frontiers | Research Topics

Advanced data-driven uncertainty optimization for planning, operation, and analysis of renewable power systems

Edited by
Lipeng Zhu, Minghao Wang, Cong Zhang, Zhenjia Lin and Ying Zhang

Published in
Frontiers in Energy Research

ISSN 1664-8714
ISBN 978-2-8325-7317-4
DOI 10.3389/978-2-8325-7317-4

Generative AI statement
Any alternative text (Alt text) provided alongside figures in the articles in this ebook has been generated by Frontiers with the support of artificial intelligence and reasonable efforts have been made to ensure accuracy, including review by the authors wherever possible. If you identify any issues, please contact us.

About Frontiers

Frontiers is more than just an open access publisher of scholarly articles: it is a pioneering approach to the world of academia, radically improving the way scholarly research is managed. The grand vision of Frontiers is a world where all people have an equal opportunity to seek, share and generate knowledge. Frontiers provides immediate and permanent online open access to all its publications, but this alone is not enough to realize our grand goals.

Frontiers journal series

The Frontiers journal series is a multi-tier and interdisciplinary set of open-access, online journals, promising a paradigm shift from the current review, selection and dissemination processes in academic publishing. All Frontiers journals are driven by researchers for researchers; therefore, they constitute a service to the scholarly community. At the same time, the *Frontiers journal series* operates on a revolutionary invention, the tiered publishing system, initially addressing specific communities of scholars, and gradually climbing up to broader public understanding, thus serving the interests of the lay society, too.

Dedication to quality

Each Frontiers article is a landmark of the highest quality, thanks to genuinely collaborative interactions between authors and review editors, who include some of the world's best academicians. Research must be certified by peers before entering a stream of knowledge that may eventually reach the public - and shape society; therefore, Frontiers only applies the most rigorous and unbiased reviews. Frontiers revolutionizes research publishing by freely delivering the most outstanding research, evaluated with no bias from both the academic and social point of view. By applying the most advanced information technologies, Frontiers is catapulting scholarly publishing into a new generation.

What are Frontiers Research Topics?

Frontiers Research Topics are very popular trademarks of the *Frontiers journals series*: they are collections of at least ten articles, all centered on a particular subject. With their unique mix of varied contributions from Original Research to Review Articles, Frontiers Research Topics unify the most influential researchers, the latest key findings and historical advances in a hot research area.

Find out more on how to host your own Frontiers Research Topic or contribute to one as an author by contacting the Frontiers editorial office: frontiersin.org/about/contact

Advanced data-driven uncertainty optimization for planning, operation, and analysis of renewable power systems

Topic editors

Lipeng Zhu — Hunan University, China

Minghao Wang — University of Macau, China

Cong Zhang — Hunan University, China

Zhenjia Lin — Hong Kong Polytechnic University, Hong Kong, SAR China

Ying Zhang — Oklahoma State University, United States

Citation

Zhu, L., Wang, M., Zhang, C., Lin, Z., Zhang, Y., eds. (2026). *Advanced data-driven uncertainty optimization for planning, operation, and analysis of renewable power systems*. Lausanne: Frontiers Media SA. doi: 10.3389/978-2-8325-7317-4

Table of contents

frontiers | Frontiers in Energy Research

TYPE Editorial
PUBLISHED 10 December 2025
DOI 10.3389/fenrg.2025.1731354

OPEN ACCESS

EDITED AND REVIEWED BY
Michael Carbajales-Dale,
Clemson University, United States

*CORRESPONDENCE
Cong Zhang,
zcong@hnu.edu.cn

RECEIVED 24 October 2025
REVISED 07 November 2025
ACCEPTED 07 November 2025
PUBLISHED 10 December 2025

CITATION
Zhang C and Liu Q (2025) Editorial: Advanced data-driven uncertainty optimization for planning, operation, and analysis of renewable power systems.
Front. Energy Res. 13:1731354.
doi: 10.3389/fenrg.2025.1731354

Editorial: Advanced data-driven uncertainty optimization for planning, operation, and analysis of renewable power systems

Cong Zhang* and Qi Liu

Hunan University, Changsha, China

KEYWORDS

data-driven optimization, renewable energy uncertainty, power system resilience, intelligent algorithms, collaborative optimization

Editorial on the Research Topic
Advanced data-driven uncertainty optimization for planning, operation, and analysis of renewable power systems

The global energy landscape is undergoing a profound transformation driven by the imperative to decarbonize power systems and integrate renewable energy at an unprecedented scale. This transition, while essential for achieving climate goals, introduces significant technical challenges stemming from the inherent uncertainty, variability, and limited inherent stability characteristics of renewable generation. The Research Topic "Advanced Data-Driven Uncertainty Optimization for Planning, Operation, and Analysis of Renewable Power Systems" addresses these critical challenges by presenting a collection of innovative studies that leverage advanced computational intelligence, robust optimization frameworks, and adaptive control paradigms to enhance the reliability, resilience, and economic efficiency of future power systems.

A predominant focus across the contributions is the development of sophisticated methodologies to quantify and manage the uncertainties associated with renewable generation and load demand. Moving beyond traditional robust optimization, several studies propose data-driven frameworks that harness historical data to construct more accurate uncertainty sets. One notable contribution introduces a polyhedral-ellipsoidal hybrid uncertainty set for industrial park microgrids, effectively reducing solution conservatism while maintaining robustness (Ru et al.). Another significant advancement employs a distributionally robust optimization approach grounded in the Wasserstein metric, demonstrating remarkable improvements in out-of-sample performance and substantial cost reductions compared to conventional methods (Li et al.). Furthermore, the integration of transmission and distribution system coordination is addressed through a bi-level planning model for distributed energy storage, which incorporates Gaussian mixture model-based chance constraints to ensure voltage security under extreme weather events (Xue et al.).

In the realm of system operation and control, the collected research presents groundbreaking strategies to mitigate the impacts of renewable intermittency on dynamic performance. The critical issue of frequency stability in low-inertia systems is tackled through a novel data-model fusion architecture that synergistically combines physics-based modeling with neural network error correction for highly

accurate frequency nadir prediction (Li et al.,). For real-time frequency regulation, an intelligent cloudbased PI controller embodies a significant leap beyond conventional control schemes, enabling adaptive parameter tuning to maintain stability under stochastic wind power fluctuations and load disturbances (Li et al.). In voltage control applications, a reinforcement learning paradigm utilizing Q-learning and voltage sensitivity analysis demonstrates superior capability in coordinating doubly-fed induction generator-based wind farms for effective voltage support during grid faults (Song et al.). Complementing these approaches, a non-linear control strategy based on logic bang-bang funnel control provides a robust solution for fault current limitation in full-scale converter-interfaced wind generators, exhibiting insensitivity to system non-linearities and external disturbances (Li et al.).

The proliferation of distributed energy resources necessitates innovative frameworks for their coordinated management and market integration. Research in this Research Topic introduces advanced game-theoretic and optimization models that balance economic objectives with technical constraints. A hierarchical bi-level optimization model, formulated within a Stackelberg game framework and incorporating soft open point technology, successfully enhances both economic efficiency and voltage security in multi-prosumer distribution systems (Lou et al.). The untapped potential of telecommunications infrastructure is harnessed through an optimal scheduling model that aggregates base station energy storage to provide voltage support services to the distribution network, based on accurate load forecasting via long short-term memory networks (Sun et al.). Additionally, the strategic integration of electric vehicles via vehicle-to-grid technology is formalized through a two-stage stochastic programming model that effectively resolves load imbalance problems in low-voltage distribution networks (Lu et al.).

Economic viability and investment efficiency are paramount for the sustainable development of renewable energy systems. Contributions in this area include a multiobjective investment portfolio optimization model based on data envelopment analysis, which identifies Pareto-optimal solutions for grid infrastructure planning under high renewable penetration (Wu et al.). For energy storage systems, a comprehensive life-cycle revenue model provides crucial insights into optimal operational strategies and economic end-of-life determination in electricity spot markets (Li et al.). The emerging concept of shared energy storage is advanced through a planning model based on the adaptive alternating direction method of multipliers, which simultaneously enhances computational efficiency, protects prosumer privacy, and improves renewable energy self-consumption (Zhao et al.).

The integration of diverse power electronic interfaces presents new stability challenges that are addressed through several pioneering studies. The dynamic interaction between grid-following and grid-forming converters during fault conditions is thoroughly analyzed, leading to the development of a hybrid fault ride-through control strategy that ensures stability through coordinated phase angle adjustment and current limitation. For power system analysis under uncertainty, a support vector regression-based interval power flow prediction method offers a computationally efficient solution for real-time assessment in distribution networks with high distributed generation penetration (Liang et al.). Addressing the fundamental need for accurate frequency response modeling, a generalized system frequency response model incorporating virtual synchronous machine technology enables comprehensive analysis of frequency dynamics in renewable-rich power systems (Song et al.). Finally, system security is further enhanced through a two-stage transient stability assessment model that integrates ensemble learning with cost-sensitive classification, significantly improving assessment accuracy for critical samples under renewable energy and load fluctuations (Lei et al.).

In synthesizing these contributions, this Research Topic demonstrates the transformative potential of data-driven optimization and intelligent control methodologies in addressing the multifaceted challenges of modern power systems. The collected research not only provides immediate solutions to pressing operational problems but also establishes foundational frameworks for the future development of resilient, efficient, and sustainable energy infrastructures. As the global energy transition accelerates, we anticipate that these advancements will inspire continued innovation and collaboration across disciplines, ultimately paving the way for a secure and decarbonized energy future.

Author contributions

CZ: Writing – review and editing. QL: Investigation, Writing – original draft.

Funding

The authors declare that no financial support was received for the research and/or publication of this article.

Conflict of interest

The author declares that the research was conducted in the absence of any commercial or financial relationships that could be construed as a potential conflict of interest.

Generative AI statement

The authors declare that no Generative AI was used in the creation of this manuscript.

Any alternative text (alt text) provided alongside figures in this article has been generated by Frontiers with the support of artificial intelligence and reasonable efforts have been made to ensure accuracy, including review by the authors wherever possible. If you identify any issues, please contact us.

Publisher's note

frontiers | Frontiers in Energy Research

TYPE Original Research
PUBLISHED 10 September 2024
DOI 10.3389/fenrg.2024.1467627

OPEN ACCESS

EDITED BY
Zhenjia Lin,
Hong Kong Polytechnic University, Hong Kong SAR, China

REVIEWED BY
Qianzhi Zhang,
Cornell University, United States
Lirong Deng,
Shanghai University of Electric Power, China
Jiehui Zheng,
South China University of Technology, China

*CORRESPONDENCE
Long Zhao,
151715352@qq.com

RECEIVED 20 July 2024
ACCEPTED 16 August 2024
PUBLISHED 10 September 2024

CITATION
Zhao L, Zhang J, Lv Q, Zhang Z, Gao P and Zhang R (2024) AADMM based shared energy storage planning for resilience improvement of renewable energy stations.
Front. Energy Res. 12:1467627.
doi: 10.3389/fenrg.2024.1467627

AADMM based shared energy storage planning for resilience improvement of renewable energy stations

Long Zhao*, Jinping Zhang, Qingquan Lv, Zhenzhen Zhang, Pengfei Gao and Ruixiao Zhang

Electric Power Research Institute, State Grid Gansu Electric Power Co., Ltd., Lanzhou, China

The exponential proliferation of renewable energy has resulted in a significant mismatch between power supply and demand, especially during extreme events. This incongruity presents challenges in efficiently harnessing renewable energy and enhancing the resilience of the power grid. To address this issue, this paper proposes shared energy storage (SES) planning based on the adaptive alternating direction method of multipliers (AADMM). The objective is to fully leverage SES, enhance the local consumption level of renewable energy, ensure power grid resilience, and reduce operational costs. First, to ensure the effective utilization of SES while minimizing initial investment and construction costs, a planning model for SES is formulated. Secondly, to maximize the benefits for multiple prosumers within the renewable energy and SES station, a profit maximization model for multiple prosumers is established. Lastly, to guarantee the privacy security of SES and multi-prosumers while optimizing computational efficiency, a distributed computing model for SES based on AADMM is developed. The results of the example show that the proposed model can not only reduce the cost of 47.96 CNY, but also increase the power self-sufficiency rate by 21.86%. In addition, compared with the traditional distributed optimization, the number of iterations of AADMM is increased by 47.05%, and the computational efficiency is increased by 54.67%. In addition, market prices have a great impact on energy trading, and the impact of market pricing on the operation of the park is not considered in our current research. In this case, our future research aims to consider how to price reasonably between prosumers and between prosumers and SES, so as to realize the stable participation of each subject in the energy market.

KEYWORDS

renewable energy, shared energy storage, planning, distributed optimization, resilience

1 Introduction

With the continuous advancement of the “dual-carbon” goals, China’s photovoltaic (PV) has experienced rapid development, with large-scale integration into the user-side becoming a future trend (He et al., 2021; Li R. et al., 2024). However, the intermittent and fluctuating characteristics of PV output poses challenges to the stable operation of traditional power grids (Peterssen et al., 2024). Generally, two-part electricity pricing is adopted in PV and energy storage integrated industrial parks. The two-part electricity price can guide prosumers to use electricity during the trough period, so as to smooth the load curve of the power system, reduce the peak load of the system, and improve the stability and

power supply capacity of the power system. Energy storage can utilize the peak-valley price difference to store energy, alleviate the impact of PV output fluctuations, and promote the local consumption of PV (Yan et al., 2023). Therefore, the two-part tariff has significant advantages in reducing power supply costs and promoting the rational application of resources.

Existing energy storage business modes are primarily divided into distributed energy storage and shared energy storage (SES) (Abdalla et al., 2023). However, the high initial investment costs and longer payback periods of distributed energy storage impose significant economic pressure on both producers and consumers. Additionally, existing distributed energy storage systems often operate in a "self-storage, self-use" mode, leading to substantial idle energy storage resources on the user-side and revealing significant issues of investment inefficiency, thus failing to achieve maximum utilization efficiency of energy storage systems (Li and Okur, 2023; Wald et al., 2023; Ji et al., 2024). In contrast, SES can complement the load demands of multiple prosumers, enhancing the efficiency of energy storage utilization and fostering a cooperative and mutually beneficial relationship between SES and prosumers (Zhu et al., 2023; Aghdam et al., 2023; Alfaverh et al., 2023). Moreover, SES can distribute the initial investment and construction costs among multiple prosumers, thereby reducing the initial investment risks for each participant. Therefore, promoting energy sharing between SES and prosumers has become the core strategy to enhance the energy efficiency and economic viability of energy parks (Ruan et al., 2024; Xie et al., 2024).

PV and energy storage integrated stations typically comprise multiple prosumers. Existing studies on SES often focus on the centralized optimization of SES and prosumers. For instance, in (Tercan et al., 2022), authors targeted communities by optimizing the capacity of distributed SES on the user-side based on energy sharing, with the objective functions of minimizing investment payback periods and line losses. In (Li L. et al., 2024), industrial parks with different electricity consumption characteristics were analyzed. It investigates energy interaction mechanisms between decentralized SES and multiple industrial users, with the optimization configuration of distributed SES aiming to maximize the overall net profit of multiple users. Additionally, a centralized optimization and scheduling model for multiple parks through electric-thermal mutual aid was proposed in (Liu Z. et al., 2023), effectively improving the overall energy utilization efficiency and operational economics by coupling different energy sources.

In the SES model, information security issues involving various prosumers pose a significant challenge. A widely adopted approach to address such challenges is the alternating direction method of multipliers (ADMM). Each prosumer can use ADMM to independently solve their respective objective utility functions. The Lagrange multipliers are updated based on the constraints, achieving interactive power balance among multiple prosumers, and SES within the PV storage park. For instance, in (Maneesha and Swarup, 2021), the ADMM algorithm was employed to solve a proposed model for the operation of multiple microgrids and obtain global interactive power quantities. Authors in (Sun et al., 2024) introduced an optimized model for combined transmission and distribution units, considering the state of charge constraints for energy storage. This model was decomposed into transmission unit combination models and distribution network economic dispatch models based on distributed optimization theory, with ADMM used for iterative solving. While these studies utilizing ADMM address privacy concerns between participants, they do not fully guarantee the solution efficiency of distributed optimization (Chen et al., 2017). In the process of solving the traditional ADMM, due to the different initial values of the penalty factor, the number of iterations is too numerous and the iteration time is too lengthy. In order to solve the above problems, some literatures propose an adaptive ADMM method to improve the solution efficiency, and the adaptive ADMM improves the distributed convergence speed by changing the penalty factor of each iteration. For example, Zhao et al. (2024) proposes a novel ADMM with adaptive penalty parameter to hedge against wind fluctuation, which further ensures improves the sensitivity of the penalty parameter. Cui et al. (2020) adopts the ADMM with adaptive penalty parameters to solve the energy cooperation between prosumers and community energy storage to improve the convergence performance. The adaptive ADMM (AADMM) promotes the convergence of variables by dynamically adjusting the penalty parameter during the iteration process, thus effectively reducing the dependence of ADMM on the initial value and avoiding the problem of slow convergence caused by improper penalty factor.

To address these issues, this paper proposes a research approach for photovoltaic and energy storage integrated park with SES planning based on the adaptive alternating direction method of multipliers (AADMM). Firstly, an SES capacity planning model is established to ensure the economic feasibility of SES configuration. Secondly, to maximize the benefits for multiple prosumers, an economic model for multiple prosumers is developed based on two-part electricity pricing. Subsequently, AADMM is applied to perform distributed optimization on the established SES capacity planning model and the economic benefit model for multiple prosumers. Finally, simulation verification is conducted in a photovoltaic storage park containing multiple prosumers.

2 Planning of SES under multiple PV stations

Independently configuring energy storage for each prosumer entails challenges such as high configuration costs, low energy storage utilization efficiency, and a reduced on-site consumption rate of new energy sources (Zhang et al., 2024). In contrast, when multiple prosumers with diverse load demands collaborate with SES, they can enhance the on-site consumption level of renewable energy, thereby reducing the operational costs of the PV station integrated park microgrid. Figure 1 illustrates the operational framework of SES in the PV integrated park studied in this paper.

The PV storage park includes N prosumers, each of which is equipped with a separate PV system, and the prosumers and SES are connected to the grid. On the premise that the PV system of the prosumer can meet its own load demand, the excess PV output can be sold to the power grid to increase its own income or stored in the SES for subsequent use; when the prosumer's PV system cannot meet its own load demand, energy can be purchased from SES or power grid (Zhang et al., 2018). SES is charged during the period when the PV output of prosumers is more and the load demand is less. Discharge in the period of low PV output, high load demand and high electricity price. Therefore, the cost of purchasing electricity from the power grid by the prosumers due to their insufficient PV power generation is reduced. At the same time,

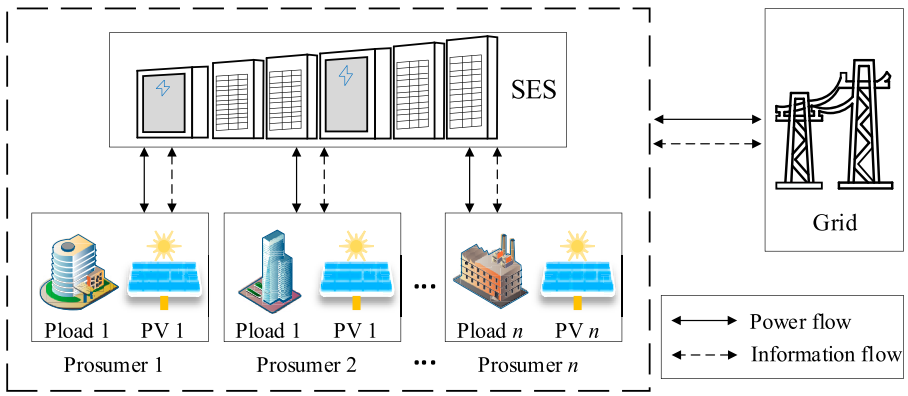

FIGURE 1
SES operating framework of multiple PV stations.

the distributed intelligent controller is embedded in the equipment of the energy system, so that the prosumers and SES can control their own energy supply and demand, perform local two-way communication and realize distributed optimization calculation.

2.1 Planning model of SES

In the context of a two-part electricity pricing mechanism, this paper establishes a SES planning model for multiple PV stations with the objective of minimizing overall costs. The approach involves three main steps: initially constructing an optimization configuration model for SES, developing a model aimed at maximizing the benefits of prosumers, and finally, formulating a collaborative SES planning model for PV stations under cooperative conditions.

The configuration of SES entails rational planning to maximize its efficiency and benefits. The objective function F_{es} for optimizing the configuration include transaction cost with the grid C_1, initial installation cost C_2, and operational cost C_3. The specific calculation formula is as follows:

$$F_{es} = \min[C_1 + C_2 + C_3] \tag{1}$$

Regarding transaction costs with the grid, a two-part electricity pricing mechanism is adopted. This mechanism includes both an energy charge based on actual electricity consumption and a demand power charge based on the user's maximum monthly demand power. SES engages in arbitrage by charging during periods of low electricity prices and discharging during periods of high prices. By shifting load demands, the user's demand is reduced, consequently lowering costs for the consumer and enhancing the benefits of SES. Therefore, the transaction cost C_1 between SES and the grid can be expressed as follows:

$$C_1 = \sum_{h\epsilon H} \lambda_h^{\mathrm{b}} q_h^{\mathrm{b}} \Delta H + \mathrm{Q}\max\left\{q_h^{\mathrm{b}}\right\} \tag{2}$$

where λ_h^{b}, Q, H, ΔH are respectively the time-of-use price, demand power price, dispatching period, and dispatching interval. q_h^{b} denotes the power bought from superior grid at time h.

The initial installation cost of SES, denoted as C_2, primarily comprises capacity and power costs (Wang YX. et al., 2024; Wang D. et al., 2024). These two components constitute the main expenses for the initial installation of the SES system and can be expressed as follows:

$$C_2 = \lambda_{\mathrm{e}} E_{\mathrm{rate}} + \lambda_{\mathrm{p}} P_{\mathrm{rate}} \tag{3}$$

where λ_{e}, λ_{p} are respectively the unit capacity and power costs, and E_{rate}, P_{rate} represent maximum rated capacity and power, respectively.

As for operation and maintenance cost of SES, it is closely associated with the charging and discharging power of the system. Variations in SES charging and discharging power directly impact the frequency and complexity of maintenance. Therefore, the operational cost of SES C_3 can be expressed as follows:

$$C_3 = \sum_{h\epsilon \mathrm{H}} C_{\mathrm{om}}\left(q_h^{\mathrm{ch}} + q_h^{\mathrm{dis}}\right)\Delta H \tag{4}$$

where C_{om} denotes unit power operation and maintenance cost coefficient of SES, and q_h^{ch}, q_h^{dis} are respectively the charge and discharge power of SES at time h.

In the process of planning SES, to ensure the stable operation of the PV station, certain inherent constraints must be satisfied (Ma et al., 2022; Jiao et al., 2021). These constraints include the following:

$$\begin{cases} 0 \le q_h^{\mathrm{ch}} \le q_{\max}^{\mathrm{ch}} \\ 0 \le q_h^{\mathrm{dis}} \le q_{\max}^{\mathrm{dis}} \\ q_h^{\mathrm{b}} \ge 0 \\ q_h^{\mathrm{ch}} q_h^{\mathrm{dis}} = 0 \\ SoC_h = (1-\rho) SoC_{h-1} + \left(\dfrac{\eta^{\mathrm{ch}} q_h^{\mathrm{ch}}}{E_{\mathrm{rate}}} - \dfrac{\eta^{\mathrm{dis}} q_h^{\mathrm{dis}}}{E_{\mathrm{rate}}}\right)\Delta H \\ E_{\mathrm{rate}} = \gamma P_{\mathrm{rate}} \\ 0.2 \le SoC_h \le 1 \\ SoC_0 = SoC_H \\ q_h^{\mathrm{ch}} + q_h^{\mathrm{b}} = q_h^{\mathrm{dis}} \end{cases} \tag{5}$$

Equation 5 represent the charging and discharging power constraints of the SES, where $q_{\max}^{\mathrm{ch}}$ and $q_{\max}^{\mathrm{dis}}$ denote the maximum charging and discharging power of SES, respectively. Equation 5 signifies the non-negativity constraint on the power absorbed by SES from the upper grid. Equation 5 represents the state of charge constraint, indicating that SES cannot simultaneously charge and discharge. Equation 5 describes the state of charge for SES, determined by the charging and discharging power at the current time and the state of charge at the previous time. Here, SoC_h and SoC_{h-1} represent the state of charge for SES in time periods h and h-1, respectively. ρ is the self-discharge coefficient, indicating the proportion of energy loss per hour, while η^{ch} and η^{dis} represent the charging and discharging efficiencies of SES, respectively. Equation 5 represents the energy rate constraint for SES, where γ is the energy rate coefficient. Equation 5 indicates that the remaining energy of SES should be between 0.2 and 1 to extend the lifespan of SES. Equation 5 states that the charging and discharging quantities of SES should remain consistent within an optimization cycle H. Equation 5 represents the power balance constraint for SES. For this problem, without loss of generality, let $(q_h^{\mathrm{ch}*}\ q_h^{\mathrm{dis}*}\ q_h^{\mathrm{b}*})$ denote the optimal solution of F_{es}.

2.2 SES planning for multiple PV prosumers sharing

For prosumer n, its operational cost, denoted as F_{pv}, encompass the transaction costs of buying and selling electricity within time period h. Utilizing the two-part pricing mechanism, the operational cost can be calculated as follows:

$$F_{\mathrm{pv}} = \min \sum_{h\in H}\left(\lambda_h^{\mathrm{b}} p_{n,h}^{\mathrm{b}} - \lambda_h^{\mathrm{s}} p_{n,h}^{\mathrm{s}}\right)\Delta H + Q\max\left\{p_{n,h}^{\mathrm{b}}\right\} \tag{6}$$

where $p_{n,h}^{\mathrm{b}}$ and $p_{n,h}^{\mathrm{s}}$ respectively represent the power bought and sold by prosumer n to the grid at time h.

In order to ensure that the prosumers can stably participate in the operation of the optical storage park, the following constraints need to be met (Zhang et al., 2022; Liu J. et al., 2023).

$$\begin{cases} p_{n,h}^{\mathrm{b}} \geq 0 \\ p_{n,h}^{\mathrm{s}} \geq 0 \\ p_{n,h}^{\mathrm{b}} p_{n,h}^{\mathrm{s}} = 0 \\ p_{n,h}^{\mathrm{load}} + p_{n,h}^{\mathrm{s}} - p_{n,h}^{\mathrm{b}} = p_{n,h}^{\mathrm{pv}} \end{cases} \tag{7}$$

where Equation 7 represent the non-negativity constraints on the power bought and sold by prosumer n within time period h. Equation 7 ensures that prosumer n cannot purchase and sell electricity at the same time. Equation 7 represents the power balance constraint, where $p_{n,h}^{\mathrm{load}}$ is the load demand of prosumer n at time h, and $p_{n,h}^{\mathrm{pv}}$ is the PV output power of prosumer n at time h. Without loss of generality, let $(p_n^{\mathrm{b}*}\ p_n^{\mathrm{s}*})$ denote the optimal solution of F_{pv}.

In order to reduce the operational cost of PV prosumers and optimize SES configuration, collaboration between prosumers and SES is essential. A planning model for minimizing the costs of PV prosumers needs to be established. Here, $p_{n,h}^{\mathrm{e}}$ represents the energy transferred to SES by prosumer n at time h, and $q_{n,h}^{\mathrm{e}}$ represents the energy received by SES from prosumer n at time h. τ_n denotes the payment made by prosumer n to SES, while π_n represents the fee accepted by SES from prosumer n. The energy-sharing configuration mechanism determines the amount of energy transferred between prosumers and SES, while the payment mechanism ensures a fair and mutually agreed upon cost-sharing for the exchanged energy. In the process of solving the SES planning for multiple PV prosumers sharing model, the energy sharing constraint shown in Equation 8 and the energy payment mechanism shown in Equation 9 need to be satisfied, as mentioned in (Wu et al., 2024).

$$p_{n,h}^{\mathrm{e}} = q_{n,h}^{\mathrm{e}} \tag{8}$$

$$\tau_n = \pi_n \tag{9}$$

where Equation 8 ensures that the energy sharing plan between prosumers and SES is consistent, that is, the energy transmitted to SES by prosumers at the same time h is the same as the energy obtained by SES from prosumers. Similarly, Equation 9 ensures that the prosumer's payment to SES is consistent with the payment obtained by SES from the prosumer at time h.

Firstly, according to Equations 1–5 and Equations 6–9, we can know the respective cost functions of SES and prosumers when they do not cooperate. Then, according to the payment mechanism of prosumers and SES shown in Equation 9, the overall objective function of SES and prosumers when they cooperate is as follows:

$$\begin{aligned} \min C = {} & C_1 + C_2 + C_3 - \sum_{n\in N}\pi_n \\ & + \sum_{h\in H}\left(\left(\lambda_h^{\mathrm{b}} p_{n,h}^{\mathrm{b}} - \lambda_h^{\mathrm{s}} p_{n,h}^{\mathrm{s}}\right)\Delta H + Q\max\left\{p_{n,h}^{\mathrm{b}}\right\}\right) + \sum_{n\in N}\tau_n \end{aligned} \tag{10}$$

SES needs to meet the following constraints when cooperating with prosumers:

$$\begin{cases} q_h^{\mathrm{ch}} + q_h^{\mathrm{b}} = \sum_{n\in N} q_{n,h}^{\mathrm{e}} + q_h^{\mathrm{dis}} \\ p_{n,h}^{\mathrm{load}} + p_{n,h}^{\mathrm{s}} = p_{n,h}^{\mathrm{pv}} + p_{n,h}^{\mathrm{b}} + p_{n,h}^{\mathrm{e}} \end{cases} \tag{11}$$

Furthermore, Equation 9 ensures that $\sum_{n\in N}\tau_n - \sum_{n\in N}\pi_n = 0$, meaning the sum of payments between PV prosumer stations and SES does not impact the overall energy costs of the entire PV stations. This implies that, in the proposed energy cooperation model, individual interests are not contradictory to societal interests. By optimizing the objective function while satisfying these constraints, the model presented in this paper aims to achieve the most effective energy cooperation strategy that minimizes costs for both SES and PV prosumers simultaneously.

3 Distributed optimization model based on AADMM

Assuming $x_n = [p_n^{\mathrm{b}}\ p_n^{\mathrm{s}}\ p_n^{\mathrm{e}}]$ represents the decision variable vector for PV prosumer n, and $y = [q_h^{\mathrm{ch}}\ q_h^{\mathrm{dis}}\ q_h^{\mathrm{b}}\ q_h^{\mathrm{e}}]$ represents the decision variable vector for SES. To avoid the exposure of private information and reduce the computational and communication burden associated with centralized optimization methods, this paper presents distributed computing to optimize the SES planning model in sharing of PV prosumers.

ADMM is a distributed algorithm used for solving large-scale convex optimization problems in statistics, machine learning, and

related fields. It offers the advantage of privacy preservation during distributed optimization scheduling. Each prosumer and SES individually solves their respective objective utility functions, achieving interactive energy balance among multiple prosumers and SES within the PV stations. Therefore, to solve the problem via ADMM, the augmented Lagrangian of the SES planning model according to Equation 10 is formulated:

$$L(x, y, \delta) = F_{es}^{ec} + F_{pv}^{ec} + \frac{1}{2}\alpha \sum_{n\in N} \left\| p_n^e - q_n^e + \frac{\delta}{\alpha} \right\|_2^2 \tag{12}$$

where let $F_{es}^{ec} = C_1 + C_2 + C_3 - \sum_{n\in N}\pi_n$ represents the SES cost of cooperation with prosumers, and $F_{pv}^{ec} = \sum_{h\in H}((\lambda_h^b P_{n,h}^b - \lambda_h^s p_{n,h}^s)\Delta H + Q\max\{p_{n,h}^b\}) + \sum_{n\in N}\tau_n$ denotes the prosumers cost of cooperation with SES. α and δ represent the penalty parameters and dual multiplier vectors associated with the coupling constraint (8).

Based on the principles of ADMM, the iterative optimization of Equation 12 is carried out (Chen et al., 2024; Zhang et al., 2021). The specific iteration equation is as follows:

$$\begin{cases} x_n(k+1) = \text{argmin} L_\alpha\left(x_n, y_g(k), \delta(k)\right) \\ y(k+1) = \text{argmin} L_\alpha\left(x_n(k+1), y, \delta(k)\right) \\ \delta_n(k+1) = \delta_n(k) + \alpha\left(p_n^e(k+1) - q_n^e(k+1)\right) \end{cases} \tag{13}$$

where $x_n(k+1) = [p_n^b(k+1), p_n^s(k+1), p_n^e(k+1)]$ represents the decision variable vector for PV prosumer n in the $(k+1)$th iteration, $y(k+1) = [q_h^{ch}(k+1), q_h^{dis}(k+1), q_h^b(k+1), q_h^e(k+1)]$ represents the decision variable vector for SES in the $(k+1)$ th iteration.

According to the definition of ADMM, by giving dual residual ε_1 and primal residual ε_2, its convergence criteria are:

$$\begin{cases} \left\| p_n^e(k+1) - p_n^e(k) \right\|_2^2 \le \varepsilon_1 \\ \left\| p_n^e(k+1) - q_n^e(k) \right\|_2^2 \le \varepsilon_2 \end{cases} \tag{14}$$

In summary, the distributed solution steps for the SES planning under multiple PV prosumers sharing model based on ADMM are as follows:

Step 1: Initialization: Set the maximum number of iterations k_{max}, set the iteration count $k = 1$, set the convergence accuracy $\varepsilon_1, \varepsilon_2$, and set the penalty factor α.

Step 2: Iterative Solution: Utilize Equation 12 to solve the SES planning model for PV prosumers. Employ Equation 13 to iteratively calculate the energy transferred from prosumers to SES, denoted as $p_{n,h}^e$, and the energy received by SES from the PV power station, denoted as $q_{n,h}^e$.

Step 3: Convergence Check: Use Equation 14 for convergence testing. If the convergence criterion is met, terminate the computation and output the results. Otherwise, set $k = k+1$, proceed to step 2 for the next round of iterative optimization, and continue until convergence.

Step 4: Output Results: x_n^* and y^* represent the optimal solutions for prosumers and SES, respectively.

In general, the ADMM algorithm is highly sensitive to the choice of penalty parameters, manifested as follows: when the penalty parameter is small, the convergence of Lagrange multipliers is slow, and when it is large, the convergence speed of decision variables is fast. This sensitivity can lead to issues such as excessive iteration counts and prolonged iteration times due to the different initial values chosen for the penalty parameter during the solution process. Therefore, this paper proposes an adaptive adjustment of the penalty parameter size to regulate the convergence speed of Lagrange multipliers and decision variables, aiming to reduce the number of iterations and convergence time in distributed computing. In summary, the adaptive update scheme based on adaptive AADMM is as follows:

$$\begin{cases} \alpha(k+1) = \begin{cases} 1/\nu\alpha(k), \|\psi(k+1)\| < \theta\|\phi(k+1)\| \\ \nu\alpha(k), \|\psi(k+1)\| > 1/\theta\|\phi(k+1)\| \\ \alpha(k), \text{otherwise} \end{cases} \\ \text{s.t.} \quad \begin{cases} \psi(k+1) = p(k+1) - q(k+1) \\ \phi(k+1) = -\alpha(k)q(k+1) - q(k) \end{cases} \end{cases} \tag{15}$$

where k represents the iteration count, while υ and θ denote the adaptive coefficients. Specifically, the adaptive coefficients $\upsilon = 3$, $\theta = 0.8$.

In summary, the flow chart of distributed optimization model based on AADMM for SES planning for multiple PV prosumers sharing is shown in Figure 2.

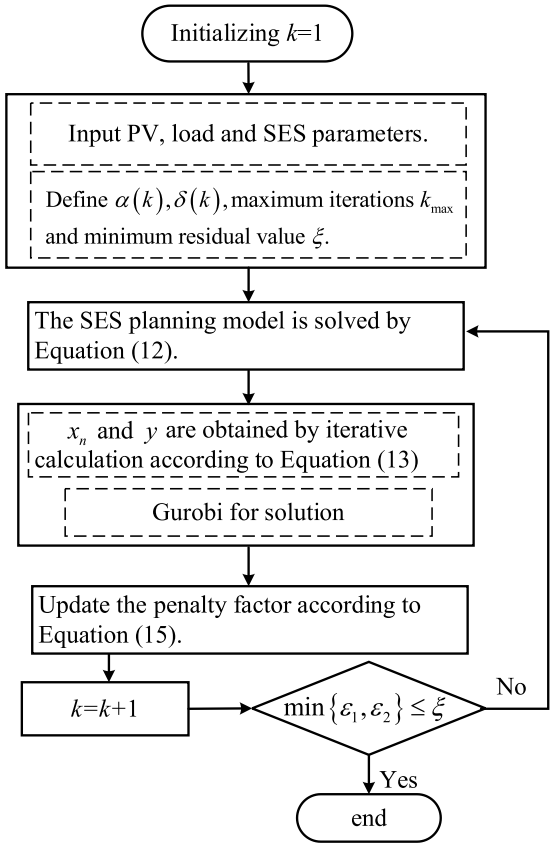

FIGURE 2
Distributed optimization model based on AADMM computational flowchart.

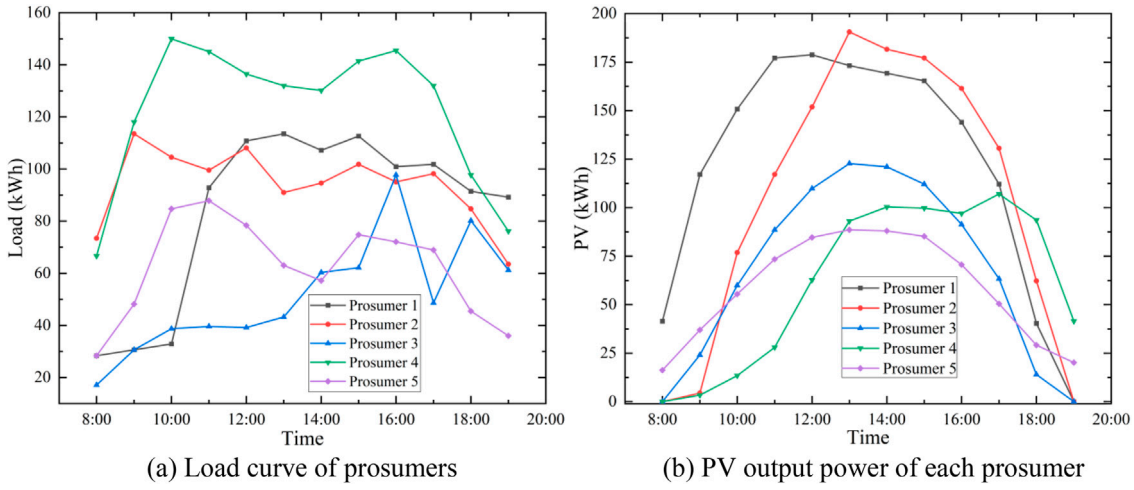

FIGURE 3
Load and PV characteristics of prosumers. **(A)** Load curve of prosumers. **(B)** PV output power of each prosumer.

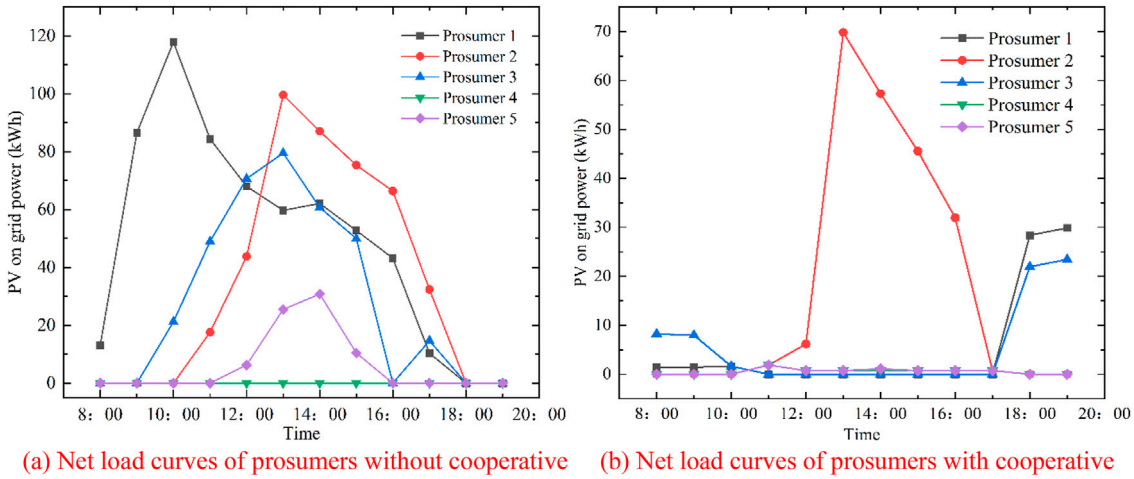

FIGURE 4
Net load curves of prosumers with and without cooperative. **(A)** Net load curves of prosumers without cooperative. **(B)** Net load curves of prosumers with cooperative.

4 Simulation and discussion

4.1 System description and parameter settings

This paper introduces data from five prosumers within a time range of 7:00–19:00, covering a period of 12 h. The load demand curve for prosumers is depicted in Figure 3A, while Figure 3B illustrates the PV output power (Liu et al., 2017). The electricity purchase price from the grid follows a two-part pricing system, where valley periods are 0:00 - 8:00 with electricity price 0.37CNY/kWh, flat periods are 12:00 - 17:00/21:00 - 24:00 with electricity 0.82CNY/kWh, and peak periods are 8:00 12:00/17:00 - 21:00 with electricity price 1.36CNY/kWh. The demand power charge is 38 CNY per month, and the on-grid power is 0.3CNY/kWh. The unit capacity cost of SES is 0.650 CNY/kWh, the unit power cost of SES is 0.245 CNY/kW, SES unit power operational cost is 0.1 CNY/kW, with charging and discharging efficiencies of 0.94 and 1.05, and an energy rate coefficient of 0.3. When using the AADMM algorithm for solution, the algorithm's iteration precision is set to 0.0001, the penalty parameter is $\alpha(1) = 0.1$, and the initial judgments are $x_n(1) = (p_n^{b^*}, p_n^{s^*}, 0)$, $y(1) = (q_h^{ch^*}, q_h^{dis^*}, q_h^{b^*}, 0)$, and $\delta = 0$.

4.2 Simulation results

When prosumers do not engage in energy cooperation with SES, the net load curve of prosumer is depicted in Figure 4A. When the PV output power of prosumers satisfies the load demand, the excess PV output is sold to the grid. However, when the PV output power is insufficient to meet the load demand, electricity needs to be

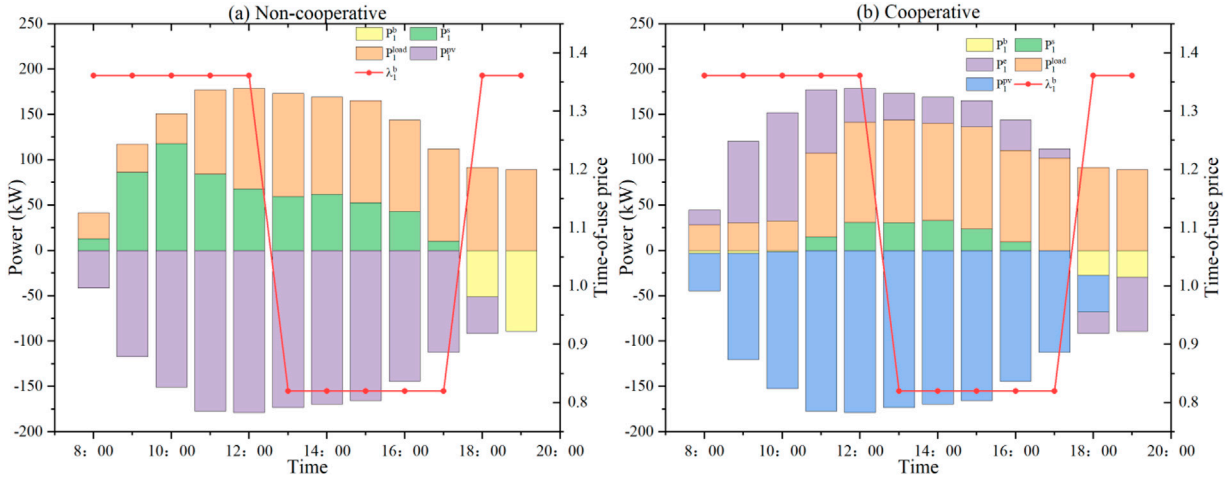

FIGURE 5
Power balance curve of user 1 with or without cooperation. **(A)** Non-corrperative. **(B)** Corrperative.

TABLE 1 Comparison of economic benefits of PV prosumers.

	Non-cooperative	Cooperative
Self-consumption (%)	71.05%	92.91%
Operational cost (CNY)	1,090.78	1,042.82

purchased from the superior grid to fulfill the demand. In this scenario, the utilization efficiency of PV is low, and it fails to achieve maximum energy efficiency and local consumption of PV power, which is easy to cause the power grid reverse heavy overload.

In the energy cooperation mode, SES stores the surplus energy from prosumers' high PV output, sells excess PV output to the grid after reaching maximum SES capacity, and shares energy with prosumers during periods of low PV output. The on-grid power of PV under energy cooperation between prosumers and SES is illustrated in Figure 4B. Through collaborative energy sharing, the PV grid power for prosumers significantly decreases. For instance, at 13:00-15:00, prosumer 2 has high PV output and low load demand, leading to the surplus PV output being sold to the grid. Overall, energy cooperation redistributes excess PV output to SES, achieving on-site consumption of PV power, and ensuring the resilience operation of the distribution network.

Table 1 presents a comparison of the economic cost for SES and prosumers under non-cooperative and cooperative modes. It is observed that SES, through peak-valley price arbitrage and on-site consumption of PV power, reduces the costs of the PV prosumers and increases the self-sufficiency. The self-sufficiency rate of prosumers increases from 71.05% to 92.91%, and the comprehensive electricity cost decreases from 1090.78 CNY to 1042.82 CNY. This implies that more PV power is locally consumed by prosumers, reducing reliance on traditional power plants, achieving "self-production and self-consumption," improving energy utilization efficiency, and reducing the overall operational cost, ultimately maximizing energy efficiency. Figure 5 shows the power balance curve of prosumer 1 with or without cooperation. As shown in Figure 5, when there is no cooperation,

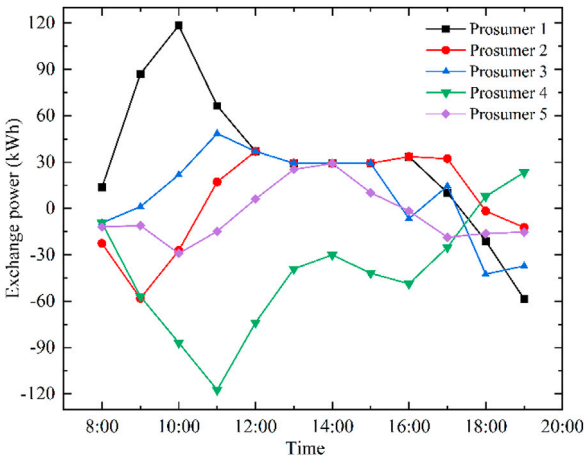

FIGURE 6
Net load curve of prosumer with SES sharing.

user 1 can only trade with the power grid, which increases the dependence on the power grid and cannot carry out peak-valley arbitrage. When user 1 cooperates with SES, the user can transfer the excess power to SES.

In the energy cooperation mode, the optimal energy-sharing curve among prosumers is illustrated in Figure 6. Prosumer 4, with low PV output and high load demand, absorbs energy to meet the demand. Other prosumers store surplus energy in SES during periods of high PV production for subsequent self-load demands. The SES planning model for the PV station optimizes SES operational scheduling strategies, taking SES state of charge as an optimization parameter to maximize economic benefits. Based on the provided data, the optimal SES capacity configuration is determined to be 333.50 kWh. Taking prosumer 2 as an example, the power optimization results are shown in Figure 7A. When its own PV output cannot meet the load demand, prosumer 2 needs to purchase electricity from the grid or SES. On the contrary,

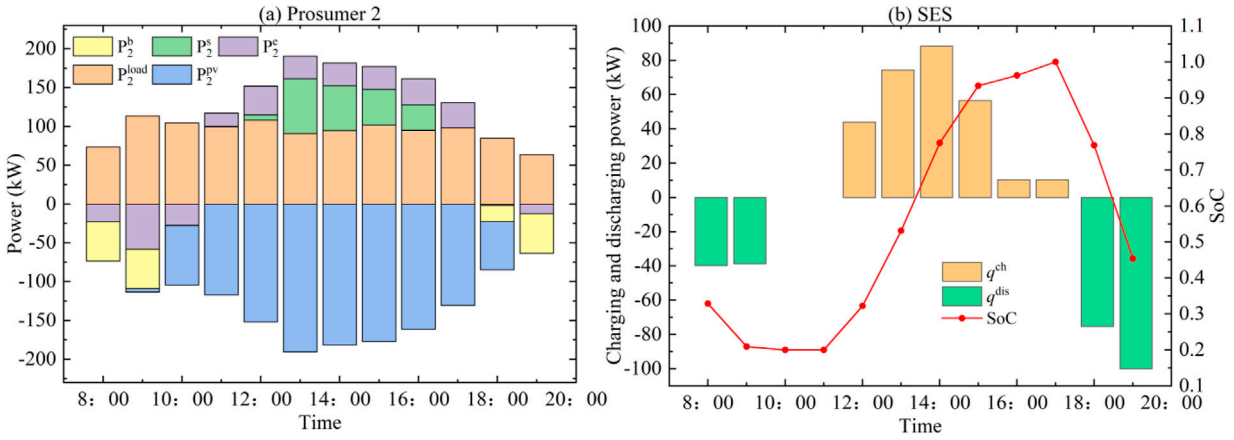

FIGURE 7
Optimization results of prosumer 2 and charging/discharing of SES under sharing. **(A)** Prosumer 2. **(B)** SES.

TABLE 2 Convergence comparison between ADMM and A-ADMM.

Initial	$\alpha = 0.1$		$\alpha = 0.3$		$\alpha = 0.5$	
	ADMM	AADMM	ADMM	AADMM	ADMM	AADMM
Iters	28	26	58	25	102	35
Times(s)	65.93	45.87	152.41	57.25	247.02	71.24

when its own PV output remains after meeting the load demand, prosumer 2 sells the remaining electricity to the grid or transmits it to SES for use by other prosumers. The SES charging and discharging power, along with the state of charge curve, are depicted in Figure 7B. The SES state of charge pattern corresponds to the time-of-use pricing periods, with discharging occurring during peak pricing hours (8:00 -9:00 and 18:00 -19:00) and coinciding with peak pricing periods. Charging occurs during standard pricing hours (13:00 -17:00) and aligns with non-peak pricing periods. The state of charge curve follows the "low charge, high discharge" characteristic typical of SES.

This paper presents AADMM to iteratively solve the SES planning for multiple PV prosumers sharing. A comparison between ADMM and AADMM algorithms is presented in Table 2. The following conclusions can be drawn from Table 2. Firstly, different penalty parameter selections require varying iteration counts and time to achieve the same algorithmic accuracy. Hence, the initial choice of the penalty parameter can impact the algorithm's iteration count and time. Secondly, for the proposed model in this paper, smaller initial penalty factors result in better convergence performance. The adaptive penalty parameter proposed in AADMM significantly reduces both the iteration count and iteration time compared to the fixed penalty parameter. Furthermore, the algorithm's improvement varies with different parameter initializations. For both ADMM and AADMM, a value of 0.3 is a preferable parameter choice. The adaptive penalty parameter in AADMM accelerates the algorithm's convergence process during the iterative stage. For instance, with a value of 0.3, the algorithm converges after 28 iterations. The convergence curves for residual errors at different time steps are illustrated in Figure 8A. At the same time, as shown in Figure 8B, taking prosumer 2 at 15: 00 as an example, as the number of iterations increases, the power transmitted by the prosumer 2 to the SES and the power received by the SES from prosumer 2 gradually tend to be consistent, reaching a global optimum. In addition, in order to show the influence of different penalty factor initial values on AADMM, this paper shows the iterative effect at α = 0.3, 0.5. As shown in Figures 9, 10, regardless of the initial value of the penalty factor, AADMM can self-adjust and ultimately achieve global optimization. This corresponds to Figure 8 and Table 2.

5 Conclusion

In order to investigate the impact of SES on prosumers, enhance prosumer self-sufficiency, reduce the operational cost, and simultaneously ensure privacy protection and expedite optimization calculations, this paper proposes a research methodology for PV prosumers with SES sharing based on AADMM. Simulation results indicate that: 1) The SES planning for multiple PV prosumers sharing model proposed in this paper can significantly reduce the cost of the optical storage park and increase the electricity self-sufficiency rate of the prosumers in the park. Compared with the optical storage park without SES, the cost is reduced by 47.96 CNY, and the electricity self-sufficiency rate is increased by 21.86%. 2) SES planning can make full use of energy storage resources, so that the prosumers in the optical storage park can reduce the cost of purchasing electricity from the grid and

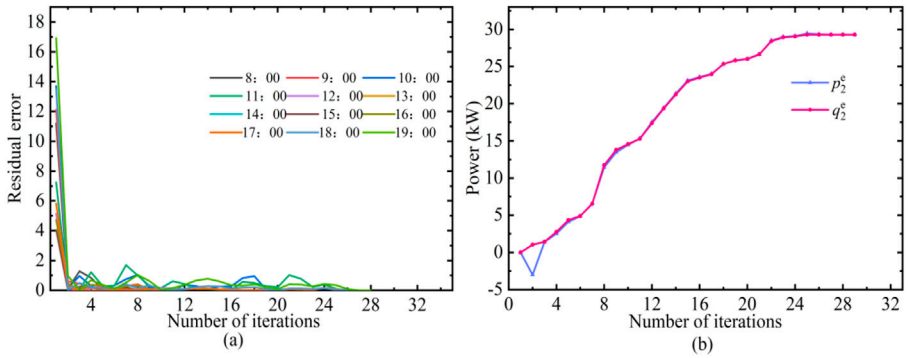

FIGURE 8
Convergence curves based on AADMM for the proposed model ($\alpha(1) = 0.1$).

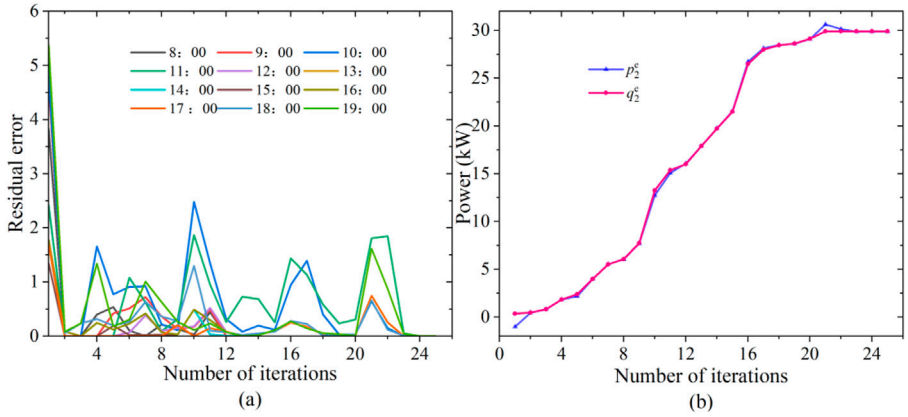

FIGURE 9
Convergence curves based on AADMM for the proposed model ($\alpha(1) = 0.3$).

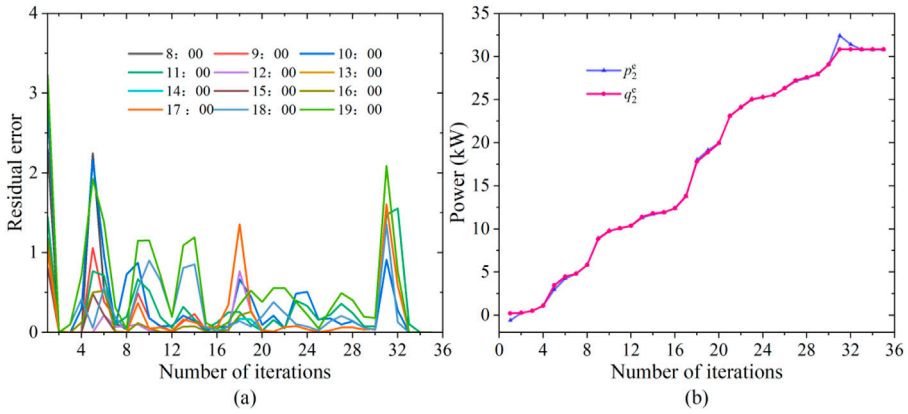

FIGURE 10
Convergence curves based on AADMM for the proposed model ($\alpha(1) = 0.5$).

improve the self-sufficiency rate of electricity. 3) The distributed optimization algorithm of AADMM is used to solve the SES planning for multiple PV prosumers sharing model. Compared with ADMM, the number of iterations and computational efficiency are increased by 47.05% and 54.67% on average. This method improves the convergence speed of the algorithm while ensuring the stability of the algorithm, and can effectively protect the privacy of each prosumer and SES.

In order to increase the electricity self-sufficiency rate of prosumers and reduce the operating cost of the optical storage park, this paper proposes the SES planning for multiple PV prosumers sharing model based AADMM. However, P2P trading can be carried out between prosumers to achieve energy sharing in the park and promote the local consumption of PV. Therefore, the P2P trading between prosumers will be the research direction of the coordinated operation of prosumers in the park in the future. In addition, market prices have a great impact on energy trading, and the impact of market pricing on the operation of the park is not considered in our current research. In this case, our future research aims to consider how to price reasonably between prosumers and between prosumers and SES, so as to realize the stable participation of each subject in the energy market.

Data availability statement

The raw data supporting the conclusion of this article will be made available by the authors, without undue reservation.

Author contributions

LZ: Conceptualization, Investigation, Writing–original draft. JZ: Conceptualization, Investigation, Validation, Supervision, Writing–review and editing. QL: Investigation, Supervision, Writing–review and editing. ZZ: Investigation, Supervision, Writing–review and editing. PG: Investigation, Supervision, Writing–review and editing. RZ: Conceptualization, Investigation, Supervision, Writing–review and editing.

Funding

The author(s) declare that financial support was received for the research, authorship, and/or publication of this article. This work was supported by State Grid Gansu Electric Power Company Science and Technology Project on Coordinated and Optimized Configuration Method of New Energy and Energy Storage for Large-scale Wind and Photovoltaic Power Transmission System Oriented to System Resilience Improvement (No. 52272223000U).

Conflict of interest

Authors LZ, JZ, QL, ZZ, PG, and RZ were employed by State Grid Gansu Electric Power Co., Ltd.

The authors declare that this study received funding from State Grid Gansu Electric Power Company. The funder had the following involvement in the study: the funders provided the necessary data in the paper, including PV and load data, and supervised the writing of the article.

Publisher's note

References

Abdalla, A. A., El Moursi, M. S., El-Fouly, T. H. M., and Hosani, K. H. A. (2023). A novel adaptive power smoothing approach for PV power plant with hybrid energy storage system. *IEEE Trans. Sustain. Energy* 14 (3), 1457–1473. doi:10.1109/tste.2023.3236634

Aghdam, F. H., Mudiyanselage, M. W., Mohammadi-Ivatloo, B., and Marzband, M. (2023). Optimal scheduling of multi-energy type virtual energy storage system in reconfigurable distribution networks for congestion management. *Appl. Energy* 333, 120569. doi:10.1016/j.apenergy.2022.120569

Alfaverh, F., Denai, M., and Sun, Y. (2023). A dynamic peer-to-peer electricity market model for a community microgrid with price-based demand response. *IEEE Trans. Smart Grid* 14 (5), 3976–3991. doi:10.1109/tsg.2023.3246083

Chen, J., Zheng, J., Wu, P., Zhang, L., and Wu, Q. (2017). Dynamic particle swarm optimizer with escaping prey for solving constrained non-convex and piecewise optimization problems. *Expert Syst. Appl.* 86, 208–223. doi:10.1016/j.eswa.2017.05.047

Chen, P., Ye, Y., Wang, H., Bu, S., Tang, Y., and Strbac, G. (2024). Holistic coordination of transactive energy and carbon emission right trading for heterogenous networked multi-energy microgrids: a fully distributed adaptive consensus ADMM approach. *Sustain. Energy Technol. Assessments* 64, 103729. doi:10.1016/j.seta.2024.103729

Cui, S., Wang, Y. W., Shi, Y., and Xiao, J. W. (2020). Community energy cooperation with the presence of cheating behaviors. *IEEE Trans. Smart Grid* 12 (1), 561–573. doi:10.1109/tsg.2020.3022792

He, W., King, M., Luo, X., Dooner, M., and Wang, J. (2021). Technologies and economics of electric energy storages in power systems: review and perspective. *Adv. Appl. Energy* 4, 100060. doi:10.1016/j.adapen.2021.100060

Ji, Z., Li, W., and Niu, D. (2024). Optimal investment decision of agrivoltaic coupling energy storage project based on distributed linguistic trust and hybrid evaluation method. *Appl. Energy* 353, 122139. doi:10.1016/j.apenergy.2023.122139

Jiao, P. H., Chen, J. J., Cai, X., Wang, L., Zhao, Y., Zhang, X., et al. (2021). Joint active and reactive for allocation of renewable energy and energy storage under uncertain coupling. *Appl. Energy* 302, 117582. doi:10.1016/j.apenergy.2021.117582

Li, L., Peng, K., Yang, X., and Liu, K. (2024b). Coordinated design of multi-stakeholder community energy systems and shared energy storage under uncertain supply and demand: a game theoretical approach. *Sustain. Cities Soc.* 100, 105028. doi:10.1016/j.scs.2023.105028

Li, N., and Okur, Ö. (2023). Economic analysis of energy communities: investment options and cost allocation. *Appl. Energy* 336, 120706. doi:10.1016/j.apenergy.2023.120706

Li, R., Hu, Y., Wang, X., Zhang, B., and Chen, H. (2024a). Estimating the impacts of a new power system on electricity prices under dual carbon targets. *J. Clean. Prod.* 438, 140583. doi:10.1016/j.jclepro.2024.140583

Liu, J., Chen, J., Yan, G., Chen, W., and Xu, B. (2023b). Clustering and dynamic recognition based auto-reservoir neural network: a wait-and-see approach for short-term park power load forecasting. *Iscience* 26 (8), 107456. doi:10.1016/j.isci.2023.107456

Liu, N., Yu, X., Wang, C., and Wang, J. (2017). Energy sharing management for microgrids with PV prosumers: a Stackelberg game approach. *IEEE Trans. Industrial Inf.* 13 (3), 1088–1098. doi:10.1109/tii.2017.2654302

Liu, Z., Chen, Y., Yang, X., and Yan, J. (2023a). Power to heat: opportunity of flexibility services provided by building energy systems. *Adv. Appl. Energy* 11, 100149. doi:10.1016/j.adapen.2023.100149

Ma, M., Huang, H., Song, X., Peña-Mora, F., Zhang, Z., and Chen, J. (2022). Optimal sizing and operations of shared energy storage systems in distribution networks: a bi-level programming approach. *Appl. Energy* 307, 118170. doi:10.1016/j.apenergy.2021.118170

Maneesha, A., and Swarup, K. S. (2021). A survey on applications of alternating direction method of multipliers in smart power grids. *Renew. Sustain. Energy Rev.* 152, 111687. doi:10.1016/j.rser.2021.111687

Peterssen, F., Schlemminger, M., Lohr, C., Niepelt, R., Hanke-Rauschenbach, R., and Brendel, R. (2024). Impact of forecasting on energy system optimization. *Adv. Appl. Energy* 15, 100181. doi:10.1016/j.adapen.2024.100181

Ruan, G., Qiu, D., Sivaranjani, S., Awad, A. S., and Strbac, G. (2024). Data-driven energy management of virtual power plants: a review. *Adv. Appl. Energy* 14, 100170. doi:10.1016/j.adapen.2024.100170

Sun, B., Jing, R., Zeng, Y., Wei, W., Jin, X., and Huang, B. (2024). Three-side coordinated dispatching method for intelligent distribution network considering dynamic capacity division of shared energy storage system. *J. Energy Storage* 81, 110406. doi:10.1016/j.est.2023.110406

Tercan, S. M., Demirci, A., Gokalp, E., and Cali, U. (2022). Maximizing self-consumption rates and power quality towards two-stage evaluation for solar energy and shared energy storage empowered microgrids. *J. Energy Storage* 51, 104561. doi:10.1016/j.est.2022.104561

Wald, D., Johnson, K., King, J., Comden, J., Bay, C. J., Chintala, R., et al. (2023). Shifting demand: reduction in necessary storage capacity through tracking of renewable energy generation. *Adv. Appl. Energy* 10, 100131. doi:10.1016/j.adapen.2023.100131

Wang, D., Zhang, C., Li, J., Zhu, L., Zhou, B., Zhou, Q., et al. (2024b). A novel interval power flow method based on hybrid box-ellipsoid uncertain sets. *IEEE Trans. Power Syst.* 39, 6111–6114. doi:10.1109/tpwrs.2024.3391921

Wang, Y. X., Chen, J. J., Zhao, Y. L., and Xu, B. (2024a). Incorporate robust optimization and demand defense for optimal planning of shared rental energy storage in multi-user industrial park. *Energy* 301, 131721. doi:10.1016/j.energy.2024.131721

Wu, Y., Wang, C., and Wang, Y. (2024). Cooperative game optimization scheduling of multi-region integrated energy system based on ADMM algorithm. *Energy* 302, 131728. doi:10.1016/j.energy.2024.131728

Xie, H., Ahmad, T., Zhang, D., Goh, H. H., and Wu, T. (2024). Community-based virtual power plants' technology and circular economy models in the energy sector: a Techno-economy study. *Renew. Sustain. Energy Rev.* 192, 114189. doi:10.1016/j.rser.2023.114189

Yan, G. J., Chen, J. J., Liu, J. Y., Chen, W., and Xu, B. (2023). Random clustering and dynamic recognition-based operation strategy for energy storage system in industrial park. *J. Energy Storage* 73, 109192. doi:10.1016/j.est.2023.109192

Zhang, C., Liu, Q., Zhou, B., Chung, C. Y., Li, J., Zhu, L., et al. (2022). A central limit theorem-based method for DC and AC power flow analysis under interval uncertainty of renewable power generation. *IEEE Trans. Sustain. Energy* 14 (1), 563–575. doi:10.1109/tste.2022.3220567

Zhang, Q., Dehghanpour, K., and Wang, Z. (2018). Distributed CVR in unbalanced distribution systems with PV penetration. *IEEE Trans. Smart Grid* 10 (5), 5308–5319. doi:10.1109/tsg.2018.2880419

Zhang, Q., Guo, Y., Wang, Z., and Bu, F. (2021). Distributed optimal conservation voltage reduction in integrated primary-secondary distribution systems. *IEEE Trans. Smart Grid* 12 (5), 3889–3900. doi:10.1109/tsg.2021.3088010

Zhang, Y. Q., Chen, J. J., Wang, Y. X., and Feng, L. (2024). Enhancing resilience of agricultural microgrid through electricity–heat–water based multi-energy hub considering irradiation intensity uncertainty. *Renew. Energy* 220, 119739. doi:10.1016/j.renene.2023.119739

Zhao, B., Qian, T., Li, W., Xin, Y., Zhao, W., Lin, Z., et al. (2024). Fast distributed co-optimization of electricity and natural gas systems hedging against wind fluctuation and uncertainty. *Energy* 298, 131420. doi:10.1016/j.energy.2024.131420

Zhu, J., Li, S., Borghetti, A., Lan, J., and Guo, T. (2023). Review of demand-side energy sharing and collective self-consumption schemes in future power systems. *iEnergy* 2 (2), 119–132. doi:10.23919/ien.2023.0006

frontiers | Frontiers in Energy Research

TYPE Original Research
PUBLISHED 13 September 2024
DOI 10.3389/fenrg.2024.1477645

OPEN ACCESS

EDITED BY
Lipeng Zhu,
Hunan University, China

REVIEWED BY
Bin Zhou,
Hunan University, China
Shiwei Xia,
North China Electric Power University, China

*CORRESPONDENCE
Haifeng Zhang,
292281350@qq.com

RECEIVED 08 August 2024
ACCEPTED 05 September 2024
PUBLISHED 13 September 2024

CITATION
Li D, Lv X, Zhang H, Meng X, Xu Z, Chen C and Liu T (2024) Cloud model-based intelligent controller for load frequency control of power grid with large-scale wind power integration. *Front. Energy Res.* 12:1477645. doi: 10.3389/fenrg.2024.1477645

Cloud model-based intelligent controller for load frequency control of power grid with large-scale wind power integration

Dexin Li, Xiangyu Lv, Haifeng Zhang*, Xiangdong Meng, Zhenjun Xu, Chao Chen and Taiming Liu

Electric Power Research Institute, State Grid Jilin Electric Power Co., Ltd., Changchun, China

The intermittent and fluctuating nature of active power output from wind power significantly affects the Load Frequency Control (LFC) in a power grid based on active power balance. To address this issue, this paper proposes a cloud-based intelligent PI controller designed to enhance the performance of LFC in smart grids with large-scale wind power integration. By using the error and the rate of change of error as the antecedent inputs of the cloud model-based controller and the tuning values of P and I as the consequent outputs of the cloud model, adaptive online tuning of the PI parameters is achieved. Based on the control rules of LFC in interconnected power grids and considering the uncertainty of wind power's active power output, the membership cloud parameters are designed, which effectively solves the problems of poor parameter robustness in traditional PI control and significant human influence on membership degrees in Fuzzy PI control. A simulation model of a dual-area interconnected power grid with wind power for LFC was built using Matlab/Simulink. Two typical disturbances, namely random fluctuations in wind power and sudden increases/decreases in load, were simulated. The simulation results demonstrate that the cloud model-based intelligent PI controller designed in this paper can effectively track the frequency variations caused by random fluctuations in wind power and exhibits strong robustness.

KEYWORDS

wind power, power grid, cloud model, load frequency control (LFC), dynamic performance

1 Introduction

In an interconnected power grid, load frequency control is an important technical means to ensure the safe, reliable, stable, and economical operation of the system (Bevrani H, 2009). With the continuous improvement in society's requirements for power quality, supply security, and reliability, the expansion of interconnected power grid scale, and the rapid development of new energy sources, traditional load frequency control methods face serious challenges and struggle to meet the performance requirements of LFC (Liang Y et al., 2024). Among these challenges, large-scale wind power, as the fastest-growing renewable energy source, has already demonstrated significant social and environmental benefits (Ratnam K et al., 2020). However, unlike conventional forms of power generation, the

primary energy source for wind power (i.e., wind energy) is difficult to predict and control accurately. Therefore, integrating large-scale wind power into the grid imposes higher demands on load frequency control in interconnected power grids (Liu et al., 2017; Liu et al., 2024).

Traditional LFC employs classical PI/PID control (Tan, 2010). However, with the integration of high-penetration renewable energy sources, the system's uncertainties are further increased. The PI/PID controllers based on linear control theory struggle to meet the control requirements of the new type of interconnected power system that exhibits strong nonlinear characteristics. Novel LFC control strategies have been continuously proposed, such as robust control methods based on linear matrix inequality design (Rerkpreedapong et al., 2003; Ojaghi and Rahmani, 2017), disturbance-insensitive sliding mode control methods (Wei M et al., 2021; Huynh et al., 2024; Tummala et al., 2018)), model predictive control methods with rolling optimization strategies (Qi X et al., 2022; Jia Y et al., 2019; Jun Zhou et al., 2024; Liu et al., 2016), and AI-based control methods (Zhang Y et al., 2022; Cam and Kocaarslan, 2005; Yan and Xu, 2020; Wadi et al., 2024). These control methods partially compensate for the shortcomings of traditional FLC, but they rely on precise mathematical models, have high control costs, and pose difficulties in design and implementation.

The cloud model, based on statistical and fuzzy mathematics, provides a unified representation of the fuzziness and randomness between linguistic values of uncertainty and precise numerical values. It achieves a natural transformation of uncertainty between qualitative concepts and their quantitative counterparts (Li D et al., 2009; Wang G et al., 2014). Currently, cloud model theory has been successfully applied in intelligent control and performance evaluation of large-scale systems. Based on a thorough analysis of LFC control characteristics in an interconnected power grid with high penetration wind power, this study proposes an intelligent PI control strategy using cloud model. The main contributions of this paper are as follows:

1) The antecedent membership cloud functions were separately constructed for Area Control Error (ACE) and its rate of change, as well as the consequent membership cloud functions for the proportional parameter P and integral parameter I of the PI controller. Based on this, a cloud-based intelligent controller for LFC was designed. Compared to traditional fuzzy control, the proposed cloud-based LFC intelligent controller in this paper achieves faster frequency control speed and higher efficiency.
2) A simulation model for LFC in a two-area interconnected power grid with high penetration wind power was built in the Matlab/Simulink environment. Two typical power disturbance events, namely random wind power fluctuation and sudden load change, were simulated. The simulation results were compared and analyzed against the LFC control effect based on Fuzzy PI control. This validation confirms the effectiveness and robustness of the intelligent PI controller based on the cloud model.

The remainder of this paper is organized as follows: Section 2 establishes the LFC model for interconnected power grid with wind power. Then, the cloud model-based intelligent PI controller for LFC is developed in Section 3. Section 4 tests the effectiveness of the proposed intelligent PI controller. The conclusions are given in Section 5.

2 Load frequency control model for interconnected power grid with wind power

The power system achieves tracking of generation power to load power by sensing frequency variations, thereby maintaining power balance and frequency stability in the grid. After the large-scale integration of wind power, the fluctuation in its active power output has, to some extent, affected the power balance state of the grid and increased the difficulty of active-power frequency control in the system.

Although multi-area power systems are strongly coupled and time-varying, LFC was designed for small fluctuations and perturbations. At this point, the system operates near a stable point, allowing for the establishment of its model using low-order linear transfer functions (Bevrani H, 2009).

In this study, the LFC model of a power system incorporating wind power is established based on conventional thermal power units, as shown in Figure 1. Before conducting a detailed derivation, the following explanations are provided for this model.

1) The objective of LFC (Load Frequency Control) in interconnected power systems is to maintain the system frequency and the power exchange between regions within a normal range. Based on this objective, the frequency deviation $\Delta f(t)$ and the power deviation on the tie line $\Delta P_{\text{tie},i}(t)$ are usually linearly combined to form a variable called Area Control Error $ACE(t)$, which serves as the control signal in the LFC problem. The $ACE(t)$ being zero is considered a criterion for measuring the stability achieved in the control area. Therefore, the ACE for the ith area, $ACE_i(t)$, can be defined as Equation 1:

$$\boldsymbol{ACE_i(t) = \Delta P_{tie,i}(t) + \beta_i \Delta f_i(t)} \tag{1}$$

where, β_i is the frequency deviation coefficient. $\Delta f_i(t)$ and $\Delta P_{tie,i}(t)$ represent the frequency deviation and tie line power deviation for the ith area, respectively.

2) The LFC system of conventional thermal power units consists of components such as a governor, non-reheat steam turbine, generator, load, tie line, and controller. Each component in the different areas is represented by an equivalent multi-machine dynamic response using a single-machine model. When there is a change in the load or an external disturbance in a specific area, the controller receives control input signals and issues control commands to adjust the position of the governor valve. This regulates the steam flow into the turbine, thereby changing the turbine's output power, affecting the generator's input power, and adjusting the active power output of the generator to achieve the control objective.
3) After meeting the set load demand in each area, the excess electricity generated by the wind power units connected to

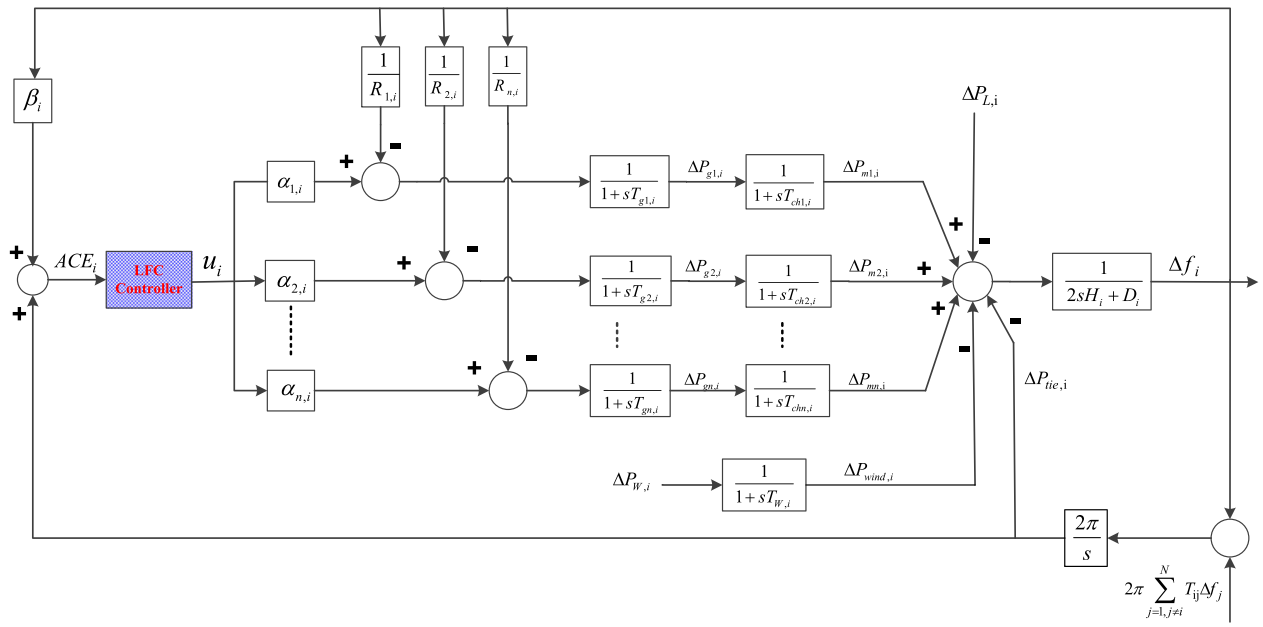

FIGURE 1
LFC model for the *i*th area in multi-area power grid with wind power.

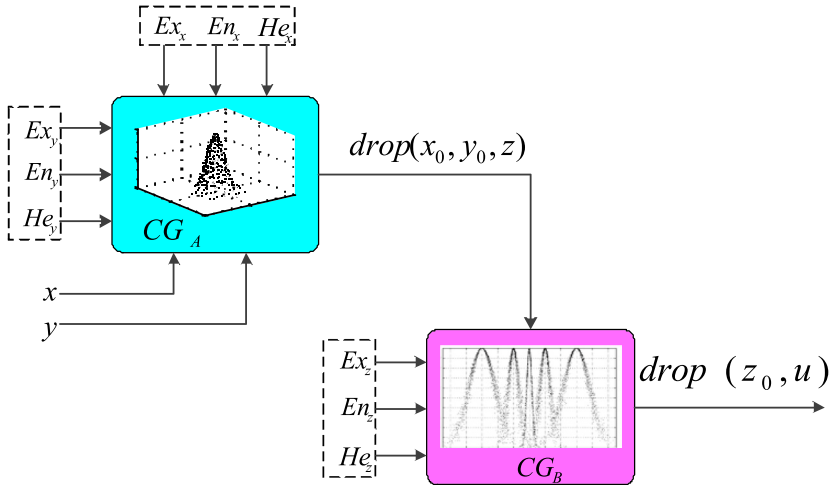

FIGURE 2
Double condition cloud generator.

each area is considered an energy-bounded external disturbance signal. In order to suppress the randomness of this disturbance, a distributed structure is formed by sharing and coordinating control information among partially interconnected controllers based on sparse optimization results. The system suppresses load variations and random disturbances by actively adjusting the control loop of the thermal power units.

The model described in Figure 1 can be represented by a set of differential equation, as shown in Equation 2.

$$\begin{cases} \Delta\dot{\boldsymbol{f}}_{\boldsymbol{i}}(\boldsymbol{t}) = \frac{\mathbf{1}}{\mathbf{2}\boldsymbol{H}_{\boldsymbol{is}}}\left(-\boldsymbol{D}_{\boldsymbol{i}}\Delta\boldsymbol{f}_{\boldsymbol{i}}(\boldsymbol{t}) + \sum_{\boldsymbol{k}=\mathbf{1}}^{\boldsymbol{n}}\Delta\boldsymbol{P}_{\boldsymbol{mk,i}}(\boldsymbol{t}) - \Delta\boldsymbol{P}_{\boldsymbol{tie,i}}(\boldsymbol{t}) - \Delta\boldsymbol{P}_{\boldsymbol{L,i}}(\boldsymbol{t}) - \Delta\boldsymbol{P}_{\boldsymbol{wind,i}}(\boldsymbol{t})\right) \\ \Delta\dot{\boldsymbol{P}}_{\boldsymbol{mk,i}}(\boldsymbol{t}) = \frac{\mathbf{1}}{\boldsymbol{T}_{\boldsymbol{chk,i}}}\left(-\Delta P_{mk,i}(t) + \Delta P_{gk,i}(t)\right) \\ \Delta\dot{\boldsymbol{P}}_{\boldsymbol{gk,i}}(\boldsymbol{t}) = \frac{\mathbf{1}}{\boldsymbol{T}_{\boldsymbol{gk,i}}}\left(-\frac{1}{R_{k,i}}\Delta f_i(t) - \Delta p_{gk,i}(t) + \alpha_{k,i}u_i(t)\right) \\ \Delta\dot{\boldsymbol{P}}_{\boldsymbol{wind,i}}(\boldsymbol{t}) = \frac{\mathbf{1}}{\boldsymbol{T}_{\boldsymbol{W,i}}}\left(-\Delta P_{wind,i(t)} + \Delta P_{w,i}(t)\right) \\ \Delta\dot{\boldsymbol{P}}_{\boldsymbol{tie,i}}(\boldsymbol{t}) = \mathbf{2}\boldsymbol{\pi}\sum_{\boldsymbol{j}=\mathbf{1},\boldsymbol{j}\neq\boldsymbol{i}}^{\boldsymbol{N}}\boldsymbol{T}_{\boldsymbol{ij}}\left(\Delta\boldsymbol{f}_{\boldsymbol{i}}(\boldsymbol{t}) - \Delta\boldsymbol{f}_{\boldsymbol{j}}(\boldsymbol{t})\right) \end{cases} \quad (2)$$

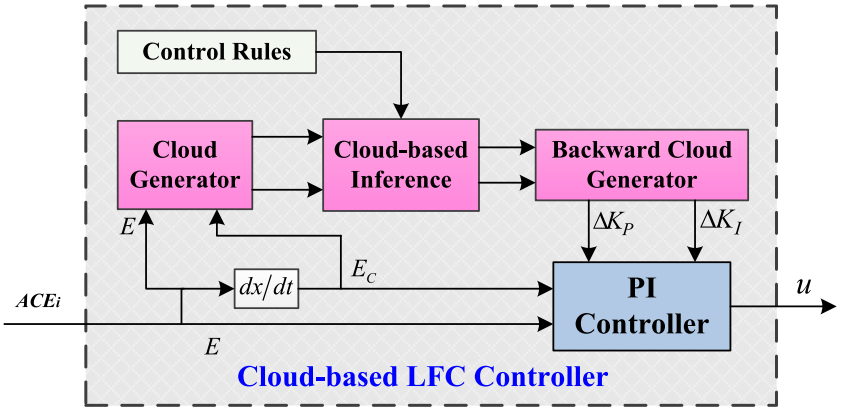

FIGURE 3
The structure of cloud PI controller for LFC.

TABLE 1 Cloud model inference rules table.

Cloud inference		*E*				
		NB	NS	ZE	PS	PB
Ec	NB	NB	NS	ZE	PS	PB
	NS	NS	NS	ZE	PS	PS
	ZE	ZE	ZE	ZE	ZE	ZE
	PS	PS	PS	ZE	NS	NS
	PB	PB	PS	ZE	NS	NB

where, H_{is} represents equivalent inertia of area *i*; $T_{chk,i}$ represents turbine time constant; $T_{gk,i}$ represents governor time constant; $T_{W,i}$ represents wind generator time constant; $\alpha_{k,i}$ represents generator ramp rate factor; $\Delta P_{mk,i}$ represents the change in mechanical power of the *k*th generators in the *i*th area; $\Delta P_{L,i}$ represents the fluctuation in active load power; $\Delta P_{wind,i}$ represents wind power deviation in the *i*th area; $\Delta P_{W,i}$ represents the fluctuation of wind power; $\Delta P_{gk,i}$ represents regulating valve position deviation; u_i represents the control variable, which refers to the output of the LFC controller. As shown in Equation 3, the output of the LFC controller can be represented as a function of *ACE* (Wood AJ et al., 1996):

$$\boldsymbol{u_i(t) = f_i(ACE_i(t))} \quad (3)$$

3 Cloud model-based intelligent PI controller for LFC

3.1 Cloud model theory

Cloud model, based on probability theory and fuzzy mathematics, uses natural language to describe the bidirectional conversion of quantitative and qualitative information, reflecting the correlation between randomness and fuzziness (Kavousi-Fard A et al., 2016; K. Zhou et al., 2024).

Definition: Let *E* be a quantitative domain on precise numerical values, and *F* be a qualitative concept on the quantitative domain *E*. If a quantitative value x is a random realization of the qualitative concept *F*, and *x* has a stable tendency with a certainty degree $\mu(x) \in [0, 1]$, where μ: $E \rightarrow [0, 1]$, $\forall x \in E$, $x \rightarrow \mu(x)$, the distribution of *x* on the domain *E* is called a cloud, and each *x* is considered a cloud droplet.

The cloud model uses three numerical characteristics to reflect the overall properties of a concept. These three numerical characteristics (Li D et al., 2009) are the Expected Value (*Ex*), Entropy (*En*), and Hyper Entropy (*He*).

The solution of the three numerical variables, i.e., the formation of the cloud model, requires the collection of a certain number of cloud droplet samples. By collecting multiple samples, the more

TABLE 2 Membership of the cloud characteristic parameters.

Qualitative concepts	*E*			*EC*			$\Delta KP\&\Delta K_I$		
	Ex	*En*	*He*	*Ex*	*En*	*He*	*Ex*	*En*	*He*
NB	−0.1	0.025	0.003	−2.45	0.5	0.005	−0.05	0.005/3	0.0002
NS	−0.04	0.02	0.002	−1.2	0.5	0.005	−0.002	0.002/3	0.00015
ZE	0	0.01	0.001	0	0.5	0.005	0	0.00033	0.00004
PS	0.04	0.02	0.002	1.2	0.5	0.005	0.002	0.002/3	0.00015
PB	0.1	0.025	0.003	2.45	0.5	0.005	0.05	0.005/3	0.0002

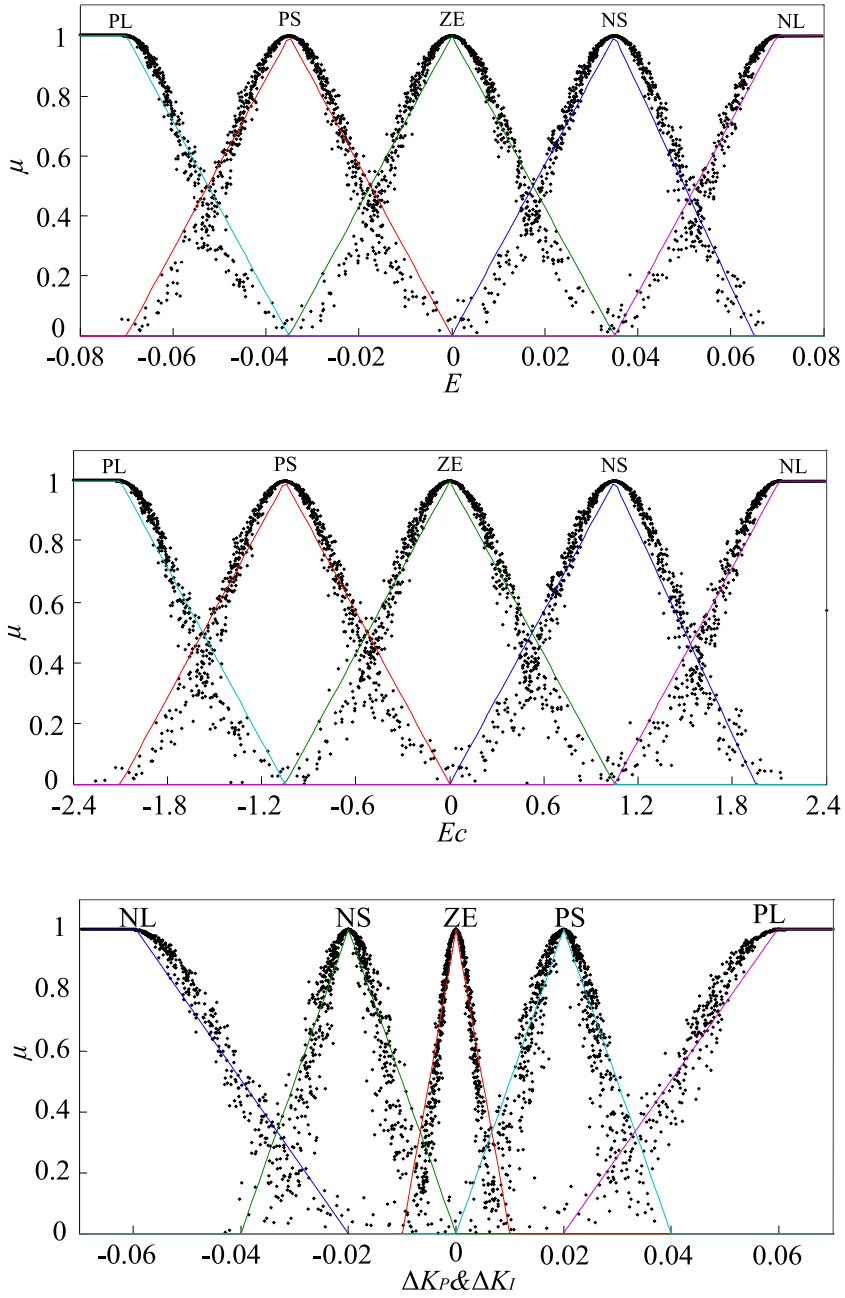

FIGURE 4
The Membership cloud diagram.

samples collected, the more accurate the obtained cloud model will be, and quantitative input preprocessing should be performed. *Ex*, *En*, and *He* can be obtained through statistical analysis of the research object's sample data using Equation 4.

$$\begin{cases} E_x = \bar{x} = \frac{1}{n}\sum_{i=1}^{n} x_i \\ E_n = \sqrt{\frac{\pi}{2}}\ \frac{1}{n}\sum_{i=1}^{n} |x_i - E_x| \\ H_e = \sqrt{s^2 - E_n^2} = \sqrt{\frac{1}{n-1}\sum_{i=1}^{n} (x_i - \bar{x}) - E_n^2} \end{cases} \tag{4}$$

This process of obtaining a cloud model composed of three numerical variables essentially refers to the statistical analysis of the sample data.

The cloud model has similarities with fuzzy mathematics, but it also has its unique aspects, particularly in how it handles uncertainty. The cloud model was proposed based on probability theory and fuzzy mathematics, aiming to address the uncertain transition between qualitative concepts and quantitative descriptions. Compared to fuzzy mathematics, the cloud model not only considers fuzziness but also incorporates randomness, providing a more comprehensive approach to uncertainty. The

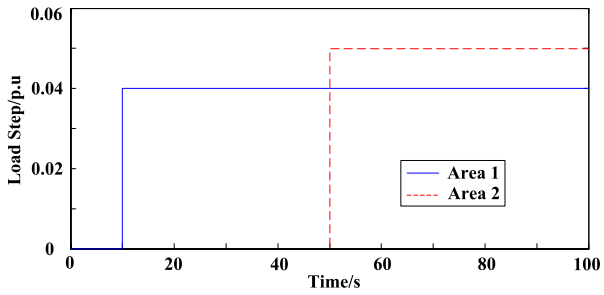

FIGURE 5
Load disturbance in Area 1 and Area 2.

cloud model describes the quantitative representation of qualitative concepts through the numerical characteristics of clouds, while fuzzy mathematics primarily deals with fuzziness, which pertains to intermediate transitions between categories of things. The successful application of the cloud model demonstrates its unique advantages in decision analysis, intelligent control, and other areas of complex systems, as it better simulates the uncertainty and fuzziness inherent in human thinking.

3.2 Rule inference of cloud model

The key to cloud model application lies in the generation of cloud droplets, and the algorithm for generating cloud droplets is called a cloud generator (CG). The cloud generator includes a forward cloud generator and a backward cloud generator (Wang G et al., 2014).

The forward cloud generator is responsible for generating cloud droplets (*drop* (x, μ)) based on the numerical characteristics of the cloud (*Ex, En, He*), which represents a mapping from qualitative to quantitative. On the other hand, the backward cloud generator is a conversion model that transforms quantitative values into qualitative concepts. The specific algorithm of the cloud generator can be found in the reference (Wang G. et al., 2014).

In control engineering, rules like "perception-action" represent logical causal relationships between concepts. Cloud models can be used to construct qualitative rule generators for control logic. Perception serves as the antecedent of control rules and can have one or more conditions. Action, on the other hand, represents detailed control actions and serves as the consequence of control rules. Both perception and action have a certain degree of uncertainty in practical engineering.

In the domain E_1, for a specific point y, the cloud generator can generate a certainty distribution *drop* (y, μ), indicating the degree of certainty that point a belongs to the qualitative concept F_1. In this case, the cloud generator is referred to as the antecedent cloud generator CG_A.

If a certainty value μ is given, where $\mu \in [0, 1]$, the cloud generator can be used to generate a cloud droplet distribution on the concept F_2 in the domain E_2 that satisfies the specified certainty. In this case, the cloud generator is referred to as the consequent cloud generator CG_B.

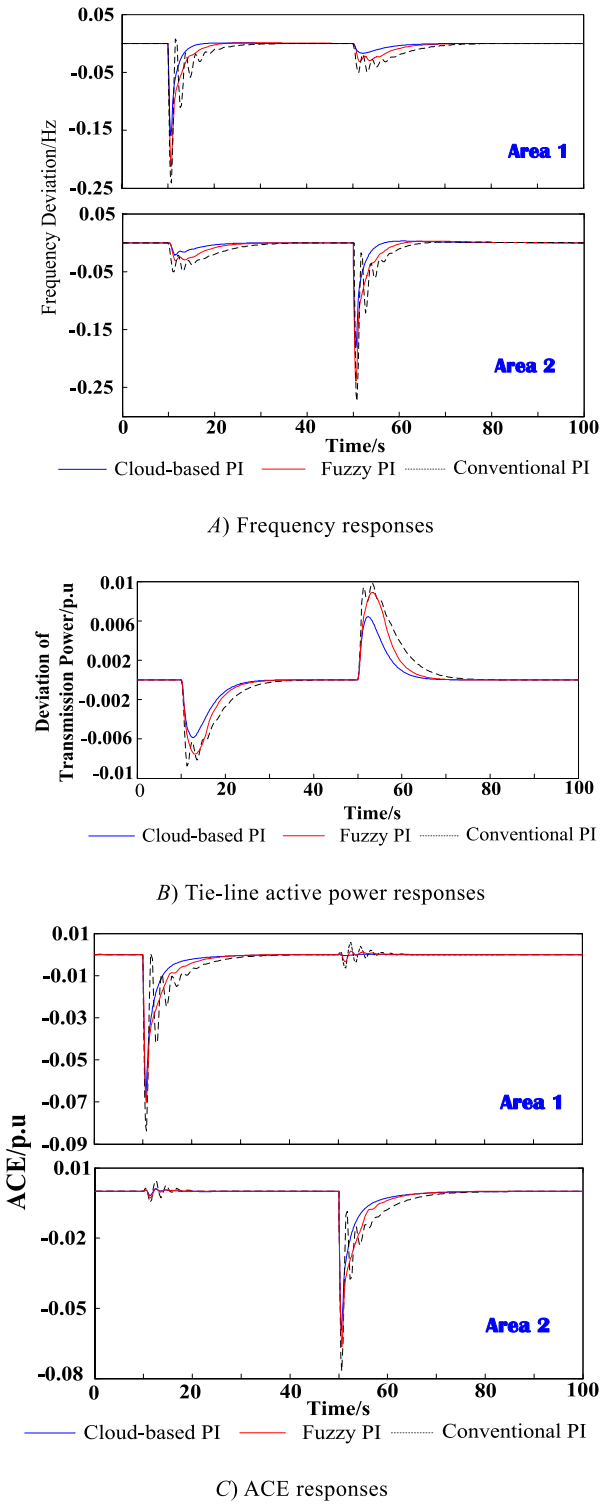

FIGURE 6
Control performance under load disturbance. **(A)** Frequency responses. **(B)** Tie-line active power responses. **(C)** ACE responses.

It is possible for a two-dimensional spatial domain to construct both a two-dimensional antecedent cloud generator and a consequent cloud generator, as shown in Figure 2.

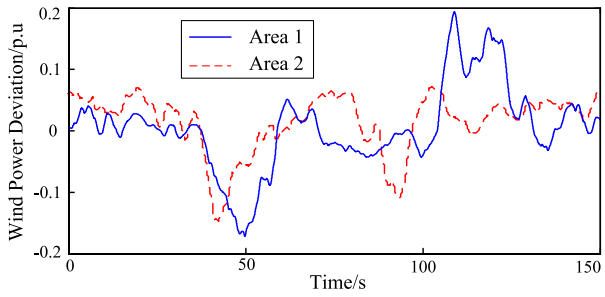

FIGURE 7
Wind power fluctuations in Area 1 and Area 2.

3.3 Design of parameter self-tuning intelligent PI controller based on cloud model

The central idea of LFC is to ensure the stable operation of system frequency and the exchange of power between areas according to planned values. However, in practical applications, due to the uncertainty of system operation, the randomness of disturbance variations, and the uncertainty in the mapping relationship between input deviations and controller outputs, LFC faces severe challenges. Cloud models can effectively address the uncertainty relationship between determinism and quantification. Therefore, by combining the cloud model with conventional PI controllers, the cloud-based PI controller can provide new opportunities for the LFC.

By using ACE (Area Control Error) and its rate of change as inputs to the antecedents of the cloud model rules and using the tuning values of P (Proportional) and I (Integral) as outputs of the entire system, a cloud model system with dual inputs and single output applicable for LFC is constructed, as shown in Figure 3. By sampling ACE, both ACE and its rate of change are input into the controller. Under the assumption that the three numerical characteristics of the cloud model are known when the antecedent of a rule is triggered by a certain input, it will randomly generate a certainty level μ. This certainty level then stimulates the consequent generators CG_P and CG_I, resulting in two sets of cloud droplets, *drop* (P, μ) and *drop* (I, μ), which represent the tuning values of P and I, respectively.

In traditional methods, the tuning of parameters P and I is mainly based on accumulated operational experience in industrial production. When selecting linguistic variable values, we need to consider both the flexibility and specificity of control rules, as well as the simplicity and feasibility of control. Therefore, based on the reference of operational experience, we will use five linguistic variable values, namely "Positive Big (PB), Positive Small (PS), Zero (ZE), Negative Small (NS), and Negative Big (NB)". The maximum membership degree for each linguistic value is "1". The range of variations for ACE and its rate of change together form a two-dimensional domain, which is then combined with the range of variations for $\triangle P$ and $\triangle I$ to create two independent biconditional cloud rule inference generators. These generators are used to dynamically tune the parameters P and I in real-time during the control process.

The cloud model inference rules applied to load frequency control are shown in Table 1.

Based on operational experience, the control rules for self-tuning the PI controller using cloud model parameters can be expressed in linguistic terms.

Region 1: ACE (Area Control Error) $\boldsymbol{E}$ = NB (Negative Big) indicates that the actual value deviates significantly from the set value, indicating a large error. Since the rate of change of ACE $\boldsymbol{E_C}$ = PB (Positive Big) indicates a rapidly increasing trend in the positive direction. Therefore, no adjustment is made to the output at this time, and the output value U = ZE (Zero), which corresponds to the last row of the first column in the cloud control Table 1.

Region 2: The $\boldsymbol{E}$ = NS (Negative Small) indicates that the actual value deviates slightly from the set value. In this case, if $\boldsymbol{E_C}$ = ZE (Zero), which means the rate of change of the error has no changing trend, the output value is required to decrease accordingly. The output value U = NS (Negative Small). This corresponds to the second column in the third row of cloud control Table 1.

Region 3: $\boldsymbol{E}$ = PS (Positive Small) indicates that the actual value is slightly lower than the set value. In this case, if $\boldsymbol{E_C}$ = NB (Negative Big), the speed error will be changed from PS to NS. Consequently, the output U = NS (Negative Small) accordingly.

After formulating cloud inference rules, the cloud intelligent controller for LFC can be designed using a cloud generator. It mainly consists of four parts: input fuzzification, cloud inference rules, cloud inference, and output defuzzification, as shown in Figure 3.

In addition to inputting cloud inference rules in advance, the cloud intelligent controller requires the definition of the input and output variable domains. Three numerical variables (*Ex*, *En*, and *He*) can be obtained by using statistical tools based on the prior data accumulated from the input and output variables during the operation or simulation process of the controlled object.

4 Simulation and analysis

4.1 Simulation model and parameters

To validate the effectiveness of the cloud model-based intelligent PI controller proposed in this paper for LFC, a simulation model for load frequency control with wind power generation was built in the Matlab/Simulink based on a two-area LFC control model.

The cloud intelligent controller utilized in the simulation process of this paper adopts the cloud inference rules shown in Table 1. Combining multiple simulation processes under different control performances, based on the changes in the values corresponding to *ACE* and the P and I parameters, the fuzzy membership parameters corresponding to the input and output variables of the controller were obtained for five qualitative concepts (Jalali N et al., 2020). The numerical variables (*Ex*, *En*, and *He*) are shown in Table 2, and the corresponding membership cloud diagrams are shown in Figure 4.

4.2 Performance analysis under load step disturbance

In order to validate the control performance of the proposed cloud-based controller under significant load impacts, load step disturbances of 0.04 p.u. and 0.05 p.u. were respectively set in

10.3389/fenrg.2024.1477645

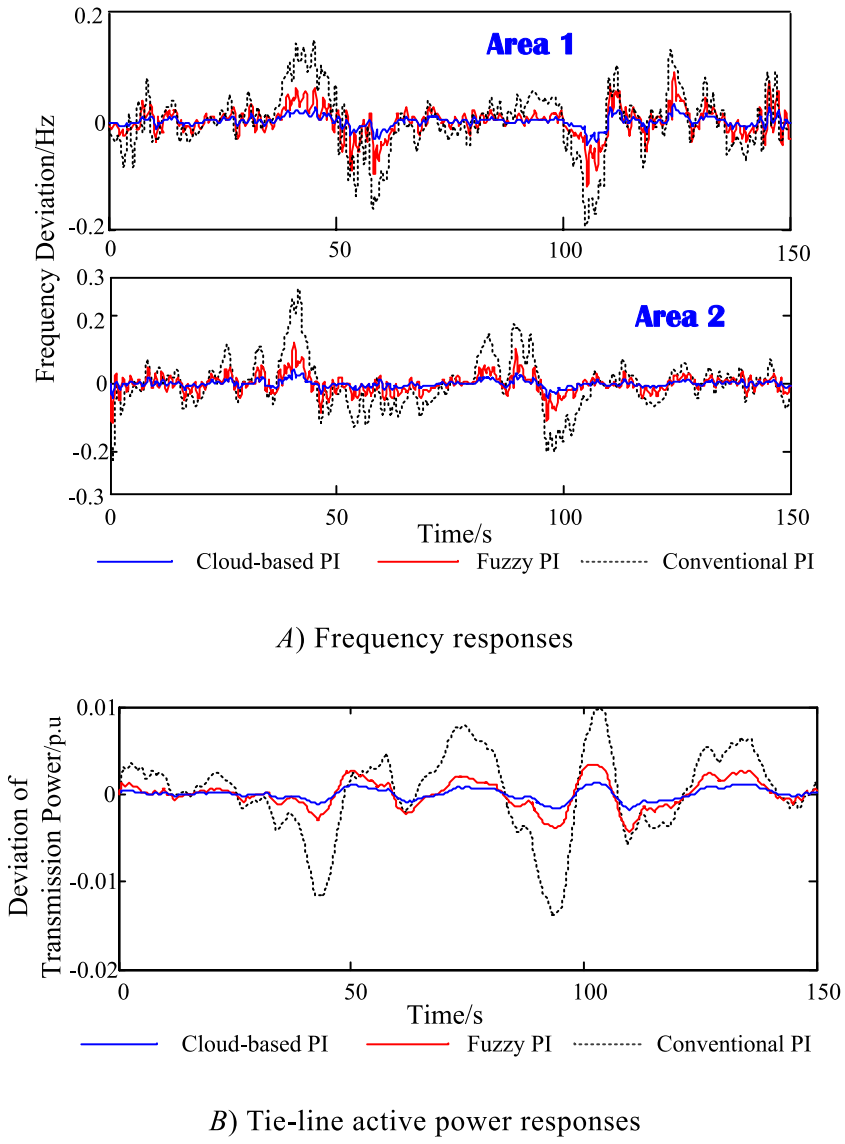

FIGURE 8
Control performance under wind power fluctuations. **(A)** Frequency responses. **(B)** Tie-line active power responses.

Area 1 and Area two at 10s and 50s, as shown in Figure 5. Both conventional PI control and Fuzzy PI control which was designed based on reference (Cam and Kocaarslan, 2005), were simultaneously employed. The time-domain responses of frequency deviation, ACE (Area Control Error), and interval transmission power deviation are shown in (Figures 6A–C), respectively.

From Figure 6, it is evident that the proposed cloud-based intelligent PI controller and Fuzzy PI controller exhibit significantly better control performance than the traditional PI control. Notably, no oscillations were observed during the frequency recovery process, which can be attributed to the adaptive adjustment of the P and I parameters of the cloud intelligent PI controller and Fuzzy PI controller. Furthermore, compared to the Fuzzy PI control, the proposed cloud-intelligent PI controller exhibits significant advantages in terms of the speed of frequency and ACE recovery.

4.3 Performance analysis under wind power fluctuations

In order to further validate the adaptability of the proposed cloud-based intelligent PI control in frequency control of power systems with wind generation, wind power generation was introduced in Area 1 and Area 2. Based on considering the aggregation effect of wind farms, a wind power sequence was generated. The deviation between the actual wind power and the predicted value is shown in Figure 7. Using the LFC model established in this study, simulations were conducted on the dynamic frequency response of a two-area system under the stochastic wind power fluctuations shown in Figure 8A). The time-domain responses of the transmission power deviation are shown in Figure 8B).

By observing the dynamic frequency response curves of the simulated results and the wind power fluctuation characteristics

shown in Figure 7, it can be observed that the LFC model established in this study effectively reflects the impact of stochastic fluctuations in active power output from large-scale wind farms on the dynamic response of the LFC.

As seen from Figures 8A, B), when there are stochastic fluctuations in the active power output of wind farms, the proposed cloud-based intelligent PI control in this study can effectively track the wind power fluctuations and provide optimal control signals for the AGC units in the region to adapt to the stochastic fluctuations in wind power, which, in turn, ensures that the system frequency and ACE fluctuate within a smaller range. On the other hand, both the Fuzzy PI and conventional PI control strategies lag behind the cloud PI control in terms of frequency recovery speed and fluctuation range, and they are unable to track the stochastic variations in wind power effectively.

In conclusion, the proposed cloud-based intelligent PI controller in this study is effective in handling uncertain wind power integration and exhibits better control performance than the Fuzzy PI control strategy. The cloud-based intelligent PI control proposed in this study is not only effective in handling typical load disturbances but also capable of tracking the stochastic fluctuations in wind power. This further validates the adaptability and robustness of the proposed cloud based intelligent PI control for LFC.

5 Conclusion

This paper designs a cloud-based intelligent PI controller based on the cloud model theory, combined with the LFC characteristics of interconnected power grids. It achieves load frequency control in interconnected power grids with high wind power penetration. The designed cloud-based intelligent controller does not rely on the mathematical model of the control system. It can be designed and implemented based on the characteristics of the controlled system and prior experience. The design process is intuitive and straightforward, without the need for tedious formula derivation. The cloud-based intelligent controller exhibits strong robustness against the uncertainty of wind power and outperforms traditional fuzzy controllers in terms of tracking time, frequency fluctuation suppression, and interval control deviation.

The three numerical characteristics, namely expectation, entropy, and hyper-entropy, directly affect the control effectiveness of the cloud-based intelligent controller. Further research is still needed to optimize these characteristic parameters based on the characteristics of the controlled system.

Data availability statement

The original contributions presented in the study are included in the article/supplementary material, further inquiries can be directed to the corresponding author.

Author contributions

DL: Data curation, Funding acquisition, Methodology, Writing–review and editing. XL: Conceptualization, Funding acquisition, Methodology, Supervision, Writing–review and editing. HZ: Methodology, Writing–original draft, Writing–review and editing. XM: Data curation, Investigation, Resources, Software, Writing–original draft. ZX: Data curation, Software, Writing–original draft. CC: Data curation, Formal Analysis, Software, Visualization, Writing–review and editing. TL: Data curation, Investigation, Methodology, Software, Writing–review and editing.

Funding

The author(s) declare that financial support was received for the research, authorship, and/or publication of this article. This publication is supported in part by grant 20230303004SF from the Jilin Province's Major Scientific and Technological Project for the High-Quality Development of "Land-based Three Gorges of Wind and Solar Energy".

Conflict of interest

Authors DL, XL, HZ, XM, ZX, CC, and TL were employed by State Grid Jilin Electric Power Co., Ltd.

Publisher's note

References

Bevrani, H. (2009). *Robust power system frequency control.* Springer.

Cam, E., and Kocaarslan, I. (2005). Load frequency control in two area power systems using fuzzy logic controller. *Energ Convers. Manage* 46, 233–243. doi:10.1016/j.enconman.2004.02.022

Huynh, V. V., Tran, P. T., Dong, C. S. T., Hoang, B. D., and Kaynak, O. (2024). Sliding surface design for sliding mode load frequency control of multiarea multisource power system. *IEEE T Ind. Inf.* 20, 7797–7809. doi:10.1109/TII.2024.3359445

Jalali, N., Razmi, H., and Doagou-Mojarrad, H. (2020). Optimized fuzzy self-tuning PID controller design based on Tribe-DE optimization algorithm and rule weight adjustment method for load frequency control of interconnected multi-area power systems. *Appl. Soft Comput.* 93 (1), 106424. doi:10.1016/j.asoc.2020.106424

Jia, Y., Dong, Z. Y., Sun, C., and Meng, K. (2019). Cooperation-based distributed economic MPC for economic load dispatch and load frequency control of interconnected power systems. *Syst. IEEE T Power Syst.* 34 (99), 3964–3966. doi:10.1109/TPWRS.2019.2917632

Jun ZhouJia, Y., and Yong, P. (2024). Robust deep Koopman model predictive load frequency control of interconnected power systems. *Electr. Pow. Syst. Res.* 226, 109948. doi:10.1016/j.epsr.2023.109948

Kavousi-Fard, A., Niknam, T., and Fotuhi-Firuzabad, M. (2016). A novel stochastic framework based on cloud theory and -modified bat algorithm to solve the distribution feeder reconfiguration. *IEEE T Smart Grid* 7 (2), 1–750. doi:10.1109/TSG.2015.2434844

Li, D., Liu, C., and Gan, W. (2009). A new cognitive model: cloud model. *Int. J. Intell. Syst.* 24 (3), 357–375. doi:10.1002/int.20340

Liang, Y., Jiaming, Q., and Xinxin, L. (2024). Load frequency control of new energy power system based on adaptive global sliding mode control. *Front. Energy Res.* 12, 1383511. doi:10.3389/fenrg.2024.1383511

Liu, X., Wang, C., Kong, X., Zhang, Y., Wang, W., and Lee, K. Y. (2024). Tube-based distributed MPC for load frequency control of power system with high wind power penetration. *IEEE T Power Syst.* 39 (2), 3118–3129. doi:10.1109/TPWRS.2023.3277997

Liu, X., Zhang, Yi, and Lee, K. Y. (2016). Robust distributed MPC for load frequency control of uncertain power systems. *Control Eng. Pract.* 56, 136–147. doi:10.1016/j.conengprac.2016.08.007

Liu, X., Zhang, Y., and Lee, K. Y. (2017). Coordinated distributed MPC for load frequency control of power system with wind farms. *IEEE T Ind. Electron* 64 (6), 5140–5150. doi:10.1109/TIE.2016.2642882

Ojaghi, P., and Rahmani, M. (2017). LMI-based robust predictive load frequency control for power systems with communication delays. *IEEE T Power Syst.* 32 (5), 4091–4100. doi:10.1109/TPWRS.2017.2654453

Qi, X., Zheng, J., and Mei, F. (2022). Model predictive control–based load-frequency regulation of grid-forming inverter–based power systems. *Front. Energy Res.* 10, 932788. doi:10.3389/fenrg.2022.932788

Ratnam, K., Palanisamy, K., and Yang, G. (2020). Future low-inertia power systems: requirements, issues, and solutions - a review. *Renew. Sust. Enst. Energ Rev.* 2020 (C), 109773. doi:10.1016/j.rser.2020.109773

Rerkpreedapong, D., Hasanovic, A., and Feliachi, A. (2003). Robust load frequency control using genetic algorithms and linear matrix inequalities. *IEEE T Power Syst.* 18 (2), 855–861. doi:10.1109/TPWRS.2003.811005

Tan, W. (2010). Unified tuning of PID load frequency controller for power systems via IMC. *IEEE T Power Syst.* 25 (1), 341–350. doi:10.1109/TPWRS.2009.2036463

Tummala, A. S. L. V., Inapakurthi, R., and Ramanarao, P. V. (2018). Observer based sliding mode frequency control for multi-machine power systems with high renewable energy. *J. Mod. Power Syst. Cle* 6 (3), 473–481. doi:10.1007/s40565-017-0363-3

Wadi, M., Shobole, A., Elmasry, W., and Kucuk, I. (2024). Load frequency control in smart grids: a review of recent developments. *Renew. Sust. Enst. Energ Rev.* 189, 114013. doi:10.1016/j.rser.2023.114013

Wang, G., Xu, C., and Li, D. (2014). Generic normal cloud model. *Inf. Sci.* 280, 1–15. doi:10.1016/j.ins.2014.04.051

Wei, M., Lin, S., Zhao, Y., Wang, H., and Liu, Q. (2021). An adaptive sliding mode control based on disturbance observer for LFC. *Front. Energy Res.* 9, 733910. doi:10.3389/fenrg.2021.733910

Wood, A. J., Bruce, F., and Wollenberg (1996). *Power generation, operation and control*. USA: John Wily and Sons, Inc.

Yan, Z., and Xu, Y. (2020). A multi-agent deep reinforcement learning method for cooperative load frequency control of a multi-area power system. *IEEE T Power Syst.* 99, 4599–4608. doi:10.1109/TPWRS.2020.2999890

Zhang, Y., Shi, X., Zhang, H., Cao, Y., and Terzija, V. (2022). Review on deep learning applications in frequency analysis and control of modern power system. *Int. J. Elec Power* 136, 107744. doi:10.1016/j.ijepes.2021.107744

Zhou, K., Lu, N., and Jiang, B. (2024). Basic probability assignment using intuitive fuzzy cloud model for information fusion and its application in fault diagnosis. *IEEE T Instrum. Meas.* 73, 1–13. doi:10.1109/TIM.2023.3334361

frontiers | Frontiers in Energy Research

TYPE Original Research
PUBLISHED 20 September 2024
DOI 10.3389/fenrg.2024.1479216

OPEN ACCESS

EDITED BY
Zhenjia Lin,
Hong Kong Polytechnic University, Hong Kong SAR, China

REVIEWED BY
Yixuan Chen,
The University of Hong Kong, Hong Kong SAR, China
Xuehan Zhang,
Fuzhou University, China
Wei Gan,
Cardiff University, United Kingdom

*CORRESPONDENCE
Yushen Gong,
254449338@qq.com

RECEIVED 11 August 2024
ACCEPTED 09 September 2024
PUBLISHED 20 September 2024

CITATION
Lu Y, Gong Y, Huang C, Gu S, Tong J and Huang W (2024) A low voltage load balancing distribution method considering street information and V2G technology application. *Front. Energy Res.* 12:1479216. doi: 10.3389/fenrg.2024.1479216

A low voltage load balancing distribution method considering street information and V2G technology application

Youfei Lu[1], Yushen Gong[2]*, Chenhui Huang[1], Shaoyuan Gu[1], Jiapeng Tong[1] and Wendong Huang[1]

[1]Guangzhou Power Supply Bureau of Guangdong Power Grid Co., Ltd., Guangzhou, China, [2]School of Electric Power Engineering, South China University of Technology, Guangzhou, China

The low-voltage distribution network (LVDN) is the final stage in delivering electric energy from power plants to consumers, and its operational condition greatly impacts many power users. While medium-voltage and high-voltage distribution networks can be managed through intelligent digital systems, load imbalance issues in LVDNs often rely on planners' experience, leading to significant limitations. With advancements in electric vehicle (EV) charging technology and vehicle-to-grid (V2G) technology, where EVs act as distributed energy storage units, bidirectional energy exchange between vehicles and the grid can now contribute to LVDN operation. This paper proposes a low-voltage load distribution planning method that integrates street information and V2G technology. A two-stage stochastic programming mixed-integer model is developed to tackle load imbalance in LVDNs, with the planning scheme derived from solving this model. A case study is presented to verify the effectiveness of the method, demonstrating that incorporating V2G technology enhances load distribution accuracy and reduces reliance on manual planning, improving network stability and operational efficiency.

KEYWORDS

low-voltage distribution network (LVDN), load balancing distribution, two-stage stochastic programming, street information, vehicle to grid (V2G)

1 Introduction

The low-voltage distribution network (LVDN) directly serves basic electricity users, acting as a crucial link between power production and power consumption. With the increasing integration of new energy sources and the introduction of advanced power equipment, the LVDN is experiencing significant transformations (Guo et al., 2023). In actual LVDN, load conditions are dynamic and subject to constant fluctuations due to various unpredictable factors, such as customer behavior, weather conditions, and public events. These variations make load imbalance an inherent challenge in such networks (Yan and Saha, 2012). As urban development accelerates, the phenomenon of "village in the city" becomes more prevalent, leading to concentrated and disorderly power loads, with pronounced regional load differences. Effective distribution network planning can mitigate load imbalance issues. LVDN planning primarily involves designing distribution transformers and low-voltage lines to form a radial network with the lowest total cost (Díaz-Dorado et al., 2001). Scheidler et al. (2018) highlights that while a large amount of

data is available for analysis in LVDNs, planning typically relies on the expertise of experienced planners. Utilizing intelligent planning methods can enhance the robustness of planning schemes, but the quality of the database information poses a significant challenge. Wang et al. (2015) employs the traditional manual planning method, gathering LVDN information for analysis to develop a distribution network planning scheme. This approach considers both the investment in grid transformation and the reduction of grid loss rates. Mateo et al. (2018) focuses on planning low-voltage feeder-level integrated distribution networks by collecting data from 79 large European distribution system operators (DSOs). However, these feeder-level distribution networks only encompass three-phase balanced urban and semi-urban low-voltage distribution networks. In Díaz-Dorado et al. (2001), a minimum Euclidean distance tree is employed to plan low-voltage radial distribution networks while considering voltage drop constraints and line losses. However, this method does not address the issue of load imbalance in the distribution network. Carpinelli et al. (2017) employs an intelligent planning method, utilizing multi-objective optimization to address load imbalance in LVDNs, thereby enhancing power quality and energy efficiency. In LVDNs, cables are typically laid along streets (Moon and Kim, 2017). Díaz-Dorado et al. (2003) focuses on planning rural power grids with fewer nodes, considering the connection between transformers and power grids but not the street layout. Verheggen et al. (2016) proposes a low-voltage distribution network planning method that accounts for both the laying of cables along streets and the inclusion of distributed generation. Similarly, Navarro and Rudnick (2009) considers the user street layout and uses a heuristic algorithm to divide the planning area into smaller sections for local analysis and optimization, ultimately optimizing the entire area. Also considers the user street layout and uses a heuristic algorithm to divide the planning area into small areas for local analysis and optimization, and finally optimizes the whole area. The aforementioned three papers focus exclusively on typical power system loads.

With the rapid development of clean energy, the number of electric vehicles (EVs) is also increasing rapidly. Studies have shown that EV charging behavior significantly impacts the power grid, causing issues such as current and voltage imbalance, line loss, and feeder overload (Boribun, 2019). For some distribution facilities, peak load may only be reached for a few hours a year. However, uncontrolled electric vehicle charging behavior often exacerbates these load peaks and negatively impacts transformer lifespan (Wu and Sioshansi, 2017). By implementing orderly charging, which involves controlling the timing and amount of EV charging load, the operation of the distribution network can be improved, and peak demand on the network can be reduced (Benetti et al., 2014). Sangob and Sirisumrannukul (2021) proposes an LVDN planning method based on sequential particle swarm optimization (PSO). This method aims to mitigate the impacts of large-scale EV usage by implementing ordered charging of EVs. Tan et al. (2016) employs a two-level planning method to minimize grid load differences by adjusting the EV charging load. Ordered charging of EVs can enhance system operation by shifting the load to off-peak hours. Moreover, if EVs can function as energy storage and participate in the adjustment of distribution network operations, peak load can be further reduced (Mets et al., 2011). EV batteries are increasingly popular as small to medium-sized energy storage solutions due to their relatively high energy density, lack of geographical restrictions, and low maintenance requirements (Pimm et al., 2018). When a large number of EV batteries are combined to act as energy storage and can send power back to the grid during peak hours, this is referred to as Vehicle-to-Grid (V2G) technology (Crozier et al., 2020). V2G technology has demonstrated significant potential in balancing electricity supply and demand (Han et al., 2012). For instance, Soares et al. (2011) proposes a particle swarm optimization (PSO) algorithm to address the optimal scheduling of energy resources, including V2G resources.

Stochastic programming is a significant branch of mathematical programming, used for modeling optimization problems that involve uncertain parameters (Shapiro and Philpott, 2007). The two-stage stochastic programming with recourse cost is the most common type, where decisions and related variables are divided into two stages (Mavromatidis et al., 2018). The first stage is typically referred to as the tactical level, involving long-term decisions that influence development over an extended period. The second stage, known as the operational level, involves more specific, shorter-term decisions. The first-stage decision must be made before the uncertain parameters are realized. Once these parameters are determined, they often differ from the expected values considered during the first stage. Consequently, the second stage incurs a recourse cost due to these differences, and the goal is to minimize this cost through second-stage decisions. Tan et al. (2014) adopts a two-stage stochastic programming method to plan the distribution network, taking into account distributed resources. Wu and Sioshansi (2017) uses a two-stage stochastic programming method to flexibly schedule EV charging times, leveraging distributed resources to mitigate the impact of load peaks on transformers.

In summary, LVDN planning is often closely linked to street information. However, due to data limitations and challenges in integrating and utilizing information, planners typically rely on limited data and design based on experience or use heuristic algorithms for support. The increasing adoption of EVs has added complexity, as their charging patterns significantly affect distribution network operations. The deployment of smart detection devices has improved data acquisition and utilization in LVDN. Nonetheless, current research falls short in integrating diverse information from these networks and using intelligent optimization methods to align long-term planning with operational scheduling while optimizing load distribution. Therefore, the paper proposes a low voltage load balancing distribution method considering street information and V2G technology applications. The proposed method employs a two-stage stochastic programming approach, the corresponding theory is illustrated in Figure 1. In the first stage, a load distribution optimization model that incorporates street information and electrical topology is established, focusing primarily on long-term load distribution planning and related constraints. In the second stage, a scheduling model utilizing V2G technology is created further to enhance the operational status of the distribution network.

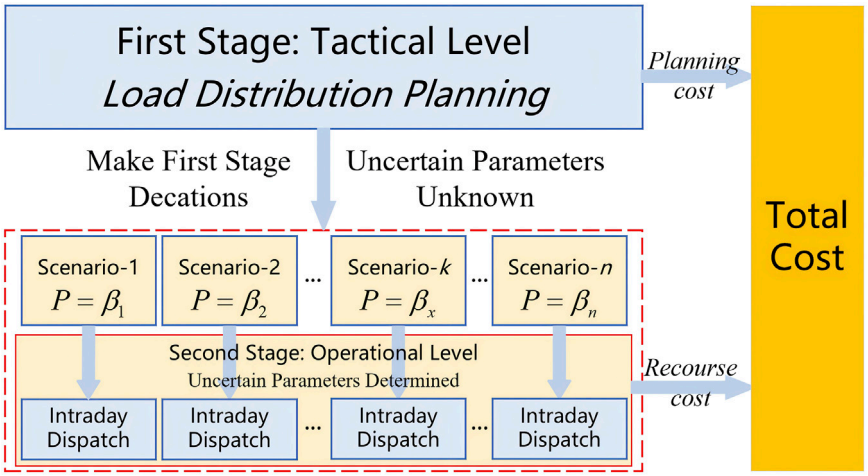

FIGURE 1
Theoretical schematic diagram of the proposed method.

TABLE 1 Road-grid coupling network concern information table.

Parameter	Description
Street Orientation	The directional layout of streets
Electrical Topology	The configuration and connections of electrical lines
Customer	Access node in the grid and historical load data

The main contributions of this paper are as follows.

1) This study contributes to the planning of low-voltage distribution networks by integrating the original load distribution with optimal load combination strategies. We propose a method to reallocate load combinations to new access nodes through analytical modeling, taking into account street orientation to determine the most efficient and cost-effective load planning pathways.
2) The approach integrates two-stage adjustments for both long-term planning and dispatch. Utilizing the pseudo load curve acquisition method, it collaboratively addresses issues such as large load fluctuations, heavy overloads in the distribution network, and load imbalance, from both planning and dispatching perspectives.

2 Distribution network modeling

In the LVDN, most distribution lines are low-voltage overhead lines, and the road network is highly coupled with the power grid. Therefore, this paper integrates electrical lines in the LVDN with street information, forming what is termed the Road-Grid Coupling Network (RGCN). The primary method for optimizing load distribution in the LVDN involves removing the load from the original line, laying low-voltage overhead lines along the street, and reconnecting the removed load to the new line. Key issues in this process include selecting the most appropriate load combination (LC) for adjustment and choosing the adjustment path with the lowest cost.

2.1 Road-grid coupling modeling

First, the street and electrical topology information related to the LVDN will be collected through the distribution operator systems (DSOs), as shown in Table 1. This table summarizes the key information required for modeling the RGCN. After collecting street direction information, the start and end nodes of the streets and the intersections of each street are anchored, and the streets are connected to establish a highway network connection model; for electrical topology information, the main focus is on the distribution and direction of electrical lines, and the line node locations are determined according to actual conditions, while the access locations of each user in the line are determined; for users, if smart meters are installed, the load data in the smart meters is read; if smart meters are not installed, the total electricity consumption information is collected for pseudo-load curve acquisition.

The cost of laying overhead lines is assessed for each street by the DSOs. This is represented by a cost coefficient c_i, which is used to determine the most cost-effective planning route.

Finally, a weighted directed topological graph of the LVDN is created. The method for assigning weights to each edge in the directed graph is described in Equation 1.

$$w_i = c_i \cdot l_i \tag{1}$$

Where w_i is the weight of the *i-th* street, c_i is the cost coefficient of the *i-th* street, and l_i is the length of the *i-th* street.

2.2 Pseudo load profile determination

The LVDN includes numerous users, making it impractical and costly to install intelligent electric meters for every user. Consequently, obtaining pseudo load profiles for low-voltage users depends on data from a limited number of users equipped with intelligent electric meters. In this paper, for users without intelligent electric meters, pseudo load profiles are utilized to

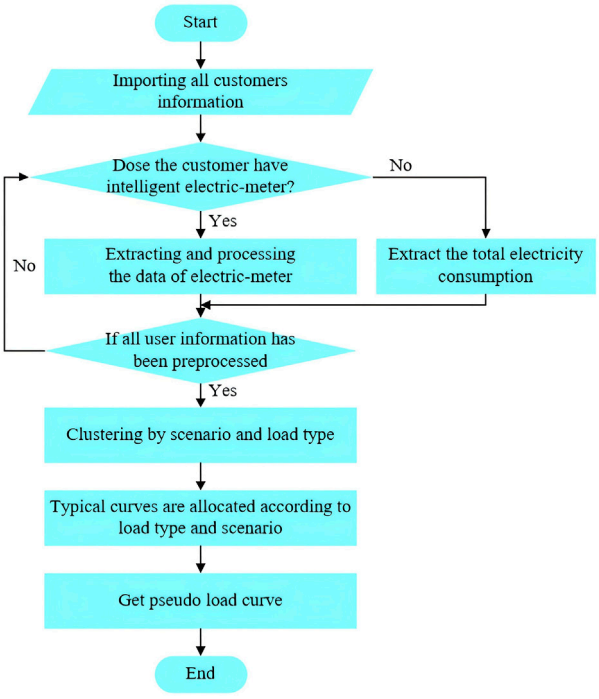

FIGURE 2
Flowchart of pseudo load profile acquisition method.

approximate their actual power consumption curves (Gahrooei et al., 2017).

First, all loads are categorized based on the electricity consumption characteristics of the users. Collect electricity usage data from all users with intelligent electric meters. After cleaning the data and filling in any gaps, cluster the typical load patterns for various load types in different scenarios according to their load types and contexts. Additionally, mark the probability of each pattern's occurrence. For loads without intelligent electric meters, assign a typical load pattern to each load based on its type and context. For example, if there are 100 A-type loads, and the clustering results for A-type loads in *scenario-I* show three load patterns (*a*, *b*, *c*) with occurrence probabilities of 50%, 30%, and 20%, respectively, then approximately 50, 30, and 20 of the 100 loads will be assigned to load patterns *a*, *b*, and *c*, respectively, in *scenario-I*. The flow chart illustrating the pseudo load profile acquisition method is shown in Figure 2.

3 Two-stage stochastic programming modeling

In the method proposed in this paper, the process is divided into two stages. The first stage is the planning stage, which spans a longer period and focuses primarily on replanning the existing load in the LVDN to mitigate issues of heavy overload and load imbalance through a limited number of load distribution adjustments. The second stage is the dispatching stage, which has a shorter period and mainly involves using V2G technology to manage EVs within the distribution network, further alleviating the problems of heavy overload and load imbalance.

This chapter addresses modeling in two distinct stages: long-term operation and short-term scheduling. After developing the models, a solver is utilized to derive collaborative planning and scheduling solutions. Ultimately, this approach aims to alleviate operational issues in the LVDN by integrating both long-term planning and short-term scheduling strategies.

3.1 Planning stage modeling

Through analysis of real-world projects, it is observed that the LVDN typically only redistributes load combinations (LCs) at the feeder endpoints. In the planning process, we begin with the load at the feeder's end, then select the most appropriate LCs along the feeder. This LC is subsequently reconnected to the most suitable node within the distribution network, which is not always the terminal node.

In Figures 3A, B show the LCs that allow replanning and that do not allow replanning, respectively. For example, in Figure 3A, black nodes 2, 3, and five represent nodes located at the end of the feeder, and the loads they connect to are the ones subject to replanning. Taking node-2 as an example, during the planning process, we can select loads *LD1-LD3* (as shown in the red frame-1 in Figure 3A). Alternatively, we can select up to k loads as an LC for planning (as shown in the red frame-2 in Figure 3A).

However, we cannot plan the load in the middle of the feeder (as shown in the red frame-1 in Figure 3B), nor can we select loads *LD1-LD3* and then add *LDk* as an LC (as shown in the red frame-2 in Figure 3B).

In the planning stage, the key decision is to determine the node of each load connected to the distribution network. For each load within the distribution network, using the *j-th* load $P^{load}{}_{j}$ as an example, we define a decision vector shown as Equation 2:

$$\boldsymbol{x}_j^{\top} = \left[\rho_{j1}, \rho_{j2}, \cdots, \rho_{jn}\right] \tag{2}$$

where the elements ρ_{jn} are all binary variables, and n is the number of nodes in the distribution network.

When making planning decisions, our goal is to minimize the total cost of the plan. The cost is calculated using the method shown as Equation 3. The cost matrix C is derived from the weighted directed topology graph developed in Chapter 2. To calculate the cost of each potential planning path for the loads, the Dijkstra shortest path algorithm is employed.

$$f_1 = \sum_{j=1}^{m}\sum_{i=1}^{n}\rho_{ji} \cdot C_{ji} \tag{3}$$

Where, C_{ji} represents the cost of replanning the *j-th* load from the original node (assumption to be the *k-th* node) to the new *i-th* node. If $k = i$, then $C_{ji} = 0$, indicating that the *j-th* load has not been replanned, and the cost is 0.

In LVDN, to avoid the formation of a closed power supply loop that could compromise safety in unexpected situations, the power supply network is typically designed to be radial. Consequently, users obtain power from only one node in the distribution network. This constraint is expressed as shown in Equation 4:

$$\sum_{i=1}^{n}\rho_{ji} = 1, \ \forall j \in \Omega_{LD} \tag{4}$$

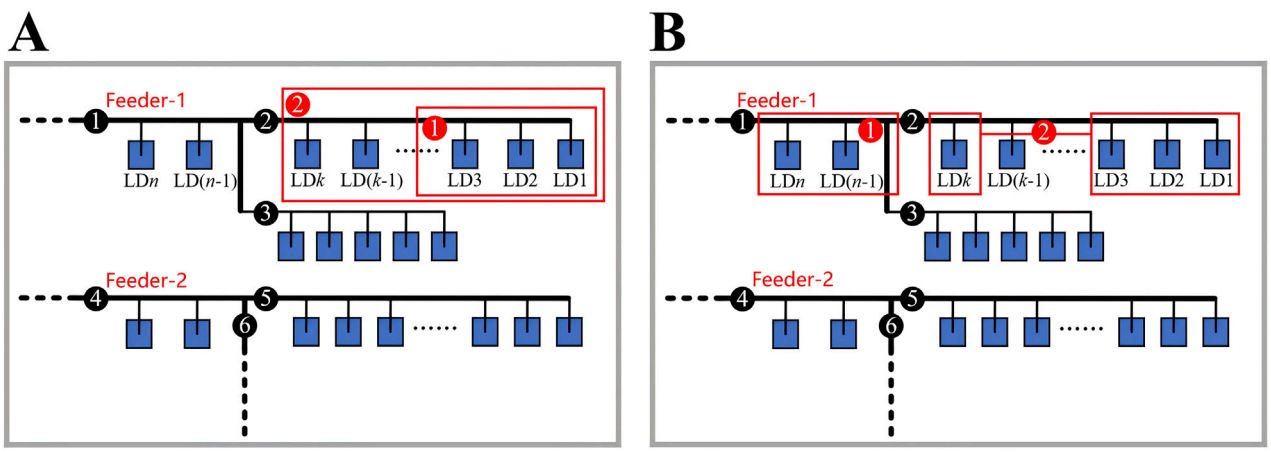

FIGURE 3
Example diagram of Load Combinations(LCs).

where Ω_{LD} is the set of all loads, and n is the total number of distribution network nodes. When $\rho_{ji} = 1$, it means that the *j-th* load access node is the *i-th* node in the distribution network.

Since all loads are already connected to the distribution network, readjusting the distribution of all loads is not feasible. During the planning stage, typically only a portion of the loads at the end of the distribution network can be redistributed. The constraint that needs to be met is shown in Equation 5, indicating that there is an upper limit on the number of loads that can be replanned:

$$\sum_{j=1}^{m}\left(1 - \boldsymbol{x}_j^{\top} \cdot \boldsymbol{x}_j\right) \le n_{\max}^{adj} \tag{5}$$

where $n_{\max}^{adj}$ means the upper limit number, and m means the number of loads. If the access node of the *j-th* load in the distribution network is redistributed, then constraint (Equation 6) needs to be satisfied:

$$\boldsymbol{x}_j^{\top} \cdot \boldsymbol{x}_j = 0 \tag{6}$$

Otherwise, constraint (Equation 7) must be met:

$$\boldsymbol{x}_j^{\top} \cdot \boldsymbol{x}_j = 1 \tag{7}$$

According to the above research results, the load connected to non-terminal nodes must adhere to the following constraint (Equation 8):

$$\boldsymbol{x}_j^{\top} \cdot \boldsymbol{x}_j = 1, j \notin \Omega_{E.N.} \tag{8}$$

where $\Omega_{E.N.}$ is the set of all end nodes.

For an end node (assuming it is node-*i*), two auxiliary decision variables are defined, as shown in Equations 9, 10:

$$A_i^{\top} = [a_{i1}, a_{i2}, \cdots, a_{in}] \tag{9}$$

$$B_i^{\top} = [b_{i1}, b_{i2}, \cdots, b_{ik}] \tag{10}$$

where a_{in} and b_{ik} are both binary variables, k is the total number of users connected to the end node-*i*; $A_i^{\top}$ is used to assist in the decision-making process for planning the users connected to end node-*i*, and $B_i^{\top}$ helps determine the LC selection for planning end node-*i*. These variables must satisfy the constraints shown in Equations 11, 12:

$$\sum_{i=1}^{n} a_{hi} = 1, \ \forall h \in \Omega_{E.N.} \tag{11}$$

$$\sum_{z=1}^{k} b_{hz} \le 1, \ \forall h \in \Omega_{E.N.} \tag{12}$$

where, if $a_{hi} = 1$, it indicates that the LC from the end node-*h* is replanned to the node-*i*; if $b_{hz} = 1$, it signifies that the *z* loads at the end of end node-*i* are replanned as an LC; if all b_{hz} values are 0, it means that the load connected to this node is not replanned. The detailed usage of these two auxiliary variables will be elaborated in the second stage.

In LVDN, it is generally preferable to connect customers to the nearest point in the distribution network. If the connection point is too far from the customer's geographical location, it can lead to cross-power-supply issues, which are detrimental to the operation and management of the power grid. Therefore, when redistributing the load, it is essential to follow the principle of proximity planning, as shown in Equation 13:

$$\sum_{i=1}^{n} \rho_{ji} \cdot D_{ji} \le R_{\max}, \ \forall j \in \Omega_{LD} \tag{13}$$

where D_{ji} represents the Euclidean distance from the *j-th* load to the *i-th* node, according to the weighted directed topological graph obtained in Chapter 2. $R_{\max}$ denotes the maximum allowable distance between the load location and the access node.

3.2 Operational stage modeling

During the operation stage, the primary objective is to utilize V2G technology to manage the charging load of EVs efficiently. This helps reduce the peak-to-valley difference in load and alleviate load imbalance. The decision variable in this stage is the EV charging load $x_{s\cdot k\cdot t}$, which operates on a smaller time scale. The subscripts

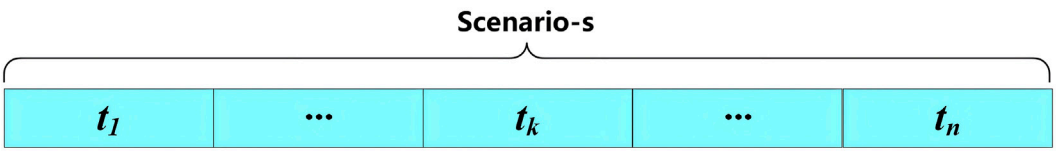

FIGURE 4
Schematic diagram of scenario sampling.

represent the charging load index, scenario, and time, respectively. Each scenario contains s_n sampling points, as illustrated in Figure 4.

In low-voltage distribution networks, significant load differences between feeders exacerbate load imbalance within the regional grid. Therefore, during project operation and maintenance, it is essential to maintain uniform load rates across feeders. The article defines the degree of load imbalance as the difference between the maximum and minimum instantaneous load rates of all feeder outlets in the distribution network at any given time. A substantial degree of load imbalance typically signals that certain feeders are overloaded. When this imbalance surpasses a specified threshold, it can lead to increased transformer heating, elevated power losses, a higher failure rate, even voltage fluctuations, and reduced equipment lifespan. The calculation method for the degree of load imbalance is defined as Equation 14:

$$\eta = \sigma_{s\cdot t\cdot \max} - \sigma_{s\cdot t\cdot \min} \tag{14}$$

where $\sigma_{s\cdot t\cdot max}$ and $\sigma_{s\cdot t\cdot min}$ are the maximum and minimum values of all feeder load rates in scenario-s, at time t.

At this stage, the optimization goal is to minimize the mathematical expectation of the degree of load imbalance across all scenarios, as shown in Equation 15, where β_s is the probability of the scenario-s occurring, and s_n is the number of typical scenarios.

$$f_2 = \sum_{s=1}^{s_n} \beta_s \cdot \frac{1}{t_n} \sum_{t=1}^{t_n} (\sigma_{s\cdot t\cdot \max} - \sigma_{s\cdot t\cdot \min}) \tag{15}$$

To facilitate the calculation of the load power at the end node (assuming node-i), auxiliary decision variables $P_{i\cdot out\cdot s\cdot t}$, $P_{i\cdot rest\cdot s\cdot t}$, and $Y^{\top}_{i\cdot s\cdot t}$ (shown as Equation 16) are introduced here:

$$Y^{\top}_{i\cdot s\cdot t} = \left[y^{s\cdot t}_{i1}, y^{s\cdot t}_{i2}, \cdots, y^{s\cdot t}_{ik} \right] \tag{16}$$

where $P_{i\cdot rest\cdot s\cdot t}$ is the remaining load value of end node-i in scenario-s at time t, and the role of $Y^{\top}_{i\cdot s\cdot t}$ is to assist in calculating the load values planned from end node-i to another node, specifically the value of $P_{i\cdot out\cdot s\cdot t}$. The element values of $Y^{\top}_{i\cdot s\cdot t}$ are obtained by accumulating the load values in order from far to near, according to the distance of the load's access to the end node before replanning. For example, the value of $y^{s\cdot t}_{i1}$ is the load value of the last load of end node-i (such as *LD1* in Figure 3A) in scenario-s at time t; and the meaning of $y^{s\cdot t}_{i2}$ is the sum of the load values of the last two loads (such as *LD1* and *LD2* in Figure 3A) in scenario-s at time t, and so on. These three auxiliary variables must satisfy the constraints in Equations 17, 18:

$$P_{i\cdot out\cdot s\cdot t} = \sum_{z=1}^{k} y^{s\cdot t}_{iz} \cdot b_{iz}, \ \forall i \in \Omega_{E.N.} \tag{17}$$

$$P_{i\cdot out\cdot s\cdot t} + P_{i\cdot rest\cdot s\cdot t} = y^{s\cdot t}_{ik} \tag{18}$$

where, according to the previous description, $y^{s\cdot t}_{ik}$ is the total load value of the end node-i in scenario-s at time t, before planning.

Based on the above analysis, the calculation method for node power in the distribution network is shown as Equation 19:

$$P^{load}_{s\cdot i\cdot t} = \begin{cases} P_{i\cdot rest\cdot s\cdot t} + \sum_{z=1}^{n^{E.N.}} P_{z\cdot out\cdot s\cdot t} \cdot a_{zi}, i \in \Omega_{E.N.} \\ \sum_{j=1}^{m} \rho_{ji} \cdot P^{LD}_{s\cdot j\cdot t} + \sum_{z=1}^{n^{E.N.}} P_{z\cdot out\cdot s\cdot t} \cdot a_{zi}, otherwise \end{cases} \tag{19}$$

where $n^{E.N.}$ is the total number of end nodes.

To ensure the distribution network's safe and stable operation, the lines' maximum instantaneous power should remain below the safety threshold, and the network should not operate under heavy overload conditions for extended periods. The constraints are shown in Equation 20:

$$\begin{cases} P_{s\cdot ij\cdot t} \le \mu \cdot {P_{ij}}^{N} \\ \sum_{t=t_0}^{t_0+T_{\max}} P_{s\cdot ij\cdot t} \le 0.8 \cdot {P_{ij}}^{N} \cdot T_{\max} \end{cases}, \forall ij \in \Omega_L, \forall s \in \Omega_s \tag{20}$$

where $P_{s\cdot ij\cdot t}$ represents the instantaneous power of the line at time t in the s-th scenario; *PN ij* is the rated power of line-ij, μ is the safety threshold parameter, $T_{\max}$ is the maximum allowable continuous overload time, Ω_L is the set of all lines, and Ω_s is the set of all scenarios.

At the same time, the distribution network should meet the power balance constraints during operation, as shown in Equation 21:

$$\begin{cases} P_{s\cdot i\cdot t\cdot in} = P^{load}_{s\cdot i\cdot t} + P_{s\cdot i\cdot t\cdot out} \\ P_{s\cdot i\cdot t\cdot in} = \sum P_{s\cdot zi\cdot t}, \forall z \in \Omega_{in} \\ P_{s\cdot i\cdot t\cdot out} = \sum_{k}^{z} P_{s\cdot ik\cdot t}, \forall k \in \Omega_{out} \\ \forall i \in \Omega_N, \forall s \in \Omega_s \end{cases} \tag{21}$$

when ignoring line losses, at any time t, the power flowing into any node (e.g., node-i) $P_{s\cdot i\cdot t\cdot in}$ should be equal to $P^{load}_{s\cdot i\cdot t}$ (the sum of the total load of the users connected to this node) plus $P_{s\cdot i\cdot t\cdot out}$ (the power flowing out of the node). $\Omega_{i\cdot in}$ is the set of starting nodes of the lines flowing into node-i, $\Omega_{i\cdot out}$ is the set of ending nodes of the lines flowing out of node-i, Ω_N is the set of all nodes.

When using V2G technology for load scheduling, to ensure the safe operation of the EV charging pile, its maximum charging and discharging power should meet the requirements specified in Equation 22:

$$-P_{d\cdot \max} \le x_{s\cdot k\cdot t} \le P_{c\cdot \max} \tag{22}$$

where $P_{c\cdot max}$ and $P_{d\cdot max}$ are the maximum charging and discharging power of the charging pile, respectively.

Since users' willingness to participate in the V2G plan varies across different periods, the proportion of users participating in the V2G plan at different times is not completely consistent. Here, we define the auxiliary decision variable P^{V2G}, which represents the charging load of the user group participating in the V2G plan. This variable satisfies Equation 23:

$$x_{s\cdot k\cdot t} = (1 - \alpha_{s\cdot t})X_{s\cdot k\cdot t} + P^{V2G}_{s\cdot k\cdot t} \tag{23}$$

Where $X_{s\cdot k\cdot t}$ is the load value when EVs are charged in an unordered manner, and $\alpha_{s\cdot t}$ is the proportion of users participating in the V2G plan at scenario-s at time t. Additionally, for users in the V2G plan, the maximum charging and discharging power constraints must also be met, as shown in Equation 24:

$$\delta_1 \cdot \alpha_{s\cdot t} \cdot X_{s\cdot k\cdot t} \le P^{V2G}_{s\cdot k\cdot t} \le \delta_2 \cdot \alpha_{s\cdot t} \cdot X_{s\cdot k\cdot t} \tag{24}$$

where δ_1 and δ_2 are the maximum charging and discharging power safety thresholds of V2G users respectively.

To ensure the safety of EV charging and battery life, and to prevent excessive current changes from impacting the power grid and batteries, the power change rate should also be controlled when scheduling EV loads, as shown in Equation 25:

$$\left|P^{V2G}_{s\cdot k\cdot t} - P^{V2G}_{s\cdot k\cdot (t-1)}\right| \le \varepsilon \cdot P_{c\cdot \max} \tag{25}$$

where ε is the maximum allowed charging rate.

For EV users, it is necessary to charge their vehicles to the specified capacity before their desired time. Therefore, in the scheduling plan, the total charging amount constraint must be met, as shown in Equation 26:

$$\sum_{t=t_0}^{t_{end}} x_{s\cdot k\cdot t} = \sum_{t=t_0}^{t_{end}} X_{s\cdot k\cdot t} \tag{26}$$

where t_0 and t_{end} are respectively the start and end times of the scheduling plan.

3.3 Modeling summary

Based on the theory of two-stage stochastic programming method, the model established in this chapter includes constraints (4)–(5), (13)and (20)–(26). The objective function of the model is shown in Equation 27:

$$\min f = \lambda_1 f_1 + \lambda_2 f_2 \tag{27}$$

where λ_1 and λ_2 are respectively the weight coefficients of the two-stage objectives.

When the model is solved, the values of the decision variables $x_j^{\top}$ and EV charging load $x_{s\cdot k\cdot t}$ are transformed into the planning method.

4 Case study

The model established in this paper is a large-scale mixed integer programming model, containing both integer and continuous variables. The commercial solver Gurobi is used to solve the problem. The computer specifications are: Intel Core™ i5-13500H, 2.60 GHz, 16 GB of memory.

4.1 Case overview

This paper uses a low-voltage distribution transformer in an urban village in Guangzhou City as an example. Figures 5, 6 are the electrical topology of the distribution network transformer and the road network coupling diagram respectively. The blue nodes in Figure 6 represent customers, and the red squares indicate distribution transformers.

The load exhibits characteristics typical of a residential area, including four categories: residential load, small commercial load, distributed photovoltaic (PV), and EV charging loads. Due to factors such as charging prices and limited charging pile capacity, most EVs charged during working hours follow a "charge-and-go" pattern. This means the owner starts charging immediately after connecting the car to the charging pile and leaves once the EV is charged to meet mileage requirements or the owner's departure time limit. Fewer users participate in the V2G plan during these hours. However, for users who charge during late night to next morning, the end time of charging is more flexible, and the proportion of users participating in the V2G plan is relatively high.

To more clearly demonstrate the continuous dispatch effect of V2G from late night to the next morning, this article takes 8:00 a.m. as the starting point, the scenario time scale is 24 h a day, and the sampling frequency is 15 min. For residential, small commercial, and EV charging loads, the load curve is closely related to whether the day is a weekday or not. Their clustering results on weekdays and non-working days show obviously different characteristics, as shown in Figures 7A–C. PV is closely related to weather conditions. Therefore, the clustering results of different scenarios according to weather conditions are shown in Figure 7D. From the results, we can see that PV output is larger on sunny days, smaller on cloudy or rainy days, and relatively smaller on cloudy days, with random fluctuations.

According to the pseudo load profile acquisition approach proposed in Chapter 2, the load profiles of all loads in the distribution network are obtained as shown in Figure 8. In this paper, PV output is regarded as loads with negative values, and all PV output is considered to be absorbed.

4.2 Case analysis

According to the scenarios generated above, the degree of load imbalance in the area before replanning reached 26.38%. In both working day and non-working day scenarios, the degree of load imbalance at 10:00 p.m. is significantly higher. In the working day scenario, the instantaneous degree of load imbalance can reach 43.71%, which is very unfavorable for the safe and stable operation of the regional distribution network.

Applying the method proposed in this paper (referred to as method 1), the load planning scheme for the region is obtained as

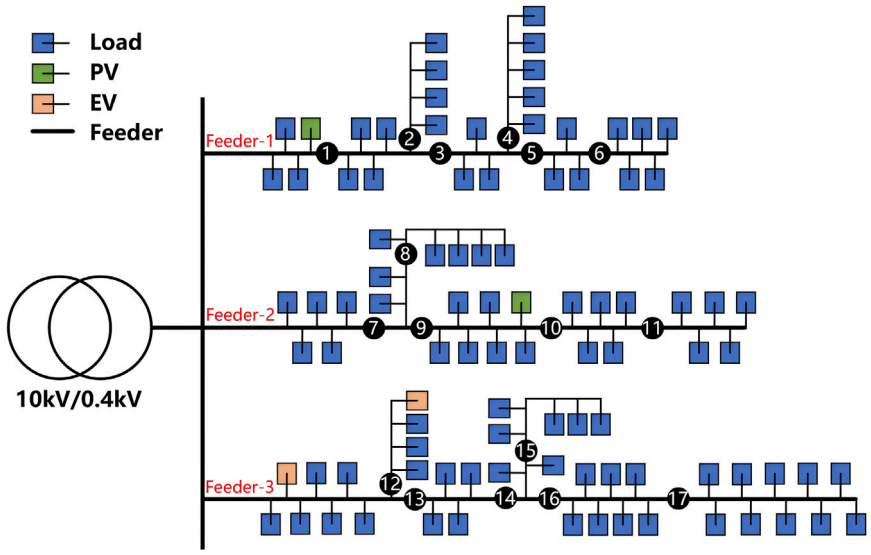

FIGURE 5
Electrical topology diagram of LVDN.

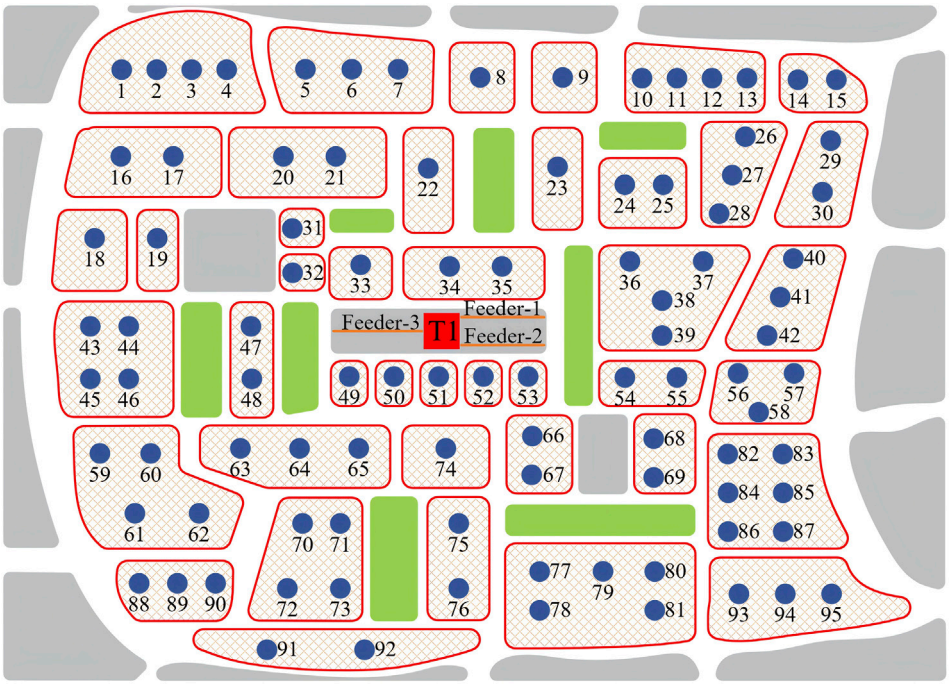

FIGURE 6
Diagram of road-grid coupling network(RGCN).

follows: load-63, 64, and 65 at the end of feeder-3 are adjusted to feeder-2, and load-77 and 78 at the end of feeder-2 are adjusted to feeder-1. The schematic diagrams of the load adjustment positions and paths are shown in Figures 9, 10.

Take EV load No. 39 as an example, the optimization results of EV charging load considering V2G technology are shown in Figure 11. During certain high-load periods, EVs connected to the distribution network act as energy storage, transmitting energy back to the distribution network. As night falls, most residential and commercial loads decrease significantly. During this period, EV charging demand rises to fulfill charging requirements. By early morning, residential and commercial loads begin to increase again. By this time, most EVs have completed charging, leading to a gradual decrease in EV load. This sequence achieves a staggered operation of various loads.

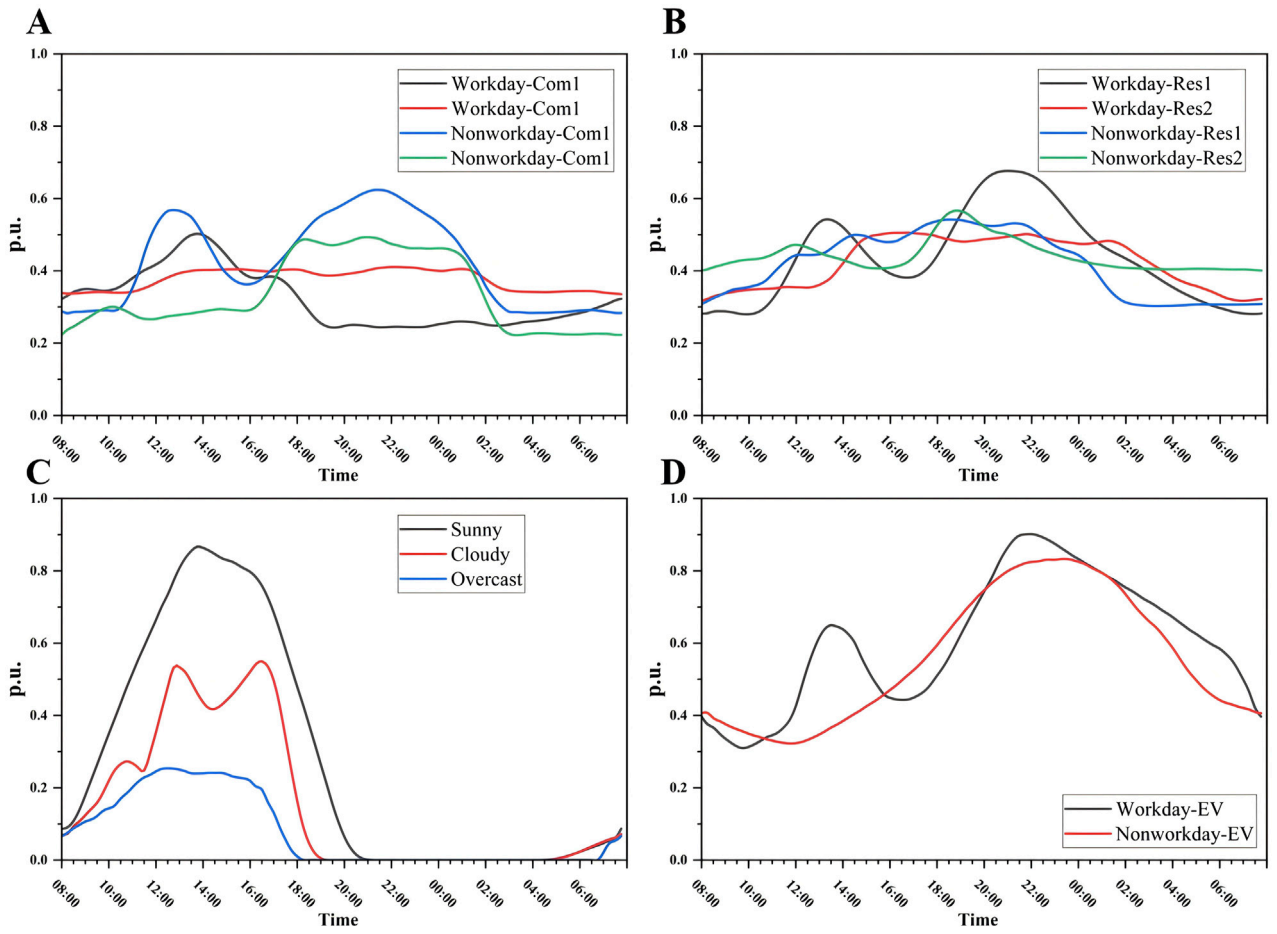

FIGURE 7
Clustering results of loads.

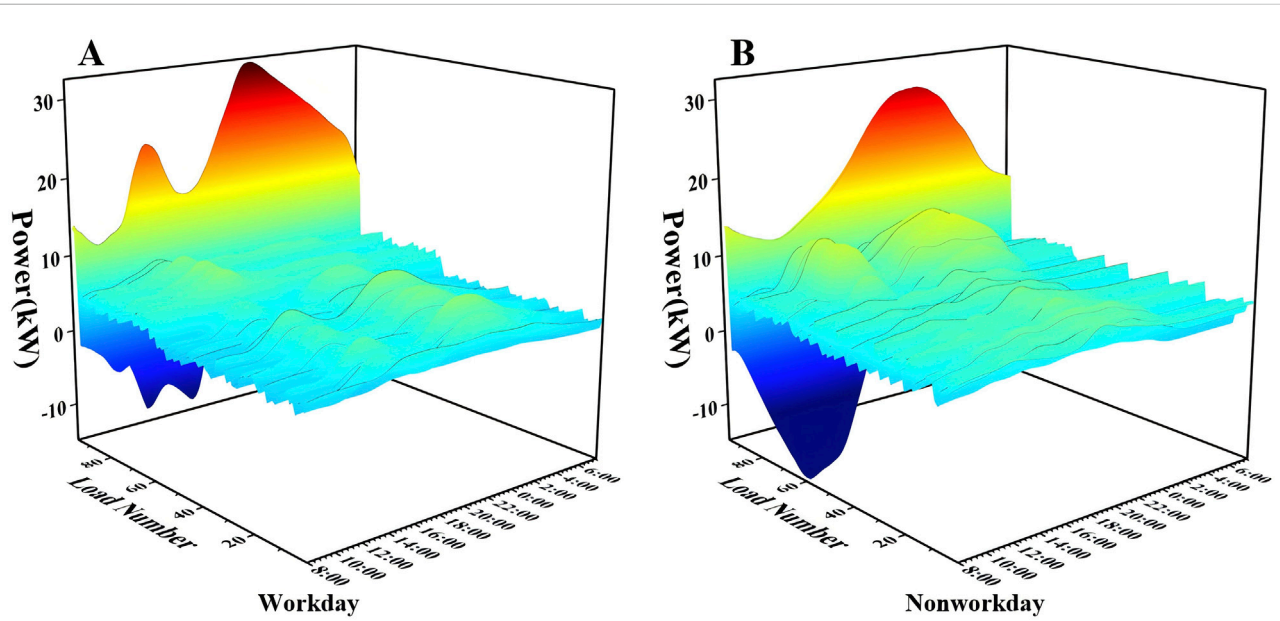

FIGURE 8
Pseudo load profiles of all loads.

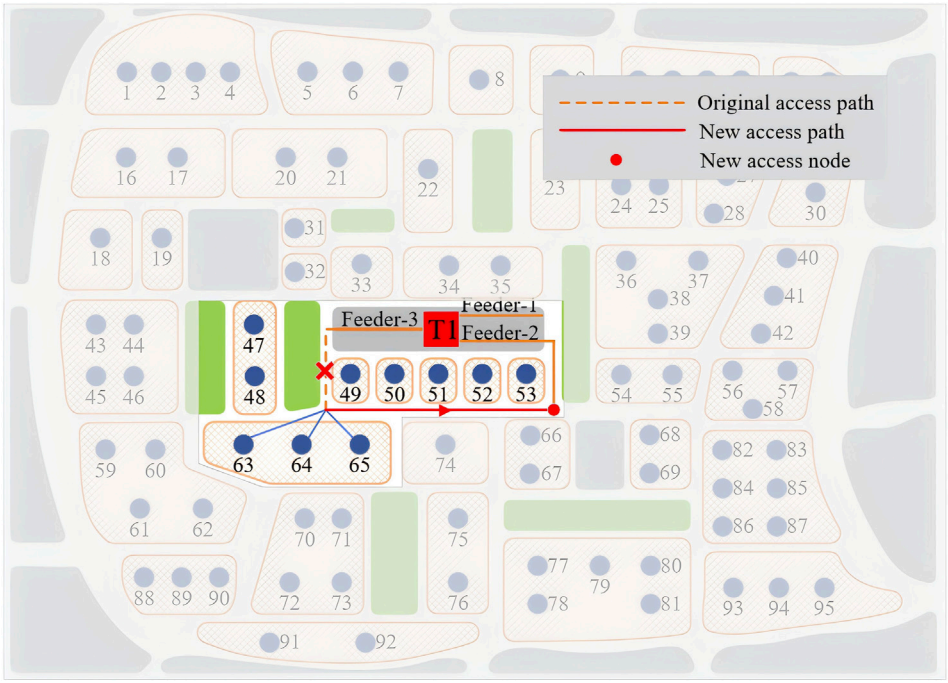

FIGURE 9
Planning scheme diagram 1.

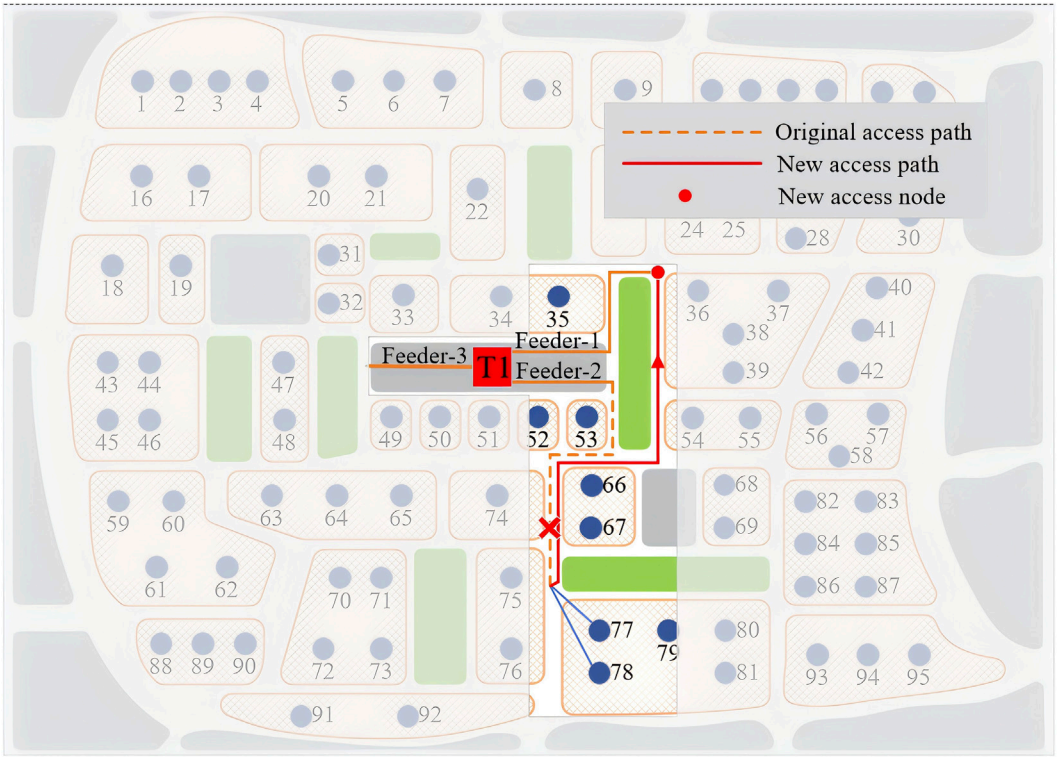

FIGURE 10
Planning scheme diagram 2.

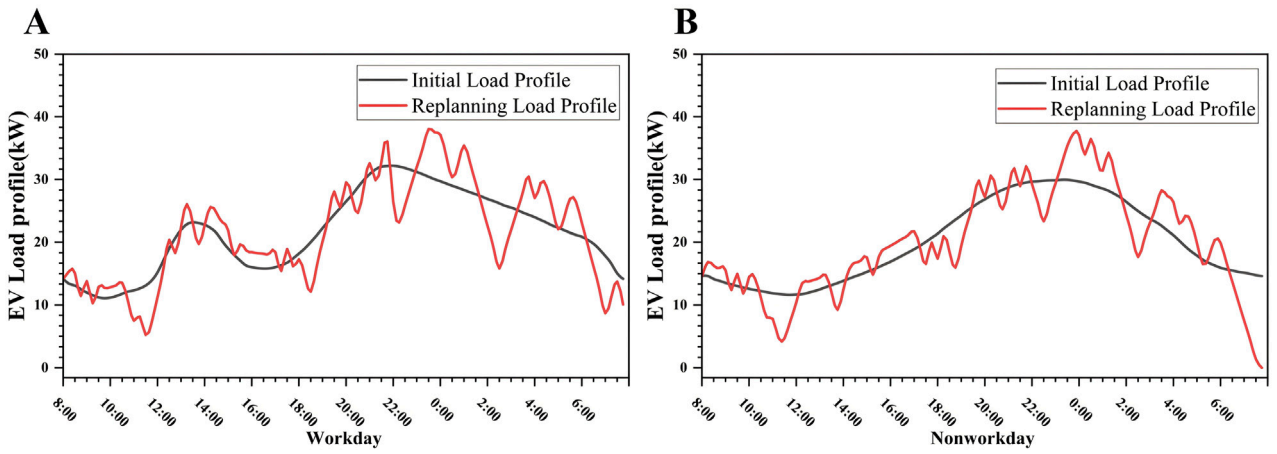

FIGURE 11
EV charging load optimization diagram.

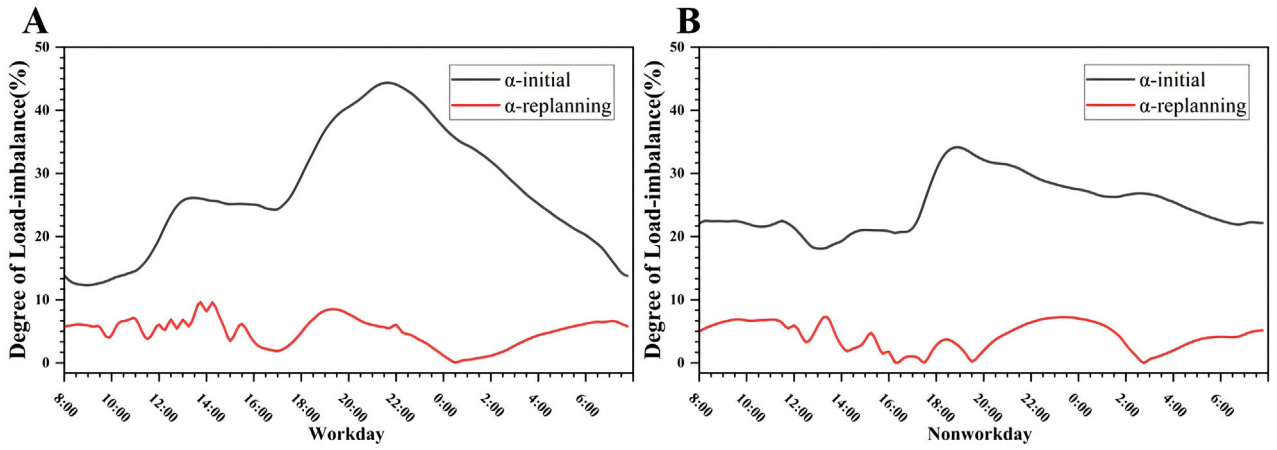

FIGURE 12
Comparison of the degree of load imbalance.

After optimizing the distribution network in the region according to the plan mentioned above, the comparison of the degree of load imbalance is shown in Figure 12. It can be seen that the degree of load imbalance has significantly decreased across different scenarios, especially around the 22:00 period in the non-working day scenario. The load imbalance phenomenon has been greatly alleviated, and the overall degree of load imbalance has dropped to 4.66%, demonstrating a significant effect.

If we only consider adjusting the distribution of loads in the distribution network without applying V2G technology (referred to as method 2), the resulting planning scheme would need to adjust load 48 along with loads 63, 64, and 65 to feeder 2. In this case, the degree of load imbalance can only be reduced to 6.87%. The planning cost and the degree of load imbalance would be higher than method 1.

If we ignore street information and only optimize network flow (referred to as method 3), the planning scheme involves adjusting load-1, 2, 3, and 4 to feeder-2, and adjusting load-64 and 65 to feeder-1. This optimizes the degree of load imbalance to 4.11%. However, the replanning routes in this scheme are longer and the planning cost is higher. Compared to the case where street information is considered, the decrease in the degree of load imbalance is insignificant. The overall economic benefits of this scheme are lower, and it can easily cause cross-power-supply issues, increasing management difficulty. The comparison of the three methods is shown in Table 2.

The method proposed in this paper comprehensively considers street information and the application of V2G technology. It achieves a relatively good adjustment in the degree of load imbalance at the lowest cost, offering high efficiency and economic benefits.

5 Conclusion

Aiming at the current problem of load imbalance in Low Voltage Distribution Networks (LVDN), this paper proposes a load-balanced distribution method that considers street information and the application of V2G technology. Its outstanding features include the

TABLE 2 Comparison of three planning methods.

Methods	Planning scheme		Planning costs	Degree of load imbalance	
	Load No.	Scheme		Before planning (%)	After planning (%)
Method 1	63, 64, 65	From feeder-3, bus-12 to feeder-2, bus-9	976.53	26.38	4.66
	77, 78	From feeder-2, bus-8 to feeder-1, bus-1			
Method 2	48, 63, 64, 65	From feeder-3, bus-12 to feeder-2, bus-9	1,131.36		6.87
	77, 78	From feeder-2, bus-8 to feeder-1, bus-1			
Method 3	1, 2, 3, 4	From feeder-3, bus-17 to feeder-2, bus-8	1,640.72		4.11
	64, 65	From feeder-3, bus-12 to feeder-1, bus-1			

incorporation of LVDN street information and the adoption of a two-stage stochastic programming approach. The method proposed in this paper effectively integrates long-term planning with short-term dispatching strategies in the distribution network. By optimizing user access nodes and incorporating V2G technology, this approach significantly mitigates the degree of load imbalance in the LVDN with minimal and more judicious adjustments. However, the load profiles used in this method are pseudo load profiles. If more accurate load profiles of all users can be obtained, the effectiveness of this method can be further enhanced.

Data availability statement

The original contributions presented in the study are included in the article/supplementary material, further inquiries can be directed to the corresponding author.

Author contributions

YL: Conceptualization, Methodology, Writing–review and editing. YG: Formal Analysis, Writing–original draft. CH: Investigation, Methodology, Validation, Writing–review and editing. SG: Investigation, Validation, Writing–review and editing. JT: Investigation, Validation, Writing–review and editing. WH: Writing–review and editing.

Funding

The author(s) declare that financial support was received for the research, authorship, and/or publication of this article. This research was funded by the R&D Project of Guangzhou Power Supply Bureau of Guangdong Power Grid, Co., Ltd, grant number No. 030103KK52220007/GDKJXM20220286.

Acknowledgments

Special thanks to all the institutions and colleagues who provided help and support for this study.

Conflict of interest

Authors YL, CH, SG, JT, and WH were employed by Guangzhou Power Supply Bureau of Guangdong Power Grid Co., Ltd.

The remaining author declares that the research was conducted in the absence of any commercial or financial relationships that could be construed as a potential conflict of interest.

The authors declare that this study received funding from Guangzhou Power Supply Bureau of Guangdong Power Grid, Co., Ltd. The funder had the following involvement in the study: conceptualization and design of the article, collection of initial data, review of the article.

Publisher's note

References

Benetti, G., Casagrande, D., Giannuzzi, G., Livi, S., and Moser, D. (2014). Real-time modeling and control of electric vehicles charging processes. *IEEE Trans. Smart Grid* 6 (3), 1375–1385. doi:10.1109/TSG.2014.2376573

Boribun, B. (2019). Modeling and analysis of the plug-in electric vehicles charging in the unbalanced radial distribution system. *Int. J. Electr. Electron. Eng. and Telecommun.* 8 (3), 133–138. doi:10.18178/ijeetc.8.3.133-138

Carpinelli, G., Celli, G., Mocci, S., Pilo, F., and Russo, A. (2017). Minimizing unbalances in low-voltage microgrids: optimal scheduling of distributed resources. *Appl. Energy* 191, 170–182. doi:10.1016/j.apenergy.2017.01.057

Crozier, C., Morstyn, T., McCulloch, M. D., and Chilvers, A. (2020). The case for Bi-directional charging of electric vehicles in low voltage distribution networks. *Appl. Energy* 259, 114214. doi:10.1016/j.apenergy.2019.114214

Díaz-Dorado, E., Cidrás Pidre, J., and Míguez García, E. (2003). Planning of large rural low-voltage networks using evolution strategies. *IEEE Trans. Power Syst.* 18 (4), 1594–1600. doi:10.1109/TPWRS.2003.818741

Díaz-Dorado, E., Miguez, E., and Cidrás, J. (2001). Design of large rural low-voltage networks using dynamic programming optimization. *IEEE Trans. Power Syst.* 16 (4), 898–903. doi:10.1109/59.962443

Gahrooei, Y. R., Khodabakhshian, A., and Hooshmand, R.-A. (2017). A new pseudo load profile determination approach in low voltage distribution networks. *IEEE Trans. Power Syst.* 33 (1), 463–472. doi:10.1109/TPWRS.2017.2696050

Guo, R., Meunier, S., Protopapadaki, C., and Saelens, D. (2023). A review of European low-voltage distribution networks. *Renew. Sustain. Energy Rev.* 173, 113056. doi:10.1016/j.rser.2022.113056

Han, Y., Chen, Y., Han, F., and Liu, K. R. (2012). "An optimal dynamic pricing and schedule approach in V2G," in Proceedings of the 2012 asia pacific signal and information processing association annual summit and conference, 03-06 December 2012 (Hollywood, CA, USA: IEEE), 1–8.

Mateo, C., Marti, J., Perez, R., Smith, P., Gangale, F., Frías, P., et al. (2018). European representative electricity distribution networks. *Int. J. Electr. Power and Energy Syst.* 99, 273–280. doi:10.1016/j.ijepes.2018.01.027

Mavromatidis, G., Orehounig, K., and Carmeliet, J. (2018). Design of distributed energy systems under uncertainty: a two-stage stochastic programming approach. *Appl. Energy* 222, 932–950. doi:10.1016/j.apenergy.2018.04.019

Mets, K., Verschueren, T., Haerick, W., Develder, C., and De Turck, F. (2011). "Exploiting V2G to optimize residential energy consumption with electrical vehicle (dis) charging," in 2011 IEEE first international workshop on smart grid modeling and simulation (SGMS), 17-17 October 2011 (Brussels, Belgium: IEEE). doi:10.1109/SGMS.2011.6089203

Moon, S.-K., and Kim, J.-O. (2017). Balanced charging strategies for electric vehicles on power systems. *Appl. Energy* 189, 44–54. doi:10.1016/j.apenergy.2016.12.025

Navarro, A., and Rudnick, H. (2009). Large-scale distribution planning—Part I: simultaneous network and transformer optimization. *IEEE Trans. Power Syst.* 24 (2), 744–751. doi:10.1109/TPWRS.2009.2016593

Pimm, A. J., Cockerill, T. T., and Taylor, P. G. (2018). The potential for peak shaving on low voltage distribution networks using electricity storage. *J. Energy Storage* 16, 231–242. doi:10.1016/j.est.2018.02.002

Sangob, S., and Sirisumrannukul, S. (2021). Optimal sequential distribution planning for low-voltage network with electric vehicle loads. *Front. Energy Res.* 9, 673165. doi:10.3389/fenrg.2021.673165

Scheidler, A., Thurner, L., and Braun, M. (2018). Heuristic optimisation for automated distribution system planning in network integration studies. *IET Renew. Power Gener.* 12 (5), 530–538. doi:10.1049/iet-rpg.2017.0394

Shapiro, A., and Philpott, A., 2007. A tutorial on stochastic programming. Available at: www.isye.gatech.edu/ashapiro/publications.html,17.

Soares, J., Sousa, T., Morais, H., Vale, Z., and Faria, P. (2011). "An optimal scheduling problem in distribution networks considering V2G," in 2011 IEEE symposium on computational intelligence applications in smart grid (CIASG), 11-15 April 2011 (Paris, French Guiana: IEEE). doi:10.1109/CIASG.2011.5953342

Tan, K. M., Ramachandaramurthy, V. K., and Yong, J. Y. (2016). Optimal vehicle to grid planning and scheduling using double layer multi-objective algorithm. *Energy* 112, 1060–1073. doi:10.1016/j.energy.2016.07.008

Tan, Y., Wang, L., Yang, F., Xiong, W., and Wang, J. (2014). A two-stage stochastic programming approach considering risk level for distribution networks operation with wind power. *IEEE Syst. J.* 10 (1), 117–126. doi:10.1109/JSYST.2014.2350027

Verheggen, L., Ferdinand, R., and Moser, A. (2016). "Planning of low voltage networks considering distributed generation and geographical constraints," in 2016 IEEE international energy conference (ENERGYCON), 04-08 April 2016 (Leuven, Belgium: IEEE). doi:10.1109/ENERGYCON.2016.7514042

Wang, L., Zhang, H., Li, Y., and Liu, J. (2015). "Research on the methods of low-voltage distribution network planning," in 2015 2nd international conference on electrical, computer engineering and electronics, May 29-31, 2015 (Jinan, China: Atlantis Press), pp.1498–1501. doi:10.2991/icecee-15.2015.282

Wu, F., and Sioshansi, R. (2017). A two-stage stochastic optimization model for scheduling electric vehicle charging loads to relieve distribution-system constraints. *Transp. Res. Part B Methodol.* 102, 55–82. doi:10.1016/j.trb.2017.05.002

Yan, R., and Saha, T. K. (2012). Investigation of voltage imbalance due to distribution network unbalanced line configurations and load levels. *IEEE Trans. Power Syst.* 28 (2), 1829–1838. doi:10.1109/TPWRS.2012.2225849

frontiers | Frontiers in Energy Research

TYPE Original Research
PUBLISHED 20 September 2024
DOI 10.3389/fenrg.2024.1472378

OPEN ACCESS

EDITED BY
Zhenjia Lin,
Hong Kong Polytechnic University, Hong Kong SAR, China

REVIEWED BY
Yiyan Sang,
Shanghai University of Electric Power, China
J. J. Chen,
Shandong University of Technology, China
Muhammad Faizan Tahir,
South China University of Technology, China

*CORRESPONDENCE
Haoheng Li,
ephoen@mail.scut.edu.cn

RECEIVED 29 July 2024
ACCEPTED 09 September 2024
PUBLISHED 20 September 2024

CITATION
Shen K, Li J, Zhang Y, Li H and Liu Y (2024) Fault current limiting control of full-scale wind power generators based on switched bang-bang scheme.
Front. Energy Res. 12:1472378.
doi: 10.3389/fenrg.2024.1472378

Fault current limiting control of full-scale wind power generators based on switched bang-bang scheme

Kankai Shen[1], Jingyi Li[1], Yaozhong Zhang[1], Haoheng Li[2]* and Yang Liu[2]

[1]Power China Huadong Engineering Corporation Limited, Hangzhou, China, [2]School of Electric Power Engineering, South China University of Technology, Guangzhou, China

This paper proposes a fault current limiting scheme (FCLS) for full-scale wind power generators based on logic bang-bang funnel control (LBFC). Different from the convention methods such as frequency droop control and sliding control, which design the control strategy according to the specific fault currents, LBFC is able to restrict various fault current within acceptable range in the shortest time, and it is robust to system nonlinearities and external disturbances. The control signal of the LBFC is bang-bang with the upper and lower limits of control variables. In the model of full-scale wind power generators connecting with the power grid, LBFC is designed to control the switches of inverter bridges when over-current is detected, and a vector controller is applied during the normal operation. Time-domain simulations were conducted with PSCAD, and the performance of LBFC was validated.

KEYWORDS

bang-bang funnel controller, fault current limiting, switching control, wind turbine generator, wind turbine

1 Introduction

Energy transition brings great challenges to the stable operation of the power grid. The transient stability of large-scale wind power penetrated power systems (WPPS) is increasingly influenced by the dynamics of wind power plants (Wang et al., 2015). Renewable power sources are connected to power grids through flexibly controlled power electronics inverters (Liu et al., 2017), which introduce completely different dynamics into power grids in comparison with synchronous generators (SGs) (Li et al., 2020). Under an extreme event, an effective control system of wind power generators can enhance the reliability of wind power generation and prevent wind farms from tripping, which helps to alleviate the power unbalance and improve the transient stability of large scale WPPSs. The reliability of future renewable energy generation is the major challenge for the development of renewable power sources (Enslin, 2016; Wu et al., 2023). To ensure that the power system can operate stably and has strong anti-disturbance ability. Much research has been done to meet these expectations and challenges.

The concept of Frequency Droop Control was initially introduced in Chandorkar et al. (1993) for regulating the operation of parallel-connected inverters in autonomous AC power grids. This control scheme involved determining the frequency and magnitude of the inverter voltage vectors using active power-frequency

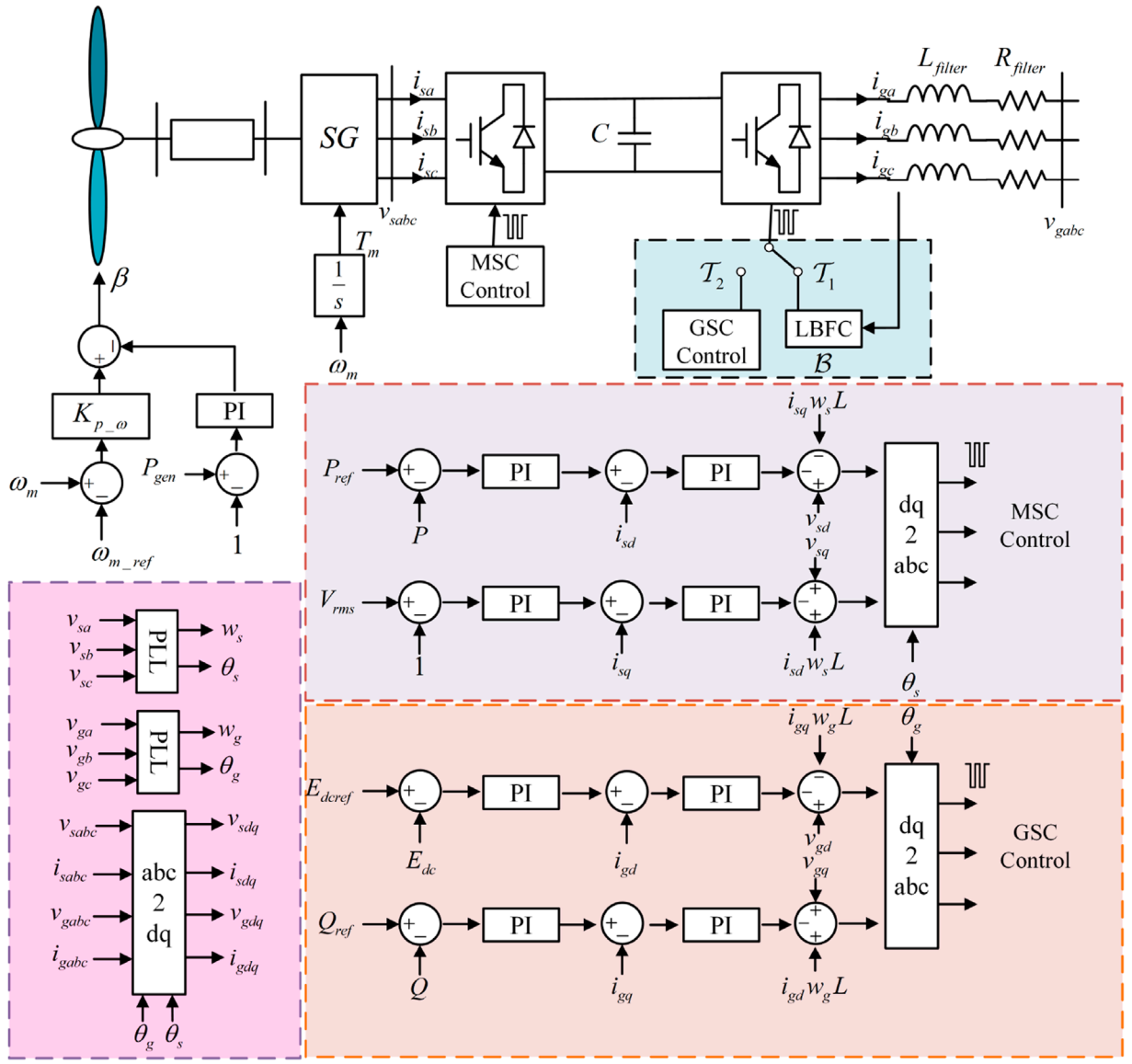

FIGURE 1
Wind power generation system.

droop and reactive power-voltage droop characteristics, as outlined in Behera and Saikia (2022); Silva et al. (2022). The primary objective of this approach was to make the parallel-connected inverters mimic the load-sharing behavior of traditional SGs to maintain a stable frequency and voltage in the external power grid (Li et al., 2021). However, it was observed that this frequency and voltage droop method exhibited a sluggish and oscillatory transient response (Guerrero et al., 2004).

To address these limitations, a phase angle droop control mechanism was introduced in Marwali et al. (2004) for the management of autonomously operating inverter-interfaced power grids. In this strategy, the regulation of the phase angle of the inverter voltage vector, as opposed to the system frequency, was accomplished by employing an active power-phase angle droop characteristic. This was done to ensure the proper distribution of loads among the parallel-connected inverters. An examination of the small-signal stability of inverter-interfaced power grids with phase angle droop controllers was carried out in Marwali et al. (2007), which affirmed the necessity of substantial angle droop gains for maintaining appropriate load sharing, especially in situations of system weakness. However, it's important to note that elevated droop gains can have an adverse impact on the overall stability of the system.

Furthermore, various nonlinear control techniques, such as fuzzy control (Jabr et al., 2011), sliding mode control (Martinez et al., 2012), and model predictive control Liu and Kong (2014) have also been applied for the integral control of the wind turbine. To ease the uncertainty and volatility caused by high penetration of renewable energy, the robustness and demand defence of grid were researched (Wang et al., 2024). Although

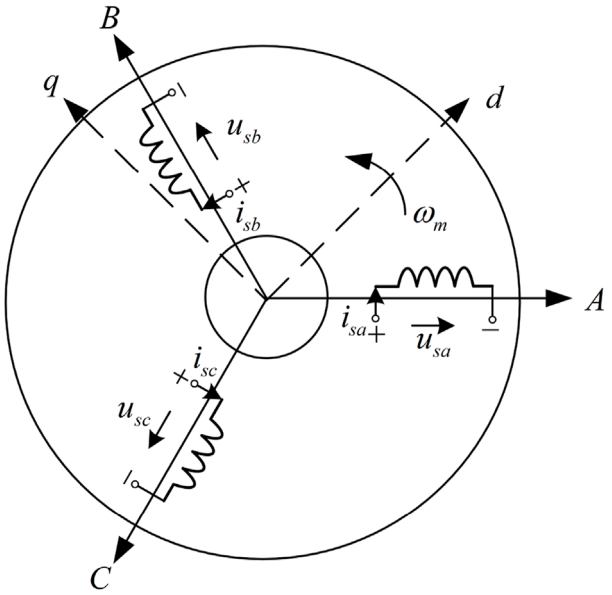

FIGURE 2
Schematic of a PMSG.

these nonlinear control methods have superior robustness to the nonlinearity and parameter uncertainty of the WPPS in contrast with linear control schemes, none of them has ever employed the maximum control energy of the converters of the permanent magnet synchronous generator (PMSG) in its control law.

In terms of improvements at the algorithmic aspect, some novel methods were used to study the stability of renewable energy generation (Chen L. et al., 2024; Liu et al., 2024). A method of combining multi-step reconfiguration with many-objective reduction is applied to deal with the power loss and load peak–valley fluctuation in distribution network (Li J. et al., 2024). Based on the neural network of dynamic recognition and auto-reservoir (Liu J. et al., 2023), the load fluctuation can be predicted. In addition, methods such as artificial intelligence and deep reinforcement learning have also been applied to study the potential of renewable power systems in terms of operation (Li et al., 2023; Li Y. et al., 2024).

Combining the advantages of linear and nonlinear control methods and exploring the potential of the already existing control system of the PMSG, bang-bang control scheme is employed here for the integral control of the PMSG to enhance the transient stability of large-scale WPPSs (Chen X. et al., 2024). The bang-bang control scheme has ever been used for the excitation control of synchronous generators in Kobayashi and Ichiyanagi (1978). The bang-bang control law is derived by solving the canonical equation of the system's Hamiltonian, which, in turn, necessitates the computation of the Hamiltonian's derivatives. Yet, the need for precise system parameters and the intricate nature of the Hamiltonian have unquestionably impeded its implementation within extensive power systems (Chen et al., 2023). A bang-bang funnel controller (BBFC) is proposed for the nonlinear system having arbitrary known relative degree (Liberzon and Trenn, 2013). Apart from the existing researches, the design of the BBFC does not require the detailed system information, and the system nonlinearity, uncertainty and the impact of external disturbances are considered (Liu et al., 2016b; Liu Y. et al., 2023). It involves logic calculation only, which facilitates its application in the computationally burdened control systems (Kang et al., 2015). Based on the advantages of inherently robust nature due to its model-free design, a LBFC of PMSG is proposed in this paper for limiting the fault current (Chen X. et al., 2024).

The contributions of the fault current limit method proposed in this paper can be summarized as follows:

- The proposed BBFC method is performed in nature coordinates with simple structure based on logical module. And it inherently robustness due to its model-free design, which brings convenience to its application.
- Benefit from the characteristics of logical switches, BBFC method has a natural advantage in fault current limiting and operates without the utilization of angular information from phase lock loop (PLL), rotational transformation.

To summarise, the paper is structured as follows. Section 2 introduces the model of PMSG and describes the type 4 wind turbine model in PSCAD. Moreover, the LBFC for fault current rejection is derived in Section 3. Comparative simulation results of the test system under the combination of LBFC and vector control alone under the disturbance of current fault scenarios are given in Section 4. Based on the results of the time-domain simulation, conclusions are drawn in Section 5, followed by the Appendix.

2 Modelling of wind turbine system

In a full-scale wind power generator, the stator of the PMSG is connected to the grid through a back-to-back converter, machine-side converter (MSC) and grid-side converter (GSC), as shown in Figure 1. During operation, changes in wind speed lead to variations in the rotor speed of the generator. The output frequency of the stator winding depends on the rotor speed. To ensure the rated frequency of the three-phase voltages and currents generated by the wind power generator, it is necessary for the MSC to convert alternating current into direct current, which is then converted back into rated frequency alternating current by the GSC, thereby achieving variable-speed constant-frequency operation. For the control aspect, vector control is used for both the MSC and GSC to achieve current decoupled control. The outer loops of MSC are active power loop and AC voltage loop. The outer loops of GSC are dc voltage loop and reactive power loop. Both sides introduced the PLL to obtain synchronous phase angle. And the switching logic can also be obtained in Figure 1. The wind turbine is a core component in the energy conversion of the full-scale wind power generator. This section models the wind power generation (WPG) system comprised of the mathematical models of the wind turbine and the PMSG.

2.1 Model of wind turbine

A wind turbine consists of several components capable of converting kinetic energy into electrical energy. The blades on the wind turbine can convert wind energy into mechanical energy,

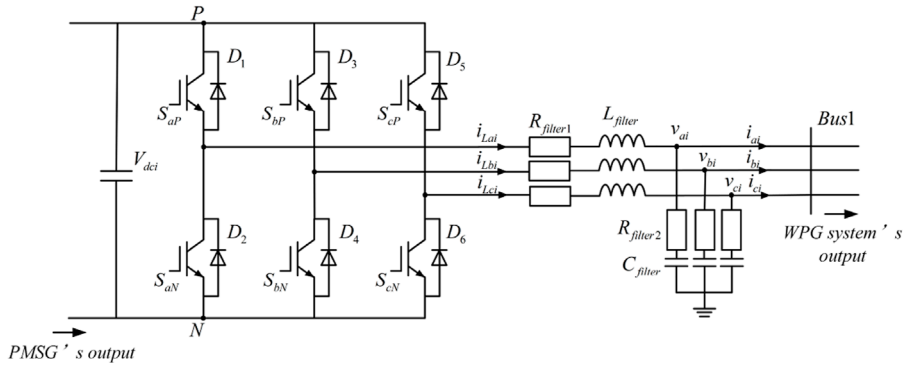

FIGURE 3
Topology of the three-phase full-bridge inverter.

TABLE 1 Parameters of WPG system.

Parameter	Value	Parameter	Value	Parameter	Value
f_{req}	60 Hz	K_{p_ω}	0.5	L_{filter1}	0.335 mH
S_{base}	200 MVA	K_{p_pitch}	10	V_{dc_base}	1.45 kV
V_{base}	33 kV	K_{i_pitch}	0.01	R_{filter2}	0 Ω
V_{source}	230 kV	$V_{\text{rated}_p\text{M}}$	0.69 kV	I_{qrefMin}	−1.5 p.u
N	100	I_{qrefMax}	1.5 p.u	x_q	1.11 p.u
R_{filter1}	1.332 Ω	I_{drefMax}	1.5 p.u	I_{drefMin}	−1.5 p.u
C_{filter1}	700 uF	ρ	$1.2kg/m^3$	v_ω	10 m/s
R	50 m	x_d	0.55 p.u	ε_0^+	0
x_{kd}	0.62 p.u	x_{kq}	1.175 p.u	φ_0^+	0.3

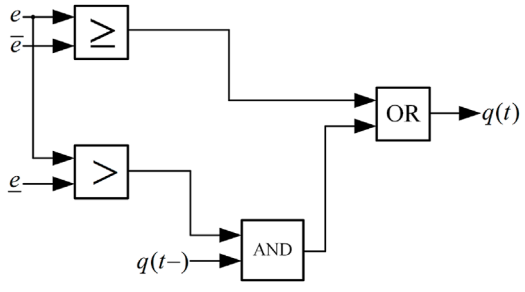

FIGURE 4
The scheme of LBFC.

which is then transmitted through the drive system to the generator, where it is further transformed into electrical energy. Therefore, the wind turbine is a primary and critical component of a WPG system, directly impacting the efficiency of wind power generation.

According to aerodynamic principles, it is possible to express the airflow power as Equation 1.

$$P_w = \frac{1}{2}\rho A v_w^3 \tag{1}$$

where ρ represents air density, under normal conditions, $\rho = 1.2kg/m^3$; A denotes swept area; v_w is wind speed.

The blades capture wind power can be expressed as Equation 2.

$$P_m = \frac{1}{2}\rho A v_w^3 C_p \tag{2}$$

where C_p denotes wind energy utilization coefficient. According to the Betz limit, the maximum theoretical value of this coefficient is 0.59. The sweep area A of the wind turbine is only related to the physical size of the wind motor, air density is equal to 0.2 generally. Under the wind speed is given, the wind energy utilization coefficient C_p determines the power obtained by wind turbine.

When the blade rotates, the ratio of the tip speed to the input wind speed is defined as the tip speed ratioλ. λ can be

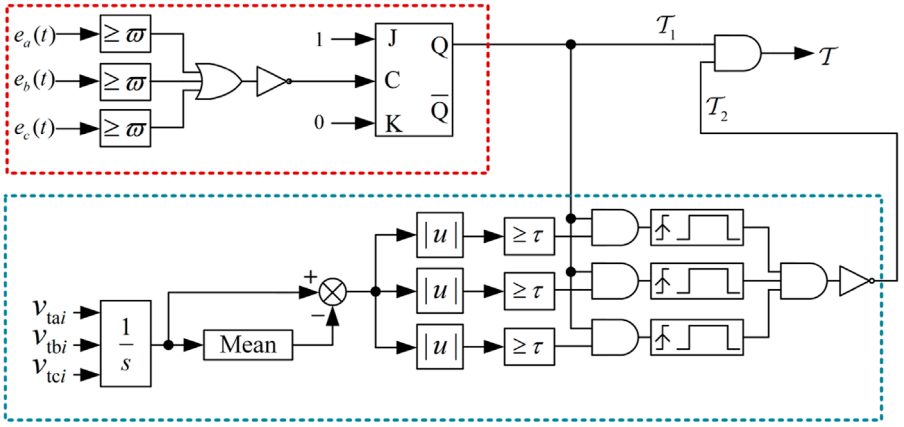

FIGURE 5
The description of the switching logic.

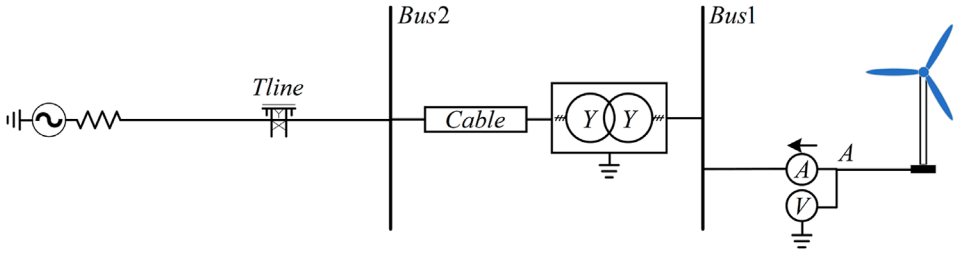

FIGURE 6
Structure of the type 4 wind turbine model.

indicated as Equation 3.

$$\lambda = \frac{\omega_m R}{v_w} \tag{3}$$

where ω_m represents the angular velocity of the blade, R represents blade radius.

For variable pitch wind turbine, C_p can be expressed as Equation 4.

$$C_p(\lambda,\beta) = 0.5176\left(\frac{116}{\lambda_i} - 0.4\beta - 5\right)e^{-\frac{21}{\lambda_i}} + 0.0068\lambda \tag{4}$$

where β represents pitch angle, λ_i is determined by Equation 5.

$$\frac{1}{\lambda_i} = \frac{1}{\lambda + 0.08\beta} - \frac{0.035}{\beta^3 + 1} \tag{5}$$

Through computing P_m, according to Equation 6, the output torque of wind turbine is obtained and inputs into the PMSG.

$$T_m = \frac{P_m}{\omega_m} \tag{6}$$

2.2 Modelling of PMSG equivalent model

PMSG uses permanent magnet material to replace the excitation winding, and the permanent magnet generates rotor excitation, which is a brushless motor. Since there is no rotor winding, its size and weight are greatly reduced, and there is no rotor winding loss.

Figure 2 shows the equivalent model of PMSG. The time domain model of PMSG in the stationary coordinate system can be represented by voltage equation, flux equation and rotor motion equation. The three-phase stator winding voltage equation can be described as Equation 7.

$$\begin{cases} u_{sa} = R_s i_{sa} + p\psi_{sa} \\ u_{sb} = R_s i_{sb} + p\psi_{sb} \\ u_{sc} = R_s i_{sc} + p\psi_{sc} \end{cases} \tag{7}$$

where u_{sa}, u_{sb}, u_{sc} represent three-phase winding phase voltage; i_{sa}, i_{sb}, i_{sc} represent three-phase winding phase current; $\psi_{sa}, \psi_{sb}, \psi_{sc}$ denote three-phase winding flux linkage; $p = \frac{d}{dt}$. Three phase winding flux equation can be written as Equation 8.

$$\begin{bmatrix} \psi_{sa} \\ \psi_{sb} \\ \psi_{sc} \end{bmatrix} = \begin{pmatrix} L_{aa} & L_{ab} & L_{ac} \\ L_{ba} & L_{bb} & L_{bc} \\ L_{ca} & L_{cb} & L_{cc} \end{pmatrix} \begin{bmatrix} i_{sa} \\ i_{sb} \\ i_{sc} \end{bmatrix} + \begin{bmatrix} \psi_{fa} \\ \psi_{fb} \\ \psi_{fc} \end{bmatrix} \tag{8}$$

where L_{aa}, L_{bb}, L_{cc} are three-phase winding inductance; $M_{ab} = M_{ba}, M_{ac} = M_{ca}, M_{bc} = M_{cb}$ denote mutual inductance between three phase windings; $\psi_{fa}, \psi_{fb}, \psi_{fc}$ denote the flux linkage between the

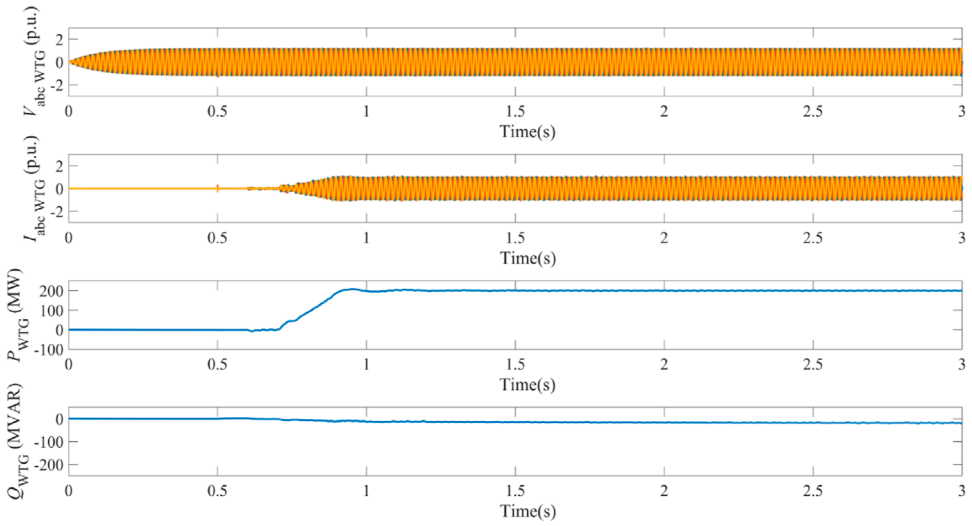

FIGURE 7
Dynamics of WPG system in steady operation.

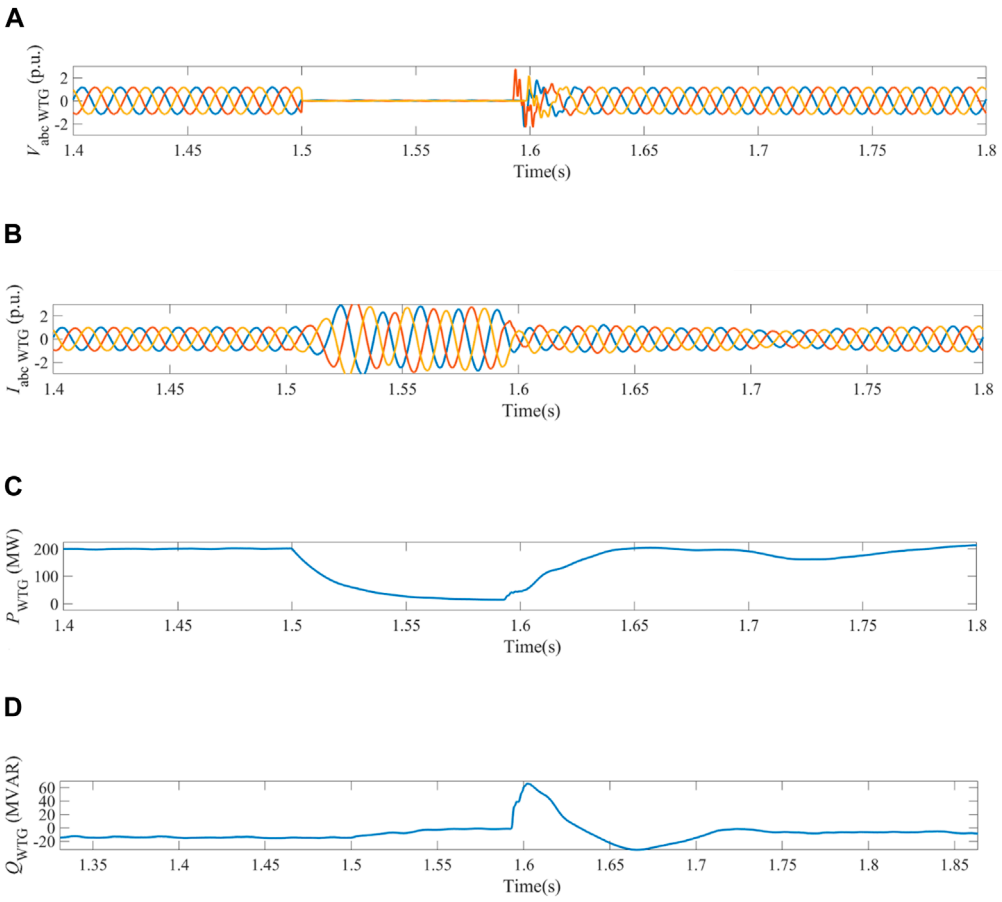

FIGURE 8
Dynamics of WPG system obtained in the case when three-phase current fault happened on bus 1 under vector control. **(A)** Three-phase voltages measured on bus 1. **(B)** Three-phase currents measured on bus 1. **(C)** Active power output of WPG system. **(D)** Reactive power output of WPG system on bus 1.

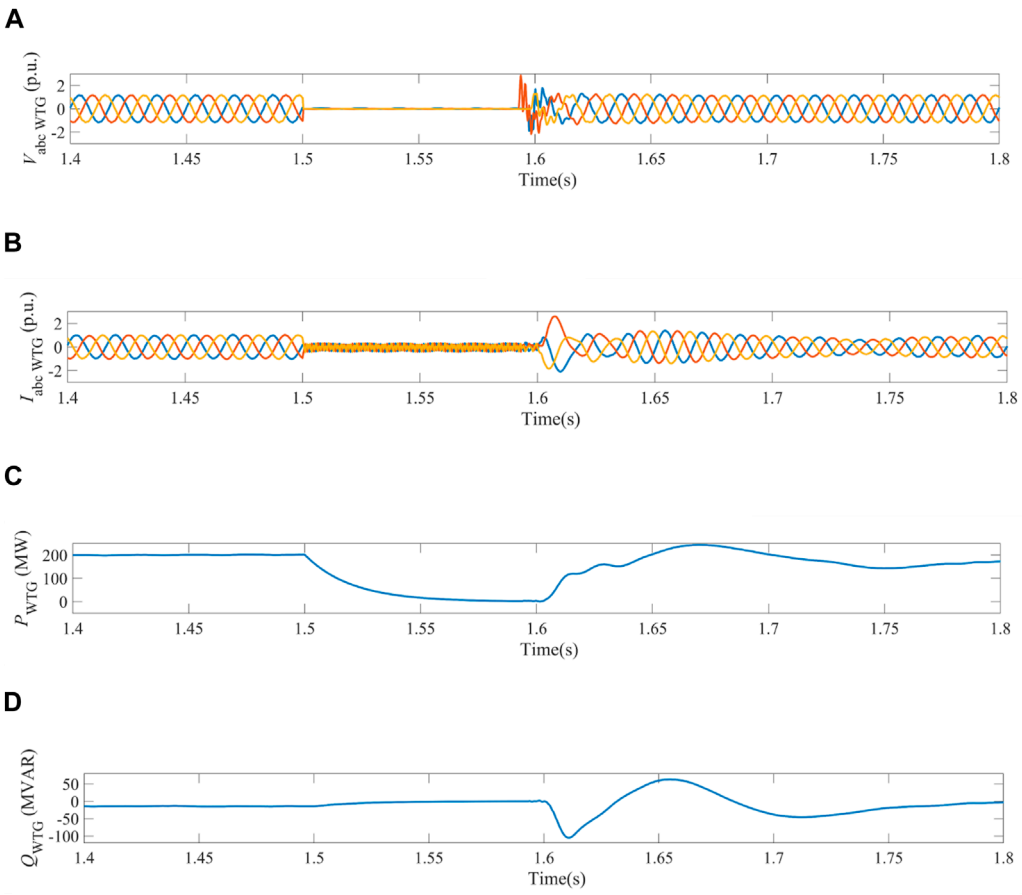

FIGURE 9
Dynamics of WPG system obtained in the case when three-phase current fault happened on bus 1 under the switching control of vector control and BBFC. **(A)** Three-phase voltages measured on bus 1. **(B)** Three-phase currents measured on bus 1. **(C)** Active power output of WPG system. **(D)** Reactive power output of WPG system on bus 1.

rotor and the stator, which can be described as Equation 9.

$$\begin{bmatrix} \psi_{fa} \\ \psi_{fb} \\ \psi_{fc} \end{bmatrix} = \psi_f \begin{bmatrix} \cos\theta \\ \cos\left(\theta - \frac{2\pi}{3}\right) \\ \cos\left(\theta + \frac{2\pi}{3}\right) \end{bmatrix} \tag{9}$$

According to the theory of permanent magnet motor, the motor motion equation can be written as Equation 10.

$$J\frac{d\omega_m}{dt} = T_e - T_m - B_m\omega_m \tag{10}$$

where T_m represents input mechanical torque, which can be acquired in (6), T_e denotes mechanical torque of PMSG; $B_m = 0$ is coefficient of rotational viscosity.

In the static coordinate system, the uneven air gap leads to the asymmetry of the fixed rotor magnetic field structure, and the projection of the rotor flux on the three-phase stator winding is related to the rotor position Angle. The mathematical model of the synchronous motor is a set of nonlinear time-varying equations related to the instantaneous position of the rotor, which is difficult to analyze and control. After Park transformation, the stator winding is equivalent to the d and q axis winding and the rotor winding are relatively stationary, so that the inductance parameters of the d and q axes become fixed, and the stator voltage, current and flux vector are all constant direct flow that is relatively stationary with the rotor. In PSCAD, the modeling of WPG system can be realized by applying coordinate transformation.

3 Fault current limiting control

3.1 Logical-based bang-bang funnel control (LBFC) design

The three-phase full-bridge inverter's topology is described in Figure 3, and all of the symbols utilized in the subsequent LBFC design process are defined in Table 1.

Obviously, the states of S_{jP} and S_{jN} are reversed, let S_{jP} serves as the working state of the switches on $j-phase$ and rewrite it as S_j^b, $S_j^b \in \{0,1\}$. Then the three-phase inverter modelling in this paper can

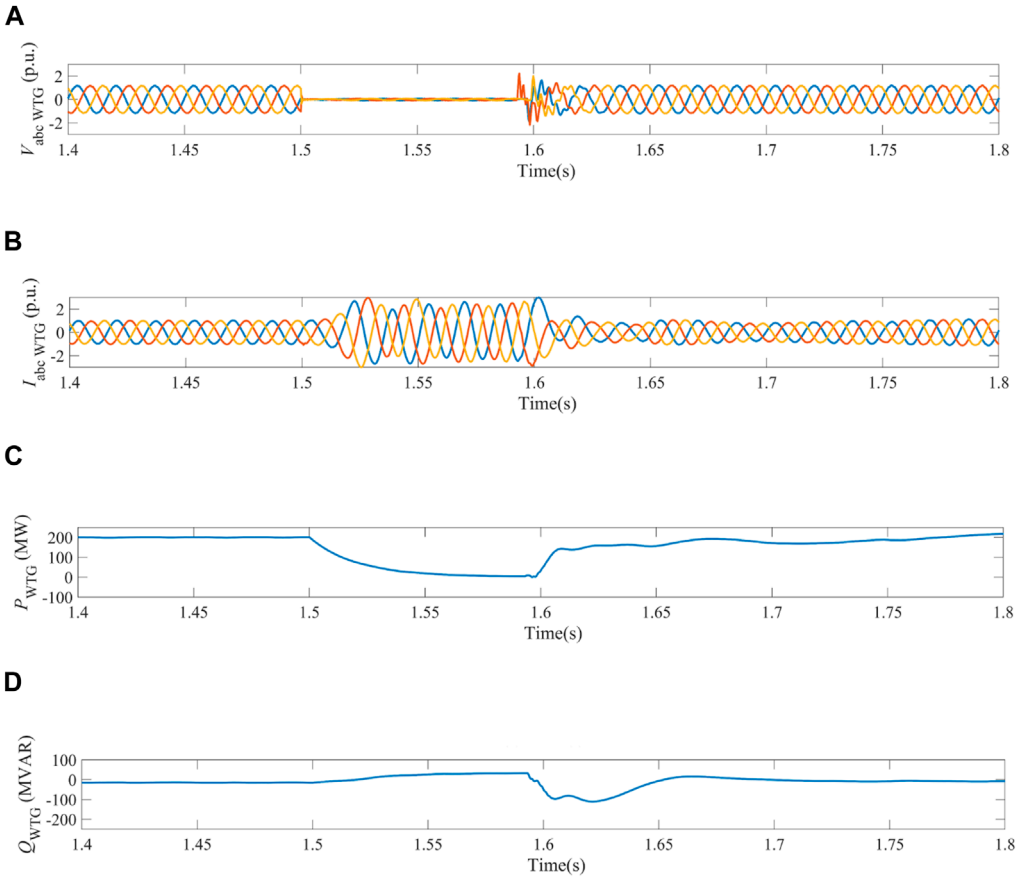

FIGURE 10
Dynamics of WPG system obtained in the case when three-phase current fault happened on bus 2 under the switching control of vector control. **(A)** Three-phase voltages measured on bus 1. **(B)** Three-phase currents measured on bus 1. **(C)** Active power output of WPG system. **(D)** Reactive power output of WPG system on bus 1.

be written as follows Equation 11.

$$\begin{cases} L_{filter} p i_{Lj} = V_{dc} S_j^b + u_{ON} - R_{filter} i_{Lj} - v_j \\ C_{filter} p u_{Cj} = i_{Lj} - i_j \\ u_{ON} = -\dfrac{V_{dc}}{3}\left(S_a^b + S_b^b + S_c^b\right) \end{cases} \tag{11}$$

where u_{ON} denotes the voltage between point O and N, u_{Cj} represents the filter capacitor voltage. The output current of the inverter would need to be controlled in this paper. As a result, the differential Equation 11 has to be stated in general linear single-input, single-output (SISO) form (Liberzon and Trenn, 2013). Then i_{Lj} is both the system's output y_j and one of the state variables, which have been set as $X_j = [i_{Lj}, u_{Cj}]$. The control variable of the system is defined as $u_j = S_j^b$. Thus the $j-phase$ system in the inverter can be given by Equations 12, 13.

$$\begin{cases} pX_j(t) = F\left(X_j\right) + G\left(X_j\right) u_j(t) \\ y_j(t) = h_j(t) \end{cases} \tag{12}$$

where

$$F\left(x_j\right) = \begin{bmatrix} -\dfrac{1}{L_{filter}}\left(R_{filter} x_1 + \dfrac{V_{dc}}{3} S_k^b + \dfrac{V_{dc}}{3} S_l^b + v_j\right) \\ \dfrac{1}{C_{filter}}\left(x_1 - i_j\right) \end{bmatrix}$$
$$G\left(x_j\right) = \begin{bmatrix} \dfrac{2V_{dc}}{3L_{filter}} \\ 0 \end{bmatrix} \tag{13}$$
$$h_j(t) = x_1(t)$$

where k and l indicate the two phases aside from $j-phase$, their operation states S_k^b and S_l^b are treated as constant variables during discussing $j-phase$ to allow the independence of logic switching control for each phase.

The order of the LBFC varies depending on the relative degree r of the system. Specifically, the relative degree of control objective $h_j(t)$ with respect to system's input $u_j(t)$ is to differentiate output $h_j(t)$ until input $u_j(t)$ explicitly appears in $h_j^r(t)$, namely, as Equation 14.

$$.h_j^{(r)}(t) = \mathcal{L}_F^r h_j(t) + \mathcal{L}_G \mathcal{L}_F^{r-1} h_j(t)\, u_j(t) \tag{14}$$

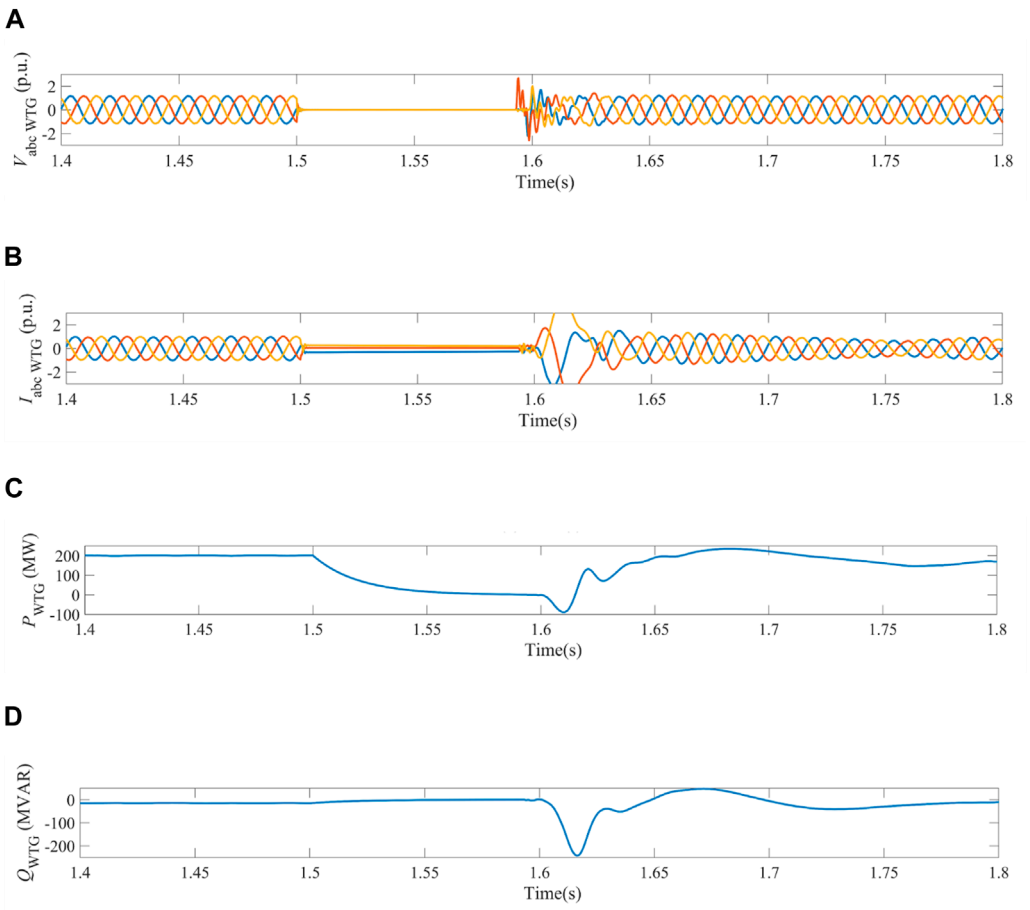

FIGURE 11
Dynamics of WPG system obtained in the case when three-phase current fault happened on bus 2 under the switching control of vector control and LBFC. **(A)** Three-phase voltages measured on bus 1. **(B)** Three-phase currents measured on bus 1. **(C)** Active power output of WPG system. **(D)** Reactive power output of WPG system on bus 1.

when $\mathcal{L}_G\mathcal{L}_F^{r-1}h_j(t) \neq 0$ holds. Thus, the approach for determining the relative degree of system (12) is shown in Equation 15.

$$\begin{aligned} h_j^{(1)}(t) &= \mathcal{L}_F h_j(t) + \mathcal{L}_G h_j(t)\, u_j(t) \\ &= -\frac{R_{filter}}{L_{filter}} x_1(t) - \frac{V_{dc}S_k^b + V_{dc}S_l^b + 3v_j}{3L_{filter}} \\ &\quad + \frac{2V_{dc}}{3L_{filter}} u_j(t) \end{aligned} \tag{15}$$

Therefore, it has $r = 1$ and the first-order LBFC would be adopted here. The switching logic of the first-order LBFC can be simply defined as Equation 16.

$$\begin{aligned} q(t) &= \mathcal{G}\left(e(t), \varphi_0^+ - \varepsilon_0^+, \varphi_0^- + \varepsilon_0^-, q(t-)\right) \\ &= \mathcal{G}\left(e(t), \bar{e}, \underline{e}, q(t-)\right) \\ &= \left[e \geq \bar{e} \vee \left(e > \underline{e} \wedge q(t-)\right)\right] \\ q(0-) &\in \{true, false\} \end{aligned} \tag{16}$$

where $q(t) \in \{true, false\}$,having $q(t-) \coloneqq lim_{\varepsilon \to 0} q(t-\varepsilon)$, is the switching logic's output deduced by the tracking error $e(t) = i_{Lji}$. The chosen funnel boundaries are shown by $\varphi_0^{\pm}$, $\varepsilon_0^{\pm}$ represent the safety distances, and the upper trigger $\bar{e}$ and lower trigger $\underline{e}$ are made up of these two. The BBFC enables to limit the fault current in the funnel through logical switching control. The funnel boundaries can be obtained by several simulation trials, combining with the limit value of current. In most instances, the value of $\varepsilon_0^{\pm}$ is set as 0. The scheme of LBFC in PSCAD can be described by Figure 4.

On the basis of $\mathcal{L}_g h_{ji}(t) = \frac{2V_{dci}}{3L_{filter}} > 0$, the control law of the LBFC designed to suppress the inverter outlet currents is given as Equation 17.

$$S_j^b(t) = \begin{cases} 0, \text{if q(t)} = \text{true} \\ 1, \text{if q(t)} = \text{false} \end{cases} \tag{17}$$

3.2 Switching strategy design

The state-dependent strategy $\mathcal{T}$, depicted in Figure 1, is the foundation upon which the switching control scheme created for the overcurrent suppression of the PMSM power system operates. It is explained in Figure 5.

Assume that following a short-circuit malfunction at the system, the absolute value of any $j-phase$ current at the inverter's outlet is $|e_j(t)|$. Then the switching strategy is stated as that the inverter bridge arm switching control switches from the GSC Control to LBFC if

$\mathcal{T}_1$ is satisfied and switches from the LBFC to the GSC Control on condition that $\mathcal{T}_2$ is satisfied, where $\mathcal{T}_1$ and $\mathcal{T}_2$ are illustrated as follows (Liu et al., 2016a):

$\mathcal{T}_1$:{$|e_j(t)| \geq \varpi$},$\mathcal{T}_2$: {The switching frequency of the control signal generated by ad LBFC reaches its maximum} $\vee$ {Signal for fault clearance, it can be $\overline{V}_{tj} > \tau$}where ϖ, τ are design parameters of the switching strategy of the system, $\overline{V}_{tj}$ is the three phase voltage of the short-circuit point.

4 Simulation verifications

PMSG power system is a part of WPG system. In order to verify the effectiveness of fault current rejection through LBFC, time domain simulations of the system considering electromagnetic transients were performed in PSCAD. In the test system, the simulation time is set to 3 s, three-phase current faults happened in 1.5 s on bus 1 and bus 2 separately, and faults were cleared after 90 ms, the type 4 wind turbine model is shown in Figure 6. At the WPG system outlet A, a multimeter is used to measure the voltage, current, active power and reactive power of the turbine output. The voltage and current are measured by unit value, and the active power and reactive power are measured by named value. The result when the system runs stably is displayed in Figure 7.

4.1 A three-phase current fault occurred on bus 1 of the WPG system at 1.5 s

On bus 1 at $t = 1.5s$, a three-phase current fault occurred. Figures 8, 9 display the dynamics of WPG system. Where the WPG system in Figure 9 is equipped with LBFC during current fault, and system in Figure 8 is only under the vector control. Due to the current fault of three-phase, the magnitudes of bus voltages dropped, and the three-phase voltages measured on bus 1 are shown in Figures 8A, 9A. Fault was cleared after 90 ms. During the current fault time, the short-circuit currents of the system without LBFC reached 3 times the nominal current value, as shown in Figure 8B.

In contrast, the switching control of vector control and LBFC had an optimizing effect on WPG system during fault time. When the short-circuit current was up to the switching criterion ϖ, the inverter bridge arm switching control was switched from the vector control to the LBFC, which in turn controlled the current the set boundary values φ_0^- to φ_0^+, as seen in Figure 9B, which represented that BBFC was able to control the fault current. Furthermore, with the magnitudes of bus voltages declined, the active power both in Figures 8C, 9C decreased. As presented in Figures 8D, 9D, WPG system's reactive power output fluctuated following the voltages' volatility when system converted from LBFC to vector control.

4.2 A three-phase current fault occurred on bus 2 of the WPG system at 1.5 s

Similarly, three-phase-to-ground fault occurred on bus 2 at 1.5*s*. The dynamics of WPG system were displayed in Figures 10, 11. When a three-phase current fault occurred at 1.5s, the three-phase voltages decreased and were close to zero during the fault time, as seen in Figures 10A, 11A. WPG system in Figure 10 utilized vector control only, while system in Figure 11 employed the switching control of vector control and LBFC. The results were the same as above content, LBFC could operate effectively, it could control the fault current of WPG system, as displayed in Figures 10B, 11B. The fault was cleared after 90 ms, when the system switched from LBFC to vector control, and voltage and current oscillations occurred during this process, which also caused active and reactive power fluctuations, as seen in Figures 10C, D and Figures 11C, D.

5 Conclusion

This paper has proposed a FCLS for the full-scale wind power generators based on LBFC. The GSC is controlled in a switched manner with the LBFC and a vector controller. When fault currents are detected, the control system of GSC switches from vector controller to LBFC, which generates independent control signals for the three-phase bridge arms.

Simulation results, obtained in the case when bus 1 and bus 2 happen three-phase-to-ground current fault on the test system, have verified that switching control in conjuction with the LBFC could enhance the dynamics of system during fault and restrain the fault current effectively. LBFC's fault current rejection avoided prolonged overcurrent, reduced the pressure on the power grid under the fault. In contrast to the original Type 4 wind turbine model in PSCAD, the switching control in conjuction with the LBFC could maintain the three-phase fault current at a low value, about 0.5 times the rated value, where 3 times the rated value without LBFC. Meanwhile, considering the simple structure and excellent ability of limiting fault current, LBFC could be applied into the area of PV system, electrochemical energy storage system and flywheel energy storage system, which helps to reduce the harm of overcurrent to the system. With the switching from LBFC to vector control after fault disappeared, the WPG system would experience an oscillation, leading to the fluctuation of voltage and current in a short time, which is also the inspiration for the future study considering the harmonic stability of the co-ordinated control of vector control and LBFC.

In terms of the difficulties of practical application, the communication delays will put forward potential challenges for the implementation of the LBFC. The sensor accuracy can also impact the performance of the LBFC, and the error of current measurement weakens the effectiveness of the controller.

Data availability statement

The raw data supporting the conclusions of this article will be made available by the authors, without undue reservation.

Author contributions

KS: Methodology, Writing–original draft. JL: Software, Writing–original draft. YZ: Validation, Writing–original

draft. HL: Writing–original draft. YL: Writing–review and editing.

Funding

The author(s) declare that no financial support was received for the research, authorship, and/or publication of this article.

Conflict of interest

Authors KS, JL, and YZ were employed by Power China Huadong Engineering Corporation Limited.

The remaining authors declare that the research was conducted in the absence of any commercial or financial relationships that could be construed as a potential conflict of interest.

Publisher's note

All claims expressed in this article are solely those of the authors and do not necessarily represent those of their affiliated organizations, or those of the publisher, the editors and the reviewers. Any product that may be evaluated in this article, or claim that may be made by its manufacturer, is not guaranteed or endorsed by the publisher.

References

Behera, M. K., and Saikia, L. C. (2022). An improved voltage and frequency control for islanded microgrid using bpf based droop control and optimal third harmonic injection pwm scheme. *IEEE Trans. Industry Appl.* 58, 2483–2496. doi:10.1109/TIA.2021.3135253

Chandorkar, M., Divan, D., and Adapa, R. (1993). Control of parallel connected inverters in standalone ac supply systems. *IEEE Trans. Industry Appl.* 29, 136–143. doi:10.1109/28.195899

Chen, L., Wen, T., Lin, Y., Liu, Y., Qin, Y., and Wu, Q.-H. (2024a). Two-stage expanding boundary algorithm to estimate domains of attraction of large-scale power systems with induction motors. *IEEE Trans. Power Syst.*, 1–13. doi:10.1109/TPWRS.2024.3413078

Chen, X., Liu, Y., Wu, Q. H., Hong, C., and Su, Y. (2024b). Direct power regulation of grid-connected voltage-source inverters based on bang-bang funnel control. *IEEE Trans. Industrial Electron.* 71, 6460–6470. doi:10.1109/TIE.2023.3306418

Chen, X., Wang, L., Liu, Y., and Wu, Q. (2023). Bang-bang funnel control of three-phase full-bridge inverter under dual-buck scheme. *IEEE Trans. Industrial Electron.* 70, 5399–5409. doi:10.1109/TIE.2022.3198247

Enslin, J. H. (2016). Power system infrastructure: do we face a complete power-electronics-based power system and energy-storage infrastructure? *IEEE Power Electron. Mag.* 3, 42–45. doi:10.1109/MPEL.2016.2551798

Guerrero, J., de Vicuna, L., Matas, J., Castilla, M., and Miret, J. (2004). A wireless controller to enhance dynamic performance of parallel inverters in distributed generation systems. *IEEE Trans. Power Electron.* 19, 1205–1213. doi:10.1109/TPEL.2004.833451

Jabr, H. M., Lu, D., and Kar, N. C. (2011). Design and implementation of neuro-fuzzy vector control for wind-driven doubly-fed induction generator. *IEEE Trans. Sustain. Energy* 2, 404–413. doi:10.1109/TSTE.2011.2160374

Kang, H., Liu, Y., Wu, Q. H., and Zhou, X. (2015). Switching excitation controller for enhancement of transient stability of multi-machine power systems. *CSEE J. Power Energy Syst.* 1, 86–93. doi:10.17775/CSEEJPES.2015.00039

Kobayashi, H., and Ichiyanagi, K. (1978). Improvement of the transient stability by optimal switching control of parallel ac-dc power systems. *IEEE Trans. Power Apparatus Syst.* PAS-97, 1140–1148. doi:10.1109/TPAS.1978.354594

Li, J., Chen, J., Wang, Y., and Chen, W. (2024a). Combining multi-step reconfiguration with many-objective reduction as iterative bi-level scheduling for stochastic distribution network. *Energy* 290, 130198. doi:10.1016/j.energy.2023.130198

Li, Y., Ding, Y., He, S., Hu, F., Duan, J., Wen, G., et al. (2024b). Artificial intelligence-based methods for renewable power system operation. *Nat. Rev. Electr. Eng.* 1, 163–179. doi:10.1038/s44287-024-00018-9

Li, Y., Fan, L., and Miao, Z. (2020). Wind in weak grids: low-frequency oscillations, subsynchronous oscillations, and torsional interactions. *IEEE Trans. Power Syst.* 35, 109–118. doi:10.1109/TPWRS.2019.2924412

Li, Y., Yu, C., Shahidehpour, M., Yang, T., Zeng, Z., and Chai, T. (2023). Deep reinforcement learning for smart grid operations: algorithms, applications, and prospects. *Proc. IEEE* 111, 1055–1096. doi:10.1109/JPROC.2023.3303358

Li, Z., Chan, K. W., Hu, J., and Guerrero, J. M. (2021). Adaptive droop control using adaptive virtual impedance for microgrids with variable pv outputs and load demands. *IEEE Trans. Industrial Electron.* 68, 9630–9640. doi:10.1109/TIE.2020.3022524

Liberzon, D., and Trenn, S. (2013). The bang-bang funnel controller for uncertain nonlinear systems with arbitrary relative degree. *IEEE Trans. Automatic Control* 58, 3126–3141. doi:10.1109/TAC.2013.2277631

Liu, J., Chen, J., Yan, G., Chen, W., and Xu, B. (2023a). Clustering and dynamic recognition based auto-reservoir neural network: a wait-and-see approach for short-term park power load forecasting. *iScience* 26, 107456. doi:10.1016/j.isci.2023.107456

Liu, X., and Kong, X. (2014). Nonlinear model predictive control for dfig-based wind power generation. *IEEE Trans. Automation Sci. Eng.* 11, 1046–1055. doi:10.1109/TASE.2013.2284066

Liu, Y., Jiang, L., Wu, Q. H., and Zhou, X. (2017). Frequency control of dfig-based wind power penetrated power systems using switching angle controller and agc. *IEEE Trans. Power Syst.* 32, 1553–1567. doi:10.1109/TPWRS.2016.2587938

Liu, Y., Lin, Z., Xu, C., and Wang, L. (2023b). Fault ride-through hybrid controller for mmc-hvdc transmission system via switching control units based on bang-bang funnel controller. *J. Mod. Power Syst. Clean Energy* 11, 599–610. doi:10.35833/MPCE.2021.000470

Liu, Y., Wu, Q. H., and Zhou, X. X. (2016a). Co-ordinated multiloop switching control of dfig for resilience enhancement of wind power penetrated power systems. *IEEE Trans. Sustain. Energy* 7, 1089–1099. doi:10.1109/TSTE.2016.2524683

Liu, Y., Wu, Q. H., and Zhou, X. X. (2016b). Coordinated switching controllers for transient stability of multi-machine power systems. *IEEE Trans. Power Syst.* 31, 3937–3949. doi:10.1109/TPWRS.2015.2495159

Liu, Y., Yao, H., Chen, Z., Pei, X., Yang, Y., and Wu, Q. H. (2024). Estimating the region of attraction of wind integrated power systems based on improved expanding interior algorithm. *IET Generation, Transm. & Distribution* 18, 2242–2257. doi:10.1049/gtd2.13201

Martinez, M. I., Tapia, G., Susperregui, A., and Camblong, H. (2012). Sliding-mode control for dfig rotor- and grid-side converters under unbalanced and harmonically distorted grid voltage. *IEEE Trans. Energy Convers.* 27, 328–339. doi:10.1109/TEC.2011.2181996

Marwali, M., Jung, J.-W., and Keyhani, A. (2004). Control of distributed generation systems - part ii: load sharing control. *IEEE Trans. Power Electron.* 19, 1551–1561. doi:10.1109/TPEL.2004.836634

Marwali, M. N., Jung, J.-W., and Keyhani, A. (2007). Stability analysis of load sharing control for distributed generation systems. *IEEE Trans. Energy Convers.* 22, 737–745. doi:10.1109/TEC.2006.881397

Silva, G. F., Donaire, A., Seron, M. M., McFadyen, A., and Ford, J. (2022). String stability in microgrids using frequency controlled inverter chains. *IEEE Control Syst. Lett.* 6, 1484–1489. doi:10.1109/LCSYS.2021.3114143

Wang, Y., Chen, J., Zhao, Y., and Xu, B. (2024). Incorporate robust optimization and demand defense for optimal planning of shared rental energy storage in multi-user industrial park. *Energy* 301, 131721. doi:10.1016/j.energy.2024.131721

Wang, Y., Meng, J., Zhang, X., and Xu, L. (2015). Control of pmsg-based wind turbines for system inertial response and power oscillation damping. *IEEE Trans. Sustain. Energy* 6, 565–574. doi:10.1109/TSTE.2015.2394363

Wu, Q.-H., Bose, A., Singh, C., Chow, J. H., Mu, G., Sun, Y., et al. (2023). Control and stability of large-scale power system with highly distributed renewable energy generation: viewpoints from six aspects. *CSEE J. Power Energy Syst.* 9, 8–14. doi:10.17775/CSEEJPES.2022.08740

frontiers | Frontiers in Energy Research

TYPE Original Research
PUBLISHED 25 September 2024
DOI 10.3389/fenrg.2024.1485135

OPEN ACCESS

EDITED BY
Minghao Wang,
University of Macau, China

REVIEWED BY
Xu Xu,
Xi'an Jiaotong-Liverpool University, China
Jiapeng Li,
Xi'an Jiaotong University, China

*CORRESPONDENCE
Mengwei Zhang,
2464152664@hnu.edu.cn

RECEIVED 23 August 2024
ACCEPTED 13 September 2024
PUBLISHED 25 September 2024

CITATION
Sun P, Zhang M, Liu H, Dai Y and Rao Q (2024) Coordinated scheduling of 5G base station energy storage for voltage regulation in distribution networks.
Front. Energy Res. 12:1485135.
doi: 10.3389/fenrg.2024.1485135

Coordinated scheduling of 5G base station energy storage for voltage regulation in distribution networks

Peng Sun, Mengwei Zhang*, Hengxi Liu, Yimin Dai and Qian Rao

College of Electrical and Information Engineering, Hunan University, Changsha, China

With the rapid development of 5G base station construction, significant energy storage is installed to ensure stable communication. However, these storage resources often remain idle, leading to inefficiency. To enhance the utilization of base station energy storage (BSES), this paper proposes a co-regulation method for distribution network (DN) voltage control, enabling BSES participation in grid interactions. In this paper, firstly, an energy consumption prediction model based on long and short-term memory neural network (LSTM) is established to accurately predict the daily load changes of base stations. Secondly, a BSES aggregation model is constructed by using the power feasible domain maximal inner approximation method and Minkowski summation to evaluate the charging and discharging potential and adjustable capacity of BSES clusters. Subsequently, a BSES demand assessment and optimal scheduling model for low voltage regulation in DN is developed. This model optimizes the charging and discharging strategies of BSES to alleviate low voltage problems in DN. Finally, the simulation results effectively verify the feasibility of the proposed optimal scheduling method of BSES for voltage regulation in DN.

KEYWORDS

5G base station energy storage, aggregation, distribution network, voltage regulation, optimal scheduling

1 Introduction

In recent years, advancements in new energy technologies have progressed rapidly, and the proportion of new energy sources such as wind energy and solar energy has been increasing. The landscape of large-scale new energy consumption remains unclear, necessitating urgent adjustments in flexible resource allocation. As the best flexible resource, energy storage can control the input and output of power and energy at different time scales, thereby improving the stability and operation characteristics of high-proportion new energy power systems, promoting flexible dispatching of power grids, and solving the adverse effects of large-scale grid-connected clean energy. However, its widespread adoption is impeded by high costs. Meanwhile, China has clearly proposed to speed up the development of new infrastructure. Operators of 5G base stations have invested in constructing numerous communication facilities and configured extensive energy storage batteries to ensure the stability and reliability of communication. However, the growing strength and stability of the distribution system have significantly enhanced the energy supply reliability of 5G base stations, making the redundant 5G BSES devices idle for a long time. Therefore, considering the unique backup

power supply requirements of energy storage resources at communication base stations, it is urgent to investigate the influence of the communication load characteristics on the backup power demand and deeply explore the schedulable potential of the backup energy storage. This will enable the efficient utilization of idle resources at 5G base stations in the collaborative interaction of the power system, fostering mutual benefit and win-win between the power grid and the communication operators.

The research on 5G base station load forecasting technology can provide base station operators with a reasonable arrangement of energy supply guidance, and realize the energy saving and emission reduction of 5G base stations. Currently, the research primarily focuses on statistical learning methods and machine learning techniques (Shang et al., 2022). In (Morosi et al., 2013), the exponential smoothing technique is used to predict the traffic in all coverage areas of the base station. In (Pan et al., 2015), a Block Regression (BR) model for base station traffic prediction considering the time correlation of base station load is proposed. Although the proposed model boasts low complexity and the mathematical formula is clear and easy to understand, it suffers from poor scalability as it constructs only a single model for all base stations. Moreover, the prediction results using these statistical learning models are not satisfactory when dealing with long-term problems, especially when predicting violently fluctuating base station network traffic data (Cheng et al., 2023). For the machine learning load forecasting model, a neural network load forecasting training method based on the maximum correntropy criterion (NTPMCC) is proposed in (Qu et al., 2013). This method takes into account the nonlinear characteristics of network load, but the overall improvement in prediction accuracy is moderate. Reference (Qu et al., 2019) introduces a base station load forecasting model that leverages spatio-temporal characteristics. To achieve this, a clustering algorithm based on artificial neural networks is employed to establish specific models for various types of base stations. Additionally, in reference (Stolojescu-Crisan, 2012), the Stationary Wavelet Transform (SWT) method is introduced during the data preprocessing stage. This method is combined with the Auto-Regressive Integrated Moving Average (ARIMA) model and Artificial Neural Networks (ANNs) to accomplish the load forecasting tasks. While the above-mentioned base station load forecasting method cannot shield the interference caused by the drastic fluctuation of 5G base station load data, which leads to a large static error in the prediction results, so there is an urgent need to study a more efficient and applicable base station load prediction method to effectively improve the base station load prediction accuracy.

Addressing the efficient utilization of flexible resources in 5G base stations, literature (Ye, 2021; Yin et al., 2022) proposes installing photovoltaic systems to enhance energy storage capabilities. However, for the existing 5G base stations that have been completed, the measure of reinstalling photovoltaic devices is difficult to implement. Several scholars have proposed a dynamic clustering method of energy storage utilizing virtual power plant technology to address the challenge that the energy storage of communication base stations with a large number and wide distribution is difficult to schedule (Suo et al., 2022; Yang et al., 2020). Nevertheless, the energy storage model is too simplified, and the spatial and temporal differences between BSES are ignored in order to improve the solution efficiency. Other studies have deeply explored the adjustable capacity of energy storage, and proposed energy storage resource aggregation optimization methods (Yang et al., 2023; Yu et al., 2023). Reference (Sajjad et al., 2016) pointed out that the idea of describing the feasible region of energy storage resource cluster operation can be divided into two kinds: top-down and bottom-up. Among them, top-down refers to the direct construction of the feasible region of cluster operation through data analysis and probabilistic modeling. From bottom to top, it refers to describing the feasible domain of a single resource first, and then aggregating multiple independent operating domains into a unified whole. Following a top-down approach, reference (Sajjad et al., 2016) estimates the flexibility level according to the probability of changing the collective behavior of aggregated users. Reference (Ma et al., 2013) developed a flexibility standard based on reinforcement learning methods to distinguish different load types, thereby assessing the total adjustment potential of resources. The current mainstream research tends to be bottom-up, considering the shortcomings of complexity, uncertainty, high computational cost and poor interpretability in constructing feasible regions directly through data analysis and probabilistic modeling. Following a bottom-up approach, reference (Müller et al., 2019) pointed out that the flexibility of each resource is mathematically regarded as a feasible region bounded by polytope, and the essence of the flexibility aggregation problem is the Minkowski sum of polytope provided by all flexible resources. However, the above method is not feasible in practical solution. As the dimension of the polyhedron increases, both the number of vertices and the permutations and combinations grow exponentially. This results in a phenomenon known as dimension explosion (Barot and Taylor, 2017; Althoff et al., 2010), significantly escalating the computational complexity of Minkowski summation. In (Müller et al., 2019), the zonotope set was proposed to aggregate distributed resource flexibility. The internal approximation method of the power feasible region ensures the feasibility of the model solution, but it also entails varying degrees of flexibility loss. The above research focuses on aggregating multiple flexible resources in the power system, but does not systematically investigate aggregation methods as backup resources for BSES. Therefore, it is necessary to thoroughly consider the characteristics of the standby power supply of the BSES resources, conduct in-depth research on its dynamic aggregation method, and quantitatively evaluate the power adjustment ability of the BSES cluster.

Research on 5G BSES in the power system focuses on integrating with the operation and dispatching of the DN (Li et al., 2022). The primary objective is to support the DN in integrating new energy consumption (Liang et al., 2023), peak shaving, valley filling (Yang et al., 2023), and optimizing economic dispatching (Chai et al., 2014). In (Jia et al., 2023), research focuses on mobile energy storage technology aimed at enhancing the consumption of distributed energy within station areas, which improves the consumption rate of new energy and ensures the stable and reliable operation of the DN in the station area. Reference (Zhang et al., 2023) proposed a model to optimize the energy storage configuration of 5G base stations. The objective is to alleviate the pressure of peak load on the power grid by minimizing the total investment over the battery system's entire lifecycle. Reference (Han et al., 2021) proposed a Stackelberg game collaborative optimization method for DN and 5G mobile network based on demand response. The DN operator (DNO) acts as the leader, selecting an optimal interactive electricity price to reduce peak-valley differences in net load. The mobile network operator (MNO), as a follower, adjusts its energy costs by responding to the electricity price set by the DNO. In (Zhou and Xu, 2021), the mobile BSES system is

used to provide local reactive power support. A day-ahead reactive power scheduling model is proposed, considering the system and the conventional reactive power compensation device, aimed at minimizing the node voltage deviation in the active DN. The above research works have established methods for BSES to participate in DN optimization and dispatch from different perspectives, but there is a lack of research related to making full use of BSES resources to participate in voltage regulation of DNs.

In summary, the existing research on 5G BSES lacks a BSES co-regulation method based on aggregation technology for voltage regulation of DNs. Therefore, in order to fill the above research gaps, this paper firstly proposes a BSES aggregation model taking into account the base station energy consumption prediction, and then proposes a BSES co-regulation method for the voltage regulation of base stations in distribution grids, which makes full use of the large amount of idle energy storage resources in 5G base stations and realizes the mutual benefits of telecommunication operators and power grids. The main contributions of this paper are as follows.

- The specific composition of 5G base station energy consumption is analysed, and a 5G base station energy consumption prediction model based on long short-term memory (LSTM) is constructed.
- Considering the power supply characteristics of BSES backup supply, we constructed a BSES aggregation model taking into account the energy consumption prediction of 5G base stations, and quantitatively evaluated the maximum adjustable capacity and charging/discharging potential of BSES.
- A BSES co-regulation method based on BSES aggregation technology for voltage regulation of DNs is proposed to quantitatively assess the minimum energy storage regulation capacity required for voltage regulation of DNs and optimize the charging and discharging strategy of each BSES based on the balanced charge state scheduling method of energy storage.

The rest of this paper is organized as follows: In Section 2, it proposes a method for predicting 5G base station energy consumption using LSTM and constructs a BSES aggregation model considering this prediction. In Section 3, it proposes a coordinated control method of BSES for low voltage governance of DN based on BSES aggregation technology. In Section 4, simulations are performed on a real distribution network test system. The conclusion is put forward in Section 5.

2 BSES aggregation method considering energy consumption prediction

2.1 5G base station energy consumption analysis and prediction model

2.1.1 5G base station energy consumption model

To meet the communication requirements of large capacity and low delay, the commissioning of new equipment has significantly improved the performance of 5G base stations compared with the previous generation base stations. At the same time, the new equipment has altered the power load characteristics of base stations. In the 5G technology framework, the 5G base station comprises macro and micro variants. The micro base station serves indoor blind spots with minimal power consumption. The macro base station exhibits greater potential for demand response. This section primarily analyzes the current mainstream commercial 5G macro base stations.

The load of a 5G base station primarily consists of communication equipment and auxiliary components. The communication equipment mainly includes Active Antenna Unit (AAU) and Base Band Unit (BBU). AAU is a combination of radio frequency unit and antenna array of 5G base station. Its main functions include converting baseband digital signal into analog signal, modulating it into high frequency radio frequency signal, and then amplifying it to enough power to be transmitted through the antenna. AAU is the most energy-consuming equipment in 5G base stations, accounting for up to 90% of their total energy consumption. Auxiliary equipment includes power supply equipment, monitoring and lighting equipment. The power supply equipment manages the distribution and conversion of electrical energy among equipment within the 5G base station. During main power failures, the energy storage device provides emergency power for the communication equipment.

A set of 5G base station main communication equipment is generally composed of a baseband BBU unit and multiple RF AAU units. Equation 1 serves as the base station load model:

$$P_{BS} = P_{\text{main}} + P_{\text{static}} \tag{1}$$

where P_{BS} is base station load; P_{main} is the base station main equipment load power and $P_{\text{main}} = P_{\text{BBU}} + n \cdot P_{\text{AAU}}$, P_{BBU} is the baseband unit power, n is the number of active antenna elements, P_{AAU} is the active antenna unit power and its size is mainly related to the base station communication load; P_{static} is the base station auxiliary equipment load power, including the base station environment equipment, transmission equipment and monitoring equipment load power, and the power remains constant.

The load change of base station mainly depends on the communication behavior of users, exhibiting significant time correlation and random fluctuations. As a special deep recurrent neural network, the LSTM network can basically smooth the interference caused by fluctuation to the training model, making it suitable for base station energy consumption prediction with large fluctuations in time series data.

2.1.2 LSTM-based energy consumption prediction model for 5G base stations

The LSTM model is an advanced extension of the Recurrent Neural Network (RNN) model, specifically designed to handle sequence data. It addresses the long-term dependency problem, enabling it to better capture long-term dependencies in sequence data. This allows the model to effectively learn patterns and features in temporal data.

According to the energy consumption characteristics of the base station, a 5G base station energy consumption prediction model based on the LSTM network is constructed to provide data support for the subsequent BSES aggregation and collaborative scheduling. The prediction flow chart is shown in Figure 1, and the specific prediction process is as follows.

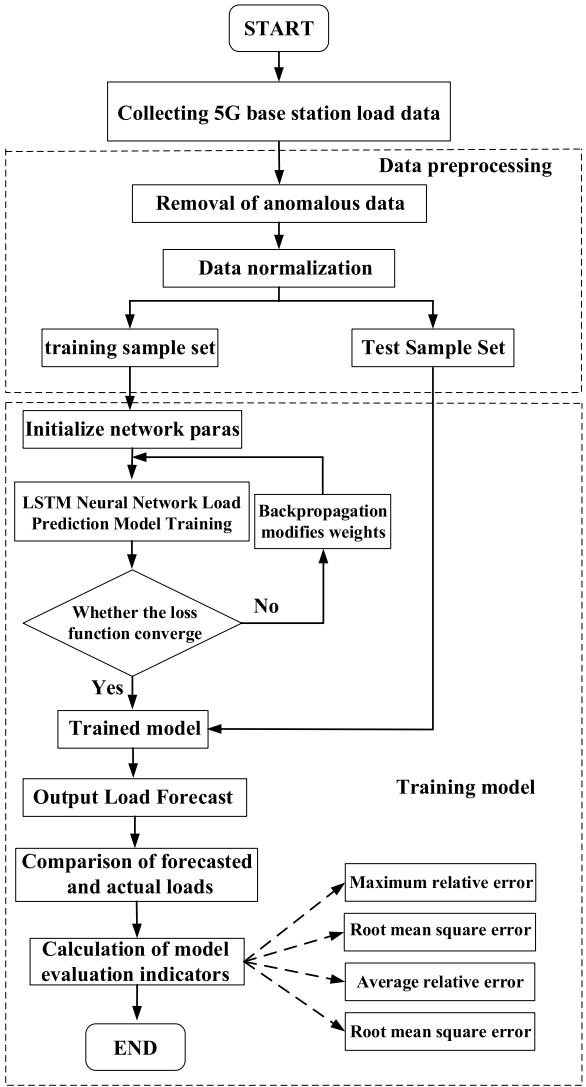

FIGURE 1
Flowchart of 5G base station load prediction based on LSTM.

Step (1) The data is collected and preprocessed. After deleting the abnormal data, the data is normalized according to Equation 2. Then, the processed data set is divided into training set and test set according to a certain proportion.

$$P_{bs} = \frac{P - P_{min}}{P_{max} - P_{min}} \tag{2}$$

where P_{bs} is the normalized historical input data; P is the historical input data before normalization; P_{min} is the minimum value of the historical input data before normalization; P_{max} is the maximum value of the historical input data before normalization.

Step (2) The LSTM model is created and the training set sample data is imported into the LSTM load forecasting model for training. The specific LSTM model principle can be referenced in (Fu, 2020).

Step (3) The test set sample data is imported into the trained model for 5G base station load forecasting, and compared with the actual 5G base station load to calculate the evaluation index of the model. The root mean square error e_{RTS}, average relative error e_{AR}, maximum relative error e_{MR} and relative error e_R are used as the evaluation indexes of prediction effect. The calculation formula is as Equations 3–6:

$$e_{RTS} = \sqrt{\frac{1}{n}\sum_{i=1}^{n}(y_i - \hat{y}_i)^2} \tag{3}$$

$$e_{AR} = \frac{1}{n}\sum_{i=1}^{n}\left|\frac{y_i - \hat{y}_i}{y_i}\right| \tag{4}$$

$$e_{MR} = \max\left(\left|\frac{y_i - \hat{y}_i}{y_i}\right|\right) \tag{5}$$

$$e_R = \left|\frac{y_i - \hat{y}_i}{y_i}\right| \tag{6}$$

where y_i is the actual load value; $\hat{y}_i$ is the load prediction value; n is the number of data sets.

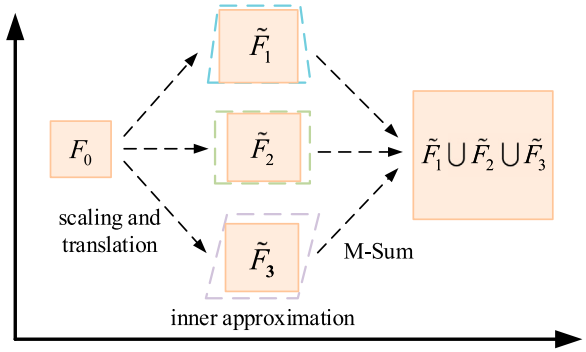

FIGURE 2
The principle of the maximum inner approximation method in the feasible domain of aggregation power.

2.2 BSES aggregation method

2.2.1 Operational model of individual BSES

The feasible domain of a single BSES power can be described as:

$$F_j = \left\{ \mathbf{p}_j^{ES} \in \mathbb{R}^T \left| \begin{array}{c} E_{j,t}^{ES} = \delta_j E_{j,t-1}^{ES} + p_{j,t}^{ES}\Delta t, \forall t \in \tau \\ -p_{j,t}^{ES,-} \le p_{j,t}^{ES} \le p_{j,t}^{ES,+}, \forall t \in \tau \\ E_{j,t}^{ES,-} \le E_{j,t}^{ES} \le E_{j,t}^{ES,+}, \forall t \in \tau \end{array} \right. \right\} \tag{7}$$

where $\mathbf{p}_j^{ES}$ is the output power of the BSES j at each moment in the time period T, while $\mathbf{p}_j^{ES} = [p_{j,1}^{ES}, p_{j,2}^{ES}, \cdots, p_{j,T}^{ES}]$; $E_{j,t}^{ES}$ is the battery residual energy state of the BSES j at time t; δ_j is the self-discharge efficiency of the BSES j; $p_{j,t}^{ES}$ is the input power of the BSES j at time t, $p_{j,t}^{ES} > 0$ indicates charging, $p_{j,t}^{ES} < 0$ indicates discharging,; is charging/discharging intervals for BSES j; $\tau = \{1, 2, \cdots, T\}$, denotes a moment in time T; $p_{j,t}^{ES,-}$ is the maximum discharge power of the BSES j; $p_{j,t}^{ES,+}$ is the maximum charge power of the BSES j; $E_{j,t}^{ES,-}$ is the value of the minimum energy state allowed for the BSES j at time t, with respect to the load size and minimum supply time at time t, $E_{j,t}^{ES,-} = t_{\min}^{d} P_t^d$, P_t^d is the predicted power of the base station energy consumption at time t, is the minimum power supply

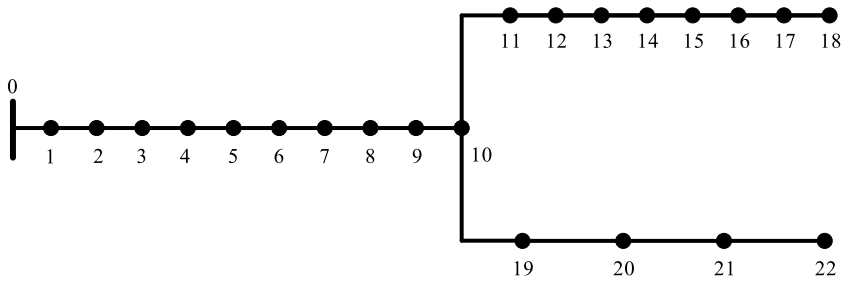

FIGURE 3
Topology of 22-node distribution network system.

TABLE 1 Line parameters.

Line	Length (km)	Resistance (Ω/km)	Reactance (Ω/km)	Current capacity (A)
0–10	13.173	0.13	0.358	503
10–16	4.176	0.91	0.38	90
16–18	1.364	0.91	0.38	90
10–20	4.266	0.91	0.38	90
20–22	4.635	0.91	0.38	90

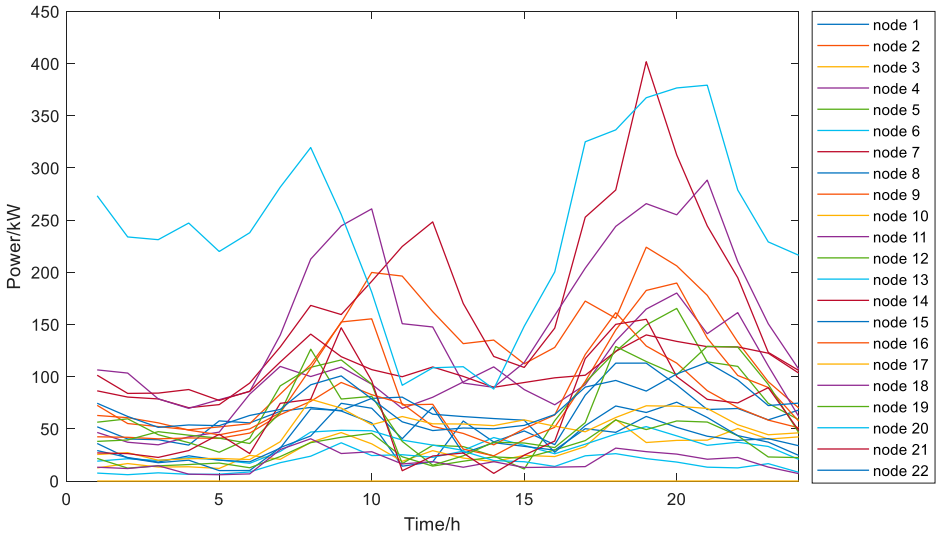

FIGURE 4
Load curve of each node.

time of the base station load, and the general minimum power supply time is 3 h; and $E_{j,t}^{ES,+}$ is the maximum energy state value of the BSES j allowed at time t.

To facilitate the derivation of the subsequent equations, Equation 7 can be written in the following compact form, as illustrated in Equation 8.

$$F_j = \left\{ \mathbf{p}_j^{ES} \in \mathbb{R}^T \middle| \mathbf{M}_j \mathbf{p}_j^{ES} \le \mathbf{N}_j \right\} \tag{8}$$

where $\mathbf{M}_j$, $\mathbf{N}_j$ are expressed as Equations 9, 10, respectively:

$$\mathbf{M}_j = \left(diag(\mathbf{I}); diag(-\mathbf{I}); \mathbf{A}_j^{-1}\mathbf{B}_j; -\mathbf{A}_j^{-1}\mathbf{B}_j \right) \tag{9}$$

$$\mathbf{N}_j = \left(\mathbf{p}_j^{ES,+}; \mathbf{p}_j^{ES,-}; \mathbf{E}_j^{ES,+} - \mathbf{A}_j^{-1}\mathbf{C}_j; -\mathbf{E}_j^{ES,-} + \mathbf{A}_j^{-1}\mathbf{C}_j \right) \tag{10}$$

where $\mathbf{I} = [1, 1, \cdots, 1]^T \in \mathbb{R}^{T\times 1}$, where $\mathbf{p}_j^{ES,+}$, $\mathbf{p}_j^{ES,-}$, $\mathbf{E}_j^{ES,+}$, $\mathbf{E}_j^{ES,-} \in \mathbb{R}^{T\times 1}$, represent maximum charging power vector, the maximum discharging vector, the maximum energy state vector and the minimum energy state vector of the BSES j in T period, respectively. $\mathbf{A}_j$, $\mathbf{B}_j$, $\mathbf{C}_j$ are expressed as Equations 11-13, respectively:

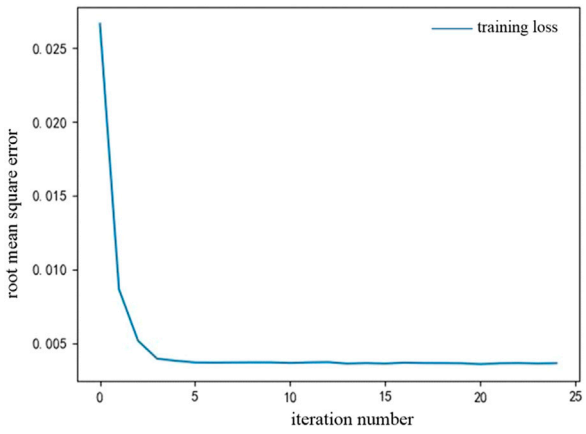

FIGURE 5
Convergence of training set error for 5G base station energy consumption prediction.

$$\mathbf{A}_j = \begin{bmatrix} 1 & 0 & 0 & \cdots & 0 \\ -\delta_j & 1 & 0 & \cdots & 0 \\ 0 & -\delta_j & 1 & \cdots & 0 \\ \vdots & \vdots & \vdots & \ddots & \vdots \\ 0 & 0 & 0 & \cdots & 1 \end{bmatrix} \tag{11}$$

$$\mathbf{B}_j = diag(\mathbf{I})\Delta t \tag{12}$$

$$\mathbf{C}_j = \left[\delta_j E_{j,0}^{ES}, 0, 0\cdots, 0\right]^T \tag{13}$$

where $\mathbf{A}_j, \mathbf{B}_j \in \mathbb{R}^{T\times T}$, $\mathbf{C}_j \in \mathbb{R}^{T\times 1}$. δ_j is the self-discharge efficiency of the BSES j. $E_{j,0}^{ES}$ is the initial capacity state of energy storage.

2.2.2 BSES aggregation model

To reduce decision-making complexity at the distribution network operator level, BSES aggregators need to aggregate the operational feasible regions of all BSES units to form the operational feasible region of the BSES cluster. The aggregated operational feasible region represents the adjustable range of the flexible resources when all BSES units are simultaneously controlled. The mathematical essence of the feasible region aggregation problem is the Minkowski sum (M-Sum). The aggregation calculation process is as follows.

The expression for the aggregated power when the number of BSES units is N is presented in Equation 14.

$$p_{i,t}^{agg} = \sum_{j=1}^{N} p_{j,t}^{ES}, \forall t \in \tau \tag{14}$$

The aggregated feasible domain F can be expressed as Equation 15:

$$F = \bigcup_{j\in\mathcal{N}} F_j \tag{15}$$

where $\cup$ is denoted as Minkowski summation; $\mathcal{N}: = [1, 2, \cdots N]$.

However, when the number of energy storage units in the base station is high, the number of sets and dimensions involved in the operation increases, and the planes describing the boundary of the feasible domain increase exponentially, which leads to the difficulty of the Minkowski summation and makes the solution of its aggregated power feasible domain non-computable. Therefore, in order to reduce the computational complexity, this paper adopts an aggregated power feasible domain maximal inner approximation method (Zhao et al., 2017), whose principle schematic is shown in Figure 2.

The feasible region aggregation problem is characterized by large computational scale and strong temporal coupling. The exact feasible region of the aggregate is often difficult to compute and typically requires approximation of the feasible region for individual objects first. Initially, a basic power feasible region F_0 is selected and subjected to scaling and translation to fit the power feasible regions of each BSES unit. Then, the Minkowski sum is performed. This method effectively addresses the computational complexity of the aggregated feasible region. The fitted power feasible region is represented as Equation 16:

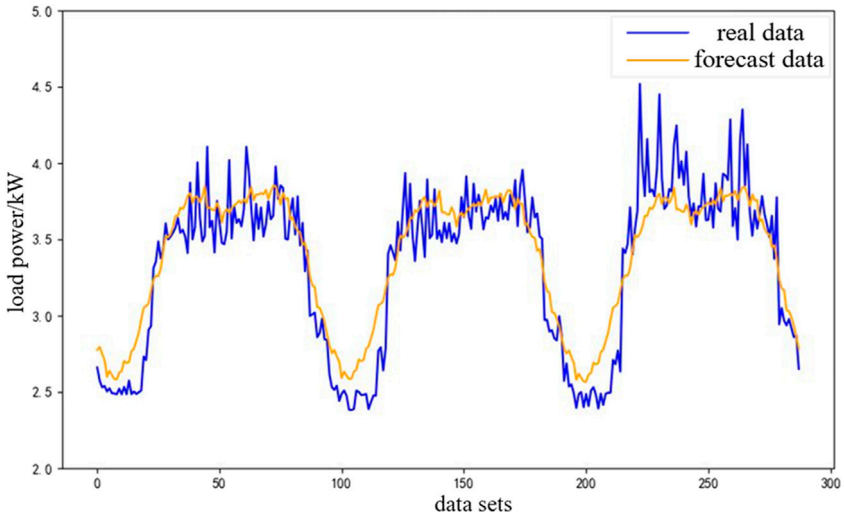

FIGURE 6
5G base station load forecast for three consecutive days.

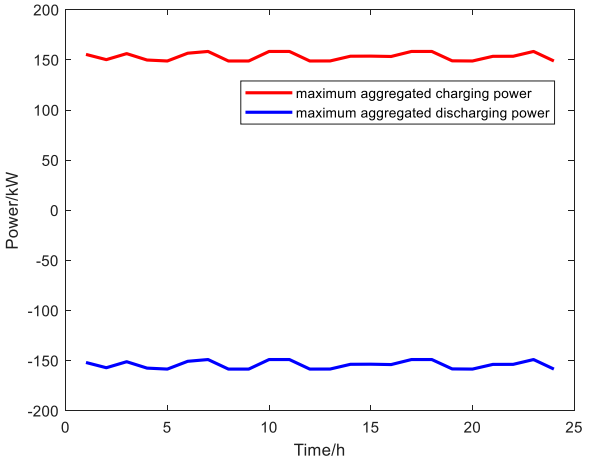

FIGURE 7
Charging and discharging potential of aggregated energy storage for 10 base stations over 24 time periods.

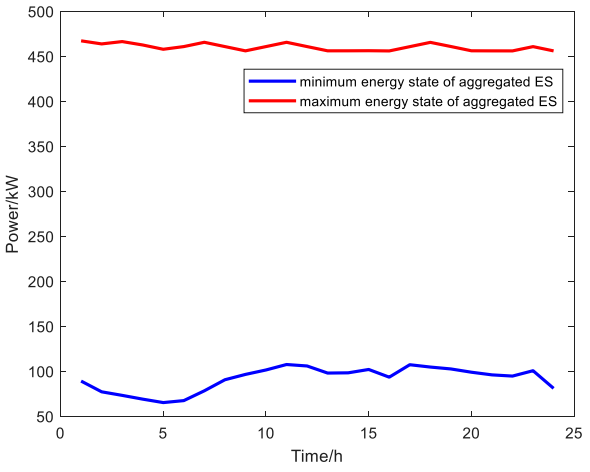

FIGURE 8
Energy state boundaries of aggregated energy storage for 10 base stations over 24 time periods.

$$\varphi_j F_0 + \boldsymbol{\mu}_j = \left\{ y_j \middle| y_j = \varphi_j \xi + \boldsymbol{\mu}_j, \forall \xi \in F_0 \right\} \tag{16}$$

where φ_j is the scaling factor; $\boldsymbol{\mu}_j$ is the translation factor, $\boldsymbol{\mu}_j \in \mathbb{R}^T$, $\mathbb{R}^T$ denotes the T-dimensional real number space; y_j denotes the power feasible domain of the BSES at each moment; ξ denotes the baseline power feasible domain at each moment.

The expression of F_0 is as follows:

$$F_0 = \left\{ \mathbf{p}_0^{ES} \in \mathbb{R}^T \middle| \begin{array}{c} E_{0,t}^{ES} = \hat{\delta} E_{0,t-1}^{ES} + p_{0,t}^{ES} \Delta t, \forall t \in \tau \\ -\hat{P}_{0,t}^{ES,-} \le p_{0,t}^{ES} \le \hat{P}_{0,t}^{ES,+}, \forall t \in \tau \\ \hat{E}_{0,t}^{ES,-} \le E_{0,t}^{ES} \le \hat{E}_{0,t}^{ES,+}, \forall t \in \tau \end{array} \right\} \tag{17}$$

where $\hat{\delta}$, $\hat{p}_{0,t}^{ES,-}$, $\hat{p}_{0,t}^{ES,+}$, $\hat{E}_{0,t}^{ES,-}$, $\hat{E}_{0,t}^{ES,+}$ are the average values of the corresponding parameters for all BSES.

Equation 17 can be written in a compact form, as show in Equation 18:

$$F_0 = \left\{ \mathbf{p}_0^{ES} \in \mathbb{R}^T \middle| \mathbf{M}_0 \mathbf{p}_0^{ES} \le \mathbf{N}_0 \right\} \tag{18}$$

where M_0 and $\mathbf{N}_0$ are expressed as Equations 19, 20, respectively:

$$\mathbf{M}_0 = \left(diag(\mathbf{I}); diag(-\mathbf{I}); \mathbf{A}_0^{-1}\mathbf{B}_0; -\mathbf{A}_0^{-1}\mathbf{B}_0 \right) \tag{19}$$

$$\mathbf{N}_0 = \left(\hat{\mathbf{p}}_0^{ES,+}; \hat{\mathbf{p}}_0^{ES,-}; \hat{\mathbf{E}}_{0,t}^{ES,+} - \mathbf{A}_0^{-1}\mathbf{C}_0; -\hat{\mathbf{E}}_{0,t}^{ES,-} + \mathbf{A}_0^{-1}\mathbf{C}_0 \right) \tag{20}$$

where $\mathbf{B_0} = \mathbf{B_n}$, $\mathbf{A_0}$'s expression is as Equation 21:

$$\mathbf{A_0} = \begin{bmatrix} 1 & 0 & 0 & \cdots & 0 \\ -\hat{\delta} & 1 & 0 & \cdots & 0 \\ 0 & -\hat{\delta} & 1 & \cdots & 0 \\ \vdots & \vdots & \vdots & \ddots & \vdots \\ 0 & 0 & 0 & \cdots & 1 \end{bmatrix} \tag{21}$$

where $\mathbf{A_0} \in \mathbb{R}^{T \times T}$. $\hat{\delta}$ is the average values of self-discharge efficiency of all BSES.

Scaling and translation of F_0 is used to fit each BSES power feasible domain F_n, when φ_j is maximum, the fitted BSES power feasible domain F_j is optimal, and the optimal parameters φ_j^* and $\boldsymbol{\mu}_j^*$ can be obtained by solving the optimization problem as shown in Equation 22:

$$\begin{aligned} &\underset{\varphi_j, \boldsymbol{\mu}_j}{\text{maximize}} \quad \varphi_j \\ &s.t. \quad \varphi_j F_0 + \boldsymbol{\mu}_j \subset F_j \\ &\varphi_j \ge 0 \end{aligned} \tag{22}$$

Let $\phi_j = \frac{1}{\varphi_j}$, $\boldsymbol{\eta}_j = -\phi_j \boldsymbol{\mu}_j$, based on Farkas' theorem, the above optimization problem expression can be transformed into Equation 23:

$$\begin{aligned} &\underset{\phi_j, \boldsymbol{\eta}_j, \mathbf{G}}{\text{minimize}} \quad \phi_j \\ &s.t. \quad \mathbf{G}\mathbf{M_0} = \mathbf{M}_j \\ &\mathbf{G}\mathbf{N_0} \le \phi_j \mathbf{N}_j + \mathbf{M}_j \boldsymbol{\eta}_j \end{aligned} \tag{23}$$

By solving the above optimization problem, the parameters φ_j and $\boldsymbol{\mu}_j$ can be obtained, so that the feasible domain of BSES aggregation power can be obtained as Equation 24:

$$F_{agg} = \left\{ \mathbf{p}_t^{agg} \in \mathbb{R}^T \middle| \begin{array}{c} E_{i,t}^{agg} = \delta_i E_{i,t-1}^{agg} + p_{i,t}^{agg} \Delta t, \forall t \in \tau \\ -p_{i,t}^{agg,-} \le p_{i,t}^{agg} \le p_{i,t}^{agg,+}, \forall t \in \tau \\ E_{i,t}^{agg,-} \le E_{i,t}^{agg} \le E_{i,t}^{agg,+}, \forall t \in \tau \end{array} \right\} \tag{24}$$

where each boundary parameter is expressed as Equations 25-28:

$$\mathbf{p}_i^{agg,-} = \varphi \hat{P}_0^{ES,-} - \boldsymbol{\mu} \tag{25}$$

$$\mathbf{p}_i^{agg,+} = \varphi \hat{P}_0^{ES,+} + \boldsymbol{\mu} \tag{26}$$

$$\mathbf{E}_i^{agg,-} = \varphi \hat{E}_0^{ES,-} - \mathbf{A}^{-1}\mathbf{B}\boldsymbol{\mu} \tag{27}$$

$$\mathbf{E}_i^{agg,+} = \varphi \hat{E}_0^{ES,+} + \mathbf{A}^{-1}\mathbf{B}\boldsymbol{\mu} \tag{28}$$

where $\varphi = \sum_{j \in \Omega_i} \varphi_j^*$, $\boldsymbol{\mu} = \sum_{j \in \Omega_i} \boldsymbol{\mu}_j^*$; Ω_i denotes the set of BSES belonging to aggregator i.

3 5G BSES co-regulation method for voltage regulation in DNs

This chapter aims to study 5G BSES participation in DN coordinated scheduling methods for optimal operation in low-voltage scenarios. It first establishes a DN model and introduces

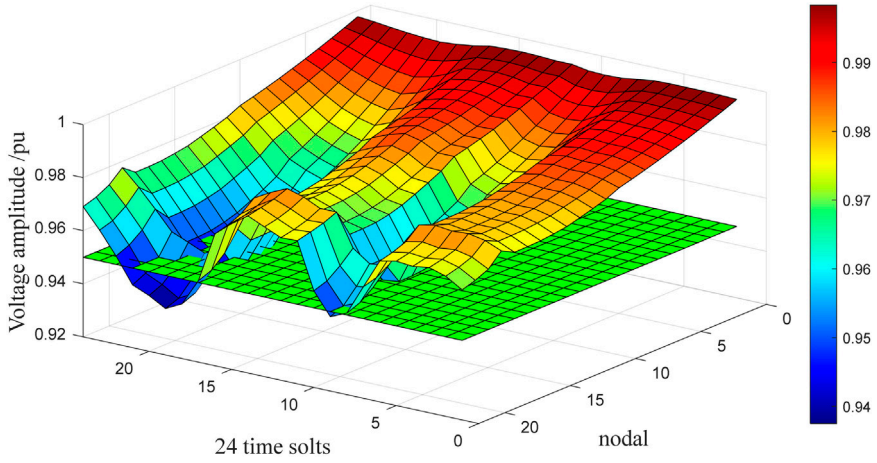

FIGURE 9
Voltage amplitude of BSES before participation in dispatch for 24 time periods.

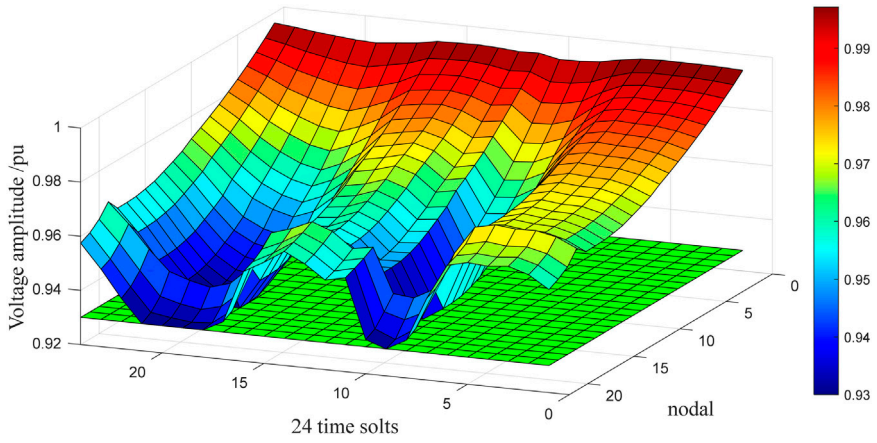

FIGURE 10
Voltage amplitude after participation of BSES in dispatch for 24 time periods.

a quantitative assessment method for low-voltage regulation demand, which guides base station operators in coordinating with the DN. The chapter then proposes a cooperative scheduling method for BSES, optimizing its charging and discharging strategies to regulate DN voltage and improve grid safety and stability.

3.1 DN modeling

3.1.1 DN topology model

Since the DN is a radial structure, the DN topology containing N nodes is defined as $G = (\mathcal{N}, \mathcal{E})$, where $\mathcal{N} = \{1, 2, ..., N\}$ and $\mathcal{E}$ represent the set of nodes and the set of lines, respectively. The substation is denoted as node 0. In addition to the substation, each node i has a unique parent node π_i and a set of child nodes directly connected to it, which are denoted by C_i. Without loss of generality, the node index is encoded in such a way that the index of each node is always greater than the index of its parent node, $\pi_i < i$. In addition, the line pointing from a node π_i to node i is labeled as line i. Therefore, the branch numbering $\mathcal{E} = \{1, 2, ..., N\}$ can be consistent with the node numbering. Let A^0 be an $N \times (N + 1)$ dimensional node association matrix. It can be expressed as Equation 29:

$$A_{ij}^0 = \begin{cases} -1 & j = i \\ 1 & j = \pi_i \\ 0 & j \neq i, \pi_i \end{cases} \tag{29}$$

where if $j = \pi_i$, $A_{ij}^0 = 1$ indicates that node j is the parent of node i and there is a line connecting node i to node j. If $A_{ij}^0 = 0$, it indicates that node j is not the parent of node i. A^0 is divided into two parts, a and A, where a represents the first column of A^0, which is the correlation matrix of node 0. A is a full-rank matrix, and therefore A is invertible.

3.1.2 DN branch-circuit current modeling

For a radial DN, the following tidal equations are used to represent the branch-circuit tidal models (Li et al., 2019).

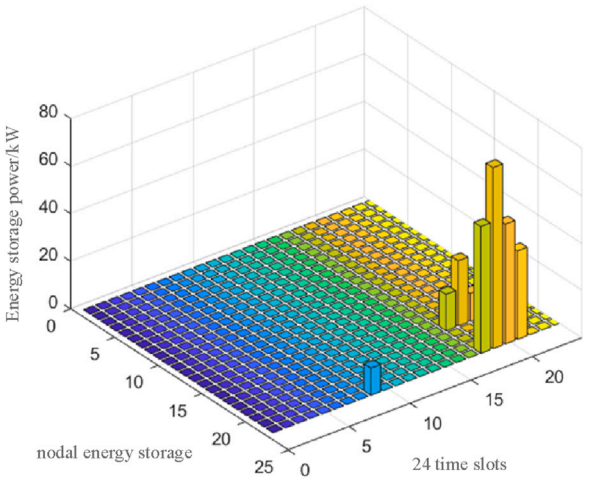

FIGURE 11
24 time periods of AES regulation requirements at each node.

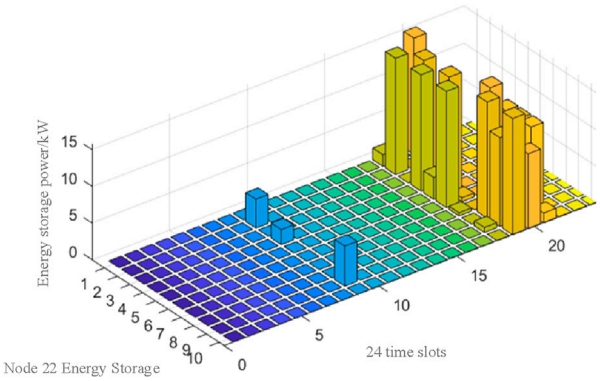

FIGURE 12
Charging and discharging of internal BSES at node 22 for 24 time periods.

$$P_i - \frac{P_i^2 + Q_i^2}{V_{\pi_i}^2} r_i + p_i = \sum_{j \in \mathbf{C}_i} P_j \quad \forall i \in \mathcal{N}/0 \tag{30}$$

$$Q_i - \frac{P_i^2 + Q_i^2}{V_{\pi_i}^2} x_i + q_i = \sum_{j \in \mathbf{C}_i} Q_j \quad \forall i \in \mathcal{N}/0 \tag{31}$$

$$V_{\pi_i}^2 - V_i^2 = 2\left(r_i P_i + x_i Q_i\right) - \left(r_i^2 + x_i^2\right) \frac{P_i^2 + Q_i^2}{V_{\pi_i}^2} \quad \forall i \in \varepsilon \tag{32}$$

Equations 30, 31 represent the active and reactive power balance at node i, respectively, and Equation 32 represents the voltage link between two neighboring nodes, Where p_i and q_i denote the active and reactive power injected at node i, respectively; P_i and Q_i denote the active and reactive power circulating on branch i, respectively; r_i and x_i denote the resistance and reactance of line i, respectively; and V_{π_i} and V_i denote the voltage magnitude of the parent node and the child node i, respectively.

Since the original branch-current models (30)–(32) are non-convex, the convex optimization solution method cannot be directly applied. To ensure the efficient solution of the problem, after approximating, and neglecting the higher terms of the equations, the linear branch-current model can be obtained as shown in Equations 33–35.

$$P_i - \sum_{j \in \mathbf{C}_i} P_j = -p_i \quad \forall i \in \mathcal{N}/0 \tag{33}$$

$$Q_i - \sum_{j \in \mathbf{C}_i} Q_j = -q_i \quad \forall i \in \mathcal{N}/0 \tag{34}$$

$$V_{\pi_i} - V_i = r_i P_i + x_i Q_i \quad \forall i \in \varepsilon \tag{35}$$

3.2 BSES demand assessment model for voltage regulation in DNs

3.2.1 Objective function

When the distribution network system experiences excessive load, certain nodes may encounter low voltage issues. These issues can be addressed by aggregators scheduling the charging and discharging actions of 5G BSES, effectively adjusting the flexible active load of the 5G base stations. From the perspective of the power grid, the aim is to resolve low voltage problems with minimal energy storage adjustment requirements. Therefore, the objective function is to minimize the energy storage adjustment demand F at each node of the base station over a day, as shown in Equation 36.

$$F = \sum_{t=1}^{T=24} \sum_{i=1}^{N_e} \left| p_{i,t}^{agg} \right| \tag{36}$$

where T is 24 time periods in a day; N_e denotes the number of node's aggregated energy storage (AES); $p_{i,t}^{agg}$ denotes the output power of node i's AES in time period t.

3.2.2 Restrictive condition

3.2.2.1 Linear branch flow model

$$P_{i,t} - \sum_{j \in \mathbf{C}_i} P_{j,t} = -p_{i,t} \quad \forall i \in \mathcal{N}/0 \tag{37}$$

$$Q_{i,t} - \sum_{j \in \mathbf{C}_i} Q_{j,t} = -q_{i,t} \quad \forall i \in \mathcal{N}/0 \tag{38}$$

$$V_{\pi_i,t} - V_{i,t} = r_i P_{i,t} + x_i Q_{i,t} \quad \forall i \in \varepsilon \tag{39}$$

Equations 37-39 represent the linear power flow constraints of the line where $p_{i,t}$ and $q_{i,t}$ denote the active and reactive power injected into node i at time t; $P_{i,t}$ and $Q_{i,t}$ denote the active and reactive power circulating on branch i at time t; r_i and x_i denote the resistance and reactance of line i; $V_{\pi_i,t}$ and $V_{i,t}$ denote the voltage magnitude of the parent node and the child node i at time t, respectively.

3.2.2.2 Nodal power balance constraints

$$p_{i,t} = -p_{i,t}^d - p_{i,t}^{agg} \tag{40}$$

$$q_{i,t} = -q_{i,t}^d \tag{41}$$

Equation 40 ensures the load active power balance of node i; Equation 41 ensures the load reactive power balance of node I, where $p_{i,t}^d$ and $q_{i,t}^d$ denote the load active power and reactive power of node i at time t respectively; $p_{i,t}^{agg}$ denote the AES output power of node i at time t.

3.2.2.3 Node voltage constraints

$$\underline{V}_i \le V_{i,t} \le \bar{V}_i \tag{42}$$

Equation 42 ensures that the node voltage of the DN does not exceed the limit. Where $\underline{V}_i$ and $\bar{V}_i$ are the maximum and minimum values allowed for the nodal voltage, respectively.

3.2.2.4 Line transmission power capacity constraints

$$P_{i,t}^2 + Q_{i,t}^2 \le S_{i,t}^2 \tag{43}$$

where $S_{i,t}$ is denoted as the maximum value of the apparent power allowed to flow through branch *i*. In order to facilitate the solution, it is necessary to linearize the line transmission power capacity constraint, as shown in Equation 44. Equation 44 ensures that the transmission power of the DN line does not exceed the limit.

$$\begin{cases} (\sqrt{2}-1)P_{i,t} + Q_{i,t} \le S_{i,t} \\ \sqrt{2}\,P_{i,t} - (\sqrt{2}-2)Q_{i,t} \le \sqrt{2}\,S_{i,t} \\ \sqrt{2}\,P_{i,t} + (\sqrt{2}-2)Q_{i,t} \le \sqrt{2}\,S_{i,t} \\ (\sqrt{2}-1)P_{i,t} - Q_{i,t} \le S_{i,t} \\ -(\sqrt{2}-1)P_{i,t} + Q_{i,t} \le S_{i,t} \\ -\sqrt{2}\,P_{i,t} - (\sqrt{2}-2)Q_{i,t} \le \sqrt{2}\,S_{i,t} \\ -\sqrt{2}\,P_{i,t} + (\sqrt{2}-2)Q_{i,t} \le \sqrt{2}\,S_{i,t} \\ -(\sqrt{2}-1)P_{i,t} - Q_{i,t} \le S_{i,t} \end{cases} \tag{44}$$

3.2.2.5 The power and energy state constraints of the AES

$$E_{i,t}^{agg} = \delta_i E_{i,t-1}^{agg} + p_{i,t}^{agg}\Delta t \tag{45}$$

$$-p_{i,t}^{agg,-} \le p_{i,t}^{agg} \le p_{i,t}^{agg,+} \tag{46}$$

$$E_{i,t}^{agg,-} \le E_{i,t}^{agg} \le E_{i,t}^{agg,+} \tag{47}$$

Equations 45-47 indicates the operational constraints of AES where $E_{i,t}^{agg}$ denotes the residual energy state of the AES *i* at time *t*; δ_i denotes the self-discharge efficiency of the AES *i*; Δt denotes the charging or discharging time period of the AES; $p_{i,t}^{agg,+}$ denotes the maximum charging power of the AES; $p_{i,t}^{agg,-}$ denotes the maximum discharging power of the AES; $E_{i,t}^{agg,+}$ denotes the maximum permissible energy state value of the AES *i* at time *t*; $E_{i,t}^{agg,-}$ denotes the minimum permissible energy value of the AES *i* at time *t*.

3.3 Cooperative scheduling model of BSES for voltage regulation in DNs

Building on the BSES demand assessment model for low voltage regulation in distribution networks, the power adjustment demand for aggregated BSES at each network node has been calculated. However, the individual BSES output at each node remains unknown. To address this, an optimized scheduling model is proposed, which balances the state of charge and optimizes BSES charging and discharging strategies to mitigate low voltage issues in the distribution network.

3.3.1 Objective function

Charging and discharging is carried out with the goal that the SOC of each base station's energy storage state of charge is close to 0.5 after scheduling, to realize the fair distribution of power among each base station's energy storage resources, as shown in Equation 48.

$$F = \sum_{j=1}^{N}\sum_{t=1}^{T}\left|SOC_{j,t}^{ES} - 0.5\right| \tag{48}$$

where N denotes the number of BSES inside the node; T denotes the BSES scheduling time period; $SOC_{j,t}^{ES} = \frac{E_{j,t}^{ES}}{E_j^B}$ denotes the SOC state of BSES *j* inside the node at time *t*, $E_{j,t}^{ES}$ denotes the remaining energy state of BSES *j* inside the node at time *t*, and E_j^B denotes the rated capacity of BSES *j* inside the node.

3.3.2 Restrictive condition

3.3.2.1 Energy storage energy balance constraints

The sum of the node's internal BSES energy should be balanced with the node's AES energy value, as described in Equation 49.

$$\sum_{j=1}^{N} E_{j,t}^{ES} = E_{i,t}^{agg} \tag{49}$$

3.3.2.2 Energy storage energy state constraints

$$E_{j,t}^{ES} = \delta_j \cdot E_{j,t-1}^{ES} + p_{j,t}^{ES}\Delta t \tag{50}$$

$$E_{j,t}^{ES,-} \le E_{j,t}^{ES} \le E_{j,t}^{ES,+} \tag{51}$$

Equation 50 illustrates the relationship between the energy stored in BSES *j* and its input power, Equation 51 shows the upper and lower bounds of energy stored in BSES *j* where δ_j denotes the self-discharge efficiency of the BSES *j*; $p_{j,t}^{ES}$ denotes the output power of the BSES *j* at time *t*; Δt denotes the BSES charging or discharging time period; $E_{j,t}^{ES,-}$ denotes the minimum energy state value allowed by the BSES *j* at time *t*; and $E_{j,t}^{ES,+}$ denotes the maximum energy state value allowed by the BSES *j* at time *t*.

3.3.2.3 Energy storage power balance constraints

$$\sum_{j=1}^{N} p_{j,t}^{ES} = p_{i,t}^{agg} \tag{52}$$

$$-p_{j,t}^{ES,-} \le p_{j,t}^{ES} \le p_{j,t}^{ES,+} \tag{53}$$

Equation 52 ensures the power balance of AES, Equation 53 enforces the lower and upper bounds to the power input of BSES *j* where $p_{j,t}^{ES,+}$ indicates the maximum charging power of the BSES; $p_{j,t}^{ES,-}$ indicates the maximum discharging power of the BSES *j*.

4 Simulation results

4.1 System data

To validate the effectiveness of the proposed method, a simulation analysis was conducted using a 22-node distribution network in a specific region. The network topology is shown in Figure 3, and the line parameters are listed in Table 1. The nodes are uniformly distributed, with the maximum and minimum node voltages set at 1.05 p. u and 0.95 p. u, respectively. The typical

daily load curve is depicted in Figure 4. In this region, the communication base stations are equipped with energy storage systems with a rated capacity of 48 kWh and a maximum charge/discharge power of 15.84 kW. The self-discharge efficiency is set at 0.99, and the state of charge (SOC) is allowed to range between a maximum of 0.9 and a minimum of 0.1.

4.2 5G BSES energy consumption prediction model results and analysis based on LSTM

The training and test datasets were imported into the LSTM-based load forecasting model for 5G base stations. The error convergence for the training and test datasets is shown in Figure 5, while the load forecasting for the test dataset samples is illustrated in Figure 6. The root mean square error (RMSE) for the test dataset samples was calculated to be 0.22 kW, with an average relative error of 0.06. As seen in Figure 5, the loss function value converges to a minimum after 24 training epochs. Figure 6 indicates that the model accurately reflects the load data trends over time, demonstrating good tracking performance. In summary, these results validate that the LSTM load forecasting model performs well in predicting the load data of 5G base stations.

4.3 Results and analysis of BSES aggregation

The simulation results for the aggregated power feasible region of 10 BSES units are shown below. Figures 7, 8 illustrate the charging and discharging potential and the energy state boundaries of the aggregated 10 base stations over 24 time periods in a day. The adjustable capacity of the aggregated energy storage is influenced by factors such as individual BSES parameters and the load size of the base stations, resulting in temporal fluctuations. The charging and discharging potential is related to the charge/discharge power parameters of each storage unit. The minimum energy state of the aggregated storage is associated with the base station load size, while the maximum energy state is linked to the rated capacity parameters of each storage unit. Therefore, the proposed BSES aggregation model can quantitatively assess the charging and discharging potential and the adjustable capacity of the controllable BSES group, providing data support for the subsequent participation of BSES in coordinated scheduling with the distribution network.

4.4 Validation results of 5G BSES co-regulation method for DN voltage regulation

4.4.1 Validation results of a BSES demand assessment model for DN voltage regulation

Based on the distribution network branch power flow model presented in this paper and utilizing existing data, the voltage magnitudes at each node of the distribution network were calculated before the participation of BSES in the scheduling across multiple time scales. Figure 9 illustrates the voltage magnitudes at each node of the distribution network over 24 time periods before BSES participated in the scheduling. As shown in the figure, low voltage phenomena (voltage magnitude per unit value less than 0.95, indicated by the green sections) occur at certain times at the end nodes of the distribution network.

Using the BSES demand assessment model proposed in this paper, and combining it with existing data, the voltage magnitudes at each node of the distribution network and the energy storage adjustment requirements for low voltage mitigation were calculated after the participation of BSES in the scheduling across multiple time scales. Figure 10 shows the voltage magnitudes at each node of the distribution network over 24 time periods after the BSES participated in the scheduling. As depicted in the figure, the coordinated scheduling of BSES effectively improves the voltage magnitudes at the end nodes, achieving low voltage mitigation. The multi-time scale adjustment requirements of the aggregated BSES power for low voltage mitigation in the distribution network nodes are shown in Figure 11.

4.4.2 Validation results of an optimal scheduling model for BSES for voltage regulation in DNs

Based on the BSES optimization scheduling model proposed in this paper and utilizing existing data, the coordinated scheduling of BSES at each node was calculated. Taking node 22 as an example for the analysis of internal BSES coordination, Figure 12 illustrates the charging and discharging conditions of BSES at node 22 over 24 time periods. The figure shows that the model can achieve coordinated scheduling of BSES, optimizing the charging and discharging strategies of the energy storage units and effectively managing low voltage issues.

5 Conclusion

In this paper, a BSES aggregation method that takes into account both the base station energy consumption and the backup power characteristics of BSES is proposed. Furthermore, with the goal of fully utilizing the energy storage resources of 5G base stations, a BSES co-regulation method for voltage regulation in DNs is proposed. The feasibility of the proposed method is verified by case analysis, and the following conclusions can be drawn.

- The 5G base station energy consumption prediction model based on LSTM proposed in this paper takes into account the energy consumption characteristics of 5G base stations. The prediction results have high accuracy and provide data support for the subsequent research on BSES aggregation and optimal scheduling.
- The BSES aggregation model proposed in this paper, which considers the prediction of base station energy consumption, accurately and quantitatively evaluates the power adjustability and adjustable capacity of BSES clusters, and enables the centralized management and scheduling of massive BSES.
- The BSES optimization scheduling model constructed in this paper for voltage regulation of DNs further exploits the dispatchable potential of BSES to participate in DN synergy and interaction. It addresses the low-voltage problem of the

DN and improves the security and stability of the grid while ensuring a sufficient and stable backup supply for 5G base stations.

Data availability statement

The original contributions presented in the study are included in the article/supplementary material, further inquiries can be directed to the corresponding author.

Author contributions

PS: Conceptualization, Data curation, Formal Analysis, Methodology, Validation, Writing–original draft. MZ: Supervision, Validation, Writing–review and editing. HL: Investigation, Methodology, Writing–original draft. YD: Investigation, Methodology, Writing–original draft. QR: Investigation, Methodology, Writing–original draft.

Funding

The author(s) declare that no financial support was received for the research, authorship, and/or publication of this article.

Conflict of interest

The authors declare that the research was conducted in the absence of any commercial or financial relationships that could be construed as a potential conflict of interest.

Publisher's note

References

Althoff, M., Stursberg, O., and Buss, M. (2010). Computing reachable sets of hybrid systems using a combination of zonotopes and polytopes. *Nonlinear Anal. Hybrid. Syst.* 4 (2), 233–249. doi:10.1016/j.nahs.2009.03.009

Barot, S., and Taylor, J. A. (2017). A concise, approximate representation of a collection of loads described by polytopes. *Int. J. Electr. Power & Energy Syst.* 84, 55–63. doi:10.1016/j.ijepes.2016.05.001

Chai, B., Chen, J., Yang, Z., and Zhang, Y. (2014). Demand response management with multiple utility companies: a two-level game approach. *IEEE Trans. Smart Grid* 5 (2), 722–731. doi:10.1109/tsg.2013.2295024

Cheng, J., Zhang, H., and Xu, J. (2023) "Traffic prediction model for telecommunication base stations based on improved WOA optimized LSTM and EMD," in *2023 IEEE 5th international conference on power, intelligent computing and systems (ICPICS)*, 1075–1084.

Fu, L. (2020) "Time series-oriented load prediction using deep peephole LSTM," in *2020 12th international conference on advanced computational intelligence (ICACI)*, 86–91.

Han, J., Liu, N., Huang, Y., and Zhou, Z. (2021). Collaborative optimization of distribution network and 5G mobile network with renewable energy sources in smart grid. *Int. J. Electr. Power & Energy Syst.* 130, 107027. doi:10.1016/j.ijepes.2021.107027

Jia, Z., Gao, H., Yang, Y., Liu, L., Li, Z., Liu, S., et al. (2023) "Research on mobile energy storage technology based on improving distributed energy consumption in substation area," in *2023 IEEE 7th information technology and mechatronics engineering conference (ITOEC)*, 156–159.

Li, C., Wang, Y., Wang, R., Liu, H., Tao, X., Zhong, H., et al. (2022) "Load recovery strategy based on mobile energy storage flexibility and DN reconfiguration," in *2022 IEEE 5th international electrical and energy conference (CIEEC)*, 2905–2910.

Li, J., Xu, Z., Zhao, J., and Zhang, C. (2019). Distributed online voltage control in active distribution networks considering PV curtailment. *IEEE Trans. Industrial Inf.* 15 (10), 5519–5530. doi:10.1109/tii.2019.2903888

Liang, H., Li, J., Deng, Y., Song, F., and Yu, X. (2023) "Optimization method for energy storage system planning based on dispatchable potential of 5G base station and cluster partition of DN," in *2023 IEEE 6th international electrical and energy conference (CIEEC)*, 4334–4340.

Ma, J., Silva, V., Belhomme, R., Kirschen, D. S., and Ochoa, L. F. (2013). Evaluating and planning flexibility in sustainable power systems. *IEEE Trans. Sustain. Energy* 4 (1), 200–209. doi:10.1109/tste.2012.2212471

Morosi, S., Piunti, P., and Del Re, E. (2013) "A forecasting driven technique enabling power saving in LTE cellular networks," in *2013 IEEE 9th international conference on wireless and mobile computing, networking and communications (WiMob)*, 217–222.

Müller, F. L., Szabó, J., Sundström, O., and Lygeros, J. (2019). Aggregation and disaggregation of energetic flexibility from distributed energy resources. *IEEE Trans. Smart Grid* 10 (2), 1205–1214. doi:10.1109/tsg.2017.2761439

Pan, H., Liu, J., Zhou, S., and Niu, Z. (2015). A block regression model for short-term mobile traffic forecasting. *IEEE/CIC Int. Conf. Commun. China (ICCC)*, 1–5. doi:10.1109/iccchina.2015.7448619

Qu, H., Ma, W., Zhao, J., and Wang, T. (2013). Prediction method for network traffic based on Maximum Correntropy Criterion. *China Commun.* 10 (1), 134–145. doi:10.1109/cc.2013.6457536

Qu, H., Zhang, Y., and Zhao, J. (2019) "A spatio-temporal traffic forecasting model for base station in cellular network," in *2019 IEEE 19th international conference on communication technology (ICCT)*, 567–571.

Sajjad, I. A., Chicco, G., and Napoli, R. (2016). Definitions of demand flexibility for aggregate residential loads. *IEEE Trans. Smart Grid* 7 (6), 2633–2643. doi:10.1109/tsg.2016.2522961

Shang, Y., Liu, J., Ma, J., Qiu, Y., Zhang, Z., and Liu, C. (2022) "A prediction method of 5G base station cell traffic based on improved transformer model," in *2022 IEEE 4th international conference on civil aviation safety and information technology (ICCASIT)*, 40–45.

Stolojescu-Crisan, C. (2012) "Data mining based wireless network traffic forecasting," in *2012 10th international symposium on electronics and telecommunications*, 115–118.

Suo, S., Kuang, X., Cheng, R., Chen, L., Huang, K., and Zhao, W. (2022) "Research of real-time monitoring and control technology for distributed energy storage based on 5G," in *2022 IEEE/IAS industrial and commercial power system asia (I&CPS asia)*, 1496–1500.

Yang, J., Lin, G., Lv, R., Gao, C., and Chen, T. (2020) "Research on construction and dispatching of virtual power plant based on reserve energy storage of communication base station," in *2020 IEEE 4th conference on energy internet and energy system integration (EI2)*, 398–403.

Yang, L., Zhang, L., Yu, K., and Ma, X. (2023) "Research on interaction between power grid and 5G communication base station storage energy," in *2023 8th asia conference on power and electrical engineering*. IEEE: ACPEE, 592–596.

Ye, G. (2021) "Research on reducing energy consumption cost of 5G Base Station based on photovoltaic energy storage system," in *2021 IEEE international conference on computer science, electronic information engineering and intelligent control technology (CEI)*, 480–484.

Yin, X., Lv, G., Wang, Z., Lu, Z., Liu, Y., and Yu, K. (2022) "Research on 5G BSES configuration taking photovoltaics into account," in *2022 7th asia conference on power and electrical engineering (ACPEE)*, 591–595.

Yu, K., Yang, L., Zhang, L., and Ma, X. (2023) "Summary of research on key technologies of 5G base station flexible resources," in *2023 8th asia conference on power and electrical engineering*. IEEE: ACPEE, 2129–2133.

Zhang, L., Yu, K., Yang, L., and Ma, X. (2023) "A study on energy storage configuration of 5G communication base station participating in grid interaction," in *2023 8th asia conference on power and electrical engineering*. IEEE: ACPEE, 608–612.

Zhao, L., Zhang, W., Hao, H., and Kalsi, K. (2017). A geometric approach to aggregate flexibility modeling of thermostatically controlled loads. *IEEE Trans. Power Syst.* 32 (6), 4721–4731. doi:10.1109/tpwrs.2017.2674699

Zhou, Q., and Xu, Y. (2021) "Reactive power optimization of active DN considering mobile energy storage," in *2021 international conference on power system technology (POWERCON)*, 1040–1044.

frontiers | Frontiers in Energy Research

TYPE Original Research
PUBLISHED 30 September 2024
DOI 10.3389/fenrg.2024.1465604

OPEN ACCESS

EDITED BY
Ying Zhang,
Oklahoma State University, United States

REVIEWED BY
Zipeng Liang,
Hong Kong Polytechnic University, Hong Kong SAR, China
Haoyong Chen,
South China University of Technology, China
Yun Liu,
South China University of Technology, China
Ge Chen,
Purdue University, United States
Haris M. Khalid,
University of Dubai, United Arab Emirates

*CORRESPONDENCE
Huaying Zhang,
zhytgyx@163.com
Qian Liu,
liuqian365@hnu.edu.cn

RECEIVED 16 July 2024
ACCEPTED 17 September 2024
PUBLISHED 30 September 2024

CITATION
Liang X, Zhang H, Liu Q, Liu Z and Liu H (2024) A support vector regression-based interval power flow prediction method for distribution networks with DGs integration.
Front. Energy Res. 12:1465604.
doi: 10.3389/fenrg.2024.1465604

A support vector regression-based interval power flow prediction method for distribution networks with DGs integration

Xiaorui Liang[1], Huaying Zhang[1]*, Qian Liu[2]*, Zijun Liu[1] and Huicong Liu[1]

[1]New Smart City High-Quality Power Supply Joint Laboratory of China Southern Power Grid, Shenzhen Power Supply Co., Ltd., Shenzhen, Guangdong, China, [2]College of Electrical and Information Engineering, Hunan University, Changsha, Hunan, China

In distribution networks with distributed generators (DGs), power generation and load demand exhibit increased randomness and volatility, and the line parameters also suffer more frequent fluctuations, which may result in significant state shifts. Existing model-driven methods face challenges in efficiently solving uncertain power flow, especially as the size of the system increases, making it difficult to meet the demand for rapid power flow analysis. To address these issues, this paper proposes an SVR-based interval power flow (IPF) prediction method for distribution networks with DGs integration. The method utilizes intervals to describe system uncertainty and employs Support Vector Regression (SVR) for model training. The input feature vector consists of the intervals of active power generation, load demand, and line parameters, while the output feature vector represents the intervals of voltage or line transmission power. Ultimately, the SVR-based IPF prediction model is established, capturing the linear mapping relationship between input data and output IPF variables. Simulation results demonstrate that the proposed method exhibits high prediction accuracy, strong adaptability, and optimal computation efficiency, meeting the requirements for rapid and real-time power flow analysis while considering the uncertainty in distribution networks with DGs integration.

KEYWORDS

data-driven method, interval power flow, support vector regression, distribution network, distributed generators

1 Introduction

1.1 Motivation

In the context of widespread integration of distributed generators (DGs) such as wind and photovoltaic (PV) power into distribution networks, power generation exhibits uncertainty due to the inherent volatility and randomness of wind and solar. In addition, load demand and line parameters also exhibit uncertainty which is caused by user consumption behaviors and environmental factors, respectively. These issues caused the power flow state in the system to undergo rapid and intricate changes. Considering these uncertainties, uncertain power flow (PF) methods are proposed by researchers. However,

most existing uncertain PF methods are model-driven. As the system scale increases, the model complexity grows, leading to a significant reduction in computational efficiency, which fails to meet the requirements for rapid assessment of system states in distribution networks. Improving the computational efficiency of uncertain PF analysis can provide assurance for real-time monitoring and dispatching of distribution systems, ensuring stable and efficient operation. There is an urgent need for efficient and rapid methods for uncertain PF analysis in distribution networks that can effectively address system uncertainty.

1.2 Focus and potential

This paper focuses on addressing the computational efficiency issues of uncertain PF, primarily in two aspects: describing system uncertainty using intervals and employing data-driven methods for PF prediction, enabling real-time interval power flow (IPF) calculations in distribution systems. The potential of this research lies in its ability to significantly enhance the real-time monitoring and operational capabilities of distribution networks with integrated DGs. By addressing the limitations of existing model-driven uncertain PF methods, the proposed approach could lead to more efficient PF analysis, particularly in the face of the increasing penetration of renewable energy sources (RES). This has offered a scalable solution for real-time PF analysis in increasingly complex and uncertain environments.

1.3 Preceding research

Commonly used methods for handling uncertainty currently include robust, probabilistic, and interval methods. Among them, the robust method is mainly used for optimization (Zheng et al., 2024), such as energy management under the uncertainty of renewable energy generation and electric vehicles (EVs) (Tan et al., 2024). When calculating power flow, the probabilistic method and interval algorithm are more frequently employed, which are called probabilistic power flow (PPF) and interval power flow (IPF). IPF has the advantages of simple modelling and high security compared with PPF. Existing IPF methods primarily consist of iterative approaches (Mori and Yuihara, 1999; Barboza et al., 2004) and optimization techniques (Zhang et al., 2017; 2018; 2023). For iterative approaches, the Interval Newton iteration was first employed. To avoid solving the equations in the Interval Newton method, the Krawczyk method was introduced. The interval problem was broken down into multiple sub-intervals, and each sub-interval was solved iteratively using the Krawczyk method (Mori and Yuihara, 1999). The Interval Newton iteration framework was combined with the Krawczyk operator in (Barboza et al., 2004), enhancing convergence performance. The introduction of the Affine Algorithm (AA) (Vaccaro et al., 2010) increased the efficiency and accuracy of solving interval nonlinear equation systems. The convergence of the Krawczyk-Moore iteration was enhanced by introducing AA, and the correlation issues of interval computation were addressed. Optimization methods, which avoid iteration and convergence problems, have gained widespread attention in recent years. The optimization model for the IPF solution was constructed by converting intervals into affine forms (Zhang et al., 2017), improving the efficiency of solving IPF. An optimization scenario method (OSM) was improved to solve IPF (Zhang et al., 2018), directly obtaining the range of power flow variables through the optimization models. In IPF analysis for distribution networks, the rise of AA has led to a trend of combining it with the Distflow model, including solving the affine Distflow model using forward-backward substitution (Cheng et al., 2023; Lyu et al., 2023) and directly establishing AA-based IPF optimization models (Leng et al., 2020; Cao et al., 2024). However, existing uncertainty analysis based on physical models suffers from the drawback of increased computational complexity, resulting in lengthy processing times, making it challenging to meet the power grid's demand for swift power flow computations.

Due to the advancements in computer and digital communication technologies, data acquisition in power systems has made significant progress. The deployment of Wide Area Measurement Systems (WAMS) has enabled the reliable collection of high-precision, wide-area synchronized electrical quantities, including voltage, current, phase angles, et al. This progress has fostered the development of data-driven power flow analysis methods, providing a solution to the issue of low efficiency in traditional model-driven power flow analysis (Fu et al., 2024). A data-driven linear PF model incorporating the support vector regression (SVR) and ridge regression (RR) algorithms was proposed in (Li et al., 2023). Similarly, a linear regression model was solved by RR to suppress the effect of data collinearity in (Chen, Y. et al., 2022). In distribution networks, the single-phase PF model is often considered. For instance, a data-driven single-phase linear PF model was introduced in (Xing et al., 2021). A data-driven convex model for hybrid AC/DC microgrids operation involving bi-directional converters was proposed in (Liang et al., 2023). Nevertheless, distribution power systems (DPSs) are generally unbalanced and it is still necessary to study linear three-phase distribution PF models. A data-driven-aided linear three-phase PF model for DPSs considering the imbalance was constructed in (Liu, Y. et al., 2022), and a data-driven piecewise linearization for distribution three-phase stochastic power flow was proposed in (Chen, J. et al., 2022), mitigating the errors of model-based PF linearization approaches. To overcome the challenge of obtaining accurate results with linear model-based data-driven methods, an approach with high adaptability to the nonlinearity of PF was proposed based on the thought of Koopman operator theory (Guo et al., 2022). What's more, a risk-free method was proposed in (Dong et al., 2022) to accelerate AC power flow with machine learning-based initiation, reducing the PF computation time. To tackle the challenges of the hidden measurement noise in the data-driven PF linearization, the problem was transformed into a regression model where the structure of the PF equations was exploited (Liu et al., 2020). Besides, the local load fluctuation suppression and its interaction with distribution system should also be addressed which brings the exact necessity towards the power flow prediction (Khalid et al., 2022; Rehman et al., 2024). Also, here the role of ancillary services and renewable energy integration should also be addressed towards covering the intermittency (Musleh et al., 2019; Sun et al., 2020). In some

cases, the database may not possess the envisioned completeness and appropriateness. There is a trend that combines the physical model-driven and data-driven. This can make up for the issues arising from incomplete data (Xing et al., 2022; Liu et al., 2021). A hybrid physical model-driven and data-driven approach for linearizing the power flow model was proposed in (Tan et al., 2020), and the linearized errors are obtained by the partial least squares regression-based data-driven approach. In the condition of lack of data, physical model parameters are introduced to assist the data-driven training process (Shao et al., 2023), and a highly scalable data-driven algorithm for stochastic AC-OPF that has extremely low sample requirements was presented in (Mezghani et al., 2020). To enhance the performance and generalization ability of the data-driven model, a physics-guided neural network was proposed to solve the PF problem by encoding different granularity of Kirchhoff's laws, and system topology into the rebuilt PF model (Hu et al., 2021). The fusion of robust principles with data-driven approaches has also enhanced the precision of data-driven methods. The worst-case errors were probabilistically constrained through distributionally robust chance-constrained programming (Liu, Y. et al., 2022; Chen et al., 2020). It also allows guaranteeing the linearization accuracy for a chosen operating point. In addition, a more comprehensive summary and discussion of existing data-driven PF linearization was presented in (Jia and Hug, 2023). For data-driven methods, support vector machine (SVM) is widely used due to its strong robustness and generalization ability, particularly excelling in scenarios with small samples and high dimensionality. Addressed to the N-k1-k2 cascading outages, the researchers employ SVM for classifier training, enabling the fast, reliable, and robust computation of active and reactive power flows (Xue and Liu, 2021). The SVM is utilized for optimal power flow with small-signal stability constraints in (Liu, J. et al., 2022), achieving high computational efficiency and economic benefits.

Although data-driven PF methods have made significant advancements, combining data-driven approaches with uncertainty still presents challenges. On the one hand, data-driven methods require a large amount of real or simulated data, which is what uncertain PF lacks. Historical data is difficult to obtain, and generating simulated data often incurs higher costs compared to deterministic PF. On the other hand, effectively integrating uncertainty into data-driven models is a challenge, as these uncertainties are often high-dimensional, increasing the complexity of modeling. In response, interval approaches offer the advantages of simple modeling and high simulation accuracy, while SVR can handle high-dimensional data, making it suited to the requirements. Therefore, this paper adopts interval modeling to represent uncertainties and selects SVR as the data-driven approach.

1.4 Contribution

This paper is dedicated to improving the computational efficiency of IPF in distribution networks to achieve real-time analyses, providing essential support for the rapid response of uncertain distribution systems with DGs integration. To this end, a method for IPF prediction in distribution networks based on SVR is proposed by combining data-driven methods with interval approaches. Accordingly, the research makes the following contributions.

Firstly, an IPF model for distribution networks based on the OSM is established considering system uncertainty as intervals. In addition to the uncertainty of power generation and load demand, the uncertainty of line parameters is also considered in this model. Due to environmental variations, the parameters of network lines exhibit a certain level of uncertainty. This consideration improves the accuracy of the model.

Secondly, an IPF prediction model is constructed using SVR based on the interval dataset generated by simulation. Different from traditional data-driven models, this model is a multi-output model that separately outputs the upper and lower bounds of the power flow results. This interval result fully considers various uncertainties in the distribution system, as the model is trained with these uncertainties incorporated.

Thirdly, the established SVR-based IPF prediction approach has been demonstrated to have high prediction accuracy and computational efficiency. The effectiveness of this approach is validated through studies on both IEEE 33bw and IEEE 69 cases. The IEEE 33bw case is primarily used to evaluate the model's accuracy, while the IEEE 69 case is mainly used to analyze the model's computational efficiency.

The IPF model for distribution networks is introduced in Section 2. The training and prediction algorithm through SVR is introduced in Section 3. The procedure of the method is introduced in Section 4. The case studies are conducted in Section 5, and conclusions in Section 6.

2 Construction of IPF model for distribution networks

2.1 Distflow formulation

The relaxed Distflow model for the radial distribution network is expressed as Equations 1–4. Before constructing the model, it is customary to assume that the transmission lines do not involve parallel grounding branches and to specify that the direction of current and power flow from node i to node j is positive.

$$v_j = v_i - 2\left(r_{ij}P_{ij} + x_{ij}Q_{ij}\right) + \left(r_{ij}^2 + x_{ij}^2\right)l_{ij},\ \forall (i,j) \in \mathbf{B} \tag{1}$$

$$P_{ij}^2 + Q_{ij}^2 \le l_{ij}v_i \Leftrightarrow \left\| \begin{matrix} 2P_{ij} \\ 2Q_{ij} \\ l_{ij} - v_i \end{matrix} \right\|_2 \le l_{ij} + v_i \tag{2}$$

$$\sum_{k:j\to k} P_{jk} - \sum_{i:i\to j}\left(P_{ij} - r_{ij}l_{ij}\right) = p_j,\ \forall j \in \mathbf{D} \tag{3}$$

$$\sum_{k:j\to k} Q_{jk} - \sum_{i:i\to j}\left(Q_{ij} - x_{ij}l_{ij}\right) = q_j,\ \forall j \in \mathbf{D} \tag{4}$$

The model is the branch power flow model after convex relaxation, where Equation 1 is the voltage equation, Equation 2 is the power equation at the sending end of the branch, Equations 3, 4 are the power balance equation. $\mathbf{B}$ and $\mathbf{D}$ are the set of branches and nodes. We set that $l_{ij} = |I_{ij}|^2$ and $v_i = |V_i|^2$, where V_i is the voltage vector of node i, and I_{ij} is the current vector flowing through branch (i, j). r_{ij} is the resistance and x_{ij} is the reactance of transmission line. P_{ij} and Q_{ij} are the active and reactive line transmission power from node i to node j, respectively. Note that more than one upstream and downstream branch is connected to

node j. p_j and q_j are the injection active and reactive power of node j, respectively, which are equal to the power generation minus the load demand, i.e., $p_j = p_j^G - p_j^L$.

2.2 Modelling of IPF based on distflow

In active distribution networks with DGs integration, the output of distributed generators and flexible loads both exhibit a certain degree of uncertainty, which has a significant impact on the safe and stable operation of the distribution networks. Therefore, it is essential to consider these uncertainties. In this paper, the interval approach is utilized to describe uncertainties, ensuring the security of system operation. Additionally, the network parameters, including line resistance and reactance, may experience variations due to external environmental factors. To make the model more practical, the uncertainties of these parameters are considered simultaneously during modelling.

In the interval approach, the active power generation and load demand, as well as line parameters are represented in interval form, and the interval results for variables such as voltage and line transmission power can be obtained. Representing the interval form in $\hat{\chi}$, where $\hat{\chi} = [\underline{\chi}, \bar{\chi}]$, the IPF model based on Distflow for distribution networks can be expressed as Equations 5–8.

$$\hat{v}_j = \hat{v}_i - 2\left(\hat{r}_{ij}\hat{P}_{ij} + \hat{x}_{ij}\hat{Q}_{ij}\right) + \left(\hat{r}_{ij}^2 + \hat{x}_{ij}^2\right)\hat{l}_{ij},\ \forall (i,j) \in \mathbf{B} \tag{5}$$

$$\left\| \begin{matrix} 2\hat{P}_{ij} \\ 2\hat{Q}_{ij} \\ \hat{l}_{ij} - \hat{v}_i \end{matrix} \right\|_2 \le \hat{l}_{ij} + \hat{v}_i,\ \forall (i,j) \in \mathbf{B} \tag{6}$$

$$\sum_{k:j\to k} \hat{P}_{jk} - \sum_{i:i\to j}\left(\hat{P}_{ij} - \hat{r}_{ij}\hat{l}_{ij}\right) = \hat{p}_j,\ \forall j \in \mathbf{D} \tag{7}$$

$$\sum_{k:j\to k} \hat{Q}_{jk} - \sum_{i:i\to j}\left(\hat{Q}_{ij} - \hat{x}_{ij}\hat{l}_{ij}\right) = \hat{q}_j,\ \forall j \in \mathbf{D} \tag{8}$$

where $\hat{p}_j = \hat{p}_j^G - \hat{p}_j^L$, $\hat{q}_j = q_j^G - \hat{q}_j^L$. $\hat{p}_j^G$ and q_j^G are the active and reactive power generation, respectively. $\hat{p}_j^L$ and $\hat{q}_j^L$ are the active and reactive load demand, respectively.

The IPF model based on Distflow can draw inspiration from the principles of OSM for its solution. In this approach, the interval uncertainties of the IPF model are regarded as variables that vary in their interval bounds, and the desired variables are set as the objective functions. Thus, it involves transforming the resolution of a set of interval nonlinear equations into variable optimization problems. The core of OSM is based on the Extreme Value Theorem through which we can get two points of conclusions. We simplify Equations 5–8 as $\boldsymbol{h}(\boldsymbol{x}) = [\underline{\boldsymbol{h}}, \bar{\boldsymbol{h}}]$ where $[\underline{\boldsymbol{h}}, \bar{\boldsymbol{h}}]$ are interval input data and $\boldsymbol{x}$ are the variables of the IPF model. The first point is that there is a fixed $\boldsymbol{x}$ corresponding to an arbitrary scenario $\boldsymbol{\xi} \in [\underline{\boldsymbol{h}}, \bar{\boldsymbol{h}}]$ in the power flow calculation. The second point is that there exists a special scenario $\xi_i^{\min}$ ($\xi_i^{\max}$) for each single variable x_i making x_i minimum (maximum) for all scenarios $\boldsymbol{\xi} \in [\underline{\boldsymbol{h}}, \bar{\boldsymbol{h}}]$. The minimum and maximum are denoted as $x_i^{\min}$ and $x_i^{\max}$, and the interval $[x_i^{\min}, x_i^{\max}]$ is the solution of x_i under the input data $[\underline{\boldsymbol{h}}, \bar{\boldsymbol{h}}]$.

From the two points of conclusions, the solution for IPF model is reduced to find $\xi_i^{\min}$ and $\xi_i^{\max}$ for each variable x_i by establishing the minimum and maximum optimization models Equation 9 of power flow variables.

$$\begin{aligned} &\min(\max)\, x_i \\ &s.t. \begin{cases} \boldsymbol{h}(\boldsymbol{x}) = \boldsymbol{\xi} \\ \underline{\boldsymbol{h}} \le \boldsymbol{\xi} \le \bar{\boldsymbol{h}} \end{cases} \end{aligned} \tag{9}$$

Taking the variable v_i in distribution networks, for example, solving the IPF model Equations 5–8 can be transformed into solving the optimization model Equation 10, and the model can be solved through commercial solvers such as CPLEX.

$$\begin{aligned} &\min(\max)\ v_i,\ \forall i \in \mathbf{D} \\ &\begin{cases} \left\| \begin{matrix} 2P_{ij} \\ 2Q_{ij} \\ l_{ij} - v_i \end{matrix} \right\|_2 \le l_{ij} + v_i,\ \forall (i,j) \in \mathbf{B} \\ v_j = v_i - 2\left(r_{ij}P_{ij} + x_{ij}Q_{ij}\right) + \left(r_{ij}^2 + x_{ij}^2\right)l_{ij},\ \forall (i,j) \in \mathbf{B} \\ \sum_{k:j\to k} P_{jk} - \sum_{i:i\to j}\left(P_{ij} - r_{ij}l_{ij}\right) = p_j,\ \forall j \in \mathbf{D} \\ \sum_{k:j\to k} Q_{jk} - \sum_{i:i\to j}\left(Q_{ij} - x_{ij}l_{ij}\right) = q_j,\ \forall j \in \mathbf{D} \\ q_j^G - \bar{q}_j^L \le q_j \le q_j^G - \underline{q}_j^L,\ \forall j \in \mathbf{D} \\ \underline{p}_j^G - \bar{p}_j^L \le p_j \le \bar{p}_j^G - \underline{p}_j^L,\ \forall j \in \mathbf{D} \\ \underline{x}_{ij}\left(\underline{l}_{ij}\right) \le x_{ij}\left(l_{ij}\right) \le \bar{x}_{ij}\left(\bar{l}_{ij}\right),\ \forall (i,j) \in \mathbf{B} \end{cases} \end{aligned} \tag{10}$$

It can be succinctly described as searching for a specific scenario $\xi_i^{\min}$ ($\xi_i^{\max}$) among all uncertain scenarios of the distribution network, which can minimize (maximize) the voltage magnitude $|V_i|$ at node i, so as to obtain the voltage interval $[V_i^{\min}, V_i^{\max}]$. Naturally, the objective function v_i of Equation 10 can also be replaced with active power transmission P_{ij} or reactive power transmission Q_{ij}.

3 IPF prediction method for distribution networks based on SVR

As the system scale increases, the efficiency of model-driven IPF analysis significantly decreases, which does not meet the current demands for rapid PF computations in distribution networks. Therefore, the data-driven approach has garnered attention for achieving faster IPF computations. The SVR has been opted for in this research due to its advantages of handling high-dimensional data, which is aligned with the characteristics of IPF analysis.

3.1 Construction of eigenvectors in IPF

In the typical SVR framework, the model is designed for single-output problems. However, in the context of IPF models, situations may arise where some nodes attain their maximum values while others reach their minimum values within the same input scenario since both input data and output variables are represented as intervals. Therefore, the SVR model for IPF is fundamentally a multiple-output problem. Corresponding to the same input scenario, the situation where different nodes attain either maximum or minimum values may vary. In such cases, training the SVR model based on the specific input and a singular minimum (or maximum) output would lead to a significant decrease in model accuracy. Based on this, the feature vectors in IPF model are established.

The well-constructed feature vectors are crucial prerequisites for ensuring the effectiveness of data-driven model learning. In the

analysis of extensive historical state data for distribution networks with DGs, it is essential to determine the input and output features for the IPF analysis at first. Given that the primary characteristic of distribution networks with DGs is the uncertainty of renewable power generation and load demand, which significantly impacts IPF analysis results, the sequence of renewable power generation and load demand for the distribution system is selected as the input eigenvector of the SVR model, and the sequence of node voltages and active line transmission power, which is indicative of power flow results, is selected as the output feature vector.

3.1.1 Construction of input eigenvector adapted to variations in source-grid-load

The uncertainty of source, grid, and load is represented in interval form for the IPF model. Therefore, the values in the input eigenvector should be intervals distinguishing from conventional eigenvectors. However, directly using interval values for training poses challenges such as computational complexity, model misfit, and difficulty in interpreting learning patterns. To address these issues, it is necessary to identify relevant parameters that can characterize interval features, such as interval midpoints and interval radii, to replace interval values during training. The midpoint of the interval is the operating point of generator, which reflects the randomness of generator output. The interval radius can reflect the fluctuation degree of uncertain data. Therefore, the interval midpoint of source and radius of source-grid-load data is used to construct the input eigenvector instead of interval values.

Take the renewable active power generation $\hat{p}_j^G = [\underline{p}_j^G, \bar{p}_j^G]$ as an example, the relationships Equations 11, 12 exist in the interval.

$$\underline{p}_j^G = p_{0,j}^G - \Delta p_j^G, \bar{p}_j^G = p_{0,j}^G + \Delta p_j^G \tag{11}$$

$$\Delta p_j^G = \sigma \cdot p_{0,j}^G \tag{12}$$

where $p_{0,j}^G$ represents the interval midpoint, Δp_j^G is the interval radius, σ is the fluctuation coefficient. The $p_{0,j}^G$ and Δp_j^G can characterize the features of the renewable active power generation interval. For a certain distribution network, the value of the input eigenvector can be changed by changing the midpoint $p_{0,j}^G$ or the fluctuation coefficient σ. Besides, the active and reactive load demands, and line parameters follow the similar principle.

The eigenvector for source includes the sequence of renewable active power generation $\Delta \boldsymbol{p}^G = \{\Delta p_1^G, \Delta p_2^G, \ldots, \Delta p_M^G\}$ and $\boldsymbol{p}_0^G = \{p_{0,1}^G, p_{0,2}^G, \ldots, p_{0,M}^G\}$, which for load includes the sequences of active and reactive load demand $\Delta \boldsymbol{p}^L = \{\Delta p_1^L, \Delta p_2^L, \ldots, \Delta p_D^L\}$, $\Delta \boldsymbol{q}^L = \{\Delta q_1^L, \Delta q_2^L, \ldots, \Delta q_D^L\}$, and which for grid includes the sequences of line parameters $\Delta \boldsymbol{r} = \{\Delta r_1, \Delta r_2, \ldots, \Delta r_B\}$, $\Delta \boldsymbol{x} = \{\Delta x_1, \Delta x_2, \ldots, \Delta x_B\}$. According to this, the input eigenvector adaptable to variations in source-grid-load can be formulated as follows:

$$\boldsymbol{X}_{in} = [\Delta \boldsymbol{p}^G, \boldsymbol{p}_0^G, \Delta \boldsymbol{p}^L, \Delta \boldsymbol{q}^L, \Delta \boldsymbol{r}, \Delta \boldsymbol{x}] \tag{13}$$

where M is the number of DGs, D is the number of nodes, B is the number of branches.

3.1.2 Construction of output feature vector

When conducting PF analysis, it is essential to consider the output features that can reflect power system quality and stability. In power flow results, node voltage or line transmission power can be used to evaluate system stability. Therefore, the node voltage is selected as output features in this paper. In IPF model, node voltages are represented as interval values, so that the output features of the SVR training model are essentially intervals. However, training the model directly with interval values as the output vector may lead to issues such as model complexity and low interpretability. To address the issues, it is preferable to choose upper and lower bounds that characterize interval features as the output feature vector. This involves establishing the SVR model with two output nodes. According to this, the output feature vector in IPF can be constructed as Equation 14.

$$\boldsymbol{Y}_{out1} = \boldsymbol{V}_{\min}, \ \boldsymbol{Y}_{out2} = \boldsymbol{V}_{\max} \tag{14}$$

Certainly, we can also construct the output feature vector as presented in Equation 15 to obtain the predictive results of line transmission power.

$$\boldsymbol{Y}_{out1} = \boldsymbol{P}_{ij,\min}, \ \boldsymbol{Y}_{out2} = \boldsymbol{P}_{ij,\max} \tag{15}$$

3.2 Modelling of SVR-based IPF prediction

Support Vector Machine (SVM) is a binary classification algorithm, and its fundamental model is a linear classifier that maximizes the margin in the feature space. The objective of SVM learning is to find a hyperplane that separates the samples, guided by the principle of maximizing the margin. This ultimately translates into solving a convex quadratic programming problem. The variant of SVM used in this research for IPF prediction is SVR, specifically designed for solving regression problems. The principle of SVR is presented in Figure 1. SVR can be categorized into three types according to the linear separability of the training data, including Linear Hard ε-SVR, Linear ε-SVR, and ε-SVR.

The original data for IPF analysis is considered linearly non-separable. Therefore, this paper selects the ε-SVR model to explore the connection between the input and output of the

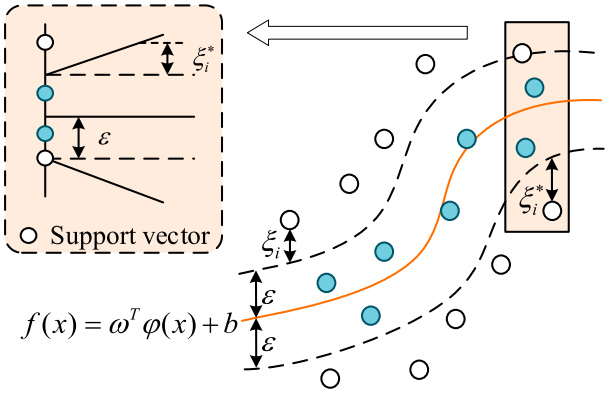

FIGURE 1
The principle of SVR.

IPF for distribution systems. Based on the constructed feature vectors in IPF, the ε-SVR model for IPF prediction is established as follows.

According to the description in 3.1, the training data set of the model can be obtained as $T = \{(\boldsymbol{X}_{in}, \boldsymbol{Y}_{out1}, \boldsymbol{Y}_{out2})_1, (\boldsymbol{X}_{in}, \boldsymbol{Y}_{out1}, \boldsymbol{Y}_{out2})_2, \ldots, (\boldsymbol{X}_{in}, \boldsymbol{Y}_{out1}, \boldsymbol{Y}_{out2})_N\}$ $\boldsymbol{X}_{in} \in \boldsymbol{R}^d$. Then divide the training data set into two groups $T_1 = \{(\boldsymbol{X}_{in}, \boldsymbol{Y}_{out1})_1, (\boldsymbol{X}_{in}, \boldsymbol{Y}_{out1})_2, \ldots, (\boldsymbol{X}_{in}, \boldsymbol{Y}_{out1})_N\}$ and $T_2 = \{(\boldsymbol{X}_{in}, \boldsymbol{Y}_{out2})_1, (\boldsymbol{X}_{in}, \boldsymbol{Y}_{out2})_2, \ldots, (\boldsymbol{X}_{in}, \boldsymbol{Y}_{out2})_N\}$, and two SVR training models Equations 16, 17 can be built for the minimum and maximum outputs depending on each group of training data.

$$\begin{aligned} &\min_{\boldsymbol{\omega}_l, \boldsymbol{b}_l} \frac{1}{2}\|\boldsymbol{\omega}_l\|^2 + C\sum_{i=1}^{N}\left(\xi_i + \xi_i^*\right) \\ &s.t. \ |(\boldsymbol{\omega}_l \cdot \boldsymbol{X}_{in}) + \boldsymbol{b}_l - \boldsymbol{Y}_{out1}| \le \varepsilon + \boldsymbol{\xi}, \\ &\xi_i, \xi_i^* \ge 0, i = 1, 2, \ldots, N \end{aligned} \tag{16}$$

$$\begin{aligned} &\min_{\boldsymbol{\omega}_u, \boldsymbol{b}_u} \frac{1}{2}\|\boldsymbol{\omega}_u\|^2 + C\sum_{i=1}^{N}\left(\xi_i + \xi_i^*\right) \\ &s.t. \ |(\boldsymbol{\omega}_u \cdot \boldsymbol{X}_{in}) + \boldsymbol{b}_u - \boldsymbol{Y}_{out2}| \le \varepsilon + \boldsymbol{\xi}, \\ &\xi_i, \xi_i^* \ge 0, i = 1, 2, \ldots, N \end{aligned} \tag{17}$$

where $\boldsymbol{\omega}_l$ and $\boldsymbol{\omega}_u$ are the normal vectors, $\boldsymbol{b}_l$ and $\boldsymbol{b}_u$ are constants, ξ_i, ξ_i^* are the slack variables, C is the penalty factor, and $C > 0$. ε represents the distance swept by the hyperplane across the regions on either side, and the "ε-band" includes all training points of each training data set.

3.3 Solving of SVR-based IPF prediction model

The SVR training models are solved in this section. To reduce the complexity of solving, the models Equations 16, 17 can be transformed into Equations 18, 19 through applying the Lagrangian function and choosing an appropriate kernel function $K(x, x')$.

$$\begin{aligned} &\min_{\boldsymbol{\alpha}_l (*) \in \mathbf{R}^{2N}} \sum_{i,j=1}^{N}\left(\alpha_{l,i}^* - \alpha_{l,i}\right)\left(\alpha_{l,j}^* - \alpha_{l,j}\right)K\left(\boldsymbol{X}_{in,i}, \boldsymbol{X}_{in,j}\right) \\ &\quad +\varepsilon\sum_{i=1}^{N}\left(\alpha_{l,i}^* + \alpha_{l,i}\right) - \sum_{i=1}^{N}\boldsymbol{Y}_{out1,i}\left(\alpha_{l,i}^* - \alpha_{l,i}\right), \\ &\quad s.t. \quad \sum_{i=1}^{N}\left(\alpha_{l,i} - \alpha_{l,i}^*\right) = 0, \\ &\quad 0 \le \alpha_{l,i}, \alpha_{l,i}^* \le C, i = 1, 2, \ldots, N \end{aligned} \tag{18}$$

$$\begin{aligned} &\min_{\boldsymbol{\alpha}_u (*) \in \mathbf{R}^{2N}} \sum_{i,j=1}^{N}\left(\alpha_{u,i}^* - \alpha_{u,i}\right)\left(\alpha_{u,j}^* - \alpha_{u,j}\right)K\left(\boldsymbol{X}_{in,i}, \boldsymbol{X}_{in,j}\right) \\ &\quad +\varepsilon\sum_{i=1}^{N}\left(\alpha_{u,i}^* + \alpha_{u,i}\right) - \sum_{i=1}^{N}\boldsymbol{Y}_{out2,i}\left(\alpha_{u,i}^* - \alpha_{u,i}\right), \\ &\quad s.t. \quad \sum_{i=1}^{N}\left(\alpha_{u,i} - \alpha_{u,i}^*\right) = 0, \\ &\quad 0 \le \alpha_{u,i}, \alpha_{u,i}^* \le C, i = 1, 2, \ldots, N \end{aligned} \tag{19}$$

where $\alpha_{l,i}, \alpha_{l,i}^*, \alpha_{u,i}, \alpha_{u,i}^*$ are the Lagrange multipliers corresponding to the inequality constraints. The optimization problems can be solved by commercial solvers. The optimal solutions are attained as $\bar{\boldsymbol{\alpha}}_l = (\bar{\alpha}_{l,1}, \bar{\alpha}_{l,1}^*, \cdots, \bar{\alpha}_{l,N}, \bar{\alpha}_{l,N}^*)^{\mathrm{T}}$ $\bar{\boldsymbol{\alpha}}_u = (\bar{\alpha}_{u,1}, \bar{\alpha}_{u,1}^*, \cdots, \bar{\alpha}_{u,N}, \bar{\alpha}_{u,N}^*)^{\mathrm{T}}$, respectively. Then the decision functions are constructed as (20) and (21), and the corresponding $\bar{\boldsymbol{b}}_l$ and $\bar{\boldsymbol{b}}_u$ can be calculated by Equations 22, 23, respectively. It is noted that $\bar{\boldsymbol{b}}$ is calculated differently depending on $\bar{\alpha}_j$ or $\bar{\alpha}_k^*$.

$$\boldsymbol{f}_{\min}(\boldsymbol{x}) = \sum_{i=1}^{N}(\bar{\alpha}_{l,i}^* - \bar{\alpha}_{l,i})K(\boldsymbol{X}_{in,i}, \boldsymbol{x}) + \bar{\boldsymbol{b}}_l \tag{20}$$

$$\boldsymbol{f}_{\max}(\boldsymbol{x}) = \sum_{i=1}^{N}(\bar{\alpha}_{u,i}^* - \bar{\alpha}_{u,i})K(\boldsymbol{X}_{in,i}, \boldsymbol{x}) + \bar{\boldsymbol{b}}_u \tag{21}$$

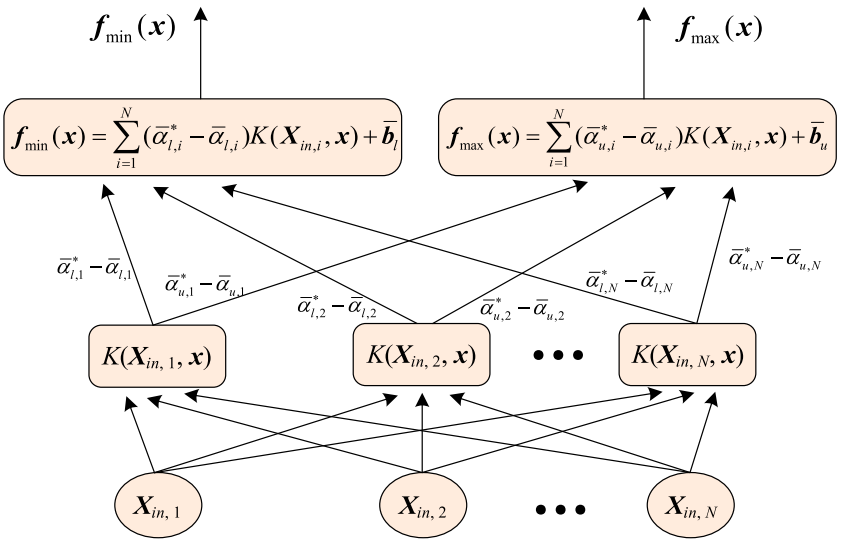

FIGURE 2
The structure of SVR training model for IPF prediction.

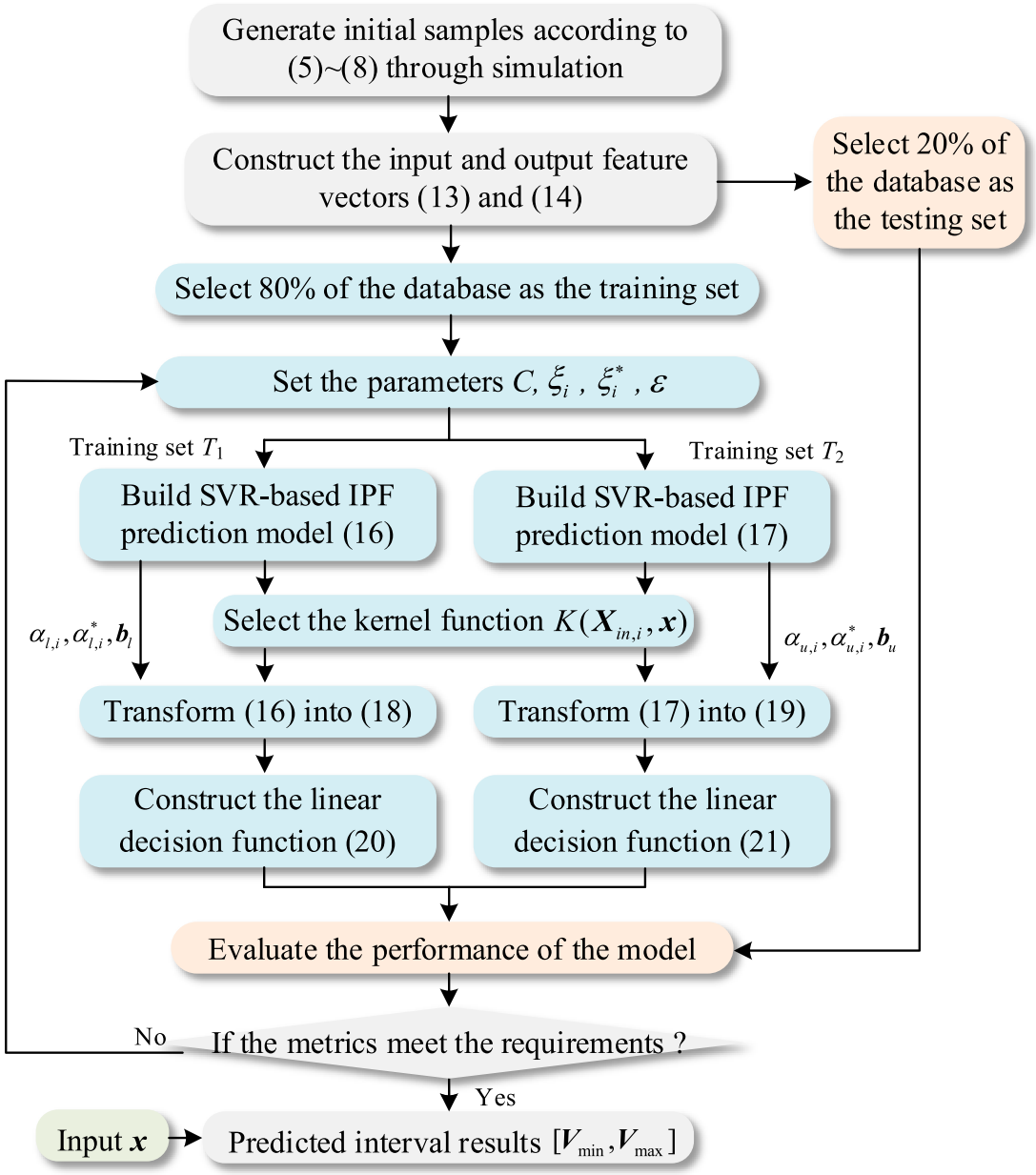

FIGURE 3
The flow chart of SVR-based IPF prediction method.

$$\bar{\boldsymbol{b}}_l = \boldsymbol{Y}_{out1,j} - \sum_{i=1}^{N}\left(\bar{\alpha}_{l,i}^* - \bar{\alpha}_{l,i}\right)K\left(\boldsymbol{X}_{in,i}, \boldsymbol{X}_{in,j}\right) + \varepsilon$$

$$\bar{\boldsymbol{b}}_l = \boldsymbol{Y}_{out1,k} - \sum_{i=1}^{N}\left(\bar{\alpha}_{l,i}^* - \bar{\alpha}_{l,i}\right)K\left(\boldsymbol{X}_{in,i}, \boldsymbol{X}_{in,k}\right) - \varepsilon \quad (22)$$

$$\bar{\boldsymbol{b}}_u = \boldsymbol{Y}_{out2,j} - \sum_{i=1}^{N}\left(\bar{\alpha}_{u,i}^* - \bar{\alpha}_{u,i}\right)K\left(\boldsymbol{X}_{in,i}, \boldsymbol{X}_{in,j}\right) + \varepsilon$$

$$\bar{\boldsymbol{b}}_u = \boldsymbol{Y}_{out2,k} - \sum_{i=1}^{N}\left(\bar{\alpha}_{u,i}^* - \bar{\alpha}_{u,i}\right)K\left(\boldsymbol{X}_{in,i}, \boldsymbol{X}_{in,k}\right) - \varepsilon \quad (23)$$

The structure of SVR training model for IPF prediction can be depicted as shown in Figure 2.

According to Figure 2, the minimum and maximum values of the power flow results, that is the interval results $[\boldsymbol{V}_{\min}, \boldsymbol{V}_{\max}]$ or $[\boldsymbol{P}_{ij,\min}, \boldsymbol{P}_{ij,\max}]$ for IPF prediction in the distribution network, are obtained based on the corresponding linear mapping relationships for any given input eigenvector.

4 The procedure of SVR-based IPF prediction method

In the SVR-based IPF prediction method for distribution networks, the first step involves establishing an IPF model for generating the initial sample database through simulation. The

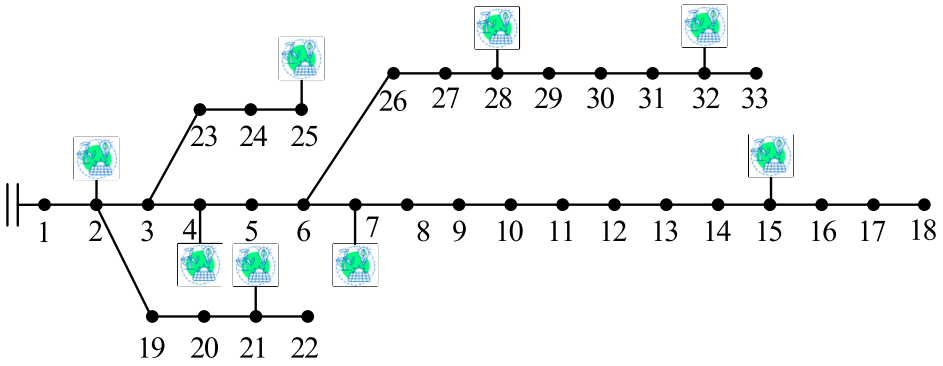

FIGURE 4
The topology of enhanced IEEE 33bw distribution network.

database includes intervals for node injections of active and reactive power, intervals for line parameter fluctuations, and corresponding intervals for node voltage. The data are then processed to construct the input and output feature vectors. Subsequently, the SVR training model is established, and the formulation of linear decision function can be determined by solving the model. Finally, when given a specific input eigenvector, the interval results for power flow variables can be predicted according to the decision function. The detailed procedure of SVR-based IPF prediction is expressed as follows and the flow chart is presented in Figure 3.

Step1. Data Generating. Generate a diverse set of initial samples according to the established IPF model Equations 5–8 through simulation, where each set comprises the interval of active and reactive node power injection fluctuations, the interval of line parameter fluctuations, and the associated node voltage intervals.

Step2. Data Preprocessing. Select and extract features from the initial samples, and construct the input and output feature vectors Equations 13, 14 for each set of data in the database according to Section 3.1. To ensure the accuracy of model training, normalize the input data. Then select 80% of the database as the training set and 20% of the database as the testing set.

Step3. IPF Prediction Model Construction. Set the parameters C, ξ_i, ξ_i^*, and ε. Then, obtain T_1 and T_2 from the training dataset, and build SVR-based IPF prediction models Equations 16, 17 depending on T_1 and T_2, respectively. Meanwhile, experiment with different kernel functions $K(\boldsymbol{X}_{in,i}, \boldsymbol{x})$ and select the one that yields the best results.

Step4. IPF Prediction Model Solving. Transform the constructed models Equations 16, 17 into Equations 18, 19, and the parameters $\alpha_{l,i}$, $\alpha_{l,i}^*$, $\alpha_{u,i}$, $\alpha_{in,i}^*\boldsymbol{b}_l$, and $\boldsymbol{b}_u$ can be obtained by solving Equations 18, 19. Then construct the linear decision functions Equation 20, 21 for predicting the minimum and maximum value of power flow variables, respectively.

Step5. Model Evaluation. Based on the testing dataset, evaluate the performance of the model using appropriate metrics, such as mean absolute error (MAE) and root mean square error (RMSE). Then determine if the metrics meet the requirements. If the metrics meet the expectations, proceed to step6; otherwise, adjust the parameters C, ξ_i, ξ_i^*, ε and return to step 3.

Step6. Interval Power Flow Prediction. Give the independent and specific input eigenvector $\boldsymbol{X}$, so that obtain the corresponding minimum voltage value $\boldsymbol{V}_{\min}$ and maximum voltage value $\boldsymbol{V}_{\max}$ through substituting $\boldsymbol{X}$ into the decision functions and De-normalization. Finally, the predicted interval results $[\boldsymbol{V}_{\min}, \boldsymbol{V}_{\max}]$ can be yielded.

5 Case studies

The performance of the proposed SVR-based IPF prediction method is tested on IEEE 33bw and IEEE 69 distribution networks on an Intel(R) Core(TM) i5 PC, 2.50 GHz processor with 8 GB RAM. The algorithm is implemented in MATLAB. The IEEE 33bw case is primarily used to validate the accuracy of the established IPF prediction model and its adaptability to various system fluctuations. Meanwhile, the IEEE 69 case is employed to verify the efficiency and real-time capability of the proposed algorithm in predicting IPF of the distribution network.

5.1 IEEE 33bw case study

The IEEE 33bw case is illustrated in Figure 4, and the case has been enhanced to include eight distributed renewable energy sources. All parameters are valued according to the per unit (p.u.) system of analysis, with 10 MVA chosen as the basic power of the test case. The detailed original power generation data for these eight DGs are presented in Table 1. The voltage limits of all buses except the slack bus are constrained to [0.9,1.1].

5.1.1 Evaluation of the model

The active power generation fluctuation ranges of DGs are assumed to be ±20% of the original data, which is also assumed on the active and reactive load demand, that is the set the fluctuation coefficient $\sigma_1 = 0.2$. Meanwhile, considering the slight fluctuations in distribution network line parameters under both internal and

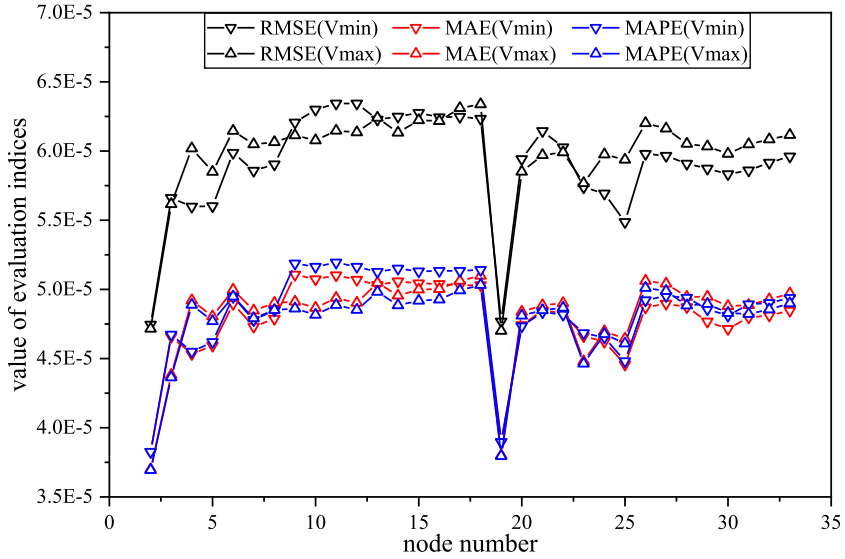

FIGURE 5
The evaluation results of RMSE, MAE and MAPE for the SVR-based IPF prediction model.

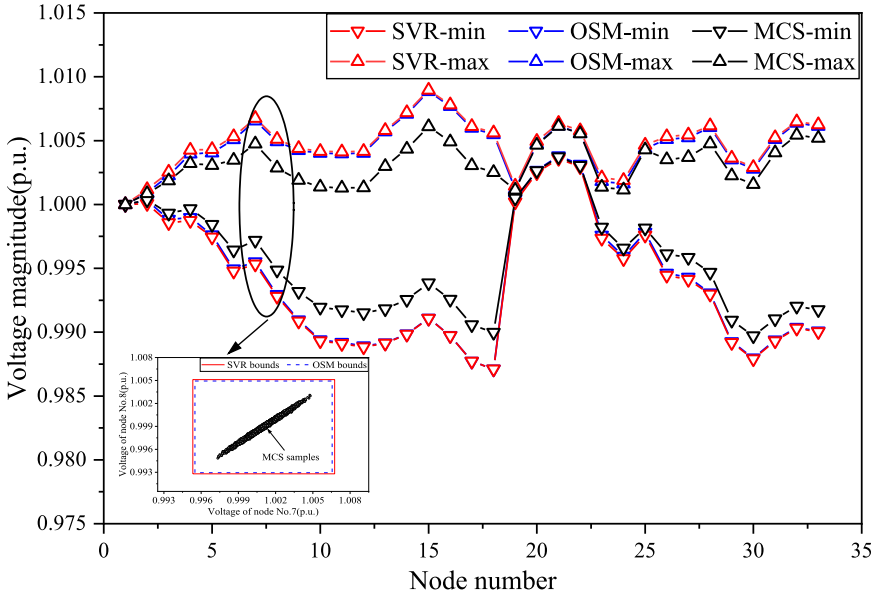

FIGURE 6
The voltage interval results obtained by SVR, OSM and MCS for IEEE 33bw case in Scenario 1.

external conditions, assume the fluctuation range is ±10% of r_{ij} and x_{ij}, that is $\sigma_2 = 0.1$. Within these ranges, 1,500 sets of initial data are randomly generated through simulation for the distribution network, where 1,200 sets are training sets, and 300 sets are testing sets. In the model training process, the parameters of SVR model are set to be C = 5,000, $\varepsilon = 0.0001$, $\xi_i = 1$. The kernel function is selected as $K(x_i, x_j) = x_i^T x_j$.

To evaluate the model's performance comprehensively and objectively, the indices of mean absolute error (MAE), root mean square error (RMSE), mean absolute percentage error (MAPE) and R2 for the testing sets are calculated in this paper. They are defined as Equations 24–27. Using these metrics together helps to avoid biases introduced by a single metric, enhancing the robustness of the evaluation.

$$MAE = \frac{1}{n}\sum_{i=1}^{n}|y_i - \hat{y}_i| \tag{24}$$

$$RMSE = \sqrt{\frac{1}{n}\sum_{i=1}^{n}(y_i - \hat{y}_i)^2} \tag{25}$$

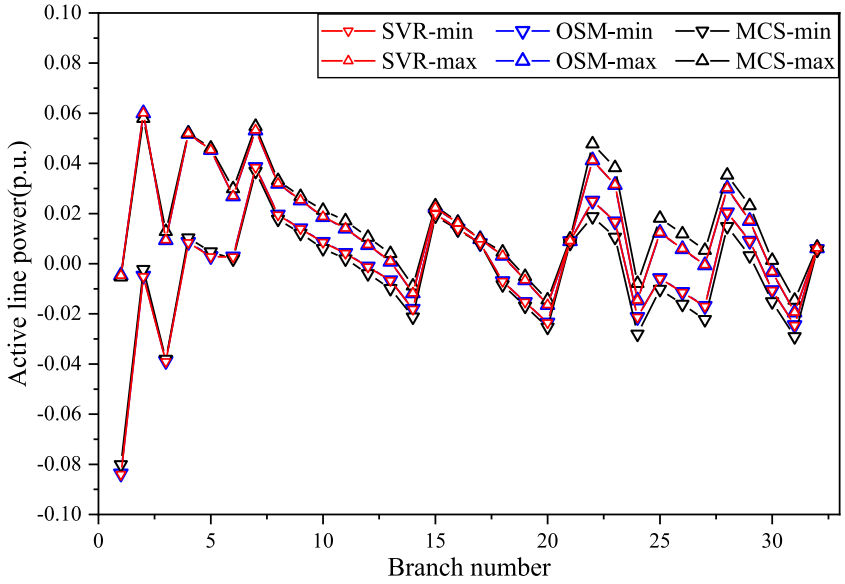

FIGURE 7
The active line power interval results obtained by SVR, OSM and MCS for IEEE 33bw case in Scenario 1.

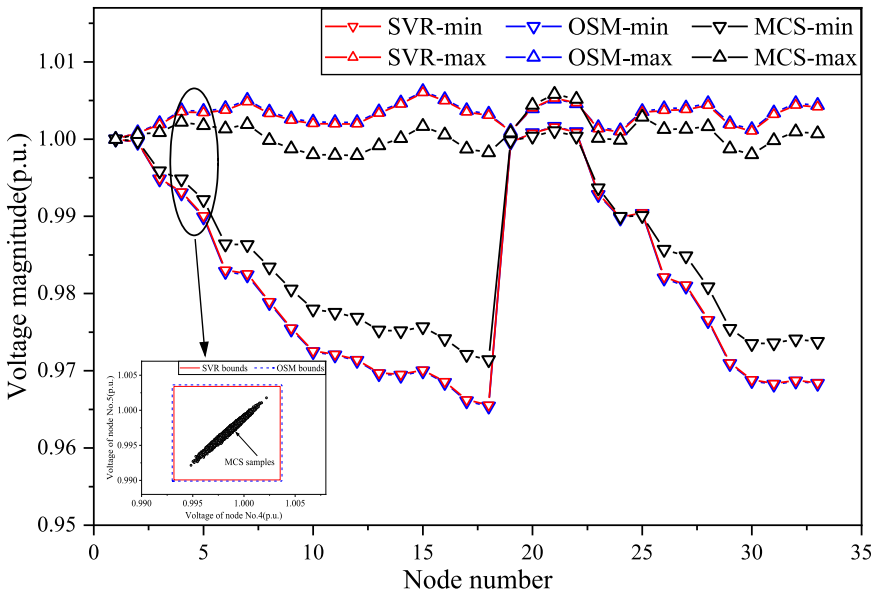

FIGURE 8
The voltage interval results obtained by SVR, OSM and MCS for IEEE 33bw case in Scenario 2.

$$MAPE = \frac{1}{n}\sum_{i=1}^{n}\left|\frac{y_i - \hat{y}_i}{y_i}\right| \tag{26}$$

$$R^2 = 1 - \frac{\sum_{i=1}^{n}(y_i - \hat{y}_i)^2}{\sum_{i=1}^{n}(y_i - \bar{y}_i)^2} \tag{27}$$

where n is the number of samples, y_i is the observed values, $\hat{y}_i$ is the corresponding model-predicted value, and $\bar{y}$ is the mean of the observed values. The evaluation results of the indices for the SVR-based IPF prediction model in IEEE 33bw case are presented in Figure 5.

It can be observed from Figure 5 that the value of the evaluation indices is ideal. For the lower and upper bounds of each node voltage, the RMSE evaluation results are within the range $[4.7 \times 10^{-5}, 6.4 \times 10^{-5}]$, the MAE evaluation results are within the range $[3.6 \times 10^{-5}, 5.2 \times 10^{-5}]$, and the MAPE evaluation results are within the range $[3.6 \times 10^{-5}, 5.3 \times 10^{-5}]$, all of which

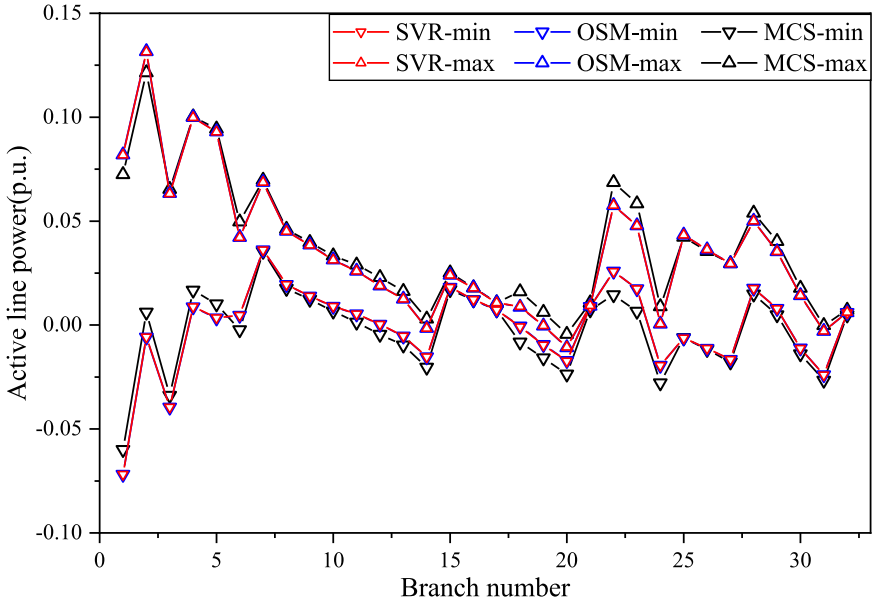

FIGURE 9
The active line power interval results obtained by SVR, OSM and MCS for IEEE 33bw case in Scenario 2.

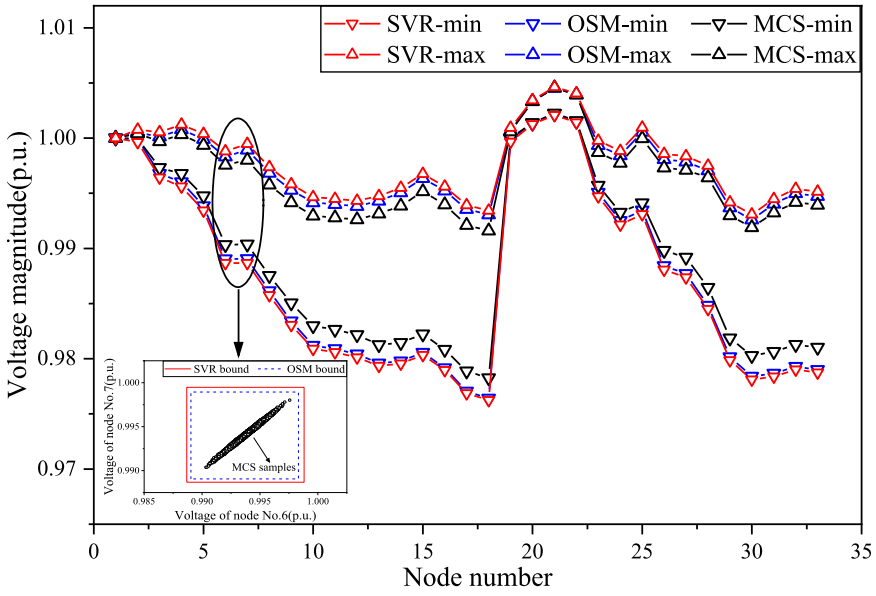

FIGURE 10
The voltage interval results obtained by SVR, OSM and MCS for IEEE 33bw case in Scenario 3.

are relatively small. Besides, the value of R2 can reach above 0.95 for both lower and upper bounds of each node voltage. These support the notion that the model's predicted values exhibit minimal deviation from the true values, indicating a strong fit of the model to the testing sets, which confirms the superior performance of the established SVR-based IPF prediction model.

5.1.2 Comparison with the OSM and MCS

To validate the accuracy and adaptability of the SVR-based IPF prediction model, three scenarios were designed to conduct the proposed method compared with the OSM (Zhang et al., 2017) and MCS. The forward-backward substitution is employed in MCS for solving general distribution network power flow. The three operating scenarios are described as follows.

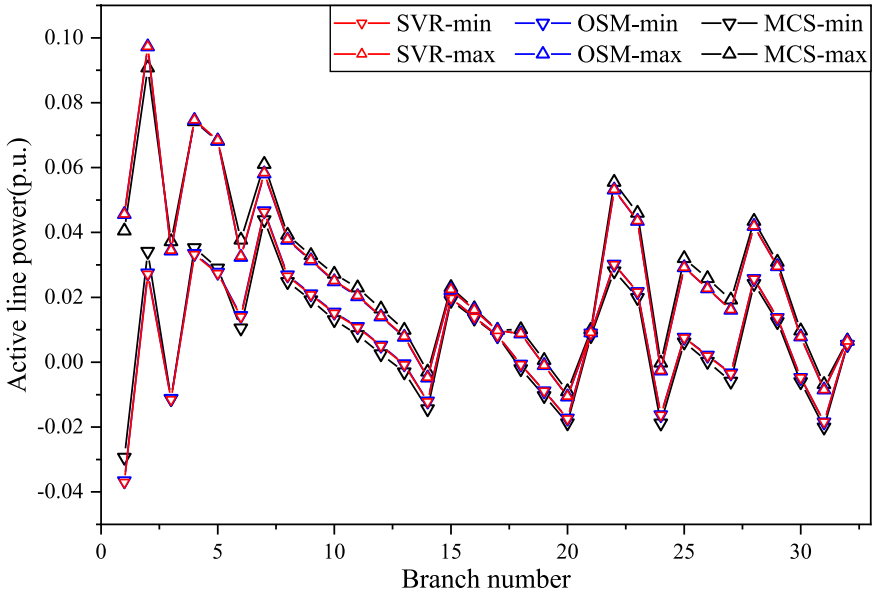

FIGURE 11
The active line power interval results obtained by SVR, OSM and MCS for IEEE 33bw case in Scenario 3.

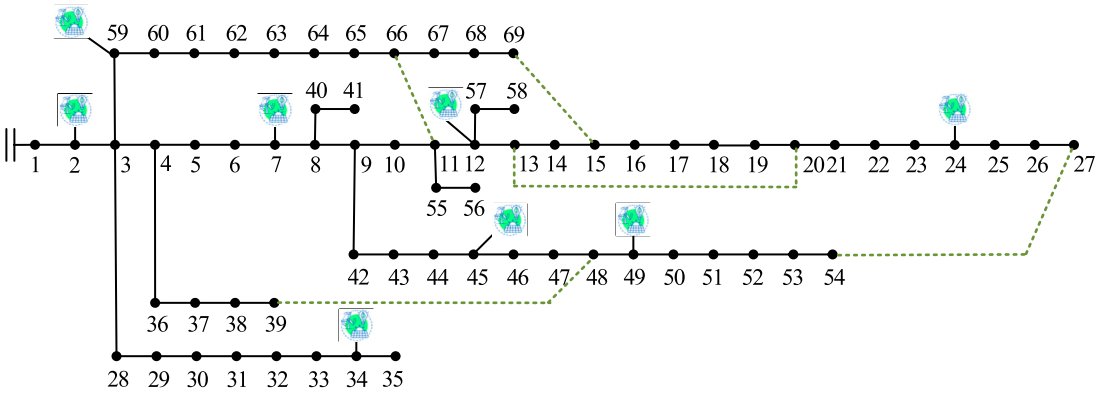

FIGURE 12
The topology of enhanced IEEE 69 distribution network.

Scenario 1: The same operating points, and the different fluctuation ranges;

Scenario 2: The different operating points, and the same fluctuation ranges;

Scenario 3: The different operating points, and the different fluctuation ranges,

where the settings of these scenarios are changed based on the training data. The operating points represent the original active power generation $\boldsymbol{p}_0^G$, and the fluctuation ranges are set by changing the fluctuation coefficients σ_1 and σ_2. They represent the randomness and volatility of uncertain data in distribution networks.

5.1.2.1 The simulation under scenario 1

In Scenario 1, the original active power generation data was the same as that in Table 1, and the fluctuation coefficients were set as $\sigma_1 = 0.1$, $\sigma_2 = 0.05$. Thus, a new set of input eigenvector $\boldsymbol{X}_{in,\mathrm{I}}$ was introduced. The parameters of SVR model were set to be C = 5,000, $\varepsilon = 0.0001$, $\xi_i = 1$, and the MCS was conducted with a sample size of 10,000 to ensure a high accuracy level. The simulation results under this scenario are demonstrated as follows.

The voltage interval results obtained by the SVR, OSM and MCS for IEEE 33bw case are presented in Figure 6, and the active line transmission power interval results are presented in Figure 7. Additionally, in Figure 6, the voltage interval boundary values of node No. 7 and No. 8 obtained by SVR and OSM are compared with the results of MCS sampling for a more intuitive presentation. It can be observed from Figure 6 that the voltage interval results obtained by SVR are very close to those acquired by the OSM, and the voltage interval range obtained by SVR and OSM is larger than that obtained by MCS. This is to be expected, because the initial data for SVR

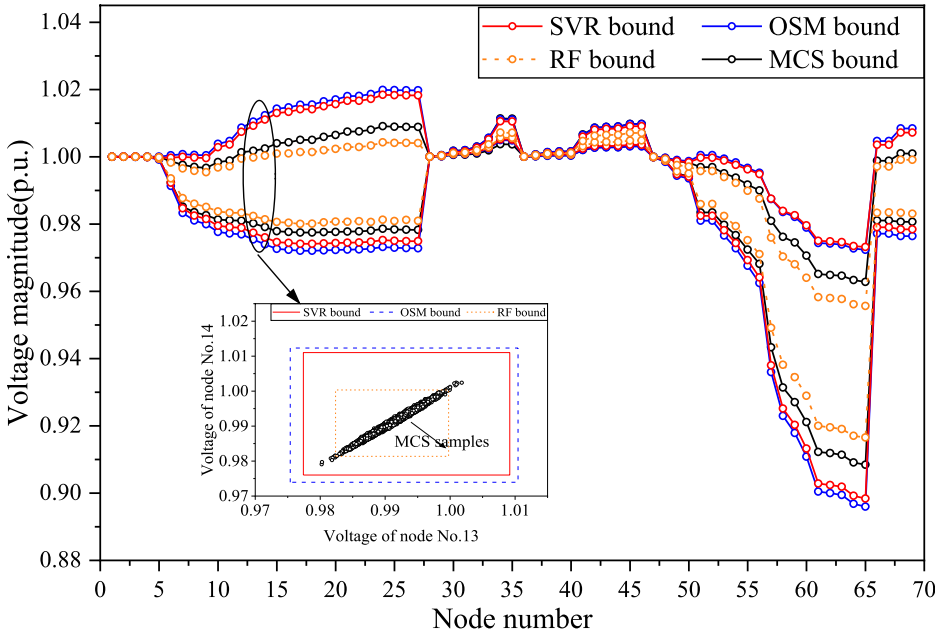

FIGURE 13
The voltage interval results obtained by SVR, RF, OSM and MCS for IEEE 69 case.

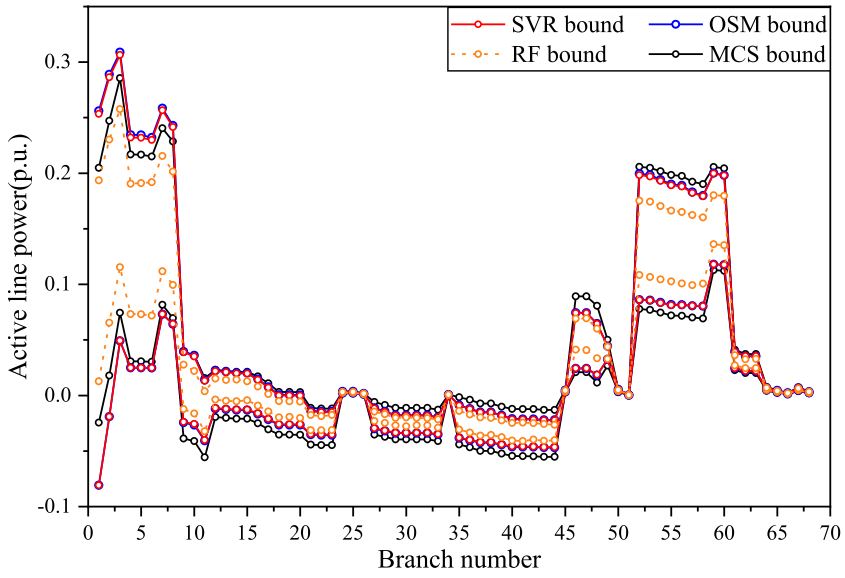

FIGURE 14
The active line power interval results obtained by SVR, RF, OSM and MCS for IEEE 69 case.

model training is generated through OSM, and the OSM takes into consideration of the extreme scenarios that are ignored by the MCS method. It can be seen from Figure 7 that the interval ranges of active line transmission power obtained by the three methods are relatively close. This is because the line transmission power is related to power generation, load demand, and line parameters, and the Distflow model for the distribution network is linear, so that the active line power results obtained by different methods are close under the same interval input values. The simulation results indicate that the established SVR-based IPF prediction method possesses high predictive accuracy and performs a strong adaptability to different fluctuations.

TABLE 1 The original power generation data of DGs for IEEE 33bw case (p.u.).

Bus number	Active power generation P_G	Reactive power generation Q_G
2	0.0800	0.0600
4	0.0570	0.0500
7	0.0510	0.0440
15	0.0420	0.0380
21	0.0380	0.0340
25	0.0600	0.0500
28	0.0400	0.0320
32	0.0490	0.0450

TABLE 2 The original power generation data of DGs for IEEE 33bw case in Scenario 2 (p.u.).

Bus number	Active power generation P_G	Reactive power generation Q_G
2	0.0720	0.0600
4	0.0545	0.0500
7	0.0490	0.0440
15	0.0355	0.0380
21	0.0320	0.0340
25	0.0515	0.0500
28	0.0335	0.0320
32	0.0405	0.0450

5.1.2.2 The simulation under scenario 2

In Scenario 2, the original active power generation data was listed in Table 2, and the fluctuation coefficients were set as $\sigma_1 = 0.2$, $\sigma_2 = 0.1$. Thus, a new set of input eigenvector $\boldsymbol{X}_{in,\mathrm{II}}$ was introduced. The parameters of SVR model and the sample size of MCS remain the same as (I).

The interval bound results obtained by the SVR, OSM, and MCS for the voltage magnitudes of nodes and the active transmission power of branches for IEEE 33bw case in Scenario 2 are presented in Figures 8, 9, respectively. Similarly, the voltage interval boundaries of nodes No. 4 and No. 5 are selected in Figure 8 for comparison with the MCS sampling results. The SVR is observed to have acquired a similar voltage range to OSM, which is wider than that of MCS. The active line power interval bounds acquired by SVR are close to that obtained by OSM and MCS. These results show that the proposed method also has high precision under scenario 2, which proves that the SVR-based IPF prediction model can adapt to different operating points.

5.1.2.3 The simulation under scenario 3

In Scenario 3, the original active power generation data was the same as that in Table 2, and the fluctuation coefficients were set as $\sigma_1 = 0.1$, $\sigma_2 = 0.05$. Thus, a new set of input eigenvector $\boldsymbol{X}_{in,\mathrm{III}}$ was introduced. The parameters of SVR model and the sample size of MCS remain the same as (I). The simulation results under this scenario are demonstrated as follows.

Scenario 3 was set up to verify the accuracy of the proposed algorithm when the operating points and fluctuation ranges change simultaneously. The interval bounds of voltage and active line power obtained by SVR, OSM, and MCS in Scenario 3 are presented in Figures 10, 11. Besides, the voltage boundaries of nodes No. 6 and No. 7 obtained by SVR and OSM are also compared with the MCS sampling results in Figure 10. It can be observed that the voltage ranges obtained by SVR and OSM are still very close, which are more conservative than those obtained by MCS. The active line power ranges acquired by the three methods remain close. The simulation results are expected. Furthermore, compared to scenario 2, the voltage and active line power interval ranges obtained by the three methods are both smaller. This is because the fluctuation ranges are reduced while the operating points remain still. The simulation in scenario 3 validates that the proposed algorithm can maintain high prediction accuracy under different operating points and fluctuation ranges.

In summary, based on simulations under different scenarios, the proposed SVR-based IPF prediction model can adapt to various operational states and environmental fluctuations. In different operating scenarios, this method achieves prediction accuracy comparable to the OSM which is model-driven. Besides, the SVR method provides a more conservative interval range than MCS, which ensures distribution system security under high-dimensional uncertainty. It demonstrates high computational accuracy and strong adaptability of the proposed approach.

5.2 IEEE 69 case study

The IEEE 69 case is applied to validate the efficiency of the proposed SVR-based IPF prediction method. The distribution network is enhanced to include eight DGs. The topology of enhanced IEEE 69 case is presented in Figure 12 and the original active and reactive power generation of DGs are shown in Table 3. All parameters are valued in p.u., and the base power is set to 10 MVA. The voltage limits of all nodes except the slack bus are constrained to [0.9, 1.1].

In IEEE 69 case, 500 sets of training data were generated under the condition of fluctuations with $\sigma_1 = 0.2$, $\sigma_2 = 0.1$. The model training parameters were set as C = 5,000, $\varepsilon = 0.0001$, $\xi_i = 1$, and the kernel function is selected as $K(x_i, x_j) = x_i^T x_j$. After the model was trained, the predictions were conducted under Scenario 3 as defined in Section 5.1.2. To further validate the model's applicability, the generator operating points were randomly selected within ± 30% of the original active power generation data. What's more, the fluctuation coefficients for power generation and load demand were set to $\sigma_1 = 0.3$, and the fluctuation coefficient for line parameters was set to $\sigma_2 = 0.15$, which aims to assess the model's adaptability under expanded fluctuation ranges. This case was carried out with SVR, OSM, and MCS as well.

To further demonstrate the advantage of the proposed SVR-based IPF method, this case additionally incorporated the Random Forest (RF) method for interval power flow prediction. To balance both prediction accuracy and efficiency, the parameters for training the RF model were set as follows: the number of decision trees was

TABLE 3 The original power generation data of DGs for IEEE 69 case (p.u.).

Bus number	Active power generation P_G	Reactive power generation Q_G
2	0.0500	0.0400
7	0.0370	0.0300
12	0.0410	0.0340
24	0.0320	0.0280
34	0.0280	0.0240
45	0.0400	0.0400
49	0.0300	0.0220
59	0.0390	0.0350

set to 100, the minimum leaf size was set to 5, and the model was configured as a regression model. Besides, the system uncertainty parameters were consistent with those described above. Considering the above all, the simulation results are presented in Figures 13, 14.

Figures 13, 14 show the voltage interval ranges and active line transmission power ranges, respectively. The voltage bounds of nodes No. 13 and No. 14 obtained by SVR, RF and OSM are depicted in Figure 13 compared with the MCS samples. It can be observed that under large-scale fluctuations, the voltage ranges obtained by the SVR and OSM are relatively close, and the error precision is determined to be 0.001 upon calculations. The error is mainly attributed to the insufficient size of the training dataset, which can be mitigated by increasing the number of training samples. However, the two methods yield very close active transmission power ranges with high prediction accuracy. Furthermore, compared to the MCS, SVR and OSM obtain wider voltage ranges, as explained in 5.1.2. This case study validates the adaptability of the proposed method to different networks and their ability to handle large fluctuation ranges.

Comparing the SVR method proposed in this paper with the RF method, the SVR method achieves higher prediction accuracy. It is evident that the prediction error using the RF method is relatively large, with an error precision of only 0.01, which shows a significant deviation from the interval results obtained by the OSM. Additionally, the interval obtained by the RF method is narrower, possibly because the predictions of the trees in the model are more concentrated and less flexible in handling extreme cases. Meanwhile, for the RF method, improving prediction accuracy requires increasing the number of decision trees, but this comes at the cost of increased computation time. Through multiple experiments, the accuracy gain from adding more decision trees was found to be negligible.

To validate the efficiency of the proposed method, the computation time of the algorithm compared to RF and OSM is shown in Table 4. The computation time includes the total time for solving voltage and line transmission power. It is noticeable that the online computation speed of the SVR-based IPF prediction method and RF prediction method is significantly faster than the OSM. Meanwhile, the online computation speed of SVR is also faster than that of RF. Besides, the offline training of SVR and RF requires more time compared to the OSM computation, and the offline training times of SVR and RF are comparable. However, the training and OSM both require significant amounts of time, which increases as the number of system nodes grows. In contrast, the online computation time of SVR is minimally affected by the system scale, and predictions are conducted based on the trained results in practical applications, so that the online computation time is more crucial.

TABLE 4 The computation time of SVR prediction method, RF prediction method, and OSM for IEEE 69 case.

	Online computation time/s	Offline training time/s
SVR prediction	0.0162	501.58
RF prediction	2.18	553.36
OSM	317.55	—

The comparison demonstrates that the proposed SVR approach achieves a significant improvement in computational efficiency over model-driven approaches and is more suitable for large-scale systems. Additionally, the SVR approach has advantages over the RF method in both computational accuracy and efficiency, demonstrating that it is more suitable for IPF analysis compared to other data-driven methods. In summary, the proposed SVR approach is more suitable for rapid and real-time PF analysis of distribution networks with DGs.

6 Conclusion

To address the uncertainty in PF and overcome the efficiency challenges faced by traditional model-driven methods, an SVR-based IPF prediction method for PF analysis in distribution networks is proposed through combining data-driven methods with interval theory. This method considers uncertainty as intervals and employs SVR for model training. The training data is generated through simulation of the established IPF model for distribution network including the intervals of node power injections, line parameters, and the minimum/maximum PF variables. Then the input and output feature vectors for IPF are constructed and the multi-output SVR-based IPF prediction model is established based on the training dataset. To assess the performance of the proposed method, several simulations are conducted both on IEEE 33bw case and IEEE 69 case.

The simulation results show that the proposed method has a good performance. Firstly, the evaluation metrics are calculated to demonstrate the method's high accuracy. Additionally, the proposed method is compared with OSM and MCS in three different scenarios, showcasing robust adaptability across different distribution network cases, operating points, and input data fluctuation ranges. The comparison of interval results obtained by SVR prediction and OSM demonstrates that the SVR approach can achieve prediction accuracy comparable to that of model-driven methods. Meanwhile, the comparative analysis of computation time with the OSM and RF demonstrates that the proposed approach significantly improves computational efficiency compared to model-driven approaches and offers better prediction accuracy and efficiency compared to other data-driven methods. In conclusion, the proposed method exhibits superior computational efficiency and accuracy, meeting the requirements for

handling power flow uncertainty and achieving real-time rapid PF analysis in distribution networks.

Data availability statement

The original contributions presented in the study are included in the article/supplementary material, further inquiries can be directed to the corresponding authors.

Author contributions

XL: Conceptualization, Methodology, Writing–original draft. HZ: Data curation, Investigation, Writing–review and editing. QL: Methodology, Validation, Writing–original draft, Writing–review and editing. ZL: Software, Writing–review and editing. HL: Investigation, Writing–original draft.

Funding

The author(s) declare that financial support was received for the research, authorship, and/or publication of this article. This work was supported by the Science and Technology Project of China Southern Power Grid (090000KK52222133/SZKJXM20222115).

Conflict of interest

Authors XL, HZ, ZL, HL were employed by Shenzhen Power Supply Co., Ltd.

The remaining author declare that the research was conducted in the absence of any commercial or financial relationships that could be construed as a potential conflict of interest.

The authors declare that this study received funding from China Southern Power Grid. The funder had the following involvement in the study: data curation, investigation, the study methodology, data analysis, and writing-review\editing.

Publisher's note

All claims expressed in this article are solely those of the authors and do not necessarily represent those of their affiliated organizations, or those of the publisher, the editors and the reviewers. Any product that may be evaluated in this article, or claim that may be made by its manufacturer, is not guaranteed or endorsed by the publisher.

References

Barboza, L. V., Dimuro, G. P., and Reiser, R. S. (2004). "Towards interval analysis of the load uncertainty in power electric systems," in *Proceedings of the international conference on probabilistic methods applied to power systems (ICPMAPS), ames, United States, 12-16 september 2004*, 538–544.

Cao, Y., Zhou, B., Chung, C. Y., Wu, T., Zheng, L., and Shuai, Z. (2024). A coordinated emergency response scheme for electricity and watershed networks considering spatio-temporal heterogeneity and volatility of rainstorm disasters. *IEEE Trans. Smart Grid.* 15 (4), 3528–3541. doi:10.1109/TSG.2024.3362344

Chen, J., Li, W., Wu, W., Zhu, T., Wang, Z., and Zhao, C. (2020). "Robust data-driven linearization for distribution three-phase power flow," in *Proceedings of the IEEE 4th conference on energy internet and energy system integration (EI2)*, 1527–1532. Wuhan, China, 30 October-01 November 2020.

Chen, J., Wu, W., and Roald, L. A. (2022). Data-driven piecewise linearization for distribution three-phase stochastic power flow. *IEEE Trans. Smart Grid.* 13 (2), 1035–1048. doi:10.1109/TSG.2021.3137863

Chen, Y., Wu, C., and Qi, J. (2022). Data-driven power flow method based on exact linear regression equations. *J. Mod. Power Syst. Clean. Energy.* 10 (3), 800–804. doi:10.35833/MPCE.2020.000738

Cheng, S., Zuo, X., Yang, K., Wei, Z., and Wang, R. (2023). Improved affine arithmetic-based power flow computation for distribution systems considering uncertainties. *IEEE Syst. J.* 17 (2), 1918–1927. doi:10.1109/JSYST.2022.3176461

Dong, M., Wiebe, D., and Shi, J. (2022). "An accelerated and risk-free AC power flow method with machine learning based initiation," in *Proceedings of the IEEE electrical power and energy conference (EPEC)*, 103–108. Victoria, Canada, 05-07 December 2022.

Fu, X., Zhang, C., Xu, Y., Zhang, Y., and Sun, H. (2024). Statistical machine learning for power flow analysis considering the influence of weather factors on photovoltaic power generation. *IEEE Trans. Neural Netw. Learn. Syst.*, 1–15. doi:10.1109/TNNLS.2024.3382763

Guo, L., Zhang, Y., Li, X., Wang, Z., Liu, Y., Bai, L., et al. (2022). Data-driven power flow calculation method: a lifting dimension linear regression approach. *IEEE Trans. Power Syst.* 37 (3), 1798–1808. doi:10.1109/TPWRS.2021.3112461

Hu, X., Hu, H., Verma, S., and Zhang, Z. L. (2021). Physics-guided deep neural networks for power flow analysis. *IEEE Trans. Power Syst.* 36 (3), 2082–2092. doi:10.1109/TPWRS.2020.3029557

Jia, M., and Hug, G. (2023). "Overview of data-driven power flow linearization," in *Proceedings of the IEEE belgrade PowerTech*, 1–6. Belgrade, Serbia, 25-29 June 2023.

Khalid, H. M., Muyeen, S. M., and Kamwa, I. (2022). An improved decentralized finite-time approach for excitation control of multi-area power systems. *Sustain. Energy Grids Netw. 31* 31, 100692. doi:10.1016/j.segan.2022.100692

Leng, S., Liu, K., Ran, X., Chen, S., and Zhang, X. (2020). An affine arithmetic-based model of interval power flow with the correlated uncertainties in distribution system. *IEEE Access* 8, 60293–60304. doi:10.1109/ACCESS.2020.2982928

Li, P., Wu, W., Wang, X., and Xu, B. (2023). A data-driven linear optimal power flow model for distribution networks. *IEEE Trans. Power Syst.* 38 (1), 956–959. doi:10.1109/TPWRS.2022.3216161

Liang, Z., Dong, Z., Li, C., Wu, C., and Chen, H. (2023). A data-driven convex model for hybrid microgrid operation with bidirectional converters. *IEEE Trans. Smart Grid.* 14 (2), 1313–1316. doi:10.1109/TSG.2022.3193030

Liu, J., Yang, Z., Zhao, J., Yu, J., Tan, B., and Li, W. (2022). Explicit data-driven small-signal stability constrained optimal power flow. *IEEE Trans. Power Syst.* 37 (5), 3726–3737. doi:10.1109/TPWRS.2021.3135657

Liu, Y., Li, Z., and Zhao, J. (2022). Robust data-driven linear power flow model with probability constrained worst-case errors. *IEEE Trans. Power Syst.* 37 (5), 4113–4116. doi:10.1109/TPWRS.2022.3189543

Liu, Y., Li, Z., and Zhou, Y. (2022). Data-driven-aided linear three-phase power flow model for distribution power systems. *IEEE Trans. Power Syst.* 37 (4), 2783–2795. doi:10.1109/TPWRS.2021.3130301

Liu, Y., Wang, Y., Zhang, N., Lu, D., and Kang, C. (2020). A data-driven approach to linearize power flow equations considering measurement noise. *IEEE Trans. Smart Grid.* 11 (3), 2576–2587. doi:10.1109/TSG.2019.2957799

Liu, Y., Xu, B., Botterud, A., Zhang, N., and Kang, C. (2021). Bounding regression errors in data-driven power grid steady-state models. *IEEE Trans. Power Syst.* 36 (2), 1023–1033. doi:10.1109/TPWRS.2020.3017684

Lyu, C., Sheng, W., Liu, K., and Dong, X. (2023). Novel affine power flow method for improving accuracy of interval power flow data in cyber physical systems of active distribution networks. *CSEE J. Power Energy Syst.* 9 (5), 1881–1892. doi:10.17775/CSEEJPES.2020.07040

Mezghani, I., Misra, S., and Deka, D. (2020). Stochastic AC optimal power flow: a data-driven approach. *Electr. Power Syst. Res.* 189, 106567. doi:10.1016/j.epsr.2020.106567

Mori, H., and Yuihara, A. (1999). "Calculation of multiple power flow solutions with the Krawczyk method," in *Proceedings of the IEEE international symposium on circuits and systems (ISCAS)*, 94–97. Orlando, USA.

Musleh, A. S., Khalid, H. M., Muyeen, S. M., and Al-Durra, A. (2019). A prediction algorithm to enhance grid resilience toward cyber attacks in WAMCS applications. *IEEE Syst. J.* 13 (1), 710–719. doi:10.1109/JSYST.2017.2741483

Rehman, A. U., Ullah, Z., Qazi, H. S., Hasanien, H. M., and Khalid, H. M. (2024). Reinforcement learning-driven proximal policy optimization-based voltage control for

PV and WT integrated power system. *Renew. Energy*. 227, 120590. doi:10.1016/j.renene.2024.120590

Shao, Z., Zhai, Q., and Guan, X. (2023). Physical-model-aided data-driven linear power flow model: an approach to address missing training data. *IEEE Trans. Power Syst.* 38 (3), 2970–2973. doi:10.1109/TPWRS.2023.3256120

Sun, Y., Zhao, Z., Yang, M., Jia, D., Pei, W., and Xu, B. (2020). Overview of energy storage in renewable energy power fluctuation mitigation. *CSEE J. Power Energy Syst.* 6 (1), 160–173. doi:10.17775/CSEEJPES.2019.01950

Tan, B., Chen, S., Liang, Z., Zheng, X., Zhu, Y., and Chen, H. (2024). An iteration-free hierarchical method for the energy management of multiple-microgrid systems with renewable energy sources and electric vehicles. *Appl. Energy*. 356, 122380. doi:10.1016/j.apenergy.2023.122380

Tan, Y., Chen, Y., Li, Y., and Cao, Y. (2020). Linearizing power flow model: a hybrid physical model-driven and data-driven approach. *IEEE Trans. Power Syst.* 35 (3), 2475–2478. doi:10.1109/TPWRS.2020.2975455

Vaccaro, A., Canizares, C. A., and Villacci, D. (2010). An affine arithmetic-based methodology for reliable power flow analysis in the presence of data uncertainty. *IEEE Trans. Power Syst.* 25 (2), 624–632. doi:10.1109/TPWRS.2009.2032774

Xing, Z., Gong, J., Lao, K. W., and Dai, N. (2021). "Single bus data-driven power estimation based on modified linear power flow model," in *Proceedings of the 6th international conference on power and renewable energy (ICPRE)* (Shanghai, China), 755–758.

Xing, Z., Lao, K. W., Gao, H., and Dai, N. (2022). "A modified data-driven power flow model for power estimation with incomplete bus data," in *Proceedings of the 12th international conference on power, energy and electrical engineering (CPEEE)*, 316–320. Shiga, Japan, 25-27 February 2022.

Xue, Y., and Liu, Y. (2021). Intelligent assessment of active and reactive power flow with satisfying accuracy for N-k1-k2 cascading outages. *J. Mod. Power Syst. Clean. Energy*. 9 (5), 986–999. doi:10.35833/MPCE.2020.000312

Zhang, C., Chen, H., Ngan, H., Yang, P., and Hua, D. (2017). A mixed interval power flow analysis under rectangular and polar coordinate system. *IEEE Trans. Power Syst.* 32 (2), 1–1429. doi:10.1109/TPWRS.2016.2583503

Zhang, C., Chen, H., Shi, K., Qiu, M., Hua, D., and Ngan, H. (2018). An interval power flow analysis through optimizing-scenarios method. *IEEE Trans. Smart Grid.* 9 (5), 5217–5226. doi:10.1109/TSG.2017.2684238

Zhang, C., Liu, Q., Zhou, B., Chung, C. Y., Li, J., Zhu, L., et al. (2023). A central limit theorem-based method for DC and AC power flow analysis under interval uncertainty of renewable power generation. *IEEE Trans. Sustain. Energy.* 14 (1), 563–575. doi:10.1109/TSTE.2022.3220567

Zheng, X., Khodayar, M. E., Wang, J., Yue, M., and Zhou, A. (2024). Distributionally robust multistage dispatch with discrete recourse of energy storage systems. *IEEE Trans. Power Syst.*, 1–14. doi:10.1109/TPWRS.2024.3369664

frontiers | Frontiers in Energy Research

TYPE Original Research
PUBLISHED 01 October 2024
DOI 10.3389/fenrg.2024.1469594

OPEN ACCESS

EDITED BY
Lipeng Zhu,
Hunan University, China

REVIEWED BY
Junjie Hu,
North China Electric Power University, China
ERSHUN DU,
Tsinghua University, China

*CORRESPONDENCE
Shuyan Zhang,
437380005@qq.com

RECEIVED 24 July 2024
ACCEPTED 13 September 2024
PUBLISHED 01 October 2024

CITATION
Li Y, Zhang S, Yang L, Gong Q, Li X and Fan B (2024) Optimal scheduling strategies for electrochemical energy storage power stations in the electricity spot market.
Front. Energy Res. 12:1469594.
doi: 10.3389/fenrg.2024.1469594

Optimal scheduling strategies for electrochemical energy storage power stations in the electricity spot market

Yuanyuan Li[1], Shuyan Zhang[1]*, Luye Yang[2], Qihang Gong[2], Xiaojing Li[2] and Biwu Fan[2]

[1]Beijing Key Laboratory of Research and System Evaluation of Power, China Electric Power Research Institute, Power Automation Department, Beijing, China, [2]PKU-Changsha Institute for Computing and Digital Economy, Changsha, China

Introduction: This paper constructs a revenue model for an independent electrochemical energy storage (EES) power station with the aim of analyzing its full life-cycle economic benefits under the electricity spot market.

Methods: The model integrates the marginal degradation cost (MDC), energy arbitrage, ancillary services, and annual operation and maintenance (O&M) costs to calculate the net profits of the EES power station. Using an iterative optimization approach, we determine the optimal MDC and analyze the economic end of life (EOL) for different types of EES power stations.

Results: By examining real-world examples from the California energy market, we find that the full life-cycle benefits of an EES power station peak when its MDC is optimal, at $45/MWh-throughput. Under these conditions, the economic and physical EOL of commercial/industrial EES power station is 9 years, while the economic EOL of residential-grade EES power station is 8 years, which is shorter than their physical EOL of 9 years.

Discussion: The study further indicates that the economic life of an EES power station is influenced by multiple factors, and operators need to determine the optimal economic EOL to maximize revenue based on battery degradation characteristics, market conditions and operational strategy.

KEYWORDS

electricity spot market, electrochemical energy storage, profit model, energy arbitrage, economic end of life

1 Introduction

With the global energy structure transition and the large-scale integration of renewable energy, research on energy storage technologies and their supporting market mechanisms has become the focus of current market domain (Zhu et al., 2024). Electrochemical energy storage (EES) not only provides effective energy storage solutions but also offers new business opportunities and operational strategies for electricity market participants. At present, the configuration of energy storage projects mainly focuses on the source-side renewable energy configuration and independent energy storage applications.

In some areas, energy storage is applied in the frequency regulation market transactions in the form of an integrated system (Zhang and Wang, 2021), (Liang et al., 2021). From the

perspective of specific practices, energy storage is primarily bundled with thermal power, wind power, and photovoltaic in the form of a consortium to participate in market transactions in the early stages (Chen et al., 2021), (Zhu et al., 2022). However, due to the small scale of EES devices in integrated systems, their effectiveness in achieving time-shifting of electrical energy and promoting peak shaving and valley filling is limited (Wang et al., 2024). With the rapid development of renewable energy, the power system urgently needs independent energy storage to participate in the electricity market (He et al., 2022). Independent EES systems, with their fast response and efficient charging and discharging characteristics, bring new vitality and opportunities to the electricity spot market, especially in promoting the integration of renewable energy, improving system reliability, and optimizing energy utilization efficiency.

From the perspective of top-level design, EES will recover most of its revenue through the electricity market, especially the spot market. The operation mechanism involves industrial and commercial users obtaining the electricity prices for each time period of the following day based on the clearing results of the day-ahead electricity market. Combining the capacity, cycle efficiency of the EES power station, and the load forecast for the next day, the charging and discharging plan of the power station is formulated. During the low price periods, the EES power station acts as an electricity demand-side participant, purchasing electricity from the grid at relatively lower prices to charge the batteries and store cheap electricity (Sakti et al., 2017), (Xu et al., 2018). During the peak price periods, which usually coincide with the peak load periods, the EES power station switches to an electricity supply-side participant, with the storage batteries supplying electricity to the load and outputting to the grid, realizing peak load shifting and obtaining price difference revenue from peak-valley price arbitrage (Padmanabhan et al., 2020; Hesse et al., 2019; Fares and Webber, 2018). Through the flexible operation of the above-mentioned dual roles, the EES power station can earn arbitrage profits from the fluctuations of intraday power load and spot prices, becoming an important profit-increasing entity in the electricity spot market. Cui et al. (2021) and his partner proposed an optimal operation strategy with the goal of maximizing the expected revenue by considering the operating cost of the storage device and the prediction deviation of the new energy generation, so as to avoid the loss of revenue caused by the prediction deviation. For the problem of bidding strategy in the integrated system electric energy spot market, the researchers propose a spot declaration strategy aiming at maximising the expected benefits, which is applied to the electric energy spot market trading (Schram et al., 2020).

When rare high price differentials become part of the revenue, a longer calendar life may be more beneficial for energy arbitrage than an extended cycle life (Kumtepeli et al., 2020). In addition, EES power stations can also utilize their flexible and fast charging and discharging regulation capabilities to provide backup services, frequency regulation, and other ancillary services to the power grid, obtaining service revenue by participating in the bidding of the electricity ancillary service market or signing long-term agreements, which becomes an important way for the commercialized operation of EES power stations.

The core elements of an EES power station are energy transmission, battery management, and potential application scenarios in the power system. As an independent entity participating in the electricity spot market, the EES power station gains revenue during the battery energy transmission process. This paper aims to construct a revenue model for an independent EES power station that comprehensively considers the above factors to analyze its economic benefits in the electricity spot market. By studying the profit model of EES power stations in the electricity spot market, under limited battery life and different electricity price fluctuations, the owners and operators of EES power stations consider the marginal degradation cost (MDC) and annual operation and maintenance (O&M) costs. At the same time, they optimize the battery charging and discharging plan through operational decisions to extend battery life and improve the revenue of the EES power station. This research provides a new perspective for the operators of EES power stations, helping them better understand the economic potential of the EES station and formulate corresponding operation strategies to maximize revenue. Furthermore, this research also contributes to promoting the healthy development and market application of EES technology.

2 Methods

2.1 EES power station profit model

As an independent market entity, the EES power station needs to interact and collaborate with the power grid and users through electricity market mechanisms and technical means to ensure project revenue. The business model of an independent EES power station participating in the electricity market transactions is shown in Figure 1. Currently, energy storage only participates in the market as a spot price taker, usually reporting quantity without reporting price. From the declaration perspective, energy storage only needs to declare the next day's charging and discharging dispatch curve in the day-ahead market. On the operation day, the charging and discharging are arranged according to the actual cleared power plan, and the actual clearing depends on the power grid dispatch arrangement. Theoretically, the power grid will prioritize dispatching according to the energy storage declaration curve, and the actual charged and discharged electricity is settled at the spot price.

Based on the analysis of the main revenue and operating costs of the EES power station, and combining the short-term dispatch and long-term decision models, this paper adopts an itemized method to calculate the net operating revenue of the EES power station over its entire life cycle. The mathematical formula of the model is as follows (1)--(8):

$$R_{ESS}max = \max_{x} R_{ESS} = \max_{x} \sum_{t \le T} \delta_t R_t(x) \tag{1}$$

$$\begin{aligned} R_t^* &= max\, R_t(P_t) = \max_{P_t \in F} RM(P_t) - C_t^{BD}(P_t) + A_s - C_{fix} \\ &= \max_{P_t \in F} \sum \left[\Pi_h \left(p_h^{dis} - p_h^{cha}\right)\right] - \sum_{h \in (t+\Delta t)} \mu_t \left(p_h^{cha} + p_h^{dis} + \varphi\right) + A_s \\ &\quad - C_{fix} \end{aligned} \tag{2}$$

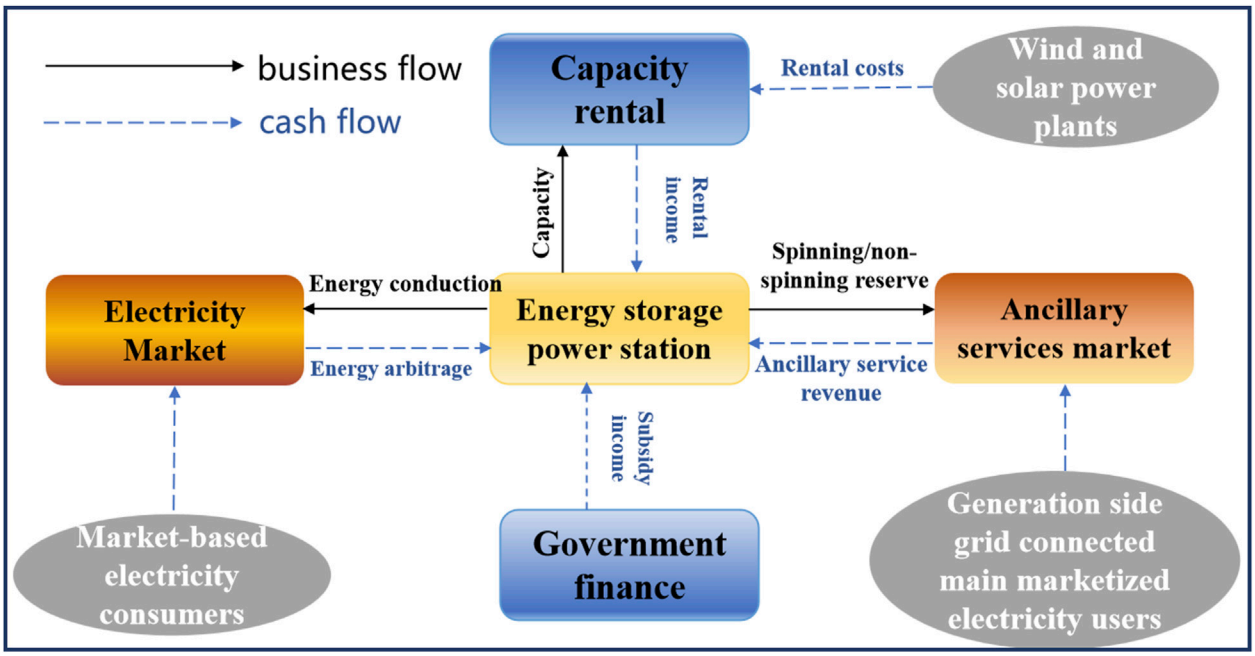

FIGURE 1
Graphical illustration of the business model for participation of EES plants in electricity market trading.

$$d_t = \sum_{\theta} 2z_t \eta_{t,\theta} \theta + \varphi \tag{3}$$

$$s.t. \sum_{t \le T} d_t(x) \le \underline{D} \tag{4}$$

$$d_t(x) \ge \varphi \tag{5}$$

$$S_c = (1-\zeta) S_{c-1} + p_h^{cha} \eta_t(H_t) - p_h^{dis} / \eta_t(H_t) \tag{6}$$

$$H_{t+1} = H_t - \frac{(\bar{H} - \underline{H}) d_t}{\underline{D}} \tag{7}$$

$$0 \le p_h^{dis},\ p_h^{cha} \le P_t \tag{8}$$

Formula 1 utilizes the exponential discount factor (δ_t) and the short-term benefits (R_t) of the EES power station to achieve the optimal long-term revenue of the EES power station under the electricity spot market, $\delta_t = (1+r)^{-\alpha}$, where r represents the discount rate, and α is the number of years the battery is used. Formula 2 calculates the short-term net revenue (R_t^*) of the EES power station by using the difference between the revenue and cost items of the EES power station, without considering the real-time market electricity deviation and using a daily settlement and monthly reconciliation method. The revenue items include market revenue, RM_t (battery charging and discharging revenue) and ancillary service revenue A_s (i.e., battery reserve revenue), while the cost items include the total battery degradation cost C_t^{BD} and the fixed operation and maintenance cost of the EES power station C_{fix} The degradation degree of the EES power station battery in period t is obtained through the sum of battery cycle degradation and calendar degradation (Formula 3), where E_t represents the battery capacity within time t, and $2E_t$ represents the total energy of charging and discharging in a cycle process. Formulas 4, 5, as boundary conditions, respectively limit the degradation and usage of the EES power station during operation to be less than the total usage before the end of the battery's physical life, and the total degradation amount in period t does not exceed the calendar degradation value of the battery. Formulas 6, 7 respectively represent the state of charge (SOC) and state of health (SOH) functions of the EES power station battery, both of which are related to the energy, battery capacity, and charging and discharging efficiency of the EES power station. Formula 8 is the boundary condition for the power generation and charging amount of the EES power station.

2.2 Parameter settings

We utilize the net revenue model of the EES power station to simulate the life-cycle operation of the energy storage power station and analyze the main revenue items of the EES power station under the electricity spot market. The main parameters and data used in the analysis case are as follows: We use the local marginal prices and non-spinning reserve service prices of the California Independent System Operator (CAISO) in 2018 to represent the price situation for each year during the battery's life cycle, with an average peak-valley price difference of about $32/MWh. The power station adopts LFP battery energy storage, with an initial battery charging and discharging efficiency of 95% and no self-discharge effect, i.e., a self-discharge rate of 0. Assuming that after operating 2000 cycles at 100% depth of discharge, the capacity retention rate of the energy storage power station is about 80% of the original battery (Ecker et al., 2014), at which point the battery energy efficiency is low, and the battery is considered to have ended its physical life. The average calendar degradation of the energy storage power station is estimated to be a 1% capacity loss per year (Schuster et al., 2016; Keil et al., 2016). Independent EES power stations require 24 h staffing, and labor operation and maintenance costs and equipment maintenance costs are relatively high. The annual operation and maintenance costs for

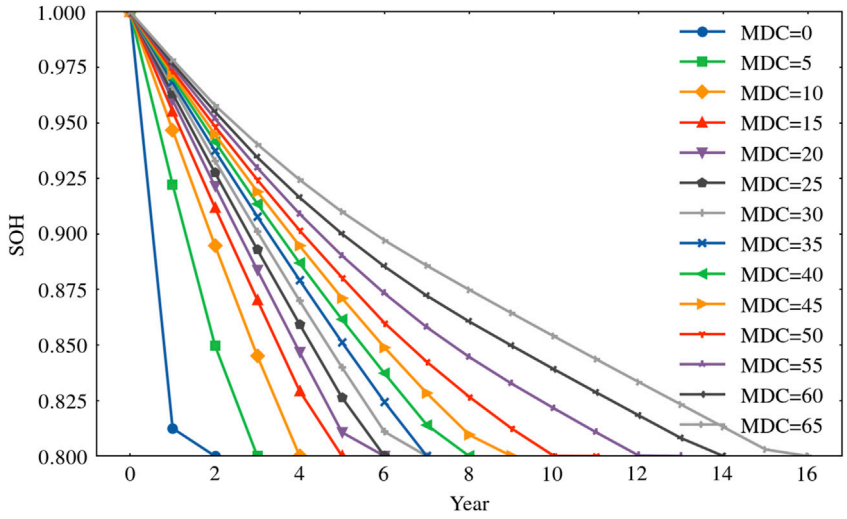

FIGURE 2
Physical life of batteries at different marginal degradation costs.

large-scale industrial-grade EES power stations and commercial and industrial EES are \$16/kW-year and \$27/kW-year, respectively (Chen et al., 2023; He et al., 2020).

3 Results

3.1 Battery life and SOH

Figure 2 demonstrates the SOH trend of battery over time, considering different marginal degradation cost (MDC) values. As the battery inevitably experience cycling degradation and performance degradation with increasing charge-discharge cycles, its SOH also shows a decreasing trend with the increase in the usage time. However, from the figure, we can observe that the larger the value of MDC, the slower the SOH decline and the longer the physical life of the battery. When MDC = 0, that is, without considering the degradation cost of the battery, the SOH of the battery has dropped to below 80% in about 2 years. In contrast, when MDC = 65, the battery's SOH can still remain above 85% after 10 years of use. This indicates that considering MDC in the operational optimization of EES power stations and moderately controlling charge-discharge power can effectively extend battery life. Therefore, MDC is also considered an opportunity cost that characterizes the long-term future value of EES power stations. In other words, if the MDC is relatively large in the battery's full life-cycle, future benefits may be higher. However, it is not the case that the higher the MDC is the better. Excessively high MDC can lead to reduced battery utilization, potentially decreasing EES benefits. Thus, it is necessary to seek a balance between prolonging the battery life and increasing the battery utilization to select the optimal MDC value.

3.2 Full life-cycle benefits of EES

We utilize an EES revenue model to evaluate the life-cycle profits of EES power stations. To determine the optimal MDC value, we employed an iterative optimization approach. We simulated the EES power station's operation over its lifetime for a range of MDC values from \$0 to \$100/MWh-throughput, in increments of \$5/MWh-throughput. For each MDC value, we calculated the total life-cycle revenue using our comprehensive model. Figure 3 illustrates the relationship between different MDCs and the profitability of EES power stations. As the MDC increases, the life-cycle revenue of EES power station rises sharply. When the MDC value increases from 0 to around \$45/MWh-throughput, the revenue grows rapidly. This indicates that within this range, the higher the MDC, the stronger the EES power station's profitability. The profits reach its peak when the MDC value is approximately \$45/MWh-throughput, which represents the optimal operating point for maximizing the EES power station's life-cycle earnings. This optimal value was identified as the MDC that resulted in the highest total revenue in our simulations. When the MDC exceeds \$45/MWh-throughput, profits begin to decline slowly. Excessively high MDC lead to accelerated battery degradation, shortened battery life and reduced overall profitability. Therefore, as the MDC value becomes increasingly large, approaching \$100/MWh-throughput, earnings begin to decrease dramatically.

For independent EES power stations, the profitability can be realized by the way of auxiliary service (specifically referring to reserve services in this context) in addition to the energy arbitrage through the participation of EES in the electricity trading in the spot market. As shown in Figure 2, at the optimal MDC (\$45/MWh-throughput), the battery's SOH decreases to 80% in the ninth year. Figure 4 illustrates the profitability of an EES power station over its entire life-cycle under optimal MDC conditions. The graph shows that the station's profitability is highest in the early stages of the project. Initially, energy arbitrage revenue is \$29.9/kW, and reserve services contribute \$14.0/kW, resulting in a total revenue of \$43.9/kW. Energy arbitrage accounts for a larger proportion of the revenue at this stage. However, as the EES power station operates over its life-cycle, battery degradation intensifies, causing a steady decline in energy arbitrage revenue. Ancillary

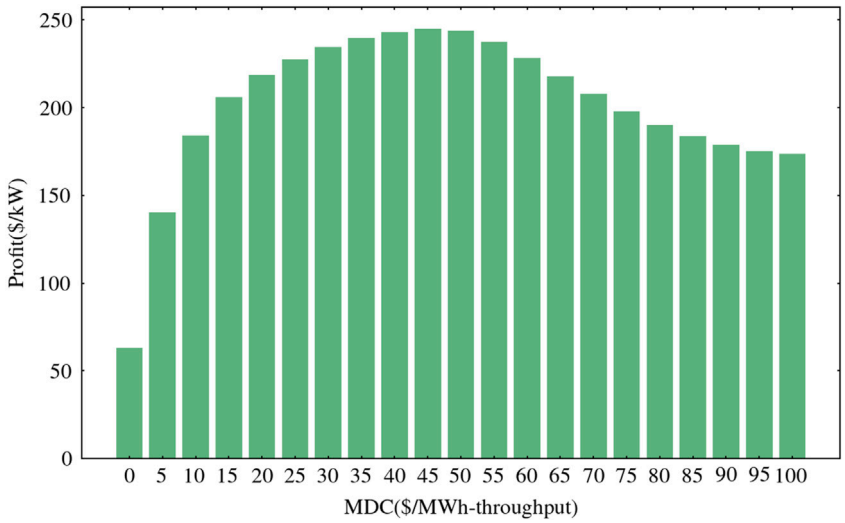

FIGURE 3
The relationship between the profits of EES and MDC.

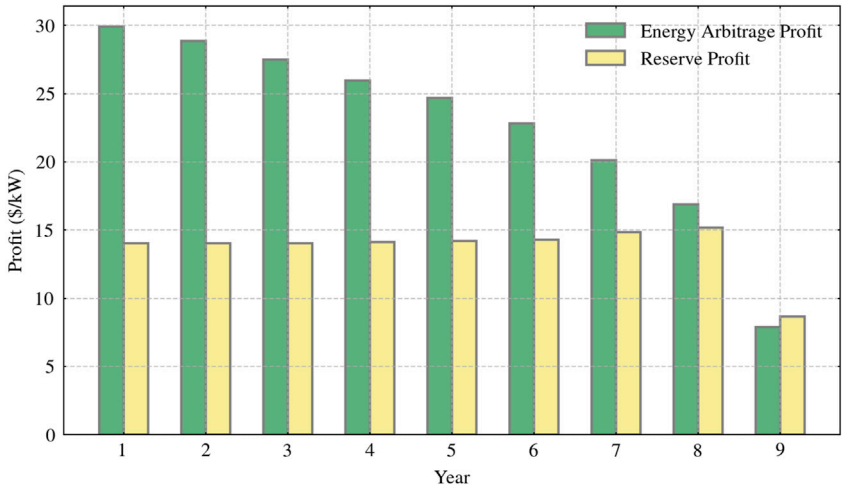

FIGURE 4
Trends in life-cycle profits of EES power stations under different operating models in the spot market.

services, being less affected by battery degradation, maintain relatively stable demand and prices for reserve service capacity. Consequently, the total annual revenue shows a downward trend. By the eighth year, energy arbitrage revenue decreases to $16.9/kW, while reserve services contribute $15.2/kW, resulting in a total revenue of $32.0/kW.

In the last year of the battery's life, all revenues drop sharply, with total revenue amounting to only $16.6/kW. This trend shows that, over time, battery degradation increases, the number of charge-discharge times used for price arbitrage increases, and both battery capacity and efficiency decrease, forcing the profitability of the power station to decline. Providing reserve services, however, has lower requirements for battery performance, needing only to maintain a certain energy and power reserve, and is thus less affected by battery degradation.

Therefore, EES power stations should focus on life-cycle profitability and plan their operational strategies accordingly. In the early stages of the project, emphasis can be placed on energy arbitrage to fully utilize battery performance and obtain high returns. As the battery degradation, the focus should gradually shift towards increasing the proportion of ancillary services to maintain a stable income.

3.3 Battery physical and economic life

Depending on the region and type of energy storage project, the fixed operation and maintenance (O&M) costs for EES power stations are estimated to range between 0 - $30/kW-year (Hledik et al., 2018). Figures 5A, B show the relationship between the

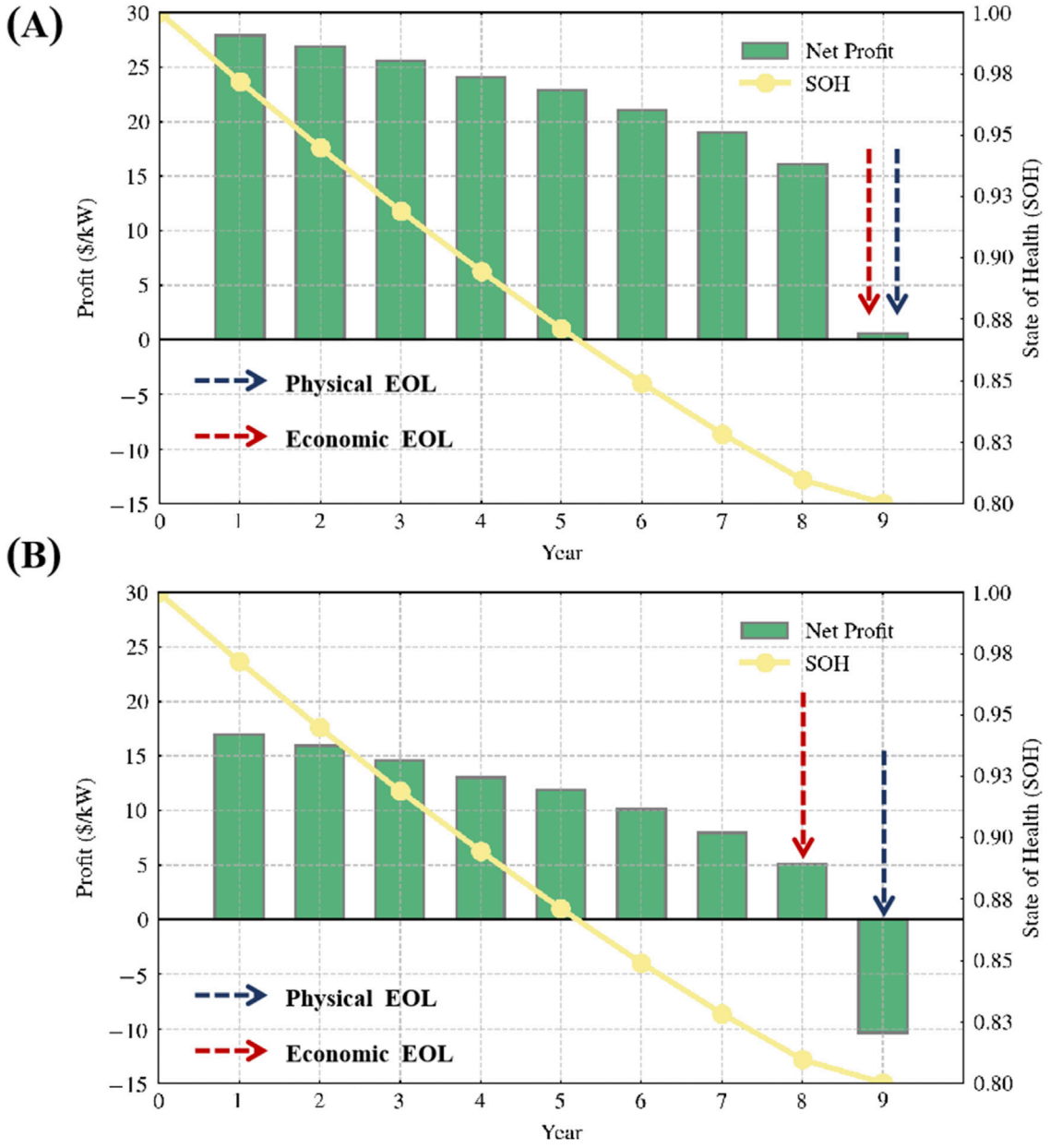

FIGURE 5
Changes in net profit from California EES power stations with battery cycle-life for different fixed O&M costs, **(A)** fixed O&M costs of $16/kW-year for commercial/industrial energy storage, and **(B)** fixed O&M costs of $27/kW-year for distributed/residential energy storage. Energy arbitrage and providing non-spinning reserve.

life-cycle net revenue and the battery's SOH for EES projects in the spot market under different O&M cost levels (16 $/kW-year for commercial/industrial energy storage, and 27 $/kW-year for distributed/residential energy storage). As the years of use increase, the battery capacity irreversibly decreases. When the SOH drops to 80%, it is typically considered the physical end of the life (EOL) of battery. He et al. (Ecker et al., 2014) proposed that if an EES project cannot achieve positive net profits during operation, this point should be considered the economic end of life for the EES power station. To analyze the net revenue situation of EES power stations in the spot market, this paper introduces the concept of the battery's economic end of life.

In this case, when the MDC is set at its optimal value ($45/MWh-throughput), the physical life of the $LiFePO_4$ battery is 9 years. However, from an economic perspective, when the annual net revenue drops to 0, the continuing operation loses its economic value even if the battery has not reached the end of its physical life. In Figure 5A, the commercial/industrial energy storage scale reaches the end of both its economic and physical life in the ninth year. For distributed/residential energy storage (Figure 5B), the economic EOL of the station (8 years) is notably shorter than its physical EOL (9 years). Higher O&M costs accelerate the decline in net revenue, causing the battery to lose its economic value before physical EOL. In other words, in the ninth year, even though the EES

power station's battery can still operate, its revenue is insufficient to cover the fixed operation and maintenance costs, resulting in no net profit for the EES power stations. At this point, the battery can be recycled or repurposed for other economically advantageous applications. This approach ensures that resources are utilized efficiently, maximizing the overall economic benefit of the energy storage system throughout its life-cycle.

4 Discussion and conclusion

EES power stations play a crucial role in power systems. However, their profitability in the electricity spot market faces uncertainties due to several factors: their limited power generation capacity, constraints in providing ancillary services, and the current imperfections in electricity market trading mechanisms. Given these challenges, the key to improving the economic benefits of small-scale EES power stations lies in how to promote their active participation in electricity market trading and maximize their advantages through reasonable scheduling and flexible operations.

This paper proposes a revenue model for EES power stations to evaluate their life-cycle profits. The model focuses on the impact of MDC on the physical EOL of batteries and incorporates annual fixed O&M costs to illustrate the net revenue of EES power stations under the electricity spot market. Additionally, the concept of economic EOL for EES power stations is introduced. Through data analysis, the paper demonstrates that using the economic EOL as the operational life for EES power stations is more meaningful than relying solely on physical EOL metrics.

Energy arbitrage and ancillary services currently represent the primary and most mature sources of revenue. In a case study of EES power station arbitrage in the California energy market, it is found that when the battery completes 2000 cycles and its capacity reduces to 80% of the original (i.e., physical EOL), the optimal MDC for the EES power station is \$45/MWh-throughput. Under these conditions, the EES power station achieves its highest life-cycle revenue. For commercial/industrial-scale EES power station, both the economic and physical EOL are 9 years. However, for residential-scale EES power station, the economic EOL is earlier than the physical EOL, at 8 and 9 years respectively. This indicates that continuing to operate the residential-scale EES power station in the ninth year would result in revenues lower than operating costs.

Therefore, operators need to carefully balance battery degradation characteristics, market conditions, and operational strategies to determine the optimal economic EOL of residential-scales. This balance is crucial for making appropriate investment and operational decisions. By considering these factors, operators can maximize the economic benefits of their residential-scales while ensuring they do not operate beyond the point where costs exceed revenues. This approach allows for more efficient use of resources and better long-term planning in the rapidly evolving energy storage market. Future research could explore the impact of emerging battery technologies on the economic lifespan of EES power stations. Additionally, investigating the potential synergies between EES power stations and other grid assets, such as renewable energy sources or demand response systems, could uncover new economic opportunities in the evolving energy landscape.

Data availability statement

The raw data supporting the conclusions of this article will be made available by the authors, without undue reservation.

Author contributions

YL: Conceptualization, Investigation, Methodology, Writing–original draft. SZ: Conceptualization, Supervision, Writing–review and editing. LY: Formal Analysis, Methodology, Software, Writing–original draft. QG: Methodology, Software, Writing–review and editing. XL: Formal Analysis, Writing–review and editing. BF: Investigation, Writing–review and editing.

Funding

The author(s) declare that financial support was received for the research, authorship, and/or publication of this article. This work was financially supported by the State Grid Corporation Headquarters Management Science and Technology Project "Research on Co-operation Technology of Multi-Level Electricity Spot Market for High Percentage of New Energy" (5108-202218280A-2-286-XG). The funder was not involved in the study design, collection, analysis, interpretation of data, the writing of this article, or the decision to submit it for publication.

Conflict of interest

The authors declare that the research was conducted in the absence of any commercial or financial relationships that could be construed as a potential conflict of interest.

Publisher's note

References

Chen, Q., Fang, X., Guo, H., He, G., Zhang, D., and Xia, Q. (2021). Participation mechanism of energy storage in electricity market: *status quo* and prospect. *Automation Electr. Power Syst.* 45 (16), 14–28. doi:10.7500/AEPS20210227001

Chen, X., Yang, Y., Wang, J., Song, J., and He, G. (2023). Battery valuation and management for battery swapping station. *Energy* 279, 128120. doi:10.1016/j.energy.2023.128120

Cui, H., Song, K., Dou, W., Nan, Z., Wang, Z., and Zhang, N. (2021). Bidding strategy of a flexible CHP plant for participating in the day-ahead energy and downregulation service market. *IEEE Access* 9, 149647–149656. doi:10.1109/ACCESS.2021.3116981

Ecker, M., Nieto, N., Kaebitz, S., Schmalstieg, J., Blanke, H., Warnecke, A., et al. (2014). Calendar and cycle life study of Li(NiMnCo)O_2-based 18650 lithium-ion batteries. *J. Power Sources* 248, 839–851. doi:10.1016/j.jpowsour.2013.09.143

Fares, R., and Webber, M. E. (2018). What are the tradeoffs between battery energy storage cycle life and calendar life in the energy arbitrage application? *J. Energy Storage.* 16, 37–45. doi:10.1016/j.est.2018.01.002

He, G., Ciez, R., Moutis, P., Kar, S., and Whitacre, J. F. (2020). The economic end of life of electrochemical energy storage. *Appl. Energy* 273, 115151. doi:10.1016/j.apenergy.2020.115151

He, X., Lou, S., Wu, Y., Liang, Y., and Chen, X. (2022). Two-stage market bidding and scheduling strategy of integrated wind power and energy. *Automation Electr. Power Syst.* 46(4), 47–55.

Hesse, H., Kumtepeli, V., Schimpe, M., Reniers, J., Howey, D., Tripathi, A., et al. (2019). Ageing and efficiency aware battery dispatch for arbitrage markets using mixed integer linear programming. *Energies* 12 (9), 999. doi:10.3390/en12060999

Hledik, R., Chang, J., Lueken, R., Pfeifenberger, J., Pedtke, J. I., and Vollen, J. (2018). *The economic potential for energy storage in Nevada*. Boston, MA: The Brattle Group, prepared for Public Utilities Commission of Nevada Governor's Office of Energy. Available at: https://www.brattle.com/wpcontent/uploads/2021/05/14618_economic_potential_for_storage_in_nevada_-_final.pdf.

Keil, P., Schuster, S. F., Wilhelm, J., Travi, J., Hauser, A., Karl, R. C., et al. (2016). Calendar aging of lithium-ion batteries i. impact of the graphite anode on capacity fade. *J. Electrochem Soc.* . 163, 1872–1880. doi:10.1149/2.0411609jes

Kumtepeli, V., Hesse, H., Schimpe, M., Tripathi, A., Wang, Y., and Jossen, A. (2020). Energy arbitrage optimization with battery storage: 3D-MILP for electro-thermal performance and semi-empirical aging models. *IEEE Access* 8, 204325–204341. doi:10.1109/ACCESS.2020.3035504

Liang, Y., Chen, X., Lou, S., Liu, Q., Lin, Q., and Deng, W. (2021). Formation mechanism analysis of cartel in frequency regulation ancillary service market in Southern China (starting from Guangdong Province). *Automation Electr. Power Syst.* 45 (15), 93–100. doi:10.7500/AEPS20201102003

Padmanabhan, N., Ahmed, M., and Bhattacharya, K. (2020). Battery energy storage systems in energy and reserve markets. *IEEE Trans. Power Syst.* 35 (1), 215–226. doi:10.1109/TPWRS.2019.2936131

Sakti, A., Gallagher, K., Sepulveda, N., Uckun, U., Vergara, C., de Sisternes, F., et al. (2017). Enhanced representations of lithium-ion batteries in power systems models and their effect on the valuation of energy arbitrage applications. *J. Power Sources.* 342, 279–291. doi:10.1016/j.jpowsour.2016.12.063

Schram, W., Alskaif, T., Lampropoulos, I., Henein, S., and Van Sark, W. G. J. H. M. (2020). On the trade-off between environmental and economic objectives in community energy storage operational optimization. *IEEET ransactions Sustain. Energy* 11 (4), 2653–2661. doi:10.1109/tste.2020.2969292

Schuster, S., Brand, M., Campestrini, C., Gleissenberger, M., and Jossen, A. (2016). Correlation between capacity and impedance of lithium-ion cells during calendar and cycle life. *J. Power Sources.* 305, 191–199. doi:10.1016/j.jpowsour.2015.11.096

Wang, D., Zhang, C., Li, J., Zhu, L., Zhou, B., Zhou, Q., et al. (2024). A novel interval power flow method based on hybrid box-ellipsoid uncertain sets. *IEEE Trans. Power Syst.* 39 (4), 6111–6114. doi:10.1109/tpwrs.2024.3391921

Xu, B., Zhao, J., Zheng, T., Litvinov, E., and Kirschen, D. (2018). Factoring the cycle aging cost of batteries participating in electricity markets. *IEEE Trans. Power Syst.* 33 (2), 2248–2259. doi:10.1109/TPWRS.2017.2733339

Zhang, H., and Wang, Y. (2021). Mechanism experience of foreign grid-side storage participating in frequency regulation auxiliary service market and its enlightenment to China. *Energy Storage Sci. Technol.* 10 (2), 766–773. doi:10.19799/j.cnki.2095-4239.2020.0370

Zhu, H., Xu, J., Liu, G., Yue, F., Yu, Z., and Zhang, X. (2022). UK policy mechanisms and business models for energy storage and their applications to China. *Energy Storage Sci. Technol.* 11 (1), 370–378. doi:10.19799/j.cnki.2095-4239.2021.0290

Zhu, L., Wen, W., Qu, Y., Shen, F., Li, J., Song, Y., et al. (2024). Robust representation learning for power system short-term voltage stability assessment under diverse data loss conditions. *IEEE Trans. Neural Netw. Learn. Syst.* 35 (5), 6035–6047. doi:10.1109/tnnls.2023.3325542

Nomenclature

Indices

t	Indices for time, typically a day
h	Indices for time, typically an hour

Parameters and constants

φ	Calendar degradation of the battery in period t
C_{fix}	Fixed operation and maintenance costs
$\underline{D}$	Total usage before the end of the battery life at 100% charge and discharge depth
ζ	Battery self-discharge rate
$\bar{H}$	EES Initial SOH
$\underline{H}$	EES Final SOH

Variables and functions

$d_t(x)$	Degradation of EES power station in period t
$RM_t(P_t)$	Market revenue of EES power station in period t
$C_t^{BD}(P_t)$	Total battery degradation cost during period t
Π_h	Regional marginal electricity price
A_s	Ancillary services revenue
z_t	Remaining capacity of EES power station
θ	Depth of charge and discharge
S_c	SOC of EES power station
$\eta_{t,\theta}$	The number of cycles of a storage power station at a certain charging depth
H_{t+1}	SOH of EES power station
p_h^{cha}	The charging amount of the energy storage system
p_h^{dis}	The discharging amount of the energy storage system
R_{ESS}	Total revenue of EES power station
δ_t	Discount factor for period t
x	Optimal marginal degradation cost
$\eta_t(S_t)$	EES power station charging and discharging efficiency
P_t	The charging and discharging amount of the EES power station during period t
μ_t	Adjusted MD for storage in time period t

frontiers | Frontiers in Energy Research

TYPE Original Research
PUBLISHED 17 October 2024
DOI 10.3389/fenrg.2024.1491846

OPEN ACCESS

EDITED BY
Cong Zhang,
Hunan University, China

REVIEWED BY
Weike Mo,
Jinan University, China
Xiaodong Zheng,
South China University of Technology, China

*CORRESPONDENCE
Fangneng Huang,
leiay@csg.cn

RECEIVED 05 September 2024
ACCEPTED 25 September 2024
PUBLISHED 17 October 2024

CITATION
Lei A, Mei Y, Ma D, Liu Z, Tao W and Huang F (2024) Two-stage transient stability assessment using ensemble learning and cost sensitivity.
Front. Energy Res. 12:1491846.
doi: 10.3389/fenrg.2024.1491846

Two-stage transient stability assessment using ensemble learning and cost sensitivity

Aoyu Lei[1], Yong Mei[1], Dexin Ma[2], Zining Liu[2], Wenwei Tao[1] and Fangneng Huang[1]*

[1]Power Dispatch and Control Center of China Southern Power Grid, Guangzhou, China, [2]China Southern Power Grid Electric Power Research Institute, Guangzhou, China

This paper proposes a novel two-stage transient stability assessment (TSA) model that integrates ensemble learning with cost sensitivity to address the challenges posed by the integration of renewable energy and load fluctuations. The model employs CNNs as positive and negative classifiers to initially evaluate samples, with consistent results output directly. In cases of inconsistency, the sample is evaluated by a fair classifier, specifically an ELM, trained on critical samples. This approach significantly enhances the classification performance and credibility of the fair classifier, especially under imbalanced conditions, thereby improving the overall efficiency and accuracy of TSA. The proposed model demonstrates superior performance compared to single-stage models and other two-stage models, achieving high accuracy and robustness in transient stability assessment, particularly for critical samples.

KEYWORDS

transient stability, cost sensitivity, critical sample, ensemble learning, sample imbalance

1 Introduction

The development of modern power systems presents new challenges to the safety of these systems. In recent years, frequent blackouts worldwide have had significant economic impacts (Wei Zhang and Zhang, 202). Transient stability is crucial to the safe operation of power systems. Once a disturbance occurs in the power system, early assessment of transient stability and timely implementation of emergency control measures can protect the system's stability (Guo et al., 2023; Meridji et al., 2023; Singh and Chauhan, 2023; Wang Y. et al., 2023; Zhu et al., 2023). Therefore, it is vital and necessary to design a TSA model that can quickly and accurately determine whether a power system will become unstable and infer the type of events that may cause instability.

Classical transient stability methods include time-domain simulation (TDS) and direct methods. TDS analyzes system stability through detailed modeling. As long as the component models and network structures are sufficiently accurate, the results are reliable. However, with the increasing complexity of power systems and rapid changes in electronic hardware, TDS-based models have become more complex, and their computational demands have increased, making TDS methods unsuitable for real-time transient stability assessment. The direct method, on the other hand, does not require numerical integration of dynamic processes and can quantitatively analyze system transient stability. However, direct method models are simple and may face applicability issues in complex power systems. Additionally, the evaluation results tend to be conservative. As a result, these methods

currently cannot fully meet the practical needs of online transient stability assessment. To date, real-world power grids still require more advanced TSA solutions that can achieve high reliability and efficiency.

The rapid development of big data offers new ideas for transient stability assessment. TSA rules can be mined from large volumes of data using machine learning (ML) methods (Liu et al., 2023; Li et al., 2024; Shao et al., 2024). Once dynamic information is received, stability results can be output within milliseconds. After discovering underlying relationships offline through ML, they can be easily applied to online TSA. This data-driven approach almost eliminates online computation time and can effectively predict system stability.

Modern power systems usually remain stable after most disturbances due to their robustness. In practical applications, events causing power system instability are rare. These rare events lead to significant imbalances between stable (majority class) and unstable (minority class) transient data distributions. The imbalance in training data leads to high misclassification rates in TSA models. Moreover, misjudging the transient stability of power systems prevents timely responses and corresponding measures, leading to safety accidents and significant economic losses. Therefore, addressing the imbalance in training data is not only crucial for improving TSA accuracy but also has practical significance.

Existing methods for addressing class imbalance can be broadly categorized into data-driven and algorithm-driven approaches. Additionally, traditional data-driven methods attempt to oversample or undersample the data so that different classes appear in equal proportions in the training data. The main drawback of sampling-based methods is that they may lose important information in undersampling or overfit the training data in oversampling. Algorithm-driven methods primarily include cost-sensitive methods (Wang H. et al., 2023; Chen et al., 2022; Lin et al., 2022; Wang et al., 2020) and ensemble learning methods (Shen, 2023; Chen and Wang, 2021; Chen et al., 2021; Zhao et al., 2022; Wu et al., 2020). References (Wang H. et al., 2023) consider the imbalance in sample distribution in space by dividing samples into different levels of training sets and training the model using cost-sensitive approaches. Reference (Shen, 2023) proposes a comprehensive transient stability state assessment method for power systems based on machine learning, using multiple classifiers to alleviate the sample imbalance problem in transient stability samples. However, its drawbacks are also evident. The ensemble learning classifiers used are often weak classifiers with low resistance to interference and increased training time. Among these methods, the application of cost sensitivity in transient stability assessment is relatively limited. Although it helps mitigate sample imbalance, its blind use may lead to overfitting and increased misclassification rates. Applying ensemble learning alone to transient stability assessment can also mitigate sample imbalance, but due to the large number of ensemble classifiers, it may result in longer training times and weaker resistance to interference.

Recently, to mitigate the imbalance in transient stability samples, references (Chen and Wang, 2021; Wang et al., 2020) adopted a two-stage assessment approach combining cost sensitivity and ensemble learning. Specifically, three models are used, with two classifiers in the first stage, each biased towards one class of samples using cost-sensitive methods. A non-cost-sensitive classifier is then trained using the same training set as a fair classifier for second-stage evaluation. Although this approach combines the advantages of cost-sensitive learning and ensemble learning, it also overcomes some disadvantages. However, this method lacks credibility, mainly because the credibility of the fair classifier is low. This is because hard samples are evaluated by a non-cost-sensitive classifier, and the evaluation results are directly output. However, since the fair classifier is not selected based on the characteristics of the input samples, highly accurate and convincing evaluation results cannot be generated.

In transient stability assessment, what truly affects misclassification and missed judgments are the hard samples. In this study, we propose a two-stage transient stability assessment model based on the integration of ensemble learning and cost sensitivity. First, the initial sample set is input into positive and negative classifiers again, and samples with inconsistent evaluation results are collected to form a critical sample set. This critical sample set is used to train the ELM (fair classifier). The model combines the strengths of cost sensitivity and ensemble learning, greatly enhancing the credibility of the fair classifier while improving the overall reliability of the model.

The rest of this paper is structured as follows: Section 2 offers an overview of the transient stability assessment (TSA) problem and introduces the proposed two-stage TSA model. Section 3 details the implementation process of the model. Section 4 presents case studies and evaluates the model's performance. Finally, Section 5 summarizes the conclusions of the paper.

2 Integrated TSA model

2.1 Transient stability assessment problem

Transient stability assessment (TSA) has become increasingly important in power systems, with the main challenge being how to overcome the inherent sample imbalance problem, which is determined by the robustness of power systems. To address the imbalance in transient stability samples, a two-stage assessment method combining cost sensitivity and ensemble learning has been widely adopted. However, due to the lack of optimization in the selection of the fair classifier, it is difficult to produce highly accurate and convincing evaluation results. The model proposed in this paper addresses the problem of transient stability assessment under imbalanced samples by considering the difficulty of classifying critical samples, combining cost sensitivity and ensemble learning, which greatly enhances the reliability of the fair classifier and the overall model reliability. Currently, the issue of sample imbalance in transient stability assessment cannot be ignored, as stable samples are the majority, unstable samples are fewer, and critical samples are even rarer. The training model must fully understand the characteristics of stable, unstable, and critical samples to classify them correctly. Therefore, solving the sample imbalance problem is crucial for transient stability assessment. The two-stage TSA model proposed in this paper aims to achieve accurate and reliable classification results even under imbalanced conditions.

2.2 Selection of positive and negative models and application of cost sensitivity

2.2.1 Selection of positive and negative models

Unlike most previous evaluation model designs, this paper designs a two-stage transient stability assessment model based on the integration of ensemble learning and cost sensitivity. The advantage of this approach is that it can combine the strengths of various models and effectively overcome the drawbacks of low accuracy, low effectiveness, and high cost caused by sample imbalance.

The positive and negative models are the foundational models in the entire two-stage framework; their results are only valid when they are consistent. Otherwise, if the results are inconsistent, the assessment will enter the next stage without directly outputting the results. Therefore, to maximize the role of the positive and negative models, cost sensitivity is applied to these models. The positive model is inclined to evaluate samples as stable, while the negative model is inclined to evaluate samples as unstable. Under this design, when the evaluation results of the positive and negative models are consistent, the input samples must be far from the boundary, indicating that the samples are either extremely stable or extremely unstable. In such cases, the positive and negative models require strong feature extraction capabilities to fully recognize samples beyond the boundary.

Convolutional Neural Networks (CNNs) possess strong nonlinear expression and pattern recognition capabilities, making them suitable for handling complex dynamic processes and nonlinear problems in power systems (Lee et al., 2023). This allows CNN-based TSA models to more accurately reflect the transient stability status of the power system based on input operational parameters. Compared to traditional time-domain and direct methods, CNN-based TSA methods offer higher assessment accuracy and faster computation speed. They can meet the requirements of online real-time prediction, providing timely and accurate power system stability analysis results for dispatchers (Gu et al., 2024). Additionally, CNN models can adapt to different power system scenarios and demands by adjusting the network structure and parameters, offering higher flexibility and scalability. In summary, applying CNNs to power system transient stability assessment has advantages such as automatic feature extraction, strong nonlinear processing capabilities, high accuracy, real-time performance, and applicability to complex systems, making it a vital tool in power system operation and control. Therefore, we select CNN as the positive and negative models. With CNN's strong feature extraction capabilities, we can effectively handle the characteristics of stable and unstable sample regions, achieving initial simple classification. Furthermore, CNN-based methods can directly use low-level measurement data as input features, extracting multi-granularity information from measurement data through multi-size convolution kernels, thereby improving the accuracy of TSA in power systems (Jin et al., 2023).

For transient stability assessment, reasonable feature selection is needed to construct samples as input. This paper focuses on selecting steady-state quantities and fault characteristics for the forward-looking prediction of transient stability (Ji et al., 2022). Therefore, bus voltage, generator active and reactive power, and load active and reactive power are chosen as input features. Relevant data are obtained from measurements or time-domain simulations and input into the CNN model. The network structure of CNN is shown in Figure 1.

Based on the input electrical quantity matrix, the convolutional layer performs local learning through convolution kernels in the CNN model. The convolution operation for each convolution kernel is as Equation 1.

$$a_{c,k} = f\left(X * W_{c,k} + b_{c,k}\right) \tag{1}$$

where $a_{c,k}$ is the output of the k-th convolutional surface, $W_{c,k}$ is the weight matrix corresponding to the k-th convolution kernel, X is the input matrix, $b_{c,k}$ is the bias term, and $f(\cdot)$ is the activation function (the ReLU function is selected here).

For the pooling layer, this paper adopts max pooling, as shown in Equation 2.

$$a_{p,k} = \max\left(a_{ij}\right), \quad i, \quad j = 1, 2, \ldots, n \tag{2}$$

where $a_{p,k}$ represents the k-th pooling surface, a_{ij} is a sub-block of the output matrix from the previous convolutional layer, and n is the dimension of the sub-block of the output matrix from the previous convolutional layer.

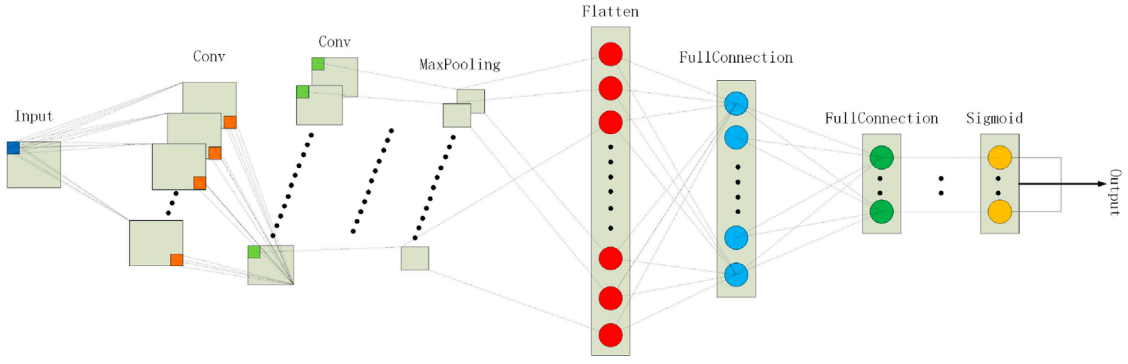

FIGURE 1
CNN network structure.

The calculation formula for the fully connected layer is as Equation 3.

$$a_{fc} = f\left(a_p W_{fc} + b_{fc}\right) \tag{3}$$

In the fully connected layer, a_{fc} represents the output, a_p represents the input, W_{fc} represents the weight matrix, and b_{fc} represents the bias term. The ReLU function is selected for the activation function.

The fully connected layer passes the output values to the output layer, and the expression of the sigmoid function in the output layer is as Equation 4.

$$\sigma(x) = \frac{1}{1+e^{-x}} \tag{4}$$

where x is the input value and $\sigma(x)$ is the function output.

2.2.2 Application of cost sensitivity

Typically, the approach to solving quantity imbalance is to assign higher weights to unstable samples. However, the misclassification of critical samples still occurs. Another approach is to assign higher weights to both imbalances simultaneously: first, higher weights are given to unstable samples, and then higher weights are assigned to misclassified samples. This approach can lead to overfitting (Kesici et al., 2023).

In this study, the model is trained by optimizing parameters to improve the fit to the training samples. The loss function is used to measure the difference between the predicted and actual values, and the impact of training samples on evaluation rules can be assessed through the loss function. This cost-sensitive approach makes the positive model inclined to evaluate samples as stable and the negative model inclined to evaluate samples as unstable.

TABLE 1 Weight coefficient matrix for model parameter modification.

Real label	Predicted label	
	Stable	Unstable
Stable	$C(1,1)$	$C(1,0)$
Unstable	$C(0,1)$	$C(0,0)$

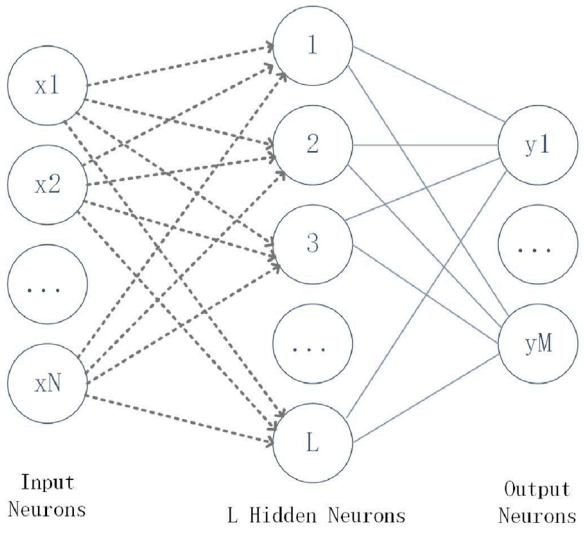

FIGURE 2
Elm network structure.

TABLE 2 Scoring table.

λ	$\lambda_2 = 0$	$\lambda_2 = 1$
$\lambda_1 = 0$	0	1
$\lambda_1 = 1$	1	2

TABLE 3 Evaluation process.

λ	First stage	Second stage	Total score
0	1	0	1
1	1	1	2
2	1	0	1

For the transient stability assessment problem, the weight correction coefficient for model parameters can be represented by Table 1.

Where $C(1,1) = C(0,0) = 0$. $C(1,0)$ and $C(0,1)$ represent the weight correction coefficients for model parameters when predicting stable conditions as unstable and unstable conditions as stable, respectively. Typically, $C(1,0) = C(0,1) = 1$.

In different scenarios, the proportion of unstable samples to stable samples in the training set often differs, which causes the model trained under imbalanced samples to have a certain bias in its discriminative results. Therefore, this paper introduces a correction factor γ to adjust for the imbalance in sample numbers in different scenarios, as shown in Equations 5, 6.

$$\gamma(0,1) = 10 \tag{5}$$

$$\gamma(1,0) = \frac{N_s}{N_{uns}} \tag{6}$$

where N_s is the number of stable samples in the training set; N_{uns} is the number of unstable samples in the training set.

By adjusting the weight correction coefficients during the evaluation model parameter correction process, the model's loss function is as follows:

$$Gp = -y^{(l)} \ln y'^{(l)} \gamma(1,0) - \left[1 - y^{(l)}\right] \ln\left[1 - y^{(l)}\right] \gamma(0,1) \tag{7}$$

The model using Equation 7 is the positive model. After applying cost sensitivity, this model tends to evaluate input samples as stable. Conversely, if the model needs to incline toward evaluating input samples as unstable, an additional correction factor β is required. Since the original model tends to evaluate samples as stable due to sample imbalance, adding the coefficient β ensures that the model tends to evaluate input samples as unstable. Similarly, it is also necessary to adjust the imbalance of the number of samples in different scenarios here, as shown in Equations 8, 9.

$$\theta(0,1) = \frac{N_s}{N_{uns}} \tag{8}$$

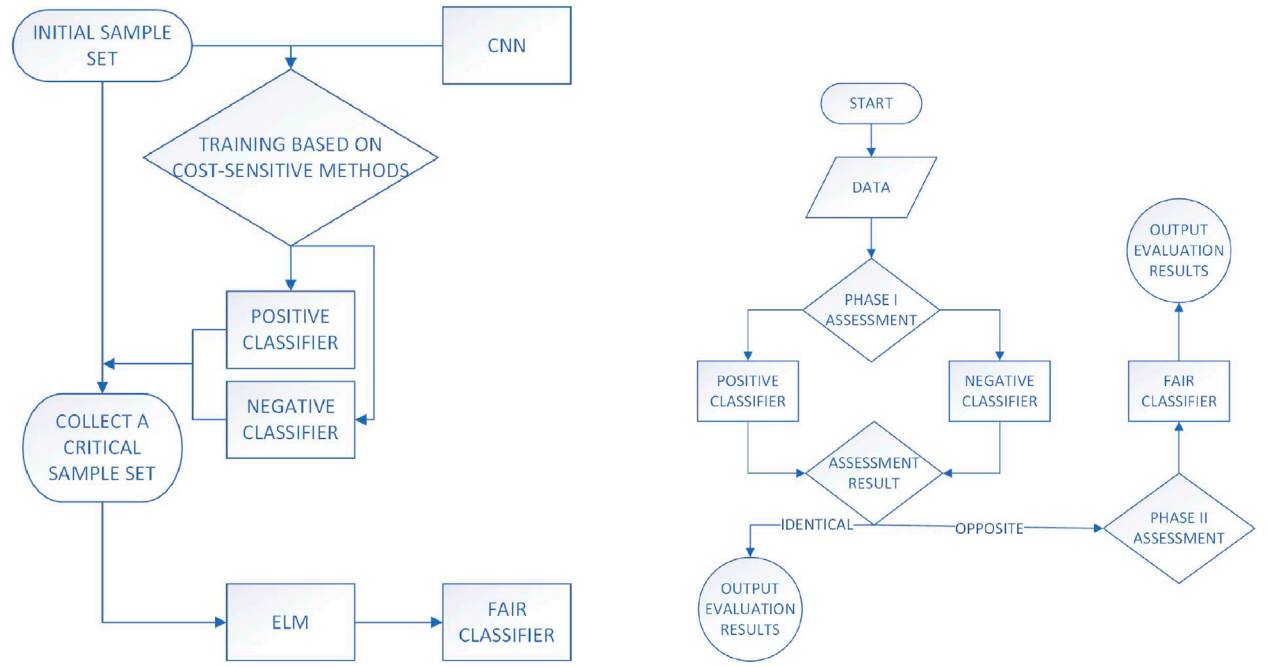

FIGURE 3
(1) Offline training; (2) Online application.

$$\theta(1,0) = 10 \tag{9}$$

When $\beta = 1$, the evaluation model merely corrects for the bias introduced by the imbalanced training samples; when $\beta > 1$, the model increases its fit to unstable samples, reducing the misclassification probability for unstable samples.

The reorganized model's loss function is shown in Equation 10.

$$Gn = -y^{(l)} \ln y'^{(l)} \theta(1,0) - \beta\left[1 - y^{(l)}\right] \ln\left[1 - y^{(l)}\right] \theta(0,1) \tag{10}$$

The negative model applies the loss function from the above equation to tend toward evaluating input samples as unstable.

2.3 Fair classifier

The fair classifier is used to classify hard samples, which are samples that the initial simple classification could not correctly categorize. Therefore, the sample set used to train the fair classifier is the critical sample set, and the model selection must consider this.

The fair classifier operates in the second stage of the assessment, requiring high accuracy and interpretability in its results. The sample set used to train the fair classifier is the critical sample set, which contains rich data information and high information entropy, requiring a suitable model to extract these features. For ELM training, the ideal sample should be data close to the stability boundary to obtain refined stability rules, allowing for effective learning of the critical region and a strong ability to correctly classify hard samples.

Given the above considerations, ELM is chosen as the fair classifier. Due to the distribution characteristics of the critical sample set, it matches the training requirements of the ELM model. If the training samples of ELM are from the critical region, the trained ELM will have a strong ability to correctly classify the critical sample set. ELM is used for training, but not with the original sample set; instead, it is trained using samples with conflicting evaluation results from two classifiers with opposing biases.

ELM can randomly select input layer parameters, and then use the Moore-Penrose generalized inverse to obtain the output layer weights with the smallest 2-norm. In ELM, only the number of hidden layer neuron nodes needs to be learned and adjusted, and the entire process does not require iteration. Figure 2 shows the ELM network structure.

Specifically, for a dataset (x_i, y_i) with N samples, where $x_i \in \mathbb{R}^n$ and $y_i \in \mathbb{R}^2$, y_i is the class label of the i-th sample, and the ELM output with M hidden layer units is shown in Equation 11.

$$f(x_j) = \sum_{i=1}^{m} \beta_i h\left(w_i x_j + b_i\right) = y_j \tag{11}$$

where $j = 1, 2, \ldots, N$; h is the activation function; $w_i \in \mathbb{R}^n$ is the weight vector of the i-th unit in the hidden layer; $\beta_i \in \mathbb{R}^2$ is the multiplier of the i-th unit in the hidden layer; and $b_i \in \mathbb{R}^1$ is the bias of the i-th unit in the hidden layer.

In ELM, the weight vector w_i and the bias b_i are randomly assigned, and the multiplier β_i can be obtained based on all the data through the Moore-Penrose generalized inverse. Therefore, there is no need for the backpropagation (BP) neural network's necessary back-adjustment process (Fuqiang et al., 2023), making ELM's calculation speed significantly faster than classification algorithms based on optimization. This reduction in calculation time also reduces the online application time of the two-stage evaluation model (Zhang et al., 2017).

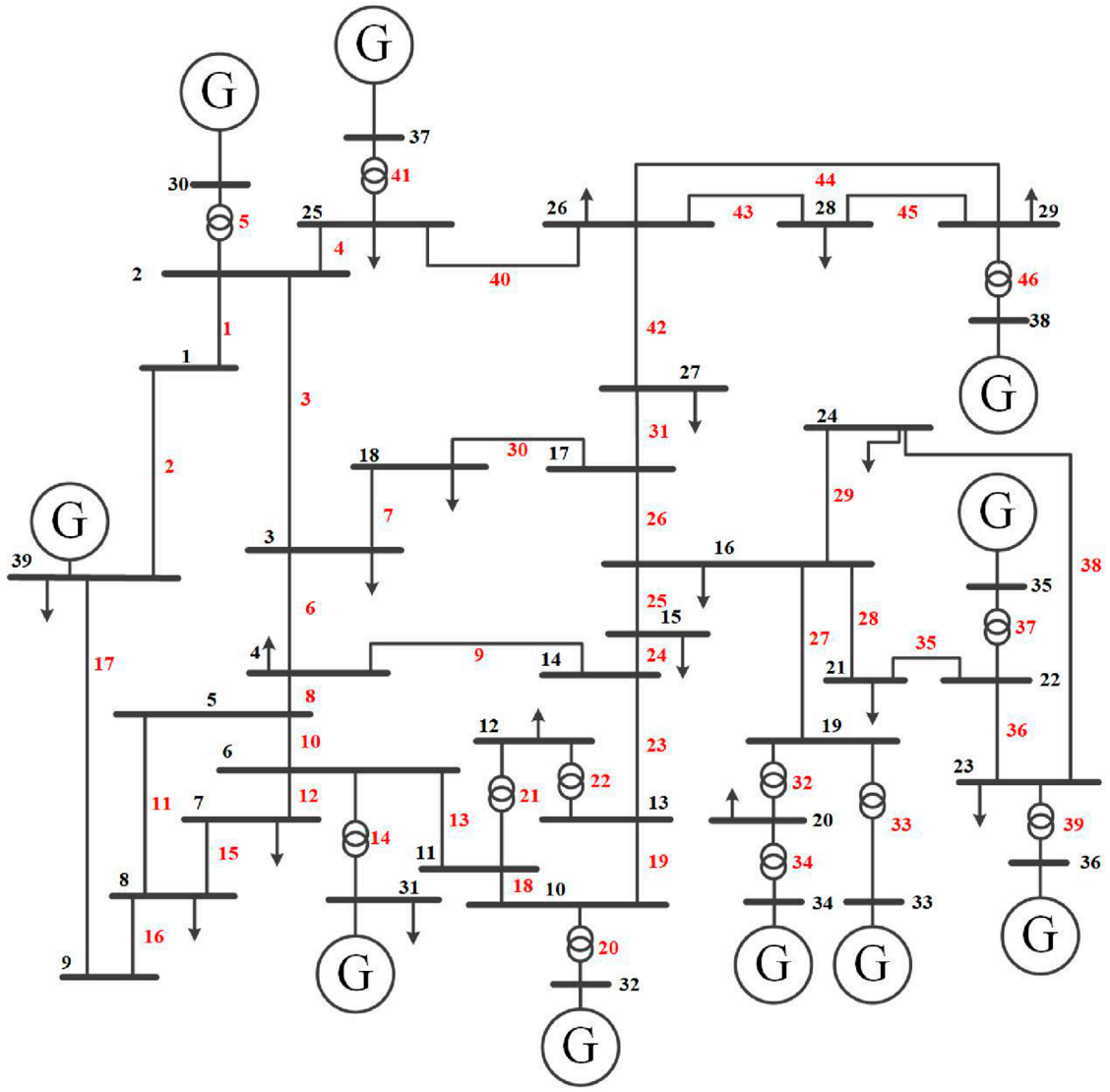

FIGURE 4
Line diagram of IEEE 39-bus power system.

TABLE 4 Weight coefficient matrix for model parameter modification.

Real label	Predicted label	
	Stable	Unstable
Stable	T_P	F_N
Unstable	F_P	T_N

TABLE 5 Comparison of single-stage and two-stage models.

Model	PACC	PFD	PFA
LSTM	0.9202	0.6535	0.4444
Two-Stage-LSTM	0.9363	0.5644	0.2903
GRU	0.9253	0.6238	0.3968
Two-Stage-GRU	0.9465	0.4257	0.2564
CNN	0.9482	0.3663	0.2727
Two-Stage-CNN	0.9533	0.2376	0.2870

2.4 Overall evaluation process

After completing all the above designs, the framework for the proposed two-stage transient stability assessment model is established. Next, the overall evaluation process is designed.

The model proposed in this study is a two-stage evaluation model, where the second stage's evaluation somewhat depends on the results of the first stage. Therefore, it is necessary to design scoring for the first-stage evaluation results to complete the evaluation logic of the first and second stages.

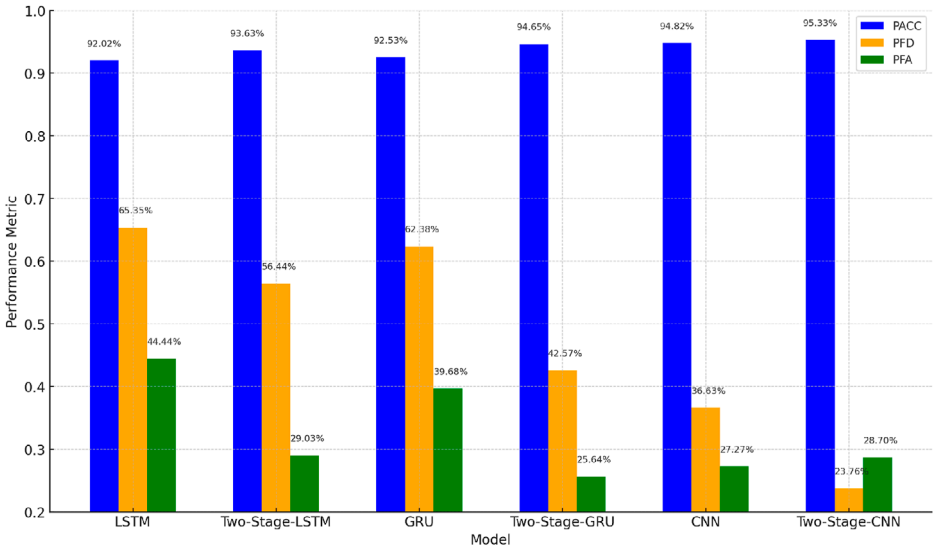

FIGURE 5
Comparison of performance between single-stage and two-stage models. Model performance improvement: two-stage vs. baseline (LSTM, GRU, CNN).

TABLE 6 Comparison of TCS-ELM with other two-stage models.

Model	PACC	PFD	PFA
TCS-ELM	0.9779	0.1584	0.1053
Two-Stage-CNN	0.9533	0.2376	0.2870
Two-Stage-GRU	0.9465	0.4257	0.2564
Two-Stage-LSTM	0.9363	0.5644	0.2903

Define $\lambda, \lambda_1, \lambda_2$, where λ is the total score of the first stage, and λ_1, λ_2 are the scores of the positive and negative classifiers, respectively.

To improve efficiency, λ_1, λ_2 are linked to the output results of the positive and negative classifiers. If the positive classifier output is stable (label 1), then λ_1 is 1; otherwise, it is 0.

Define $\lambda = \lambda_1 + \lambda_2$, the scoring logic is summarized in Table 2.

According to the model logic proposed in this paper, the first-stage evaluation results are credible, and the evaluation results are directly output only when the positive and negative classifier outputs are consistent. This occurs when λ is 0 or 2, meaning the first-stage evaluation results are reliable, and there is no need for the second-stage evaluation. If the positive and negative classifier outputs are inconsistent, the first-stage evaluation results are unreliable, and λ equals 1, then the process proceeds to the second-stage evaluation.

The overall evaluation process can be simplified as shown in Table 3.

As shown in Table 3, when the total score is 1, the second-stage evaluation result is output as the model's evaluation result. When the total score is 2, that is, when λ equals 1, the first-stage evaluation result is credible, and the first-stage evaluation result is output as the model's evaluation result.

3 Implementation process of the integrated TSA model

After selecting a specific example system, transient stability simulations are performed to collect steady-state data and create the initial sample set.

Based on the obtained initial dataset, the positive and negative classifiers are trained separately. After training, the initial dataset is re-input into the trained positive and negative classifiers for evaluation, and the critical dataset is organized based on the differing evaluation results from the positive and negative classifiers.

Since the fair classifier needs to correctly classify critical samples, ELM is selected as the fair classifier. By training ELM using the critical sample set, the ability of ELM to correctly classify critical samples is greatly enhanced, meeting the requirements of the fair classifier. The construction of the integrated TSA model is then completed.

When evaluating real-time data obtained from the power system, the measured data is input into the positive and negative classifiers for evaluation. If the evaluation results are consistent, the results are output, completing the assessment; if the evaluation results are inconsistent, the measured data is input into the fair classifier, and the evaluation results from the fair classifier are output, completing the assessment. The specific implementation process is shown in Figure 3.

(1): Offline Training
(2): Online Application

4 Case analysis

Taking the New England 10-generator, 39-bus system as a case study, as shown in the Figure 4, the entire bus system is divided into four regions according to adjacent buses. Four different

load levels, 80%, 90%, 110%, and 120%, are considered, and each region is assigned a different load level, resulting in 256 different power flows,256 different operating modes. The generator output is adjusted accordingly to ensure the convergence of power flow calculations. The fault is set as a three-phase short-circuit fault, and an N-1 scan is performed on the system by sequentially setting faults on different lines. The fault duration is set to 0.2 s on lines without transformers, with the fault point located at 50% of the line's length. On lines with transformers, the fault point is set at the head section of the line.

The selection of input features including bus voltage, generator active power and reactive power, as well as load active power and reactive power, is indeed widely used in data-driven transient stability assessment (Li et al., 2021; Du et al., 2021). Bus voltage reflects the system's voltage levels and can serve as an early warning for instability. Generator active power and reactive power respectively influence frequency stability and voltage regulation. Load active power affects the system's energy balance, while load reactive power is crucial for voltage stability. These features provide a solid foundation for predictive transient stability assessment.

A total of 11,776 samples are generated. By sampling from these 11,776 simulated samples, the training set, testing set, and validation set are obtained in a ratio of 8:1:1.

Transient stability assessment in power systems includes two categories: stable and unstable. The criterion for stability is the transient stability index (TSI). The details are given in Equation 12.

$$t_{TSI} = \frac{360° - |\Delta\delta_{\max}|}{360° + |\Delta\delta_{\max}|} \tag{12}$$

When the maximum rotor angle difference among generators exceeds 360°, TSI is less than 0, and the system is considered unstable; when the rotor angle difference is less than 360°, TSI is greater than 0, and the system is considered stable.

The following indicators are set as in Equations 13–15 to evaluate the performance of the model:

$$P_{ACC} = \frac{T_p + T_N}{T_p + F_p + T_N + F_N} \cdot 100\% \tag{13}$$

$$P_{FD} = \frac{F_p}{F_p + T_N} \cdot 100\% \tag{14}$$

$$P_{FA} = \frac{F_N}{T_p + F_N} \cdot 100\% \tag{15}$$

After the training, the model is tested from the test set, and the performance test results of the model are obtained. At the same time, existing Two-Stage models (such as two-stage-LSTM, two-stage-GRU) are tested, which all use the same neural network (such as LSTM or GRU) for positive and negative sample classification and fair classification tasks. The weight coefficient matrix used for model parameter correction is shown in Table 4. Firstly, transient stability evaluation experiments were conducted on the single-stage model and the two-stage model, and the results were recorded and summarized as shown in Table 5.Vertical comparison shows that the two-stage method proposed in this paper outperforms the single-stage method in all indicators, with a significant reduction in misclassification rates and a marked improvement in classification accuracy. This validates the effectiveness of the two-stage model in complex tasks compared to a single model. Figure 5 shows the bar chart comparison of the performance between single-stage and two-stage models.Based on these findings, we further explored the effects of different neural network combinations within the two-stage framework. As such, this paper proposes the TCS-ELM model (Two-Stage Cost-Sensitive Ensemble Learning Model), using CNN for positive and negative sample classification in the first stage and ELM for fair classification in the second stage, fully leveraging CNN's feature extraction strengths and ELM's efficient classification capabilities. Table 6 shows the performance testing results of various two-stage models and the proposed TCS-ELM

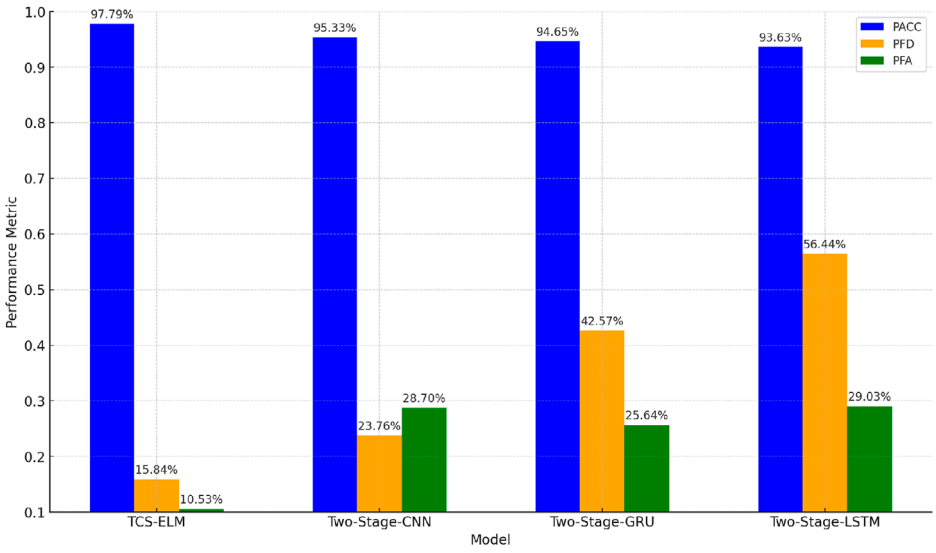

FIGURE 6
Comparison of performance between single-stage and two-stage models. Performance comparison of 4 deep learning models.

model.Results indicate that the proposed TCS-ELM model, by using CNN in the first stage for stronger feature extraction capabilities and ELM in the second stage for improved classification accuracy, outperforms other two-stage models (such as Two-Stage-LSTM and Two-Stage-GRU) in all indicators, particularly exhibiting higher accuracy and robustness when handling critical samples. This demonstrates that the TCS-ELM model combines the advantages of CNN and ELM in their respective stages, significantly enhancing overall performance. Figure 6 presents the bar chart comparison of the performance between TCS-ELM and other two-stage models.

5 Conclusion

In conclusion, the two-stage transient stability assessment model proposed in this paper, which leverages a combination of cost sensitivity and ensemble learning, addresses the key challenge of sample imbalance while exhibiting robust classification capabilities, particularly for hard-to-classify samples. By integrating these advanced techniques, the model demonstrates exceptional performance, achieving high levels of accuracy without compromising the reliability and credibility of the evaluation results.

In contrast to widely used transient stability assessment methods, this model successfully overcomes several of their inherent limitations. Traditional models often struggle to balance speed, accuracy, and reliability, particularly in cases where the data distribution is uneven or where outliers skew the results. The proposed model not only mitigates these issues but also delivers rapid assessments, making it highly efficient for real-time or near-real-time applications. Its ability to provide convincing and trustworthy evaluations further strengthens its utility in practical scenarios where precise and timely decision-making is crucial, such as in power grid operations and other dynamic systems.

By offering a superior balance of speed, accuracy, and evaluation credibility, this model stands out as a significant advancement in the field of transient stability assessment, offering a practical solution that is both scalable and adaptable to diverse operating conditions.

Data availability statement

The raw data supporting the conclusions of this article will be made available by the authors, without undue reservation.

Author contributions

AL: Writing–original draft. YM: Writing–review and editing. DM: Writing–review and editing. ZL: Writing–review and editing. WT: Writing–review and editing. FH: Writing–original draft.

Funding

The author(s) declare that financial support was received for the research, authorship, and/or publication of this article. This study received funding from the Science and Technology Project of China Southern Power Grid Co. Ltd. (ZDKJXM20210063).

Conflict of interest

The authors declare that the research was conducted in the absence of any commercial or financial relationships that could be construed as a potential conflict of interest.

The authors declare that this study received funding from the Science and Technology Project of China Southern Power Grid Co. Ltd. (ZDKJXM20210063). The funder had the following involvement with the study: the study design, the writing of this article.

Publisher's note

References

Chen, Q., Lin, N., and Wang, H. (2021). Transient stability assessment model with parallel structure and data augmentation. *Int. Trans. Electr. Energy Syst.* 31, 12872. doi:10.1002/2050-7038.12872

Chen, Q., and Wang, H. (2021). Time-adaptive transient stability assessment based on gated recurrent unit. *Int. J. Electr. Power and Energy Syst.* 133, 107156. doi:10.1016/j.ijepes.2021.107156

Chen, Q., Wang, H., and Lin, N. (2022). Imbalance correction method based on ratio of loss function values for transient stability assessment. *CSEE J. Power Energy Syst*.

Du, Y., Hu, Z., and Wang, F. (2021). A hierarchical power system transient stability assessment method considering sample imbalance. *Energy Rep.* 7, 224–232. doi:10.1016/j.egyr.2021.08.052

Fuqiang, L., Shihua, T., Yan, Z., Xiaohui, S., Pengcheng, H., and Zhu, L. (2023). Application of ssa-bp neural network in uav point cloud hole repair. *Bull. Surv. Mapp.*, 130.

Gu, T., Li, B., Xiao, L., Xu, Y., Mao, J., Yuan, M., et al. (2024). "Power system transient stability assessment based on svm-smote and one-dimensional convolutional neural network," in 2024 IEEE 2nd international conference on power science and Technology (ICPST) (IEEE), 562–568.

Guo, W., Qureshi, N. M. F., Jarwar, M. A., Kim, J., and Shin, D. R. (2023). Ai-oriented smart power system transient stability: the rationality, applications, challenges and future opportunities. *Sustain. Energy Technol. Assessments* 56, 102990. doi:10.1016/j.seta.2022.102990

Ji, J., Wu, J., Wang, Y., Shi, F., and Li, B. (2022). Power system transient voltage stability assessment based on deep residual network. *Power Syst. Technol.* 46, 2500–2511.

Jin, W., Zhou, B., Althubiti, S. A., Alsenani, T. R., and Ghoneim, M. E. (2023). Transient stability assessment of power systems using support vector regressor and convolution neural network. *Sustain. Comput. Inf. Syst.* 37, 100826. doi:10.1016/j.suscom.2022.100826

Kesici, M., Mahdi, M., Yaslan, Y., Seker, S., and Genc, I. (2023). A novel integrated framework for real-time prediction of transient instabilities in power systems with their severity levels using deep learning. *Sustain. Energy, Grids Netw.* 36, 101221. doi:10.1016/j.segan.2023.101221

Lee, H., Kim, J., Park, J. H., and Chung, S.-H. (2023). Power system transient stability assessment using convolutional neural network and saliency map. *Energies* 16, 7743. doi:10.3390/en16237743

Li, J., Yang, H., Yan, L., Liu, D., Li, Z., and Xia, Y. (2021). Integrated assessment method for transient stability of power system under sample imbalance. *Automation Electr. Power Syst.* 45, 34–41.

Li, Y., Cao, J., Xu, Y., Zhu, L., and Dong, Z. Y. (2024). Deep learning based on transformer architecture for power system short-term voltage stability assessment with class imbalance. *Renew. Sustain. Energy Rev.* 189, 113913. doi:10.1016/j.rser.2023.113913

Lin, J., Cai, R., and Zheng, Z. (2022). A transient stability assessment model based on fault severity assignment. *Front. Energy Res.* 10, 822729. doi:10.3389/fenrg.2022.822729

Liu, F., Wang, X., Li, T., Huang, M., Hu, T., Wen, Y., et al. (2023). An automated and interpretable machine learning scheme for power system transient stability assessment. *Energies* 16, 1956. doi:10.3390/en16041956

Meridji, T., Joós, G., and Restrepo, J. (2023). A power system stability assessment framework using machine-learning. *Electr. Power Syst. Res.* 216, 108981. doi:10.1016/j.epsr.2022.108981

Shao, Z., Wang, Q., Cao, Y., Cai, D., You, Y., and Lu, R. (2024). A novel data-driven lstm-saf model for power systems transient stability assessment. *IEEE Trans. Industrial Inf.* 20, 9083–9097. doi:10.1109/tii.2024.3379629

Shen, J. (2023). Em-tsa: an ensemble machine learning-based transient stability assessment approach for operation of power systems. *Math. Biosci. Eng.* 20, 8226–8240. doi:10.3934/mbe.2023358

Singh, M., and Chauhan, S. (2023). A hybrid-extreme learning machine based ensemble method for online dynamic security assessment of power systems. *Electr. Power Syst. Res.* 214, 108923. doi:10.1016/j.epsr.2022.108923

Wang, H., Hu, L., and Zhang, Y. (2023a). Svm based imbalanced correction method for power systems transient stability evaluation. *ISA Trans.* 136, 245–253. doi:10.1016/j.isatra.2022.10.039

Wang, H., Wang, Q., and Chen, Q. (2020). Transient stability assessment model with improved cost-sensitive method based on the fault severity. *IET Generation, Transm. and Distribution* 14, 4605–4611. doi:10.1049/iet-gtd.2020.0967

Wang, Y., Sun, Y., Li, Y., Feng, C., and Chen, P. (2023b). Risk assessment of power imbalance for power systems with wind power integration considering governor ramp rate of conventional units. *Electr. Power Syst. Res.* 217, 109111. doi:10.1016/j.epsr.2022.109111

Wei Zhang, Q. Z., and Zhang, C. (2024). Spatial-temporal resilience assessment of distribution systems under typhoon coupled with rainstorm events. *IEEE Trans. Industrial Inf.* doi:10.1109/TII.2024.3450079

Wu, J., Zhang, R., Ji, J., and Li, B. (2020). Two-stage transient stability prediction method of power system considering cost of misdetection and false alarm. *Automation Electr. Power Syst.* 44, 44–56.

Zhang, L., Hu, X., Li, P., Shi, F., and Yu, Z. (2017). "Elm model for power system transient stability assessment," in *2017 Chinese automation congress (CAC)* (IEEE), 5740–5744.

Zhao, D., Xie, J., Wang, C., Wang, H., Jiang, W., and Wang, Y. (2022). On-line transient stability assessment of a power system based on bagging ensemble learning. *Power Syst. Prot. control* 50, 1–10.

Zhu, L., Wen, W., Li, J., and Hu, Y. (2023). Integrated data-driven power system transient stability monitoring and enhancement. *IEEE Trans. Power Syst.* 39, 1797–1809. doi:10.1109/tpwrs.2023.3266387

frontiers | Frontiers in Energy Research

TYPE Original Research
PUBLISHED 29 October 2024
DOI 10.3389/fenrg.2024.1501181

OPEN ACCESS

EDITED BY
Zhenjia Lin,
Hong Kong Polytechnic University, Hong Kong SAR, China

REVIEWED BY
Licheng Wang,
Zhejiang University of Technology, China
Yue Wang,
China Agricultural University, China

*CORRESPONDENCE
Lisen Wang,
wanglisen@hnu.edu.cn

RECEIVED 24 September 2024
ACCEPTED 21 October 2024
PUBLISHED 29 October 2024

CITATION
Li H, Wang L, Qi S, Wang Z, Wang Y, Zhou S and Zheng W (2024) Power system frequency nadir prediction based on data-driven and power-frequency polynomial fitting. *Front. Energy Res.* 12:1501181. doi: 10.3389/fenrg.2024.1501181

Power system frequency nadir prediction based on data-driven and power-frequency polynomial fitting

Hongxin Li[1], Lisen Wang[2]*, Sirui Qi[1], Ziqiang Wang[1], Yanting Wang[2], Shichen Zhou[2] and Wenwei Zheng[2]

[1]Shenzhen Power Supply Co., Ltd., Shenzhen, China, [2]College of Electrical and Information Engineering, Hunan University, Changsha, Hunan, China

As the proportion of renewable energy and power electronics equipment continues to rise, the level of rotational inertia decreases considerably, resulting in severe frequency stability challenges to the power grid. It is of great significance to accurately predict the frequency nadir following a large disturbance. This paper proposes a novel data-model fusion-driven approach for the prediction of frequency nadir. As the physics-driven part, a Simplified Prediction Model (SPM) based on power-frequency polynomial fitting is developed to quickly produce the frequency nadir. As the data-driven part, Back Propagation Neural Network (BPNN) is deployed to correct the errors of the SPM to achieve more accurate results. This serial integration scheme not only obtains the final prediction result with higher accuracy, but also meets the computational efficiency requirements of online prediction. Compared with existing integration-driven methods, SPM only focuses on the active power-frequency characteristics of the system, which retains the most critical effects and greatly reduces the dependence of BPNN on sample data quality. Case studies on a modified IEEE 39-bus system verify the effectiveness of the proposed approach.

KEYWORDS

low inertia, frequency nadir, frequency stability, frequency response, renewable energy

1 Introduction

In order to realize the "dual carbon" development strategy, it is urgent to accelerate the construction of a new power system. With the large-scale integration of clean and low-carbon energy resources such as wind power and photovoltaic generation, the power system with synchronous machines as the main body has gradually evolved to the system with renewable energy as the main body, showing an increasingly decrease trend of rotational inertia level, and the system's frequency response capability is weakened remarkably. Consequently, the frequency stability of the power system is facing severe challenges under large power disturbances.

Frequency is one of the basic indicators to describe the operating state of the power system. The frequency nadir consists of the maximum frequency deviation and the frequency nadir time. It is not only the key indicator to judge whether the frequency is out of the limit, but also regarded as the decision-making basis for

appropriate frequency regulation control. It is very important to quickly and reliably predict the frequency nadir for frequency stability evaluation and control of large power systems (Hatziargyriou et al., 2021).

At present, there are three typical methods to predict the frequency nadir following disturbances: time-domain simulation method, simplified model based method, and data-driven method. The time-domain simulation is the most common used method for analyzing the frequency response of a power grid, which builds a time-domain model of each element of the system (including different generation units with nonlinear control links), and converts it into a series of differential algebraic equations to iteratively calculate the accurate numerical solutions of each state quantity of the power grid (Wen et al., 2023). Common time-domain simulation software includes PSASP, PSD-BPA, DIgSILENT/PowerFactory and PSS/E, etc. However, the time-domain simulation method is often time-consuming when analyzing large-scale power systems, which is more suitable for offline analysis of power grid planning and accident recurrence, but not for real-time online analysis of power grids with strong timeliness requirements. The simplified model method usually solves the dynamic process of the frequency response by retaining the rotor equation of motion and the governor model, such as the average system frequency (ASF) model (Chan et al., 1972) and the system frequency response (SFR) model (Anderson and Mirheydar, 1990; Liu et al., 2020; Egido et al., 2009) decouple power and frequency by breaking the frequency closed loop, and the analytical calculation of the frequency nadir is realized; Shen et al., 2021; Wang et al., 2022b propose multi-machine equivalent SFR models and derive their closed-form solutions to solve the frequency response of power systems with two or three regions. In summary, the simplified model is suitable for online analysis scenarios with high speed requirements, but the prediction accuracy needs to be further improved. With the rapid popularization of wide area measurement system (WAMS) in power grids, Phasor Measurement Unit (PMU) and Supervisory Control And Data Acquisition (SCADA) systems can obtain massive amounts of information about the operation of the power grid in real time, making machine learning based on data analysis more and more widely used in the power system (Kamruzzaman et al., 2021; Yi et al., 2021; Bo et al., 2022). Data-driven method can effectively deal with the nonlinear and complex problems of physical models, and provide new solutions for the establishment of frequency models of complex power systems solutions. However, its prediction accuracy is heavily dependent on the quantity and quality of sample data, the generalization ability is insufficient and the prediction results often lack interpretability.

In order to meet the practical needs of the power system, the simplified model can be combined with data-driven methods, integrating the advantages of both methods, so as to improve the overall performance and be suitable for solving complex physical problems. Feng et al., 2021 discusses the feasibility of integrating model-driven methods and data-driven methods for online frequency stability evaluation. Han et al. (2022) embeds frequency-response related physics in gated recurrent unit neural networks through the basic input eigenquants and the embedded physical knowledge, new input eigenquants are formed and used for model training. However, how to efficiently combine the accurately modeled frequency response model and the data-driven model to achieve complementary advantages remains to be studied.

In this paper, the problem of frequency nadir prediction of a high proportion of renewable energy power systems under large power deficit is studied. Due to the computing speed requirements for real-time applications, a Simplified Prediction Model (SPM) based on system frequency response equivalent is developed. Compared with the traditional frequency response model (Yang et al., 2022), the SPM uses polynomials of different orders to fit the power frequency characteristics of each frequency modulation resource, including synchronous generator, renewable energy, load, and HVDC, so as to analyze and calculate the maximum deviation of the frequency and the frequency nadir time, which has the advantages of low identification difficulty, simple form, and less required information. Therefore, the SPM is selected to be a physical-driven link in this paper to ensure the high computational speed of the fusion model.

The complexity of the data model is positively correlated with the predicted effect, and at the same time, higher requirements are put forward for the quality of data samples. Since this paper only focuses on the active power-frequency characteristics of the power system, in the serial ensemble approach, the role of the data model is to correct the predictions of the physical model, rather than to fit the complex physical mechanisms of the entire power grid. As a shallow neural network, BPNN (Back Propagation Neural Network) has good self-learning, self-adaptive, nonlinear mapping, and generalization capabilities. Therefore, in order to ensure the feasibility and accuracy of the integration-driven method, BPNN is used as the part of the data model.

The serial ensemble method (Wang et al., 2019) is implemented to introduce the SPM to obtain the initial prediction results, which can ensure the prediction efficiency and reduce the dependence of the data model on sample data. The BPNN is deployed to correct the error of the initial prediction results of the physical model. Simulation results on a modified IEEE 39-bus system show that the data-model fusion-driven method can predict the frequency nadir with high accuracy and speed, and provide more reliable indices and basis for the frequency stability analysis and control of the power system.

2 SPM modeling and analytical solution

The frequency response characteristics of the power system with a high proportion of renewable generation are mainly affected by the synchronous generators, load frequency characteristics, auxiliary frequency control strategies of renewable energy units and HVDC links. According to the respective power-frequency response characteristics, the modeling and analysis of each type of frequency modulation resources are explained in this section.

2.1 Power-frequency characteristics of synchronous generators

The mechanical power output curve of a typical synchronous generator governor under power step disturbance can be simply divided into three sections according to its change characteristics, namely, the fast change section, the constant velocity change section,

and the steady-state output section. The generator governor changes the output power by changing the prime mover valve, so as to suppress the unbalanced power, and finally restore the frequency to a quasi-steady state. The complete curve change process can be represented by the following higher-order polynomial (Equation 1):

$$\Delta P_G(f) = K_G^0 + K_G^1 \frac{d\Delta f}{dt} + K_G^2 \left(\frac{d\Delta f}{dt} \right)^2 + K_G^3 \left(\frac{d\Delta f}{dt} \right)^3 + \ldots + K_G^n \left(\frac{d\Delta f}{dt} \right)^n \quad (1)$$

where ΔP_G is the mechanical power deviation output by the synchronous generator governor; K_G^0, K_G^1, and K_G^2 are the polynomial coefficients related to the rate of change of each order.

For synchronous generator governors, the higher the order of the above polynomials, the more accurate the power-frequency response characteristic curve of the generator governor in this scenario can be described. However, at the same time, the introduction of higher-order polynomials will bring more cumbersome workload to frequency stability online evaluation, which will seriously slow down the computational speed. For the frequency nadir, the corresponding time coordinates are often located in the uniform velocity change segment, so only the first two curve change links need to be accurately modeled.

Taking the GS-TB type governor in the PSD-BPA software as an example, given a load disturbance of 35 MW, the system frequency deviates. The actual response curve of the governor and its polynomial fitting curves of different orders are compared as shown in Figure 1. It can be seen that the second-order polynomial can accurately fit the power output curve of the governor within the time scale from the moment of fault occurrence to the frequency nadir. Therefore, the second-order polynomial is utilized to describe the active power frequency characteristics of the generator governor before the frequency nadir is reached, and the expression is:

$$\Delta P_G(f) = K_G^0 + K_G^1 \frac{d\Delta f}{dt} + K_G^2 \left(\frac{d\Delta f}{dt} \right)^2 \quad (2)$$

2.2 Power-frequency characteristics of the active participation of renewable energy units in frequency regulation

Under the conventional control strategy, renewable energy units do not actively participate in the frequency regulation, which leads to a significant reduction in the inertia of the system and a weakening of the frequency control capability. Many studies have been conducted to improve the control strategy to enable them to participate in the support of the power grid frequency. To this end, most of the current renewable energy stations achieve auxiliary frequency response by implementing measures such as virtual synchronous control, virtual inertia control, and droop control. The purpose of these control schemes is to enable the renewable energy stations to simulate the characteristics of the frequency response of synchronous generators through the control of power electronic inverters and algorithms. The active power-frequency characteristics of a renewable energy unit considering virtual inertia and droop control can be expressed as:

$$\Delta P_R(f) = K_d \Delta f + K_v \frac{d\Delta f}{dt} \quad (3)$$

where K_d is the equivalent droop coefficient of the renewable energy unit, and K_v is the equivalent virtual inertia coefficient.

2.3 Frequency characteristics of the load

When the frequency changes, the active power absorbed by the load from the grid also changes, which is the frequency characteristic of the load. In the dynamic process prior to the frequency reaches its nadir following the disturbance, the power-frequency dynamic characteristics of the load can be simplified as follows:

$$\Delta P_L(f) = K_p^1 \Delta f + K_p^0 \quad (4)$$

where ΔP_L is the power deviation of the active load of the system; K_P^0 and K_P^1 are the frequency-dependent load factors of each order.

2.4 Frequency characteristics of the HVDC frequency limiter

For the high proportion of renewable energy grids, the frequency characteristics can be improved by suppressing the change of electromagnetic power of the generator through the fast and controllable function of HVDC power, reducing the deviation between the generator and the mechanical power. An HVDC frequency limiter can be used to respond to the frequency deviation of the grid and automatically modulate the HVDC power. When the power for HVDC modulation preparation is sufficient, the power-frequency dynamic characteristics can be expressed by the following formula:

$$\Delta P_{FLC}(f) = K_m \Delta f + \int K_I \Delta f dt \quad (5)$$

where ΔP_{FLC} is the power deviation of the HVDC modulator of the system; K_m is the frequency-dependent gain factor, K_I is the integral coefficient. The role of the integration link is mainly reflected in the reduction of the steady-state frequency deviation, and this paper only focuses on the maximum frequency deviation in the frequency response process, and the role of integration control FLC can be ignored. As a result, the power response of FLC control can be further simplified, as shown in Equation 6.

$$\Delta P_{FLC}(f) = K_m \Delta f \quad (6)$$

2.5 Polynomial fitting of power–frequency characteristics

For the power system with a high proportion of renewable energy generation, this paper mainly focuses on the stage when the frequency drops to the nadir under the high power shortage, according to the rotor swing equation:

$$2H_{sys} \frac{df(t)}{dt} = \Delta P_{\mathrm{m}} - P_{\mathrm{d}} - D_{sys} \Delta f(t) \quad (7)$$

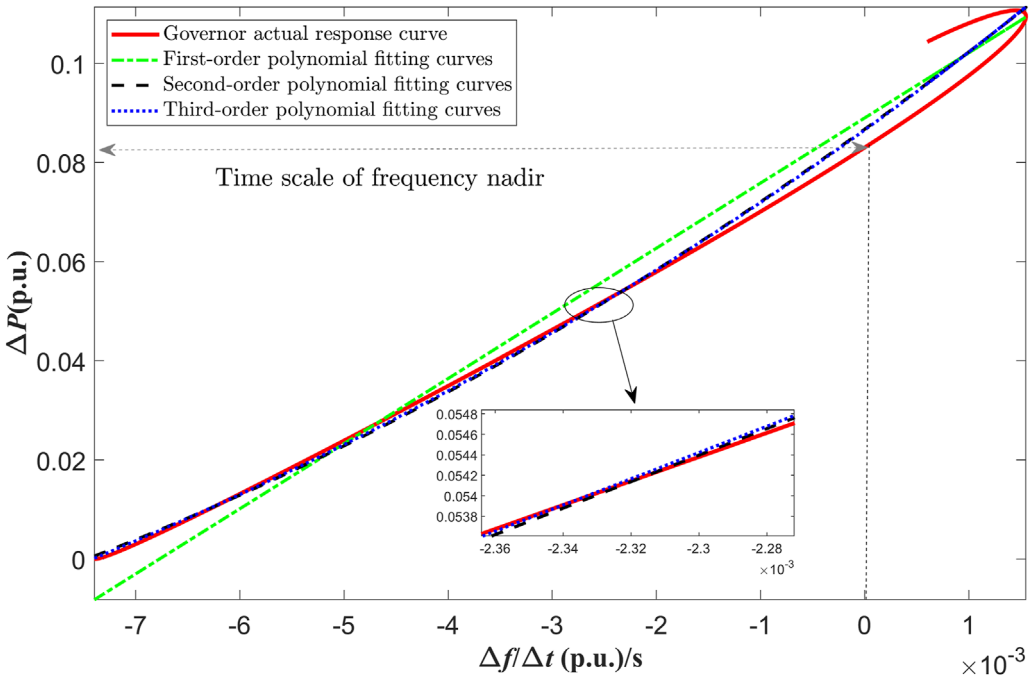

FIGURE 1
The active power-frequency characteristic curve and its fitting results of the GS-TB type governor.

where H_{sys} and D_{sys} are the equivalent inertia and damping constants of the system, Δf is the frequency deviation, P_d is the active disturbances suffered by the system, and ΔP_m is the active output of the resources participating in the primary frequency modulation.

Substituting Equations 2–6 into Equation 7, the following equation can be obtained:

$$\Delta f = a\left(\frac{d\Delta f}{dt}\right)^2 + b\frac{d\Delta f}{dt} + c, \Delta f \in [0, \Delta f_{\max}] \tag{8}$$

Where

$$a = \frac{K_G^2}{D_{sys} + K_p^1 - K_d - K_m}, b = \frac{K_G^1 + K_v - 2H_{sys}}{D_{sys} + K_p^1 - K_d - K_m}, c = \frac{K_G^0 - K_p^0}{D_{sys} + K_p^1 - K_d - K_m} \tag{9}$$

From the above equations, it can be seen that the rate of change of the system frequency with time and the frequency deviation show a second-order polynomial relationship before the system frequency falls to the nadir, which provides a theoretical basis for the subsequent identification of system parameters and online fitting prediction of the frequency. Although Equation 8 does not explicitly include the relevant variables of renewable energies, it can be seen from Equation 9 that the polynomial parameters identified by the measurement data actually reflect the virtual inertia control and droop control characteristics of renewable energies, and the changes in the operation mode and inertia level of the system are also reflected by the parameters of the second-order polynomial.

2.6 Simplified frequency nadir prediction model

Considering that when the frequency of the system reaches the extreme point, there will be $d\Delta f/dt = 0$. According to the correlation properties of the quadratic function, to meet the above conditions, the function image corresponding to Equation 8 must be symmetric with respect to the y-axis, and one obtains (Equation 10):

$$b = 0 \tag{10}$$

The frequency nadir can thus be solved by:

$$\Delta f_{\max} = c \tag{11}$$

Further analysis of the above quadratic function can be rewritten as (Equation 12):

$$\sqrt{\frac{a}{\Delta f - c}}d\Delta f = dt \tag{12}$$

For the left and right integrals, one obtains (Equation 13):

$$t = 2\sqrt{-ac} - \sqrt{a(\Delta f - c)} \tag{13}$$

The time of the frequency nadir can be calculated by:

$$t_{nadir} = 2\sqrt{-ac} \tag{14}$$

Equations 11, 14 are the SPM's expressions proposed in this section. Since it can reflect the characteristics of various frequency modulation resources, the model is suitable for power systems with a high proportion of renewable generation.

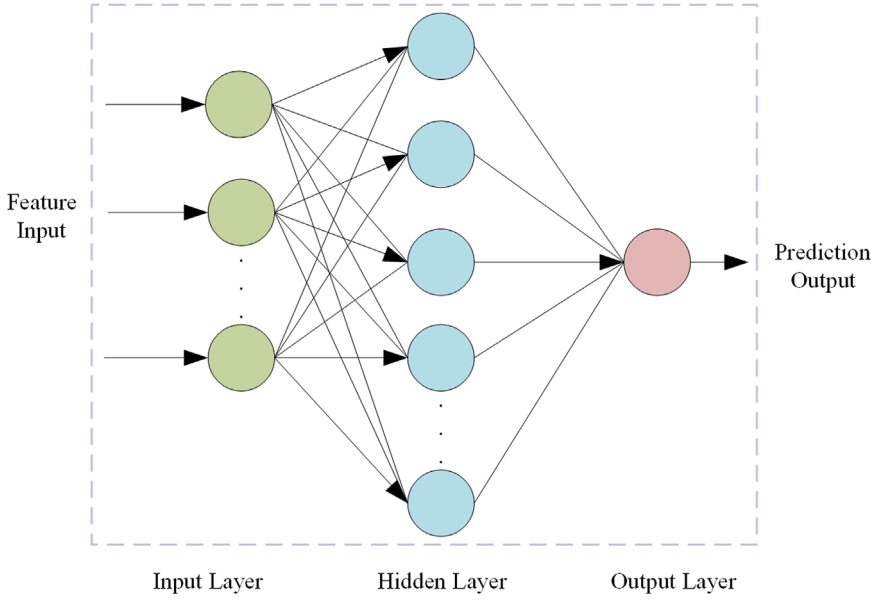

FIGURE 2
Structure diagram of the BPNN algorithm.

3 BPNN modeling and feature selection

3.1 BPNN algorithm

BP neural network, is a multilevel feedforward network structure trained on an error backpropagation algorithm. It adjusts the network weights by passing information forward layer by layer, comparing it to the desired output at the output layer, and then propagating the error backwards to each layer until the preset accuracy requirements are achieved (Wang et al., 2022a). The network topology is shown in Figure 2.

A two-layer feed-forward network with sigmoid hidden neurons and linear output neurons (fitnet), can fit multi-dimensional mapping problems arbitrarily well, given consistent data and enough neurons in its hidden layer. BPNN can obtain the best training results by continuously adjusting the number of neurons in the hidden layer. Considering that the input and output of SPM-BPNN are the maximum frequency deviation and their corresponding time, the number of neurons in the hidden layer is finally determined to be 4 after simulation tests.

3.2 Feature extraction

For the data-driven model, it is necessary to analyze the key factors affecting the frequency nadir in combination with the dynamic process of frequency response to select the eigenvalues, and the frequency response characteristics of the power system are mainly related to the active disturbance amplitude and the physical parameters of the frequency modulation unit.

The essential reason for the dynamic change of system frequency is that there is a power imbalance in the system, which leads to an imbalance between electromagnetic torque and mechanical torque, and ultimately leads to a change in motor speed. Therefore, the active power deficit of the system is a key factor affecting the frequency nadir.

For synchronous generators, the inertia, as a measure of the magnitude of inertia, reflects the rotor energy of the generator set, that is, the difficulty of changing the rotor state. Therefore, the equivalent inertia constant of the system is also a key factor influencing the frequency nadir.

Conventional generator units have the capability of primary frequency modulation, and can also participate in the frequency response when the renewable energy station imposes a specific control strategy. Therefore, the basic parameters of the governor, the virtual inertia coefficient and the equivalent droop coefficient are also the key factor influencing the frequency nadir.

In the process of HVDC FLC participating in frequency modulation, with the increase of frequency deviation, the rapid increase of HVDC power can correspondingly increase the electromagnetic power of the unit, thereby eliminating the unbalanced power, significantly suppressing the high-frequency deviation amplitude, and improving the frequency recovery characteristics. Therefore, the basic parameters of the HVDC frequency modulator are also factors that affect the frequency nadir.

Based on the above analysis, it is necessary to select key variables as input features of BPNN. For the physical data fusion model, BPNN only needs to correct the initial prediction results of the SPM, so its input features can only be the frequency nadir obtained by the SPM.

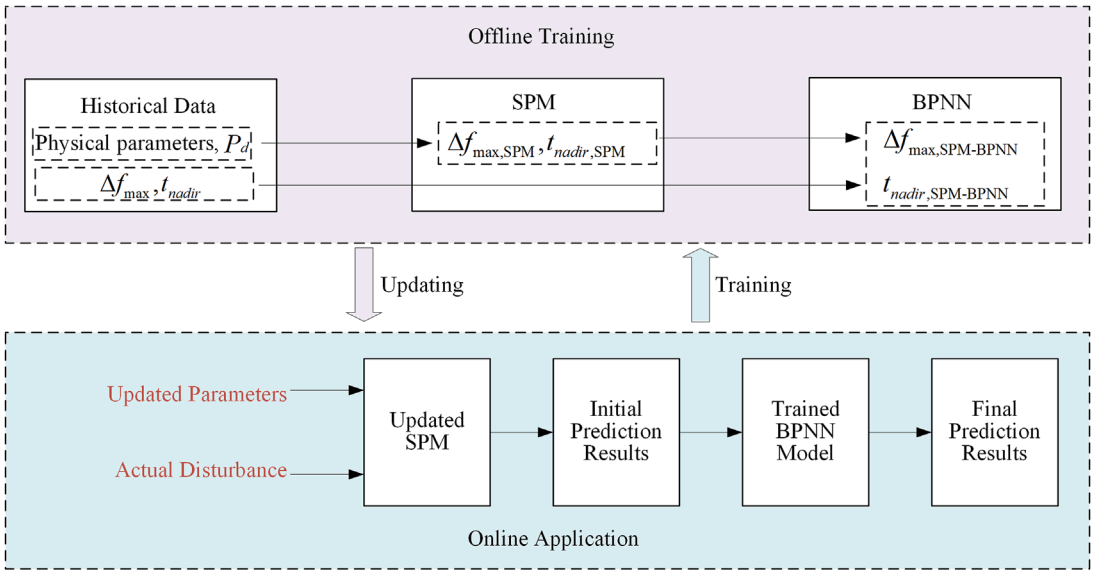

FIGURE 3
SPM-BPNN fusion modeling scheme.

4 SPM-BPNN fusion modeling

The serial scheme is used to fuse the SPM with the BPNN model to construct the SPM-BPNN model to achieve the purpose of complementing each other's advantages. Figure 3 shows the schematic diagram of the SPM-BPNN integrated modeling, which includes both offline training and online application.

4.1 Offline training

During offline training, the physical parameters, power deficit, and actual frequency nadir of the generation units are obtained from the frequency historical data or simulation data. The SPM quickly obtains the initial frequency nadir according to the physical parameters and power deficit of the frequency modulation units, and takes it as the input feature of the BPNN, and the actual frequency nadir as the output feature. The input and output features are normalized and fed into the BPNN for offline training. Finally, the trained BPNN model is used to calculate the frequency nadir online.

4.2 Online application

In the online calculation, the power deficit of the system can be measured by the WAMS and the physical parameters of the generation units can be accessed online. Based on these parameters, the SPM can compute the initial results. Then, the trained BPNN model is used to correct the initial results to obtain the final frequency nadir point. As the operating scenarios of the power system change, the parameters of the physical model also need to be updated accordingly.

5 Case studies

5.1 Case system introduction

In order to verify the effectiveness and accuracy of the SPM-BPNN fusion model proposed in this paper, a modified IEEE 39 bus system is introduced. The reference frequency is 50 Hz, and its topology is shown in Figure 4, which includes seven synchronous generator units, three renewable energy stations, one feed-in HVDC, and 6,148.6 MW load. All renewable energy stations participate in the frequency response, and the total penetration ratio is 27.9%.

The simulation is carried out using the MATLAB/Simulink simulation platform. By randomly sampling the system parameters and invoking Simulink for simulation, a large number of data samples that meet the requirements of the data model can be generated. The actual value of the frequency nadir following perturbation is taken as the output, and the dataset is divided into training samples and test samples according to a certain proportion. The training samples are used to complete the learning of BPNN, and finally the frequency feature prediction model driven by data-model fusion is obtained.

5.2 The selection of the active power-frequency characteristic fitting time window

For various working conditions in the online prediction process, the parameters of SPM need to be identified online based on the measurement data, so the accuracy of the prediction is affected by the long time window of the data. However, due to the differences between the working conditions, the offline determination of the input data time series length is not the optimal choice for some online working conditions (Yan and Xu 2019). If the

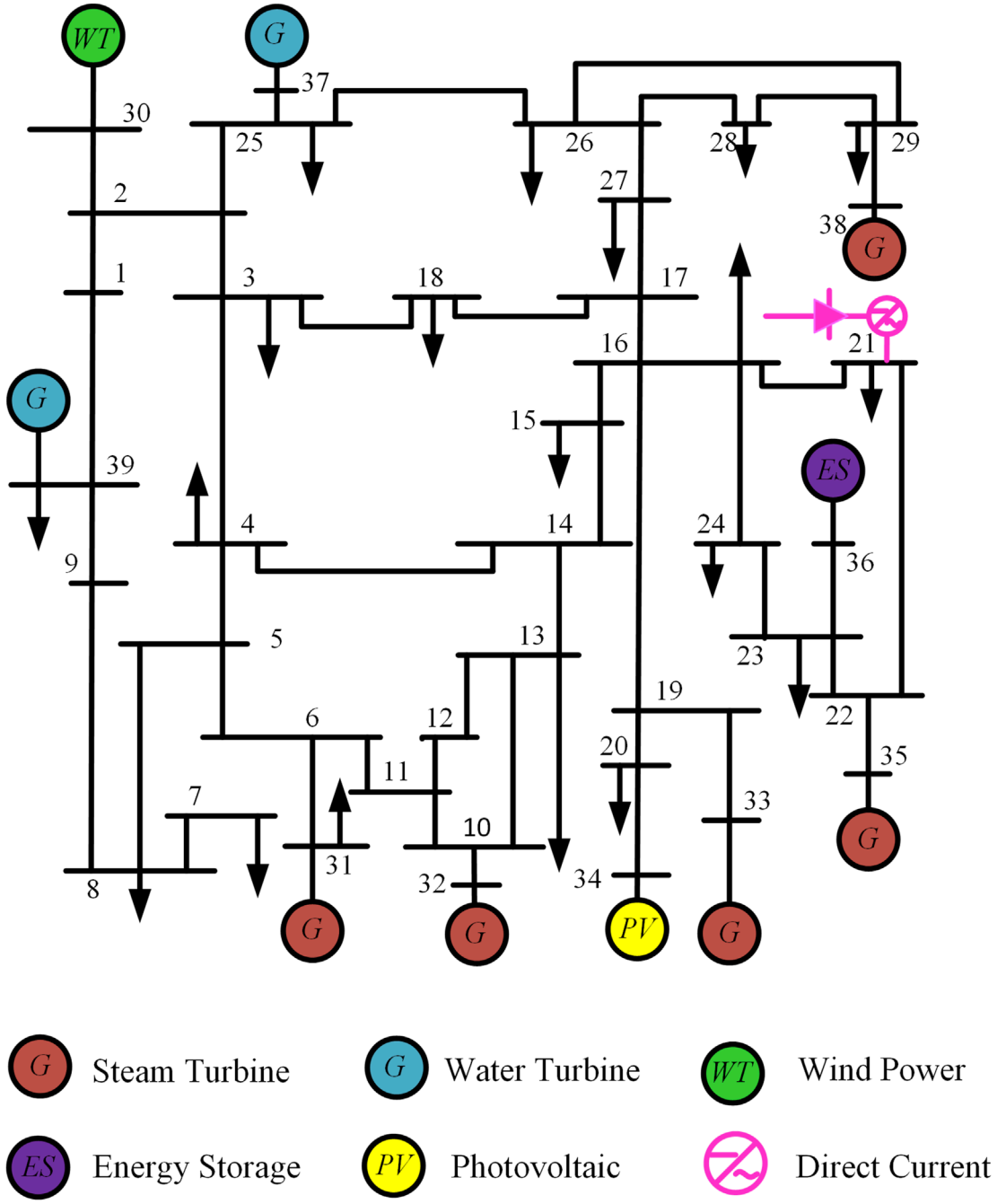

FIGURE 4
The improved IEEE 39-bus system topology diagram.

input data is too short, the prediction method will not obtain enough transient information, and the prediction accuracy will be reduced. If the input data takes too long, the forecasting method will collect "redundant" information, resulting in a decrease in forecasting speed.

In order to solve this problem, taking the data sample obtained in this simulation as an example, the occurrence time of the maximum frequency deviation of COI frequency obtained by the simulation is statistically analyzed. In the low-frequency scenario, the time range is 0.98–4.9s (the system disturbance time is t = 0 s), so the length of the effective data input of the model should not exceed 0.98s. Considering the single run time of the SPM-BPNN (0.01413s on average) and the control reaction time that needs to be reserved for emergency control measures (e.g., low-frequency load shedding), the prediction model proposed in this paper chooses to collect the disturbance moment (500 ms) and the previous data to fit the active power-frequency characteristics of the system, and then achieves a mapping relationship with the real frequency nadir

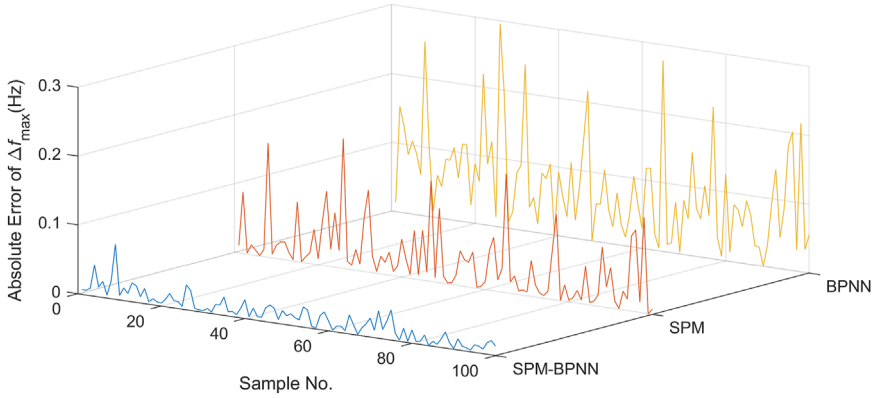

FIGURE 5
The prediction error comparison of Δf_{max}.

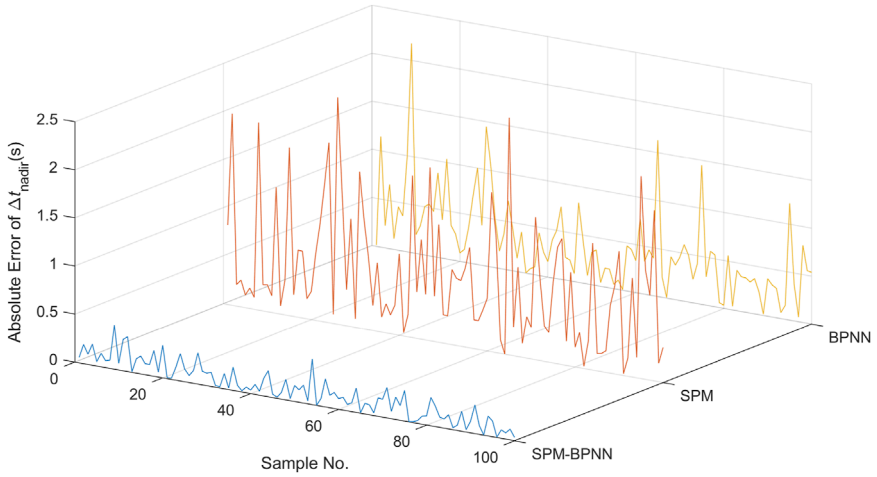

FIGURE 6
The prediction error comparison of frequency nadir time.

TABLE 1 The performance indices and comparison of Δf_{max}.

	SPM	BPNN	SPM-BPNN
MAPE (%)	0.1067	0.3258	0.0630
RMSE (Hz)	0.0563	0.1043	0.0185
MAE (Hz)	0.0364	0.0817	0.0141

TABLE 2 The performance indices and comparison of frequency nadir time.

	SPM	BPNN	SPM-BPNN
MAPE (%)	0.3003	0.1928	0.0632
RMSE (s)	0.9286	0.5725	0.1679
MAE (s)	0.7130	0.4344	0.1316

through the correction of BPNN. The selection of a shorter time window can ensure the efficiency of online prediction, and strive for more time for the system's frequency emergency control and low-frequency load shedding. The introduction of BPNN can ensure high calculation accuracy and make the prediction results more convincing.

5.3 Result analysis

The proposed SPM-BPNN model is compared with the SPM model and the BPNN model in terms of prediction speed and prediction accuracy.

The prediction time of SPM, BPNN and SPM-BPNN models are 1.47 ms, 13.61 ms and 14.13 ms. Compared with a single

data or physical model, the SPM-BPNN model proposed in this paper does not have significant advantages in prediction speed, but it can still predict the frequency nadir online at a faster speed.

In the field of machine learning, the performance of regression models is usually evaluated by three metrics: Mean Absolute Error (MAE), Mean Absolute Percentage Error (MAPE), and Root Mean Square Error (RMSE). In this paper, these three indicators are used to evaluate the prediction accuracy of the SPM-BPNN model and the existing SPM and BPNN models.

As shown in Figures 5, 6, the prediction accuracy of SPM-BPNN is significantly higher than that of a single SPM or BPNN model. As shown in Tables 1, 2, the performance indicators of the SPM-BPNN model are much smaller than those of other models, which indicates that even under different working conditions and disturbance scenarios, the prediction accuracy can be maintained, and the requirements for sample data are reduced, and the interpretability and generalization ability are stronger than those of the single data model, and has great robustness.

From the accuracy evaluation results in Tables 1, 2, it can be seen that the frequency prediction model driven by data-model fusion proposed in this paper has better performance than the two sub-models in various evaluation indicators. The results of Figures 5, 6 show that the average absolute error of SPM-BPNN is 61.26%, 82.74%, 81.54% and 69.7%, respectively, compared with single SPM and BPNN. The serial method is used to fuse the two sub-models, which effectively improves the accuracy of frequency prediction.

Generally speaking, when the prediction results of the sub-model are more accurate, the SPM-BPNN model can also get better prediction results, but when the prediction accuracy of some samples is poor due to the small number of training samples of BPNN, SPM-BPNN can give full play to the advantages of model and data fusion, effectively modify the prediction results, and greatly reduce the prediction error. However, this does not mean that BPNN is not suitable for the prediction of transient frequencies in power systems. Therefore, choosing the right data model is the key to improve the performance of the fusion model.

6 Conclusion

In this paper, a frequency nadir prediction method based on SPM and BPNN is proposed, which implements the serial integration scheme to combine SPM and BPNN to achieve the purpose of complementing each other's advantages. Simulation results show that the proposed approach can not only improve the frequency nadir prediction accuracy, but also ensure that the prediction efficiency meets the requirements of online calculation. Constrained by the inherent limitations of analytical methods, this paper only focuses on major influencing factors of the frequency response and ignores minor factors such as reactive power-voltage characteristics, more in-depth study related to this issue can be conducted in future work. We will further investigate the effective combination of different integration methods and different data models to achieve more accurate prediction of the frequency response. It is worth noting that the frequency prediction method proposed in this paper only predicts the extreme value of the center frequency of inertia following the disturbance of the power system. In the next step, the dynamic frequency characteristics of various nodes in the power system can be predicted, so as to study the spatial distribution characteristics of the frequency following a disturbance, and use this as the basis to implement more efficient distributed frequency emergency control measures.

Data availability statement

The raw data supporting the conclusions of this article will be made available by the authors, without undue reservation.

Author contributions

HL: Conceptualization, Investigation, Supervision, Validation, Writing–review and editing. LW: Conceptualization, Investigation, Writing–original draft, Writing–review and editing. SQ: Investigation, Supervision, Writing–review and editing. ZW: Investigation, Supervision, Writing–review and editing. YW: Investigation, Supervision, Writing–review and editing. SZ: Conceptualization, Investigation, Supervision, Writing–review and editing. WZ: Investigation, Supervision, Writing–review and editing.

Funding

The author(s) declare that financial support was received for the research, authorship, and/or publication of this article. This research was supported by the Science and Technology Project of China Southern Power Grid (090000KK52222151).

Conflict of interest

Authors HL, SQ, and ZW were employed by Shenzhen Power Supply Co., Ltd.

The remaining authors declare that the research was conducted in the absence of any commercial or financial relationships that could be construed as a potential conflict of interest.

Publisher's note

References

Anderson, P. M., and Mirheydar, M. (1990). A low-order system frequency response model. *IEEE Trans. Power Syst.* 5 (3), 720–729. doi:10.1109/59.65898

Bo, Y., Yijun, C., Wei, Y., Zhongtuo, S., and Hongchun, S. (2022). Review on stability assessment and decision for power systems based on new-generation artificial intelligence Technology. *Automation Electr. Power Syst.* 46 (22), 200–223. doi:10.7500/AEPS20220114001

Chan, L., Dunlop, R. D., and Schweppe, F. (1972). Dynamic equivalents for average system frequency behavior following major distribances. *IEEE Trans. Power Apparatus Syst. PAS-* 91 (4), 1637–1642. doi:10.1109/tpas.1972.293340

Egido, I., Fernandez-Bernal, F., Centeno, P., and Rouco, L. (2009). Maximum frequency deviation calculation in small isolated power systems. *IEEE Trans. Power Syst.* 24 (4), 1731–1738. doi:10.1109/tpwrs.2009.2030399

Feng, L., Qi, W., jianxiong, H., and Yi, T. (2021). Combined data-driven and knowledge-driven methodology research advances and its applied prospect in power systems. *Proc. CSEE* 41 (13), 4377–4390.

Han, Z., Cheng, W., and Tianshu, B. (2022). Online fast frequency calculation after power system disturbance based on fusion of physics and data knowledge. *Power Syst. Technol.* 46 (11), 4325–4335.

Hatziargyriou, N., Milanovic, J., Rahmann, C., Ajjarapu, V., Canizares, C., Erlich, I., et al. (2021). Definition and classification of power system stability – revisited and extended. *IEEE Trans. Power Syst.* 36 (4), 3271–3281. doi:10.1109/tpwrs.2020.3041774

Kamruzzaman, M., Duan, J., Shi, D., and Benidris, M. (2021). A deep reinforcement learning-based multi-agent framework to enhance power system resilience using shunt resources. *IEEE Trans. Power Syst.* 36 (6), 5525–5536. doi:10.1109/tpwrs.2021.3078446

Liu, L., Li, W., Ba, Y., Shen, J., Jin, C., and Wen, K. (2020). An analytical model for frequency nadir prediction following a major disturbance. *IEEE Trans. Power Syst.* 35 (4), 2527–2536. doi:10.1109/tpwrs.2019.2963706

Shen, J., Li, W., Liu, L., Jin, C., Wen, K., and Wang, X. (2021). Frequency response model and its closed-form solution of two-machine equivalent power system. *IEEE Trans. Power Syst.* 36 (3), 2162–2173. doi:10.1109/tpwrs.2020.3037695

Wang, Q., Li, F., Tang, Y., and Xu, Y. (2019). Integrating model-driven and data-driven methods for power system frequency stability assessment and control. *IEEE Trans. Power Syst.* 34 (6), 4557–4568. doi:10.1109/tpwrs.2019.2919522

Wang, X., Ding, Q., Li, Z., Zeng, H., Zou, N., Wang, Z., et al. (2022a). "FNP-BPNN integrated model for power system frequency nadir prediction," in *2022 IEEE sustainable power and energy conference (iSPEC)*, 1–5.

Wang, X., Li, W., Shen, J., Zhao, S., and Zhang, Q. (2022b). A three-machine equivalent system frequency response model and its closed-form solution. *Int. J. Electr. Power and Energy Syst.* 142, 108344. doi:10.1016/j.ijepes.2022.108344

Wen, J., Jiang, L., Zhu, J., Qiu, Z., and Chu, C.-C. (2023). "Design of data distributed service-based distributed Co-simulation platform of power systems," in *2023 IEEE industry applications society annual meeting (IAS)*, 1–7.

Yan, Z., and Xu, Y. (2019). Data-driven load frequency control for stochastic power systems: a deep reinforcement learning method with continuous action search. *IEEE Trans. Power Syst.* 34 (2), 1653–1656. doi:10.1109/tpwrs.2018.2881359

Yang, S., Meng, Q., Zhang, Y., Hao, Z., and Zhang, B. (2022). *Simplified prediction model of frequency nadir for power systems penetrated with renewable energy*. IEEE Power and Energy Society General Meeting PESGM, 1–5.

Yi, Z., Hengxu, Z., Changgang, L., and Tianjiao, P. (2021). Review on deep learning applications in power system frequency analysis and control. *Proc. CSEE* 41 (10), 3392–3406.

frontiers | Frontiers in Energy Research

TYPE Original Research
PUBLISHED 06 November 2024
DOI 10.3389/fenrg.2024.1478040

OPEN ACCESS

EDITED BY
Cong Zhang,
Hunan University, China

REVIEWED BY
Yang Liu,
South China University of Technology, China
Zhenjia Lin,
Hong Kong Polytechnic University, Hong Kong SAR, China

*CORRESPONDENCE
Jiajia Chen,
jjchen@sdut.edu.cn

RECEIVED 09 August 2024
ACCEPTED 01 October 2024
PUBLISHED 06 November 2024

CITATION
Li Y, Li K, Fan R, Chen J and Zhao Y (2024) Multi-objective planning of distribution network based on distributionally robust model predictive control.
Front. Energy Res. 12:1478040.
doi: 10.3389/fenrg.2024.1478040

Multi-objective planning of distribution network based on distributionally robust model predictive control

Yudun Li[1,2], Kuan Li[1,2], Rongqi Fan[3], Jiajia Chen[4]* and Yanlei Zhao[4]

[1]State Grid Shandong Electric Power Research Institute, Jinan, China, [2]State Grid Shandong Electric Power Company, Jinan, China, [3]Shandong Smart Grid Technology Innovation Center, Jinan, China, [4]Shandong University of Technology, Zibo, China

The uncoordinated integration of numerous distributed resources poses significant challenges to the safe and stable operation of distribution networks. To address the uncertainties associated with the intermittent output of distributed power sources, we propose a multi-objective planning strategy for distribution networks based on distributionally robust model predictive control (MPC). Initially, an error fuzzy set is established on a Wasserstein sphere using historical data to enhance out-of-sample performance. Next, a multi-objective optimization framework is constructed, balancing returns and risks, and is subsequently converted into a single-objective solution using value-at-risk conditions. This is followed by the implementation of multi-step rolling optimization within the model predictive control framework. We have linearized the proposed model using the linearized power flow method and conducted a thorough validation on an enhanced IEEE 37-node test system. Distributionally robust optimization (DRO) has been shown to reduce costs by a significant 29.16% when compared to an RO method. Moreover, the energy storage capacity required has been notably reduced by 33.33% on the 29-node system and by 20% on the 35-node system. These quantified results not only demonstrate the substantial economic efficiency gains but also the enhanced robustness of our proposed planning under the uncertainties associated with renewable energy integration.

KEYWORDS

distributionally robust optimization, model predictive control, uncertainty, distribution network planning, distributed resources

1 Introduction

With the advancement of new power system construction, distribution networks are evolving toward source-network-load-storage integration and collaborative interaction (Castro et al., 2024). The integration of large-scale distributed photovoltaic (PV) systems with uncertain output transforms distribution networks from radial passive structures into multi-power structures. This shift complicates power flow management and significantly impacts operational characteristics, leading to increased planning challenges (Zhang et al., 2023a; Esfahani et al., 2024). Addressing the capacity and scientific management of distributed power supplies and energy storage devices has thus become a research hotspot.

Many scholars have explored distribution network planning (Wang et al., 2024a; de Lima et al., 2024). For example, Pan et al. (2023) propose a collaborative planning method for distribution network and multi-energy systems, balancing multi-agent interests and improving analysis and calculation efficiency. Chen et al. (2017) introduce a multi-objective programming model based on game theory, considering the interests of source-grid-load multi-agents in a power market environment and using a particle swarm optimization algorithm for iterative optimization. Wang et al. (2022) propose a framework that considers energy storage allocation and bi-level planning of the distribution network, and the results show that this framework achieves low carbon emissions and improved economics. Subbaramaiah and Sujatha (2023) propose a multi-objective distribution network planning scheme that reduces power losses and identifies optimal wind power locations. However, these studies do not account for the impact of intermittent distributed PV output, potentially overestimating the system's risk resilience.

Scholars have increasingly recognized the pivotal role of energy storage in addressing the challenges of integrating high levels of renewable energy sources (Liu et al., 2023; Ma et al., 2024). For instance, Zheng et al. (2023) introduce an optimization framework for energy storage allocation in distribution networks with a significant penetration of photovoltaic (PV) systems. This approach addresses the source-load imbalance and voltage regulation issues, thereby reducing power losses and operational costs. Another notable contribution is made by Zhang et al. (2024), who present a method for the concurrent optimization of battery storage configuration and distribution network operations. The study demonstrates that energy storage can effectively smooth power fluctuations and enhance the network's resilience to fault disturbances. Through planning, the capacity of energy storage in the distribution network can increase the local consumption rate of renewable energy, reduce the system operating costs, and reduce the impact of PV uncertainty on the distribution network (Ba-swaimi et al., 2024; Li et al., 2024a). However, the above literature does not consider the risk assessment component in the energy storage configuration process.

Methods such as stochastic optimization, robust optimization, and distributionally robust optimization (DRO) are commonly used to address the uncertainty in high-proportion renewable energy predictions. Stochastic optimization assumes prediction errors follow specific probability distributions and uses manageable probability constraints (Wang et al., 2024b; Zhang et al., 2022; Li et al., 2024b). Robust optimization finds optimal solutions under worst-case scenarios, often resulting in overly conservative outcomes. DRO, on the other hand, uses real data to generate fuzzy sets and estimate distribution parameters, making it more suitable for complex, high-dimensional, multi-constraint problems (Skalyga et al., 2023). However, these constraints can turn the problem into a non-convex, nonlinear stochastic optimization challenge. Thus, a comprehensive approach that considers both economic benefits and operational safety is required. DRO focuses on establishing fuzzy sets with a flexible and diverse optimization framework. The Wasserstein distance, a measure of the difference between probability distributions, accurately describes similarities and differences by considering shape and weight information (Lu and Zhou, 2024).

Based on this analysis, the main contributions of this study are: (1) We consider energy storage capacity configuration and use a radius-controllable Wasserstein ball to construct a fuzzy set that achieves good out-of-sample performance, mitigating data overfitting and use distributed robust methods to balance robustness and economy. (2) Utilizing conditional value at risk (CVaR), we define optimization objectives for operation cost and constraint violation risk, transforming the multi-objective problem into a single-objective solution. (3) In order to reduce the error in PV forecasting, we implement rolling optimization within the model predictive control (MPC) framework.

2 Distributionally robust multi-objective model based on a Wasserstein sphere

2.1 Fuzzy set model based on a Wasserstein ball

Currently, there are two primary methods to model constraint distribution in distributionally robust optimization (DRO). One method involves moment-based fuzzy sets, such as unimodality (Zhang et al., 2021), symmetry (Wang et al., 2024c), and directional derivatives (Jiao et al., 2021), where fuzzy sets are defined as confidence intervals based on goodness-of-fit tests. The other method treats the fuzzy set as a ball in probability space, with the radius determined by metrics such as the Wasserstein metric, Kullback–Leibler divergence, and Prohorov metric.

Among these, the Wasserstein distance is particularly effective in measuring differences between two probability distributions. By considering both the shape and weight information of the distributions, it accurately captures the similarities and differences between them. In this paper, we construct fuzzy sets using the Wasserstein metric to achieve better out-of-sample performance and enhanced flexibility with radius control. Esfahani et al. (2024) demonstrated the effectiveness of data-driven Wasserstein metrics in solving distributed robust optimization re-representation problems. Inspired by this, our study employs the Wasserstein ball to construct fuzzy sets derived from limited prediction error data, thus achieving controllable data sets. Assuming the uncertainty set is a polyhedron, the prediction error ξ constitutes the data set $\Pi = \{\xi \in R^{N_\xi}: H\xi \le d_\xi\}$, as shown in Equation 1:

$$E^Q[\| \xi \|] = \int_\Pi \| \xi \| Q(d\xi) < \infty, \tag{1}$$

where $\| \cdot \|$ represents the norm, and $E^Q[\cdot]$ denotes the expectation operation under the Q distribution. The Wasserstein distance d_w is defined to represent the distance of all probability distributions Q of data set Π in space $m(\Pi)$. Let F be the set of all Lipschitz continuous functions f, and the constant is less than or equal to 1. The Wasserstein distance, as articulated by Equation 2, is a metric that grows with the number of samples, causing the fuzzy set to contract and ultimately converge to the true distribution. This convergence offers a more accurate and realistic portrayal of PV uncertainty (Skalyga et al., 2023). The Wasserstein distance

$\forall Q_1, Q_2 \in m(\Pi)$ between the empirical distribution d_w and the true distribution is calculated as follows:

$$d_w(Q_1, Q_2) = \max_{f \in F} \left[\begin{array}{c} \int_{\Pi} f(\xi) Q_1(d\xi) \\ -\int_{\Pi} f(\xi) Q_2(d\xi) \end{array} \right]. \tag{2}$$

The Wasserstein metric quantifies the minimum "distance" required to morph one probability distribution into another. The fuzzy set is delineated by encompassing all distributions within a controllable Wasserstein radius centered on the uniform empirical distribution derived from the training dataset, like Equation 3.

$$\hat{\mathbb{P}}^{N_s} = \left\{ Q \in m(\Pi) : d_w\left(\hat{P}^{N_s}, Q\right) \leq \gamma \right\}, \tag{3}$$

where $\hat{\mathbb{P}}^{N_s}$ contains all distributions $\hat{P}^{N_s}$ in a Wasserstein sphere with radius γ centered on the uniform empirical distribution. By adjusting the radius γ, the ball contains a true distribution P with a specified confidence level and good performance guarantee.

2.2 System optimization objective

The optimization goal of the system is to seek the balance between the operation cost and risk of the distribution network. Therefore, the objective function includes the sum of the operating cost function J_{cost} and the violation constraint risk function J_{risk}, namely Equation 4:

$$f = J_{\text{cost}} + J_{\text{risk}}. \tag{4}$$

1) The operating cost function J_{cost} is calculated as follows, as expressed in Equation 5:

$$J_{\text{cost}} = C_{\text{buy}} - C_{\text{sell}} + C_{\text{pre}} + C_{\text{cur}} + C_{\text{car}}, \tag{5}$$

where C_{buy}, C_{sell}, C_{pre}, C_{cur}, and C_{car} are electricity purchase cost, electricity sales income, operation, and maintenance cost, abandoned light cost, and carbon subsidy cost, respectively. The specific equations are expressed as Equations 6, 9 respectively

$$\begin{aligned} C_{\text{buy}} - C_{\text{sell}} = & \sum_{n \in N} a^t_{1,n} \left[P^t_{\text{l},n} + P^t_{\text{B},n} - (1 - \alpha^t_n) P^t_{\text{av},n} \right] \\ & + \sum_{n \in N} a^t_{2,n} \left[Q^t_{\text{l},n} - Q^t_{\text{av},n} \right] \\ & + \sum_{n \in N} a^t_{3,n} \left[(1 - \alpha^t_n) P^t_{\text{av},n} - P^t_{\text{l},n} - P^t_{\text{B},n} \right], \end{aligned} \tag{6}$$

where $P^t_{l,n}$ and $Q^t_{l,n}$ respectively represent the active and reactive power load of t bus $n \in N$ at the moment, $N = (1, 2, 3, \cdots, n)$ indicates the bus set, $P^t_{\text{av},n}$ and $Q^t_{\text{av},n}$ are the available active and reactive power generated by PV, respectively, and $P^t_{\text{B},n}$ denotes the charging and discharging power of the energy storage. The power reduction factor $\alpha^t_n \in [0, 1]$ is used to prevent the overvoltage hazard caused by high PV penetration. $a^t_{1,n}$ and $a^t_{2,n}$ represent the active and reactive power purchase prices, respectively, and $a^t_{3,n}$ refers to the active power sale price.

$$C_{\text{pre}} = \sum_{n \in N_{\text{av}}} a_{\text{av}} P^t_{\text{av},n} + \sum_{n \in N_{\text{B}}} a_{\text{B}} P^t_{\text{B},n}, \tag{7}$$

where $n \in N_{\text{av}}$ and $n \in N_{\text{B}}$ are the buses where the PV and energy storage are located, respectively; a_{av} and a_{B} are respectively the maintenance costs of unit power PV and energy storage.

$$C_{\text{cur}} = \sum_{n \in N_{\text{av}}} a^t_{4,n} \left[\alpha^t_n P^t_{\text{av},n} \right], \tag{8}$$

where $a^t_{4,n}$ represents the cost of discarding light.

$$C_{\text{car}} = \sum_{n \in N} a^t_{5,n} P^t_{\text{av},n}, \tag{9}$$

where $a^t_{5,n}$ denotes the government's carbon subsidy unit price for PV power generation.

2) The violation constraint risk function J_{risk} is computed as follows:

The risk function J_{risk} related to constraint violation encompasses the sum of the CVaR of the set of network and device constraint functions. This approach is supported by recent research in the field of energy systems and distribution network planning, as evidenced by Ren et al. (2024) and Chen et al. (2024). Specifically defined by Fan et al. (2023) and Zhang et al. (2023b), the CVaR measure is used to quantify the tail risk imposed by uncertainties, providing a more comprehensive assessment of risk than traditional measures

$$J^t_{\text{risk}} = \sum_{i=1}^{N_l} \text{CVaR}^{\beta}_{\mathbb{P}} \left[l_i(x_t, u_t, \xi_t) \right], \tag{10}$$

where N_l is the constraint set, and $\beta \in (0, 1]$ represents the CVaR confidence level of the random variable ξ_t under the $\mathbb{P}$ distribution. The specific details will be derived in the next section.

2.3 System constraints

2.3.1 PV output constraint

The distributed PV is connected to the distribution network through the inverter, and the relationship curve of the active and reactive power output characteristics is shown in Figure 1.

The relationship between the adjustable reactive power of the PV inverter on bus $n \in N$ and the inverter capacity $F_{\text{av},n}$ can be expressed as follows, namely Equation 11:

$$\sqrt{\left[(1 - \alpha^t_n) P^t_{\text{av},n} \right]^2 + \left(Q^t_{\text{av},n} \right)^2} \leq F_{\text{av},n}, \quad n \in N. \tag{11}$$

The reactive power output is limited by the power factor angle θ_n to be Equation 12

$$\left| Q^t_{\text{av},n} \right| \leq \tan(\theta_n) \left[(1 - \alpha^t_n) P^t_{\text{av},n} \right], \quad n \in N, \tag{12}$$

where the power factor angle θ_n of PV is also limited by $0 < \cos(\theta_n) \leq 1$.

10.3389/fenrg.2024.1478040

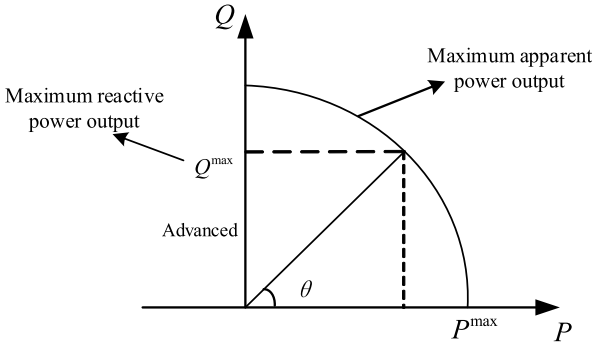

FIGURE 1
Distributed PV active and reactive power output characteristics.

2.3.2 Energy storage constraints

$$D_{es,n}^{t+1} = D_{es,n}^{t} + \eta_c P_{B_{c,n}}^{t} T - \frac{1}{\eta_d} P_{B_{d,n}}^{t} T, \quad n \in N, \tag{13}$$

where Equation 13 demonstrates the state-of-charge constraints for energy storage. T indicates the duration interval of $(t, t+1]$; $D_{es,n}^{t}$ denotes the state of charge of the energy storage device on the bus n; η_c and η_d are the charging and discharging efficiency, respectively. $P_{B_{c,n}}^{t}$ and $P_{B_{d,n}}^{t}$ represent the charging and discharging power stored at moment t, respectively. The charge/discharge power also satisfies $P_{B_{c,n}}^{t} P_{B_{d,n}}^{t} = 0$. The inequality constraints of energy storage capacity and power limit are Equation 14:

$$D_{es,n}^{min} \le D_{es,n}^{t} \le D_{es,n}^{max}, P_{B,n}^{min} \le P_{B,n}^{t} \le P_{B,n}^{max}, \tag{14}$$

where $D_{es,n}^{min}$ and $D_{es,n}^{max}$ are the minimum and maximum capacities of energy storage equipment, respectively; $P_{B,n}^{min}$ and $P_{B,n}^{max}$ represent respectively the impulse and discharge power limits.

2.3.3 Distribution network model

Suppose that the distribution network with N buses, $N = 1, 2, 3, \cdots, n$, $\boldsymbol{\Gamma} \subset N \times N$ represents the line connection matrix. Let $V_i^t \in C$ and $I_i^t \in C$ denote the voltage and current at node i at time t, $i \in N$, $\boldsymbol{V}^t = [V_1^t, V_2^t, \cdots, V_N^t]^T \in C^N$, and $\boldsymbol{I}^t = [I_1^t, I_2^t, \cdots, I_N^t]^T \in C^N$. Let $z_{ij} \in \boldsymbol{Z}$ represent the impedance between node i and node j, then the line admittance $y_{ij} = 1/z_{ij} = g_{ij} + jb_{ij}$, where $g_{ij} \in \boldsymbol{G}$ and $b_{ij} \in \boldsymbol{B}$ represent the conductance and susceptance between nodes, respectively. The bus bar is modeled using the Pi model, and the matrix y_{ij} of the admittance $\boldsymbol{Y}_{ij} \in C^{N \times N}$ can be expressed as Equation 15:

$$\boldsymbol{Y}_{ij} = \begin{cases} \sum_{l \sim i} y_{il} + y_{ii}, & i = j \\ -y_{ij}, & (i,j) \in \boldsymbol{\Gamma} \\ 0, & (i,j) \notin \boldsymbol{\Gamma}, \end{cases} \tag{15}$$

where $l \sim i$ means that the node i is connected to j. According to Kirchhoff's law and Ohm's law, $\boldsymbol{I}^t = \boldsymbol{Y}_{ij} \boldsymbol{V}^t$. Network complex power injection can be expressed as follows:

$$\boldsymbol{S}^t = \boldsymbol{V}^t (\boldsymbol{I}^t)^* = \mathrm{diag}(\boldsymbol{V}^t)(\boldsymbol{Y}\boldsymbol{V}^t)^*, \tag{16}$$

where the superscript "*" represents the conjugate operation, and the complex power $\boldsymbol{S}^t = [S_1^t, S_2^t, \cdots, S_N^t]^T$ can be decomposed into $S_i^t = P_i^t + jQ_i^t$ in the rectangular coordinate, where P_i^t and Q_i^t represent the active power and reactive power injected by the node, respectively.

3 Multi-objective planning based on DROMPC

3.1 Dynamic characteristics with MPC

Consider N_d grid-connected devices, including a traditional generator, an inverter-based distributed power supply, and time-varying load. Energy storage devices, such as batteries and plug-in electric vehicles, can be used both as generators and as loads. The power flow of each controllable device is modeled by a discrete linear dynamic system as follows Equation 17:

$$x_{t+1}^d = \bar{A}^d x_t^d + \bar{B}^d u_t^d, \tag{17}$$

where the state variable $x_t^d \in R^{n_d}$ of the device d at the time t, the dynamic matrix $\bar{A}^d \in R^{n_d \times n_d}$, and the coefficient input matrix $\bar{B}^d \in R^{n_d \times m_d}$ of the control variable $u_t^d \in R^{m_d}$. The first element of x_t^d corresponds to the output power of device d to the distribution network at t time.

Let the control domain be H; then, the matrix form of system evolution can be expressed as Equation 18:

$$\boldsymbol{x}_t^d = \boldsymbol{A}_t^d x_0^d + \boldsymbol{B}_t^d \boldsymbol{u}_t^d, \tag{18}$$

where $\boldsymbol{x}_t^d$ is the state vector, $\boldsymbol{x}_t^d = [x_1^d, x_2^d, \cdots, x_t^d]^\top$ contains all the state variables in the control domain; $\boldsymbol{u}_t^d$ denotes the control matrix, and $\boldsymbol{u}_t^d = [u_0^d, u_1^d, \cdots, u_{t-1}^d]^\top$. The calculation formulas of $\boldsymbol{A}_t^d$ and $\boldsymbol{B}_t^d$ can be expressed as Equation 19:

$$\boldsymbol{A}_t^d = \begin{bmatrix} \bar{A}^d \\ \left(\bar{A}^d\right)^2 \\ \vdots \\ \left(\bar{A}^d\right)^t \end{bmatrix}, \boldsymbol{B}_t^d = \begin{bmatrix} \bar{B}^d & 0 & \cdots & 0 \\ \bar{A}^d \bar{B}^d & \bar{B}^d & \cdots & 0 \\ \vdots & \vdots & \vdots & \vdots \\ \left(\bar{A}^d\right)^{t-1} \bar{B}^d & \cdots & \bar{A}^d \bar{B}^d & \bar{B}^d \end{bmatrix}. \tag{19}$$

3.2 Linearized approximate power flow

In this paper, the linearization method of literature (Alizadeh and Capitanescu, 2022) is used to linearize the power flow model shown in Equation 16. In a balanced, symmetrical distribution network, the common coupling point connected to the power grid is denoted as node 0, serving as the bus set that connects the load and the distributed generator.

The complex form of the node voltage is $V_n^t = |V_n^t| e^{j \angle V_n^t}$, and the node injection current is expressed as $I_n^t = |I_n^t| e^{j \angle I_n^t}$, where $|V_n^t|$ and $|I_n^t|$ correspond to the root mean square value, and $\angle V_n^t$ and $\angle I_n^t$ are the relative phase angles of voltage and current, respectively. The node 0 denotes the slack node, and the other nodes are the PQ nodes that inject complex power. The admittance matrix can be divided into

$$\begin{bmatrix} I_0^t \\ \boldsymbol{I}^t \end{bmatrix} = \begin{bmatrix} y_{00} & \bar{y}^{\top} \\ \bar{y} & \boldsymbol{Y} \end{bmatrix} \begin{bmatrix} V_0 \\ \boldsymbol{V}^t \end{bmatrix}, \tag{20}$$

where V_0 is the slack bus voltage; I_0^t is the current injected into the slack bus at time t; y_{00} is the self-admittance of the slack node; $\bar{y}$ indicates transfer admittance.

The injection power presented in Equation 20 can be formulated as follows:

$$\boldsymbol{S}^t = \mathrm{diag}(\boldsymbol{V}^t)(\boldsymbol{Y}^*(\boldsymbol{V}^t)^* + \bar{y}^*(V_0^t)^*). \tag{21}$$

Assuming that $\bar{V} = |\bar{V}|\angle\boldsymbol{\theta}$ is a preset nominal voltage value, and ΔV^t represents the difference between the actual voltage and the nominal voltage, the voltage can be expressed as $\boldsymbol{V}^t = \bar{V} + \Delta\boldsymbol{V}^t$. Then, Equation 21 becomes Equation 22:

$$\boldsymbol{S}^t = \mathrm{diag}(\bar{V} + \Delta\boldsymbol{V}^t)(\boldsymbol{Y}^*(\bar{V} + \Delta\boldsymbol{V}^t)^* + \bar{y}^*V_0^*). \tag{22}$$

Ignoring the influence of the higher-order term $\mathrm{diag}(\Delta\boldsymbol{V}^t)\boldsymbol{Y}^*(\Delta\boldsymbol{V}^t)^*$, the power constraint equation is transformed into Equation 23:

$$\Lambda\Delta\boldsymbol{V}^t + \Phi(\Delta\boldsymbol{V}^t)^* = \boldsymbol{S}^t + \Psi, \tag{23}$$

where

$\Lambda = \mathrm{diag}(\boldsymbol{Y}^*\bar{V}^* + \bar{y}^*V_0^*)$;

$\Phi = \mathrm{diag}(\bar{V})\boldsymbol{Y}^*, \Psi = -\mathrm{diag}(\bar{V})(\boldsymbol{Y}^*\bar{V}^* + \bar{y}^*V_0^*)$。

Given $\Lambda = 0_{N\times N}$ and $\psi = 0_N$, the nominal voltage is $\bar{V} = \boldsymbol{Y}^{-1}\bar{y}V_0$, and the linearized power is expressed as $\boldsymbol{S}^t = \mathrm{diag}(\bar{V})\boldsymbol{Y}^*(\Delta\boldsymbol{V}^t)^*$. The voltage deviation becomes Equation 24:

$$\Delta\boldsymbol{V}^t = \boldsymbol{Y}^{-1}\mathrm{diag}^{-1}(\bar{V}^*)(\boldsymbol{S}^t)^*. \tag{24}$$

Let $\boldsymbol{Z}_R$ be the real part of the impedance and $\boldsymbol{Z}_I$ be the imaginary part of the impedance, then $\boldsymbol{Y}^{-1} = (\boldsymbol{G} + j\boldsymbol{B})^{-1} = \boldsymbol{Z}_R + j\boldsymbol{Z}_I$. Taking M and N as the active and reactive component coefficients, respectively, $\Delta\boldsymbol{V}^t$ is expanded in the form of rectangular coordinates as Equation 25:

$$\begin{aligned} M &= \left(\boldsymbol{Z}_R\mathrm{diag}\left(\frac{\cos(\theta)}{|\bar{V}|}\right) - \boldsymbol{Z}_I\mathrm{diag}\left(\frac{\sin(\theta)}{|\bar{V}|}\right)\right), \\ N &= \left(\boldsymbol{Z}_I\mathrm{diag}\left(\frac{\cos(\theta)}{|\bar{V}|}\right) - \boldsymbol{Z}_R\mathrm{diag}\left(\frac{\sin(\theta)}{|\bar{V}|}\right)\right). \end{aligned} \tag{25}$$

The voltage amplitude is approximately equal to $|\bar{V}| + R(\Delta\boldsymbol{V}^t)$, $R(\cdot)$ represents the real part operation, and $\mathbb{I}$ indicates the unit matrix. Referring to the linear relationship between voltage and power, the voltage amplitude is finally expressed as Equation 26:

$$\boldsymbol{V}^{\mathrm{t}}[p^t, q^t] = M(\mathbb{I} - \mathrm{diag}\{\alpha_n^t\})P_{\mathrm{av},n}^t + NQ^t + |\bar{V}|. \tag{26}$$

The voltage constraint is shown in Equation 27:

$$\boldsymbol{V}^{\mathrm{t}}[p^t, q^t] - \boldsymbol{V}^{\max} \le 0, \boldsymbol{V}^{\min} - \boldsymbol{V}^{\mathrm{t}}[p^t, q^t] \le 0, \tag{27}$$

where $\boldsymbol{V}^{\min}$ and $\boldsymbol{V}^{\max}$ are the matrix forms of the lower limit $V^{\min}$ and the upper limit $V^{\max}$ of the line voltage, respectively.

3.3 DROMPC for distribution network planning

In this paper, the device constraints and voltage constraints under different times and nodes can be summarized as follows:

$$\begin{cases} E\boldsymbol{\mathcal{R}}[\boldsymbol{V}^{\mathrm{t}}[p^t, q^t] - \boldsymbol{V}^{\max} \le 0] \\ E\boldsymbol{\mathcal{R}}[\boldsymbol{V}^{\min} - \boldsymbol{V}^{\mathrm{t}}[p^t, q^t] \le 0] \\ E\boldsymbol{\mathcal{R}}[\mathbf{T}_d^t\boldsymbol{x}_t^d + \mathbf{U}_d^t\boldsymbol{u}_t^d + \mathbf{Z}_d^t\boldsymbol{\xi}_t - \omega_d \le 0], \end{cases} \tag{28}$$

where $\boldsymbol{\mathcal{R}}[\cdot]$ denotes the general transformation from inequality constraints to random form. $\mathbf{T}_d^t\boldsymbol{x}_t^d + \mathbf{U}_d^t\boldsymbol{u}_t^d + \mathbf{Z}_d^t\boldsymbol{\xi}_t - \omega_d \le 0$ contains various local constraints of grid-connected equipment; $\mathbf{T}_d^t$, $\mathbf{U}_d^t$, and $\mathbf{Z}_d^t$ are the coefficient matrices of equipment state variables, control variables, and uncertain errors, respectively. ω_d is a local constraint parameter. In this paper, CVaR is used to re-describe the voltage affine constraints, and the remaining constraints are evaluated by sample average.

Define an affine constraint set $\boldsymbol{\mathcal{V}}_t$ containing N_l Equation 28, where each affine constraint can be expressed as Equation 29:

$$\mathcal{C}_o^t(\mathbf{y}_t, \xi_t) = \left[\bar{\mathcal{A}}(\mathbf{y}_t)\right]_o\xi_t + \left[\bar{\mathcal{B}}(\mathbf{y}_t)\right]_o, \tag{29}$$

where $\mathcal{C}_o^t(\cdot)$ is the $o, o = 1, \cdots, N_l$ affine constraint in $\boldsymbol{\mathcal{V}}_t$. The decision variable $\mathbf{y}_t$ includes the PV reduction variable α_n^t and the controllable device setting point. The CVaR constrained at confidence level β in A $\boldsymbol{\mathcal{V}}_t$ is calculated as follows Equation 30:

$$\inf_{\kappa_o^t} E_{\xi_t}\left\{\left[\mathcal{C}_o^t(\mathbf{y}_t, \xi_t) + \kappa_o^t\right]_+ - \kappa_o^t\beta\right\} \le 0, \tag{30}$$

where κ_o^t is an auxiliary variable. The expected operation in the above equation can be restated as Equation 31:

$$\bar{\mathcal{Q}}_o^t = \max_{k=1,2}[\langle\bar{\mathbf{a}}_{ok}(\mathbf{y}_t), \xi_t\rangle + \bar{\mathbf{b}}_{ok}(\kappa_o^t)]. \tag{31}$$

Because the result is the maximum of two affine functions, the expression is convex in $\mathbf{y}_t$ for each fixed ξ_t. The risk objective shown in Equation 10 is expressed by the distributionally robust optimization form of CVaR as follows Equation 32:

$$\hat{J}_{\mathrm{risk}}^t = \sum_{t=1}^{H}\sum_{o=1}^{N_l}\sup_{Q_t\in\hat{\mathbb{P}}_t^{N_s}} E^{Q_t}\max_{k=1,2}\left[\langle\bar{\mathbf{a}}_{ok}(\mathbf{y}_t), \hat{\xi}_t\rangle + \bar{\mathbf{b}}_{ok}(\kappa_o^t)\right]. \tag{32}$$

The above multi-objective DRO is equivalently restated as a single-objective quadratic programming using the method of Lin et al. (2023). The objective is to minimize the total worst-case CVaR of the function and affine constraints. The specific form of the subproblem of MPC is as follows Equation 33:

$$\begin{aligned} &\left\{\inf_{\substack{\omega_{1,n},\omega_{2,n},\\ \mathbf{y}_t,\kappa_o^t}}\sum_{t=1}^{H}\left\{\mathrm{E}\left[\hat{J}_{\mathrm{cost}}^t\right] + \sup_{Q_t\in\hat{\mathbb{P}}_t^{N_s}}\sum_{o=1}^{N_l}\mathrm{E}^{Q_t}\left[\bar{\mathcal{Q}}_o^t\right]\right\}\right. \\ &= \inf_{\substack{\omega_{1,n},\omega_{2,n},\\ \mathbf{y}_t,\kappa_o^t,\\ \lambda_o,s_{io}^t,\varsigma_{iko}^t}}\sum_{t=1}^{H}\left\{\mathrm{E}\left[\hat{J}_{\mathrm{cost}}^t\right] + \sum_{o=1}^{N_l}\left(\lambda_o\gamma_t + \frac{1}{N_s}\sum_{i=1}^{N_s}s_{io}^t\right)\right\} \\ &\quad \text{s.t.} \quad (\bar{\mathbf{b}}_{ok}(\kappa_o^t) + \langle\bar{\mathbf{a}}_{ok}(\mathbf{y}_t), \hat{\xi}_t^i\rangle \le s_{io}^t \parallel \varsigma_{iko}^t \end{aligned}$$

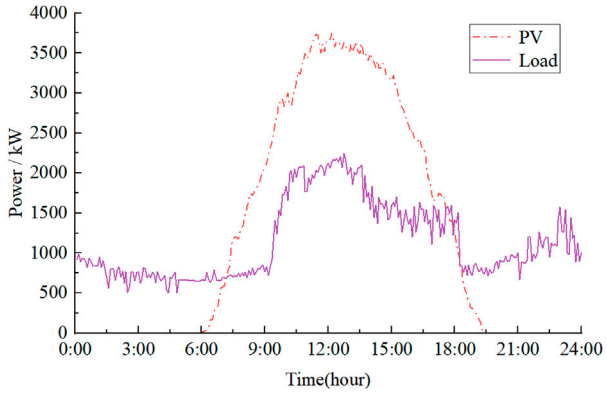

FIGURE 2
Curves of available PV power and total load demand.

$$-\bar{\mathbf{a}}_{ok}(\mathbf{y}_t)\|_{\infty} \le \lambda_o^t \varsigma_{iko}^t \ge 0 \frac{1}{N_s}\sum_{i=1}^{N_s}\left[\left[(1-\alpha_n^t)\hat{P}_{\mathrm{av},n}^{t,i}\right]^2\right.$$

$$+(Q_n^t)^2 - \bar{S}_n^2 + \varpi_{1,n}^t]_+ \le \varpi_{1,n}^t \beta \frac{1}{N_s}\sum_{i=1}^{N_s}\left[\tan(\theta_n)\left[(1-\alpha_n^t)\hat{P}_{\mathrm{av},n}^{t,i}\right]\right.$$

$$-|Q_n^t| + \varpi_{2,n}^t]_+ \le \varpi_{2,n}^t \beta$$

Equations (13) − (14), (33)

where $\varpi_{1,n}^t$, $\varpi_{2,n}^t$, and κ_o^t are auxiliary variables of CVaR, λ_o^t, s_{io}^t, and ς_{iko}^t are auxiliary variables of distributionally robust Wasserstein sphere reconstruction (Dong et al. (2024)). The power factor constraint and apparent power constraint are processed by sample average.

4 Simulation and discussion

4.1 System description and parameter settings

To verify the effectiveness of the proposed optimization framework, we conducted simulations using the improved IEEE 37-bus system, with network parameters derived from Reference Chen et al. (2023). The modified network is a single-phase equivalent network, as shown in Figure 2, and includes 21 PV inverters. Table 1 lists their positions and capacities. Figure 3 displays the total available PV power and total load demand throughout the day. The energy storage charge and discharge efficiency are set at 90%.

In this verification case, the upper and lower limits of voltage optimization are set to $V^{\min} = 0.95$ p.u. and $V^{\max} = 1.05$ p.u., respectively. The power factor is set to 0.9. The optimization decision interval is set to 5 min. The remaining parameters are shown in Table 2. Aiming at the difficulty and complexity of solving the distributed robust optimization problem, the cvx convex optimization toolbox is called in MATLAB for calculation.

4.2 Simulation results

Table 3 now includes a comprehensive comparison of energy storage planning results using the DRO-based MPC method proposed in this paper, along with the RO and SO methods for the 29th and 35th nodes. The table provides specific numerical values for the energy storage configurations obtained through each method. Table 4 presents a detailed comparison of operating costs under various strategic planning methods. The table now includes exact figures for the maximum, mean, and standard deviation of total operating costs for each method.

The quantified results, as shown in Table 3, indicate that the use of the DRO method leads to a 29.16% reduction in cost compared to the RO method, with energy storage capacities reduced by 33.33% and 20% on the 29- and 35-node systems, respectively. Furthermore, Table 4 reveals that the DRO method achieves maximum, mean, and standard deviation values of total operating costs that are 12.5%, 0.75%, and 51.3% lower than those obtained using the RO method, respectively.

These improvements are attributed to the DRO method's ability to utilize real data, offering more flexible and reliable planning support. This approach avoids the excessive conservatism and economic sacrifices associated with the RO method, which adopts a worst-case distribution strategy, and the SO method, which, despite using a preset probability distribution for energy storage capacity configuration, lacks adaptability in actual scheduling.

The SO, RO, and DRO methods are used for optimization under the same planning scheme. Figure 4 shows the system operation cost

TABLE 1 Location and capacity of PV and energy storage.

Node	PV(kW)/ES(kWh)	Node	PV(kW)/ES(kWh)	Node	PV(kW)/ES(kWh)
4	150/-	17	360/-	30	360/-
7	300/-	20	450/-	31	500/-
9	300/100	22	150/-	32	330/250
10	600/100	23	500/-	33	500/-
11	660/-	26	300/-	34	450/-
13	360/-	28	500/50	35	450/-
16	600/-	29	300/-	36	450/200

10.3389/fenrg.2024.1478040

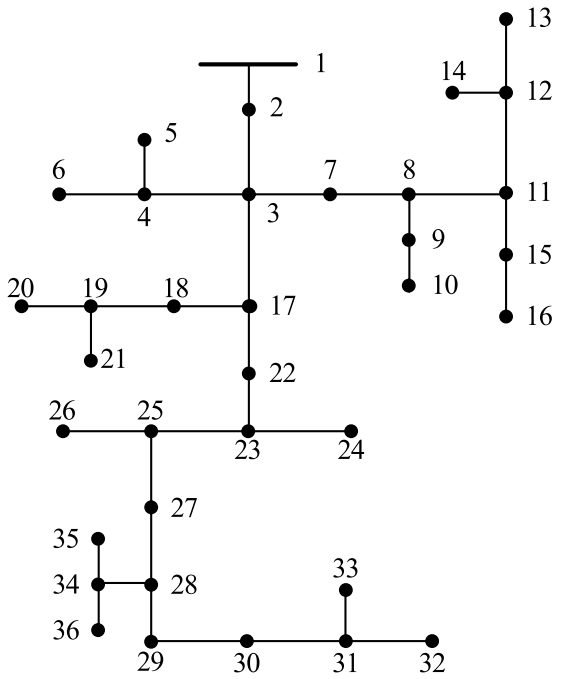

FIGURE 3
Improved IEEE 37-node test system.

from 10:00 to 15:00 for each method. Table 3 presents the maximum, minimum, average, and standard deviation of the system operation costs under these different methods. The results indicate that the proposed method outperforms the traditional RO method in terms of operation cost and demonstrates better economic efficiency. Although the proposed method is less economical than the SO method, it has a smaller skewness, leading to smoother system operation under uncertainty.

Figure 5 shows the operating voltages under the three planning strategies. It is evident that under the SO method, high uncertainty impacts lead to voltage limit violations due to excessive emphasis on economic factors, significantly reducing system robustness. The proposed method considers worst-case planning results by solving the distribution cluster containing the empirical distribution, aligning better with the modeling of uncertain outputs from different renewable energy sources, and thus offers stronger robustness than traditional stochastic optimization.

In summary, the DRO-based MPC method proposed in this paper effectively balances the relationship between economic efficiency and robustness. The proposed planning comprehensively addresses the probability of prediction errors. The average reduction in PV power achieved with this strategy is 645.510 kW, providing an effective control approach for managing significant deviations in PV predictions. Although ensuring voltage security and stability, the proposed strategy increases the average power reduction by 36.851%, thereby enhancing the distribution network's robustness in handling the uncertainties associated with renewable energy predictions.

Table 5 presents a comparative analysis of system costs and PV consumption rates under two scenarios for the IEEE 37-node system. "Case 1" includes energy storage configuration, while "Case 2" does not. The data clearly show that including energy

TABLE 2 System parameters

Parameter	Value	Parameter	Value	Parameter	Value
$a^t_{1,n}$	0.6 CNY/kW	$a^t_{4,n}$	0.6 CNY/kW	a_B	0.04 CNY/kW
$a^t_{2,n}$	0.6 CNY/kW	$a^t_{5,n}$	0.2 CNY/kW	β	0.01
$a^t_{3,n}$	0.4 CNY/kW	a_{av}	0.06 CNY/kW		

TABLE 3 Energy storage configuration under different strategic planning schemes.

Method	29-Node	35-Node	Cost/10^4CNY
RO	300 kWh	150 kWh	48
SO	150 kWh	80 kWh	26
DRO	200 kWh	120 kWh	34

TABLE 4 Comparison of operating costs under different strategic planning schemes.

Method	Total operating cost/10^4CNY			
	Minimum value	Maximum value	Mean value	Standard deviation
RO	76.26	110.73	92.08	7.60
SO	72.21	91.35	80.96	4.04
DRO	79.28	96.91	85.16	3.70

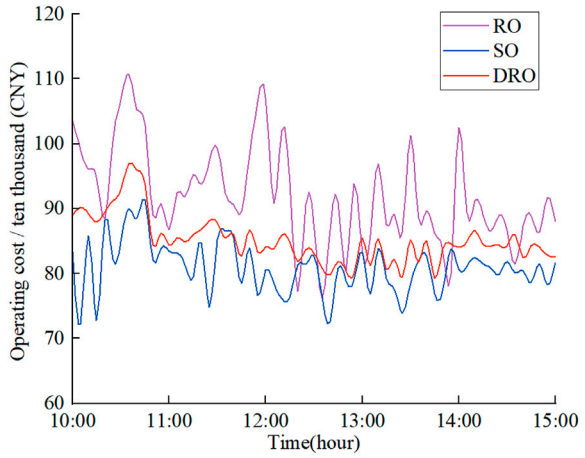

FIGURE 4
Operating costs under different strategic planning.

storage leads to a 2.85% reduction in system cost and a 1.2% increase in the PV in-situ consumption rate.

Figure 6A illustrates the purchased and sold power from the substation for the IEEE 37-node system. Figure 6B depicts the charging and discharging patterns of the energy storage system. These figures demonstrate how excess PV output is stored during periods of low demand and utilized during high demand, effectively performing peak-shaving and load-balancing functions that enhance the economic efficiency and reliability of the distribution network.

4.3 The influence of different Wasserstein spheres

To illustrate the impact of the Wasserstein sphere radius on planning results, various radius values are used to compare the total operational costs. As shown in Table 6, increasing the radius of the Wasserstein sphere results in a broader coverage of uncertainties by the fuzzy set. This broader coverage leads to more conservative decision-making, which in turn raises operating costs but results in a smoother operational mode. Consequently, the proposed method allows for more flexible control of robustness and economic efficiency by adjusting the radius of the Wasserstein sphere.

5 Conclusion

This paper introduces a multi-objective planning approach for DRO power systems utilizing MPC to tackle the uncertainty challenges posed by high levels of renewable energy integration in distribution networks. The proposed method offers a flexible balance between economic efficiency and operational robustness. The key quantitative conclusions drawn from our analysis are:

(1) The DRO-MPC approach significantly mitigates the impact of uncertainty from large-scale distributed PV output on

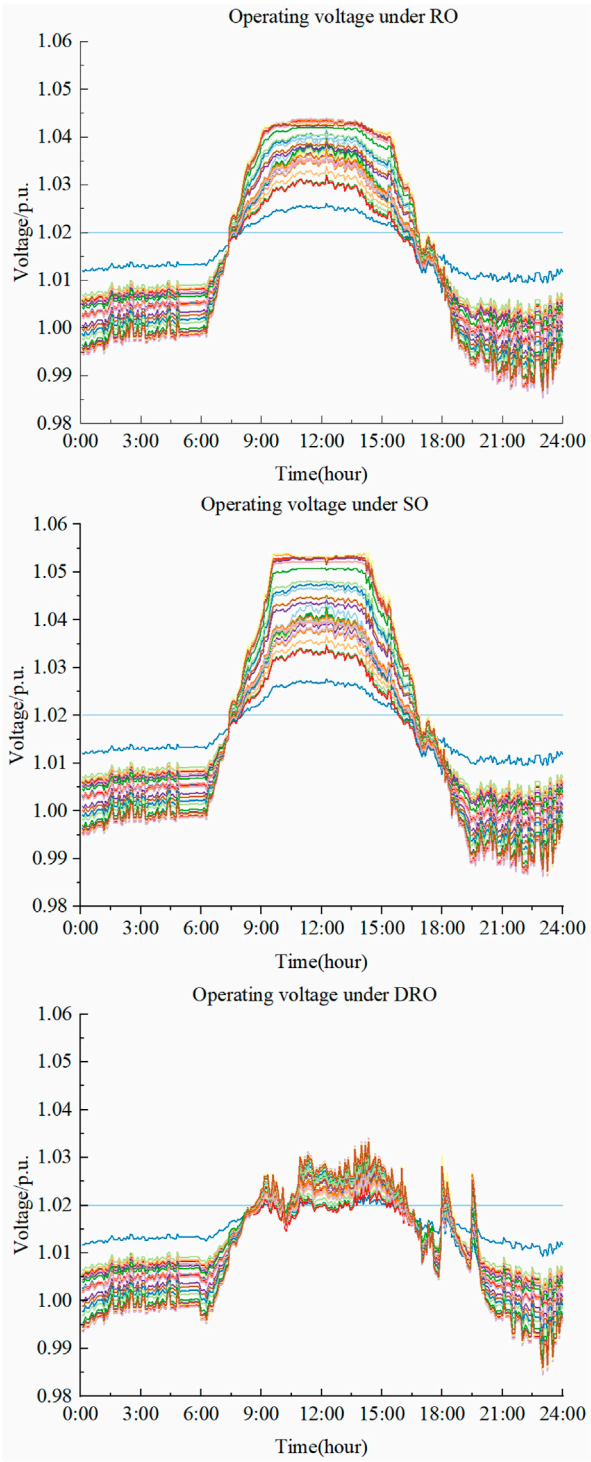

FIGURE 5
Operating voltage under different strategic planning.

TABLE 5 Results of total operating cost and PV consumption rate on the IEEE 37-node system.

	Total operating cost/ 104CNY	Local consumption rate/%
Case 1	34	98.48
Case 2	35	97.31

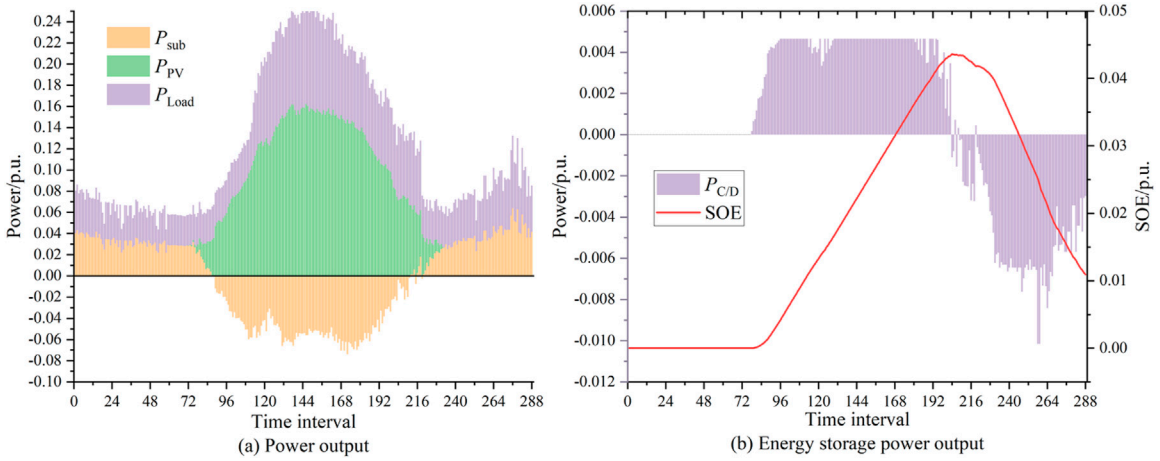

FIGURE 6
Optimal operation results of the IEEE 37-inode system.

TABLE 6 Impact of different Wasserstein sphere radii on planning results.

γ	Total operating cost/10^4CNY			
	Minimum value	Maximum value	Mean value	Standard deviation
0	78.76	96.63	84.84	3.76
0.001	79.28	96.91	85.16	3.70
0.002	79.68	97.58	85.92	3.57

distribution network planning. It enhances economic efficiency and maintains system robustness, reducing costs by 29.16% compared to the RO method. Additionally, the energy storage capacity is optimized, resulting in a 33.33% reduction on the 29-node system and a 20% reduction on the 35-node system.

(2) By transforming the computationally intensive multi-objective problem into a streamlined single-objective solution, our method overcomes the limitations inherent in traditional multi-objective optimization approaches.

(3) The planning scheme's adaptability is further enhanced by the variable radius of the Wasserstein sphere, allowing for greater flexibility and tailored responses to different operational scenarios.

Data availability statement

The original contributions presented in the study are included in the article/supplementary material; further inquiries can be directed to the corresponding author.

Author contributions

YL: conceptualization, funding acquisition, and writing–original draft. KL: investigation, methodology, and writing–original draft. RF: investigation, methodology, and writing–original draft. JC: conceptualization, supervision, and writing–review and editing. YZ: supervision and writing–review and editing.

Funding

The author(s) declare that financial support was received for the research, authorship, and/or publication of this article.

Conflict of interest

Authors YL and KL, were employed by State Grid Shandong Electric Power Research Institute and State Grid Shandong Electric Power Company.

The remaining authors declare that the research was conducted in the absence of any commercial or financial relationships that could be construed as a potential conflict of interest.

The authors declare that this study received funding from the State Grid Shandong Electric Power Company Technology Project on Renewable Energy Dominated Regional Power Grid Islanding Mechanism and High Reliability Control and Protection Technology (No. 52062623S034). The funder had the following involvement in the study: design, collection, analysis, interpretation of data, and the writing of this article.

Publisher's note

References

Alizadeh, M. I., and Capitanescu, F. (2022). A tractable linearization-based approximated solution methodology to stochastic multi-period AC security-constrained optimal power flow. *IEEE Trans. Power Syst.* 38 (6), 5896–5908. doi:10.1109/tpwrs.2022.3220283

Ba-swaimi, S., Verayiah, R., Ramachandaramurthy, V. K., and Alahmad, A. K. (2024). Long-term optimal planning of distributed generations and battery energy storage systems towards high integration of green energy considering uncertainty and demand response program. *J. Energy Storage* 100, 113562. doi:10.1016/j.est.2024.113562

Castro, F., Canizes, B., Soares, J., Almeida, J., and Vale, Z. (2024). Comprehensive framework for distribution network multi-investment expansion planning: emissions, uncertainty, and resource remuneration integration. *Energy Convers. Manag.* 316, 118734. doi:10.1016/j.enconman.2024.118734

Chen, H., Gao, P., Liu, K., Chen, L., and Huang, W. (2024). Joint expansion planning for data centers and distribution networks based on conditional value-at-risk theory considering low carbon characteristics. *Electr. Power Syst. Res.* 229, 110162. doi:10.1016/j.epsr.2024.110162

Chen, J., Zheng, J., Wu, P., Zhang, L., and Wu, Q. (2017). Dynamic particle swarm optimizer with escaping prey for solving constrained non-convex and piecewise optimization problems. *Expert Syst. Appl.* 86, 208–223. doi:10.1016/j.eswa.2017.05.047

Chen, Y., Jacob, R. A., Gel, Y. R., Zhang, J., and Poor, H. V. (2023). Learning power grid outages with higher-order topological neural networks. *IEEE Trans. Power Syst.* 39 (1), 720–732. doi:10.1109/tpwrs.2023.3266956

de Lima, T. D., Lezama, F., Soares, J., Franco, J. F., and Vale, Z. (2024). Modern distribution system expansion planning considering new market designs: review and future directions. *Renew. Sustain. Energy Rev.* 202, 114709. doi:10.1016/j.rser.2024.114709

Dong, G., Zhu, Z., Lou, Y., Yu, J., Wu, L., and Wei, J. (2024). Optimal charging of lithium-ion battery using distributionally robust model predictive control with Wasserstein metric. *IEEE Trans. Industrial Inf.* 20 (5), 7630–7640. doi:10.1109/tii.2024.3363079

Esfahani, M., Alizadeh, A., Amjady, N., and Kamwa, I. (2024). A distributed VPP-integrated co-optimization framework for energy scheduling, frequency regulation, and voltage support using data-driven distributionally robust optimization with Wasserstein metric. *Appl. Energy* 361, 122883. doi:10.1016/j.apenergy.2024.122883

Fan, W., Tan, Z., Li, F., Zhang, A., Ju, L., Wang, Y., et al. (2023). A two-stage optimal scheduling model of integrated energy system based on CVaR theory implementing integrated demand response. *Energy* 263, 125783. doi:10.1016/j.energy.2022.125783

Jiao, P. H., Chen, J. J., Cai, X., Wang, L., Zhao, Y., Zhang, X., et al. (2021). Joint active and reactive for allocation of renewable energy and energy storage under uncertain coupling. *Appl. Energy* 302, 117582. doi:10.1016/j.apenergy.2021.117582

Li, J. Y., Chen, J. J., Wang, Y. X., and Chen, W. (2024b). Combining multi-step reconfiguration with many-objective reduction as iterative bi-level scheduling for stochastic distribution network. *Energy* 290, 130198. doi:10.1016/j.energy.2023.130198

Li, Z., Pu, H., and Li, T. (2024a). Knowledge mapping and evolutionary analysis of energy storage resource management under renewable energy uncertainty: a bibliometric analysis. *Front. Energy Res.* 12, 1394318. doi:10.3389/fenrg.2024.1394318

Lin, Z., Wu, Q., Chen, H., Ji, T., Xu, Y., and Sun, H. (2023). Scenarios-oriented distributionally robust optimization for energy and reserve scheduling. *Ieee Trans. Power Syst.* 38 (3), 2943–2946. doi:10.1109/tpwrs.2023.3244018

Liu, J., Chen, J., Yan, G., Chen, W., and Xu, B. (2023). Clustering and dynamic recognition based auto-reservoir neural network: a wait-and-see approach for short-term park power load forecasting. *Iscience* 26 (8), 107456. doi:10.1016/j.isci.2023.107456

Lu, X., and Zhou, K. (2024). A distributionally robust optimization approach for optimal load dispatch of energy hub considering multiple energy storage units and demand response programs. *J. Energy Storage* 78, 110085. doi:10.1016/j.est.2023.110085

Ma, S., Liu, L., and Cheng, H. (2024). Power generation–network–load–energy storage co-planning under uncertainty. *Front. Energy Res.* 12, 1355047. doi:10.3389/fenrg.2024.1355047

Pan, Y., Zhu, M., Lv, Y., Yang, Y., Liang, Y., Yin, R., et al. (2023). Building energy simulation and its application for building performance optimization: a review of methods, tools, and case studies. *Adv. Appl. Energy* 10, 100135. doi:10.1016/j.adapen.2023.100135

Ren, C., Wei, Z., Zhou, Y., Chen, S., Han, H., Sun, G., et al. (2024). Distributionally robust CVaR optimization for resilient distribution system planning with consideration for long-term and short-term uncertainties. *Reliab. Eng. & Syst. Saf.* 251, 110378. doi:10.1016/j.ress.2024.110378

Skalyga, M., Amelin, M., Wu, Q., and Söder, L. (2023). Distributionally robust day-ahead combined heat and power plants scheduling with Wasserstein Metric. *Energy* 269, 126793. doi:10.1016/j.energy.2023.126793

Subbaramaiah, K., and Sujatha, P. (2023). Optimal DG unit placement in distribution networks by multi-objective whale optimization algorithm & its techno-economic analysis. *Electr. Power Syst. Res.* 214, 108869. doi:10.1016/j.epsr.2022.108869

Wang, C., Liu, C., Chen, J., and Zhang, G. (2024a). Cooperative planning of renewable energy generation and multi-timescale flexible resources in active distribution networks. *Appl. Energy* 356, 122429. doi:10.1016/j.apenergy.2023.122429

Wang, D., Zhang, C., Li, J., Zhu, L., Zhou, B., Zhou, Q., et al. (2024b). A novel interval power flow method based on hybrid box-ellipsoid uncertain sets. *IEEE Trans. Power Syst.* 39 (4), 6111–6114. doi:10.1109/tpwrs.2024.3391921

Wang, H., Shen, X., and Liu, J. (2022). Planning of new distribution network considering green power certificate trading and carbon emissions trading. *Energies* 15 (7), 2435. doi:10.3390/en15072435

Wang, Y. X., Chen, J. J., Zhao, Y. L., and Xu, B. (2024c). Incorporate robust optimization and demand defense for optimal planning of shared rental energy storage in multi-user industrial park. *Energy* 301, 131721. doi:10.1016/j.energy.2024.131721

Zhang, C., Liu, Q., Zhou, B., Chung, C. Y., Li, J., Zhu, L., et al. (2022). A central limit theorem-based method for DC and AC power flow analysis under interval uncertainty of renewable power generation. *IEEE Trans. Sustain. Energy* 14 (1), 563–575. doi:10.1109/tste.2022.3220567

Zhang, H., Wang, J., Zhao, X., and Yang, J. (2023b). Risk-assessment of carbon-dioxide recycling in a gas-fired power plant using CVaR-based convex optimization. *J. Clean. Prod.* 416, 137898. doi:10.1016/j.jclepro.2023.137898

Zhang, Q., Guo, Y., Wang, Z., and Bu, F. (2021). Distributed optimal conservation voltage reduction in integrated primary-secondary distribution systems. *IEEE Trans. Smart Grid* 12 (5), 3889–3900. doi:10.1109/tsg.2021.3088010

Zhang, Q., Yan, J., Gao, H. O., and You, F. (2023a). A systematic review on power systems planning and operations management with grid integration of transportation electrification at scale. *Adv. Appl. Energy* 11, 100147. doi:10.1016/j.adapen.2023.100147

Zhang, Y. Q., Chen, J. J., Wang, Y. X., and Feng, L. (2024). Enhancing resilience of agricultural microgrid through electricity–heat–water based multi-energy hub considering irradiation intensity uncertainty. *Renew. Energy* 220, 119739. doi:10.1016/j.renene.2023.119739

Zheng, F., Meng, X., Xu, T., Sun, Y., and Wang, H. (2023). Optimization method of energy storage configuration for distribution network with high proportion of photovoltaic based on source–load imbalance. *Sustainability* 15 (13), 10628. doi:10.3390/su151310628

frontiers | Frontiers in Energy Research

TYPE Original Research
PUBLISHED 04 December 2024
DOI 10.3389/fenrg.2024.1505582

OPEN ACCESS

EDITED BY
Cong Zhang,
Hunan University, China

REVIEWED BY
ShunLin Zheng,
North China Electric Power University, China
Yuchen Fang,
Dalian University of Technology, China
Mengfan Zhang,
Royal Institute of Technology, Sweden

*CORRESPONDENCE
Guodong Guo,
1622063776@qq.com

RECEIVED 03 October 2024
ACCEPTED 06 November 2024
PUBLISHED 04 December 2024

CITATION
Xue Y, Zhang K, Wang Z, Guo G, Liu D, Shi R and Huang S (2024) Planning of distributed energy storage with the coordination of transmission and distribution systems considering extreme weather.
Front. Energy Res. 12:1505582.
doi: 10.3389/fenrg.2024.1505582

Planning of distributed energy storage with the coordination of transmission and distribution systems considering extreme weather

Yawei Xue[1], Ke Zhang[2], Zhidong Wang[1], Guodong Guo[1]*, Dong Liu[1], Rui Shi[2] and Shengjin Huang[3]

[1]State Grid Economic and Technological Research Institute Co., Ltd., Beijing, China, [2]State Grid Corporation of China, Beijing, China, [3]School of Electrical Engineering, Xi'an Jiaotong University, Xi'an, Shaanxi, China

As the penetration level of renewable energy is continuously growing, it is essential for transmission and distribution system operators to collaborate on optimizing the siting and sizing of distributed energy storage to enhance the operational flexibility and economic efficiency. Given the frequent occurrence of extreme weather in recent years, the planning should also account for such factors. Hence, a planning method of distributed energy storage with the coordination of transmission and distribution systems considering extreme weather is proposed. Firstly, a Gaussian mixture model-based chance constraint is established to describe the uncertainty of wind and solar power, ensuring high confidence that the bus voltage of the distribution system is within a safe range. Secondly, aiming to maximize the social welfare, a bi-level planning model for distributed energy storage is developed. The upper-level addresses the siting and sizing issues of distributed energy storage, while the lower-level characterizes the day-ahead clearing problem of power market. By leveraging Karush-Kuhn-Tucker (KKT) conditions and linearization techniques, the bi-level model is transformed into a single-level mixed integer linear programming model that is easier to solve. Finally, numerical analysis is conducted on a modified IEEE 24-node system combined with two IEEE 33-node systems. The case study verifies the effectiveness of the proposed model.

KEYWORDS

transmission and distribution coordination, bi-level optimization, energy storage sizing and siting, market clearing, uncertainty, extreme weather

1 Introduction

Global climate change and the rapid development of new energy technologies have introduced significant challenges to the safe and stable operation of power grids. Energy storage, as a flexible resource, plays a crucial role in ensuring the stability of power systems. In recent years, the trend toward clean power generation has gained prominence (Li, H. et al., 2021). With the increasing integration of distributed wind and photovoltaic power, the configuration of an appropriate amount of energy

storage on the distribution network side has emerged as a critical issue. To enhance the operational flexibility and economic efficiency of the power system, while also leveraging the benefits of energy storage on the distribution network side, it is essential for the transmission system operator (TSO) and the distribution system operator (DSO) to collaborate closely in optimizing the siting and sizing of distributed energy storage.

The key to promoting renewable energy consumption through energy storage lies in optimizing the location and scale of energy storage systems. Work in (Tang et al., 2022) developed a location and capacity model for energy storage aimed at minimizing bus voltage fluctuations, energy storage investment costs and load fluctuation; Works (Fernández-Blanco et al., 2016; Pandžić et al., 2014) employed lossless DC power flow to approximate the transmission network while disregarding distribution network constraints. However, energy storage resources are typically situated within the distribution system and provide services to both transmission and distribution systems; Work in (Yao et al., 2022) introduced a joint planning method for transmission and storage that takes into account the complementarity of wind and solar energy, thereby enhancing the consumption levels of these renewable sources; Work in (Hua et al., 2020) proposed a control strategy for battery energy storage that considers the feasible domain of wind power acceptance to improve both the transmission and consumption; Work in (Zhao et al., 2022) established an optimization planning model for distributed energy storage in active distribution networks, utilizing an error scenario simulation method to mitigate the impact of photovoltaic output randomness on energy storage configuration planning. Notably, these studies have not established a unified framework for coordinating transmission and distribution to optimize energy storage investment planning.

Numerous studies have addressed the dual-sided uncertainties associated with renewable energy generation and load. Work in (Peker et al., 2018) introduced a two-stage stochastic programming model aimed at jointly optimizing transmission line and energy storage investment; Work in (Li et al., 2024) proposed a bi-level optimization model for the siting and sizing of distributed electrochemical energy storage, utilizing typical day scenarios while accounting for the uncertainties in to renewable energy output; Work in (Qian et al., 2020) considered the impact of wind power and photovoltaic output uncertainties on new energy bases' power transmission, modeling the operational characteristics of these bases, DC channels and receiving power grids separately, and suggested a stochastic planning method for DC transmission of new energy bases based on scenario analysis. Work in (Li et al., 2019) developed a multi-objective optimization cooperative planning model for renewable energy and energy storage, taking into consideration reliability and renewable energy penetration. Work in (Wang et al., 2024) introduced a novel interval power flow (NIPF) method based on a hybrid uncertain set, which effectively addresses input data uncertainties, including active power generation from renewable sources (such as wind and photovoltaic) and load demand. Some studies have insufficient descriptions of the predicted output of renewable energy, which makes it difficult to fully reflect the output range of renewable energy, or are often too conservative in order to cover the output range.

In the context of power grid planning influenced by extreme weather, work in (Li et al., 2023) proposed a multi-level planning method for energy storage power stations within distribution networks, which accounts for the spatiotemporal correlation of compound natural disasters; Work in (Ma et al., 2020) introduced a power grid resilience evaluation index and developed a bi-level planning model for the location and capacity of flexible resources during typhoon disasters, with the objective of optimizing both the index and economic outcomes.; Work in (Yuan et al., 2016) presented a novel flexible distribution system planning model based on two-stage robust optimization aimed at minimizing the total load reduction during natural disasters; Work in (Wang et al., 2023) proposed a new method for the location and capacity planning of energy storage systems based on extreme scenarios. Some studies focus solely on power grid planning under extreme scenarios, neglecting a comprehensive consideration of the impacts of both conventional and extreme scenarios.

Despite the extensive research on the planning and operation models of distributed energy storage in conjunction with renewable energy, several research gaps remain: 1) The investment planning of distributed energy storage is seldom addressed within a unified TSO-DSO framework. 2) The uncertainty associated with the forecast error of renewable energy generation on a typical day is often overlooked. 3) Many of these planning models fail to comprehensively consider the effects of conventional scenarios and extreme weather events. To address these deficiencies, this paper introduces a bi-level planning model for distributed energy storage that incorporates the influence of extreme weather on transmission and distribution coordination. The upper model aims to minimize the investment and operational costs for the DSO, while the lower model seeks to maximize social welfare, thereby modeling the electricity market clearing at the transmission network level. This model effectively leverages distributed energy resources and flexibility at both the distribution and transmission network levels.

The main contributions of this paper are as follows.

1) Unlike traditional methods for configuring energy storage in distribution networks, this study establishes a storage investment planning decision model for distributed renewable energy across multiple distribution networks, incorporating the collaborative participation of DSO and TSO in the market.
2) The planning model fully accounts for the uncertainty associated with renewable energy, modeling the forecast error of daily renewable energy generation using a Gaussian mixture model in conjunction with a chance constraint method.
3) In contrast to conventional planning methods that rely on typical days, this research considers the impact of extreme weather on planning; extreme weather scenarios are extracted based on a robustness framework that incorporates both maximum and minimum model parameters.

The organization of this paper is as follows: Section 2 introduces the bi-level programming model for distributed energy storage under the coordination of transmission and distribution. Section 3 presents a solution to the bi-level optimization problem. Case

studies are discussed in Section 4, followed by conclusions in Section 5.

2 Model structure and problem formulation

2.1 Stochastic bi-level investment model

The proposed bi-level optimization model for distributed energy storage planning is illustrated in Figure 1. The upper level addresses the location and scale of energy storage within the distribution network, aiming to minimize the total investment and operational costs. The lower level focuses on the day-ahead power market clearing problem, which seeks to maximize social welfare, defined as the load benefit minus the generator costs, while adhering to the constraints of the transmission network. Furthermore, the upper-level problem establishes the operational framework for the distribution network and the power transactions with the upstream power grid, with the power transaction decisions serving as input parameters for the lower-level problem. The lower-level problem subsequently provides feedback on market clearing results, including dispatch and pricing, which are utilized in the upper-level problem to compute the expected market income for all users associated with the distribution network.

To account for the effects of extreme weather, particularly the prevalence of typhoons, this study emphasizes scenario robustness. Historical data has been employed to categorize a year into four conventional scenarios and one extreme weather scenario, based on adjustments to the wind and solar output sequences during typhoon conditions. The corresponding outputs for wind and solar energy are specified, with their uncertainties characterized through prediction error and modeled using the chance constraint method. Investment planning is conducted for a single target year following the static investment analysis method (Liu et al., 2017), while operational decisions are optimized for each representative day.

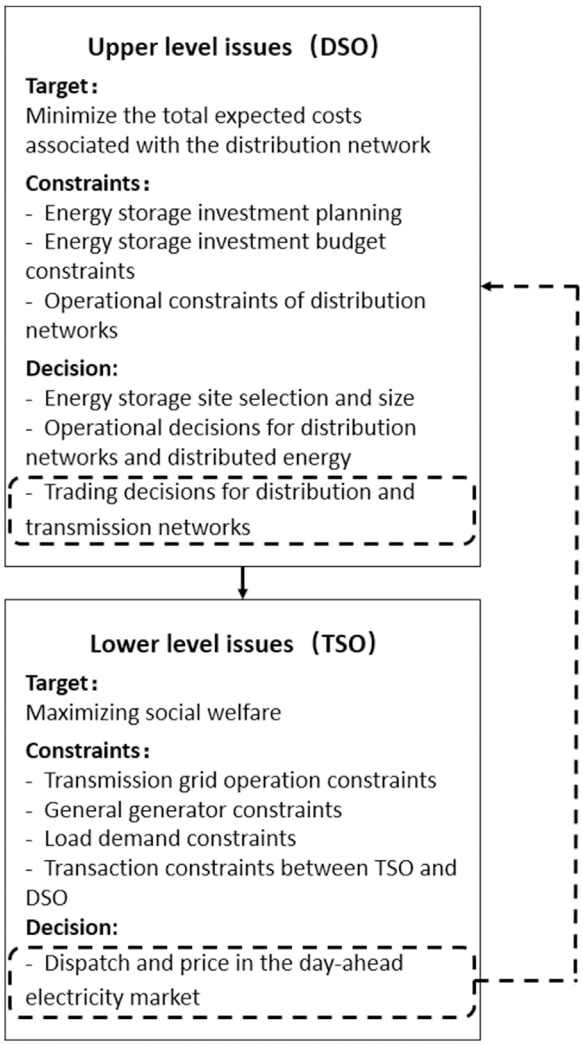

FIGURE 1
A bi-level planning model for distributed energy storage in transmission and distribution coordination.

2.2 Upper-level problem: Siting and sizing of distributed energy storage

The upper problem minimizes the total cost of the distribution network over the course of the year, which includes both the annual energy storage investment cost ($C^{inv,a}$) and the annual distribution network operation cost, as demonstrated in (1). The latter encompasses the electricity cost ($\sum_{\omega\in\Omega} C_{\omega}^{DN}$) associated with the distribution network's transactions with the upstream transmission network and the operating costs ($\sum_{\omega\in\Omega} C_{\omega}^{oper}$) of distributed energy resources (DERs):

$$\min X^{U} \sum_{\omega\in\Omega} \left(C_{\omega}^{DN} + C_{\omega}^{oper}\right) + C^{inv,a} \tag{1}$$

In this context, Equation 2 details the calculation of the distribution network in conjunction with the upstream grid, while Equations 3, 4 outline the operating costs of DERs and the annualized investment cost of energy storage, respectively.

$$C_{\omega}^{DN} = \pi_{\omega} \cdot \sum_{i\in N^{m}} \sum_{t\in H} \left(\lambda_{it\omega} \cdot \left(p_{it\omega}^{+} - p_{it\omega}^{-}\right)\right) \tag{2}$$

$$C_{\omega}^{oper} = \pi_{\omega} \cdot \sum_{i\in N^{m}} \left(\sum_{t\in H} \left(\sum_{i\in B_i^{es}} c^{es} \cdot \left(dis_{int\omega} + ch_{int\omega}\right) + \sum_{i\in B_i^{w}} c^{w} \cdot \tilde{g}_{int\omega}^{w} + \sum_{i\in B_i^{pv}} c^{pv} \cdot \tilde{g}_{int\omega}^{pv} \right) \right) \tag{3}$$

$$C^{inv,a} = \sum_{i\in N^{m}} \left(\sum_{n\in B_i^{es}} \left(C^{e,a} \cdot K_{in}^{e} + C^{p,a} \cdot K_{in}^{p}\right) \right) \tag{4}$$

Where: π_{ω} represents the number of typical days; N^{m} represents the set of transmission network nodes connected to the distribution network; H represents the scheduling time range; B_i^{w} and B_i^{pv} respectively represent the bus set of wind power and photovoltaic power generation devices installed on the distribution network. Due to geographical restrictions, B_i^{es} represents the bus set eligible for installing energy storage devices in the distribution network i ($B_i^{w}, B_i^{pv}, B_i^{es} \subseteq B_i, \forall i \in N_m$); Ω represents a group of typical days; $\lambda_{it\omega}$ represents the node marginal price of the transmission network bus

connected to the root node of the distribution network; $ch_{int\omega}/dis_{int\omega}$ represent the charging/discharging power of energy storage; $\tilde{g}^{w}_{int\omega}$ and $\tilde{g}^{pv}_{int\omega}$ respectively represent the output power of wind power and photovoltaic units; p^{-}_{itw} represents the amount of electricity injected from DSO to TSO, and p^{+}_{itw} *vice versa*; K^{e}_{in} and K^{p}_{in} respectively represent the energy and power capacity of energy storage; c^{w}, c^{pv} and c^{es} respectively represent the operating costs of wind power, photovoltaic and energy storage devices.

Equation 2 represents the electricity transaction cost associated with the distribution network's participation in the day-ahead electricity market. Equation 3 outlines the operating cost of DERs on a typical day ω, while the annualized investment cost of energy storage is detailed in (4). Notably, the parameters $C^{e,a}$ and $C^{p,a}$ are the annualized costs using the net present value method, calculated as follows (Pandžić et al., 2014):

$$C^{a} = C \cdot \frac{\Gamma \cdot (1+\Gamma)^{\Lambda}}{(1+\Gamma)^{\Lambda} - 1} \tag{5}$$

Where: Γ is the annual discount rate; Λ is the equipment life.

Investment decisions (K^{e}_{in}, K^{p}_{in}) are constrained by geography and technology, with certain capacity constraints and available investment budget constraints:

$$0 \le K^{e}_{in} \le \overline{K^{e}_{in}}, \forall i \in N^{m}, n \in B^{es}_{i} \tag{6}$$

$$0 \le K^{p}_{in} \le \overline{K^{p}_{in}}, \forall i \in N^{m}, n \in B^{es}_{i} \tag{7}$$

$$\rho \cdot K^{p}_{in} = K^{e}_{in}, \forall i \in N^{m}, n \in B^{es}_{i} \tag{8}$$

$$C^{inv} \le \overline{C^{inv}} \tag{9}$$

Where: $\overline{K^{e}_{in}}$ and $\overline{K^{p}_{in}}$ represent the energy and power capacity of the maximum energy storage device that can be installed, respectively; ρ represents the energy-to-power ratio of the energy storage device; C^{inv} represents the energy storage investment cost, and $\overline{C^{inv}}$ represents the energy storage investment budget.

Equations 6, 7 delineate the energy and power limitations for the areas (nodes) within the distribution network eligible for energy storage installation, while Equation 8 restricts the energy-to-power ratio of the energy storage device. Equation 9 indicates that the total investment cost must not exceed the allocated investment budget.

In addition, due to the operational characteristics of energy storage, its dispatch operation is subject to specific constraints on a typical day ω.

$$0 \le dis_{int\omega}, ch_{int\omega} \le K^{p}_{in}, \forall i \in N^{m}, n \in B^{es}_{i}, t \in H, \omega \in \Omega \tag{10}$$

$$dis_{int\omega} \le \Phi \cdot w_{int\omega}, \forall i \in N^{m}, n \in B^{es}_{i}, t \in H, \omega \in \Omega \tag{11}$$

$$ch_{int\omega} \le \Phi \cdot (1 - w_{in\omega}), \forall i \in N^{m}, n \in B^{es}_{i}, t \in H, \omega \in \Omega \tag{12}$$

$$w_{int\omega} \in \{0,1\}, \forall i \in N^{m}, n \in B^{es}_{i}, t \in H, \omega \in \Omega \tag{13}$$

$$SOE_{int\omega} = SOE_{in0\omega} - \sum_{\tau=1}^{t} \left(dis_{in\tau\omega}/\eta^{d} - ch_{in\tau\omega} \cdot \eta^{c} \right), \quad \forall i \in N^{m}, n \in B^{es}_{i}, t \in H, \omega \in \Omega \tag{14}$$

$$0 \le SOE_{intw} \le K^{e}_{in}, \forall i \in N^{m}, n \in B^{es}_{i}, t \in H, \omega \in \Omega \tag{15}$$

$$SOE_{inT\omega} \ge \beta \cdot SOE_{in0\omega}, \forall i \in N^{m}, n \in B^{es}_{i}, \omega \in \Omega \tag{16}$$

Where: $SOE_{int\omega}$ represents the energy state of the energy storage device; Φ is a large constant.

Equations 10–13 delineate the charge and discharge state of the energy storage device. The binary variable $w_{int\omega}$ represents the operating state of the energy storage device, taking a value of one during discharge and 0 during charging. Equation 16 indicates that the energy state of the energy storage device at the end of the scheduling period must be no less than β times of its energy at the beginning.

The output from distributed power sources, such as photovoltaics and wind power, is significantly influenced by climatic conditions. This influence is particularly pronounced during extreme weather events, where the output from wind and solar sources can become markedly abnormal and irregular. Consequently, the output from these sources exhibits increased volatility and uncertainty. To capture these effects, this article presents predicted outputs for wind and solar power under both normal and extreme scenarios, derived from historical data. It is important to note that the likelihood of extreme scenarios occurring is considerably lower. The chance constraint method is employed to strike a balance between conservatism and optimism, with the uncertainty in wind and solar power output characterized by the variability of prediction errors. Therefore, the outputs from wind power and photovoltaics should satisfy the following sufficiency conditions:

$$\tilde{g}^{w}_{int\omega} = g^{w}_{int\omega} + \Delta\tilde{g}^{w}_{int\omega}, \forall n \in B^{w}_{i}, \forall i \in N^{m}, t \in H, \omega \in H \tag{17}$$

$$g^{w}_{int\omega} = W_{it\omega} \cdot K^{w}_{in}, \forall n \in B^{w}_{i}, \forall i \in N^{m}, t \in H, \omega \in H \tag{18}$$

$$\Pr\left(\Delta g^{w-}_{int\omega} \le \Delta\tilde{g}^{w}_{int\omega} \le \Delta g^{w+}_{int\omega}\right) \ge \hbar^{w}, \forall n \in B^{w}_{i}, \forall i \in N^{m}, t \in H, \omega \in H \tag{19}$$

$$\tilde{g}^{pv}_{int\omega} = g^{pv}_{int\omega} + \Delta\tilde{g}^{pv}_{int\omega}, \forall n \in B^{pv}_{i}, \forall i \in N^{m}, t \in H, \omega \in H \tag{20}$$

$$g^{pv}_{int\omega} = \eta^{pv} \cdot I_{it\omega} \cdot K^{pv}_{in}, \forall n \in B^{pv}_{i}, \forall i \in N^{m}, t \in H, \omega \in H \tag{21}$$

$$\Pr\left(\Delta g^{pv-}_{int\omega} \le \Delta\tilde{g}^{pv}_{int\omega} \le \Delta g^{pv+}_{int\omega}\right) \ge \hbar^{pv}, \forall n \in B^{pv}_{i}, \forall i \in N^{m}, t \in H, \omega \in H \tag{22}$$

Where: K^{w}_{in} and K^{pv}_{in} are the installed capacity of wind power and photovoltaic power generation respectively.

Equation 17 indicates that the output of wind power $(\tilde{g}^{w}_{int\omega})$ consists of the predicted value $(g^{w}_{int\omega})$ and the predicted error $(\Delta\tilde{g}^{w}_{int\omega})$. Equation 18 determines the size of the predicted wind power output, where $W_{it\omega}$ is the wind intensity coefficient (Baringo and Conejo, 2011). The size of the wind power output prediction error is limited, and its probability in the interval $[\Delta g^{w-}_{int\omega}; \Delta g^{w+}_{int\omega}]$ must be greater than the given confidence level $(\hbar)$, as shown in Equation 19. Equations 20, 21 describe the photovoltaic output, which is similar to wind power, where the predicted value of photovoltaic output is calculated based on the photovoltaic energy output coefficient $(I_{it\omega})$ and the photovoltaic panel output efficiency (η^{pv}) (Xu et al., 2020), and $\hbar^{pv}$ is the confidence level.

The power flow of the distribution network adopts the linearized Distflow model, which is widely used in distribution systems. The complete model is shown in Equations 23–29.

$$\sum_{k\in\Omega_d^i(n)} f^p_{i(nk)t\omega} = \sum_{k\in\Omega_p^i(n)} f^p_{i(jk)t\omega} - D_{int\omega} + \tilde{g}^w_{int\omega} + \tilde{g}^{pv}_{int\omega} + dis_{int\omega} - ch_{int\omega},$$
$$\forall i \in N^m, n \in B_i, t \in H, \omega \in \Omega \tag{23}$$

$$\sum_{k\in\Omega_d^i(n)} f^q_{i(nk)t\omega} = \sum_{k\in\Omega_p^i(n)} f^q_{i(jk)t\omega} - \delta^d_{in}\cdot D_{int\omega} + \delta^w_{in}\cdot \tilde{g}^w_{int\omega} + \delta^{pv}_{in}\cdot \tilde{g}^{pv}_{int\omega},$$
$$\forall i \in N^m, n \in B_i, t \in H, \omega \in \Omega \tag{24}$$

$$\tilde{V}_{int\omega} = \tilde{V}_{ijt\omega} - 2\cdot\left(r_{i(jn)}\cdot f^p_{i(jn)t\omega} + x_{i(jn)}\cdot f^q_{i(jn)t\omega}\right), \forall i \in N^m, n \in B_i, t \in H, \omega \in \Omega \tag{25}$$

$$\sum_{k\in\Omega_d^i(n_0)} f^p_{i(n_0k)t\omega} = p^+_{it\omega} - p^-_{it\omega}, \forall i \in N^m, n \in B_i, t \in H, \omega \in \Omega \tag{26}$$

$$\left(f^p_{i(nk)t\omega}\right)^2 + \left(f^q_{i(nk)t\omega}\right)^2 \le \left(\overline{f^S_{i(nk)}}\right)^2, \forall i \in N^m, (nk) \in L^D_i, t \in H, \omega \in \Omega \tag{27}$$

$$\tilde{V}_{in_0tw} = V_0, \forall i \in N^m, t \in H, \omega \in \Omega \tag{28}$$

$$\Pr\left(V_0 - \Delta\overline{V} \le \tilde{V}_{intw} \le V_0 + \Delta\overline{V}\right) \ge \check{\lambda}, \forall i \in N^m, n \in B_i/n_0, t \in H, \omega \in \Omega \tag{29}$$

Where: $f^p_{i(nk)t\omega}$ and $f^q_{i(nk)t\omega}$ represent the active and reactive power flowing through the branch nk of the distribution network i in a typical day ω, respectively; $\Omega^i_{d/p}(n)$ represents the set of rear/front nodes connected to the distribution network node n; $V_{int\omega}$ represents the square value of the voltage amplitude of the distribution network nodes; $D_{int\omega}$ represents the load of each node in the distribution network; $\delta^{d/w/pv}$ are the parameters for converting active power into reactive power.

The branch power flow equations are presented in (23)–(25). The voltage difference between the buses at both ends of the node branch is related to the active and reactive power flows of the branch, as shown in Equation 25. The active power balance in the transmission line connected to the root node of the distribution network (i.e., the node linked to the transmission network) is n_0 shown in Equation 26. Equation 27 sets the apparent power capacity of the line ($\overline{f^S_{i(nk)}}$), which is a quadratic inequality constraint and can be linearized by polygonal interior approximation (Akbari and Bina, 2014). The bus voltage limit is shown in Equations 28, 29. It should be noted that V_0 is the reference voltage. If the bus is the root bus, the bus voltage is set to the reference voltage, as shown in Equation 28. Otherwise, the bus voltage should be within the given interval specified in Equation 29, and the chance constraint ensures the system voltage safety with a high probability ($\check{\lambda}$).

Equations 30, 31 impose limits on the amount of electricity that the distribution network can trade with the upstream grid, in accordance with the capacity of the substations that connect the transmission grid and the distribution grid. The binary variable $h_{it\omega}$ ensures that the distribution network can either supply power to or draw power from the transmission grid during specific time periods within a typical day ω, as shown in Equation 32.

$$0 \le o_{it\omega} \le h_{it\omega}\cdot\overline{p_i}, \forall i \in N^m, t \in H, \omega \in \Omega \tag{30}$$

$$0 \le b_{it\omega} \le \left(1 - h_{it\omega}\right)\cdot\overline{p_i}, \forall i \in N^m, t \in H, \omega \in \Omega \tag{31}$$

$$h_{it\omega} \in \{0,1\}, \forall i \in N^m, t \in H, \omega \in \Omega \tag{32}$$

Where: $o_{it\omega}/b_{it\omega}$ represents the quantity provided/bid by the distribution network to the power market; $\overline{p_i}$ represents the capacity of the substations connecting the distribution network to the upstream transmission network.

Finally, the decision variable set (X^U) of the upper-level problem includes the investment variables and the distribution network scenario-related operation phase variable set, namely, $X^U = \{K^e_{in}, \tilde{g}^w_{int\omega}, \tilde{g}^{pv}_{int\omega}, o_{it\omega}, b_{it\omega}, dis_{int\omega}, ch_{int\omega}, w_{int\omega}, SOE_{int\omega}, f^p_{i(nk)t\omega}, f^q_{i(nk)t\omega}, V_{int\omega}\}$.

2.3 Lower-level problem: Day-ahead electricity market clearing problem

The underlying problem is the day-ahead electricity market clearing problem at the transmission network level, which is performed on each typical day with the goal of maximizing social welfare, as shown in Equations 33–41.

$$\min X^L_\omega \sum_{t\in H}\left(\sum_{i\in N^g} c^g_{it}\cdot p^g_{it\omega} - \sum_{i\in N^d} c^d_{it}\cdot p^d_{it\omega} + \sum_{i\in N^m}\left(c^-_{it}\cdot p^-_{it\omega} - c^+_{it}\cdot p^+_{it\omega}\right)\right), \forall \omega \in \Omega \tag{33}$$

$$-p^g_{it\omega} + p^d_{it\omega} - p^-_{it\omega} + p^+_{it\omega} + \sum_{j\ne i} y_{ij}\cdot\left(\theta_{it\omega} - \theta_{jt\omega}\right) = 0; \left(\lambda_{it\omega}\right), \forall i \in N^g, t \in H, \omega \in \Omega \tag{34}$$

$$0 \le p^g_{it\omega} \le \overline{p^g_i}; \left(\underline{\phi^g_{it\omega}}, \overline{\phi^g_{it\omega}}\right), \forall i \in N^g, t \in H, \omega \in \Omega \tag{35}$$

$$RD_i \le p^g_{it\omega} - p^g_{i(t-1)\omega} \le RU_i; \left(\phi^{grd}_{it\omega}, \phi^{gru}_{it\omega}\right), \forall i \in N^g, t > 1, \omega \in \Omega \tag{36}$$

$$RD_i \le p^g_{it\omega} - p^g_{i0\omega} \le RU_i; \left(\phi^{grd}_{it\omega}, \phi^{gru}_{it\omega}\right), \forall i \in N^g, t = 1, \omega \in \Omega \tag{37}$$

$$0 \le p^d_{it\omega} \le \overline{p^d_i}; \left(\underline{\phi^d_{it\omega}}, \overline{\phi^d_{it\omega}}\right), \forall i \in N^d, t \in H, \omega \in \Omega \tag{38}$$

$$0 \le p^-_{it\omega} \le o_{it\omega}; \left(\underline{\phi^{p-}_{it\omega}}, \overline{\phi^{p-}_{it\omega}}\right), \forall i \in N^m, t \in H, \omega \in \Omega \tag{39}$$

$$0 \le p^+_{it\omega} \le b_{it\omega}; \left(\underline{\phi^{p+}_{it\omega}}, \overline{\phi^{p+}_{it\omega}}\right), \forall i \in N^m, t \in H, \omega \in \Omega \tag{40}$$

$$-\overline{T_{ij}} \le y_{ij}\cdot\left(\theta_{it\omega} - \theta_{jt\omega}\right) \le \overline{T_{ij}}; \left(\underline{\phi^l_{(ij)t\omega}}, \overline{\phi^l_{(ij)t\omega}}\right), \forall (ij) \in L^T, i < j, t \in H, \omega \in \Omega \tag{41}$$

Where: $X^L_\omega = \left\{p^g_{it\omega}, p^d_{it\omega}, p^-_{it\omega}, p^+_{it\omega}, \theta_{it\omega}\right\}$ is the set of decision variables for the lower-level problem, mainly the scenario-related operation phase variables of the transmission network; N^d and N^g respectively represent the set of transmission network nodes connecting load aggregators and conventional generators; L^T represents the set of branches of the transmission network; $c^{\downarrow}_{it}$ and $c^{\uparrow}_{it}$ are the supply and demand quotations of the distribution network, respectively, c^g_{it} is the quotation of the generator, c^d_{it} is the quotation of the load aggregator; $p^g_{it\omega}$ represents the active output power of the conventional generator; $p^g_{it\omega}$ represents the active power required by the load aggregator.

TSO clears the day-ahead electricity market for each typical day by minimizing social costs, as shown in Equation 33. The power flow of the transmission network adopts the DC power flow model. Equation 34 represents the power balance of the distribution network node. Equation 35 imposes a limit on the maximum output active power of conventional generators, while Equation 38 restricts the maximum active power required by the load aggregator. Equations 36, 37 detail the ramping capabilities of conventional generators. The power trading volume between the transmission and distribution networks is constrained to a specific range, as indicated in Equations 39, 40. Equation 41 establishes a limit on the active power flow within the transmission line. Additionally, the dual variables associated with each constraint are presented after the semicolon, with the voltage phase angle of the reference bus set to zero.

In summary, the upper model transfers the power trading decision between the transmission and distribution networks to the lower model, which in turn provides feedback on the node prices for each time period of the day. Based on these node prices at the boundary of the transmission and distribution networks, energy storage systems optimize their charging and discharging strategies by purchasing electricity (charging) during low-price periods and selling electricity (discharging) during high-price periods. This approach enhances economic benefits and regulates the system, ultimately leading to a reduction in the operational costs of the distribution network.

2.4 Typical day scene generation of wind and solar output

2.4.1 Conventional typical day scene generation

The selection of scenarios in this paper is based on actual annual intra-day output data for wind and solar power, resulting in a total of 365 scenarios. The large number of scenarios can significantly increase computational load, leading to lower solution efficiency and reduced flexibility. Therefore, it is essential to reduce the original scenarios to obtain typical output scenario data for wind and solar, ensuring both the diversity of scenarios and the efficiency of model solving. This study employs the K-means clustering algorithm to achieve this reduction and obtain typical output scenarios for wind and solar.

The scenario reduction process based on the K-means clustering algorithm is as follows.

1) Select K initial cluster centers from all samples;
2) Assign data points: Calculate the distances from the remaining data points to each cluster center and assign each data point to the cluster center with the closest distance;
3) Update the cluster center: Recalculate the cluster center point based on the assigned data points, establishing it as the new center of the cluster;
4) Iteration: Repeat the above steps until the cluster center no longer changes.

2.4.2 Generation of typical daily scenarios for extreme weather considering robustness

Conventional scenarios may not adequately capture the impact of extreme weather on wind and solar output. Given the significant influence of typhoons on renewable energy generation and to reduce model complexity, it is necessary to establish a separate typical day scenario for typhoon extreme weather. Additionally, a single wind field model (Batts model) is used, without considering the coupling effects of typhoons with associated disasters, such as the coupling of typhoons with rainstorm events (Zhang et al., 2024).

Batts model is a relatively mature wind field model. This paper uses the Batts model to estimate the real-time maximum wind speed in the typhoon-affected area. The parameters of the initial pressure difference, typhoon moving speed and typhoon moving direction probability distribution in the model are estimated empirically in the literature (Liu et al., 2020). The typhoon center pressure difference and typhoon moving speed should obey the log-normal probability distribution, and the typhoon moving direction should obey the binormal distribution, as shown in Equations 42–44.

$$f(\Delta H) = \frac{1}{\Delta H \sigma_1 \sqrt{2\pi}} \exp\left(-\frac{(\ln \Delta H - \mu_1)^2}{2\sigma_1^2}\right) \tag{42}$$

$$f(v_T) = \frac{1}{v_T \sigma_2 \sqrt{2\pi}} \exp\left(-\frac{(\ln v_T - \mu_2)^2}{2\sigma_2^2}\right) \tag{43}$$

$$f(\theta) = \frac{\alpha}{\sigma_3 \sqrt{2\pi}} \exp\left[-\frac{(\theta - \mu_3)^2}{2\sigma_3^2}\right] + \frac{1-\alpha}{\sigma_4 \sqrt{2\pi}} \exp\left[-\frac{(\theta - \mu_4)^2}{2\sigma_4^2}\right] \tag{44}$$

Where: ΔH is the initial pressure difference between the typhoon center and the periphery; v_T is the typhoon translation speed; θ is the typhoon translation direction angle; in this paper, set $\mu_1 = 2.9001$, $\sigma_1 = 0.627$, $\mu_2 = 2.6680$, $\sigma_2 = 0.5185$, $\mu_3 = 73.3392$; $\mu_4 = 7.2084$, $\sigma_3 = 22.5891$, $\sigma_4 = 70.3532$, and $\alpha = 0.503$.

The wind and solar output rules under typhoon weather are set as follows: when a typhoon occurs, the photovoltaic output level at each moment is randomly reduced to half or less than that in normal weather. The specific proportional coefficient (R_t^T) is obtained by sampling according to the uniform distribution, as shown in Equations 45, 46; the wind power output level at each moment is related to the real-time maximum wind speed in the area affected by the typhoon. When the maximum wind speed exceeds the set wind turbine cut-out wind speed, the wind power output is reduced to 0, as shown in Equation 47. If it does not exceed the cut-out wind speed, it will not be affected.

$$R_t^T \sim U(0, 0.5) \tag{45}$$

$$\tilde{P}_t^{pv,T} = P_t^{pv} \times R_t^T \tag{46}$$

$$\tilde{P}_t^{w,T} = 0 \tag{47}$$

The calculation formula for the real-time maximum wind speed is shown in Equation 48. The derivation process can be found in (Liu et al., 2020) and will not be repeated here. After sampling the initial pressure difference ΔH, typhoon translation speed v_T and

typhoon movement direction from Equations 42–44, the maximum wind speed at each moment can be calculated by substituting the coastline angle of the typhoon-affected area φ into (48).

$$v_{r_{\max}}(t) = 6.029\sqrt{0.75\Delta H - 0.508\left[1+\sin\left(\varphi-\theta\right)t\right]} + 0.5v_T \quad (48)$$

The wind and solar power output sequence correction method under typhoon weather described in Equations 45–47, the actual annual wind and solar power output data is corrected, and 365 possible wind and solar power output sequence data under typhoon weather can be obtained. In order to reflect the robustness of extreme scenarios, this paper takes the amount of electricity purchased by the distribution network to the transmission network as an indicator to find the worst scenario as a typical daily scenario of typhoon extreme weather.

The extreme scenario set is formed by a series of wind and solar output scenarios corrected by the wind and solar output sequence under typhoon weather, which is recorded as E. Auxiliary variables are introduced ξ to represent the power purchased by the distribution network under the worst scenario, and the auxiliary problem is solved to obtain the worst scenario of wind and solar output under typhoon weather, which is as follows:

$$\min \xi_\omega = \sum_{i\in N^m}\sum_{t\in H}\left(b_{it\omega} - o_{it\omega}\right), \forall\omega \in E \quad (49)$$

$$\xi = \max \xi_\omega, \forall\omega \in E \quad (50)$$

Where: ξ_ω is the auxiliary variable introduced for the auxiliary problem, which represents the minimum power purchase required for the normal operation of the distribution network based on the existing wind and solar installed capacity under the extreme scenario ω.

The auxiliary problem is framed as a bi-level optimization problem in the form of max-min. The constraints governing this problem are the real-time operational constraints of the distribution network, specifically outlined in Equations 17–32, with Equation 23 requiring substitution with the following

$$\sum_{k\in\Omega_d^i(n)} f^p_{i(nk)t\omega} = \sum_{k\in\Omega_p^i(n)} f^p_{i(jk)t\omega} - D_{int\omega} + \tilde{g}^w_{int\omega} + \tilde{g}^{pv}_{int\omega} \quad (51)$$

In addition, it should be noted that the auxiliary problem constraints are a set of extreme scenarios $\omega \in E$.

To summarize, the steps to ascertain the worst-case scenario for wind and solar power output during typhoon weather are as follows.

1) The actual annual data is processed using the wind and solar power output sequence correction method tailored for typhoon weather, resulting in an initial set of extreme scenarios for wind and solar power output.
2) By substituting this set of extreme scenarios into the auxiliary problem, we can derive the auxiliary variable corresponding to these extreme scenarios and subsequently identify the worst scenario associated with the auxiliary variable.

2.5 Overall model structure

In summary, the proposed complete model is as follows:

$$\min_{X^U\cup X^L} \sum_{\omega\in\Omega}\left(C^{DN}_\omega + C^{oper}_\omega\right) + C^{inv,a} \quad (52a)$$

$$s.t.(6)-(41) \quad (52b)$$

Where: $X^U = \{K^e_{in}, \tilde{g}^w_{int\omega}, \tilde{g}^{pv}_{int\omega}, o_{it\omega}, b_{it\omega}, dis_{int\omega}, ch_{int\omega}, w_{int\omega}, SOE_{int\omega}, f^p_{i(nk)t\omega}, f^q_{i(nk)t\omega}, V_{int\omega}\}$ represents the set of decision variables of the upper optimization model, including investment variables and distribution network scenario-related operation phase variables; $X^L = \{p^g_{it\omega}, p^d_{it\omega}, p^-_{it\omega}, p^+_{it\omega}, \theta_{it\omega}, \forall\omega\}$ represents the decision variables of the lower optimization model, which are the scenario-related operation phase variables of the transmission network.

The upper optimization goal is to minimize the total investment and operation cost of the distribution network, and the participating entity is the distribution network; the lower optimization goal is to maximize social welfare, and the participating entities are power generators, load aggregators and distribution networks. The power transactions and capital transactions between the upper and lower participating entities are shown in Figure 2:

Obviously, the proposed model represents a bi-level optimization problem that cannot be solved directly. Additionally, the chance constraint poses significant challenges. Consequently, the subsequent section will demonstrate how to convert the chance constraint and the objective function into a tractable mixed-integer linear programming (MILP) formulation. This transformation will allow the bi-level optimization problem to be reformulated as a single-level optimization problem, effectively handling its nonlinear terms and yielding a directly solvable MILP problem.

3 Solutions

The original problem cannot be addressed directly. This section will outline the methodology for transforming the bi-level optimization problem into a MILP problem. First, a Gaussian mixture model will be employed to express the opportunity constraints associated with renewable energy as deterministic constraints. Second, voltage will be articulated as a function of random power injection, with the inherent uncertainty in voltage being characterized by the output of renewable energy. This approach will convert the voltage-related opportunity constraints into deterministic constraints. Finally, the KKT optimality condition will be utilized to reformulate the bi-level optimization problem into a single-level problem. Subsequently, the complementary relaxation conditions and the remaining bilinear terms will be linearized into linear terms using the Big M method and duality relations, ultimately resulting in the transformation of the model into a single-layer MILP framework.

3.1 Chance-constrained deterministic representation

3.1.1 Opportunity-constrained conversion of renewable energy output based on GMM

3.1.1.1 Forecasted output distribution of renewable energy

As mentioned above, the uncertainty of wind and solar power output can be characterized by the uncertainty of prediction error. Affected by the central limit theorem, the prediction

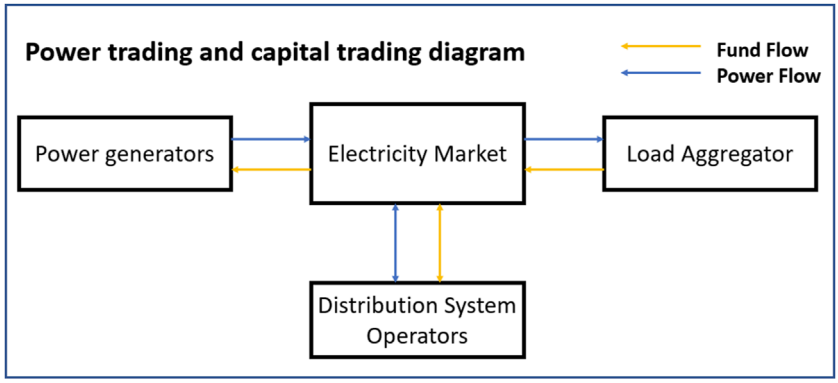

FIGURE 2
Electricity trading and capital trading chart.

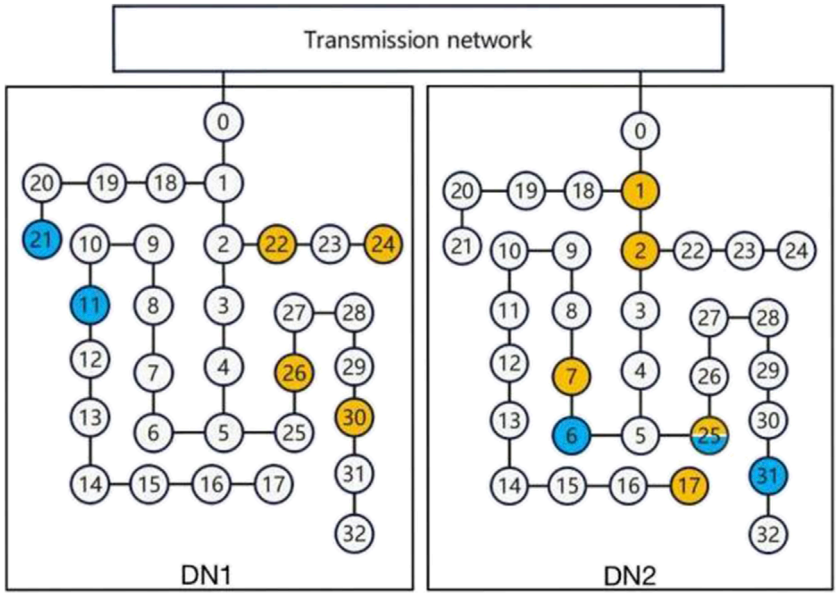

FIGURE 3
Schematic diagram of the dual IEEE 33-node power distribution test system (yellow indicates photovoltaic resources and blue indicates wind power resources).

TABLE 1 Nodes suitable for energy storage installation.

	Suitable distribution network nodes					
Distribution network 1	5	8	16	21	22	28
Distribution network 2	1	2	8	15	25	30

error is described by Gauss Mixed Model (GMM). The random vector $\boldsymbol{X} = [X_{1,t}, X_{2,t}, \cdots, X_{k,t}]^{\mathrm{T}}$ is used to represent the output power prediction error of k renewable energy sources at time t. Then the probability density function (PDF) of $\boldsymbol{X}$ can be expressed by GMM (Wang et al., 2016):

$$f_X(\boldsymbol{x}) = \sum_{m=1}^{M} \pi_m N_m(\boldsymbol{x}|\boldsymbol{\mu_m}, \boldsymbol{\sigma_m}) \tag{53}$$

$$\sum_{m=1}^{M} \pi_m = 1, \pi_m > 0 \tag{54}$$

$$N_m(\boldsymbol{x}|\boldsymbol{\mu_m}, \boldsymbol{\sigma_m}) = \frac{\exp\left\{-1/2(\boldsymbol{x}-\boldsymbol{\mu_m})^{\mathrm{T}}\boldsymbol{\sigma}_m^{-1}(\boldsymbol{x}-\boldsymbol{\mu_m})\right\}}{(2\pi)^{K/2}|\boldsymbol{\sigma}_m|^{1/2}} \tag{55}$$

Where: $\sum = \{\pi_m, \boldsymbol{\mu}_m, \boldsymbol{\sigma}_m | m = 1, 2, \ldots, M\}$ represents the parameter set of the Gaussian mixture model, where the Gaussian

TABLE 2 Distribution overview of renewable energy (MW).

		Distribution network 1					Distribution network 2				
Wind power	node	11	16	18	19	21	6	25	27	29	31
	capacity	10.5	0	0	0	10	20	20	0	0	4
Photovoltaic power	node	16	22	24	26	30	1	2	7	17	25
	capacity	0	2	8	20	8	10	10	4	10	4

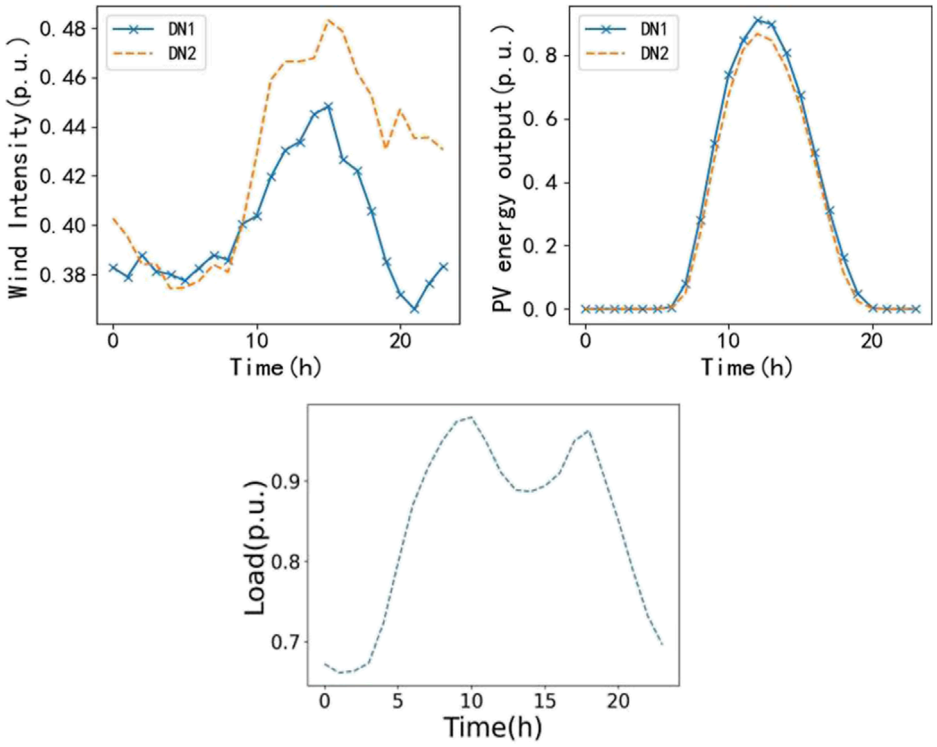

FIGURE 4
Weighted average of load, predicted wind power and PV intensity under conventional scenarios.

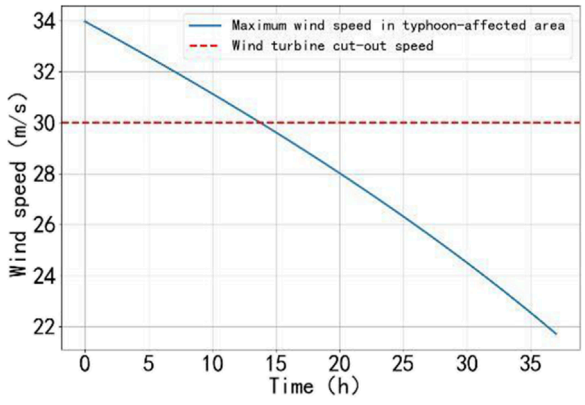

FIGURE 5
Changes of maximum wind speed in typhoon-affected areas.

mixture model is composed of Gaussian components; π_m represents the weight of each Gaussian distribution; $N_m(\boldsymbol{x}|\boldsymbol{\mu}_m, \boldsymbol{\sigma}_m)$ represents the *mth* multivariate Gaussian component, whose mean vector is $\boldsymbol{\mu}_m$ and the covariance matrix is $\boldsymbol{\sigma}_m$.

By adjusting the parameter set $\sum$, GMM can characterize different types of non-Gaussian correlated random variables. Therefore, GMM is suitable for modeling the uncertainty in the output distribution of renewable energy. Specifically, based on the historical data of the prediction error of the active output of wind power and photovoltaic power, the parameter set $\sum$ can be obtained, and then the Gaussian mixture distribution of the prediction error can be obtained.

3.1.1.2 Opportunity-constrained conversion of wind and solar output

Assume that the random variable $Y = \boldsymbol{ax} = [a_1, \ldots, a_r, \ldots a_k]\boldsymbol{X}$, if $\boldsymbol{a} = [0, \ldots, 1, \ldots 0]$ $(a_r = 1)$, then $Y = Y_r$ represents the output power of the *rth* renewable energy source. Generally speaking, the

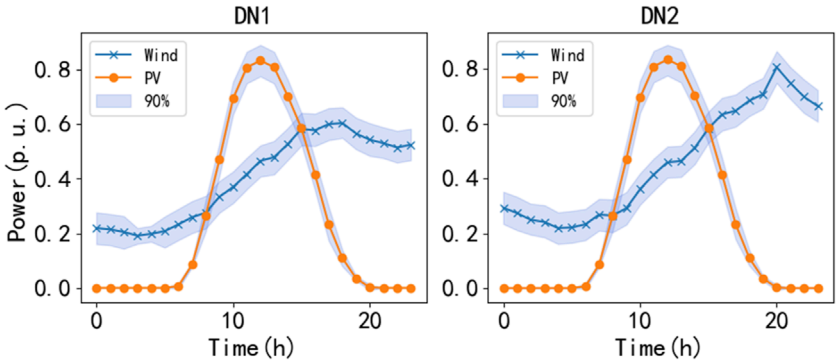

FIGURE 6
Predicted wind and solar power output power and its confidence interval under nor-mal circumstances.

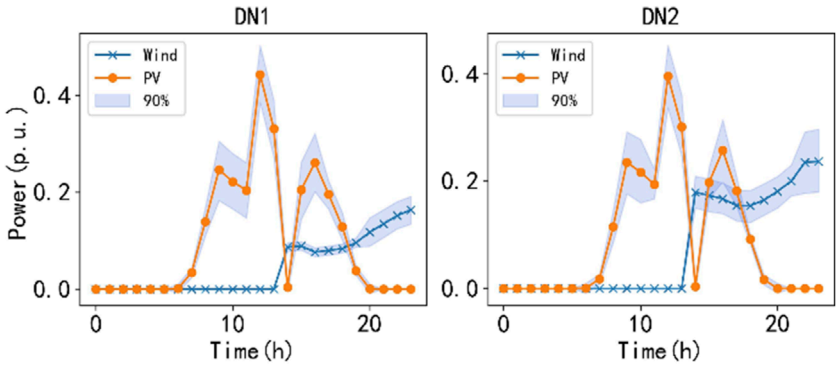

FIGURE 7
Predicted wind and solar output power along with their confidence intervals under extreme weather conditions.

linear combination of multivariate Gaussian distribution variables also obeys Gaussian distribution. Therefore, the probability density function of the random variable Y is:

$$f_Y(y) = \sum_{m=1}^{M} \pi_m N_m\left(y|\boldsymbol{a}\boldsymbol{\mu}_m, \boldsymbol{a}\boldsymbol{\sigma}_m\boldsymbol{a}^{\mathrm{T}}\right) \tag{56}$$

The cumulative distribution function (CDF) of the Gaussian distribution can be calculated as follows:

$$CDF_Y(y) = \int_{\zeta \le y} f_Y(\zeta)d\zeta = \sum_{m=1}^{M} \omega_m \cdot norm.cdf(f_m(y)) \tag{57}$$

$CDF(\cdot)$ in the interval $[-\infty, \infty]$, so it can be calculated using the binary search method $CDF^{-1}(\cdot)$. On this basis, the equivalent transformation of the chance constraints Equations 19, 22 is given:

$$CDF^{-1}_{\Delta g^{w}_{int\omega}}\left(\frac{1-\hbar^{w}}{2}\right) \le \Delta\tilde{g}^{w}_{int\omega} \le CDF^{-1}_{\Delta g^{w}_{int\omega}}\left(\frac{1+\hbar^{w}}{2}\right), \quad \forall i \in N^{m}, n \in B^{w}_{i}, t \in H, \omega \in \Omega \tag{58}$$

$$CDF^{-1}_{\Delta g^{pv}_{int\omega}}\left(\frac{1-\hbar^{pv}}{2}\right) \le \Delta\tilde{g}^{pv}_{int\omega} \le CDF^{-1}_{\Delta g^{pv}_{int\omega}}\left(\frac{1+\hbar^{pv}}{2}\right), \quad \forall i \in N^{m}, n \in B^{pv}_{i}, t \in H, \omega \in \Omega \tag{59}$$

Therefore, the opportunity constraints related to renewable energy output are transformed into deterministic constraints through the Gaussian mixture model.

3.1.2 Opportunity-constrained conversion of voltage

3.1.2.1 Node injection power represents node voltage

Equation 29 implicitly relies on uncertainty. In order to interpret (29) in a straightforward way, the voltage should be reformulated as an expression related to the random injected power. Existing studies have shown that in the LinDistFlow model, the node voltage of the radial distribution system is linearly related to the injected power of all nodes.

The amount of active/reactive power ($p^{in}_{int\omega}/q^{in}_{int\omega}$) injected into each node of the distribution network is equal to the total output power of local renewable energy minus the load, and the injected active (or reactive) power is equal to the power outflow of the node. For this purpose, Equations 23, 24, 26 are restated as shown in Equations 60–64:

$$p^{in}_{in_0t\omega} = p^{+}_{it\omega} - p^{-}_{it\omega} + \tilde{g}^{w}_{in_0t\omega} + \tilde{g}^{pv}_{in_0t\omega} + dis_{in_0t\omega} - ch_{in_0t\omega} - D_{in_0t\omega}, \forall i \in N^{m}, t \in H, \omega \in \Omega \tag{60}$$

TABLE 3 Technical parameters and cost parameters of conventional units.

Generator number	Transmission network node	Maximum output (MW)	Maximum up/down ramp (MW/h)	Initial output (MW)	Price (€/MWh)
G1	1	152	120	76	43.488
G2	2	152	120	76	43.488
G3	7	350	350	0	51.93
G4	13	591	240	0	71.037
G5	15	60	60	0	54.099
G6	15	155	155	0	9.468
G7	16	155	155	124	9.468
G8	18	400	280	240	4.923
G9	21	400	280	240	4,923
G10	22	300	300	240	0.9
G11	23	310	180	248	9,468
G12	23	350	240	280	26,901

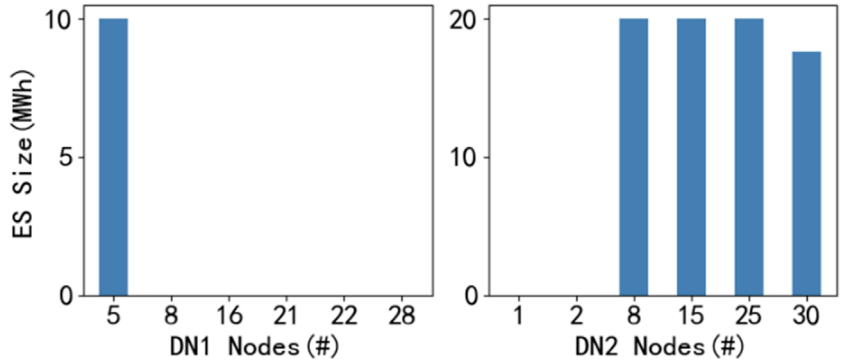

FIGURE 8
Sitting and sizing of energy storage.

$$p^{in}_{int\omega} = \tilde{g}^{w}_{int\omega} + \tilde{g}^{pv}_{int\omega} + dis_{int\omega} - ch_{int\omega} - D_{int\omega}, \forall i \in N^m, \quad n \in B_i / n_0, t \in H, \omega \in \Omega \tag{61}$$

$$q^{in}_{int\omega} = \delta^{w}_{in} \cdot \tilde{g}^{w}_{int\omega} + \delta^{pv}_{in} \cdot \tilde{g}^{pv}_{int\omega} - \delta^{d}_{in} \cdot D_{int\omega}, \forall i \in N^m, \quad n \in B_i, t \in H, \omega \in \Omega \tag{62}$$

$$p^{in}_{int\omega} = \sum_{k \in \Omega^i_p(n)} f^{p}_{i(jk)t\omega} - \sum_{k \in \Omega^i_d(n)} f^{p}_{i(nk)t\omega}, \forall i \in N^m, n \in B_i, t \in H, \omega \in \Omega \tag{63}$$

$$q^{in}_{int\omega} = \sum_{k \in \Omega^i_p(n)} f^{q}_{i(jk)t\omega} - \sum_{k \in \Omega^i_d(n)} f^{q}_{i(nk)t\omega}, \forall i \in N^m, n \in B_i, t \in H, \omega \in \Omega \tag{64}$$

The injected power of the distribution network also considers the root node (n_0). Therefore, the voltage can be restated as an expression related to the random injected power, as shown in Equation 65.

$$\tilde{V}_{int\omega} - V_0 = \sum_{j \in B^{es}_i} \left(z^{es}_{jint\omega} \cdot \left(dis_{ijt\omega} - ch_{ijt\omega} \right) \right) + \sum_{j \in B^{w}} \left(z^{w}_{jint\omega} \cdot \tilde{g}^{w}_{ijt\omega} + z'^{w}_{jint\omega} \cdot \delta^{w}_{ijt\omega} \cdot \tilde{g}^{w}_{ijt\omega} \right) + \sum_{j \in B^{pv}_i} \left(z^{pv}_{jint\omega} \cdot \tilde{g}^{pv}_{ijt\omega} + z'^{pv}_{jint\omega} \cdot \delta^{pv}_{ijt\omega} \cdot \tilde{g}^{pv}_{ijt\omega} \right) - \sum_{j \in B_i} \left(z^{d}_{jint\omega} \cdot D_{ijt\omega} \right), \quad \forall i \in N^m, n \in B_i, t \in H, \omega \in \Omega \tag{65}$$

TABLE 4 Specific configuration of energy storage.

Distribution network 1		Distribution network 2	
Node	Energy storage capacity (MWh)	Node	Energy storage capacity (MWh)
5	10	1	0
8	0	2	0
1 6	0	8	20
21	0	15	20
22	0	25	20
28	0	30	17.65

Where: $z^{w}_{jint\omega}$, $z^{pv}_{jint\omega}$ and $z^{d}_{jint\omega}$ are distribution coefficients related to the distribution network structure and power flow.

Therefore, the voltage safety constraint directly related to uncertainty is expressed as shown in Equation 66.

$$\Pr\left\{\begin{array}{l}-\Delta\overline{V}\le\sum_{j\in B_i^{es}}\left(z^{es}_{jint\omega}\cdot\left(dis_{ijt\omega}-ch_{ijt\omega}\right)\right)+\sum_{j\in B_i^{w}}\left(z^{w}_{jint\omega}\cdot\tilde{g}^{w}_{ijt\omega}+z'^{w}_{jint\omega}\cdot\delta^{w}_{ijt\omega}\cdot\tilde{g}^{w}_{ijt\omega}\right)\\ \sum_{j\in B_i^{pv}}\left(z^{pv}_{jint\omega}\cdot\tilde{g}^{pv}_{ijt\omega}+z'^{pv}_{jint\omega}\cdot\delta^{pv}_{ijt\omega}\cdot\tilde{g}^{pv}_{ijt\omega}\right)-\sum_{j\in B_i}\left(z^{d}_{jint\omega}\cdot D_{ijt\omega}\right)\le\Delta\overline{V}\end{array}\right\}\ge\lambda,\forall i\in N^{m},n\in B_i,t\in H,\omega\in\Omega \tag{66}$$

3.1.2.2 Voltage opportunity constrained conversion

As shown in Equation 66, voltage can be expressed by node injection power. Equations 58, 59 show that the opportunity constraints related to renewable energy output can be transformed into deterministic constraints, and the uncertainty implicit in node injection power comes from the output of renewable energy. Therefore, in order to ensure that the probability of the voltage amplitude within the safety interval is greater than the given confidence level (λ), it is only necessary to ensure that the output of renewable energy meets the requirements of the confidence level, and Equation 66 can be restated as Equation 67.

$$-\Delta\overline{V}\le\left\{\begin{array}{c}\sum_{j\in B_i^{es}}\left(z^{es}_{jint\omega}\cdot\left(dis_{ijt\omega}-ch_{ijt\omega}\right)\right)-\sum_{j\in B_i}\left(z^{d}_{jint\omega}\cdot D_{ijt\omega}\right)+\\ \sum_{j\in B_i^{pv}}\left(\left(z^{pv}_{jint\omega}+z'^{pv}_{jint\omega}\cdot\delta^{pv}_{ijt\omega}\right)\cdot\left(g^{pv}_{ijt\omega}+CDF^{-1}_{\Delta g^{pv}_{int\omega}}\left(1-\lambda^{1/2}\right)\right)\right)+\\ \sum_{j\in B_i^{w}}\left(\left(z^{w}_{jint\omega}+z'^{w}_{jint\omega}\cdot\delta^{w}_{ijt\omega}\right)\cdot\left(g^{w}_{ijt\omega}+CDF^{-1}_{\Delta g^{w}_{int\omega}}\left(1-\lambda^{1/2}\right)\right)\right)\end{array}\right\}\le-\Delta\overline{V},\forall i\in N^{m},n\in B_i,t\in H,\omega\in\Omega \tag{67}$$

Therefore, the chance constraint Equation 29 is transformed into a deterministic constraint.

3.2 KKT optimality condition

KKT conditions are widely used to solve nonlinear models. The lower-level market clearing problem is a linear programming problem, in which the stationary condition is obtained by taking the first order derivative of the lower-level decision variables based on the Lagrangian function of the lower-level problem. For example, ($p^{d}_{it\omega}$):

$$-c^{d}_{it}+\lambda_{it\omega}-\underline{\phi^{d}_{it\omega}}+\overline{\phi^{d}_{it\omega}}=0,\forall i\in N^{d},t\in H,\omega\in\Omega \tag{68}$$

The same is true for the remaining variables, with Equation 68 representing all stationary conditions. Similarly, the feasibility condition and complementary slack condition are obtained by taking constraint Equation 38 as an example:

$$0\le\underline{\phi^{d}_{it\omega}}\perp p^{d}_{it\omega}\ge0,\forall i\in N^{d},t\in H,\omega\in\Omega \tag{69a}$$

$$0\le\overline{\phi^{d}_{it\omega}}\perp-p^{d}_{it\omega}+\overline{p^{d}_{it\omega}}\ge0,\forall i\in N^{d},t\in H,\omega\in\Omega \tag{69b}$$

The symbol $\perp$ represents complementarity. The same is true for the other constraints. Equation 69 refers to all complementary relaxation conditions.

The nonlinearity caused by the complementary relaxation condition is linearized using the large M method (Wang et al., 2011). Taking Equations 69a, 69b as an example, they can be restated as the following constraints:

$$0\le\underline{\phi^{d}_{it\omega}}\le M\cdot b^{d,1}_{it\omega},\forall i\in N^{d},t\in H,\omega\in\Omega \tag{70a}$$

$$0\le p^{d}_{it\omega}\le M\cdot\left(1-b^{d,1}_{it\omega}\right),\forall i\in N^{d},t\in H,\omega\in\Omega \tag{70b}$$

$$0\le\overline{\phi^{d}_{it\omega}}\le M\cdot b^{d,2}_{it\omega},\forall i\in N^{d},t\in H,\omega\in\Omega \tag{70c}$$

$$0\le-p^{d}_{it\omega}+\overline{p^{d}_{it\omega}}\le M\cdot\left(1-b^{d,2}_{it\omega}\right),\forall i\in N^{d},t\in H,\omega\in\Omega \tag{70d}$$

Where: $b^{d,1}_{it\omega}$ and $b^{d,2}_{it\omega}$ are binary variables; M is a large constant.

For simplicity, Equation 70 is used to refer to the constraints after all feasibility conditions and complementary slack conditions are processed by the big M method.

In order to deal with the nonlinearity in the objective function related to the expression of (2), the linear programming duality theorem can be used to obtain the following expression, as shown in (71):

$$\begin{aligned}C^{DN}_{\omega}=\pi_{\omega}\cdot\sum_{t\in H}\Bigg(&\sum_{i\in N^{g}}\left(c^{g}_{it}\cdot p^{g}_{it\omega}+\overline{\phi^{g}_{it\omega}}\cdot\overline{P^{g}_{i}}\right.\\&\left.+\phi^{grd}_{it\omega}\cdot RD_i+\phi^{gru}_{it\omega}\cdot RU_i\right)+\sum_{i\in N^{d}}\\&-\left(c^{d}_{it}\cdot p^{d}_{it\omega}+\overline{\phi^{d}_{it\omega}}\cdot\overline{P^{d}_{it\omega}}\right)+\sum_{i<j,(i,j)\in L}\Bigg(\overline{T_{ij}}\cdot\underline{\phi^{l}_{(ij)t\omega}}\\&\left.+\overline{T_{ij}}\cdot\overline{\phi^{l}_{(ij)t\omega}}\right)\Bigg)\end{aligned} \tag{71}$$

The final model is as follows:

$$\min_{X^{U}\cup X^{L}}\sum_{\omega\in\Omega}\left(C^{DN}_{\omega}+C^{oper}_{\omega}\right)+C^{inv,a} \tag{72a}$$

$$\begin{aligned}&s.t.(6)-(18),(20)-(21),(23)-(28),\\&(30)-(32),(34),(58)-(59),(67)-(68),(70)\end{aligned} \tag{72b}$$

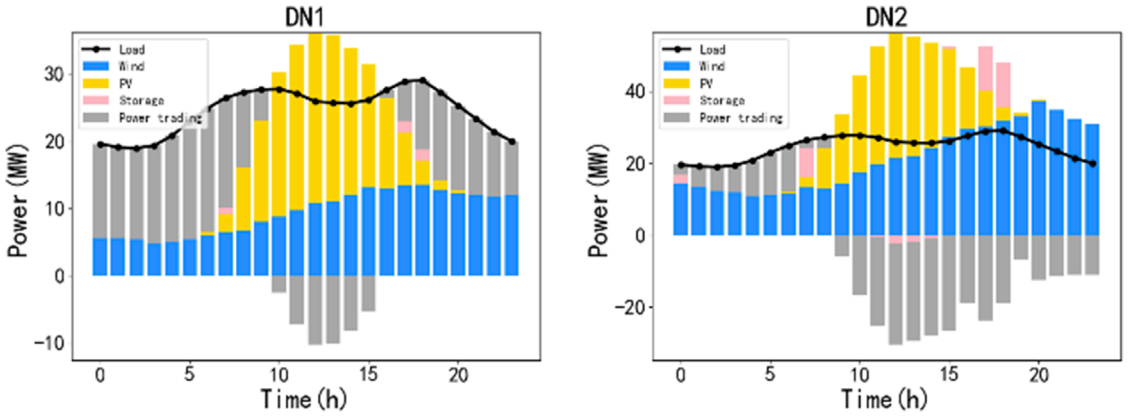

FIGURE 9
Power balance of distribution networks under a typical day.

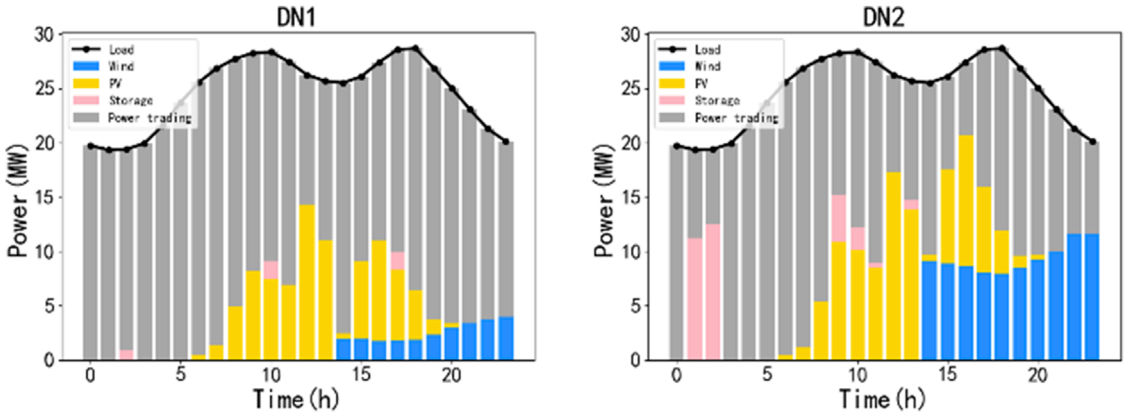

FIGURE 10
Power balance of distribution network under extreme weather conditions.

4 Case study

4.1 Example setup

The modified IEEE 24 node transmission network was combined with two IEEE 33 node distribution networks for testing. The root nodes of the two distribution networks were connected to nodes 4 and 9 of the transmission network respectively. The distribution system is shown in Figure 3. The energy storage investment occurs in the two distribution networks, and renewable energy is also distributed on the distribution networks.

Table 1 lists the distribution network nodes suitable for energy storage investment. The distribution profile of renewable energy is shown in Table 2. The load and renewable energy generation profile is based on the actual annual data of a certain place. Wind power and photovoltaic are located in two different locations of the place. Based on the K-means clustering algorithm, the annual wind and solar power output data are processed to obtain 4 typical days of conventional scenarios. Figure 4 describes the weighted average of the conventional scenario of load, wind power and photovoltaic output. Let the maximum wind speed of the wind turbine be 30 m/s. Based on the typhoon model, the maximum wind speed change in the typhoon-affected area is obtained, as shown in Figure 5. It can be seen that the wind turbine was in a shutdown state in the first 14 h. Then, based on the wind and solar power output sequence correction method under typhoon weather, the worst scenario under typhoon weather is obtained with the maximum power purchase of the distribution network as the indicator, as shown by the solid line in Figure 7.

The prediction output error is simulated based on the Gaussian mixture model, and 1,000 samples are analyzed for each prediction value. The predicted wind power and photovoltaic output power and their confidence intervals under a conventional scenario and an extreme scenario are shown in Figures 6, 7, respectively. In the case studied, the confidence level $\hbar$ and λ are set to 90%. The safety interval of the square of the voltage amplitude is [0.81, 1.21].

Assume that the investment cost of energy storage is C^e = 20€/kW and C^p = 500€/kW, the operating costs of wind power, photovoltaic power and energy storage are = 3.5€/MW, = 2.5€/MW, = 0.5€/MW respectively, c^w the service c^{pv} life of energy c^{es} storage

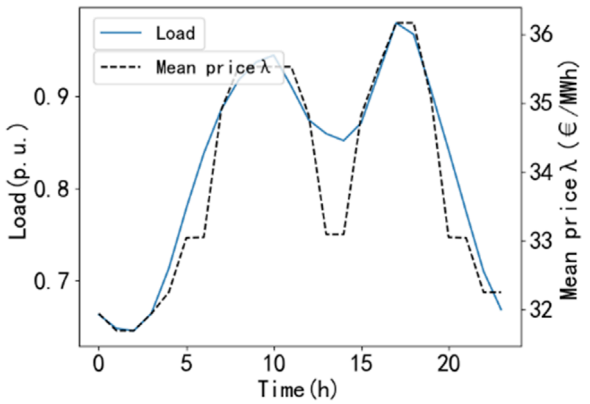

FIGURE 11
Transmission network load intensity and average electricity price.

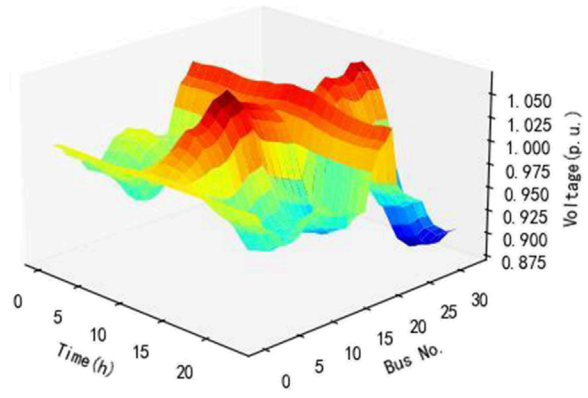

FIGURE 14
Voltage fluctuations at nodes (distribution network 1) throughout a typical day.

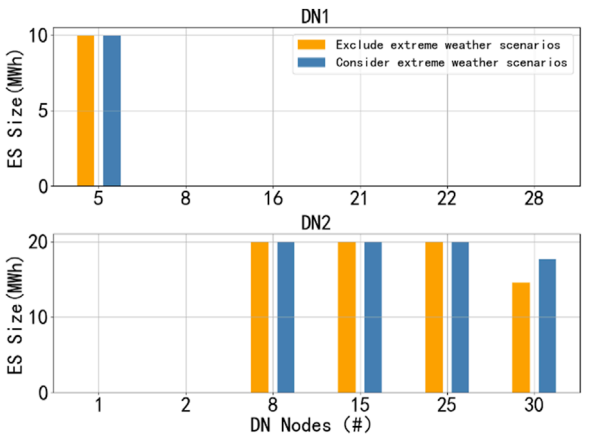

FIGURE 12
Comparison of energy storage planning with and without considering extreme weather scenarios.

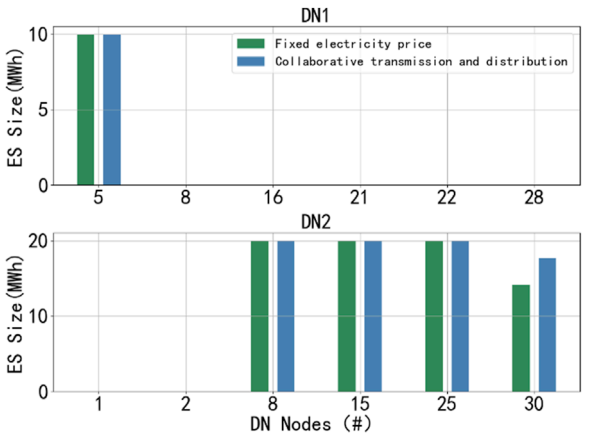

FIGURE 13
Comparison of energy storage planning with and without extreme weather scenarios.

is 15 years, and the annual discount rate is 5% (Λ = 15, Γ = 0.05). For each distribution network node eligible for energy storage installation, the maximum installed capacity is set to $\overline{K_{in}^{e}}$ = 20 MW h. The charging and discharging efficiency of the energy storage device is $\eta^{c} = \eta^{d} = 0.93$. The initial charging state of the energy storage device is assumed to be 50%, and at the end of the day, the charging state is at least 10% ($\beta = 0.1$). The technical parameters and cost parameters of the conventional unit are shown in Table 3. The power factor of wind power and photovoltaic power generation is assumed to be 0.95, and the efficiency of photovoltaic panel output is. η^{pv} = 0.95 The maximum power that can pass through the connection point $\overline{p_i}$ (substation) between the transmission network and the distribution network is = 46 MW. The purchase price of renewable energy on the distribution network when participating in the market is c_{it}^{+} = 450 €/MW, otherwise c_{it}^{-} = 0 €/MW to ensure that it can always be cleared in the day-ahead electricity market. Finally, the total budget for energy storage investment is set to $\overline{C^{inv}} = 20 \cdot 10^{6}$ €, and the locational marginal price (LMP) is calculated by the market clearing model.

4.2 Siting and sizing decisions

The planning results of energy storage site selection and scale are shown in Figure 8, and the specific configuration is shown in Table 4. It can be seen that the energy storage investment on distribution network 2 is higher than that on distribution network 1. This is mainly because distribution network 2 has better wind resources (see Figure 4) and has larger wind power and photovoltaic installed capacity. Therefore, its renewable energy generation is much larger than that of distribution network 1, and the corresponding energy storage investment will also be larger.

The energy storage investment on distribution network one is only distributed in node 5, because node 5 is the intersection of the branches where nodes 11, 26 and 40 are located, and it is also the only branch flowing to the root node. Installing energy storage here can effectively alleviate the congestion of the line. The energy storage investment in Distribution Network 2 is solely distributed at nodes 8, 15, 25, and 30, with no energy storage investment at

nodes one and 2. This planning combination is mainly determined by the distribution of renewable energy generation, load distribution and grid structure. Node 25 has the largest wind power installed capacity and a lot of photovoltaic capacity, which determines that the energy storage investment of node 25 should be large. The nodes near nodes 8 and 15 are equipped with large-capacity wind power or photovoltaic units, and node 31 adjacent to node 30 has a large load. Therefore, it is reasonable to invest a lot of energy storage in these three nodes, which can effectively alleviate the congestion of adjacent nodes and lines. Nodes one and 2 are adjacent to the root node of the distribution network, which are mainly responsible for receiving or sending the transaction electricity between the distribution network and the upstream power grid, so there is no urgent need for energy storage.

The investment cost of the energy storage decision is $90.57 \cdot 10^5$ €, the annualized investment and operating cost of the distribution network is $32.57 \cdot 10^5$ €, and the annualized generation cost of the thermal power units is $154.0 \cdot 10^6$ €. TSO benefit from renewable energy because expensive transmission-level electricity production is replaced by low-cost renewable energy units in the generation mix. More specifically, the annualized generation cost of the thermal power units (the generation cost without renewable energy is $158.31 \cdot 10^6$ €) has decreased by 2.72%, while it has decreased by 0.042% relative to the case without energy storage, because the capacity of energy storage is small relative to the load of the transmission network, so the degree of reduction is not very significant.

4.3 Overview of clearing electricity prices and system operation

The power balance of the distribution network in a normal scenario and extreme weather is shown in Figures 9, 10 respectively. Compared with the normal scenario, the output of photovoltaic and wind power is partially limited by extreme weather, and the distribution network needs to purchase more electricity to meet energy demand.

The load demand intensity and average electricity price in the region on a typical day are shown in Figure 11. For the electricity market, at the clearing price level, the amount of electricity that users are willing and able to purchase is exactly equal to the amount of electricity that the power generation side is willing and able to supply. Generally speaking, the power generation costs of various thermal power units are different, and the bids participating in the bidding are also different.

Therefore, when the user side demand is certain, the bids are usually won in order from small to large. When the load demand is small, the average electricity price in the area is also relatively small.

4.4 Impact of extreme weather scenarios on energy storage planning

In order to demonstrate the impact of extreme weather scenarios on energy storage planning, the following two scenarios are set up for analysis.

1) Scenario 1: Extreme weather scenarios are not considered in energy storage planning;
2) Scenario 2: Consider extreme weather scenarios in energy storage planning.

As shown in Figure 12, the energy storage planning under the two scenarios is shown. It can be seen from the figure that although the energy storage planning of the distribution network under the two scenarios is generally similar, in scenario 2, the energy storage capacity of node 30 in distribution network 2 is increased by 3.09 MW compared with scenario 1, that is, the total energy storage capacity of scenario 2 is greater than that of scenario 1. This is because considering the greater uncertainty and growth in electricity demand brought about by extreme weather scenarios, increasing energy storage capacity helps maintain power balance. However, due to the low probability of extreme weather scenarios, the increase in energy storage capacity is relatively small relative to the change in the overall energy storage plan.

In addition, the investment cost of energy storage planning in scenario one is $87.37 \cdot 10^5$ €, and scenario 2 increases by 3.66% compared to scenario 1. Therefore, in energy storage planning, if decision makers pay attention to the impact of extreme weather, this may lead to higher costs, but the increase in energy storage capacity will improve flexible adjustment capabilities, thereby ensuring power reliability.

4.5 Impact of transmission and distribution coordination on energy storage planning

In order to demonstrate the impact of transmission and distribution coordination on energy storage planning, the following two scenarios are set up for analysis.

1) Scenario 1: The transmission and distribution grid conducts electricity trading at a fixed price;
2) Scenario 2: Determine the transaction price of transmission and distribution network based on the proposed model.

By comparing scenarios with fixed transmission and distribution network transaction prices, it demonstrates the role of transmission-distribution coordination mechanisms in dynamically changing transaction prices, thereby affecting the investment planning for energy storage. Figure 13 compares the energy storage planning under the two scenarios. The results show that the energy storage scale increases by 3.47 MW when the distribution network participates in the market bidding mechanism under the transmission and distribution coordination compared with the fixed transaction electricity price. This is mainly because under the transmission and distribution coordination mechanism, the electricity price will change dynamically according to market demand and supply conditions. This potential economic return encourages more energy storage investment, resulting in an increase in the scale of energy storage.

For example, under a fixed electricity price, the total investment and operating cost of the distribution network

is $32.70 \cdot 10^5$ €, which is 0.40% higher than that under the transmission and distribution coordination condition. It is precisely because under a fixed electricity price, energy storage cannot use electricity price fluctuations to optimize charging and discharging strategies, resulting in a slight increase in overall operating costs. On the contrary, under the transmission and distribution coordination mechanism, energy storage can dynamically adjust according to market demand and supply conditions to achieve higher economic benefits, thereby reducing the total operating cost of the distribution network.

4.6 Fluctuation of voltage at distribution network nodes

Figure 14 shows the variation of the square of the voltage amplitude at all nodes of distribution network one during a day.

The square of the minimum and maximum voltage amplitudes during the day is 0.8744p.u. and 1.0691p.u. Since all voltages are within the safety range, network security is guaranteed. Therefore, in the case studied, the voltage security constraint has little effect on the planning and operation results.

5 Conclusion

Based on the TSO-DSO coordination framework, this paper establishes a distributed energy storage investment problem model considering extreme weather. Distributed energy storage power stations are installed in multiple distribution networks to obtain greater social welfare and renewable energy utilization. A stochastic bi-level investment planning model is established. The KKT condition, strong duality theory and linearization technology are used to transform the bi-level model into a single-level MILP model that is easy to solve. A chance constraint method based on a Gaussian mixture model is proposed to deal with the uncertainty of renewable energy power. This method can strike a balance between conservatism and optimism. A case study based on the transmission and distribution network system is carried out to verify the proposed model and method. The results show that the model considers the impact of extreme weather scenarios and optimizes the energy storage planning of the distribution network. Compared with not considering extreme weather, although the energy storage investment cost increases by 3.66%, it helps to improve the system's flexible adjustment ability; considering the transmission and distribution collaborative conditions, the total investment and operation cost of the distribution network is reduced by 0.40%. In future research work, it is possible to consider adding system reliability indicators to improve the model, and consider studying more efficient solution methods to deal with the situation where the model is complex and difficult to solve due to the increase in extreme weather scenarios.

Data availability statement

The original contributions presented in the study are included in the article/supplementary material, further inquiries can be directed to the corresponding author.

Author contributions

YX: Investigation, Methodology, Writing–original draft. KZ: Data curation, Investigation, Writing–review and editing. ZW: Methodology, Validation, Writing–original draft, Writing–review and editing. GG: Software, Writing–review and editing. DL: Investigation, Writing–original draft. RS: Validation, Writing–original draft. Shengjin Huang: Software, Writing–original draft.

Funding

The author(s) declare that financial support was received for the research, authorship, and/or publication of this article. This work was supported by State Grid Corporation Science and Technology Project (No. 5419-202356379A-2-3-XG).

Conflict of interest

Authors YX, ZW, GG, and DL were employed by State Grid Economic and Technological Research Institute Co., Ltd.

Authors KZ and RS were employed by State Grid Corporation of China.

The remaining authors declare that the research was conducted in the absence of any commercial or financial relationships that could be construed as a potential conflict of interest.

The authors declare that this study received funding from State Grid Corporation Science and Technology Project. The funder had the following involvement in the study: collection, analysis, interpretation of data and the decision to submit it for publication.

Generative AI statement

The author(s) declare that no Generative AI was used in the creation of this manuscript.

Publisher's note

References

Akbari, T., and Bina, M. T. (2014). A linearized formulation of AC multiyear transmission expansion planning: a mixed-integer linear programming approach. *Electr. Power Syst. Res.* 114, 93–100. doi:10.1016/j.epsr.2014.04.013

Baringo, L., and Conejo, A. J. (2011). Wind power investment: a benders decomposition approach. *IEEE Trans. Power Syst.* 27 (1), 433–441. doi:10.1109/TPWRS.2011.2167764

Fernández-Blanco, R., Dvorkin, Y., Xu, B., Wang, Y., and Kirschen, D. S. (2016). Optimal energy storage siting and sizing: a WECC case study. *IEEE Trans. Sustain. Energy* 8 (2), 733–743. doi:10.1109/TSTE.2016.2616444

Hua, S., Li, J., Wang, T., Zhang, J., Hu, D., and Ge, Y. (2020). Control strategy of wind power transmission improvement by considering the battery energy storage in the feasible area of wind power acceptance. *Jilin Electr. Power* 48 (2), 5–10. doi:10.16109/j.cnki.jldl.2020.02003

Li, H., Liu, D., Qing, J., Han, X., Zhao, P., Sun, Y., et al. (2024). Stochastic planning method for UHVDC transmission of renewable energy power base considering wind and photovoltaic output uncertainties. *Power Syst. Technol.* 48 (7), 2795–2803. doi:10.13335/j.1000-3673.pst.2023.1888

Li, H., Liu, D., and Yao, D. (2021). Analysis and reflection on the development of power system towards the goal of carbon emission peak and carbon neutrality. *Proc. CSEE* 41 (18), 6245–6259.

Li, J., Wang, Z., Da, Z., Ren, Y., Jin, Y., and Zhou, B. (2023). Multi-level planning method of energy storage stations for resilient distribution networks considering spatio-temporal correlation of severe weather. *Power Syst. Prot. Control* 51 (9), 128–137. doi:10.19783/j.cnki.pspc.221212

Li, R., Wang, W., Wu, X., Tang, F., and Chen, Z. (2019). Cooperative planning model of renewable energy sources and energy storage units in active distribution systems: a bi-level model and Pareto analysis. *Energy* 168, 30–42. doi:10.1016/j.energy.2018.11.069

Liu, X., Hou, K., Jia, H., Zhao, J., Mili, L., Jin, X., et al. (2020). A planning-oriented resilience assessment framework for transmission systems under typhoon disasters. *IEEE Trans. Smart Grid* 11 (6), 5431–5441. doi:10.1109/TSG.2020.3008228

Liu, Z., Yang, P., and Xu, Z. (2017). Capacity allocation of integrated energy system considering typical day economic operation. *Electr. Power Constr.* 38 (12), 51–59. doi:10.3969/j.issn.1000-7229.2017.12.007

Ma, L., Wang, H., Lu, Z., and Zhen, L. (2020). Flexible resource planning for improving distribution network resilience under typhoon disasters considering relevance impact. *Automation Electr. Power Syst.* 46 (7), 60–68. doi:10.7500/AEPS20210902005

Pandžić, H., Wang, Y., Qiu, T., Dvorkin, Y., and Kirschen, D. S. (2014). Near-optimal method for siting and sizing of distributed storage in a transmission network. *IEEE Trans. Power Syst.* 30 (5), 2288–2300. doi:10.1109/TPWRS.2014.2364257

Peker, M., Kocaman, A. S., and Kara, B. Y. (2018). Benefits of transmission switching and energy storage in power systems with high renewable energy penetration. *Appl. Energy* 228, 1182–1197. doi:10.1016/j.apenergy.2018.07.008

Qian, D., Zeng, P., Sun, K., Xu, C., and Xu, Z. (2020). A planning method for the placement and sizing of distributed energy storage system considering the uncertainty of renewable energy sources. *Energy Storage Sci. Technol.* 9 (1), 162–169. doi:10.12028/j.issn.2095-4239.2019.0156

Tang, W., Lu, J., Chen, H., Yuan, Y., Lv, X., Chen, J., et al. (2022). "Optimal research on siting and sizing of energy storage in distribution network," in *2022 5th international conference on power and energy applications (ICPEA)* (IEEE), 398–402. doi:10.1109/ICPEA56363.2022.10052359

Wang, D., Zhang, C., Li, J., Zhu, L., Zhou, B., Zhou, Q., et al. (2024). A novel interval power flow method based on hybrid box-ellipsoid uncertain sets. *IEEE Trans. Power Syst.* 39 (4), 6111–6114. doi:10.1109/TPWRS.2024.3391921

Wang, H., Zhang, W., and Liu, Y. (2016). Measurement placement in active distribution networks considering output uncertainty of distributed generators. *Automation Electr. Power Syst.* 40 (12), 9–14. doi:10.7500/AEPS20160314010

Wang, L., Li, Y., and Jin, S. (2011). A new algorithm for linear programming—improved Big-M method. *J. Logist. Eng. Univ.* 27 (3), 92–96. doi:10.3969/j.issn.1672-7843.2011.03.017

Wang, X., Gao, X., Wang, Y., Shi, Y., Zheng, H., Yao, Y., et al. (2023). "Energy storage siting and capacity planning considering voltage flexibility under extreme scenarios," in *2023 IEEE 7th conference on energy internet and energy system integration (EI2)* (IEEE), 1082–1089. doi:10.1109/EI259745.2023.10512477

Xu, X., Li, J., Xu, Y., Xu, Z., and Lai, C. S. (2020). A two-stage game-theoretic method for residential PV panels planning considering energy sharing mechanism. *IEEE Trans. Power Syst.* 35 (5), 3562–3573. doi:10.1109/TPWRS.2020.2985765

Yao, T., Liu, Q., Liu, J., Liu, H., Huang, J., Zhang, L., et al. (2022). Research on joint planning methods for energy storage and transmission network considering complementarity of wind power and PV. *Power Syst. Clean Energy* 38 (7), 118–126. doi:10.3969/j.issn.1674-3814.2022.07.015

Yuan, W., Wang, J., Qiu, F., Chen, C., Kang, C., and Zeng, B. (2016). Robust optimization-based resilient distribution network planning against natural disasters. *IEEE Trans. Smart Grid* 7 (6), 2817–2826. doi:10.1109/TSG.2015.2513048

Zhang, W., Zhang, C., Zhou, Q., Li, J., Zhu, L., Cao, S., et al. (2024). Spatial–Temporal resilience assessment of distribution systems under typhoon coupled with rainstorm events. *IEEE Trans. Industrial Inf.*, 1–10. doi:10.1109/TII.2024.3450079

Zhao, J., Su, J., Pan, F., Yang, Y., Chen, M., and Zhang, Y. (2022). Dual objective optimization planning of distributed energy storage for active distribution network considering photovoltaic fluctuations. *Renew. Energy Resour.* 40 (11), 1546–1553. doi:10.3969/j.issn.1671-5292.2022.11.019

frontiers | Frontiers in Energy Research

TYPE Original Research
PUBLISHED 18 December 2024
DOI 10.3389/fenrg.2024.1521209

OPEN ACCESS

EDITED BY
Minghao Wang,
University of Macau, China

REVIEWED BY
Weicheng Liu,
Tsinghua University, China
Ning Tong,
Guangdong University of Technology, China

*CORRESPONDENCE
Yang Liu,
1015473572@qq.com

RECEIVED 01 November 2024
ACCEPTED 22 November 2024
PUBLISHED 18 December 2024
CORRECTED 19 June 2025

CITATION
Song Y, Zhang Y, Zhang S, Liu F, Su Y and Liu Y (2024) System frequency response model and droop coefficient setting considering renewable energy participation in frequency regulation.
Front. Energy Res. 12:1521209.
doi: 10.3389/fenrg.2024.1521209

System frequency response model and droop coefficient setting considering renewable energy participation in frequency regulation

Yuyan Song, Yongjie Zhang, Shuai Zhang, Fang Liu, Yunche Su and Yang Liu*

State Grid Sichuan Electric Power Company, Sichuan, China

The highly uncertain and uncontrollable power output of renewable energy sources (RES), when integrated into power systems at high penetration levels, reduces system inertia and introduces uncertain changes in system structure, parameters, and frequency response characteristics. This renders traditional frequency regulation analysis methods and frequency response models inapplicable, lacking a generalized model to describe renewable energy's participation in frequency regulation. Thus, this paper proposes a method where RES utilize suitable means to reduce load, thereby contributing to frequency regulation. Furthermore, employing Virtual Synchronous Machine (VSM) technology, these renewable energy units emulate the inertia and droop characteristics of Synchronous Generators (SG), enabling their equivalent modeling alongside traditional generators within a single-machine aggregate model. An SFR (System Frequency Response) model integrating renewable energy's frequency regulation has been established. This model enables the analysis of the relationships between the system's equivalent droop coefficient and the frequency nadir, nadir time, and quasi-steady-state point. Furthermore, the required equivalent droop coefficients are proposed for various sending-end system capacities and operating conditions. Finally, the model's validity and accuracy are confirmed through a modified WSCC 4-machine 10-bus system, offering theoretical underpinnings for stable system operation and optimized operational planning.

KEYWORDS

renewable energy sources, SFR, droop coefficient, WSCC, VSM

1 Introduction

Compared to traditional synchronous systems, the extensive integration of high-proportion electronic RES has substituted for some SG, resulting in a gradual reduction in system inertia and relatively weaker frequency regulation capability due to the decoupling characteristics of renewable energy power electronics and their maximum power tracking mode. In addition, the application of UHV large-capacity cross-regional DC transmission has blocked the cross-regional inertia support and power response under disturbances, seriously deteriorating the system frequency stability under large disturbances (Shi et al., 2018a; Ahmadi and Ghasemi, 2014; Wright et al., 2019; Lin et al., 2023). In interconnected

power systems, frequency stability is an important indicator reflecting power quality, mainly representing the balance state of active power in power systems (Xue et al., 2024; Yin et al., 2024; Grebla et al., 2020; Mei et al., 2024). In traditional power systems, frequency control is primarily achieved by regulating the active power output of generator sets, enabling the system's generation power to follow changes in system load power, thereby achieving active power balance across the entire system. This function is commonly referred to as LFC (Load Frequency Control) (Wu et al., 2023a). However, in power systems with a high penetration of renewable energy, the uncertainty of renewable energy output becomes a critical factor affecting the active power balance of the system (Wu et al., 2023b). Compared to traditional load disturbances, renewable energy output disturbances are more severe and highly unpredictable, posing challenges to the current load frequency control techniques, which lack suitable representation and handling of this uncertainty. The integration of high proportions of renewable energy inevitably has adverse effects on the quality and stability of frequency control (Zhixuan et al., 2024). Furthermore, renewable energy units exhibit significantly different frequency response characteristics from traditional energy units. Their replacement of traditional units leads to uncertain changes in system structure, parameters, and frequency response characteristics, further complicating frequency control (Rongpeng and Yang, 2024).

In response to the aforementioned issues regarding frequency response characteristics arising from the high integration of renewable energy, extensive research has been conducted by scholars both domestically and internationally. In Reference (Altaf et al., 2022), the study of the system's frequency dynamic response through the ASF (Average System Frequency) is proposed. This model equates all generators in the system to a single-machine model while retaining the original turbine-governor systems of each unit. However, as the number of generators continues to increase, the proliferation of turbine-governor systems limits the applicability of this method. Building upon the ASF model, Reference (Quan and Pan, 2017) further simplifies the turbine-governor systems through equivalent aggregation, thereby approximating the entire power grid as a single-machine model with a centralized load model. The SFR model significantly reduces the order of the frequency response analysis model, enabling the calculation of analytical solutions for maximum frequency deviations and corresponding times under given disturbances. It is currently the most commonly used model for frequency response analysis. Reference (Xiaolin et al., 2021) established a two-stage distributionally robust unit commitment model for power systems with wind farms, based on the ASF model and its simplified SFR model, considering virtual inertia control and droop control of wind farms. Reference (Fan et al., 2020) employed the system SFR model to analyze the impact of key frequency control parameters, including inertia time constant, frequency regulation deadband, and governor droop, on system frequency response characteristics. Reference (Bo et al., 2020) developed an SFR model incorporating wind turbine integration, derived dynamic frequency quantification metrics, and constructed a unit commitment optimization model for wind-integrated systems considering dynamic frequency constraints. Reference (Malekpour et al., 2021) integrated wind power virtual inertia control into the traditional SFR model and analyzed its effect on system frequency response. Reference (Chang-gang et al., 2009) proposed a power system frequency dynamic analysis method based on the DC power flow method, which ignores the impact of reactive power-voltage variations on frequency dynamics and uses the DC power flow method to describe the system network flow equations, considering only generator motion equations and turbine-governor dynamics, with iterative integration methods to calculate post-disturbance system frequency dynamics. Reference (Banarkar et al., 2006) established equivalent models for SG, wind farms, and loads, using wind power fluctuations and frequency deviations as input and output variables, respectively, thereby simplifying a multi-machine system to a single-machine system. This enabled the establishment of a frequency-domain transfer function between system power fluctuations and frequency deviations, which was then used to analyze system frequency dynamics with the SFR model. Reference (Nguyen et al., 2015) quantitatively analyzed the impact of wind power integration on system equivalent inertia and damping constants. Through the modification of traditional SFR model parameters, it proposed an SFR model that considers wind power integration and derived the corresponding time-domain expression for maximum frequency deviation. Reference (Shi et al., 2018b) introduced an analytical method to aggregate a multi-machine SFR model into a single-machine model. Validation studies demonstrated that the proposed aggregated SFR model accurately represents the multi-machine SFR model.

This paper based on the mechanism of traditional thermal power unit inertia and primary frequency regulation (PFR) for system frequency adjustment, employs the SFR method to analyze the impact of various factors on system frequency dynamic characteristics after the participation of renewable energy units in frequency regulation. Considering the involvement of renewable energy units in frequency regulation, the SFR model is improved to derive expressions and correlations for the initial rate of frequency change, maximum frequency deviation, and steady-state frequency deviation. Through theoretical analysis, the mechanism of operating conditions influencing the frequency regulation capability of renewable energy units and system frequency dynamic behavior is revealed. The effectiveness of this improved SFR model is verified through simulations on the modified WCSS 4-machine 10-bus system.

2 Frequency response model

The frequency response characteristic of a power system refers to the variation in system frequency under unbalanced power conditions. This characteristic is influenced by factors such as the magnitude of the disturbing power, the inertia of prime movers, and the regulation characteristics of governors.

Under conditions that do not lead to power angle instability or voltage instability, the impact of reactive power and voltage variations can be neglected to focus on the primary relationship between frequency and active power, highlighting the main influencing factors. To reduce the computational burden and complexity of frequency dynamic analysis, this paper, based on the premise of a unified frequency across the entire grid, disregards spatial frequency variations and power angle stability issues. It

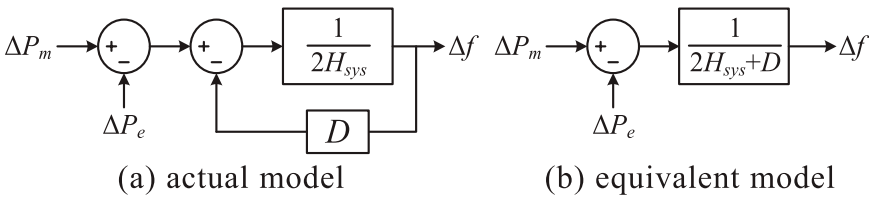

FIGURE 1
(A) actual model. **(B)** equivalent model. Equivalent model of load and traditional generator.

aggregates the rotor motion equations of all generators in the system into an equivalent single-generator model with centralized loads, thereby deriving the system's SFR.

2.1 SFR of prime mover and governor

The rotor motion equation of a synchronous generator describes the variation in rotor speed under unbalanced torque when fluctuations occur in the mechanical power output by the prime mover or the electromagnetic power output by the synchronous machine. It can be expressed as:

$$\Delta P_m - \Delta P_e = 2H_{sys}\frac{d\Delta f}{dt} \tag{1}$$

where ΔP_m is the mechanical power output of the prime mover; ΔP_e is the electromagnetic power output of the synchronous machine; Δf is the frequency variation (since the frequency f is directly proportional to the rotor angular velocity ω, for a more intuitive representation of the power-frequency relationship, the frequency deviation Δf will be used as a substitute for the angular velocity variation $\Delta\omega$; H_{sys} represents the equivalent inertia time constant of the generator set:

$$H_{sys} = \frac{\sum_{i=1}^{n} H_i S_i}{\sum_{i=1}^{n} S_i} = \frac{\sum_{i=1}^{n} H_i S_i}{S_{B(SG)}} \tag{2}$$

where n represents the number of synchronous units in the system, S_i and H_i are their respective rated capacities and inertia time constants, while $S_{B(SG)}$ denotes the total rated capacity of conventional SG. The system load's response to frequency deviations is primarily encapsulated in the load damping constant D. When a frequency deviation occurs, the variation in load power is given by:

$$\Delta P_L = D\Delta f \tag{3}$$

where ΔP_L represents the power variation of frequency-sensitive loads, and D is the load damping constant. Applying Laplace transforms to Equations 1 and 3 yields the equivalent model of the generator and load, as illustrated in Figure 1A. Figure 1B depicts the simplified version of this model.

Traditional thermal power generation units employ steam turbines as their prime movers, and the mechanical power output of the prime mover can be controlled by adjusting the valve opening of the steam turbine. The process of loading and unloading the steam chamber and inlet pipe takes a certain amount of time. Therefore, the process of load-frequency control through regulating the steam flow passing through the steam turbine using control valves can be represented by an inertial element with a time constant T_t, as shown in Figure 2. The value of the time constant T_t typically ranges from 0.2 to 0.3 s.

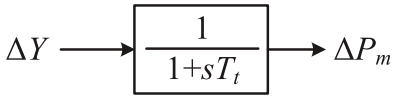

FIGURE 2
Equivalent model of prime motor.

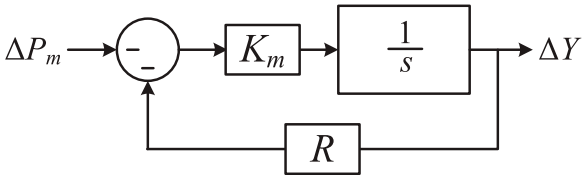

FIGURE 3
Equivalent model of governor with droop control.

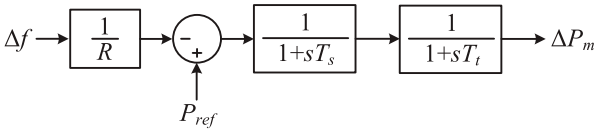

FIGURE 4
Equivalent model of governor and prime motor.

To distribute loads among multiple generator set reasonably, the governor system should be capable of reducing rotational speed when load power increases. This regulating characteristic can be achieved using an integral element with steady-state feedback, as illustrated in Figure 3.

In the figure, R represents the equivalent droop coefficient of the generator set, which physically signifies the ratio between the frequency variation and the change in generator output power. By simplifying Figure 3 and combining it with Figure 2, we obtain

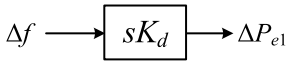

FIGURE 5
Frequency response model of RES under virtual inertia control.

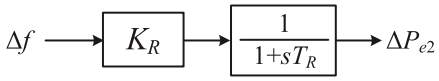

FIGURE 6
Frequency response model of RES under droop control.

the equivalent model of the prime mover and governor as shown in Figure 4, where $T_s = 1/(K_m R)$ represents the inertia time constant of the governor.

2.2 Frequency regulation-capable SFR for RES

From Equations 1–3, it is evident that during active power disturbances in a power system containing synchronous machines, the system frequency undergoes an abrupt change. The generator sets, due to their rotational inertia, can provide energy proportional to the rate of frequency change, offering transient support to the system frequency. Larger inertia time constants of the generator set result in the release of more rotational kinetic energy. However, renewable energy systems such as wind and solar power generation are typically characterized by low inertia, and their output power is decoupled from the grid frequency, rendering them incapable of responding to frequency variations. With a high penetration of these renewable sources into the power system, the overall system inertia inevitably decreases, reducing the rotational inertia available to counter frequency changes and leading to degradation of frequency dynamic performance.

The VSM technology enables renewable energy interfaces, such as converters, to mimic the virtual inertia characteristics of synchronous machines by appending control loops. The basic working principle involves adjusting the output power of renewable energy units in response to frequency deviations during system disturbances, thereby equipping them with the capability to respond to frequency variations. Analogous to the rotational inertia effect of synchronous machines, the variation in output power of renewables through virtual inertia control in response to frequency changes is given by:

$$\Delta P_{e1} = K_d \frac{d\Delta f}{dt} \tag{4}$$

where ΔP_{e1} is variation in output power of renewable energy units under virtual inertia control, where k_d represents the virtual inertia coefficient. Applying the Laplace transform to Equation 4 yields the SFR of renewables equipped with virtual inertia characteristics, as depicted in Figure 5.

To achieve a reasonable load distribution among multiple generator sets, traditional energy sources, under the influence of droop-equipped governors, exhibit a characteristic where output power increases with load increase. In contrast to rotational inertia, which provides transient support to the system frequency, the droop characteristic of generator sets reduces the steady-state error in system frequency after disturbances. The droop rate of generator sets can be expressed by Equation 5:

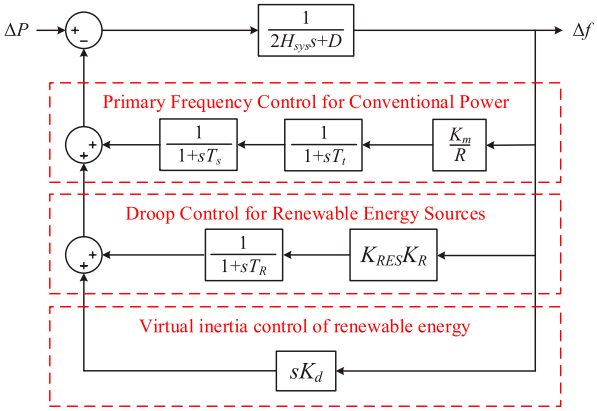

FIGURE 7
SFR model considering frequency control capability of renewable energy.

$$R(\%) = \left(\frac{\omega_{NL} - \omega_{FL}}{\omega_0}\right) \tag{5}$$

The magnitude of PFR capability in generator sets is intimately tied to their droop rates. When integrating low-inertia sources such as large wind farms or photovoltaic power stations into the grid, they are typically required to possess a certain level of PFR capability. By leveraging VSM technology to control the inverters of renewable energy interfaces, RES can exhibit a similar droop characteristic to traditional energy sources during frequency variations. In contrast to virtual inertia control, which can instantly respond to frequency changes, inverters executing droop control for frequency regulation require a certain time delay. Compared to the governor dynamics of traditional energy sources, the SFR of RES with droop characteristics is illustrated in Figure 6.

Where K_R is the droop control coefficient of RES, also known as the PFR gain, is denoted as T_R, which represents the droop control time constant. ΔP_{e2} signifies the variation in output power of renewable energy units under the influence of droop control.

2.3 SFR considering the integration RES

After renewable energy units acquire virtual inertia and droop characteristics similar to synchronous machines through VSM technology, these converter-based power sources can be aggregated with synchronous machines into a single-machine equivalent model. The SFR that considers the frequency regulation capability of renewables is depicted in Figure 7.

Where K_{RES} and K_m represent the proportions of actual output power contributed by renewable energy units and thermal power units, respectively, to the total system generation.

Without considering the virtual inertia provided by non-synchronous power sources, after replacing synchronous units with non-synchronous power sources of equal capacity, the system equivalent inertia time constant based on the total rated capacity of the system can be expressed by Equation 6:

$$H'_{SYS} = \frac{\sum_{i=1}^{n-m} H_i S_i}{\sum_{i=1}^{n-m} S_i + S_{B(NSG)}} = \frac{\sum_{i=1}^{n} H_i S_i - \sum_{i=m+1}^{n} H_i S_i}{\sum_{i=1}^{n-m} S_i} = H_{SYS} - \Delta H \quad (6)$$

where ΔH represents the equivalent inertia time constant of the synchronous units that have been replaced by non-synchronous power sources.

From an energy perspective, replacing synchronous units with non-synchronous power sources of equal capacity directly reduces the number of conventional synchronous units in operation. Consequently, the total rotational kinetic energy of the system decreases as the number of synchronous units diminishes, leading directly to a reduction in the system's equivalent inertia level.

Under the premise of not considering the participation of asynchronous power sources in PFR, after replacing synchronous units with asynchronous power sources of equal capacity, the mechanical power gain coefficient of steam turbines, K_m can be expressed by Equation 7:

$$K'_{ms} = \frac{S'_{B(s)}}{S'_{B(SG)} + S_{B(NSG)}} = \frac{S_{B(s)} - \Delta S_{B(s)}}{S_{B(SG)}} = K_{ms} - \Delta K_{ms} \quad (7)$$

where $\Delta S_{B(s)}$ refers to the capacity of hydraulic turbines and steam turbines that have been replaced by non-synchronized power sources. ΔK_{ms} represents the variation in the mechanical power gain coefficient for hydraulic turbines and steam turbines.

Accordingly, the equivalent droop coefficient of the system, R' can be expressed by Equation 8:

$$\frac{1}{R'} = \frac{1}{R_{sys}} - \frac{1}{R_s}\Delta K_{ms} = \frac{1}{R_{sys}} - \frac{1}{\Delta R} \quad (8)$$

where ΔR represents the variation in the equivalent droop coefficient of the system after it has been partially replaced by non-synchronous power sources.

In summary, since the total system capacity remains unchanged, replacing synchronous units with non-synchronous power sources of equal capacity directly alters the number of conventional synchronous units in operation. Consequently, the number of prime movers and governors of generating units decreases accordingly, leading to a gradual weakening of the frequency regulation capability of the governor system of generating units. Therefore, when synchronous units are replaced by non-synchronous power sources, the equivalent droop coefficient R' of the system gradually increases, which is equivalent to reducing the system's PFR capability.

The SFR shown in Figure 7 can be further simplified, and by letting $H_{SYS} = H_{sys} + K_d$, the rotational inertia of conventional units and the virtual inertia of renewable energy units can be aggregated into the overall system inertia. Consequently, the SFR can be expressed as:

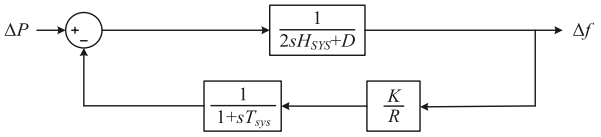

FIGURE 8
Simplified SFR model considering frequency control capability of renewable energy.

Where T_{sys} represents the equivalent response time constant of the system, and K denotes the participation factor of renewable energy in frequency regulation, as shown in Equation 9.

$$K = 1 - k_{SG} + k_{RE} \quad (9)$$

where k_{SG} is the replaced portion of synchronous machines is denoted as the proportion of substitution, and k_{RE} represents the proportion of power electronic sources that provide both inertia and frequency regulation (if power electronic sources do not provide frequency regulation, then $k_{RE} = 0$). At this point, the equivalent inertia of the system is H_{SYS}, and the equivalent droop coefficient is K/R. For simplicity, this equivalent model is used in subsequent analysis to investigate the impact of PFR parameters on the system.

3 The relationship between frequency variation and model parameters

3.1 SFR considering the integration RES

Based on the SFR derived in the previous section from Figure 8, the transfer function from load disturbance to frequency variation can be expressed by Equation 10:

$$\Delta f = \left[\frac{\omega_n^2}{K(D + R^{-1})}\right]\left[\frac{(1 + T_{SYS}s)P_d}{s(s^2 + 2\zeta\omega_n + \omega_n^2)}\right] \quad (10)$$

Where ω_n and ζ represent the undamped natural frequency and damping ratio, respectively, and their expressions are shown in Equation 11:

$$\begin{cases} f_n^2 = \dfrac{DR + K}{2H_{SYS}RT_{SYS}} \\ \zeta = \left[\dfrac{2H_{SYS}R + (DR + K)T_{SYS}}{2(DR + K)}\right] f_n \end{cases} \quad (11)$$

Assuming the magnitude of the disturbance is ΔP, applying the Laplace inverse transform to Equation 10 yields the expression of the system frequency response in the time domain, enabling the further derivation of evaluation parameters for the dynamic characteristics of system frequency, as shown in Equation 12.

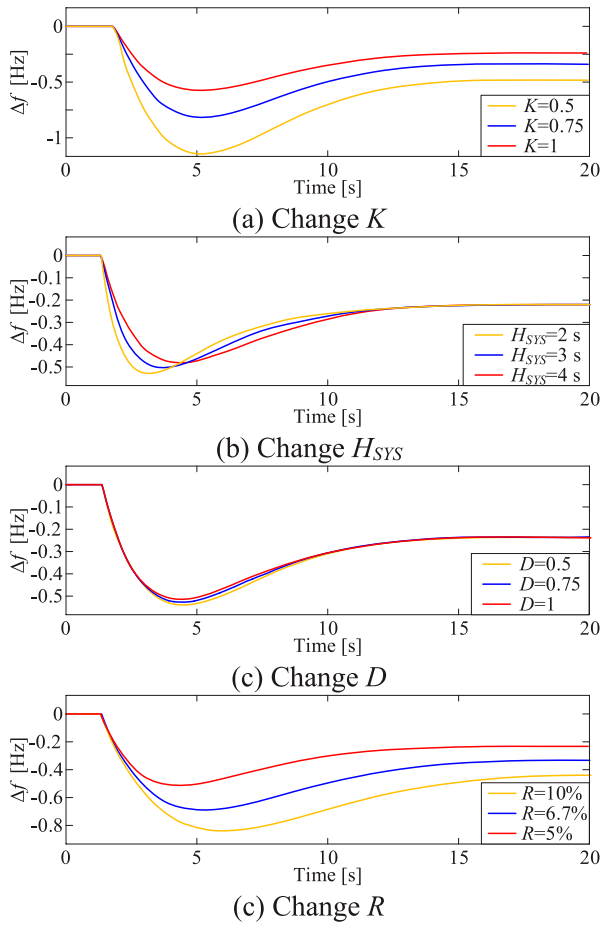

FIGURE 9
(A) Change K. **(B)** Change H_{SY}. **(C)** Change D. The characteristic of system frequency response.

$$\begin{cases} \Delta f(t) = \dfrac{R\Delta P}{DR+K}\left[1+\alpha e^{-\zeta\omega_n t}\sin\left(\omega_r t+\phi\right)\right] \\ \omega_r = \omega_n\sqrt{1-\zeta^2} \\ \alpha = \sqrt{\dfrac{1-2T_{SYS}\zeta\omega_n+T_{SYS}^2\omega_n^2}{1-\zeta^2}} \\ \phi = \arctan\left(\dfrac{\omega_r T_{SYS}}{1-\zeta f_n T_{SYS}}\right)-\arctan\left(\dfrac{\sqrt{1-\zeta^2}}{-\zeta}\right) \end{cases} \tag{12}$$

At $t = 0$, the maximum rate of change of frequency (RoCoF) can be obtained. Based on the above analysis, it can be concluded that:

$$\left.\frac{d\Delta f}{dt}\right|_{t=0} = \frac{\Delta P}{2H_{SYS}+K} \tag{13}$$

At $t = \infty$, the quasi-steady-state frequency deviation of the system can be obtained.

$$\Delta f_{set} = \Delta f(\infty) = \frac{\Delta P}{D+K/R} \tag{14}$$

Using typical parameters from the reference (Banarkar et al., 2006) as the model's parameters, and under a power disturbance of 10% of the synchronous generator capacity, the system frequency response curves are compared after wind turbines replace SG at different proportions, as shown in Figure 9.

From Figure 9A, it can be observed that as the proportion of wind power replacing SG increases (K decreases), the maximum frequency deviation, the maximum rate of change of frequency, and the quasi-steady-state frequency deviation all exhibit an increasing trend. Thus, all three evaluation indicators of system frequency response deteriorate, undoubtedly indicating that wind power integration has a negative impact on system frequency response characteristics, and this negative impact becomes more severe with an increasing proportion of wind power integration.

Figure 9B demonstrates that variations in H_{SYS} affect the magnitude of the system frequency rate of change post-disturbance. A smaller H_{SYS} results in a larger frequency rate of change throughout the PFR process, including an increased maximum value at the initial moment of the disturbance, consistent with the formula for calculating the maximum frequency rate of change given in Equation 13. Additionally, H_{SYS} significantly influences the system's frequency nadir, with a smaller H_{SYS} leading to an earlier occurrence of the nadir and a larger maximum frequency deviation at this point.

According to Figure 9C, changes in D primarily impact the system maximum frequency deviation. A smaller D results in a larger maximum frequency deviation. While Equation 14 indicates that D also influences the quasi-steady-state frequency deviation, this effect is generally limited due to the typically small damping coefficients in power systems.

Finally, Figure 9D shows that variations in R affect the quasi-steady-state frequency deviation. A larger R delays the occurrence of the frequency nadir and leads to a larger maximum deviation at this point, as well as a larger quasi-steady-state frequency deviation.

3.2 The requirement of the droop coefficient

According to above section, the K and R significantly influence the Δf_{set}. Thus, the relationship between K, R, and Δf_{set} needs to be further establish to control the value of Δf_{set} under different conditions of K by adjusting R.

According to Equation 14, the R can be calculated by: Equation 12:

$$R = \frac{K\Delta f_{set}}{\Delta P-\Delta f_{set}D} \tag{15}$$

It can be seen that the governing coefficient is directly proportional to K, while it is inversely prwxoportional to ΔP and D. Assuming a permissible quasi-steady-state frequency deviation of Δf_{set} = 0.2 Hz, the required droop coefficient R of the system is dependent on K, the integration of power electronic sources, and the active power disturbance ΔP. When the frequency regulation contribution of power electronic sources in the system decreases, an increase in the droop coefficient is necessary. Conversely, a larger active power disturbance requires a reduction in the equivalent droop coefficient to stabilize the system frequency.

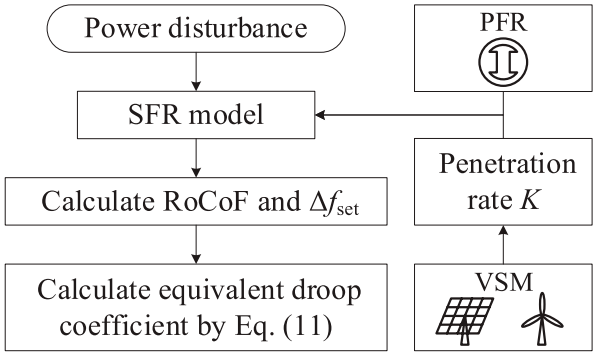

FIGURE 10
Flowchart of the droop coefficient Setting.

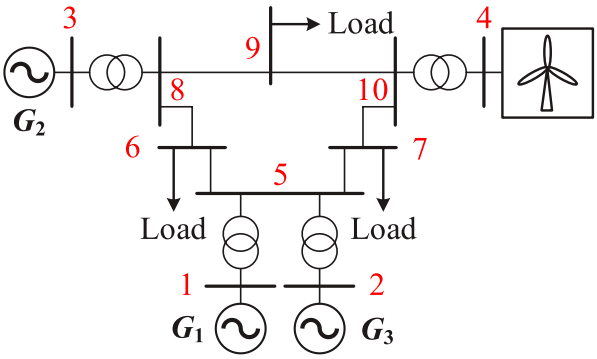

FIGURE 11
Modified WSCC 4-machine 10-bus system .

Finally, a flowchart is given by Figure 10 to obtain the equivalent droop coefficient R based on the proposed SFR in this paper.

4 Case studies

In this chapter, the test case employs the WSCC 4-machine 10-bus system, with a simulation model built on PSCAD to validate the effectiveness of the proposed SFR. The RES are modeled as common Direct-Drive Wind Turbines, as depicted in Figure 11. Generators 1, 2, 3, and Wind Turbines have a rated capacity of 20 MVA each. The system load is 75MW, and the system's equivalent inertia constant is 4s. The system feeder line, transformer, load, and frequency regulation parameters are shown in Tables A1–A3. The system equivalent original droop coefficient R is set as 3%, with a renewable energy frequency regulation contribution ratio $K = 1$ and equivalent damping constant D is set as 1.

4.1 Performance of the proposed SFR

In order to verify the accuracy of the proposed SFR model, the active power disturbances of the load increase are respectively set as 8 MW, 12 MW, 16 MW (accounting for 10%, 15%, 20% of the system capacity separately) in PSCAD simulation model and SFR model. The frequency response curves and the errors between the PSCAD and SFR are respectively shown in Figure 12 and Table 1.

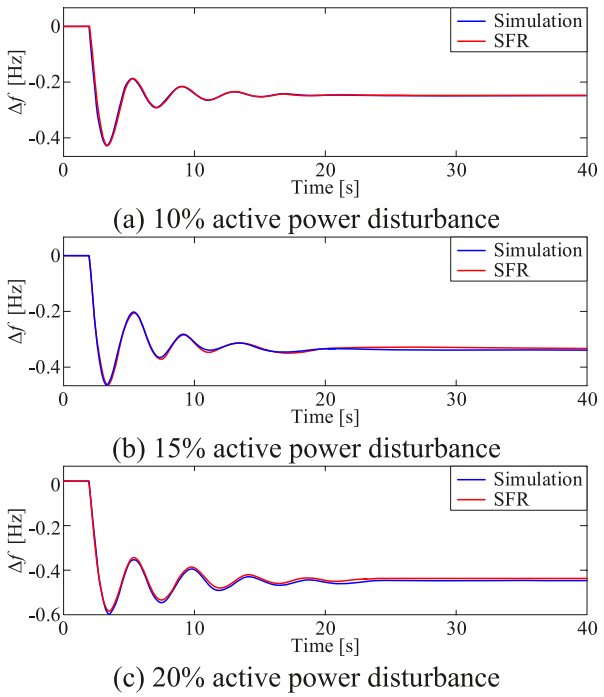

FIGURE 12
(A) 10% active power disturbance. **(B)** 15% active power disturbance. **(C)** 20% active power disturbance. Comparison results of system frequency response.

From the above figure and table, it can be observed that the output of the SFR model closely matches the results of the time-domain simulation under various load increment scenarios. Even in the case of 20% load increment, which caused a frequency drop of 0.46Hz, the error in the minimum frequency value was only 2.377%. These simulation results convincingly demonstrate the effectiveness of the proposed SFR model.

4.2 Performance of the droop coefficient adjustment

When the system suffers a 20% active power disturbance (18 MW), to maintain the quasi-steady-state deviation Δf_{set} = 0.23 Hz, substituting parameters into Equation 15 yields a equivalent droop coefficient of 1.4%. As shown in Figure 13, which compares the frequency response curves before and after the adjustment, by appropriately modifying the droop coefficient, the quasi-steady-state deviation Δf_{set} can be maintained at 0.23 Hz even under larger active power disturbances.

Under the scenario that the proportion of new energy sources participating in frequency regulation decreases, the overall frequency regulation capability of the system declines, leading to a shift in the demand for the droop coefficient.

TABLE 1 Error between the PSCAD model and SFR model.

Load increase	8 MW (10%)	12 MW (15%)	16 MW (20%)
Lowest frequency point	0 Hz	0.001 Hz	0.002 Hz
steady-state frequency value	0.001 Hz	0.002 Hz	0.002 Hz

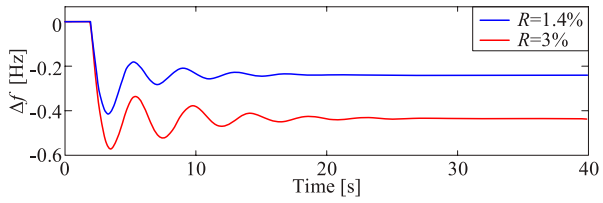

FIGURE 13
Comparison results after changing *R*.

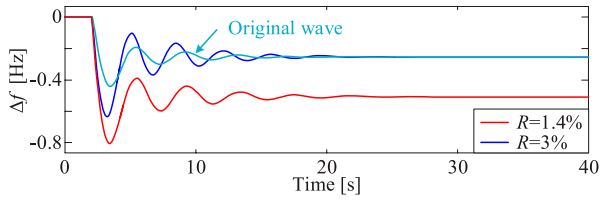

FIGURE 14
Comparison results after changing *K*.

Keeping the power disturbance scenario in IV.A unchanged, the proportion of wind turbines participating in frequency regulation K is set to 0.5 and the simulation results are shown in Figure 14.

Compared to the 10%-power-disturbance original waveform in IV.A, the decrease in K results in a deterioration of the system frequency stability, manifested by enlarged frequency fluctuations and an increase in Δf_{set}. To keep the Δf_{set} to its initial value of 0.23 Hz, substituting the relevant parameters into Equation 14, yields a required R of 1.4%. As shown in Figure 14, upon adjusting R using the proposed method, Δf_{set} is successfully reinstated to meet the original specification in IV.A, despite the reduction in K. However, due to the diminished participation of wind turbines in frequency regulation, the frequency fluctuation profile exhibits greater deviations compared to the original waveform.

To verify the impact of D on frequency regulation effectiveness, keeping the 10%-power-disturbance scenario outlined in Section 4.1 unchanged, the equivalent damping constant D is set to 0.5 and the simulation results are shown in Figure 15. According to Equation 15, the $\Delta f_{set}D$ is much smaller than ΔP, so the impact of $\Delta f_{set}D$ can be ignored, the droop regulation coefficient calculated by Equation 15 has not changed significantly. Thus, the droop coefficient doesn't need to be adjusted with the change of D.

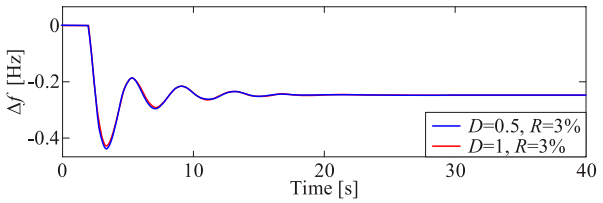

FIGURE 15
Comparison results after changing *D*.

5 Conclusion

This paper focuses on power systems with a high penetration of RES. A SFR is established to investigate the frequency response characteristics and the selection of droop coefficient post RES integration. The key contributions and innovations of this work are summarized as follows:

(1) For RES systems equipped with virtual inertia, an SFR model is established, which incorporates the participation of RES in frequency regulation. This SFR model is utilized to analyze the impact of various system equivalent parameters on frequency regulation. Through theoretical derivation, the relationship between the system's governing coefficient, renewable energy penetration rate, and frequency disturbances is established, revealing the required droop coefficient under different frequency disturbance and RES penetration rate.

(2) The accuracy of the proposed SFR model is experimentally validated, confirming its ability to accurately reflect the changes in system parameters such as larger power disturbances or variations in the RES participation ratio in frequency regulation. This ensures that the calculated governing coefficient effectively responds to these changes, maintaining the frequency regulation results within the operational requirements of the power system.

Data availability statement

The raw data supporting the conclusions of this article will be made available by the authors, without undue reservation.

Author contributions

YyS: Writing–original draft, Writing–review and editing. YZ: Writing–review and editing. SZ: Writing–review and editing. FL: Writing–review and editing. YuS: Writing–review and editing. YL: Writing–original draft, Writing–review and editing.

Funding

The author(s) declare that financial support was received for the research and/or publication of this article. This work was supported by Science and Technology Project of State Grid Sichuan Electric Power Company, Research on Key Technologies of Coordinated Active Support between Renewable Energy Clusters and LCC HVDC, (No. B7199624M001).

Conflict of interest

Authors YS, YZ, SZ, FL, YS and YL were employed by State Grid Sichuan Electric Power Company.

The author declares that this study received funding from State Grid Sichuan Electric Power Company. The funder participated in the study design, data collection, and data interpretation, and made the decision to submit the manuscript for publication.

Correction note

A correction has been made to this article. Details can be found at: 10.3389/fenrg.2025.1634727.

Generative AI statement

The author(s) declare that no Generative AI was used in the creation of this manuscript.

Publisher's note

All claims expressed in this article are solely those of the authors and do not necessarily represent those of their affiliated organizations, or those of the publisher, the editors and the reviewers. Any product that may be evaluated in this article, or claim that may be made by its manufacturer, is not guaranteed or endorsed by the publisher.

References

Ahmadi, H., and Ghasemi, H. (2014). Security-constrained unit commitment with linearized system frequency limit constraints. *IEEE Trans. POWER Syst.* 29 (4), 1536–1545. doi:10.1109/tpwrs.2014.2297997

Altaf, M. W., Arif, M. T., Saha, S., Islam, S. N., Haque, M. E., and Oo, A. M. T. (2022). Effective ROCOF-based islanding detection technique for different types of microgrid. *IEEE Trans. INDUSTRY Appl.* 58 (2), 1809–1821. doi:10.1109/tia.2022.3146094

Banarkar, H., Luo, C., and Ooi, B. T. (2006). "Power system response to wind power fluctuations," in *2005/2006 IEEE/PES transmission and distribution conference and exhibition*. Dallas, TX, USA.

Bo, W., Deyou, Y., and Guowei, C. (2020). Dynamic frequency constraint unit commitment in large-scale wind power grid connection. *Power Syst. Technol.* 44 (7), 2513–2519. doi:10.13335/j.1000-3673.pst.2019.2088

Chang-gang, L., Yu-tian, L., and Heng-xu, Z. (2009). Power system frequency response analysis based on the Direct current load flow. *Proc. CSEE* 29 (34), 36–41.

Fan, W., Haifeng, L., and Guoyi, X. (2020). Influence of key parameters of frequency control on frequency characteristics of power grid and sensitivity analysis. *Power Syst. Prot. Control* 48 (20), 1–8. doi:10.19783/j.cnki.pspc.191452

Grebla, M., Yellajosula, J. R. A. K., and Høidalen, H. K. (2020). Adaptive frequency estimation method for ROCOF islanding detection relay. *IEEE Trans. POWER Deliv.* 35 (4), 1867–1875. doi:10.1109/tpwrd.2019.2956200

Lin, J., Liu, B., and Xiao, H. (2023). Frequency characteristics of receiving end power grid for large-scale offshore wind power access. *Guangdong Electr. Power* 36 (3), 23–31.

Malekpour, M., Kiyoumarsi, A., and Gholipour, M. (2021). 'Analytical system frequency response model with virtual synchronous wind turbines. *IET Generation, Transm. Distribution* 15 (6), 2618–2631. doi:10.1049/gtd2.12204

Mei, Y., Gao, Y., and Li, C. (2024). Dynamic simulation study of the whole process of isolated network operation considering new energy connection. *Guangdong Electr. Power* 37 (1), 68–75.

Nguyen, N., Almasabi, S., and Mitra, J. (2015). "Estimation of penetration limit of variable resources based on frequency deviation," in *2015 north American power symposium (NAPS)* (Charlotte, NC, USA), 1–6.

Quan, R., and Pan, W. (2017). "A low-order system frequency response model for DFIG," in *Distributed wind power generation systems based on small signal analysis*. Energies.

Rongpeng, X., and Yang, W. (2024). Technical transformation of grid friendly power control system for doubly-fedInduction wind farm. *GUANGDONGELECTRICPOWER* 37 (6), 43–52.

Shi, Q., Li, F., and Cui, H. (2018a). Analytical method to aggregate multi-machine SFR model with applications in power system dynamic studies. *IEEE Trans. POWER Syst.* 33 (6), 6355–6367. doi:10.1109/tpwrs.2018.2824823

Shi, Q., Li, F., and Cui, H. (2018b). Analytical method to aggregate multi-machine SFR model with applications in power system dynamic studies. *IEEE Trans. Power Syst.* 33 (6), 6355–6367. doi:10.1109/tpwrs.2018.2824823

Wright, P. S., Davis, P. N., Johnstone, K., Rietveld, G., and Roscoe, A. J. (2019). Field measurement of frequency and ROCOF in the presence of phase steps. *IEEE Trans. Instrum. Meas.* 68 (6), 1688–1695. doi:10.1109/tim.2018.2882907

Wu, Z., Tian, E., and Chen, H. (2023a). Covert attack detection for LFC systems of electric vehicles: a dual time-varying coding method. *IEEE/ASME Trans. Mechatronics* 28 (2), 681–691. doi:10.1109/tmech.2022.3201875

Wu, Z., Tian, E., and Chen, H. (2023b). Control methods of VSC converters for grid-following/forming operation under grid-side faults in PV energy storage systems. *GUANGDONG Electr. POWER* 36 (12), 47–56.

Xiaolin, G., Ya, L., and Yang, F. (2021). Distributed robust unit commitment considering the whole process of inertia support and frequency regulations. *Proc. CSEE* 41 (12), 4043–4058. doi:10.13334/j.0258-8013.pcsee.200974

Xue, Y., Chen, Y., Zheng, W., Tang, Y., Li, Z., Yang, C., et al. (2024). Sharing of primary frequency response using LCC-HVDC. *IEEE Trans. POWER Deliv.* 1 (1), 2457–2469. doi:10.1109/tpwrd.2024.3415052

Yin, H., Qiu, W., Wu, Y., You, S., Tan, J., Hoke, A., et al. (2024). Field measurement and analysis of frequency and RoCoF for low-inertia power systems. *IEEE Trans. INDUSTRIAL Electron.* 71 (7), 7996–8006. doi:10.1109/tie.2023.3303622

Zhixuan, L., Chen, Y., and Ying, X. (2024). Review of frequency stability analysis and control research of multi-area asynchronous interconnected systems. *Power Syst. Technol.* 1 (1), 1–25.

Appendix

TABLE A1 Feeders parameter.

Number	R/pu	X/pu	B/pu
5–6	0.01	0.085	0.088
5–7	0.017	0.092	0.079
6–8	0.032	0.161	0.153
7–10	0.039	0.17	0.179
8–9	0.0085	0.072	0.0745
9–10	0.0119	0.1008	0.1045

TABLE A2 Transformers parameter.

Number	X/pu	Ratio	Capacity
1	0.0576	16/230	100
2	0.0625	16/230	80
3	0.0586	16/230	80

TABLE A3 Loads parameter.

Number	*P*/MW	*Q*/MW
6	30	11
7	20	7
9	25	8

TABLE A4 Speed control parameters of steam turbines.

Generator	R_s/pu	T_s/s	T_t/s
1	0.04	0.025	0.1
2	0.04	0.025	0.1
3	0.04	0.025	0.1

Nomenclature

Abbreviations

RES	Renewable Energy Sources
RoCoF	Rate of Change of Frequency
SFR	System Frequency Response
SG	Synchronous Generators
VSM	Virtual Synchronous Machine

Symbols

D	Load damping constant
Δf	Frequency variation
Δf_{set}	Steady-state frequency deviation
H_i	Respective inertia time constants
H_{sys}	Generator's equivalent inertia time constant
H_{SYS}	Equivalent inertia time constant for SFR
k_d	Virtual inertia coefficient
k_{RE}	Proportion for RES
k_{RE}	Proportion for SG
K_m	Gain coefficient for SG
K_R	Droop control coefficient for RES
K_{RES}	Gain coefficient for RES
n	The number of synchronous units
ΔP_e	Electromagnetic power output
ΔP_{e1}	Power output variation for RES
ΔP_L	Power variation of frequency-sensitive loads
ΔP_m	Mechanical power output
R	Equivalent droop coefficient
$S_{\mathrm{B(SG)}}$	total rated capacity of SG
S_i	Respective rated capacities
T_s	Inertia time constant for SG
T_{sys}	Equivalent response time constant for SFR
T_t	Time constant for SG
Δ_ω	Angular velocity variation

frontiers | Frontiers in Energy Research

TYPE Correction
PUBLISHED 19 June 2025
DOI 10.3389/fenrg.2025.1634727

OPEN ACCESS

APPROVED BY
Frontiers Editorial Office,
Frontiers Media SA, Switzerland

*CORRESPONDENCE
Yang Liu,
1015473572@qq.com

RECEIVED 25 May 2025
ACCEPTED 30 May 2025
PUBLISHED 19 June 2025

CITATION
Song Y, Zhang Y, Zhang S, Liu F, Su Y and Liu Y (2025) Correction: System frequency response model and droop coefficient setting considering renewable energy participation in frequency regulation.
Front. Energy Res. 13:1634727.
doi: 10.3389/fenrg.2025.1634727

Correction: System frequency response model and droop coefficient setting considering renewable energy participation in frequency regulation

Yuyan Song, Yongjie Zhang, Shuai Zhang, Fang Liu, Yunche Su and Yang Liu*

State Grid Sichuan Electric Power Company, Sichuan, China

KEYWORDS

renewable energy sources, SFR, droop coefficient, WSCC, VSM

A Correction on
System frequency response model and droop coefficient setting considering renewable energy participation in frequency regulation

by Song Y, Zhang Y, Zhang S, Liu F, Su Y and Liu Y (2024). Front. Energy Res. 12:1521209. doi: 10.3389/fenrg.2024.1521209

In the published article, there was an error in **Affiliation(s)** Instead of "[State Grid Sichuan Economic Research Institute, Sicuan, China]", it should be "[State Grid Sichuan Electric Power Company, Sichuan, China]".

In the published article, there was an error in the **Funding** statement. [The author(s) declare that no financial support was received for the research and/or publication of this article]. The correct Funding statement appears below.

Funding

The author(s) declare that financial support was received for the research and/or publication of this article. This work was supported by Science and Technology Project of State Grid Sichuan Electric Power Company, Research on Key Technologies of Coordinated Active Support between Renewable Energy Clusters and LCC HVDC, (No. B7199624M001).

In the published article, there was an error in the Conflict of Interest statement. The corrected statement appears below.

Conflict of interest

Authors YS, YZ, SZ, FL, YS and YL were employed by State Grid Sichuan Electric Power Company.

The author declares that this study received funding from State Grid Sichuan Electric Power Company. The funder participated in the study design, data collection, and data interpretation, and made the decision to submit the manuscript for publication.

Publisher's note

frontiers | Frontiers in Energy Research

TYPE Original Research
PUBLISHED 20 January 2025
DOI 10.3389/fenrg.2024.1517505

OPEN ACCESS

EDITED BY
Minghao Wang,
University of Macau, China

REVIEWED BY
Carlos Andres Garcia-Vazquez,
University of Cádiz, Spain
Quan Li,
University College Dublin, Ireland

*CORRESPONDENCE
Fengyi Deng,
2623615326@qq.com

RECEIVED 26 October 2024
ACCEPTED 27 December 2024
PUBLISHED 20 January 2025

CITATION
Zhai B, Liang S, Xu Z, Deng F, Chen J and Wu H (2025) Analysis of transient characteristics and fault ride-through control of hybrid grid-tied converters with grid-following and grid-forming.
Front. Energy Res. 12:1517505.
doi: 10.3389/fenrg.2024.1517505

Analysis of transient characteristics and fault ride-through control of hybrid grid-tied converters with grid-following and grid-forming

Baoyu Zhai[1], Shuchao Liang[1], Zhi Xu[1], Fengyi Deng[2]*, Junru Chen[2] and Haiyang Wu[1]

[1]Electric Power Research Institute of State Grid Xinjiang Electric Power Co., Ltd., Urumqi, Xinjiang, China, [2]Department of Electrical Engineering, Xinjiang University, Urumqi, Xinjiang, China

When the Grid-Following (GFL) and the Grid-Forming (GFM) converters are hybrid-connected to the grid, they are coupled through the grid impedance. During grid faults, the transient characteristics of the two converters become more complex due to this coupling. If one of the converters experiences stability issues, it affects the other, making fault ride-through challenging. A mathematical model for the hybrid grid-connected system of the two converters is first established to analyze the existence conditions of the equilibrium point. Using the phase-plane method, the mutual influence mechanism during faults is revealed. Subsequently, a method to adjust the GFM phase angle based on the degree of voltage sag is proposed, which also improves the phase-locked loop (PLL) of the GFL. The influence of GFL current injection is considered to limit the GFM fault current, thereby achieving hybrid fault ride-through control. Finally, the simulation verifies the effectiveness of the proposed control strategy. The results show that the proposed method can adjust the phase angle to support the grid, ensuring that the GFM outputs more reactive current within the maximum allowable current range. Meanwhile, the GFL injects current according to grid guidelines, effectively preventing overcurrent and phase angle instability of the converters.

KEYWORDS

grid-following converter, grid-forming converter, hybrid grid-connected system, stability, hybrid fault ride-through control

1 Introduction

With the implementation of carbon peaking and carbon neutrality policies, the development and application of renewable energy have progressively become essential pathways toward achieving green, low-carbon, and sustainable development goals (Huang et al., 2024). The share of non-synchronous generation in power systems is steadily increasing, resulting in high proportions of renewable energy and power electronic devices becoming defining features of modern power systems (Gu and Green, 2023). A high proportion of new energy and power electronic equipment has become a notable characteristic of power systems. In order to provide the system support, a serial of the control is implemented into the Inverter-Based Resources (IBR). In general, the control of

the IBR can be classified into the GFL and GFM. It is worth noting that using GFL as the main grid - connected devices does not provide sufficient inertia and damping for the system, resulting in a further decrease in system inertia, which jeopardizes the safe operation of the power system. GFM, which possess the characteristics of a synchronous generator, have garnered widespread attention. Compared to GFL, they can effectively function as a voltage source, allowing them to regulate system voltage and frequency and provide necessary inertia and damping support. Nevertheless, GFL still have advantages that GFM cannot replace. On the other hand, the current new energy power stations are equipped with GFL, making it impractical to replace them all with GFM. Therefore, a feasible alternative is to modify some of the already installed converters to grid-forming control. This implies that in future power systems, both grid-following and GFM will coexist (Zhao and Flynn, 2022).

Both GFL and GFM converters achieve frequency and voltage support functions. However, due to their different roles in the power system, their transient responses will also differ (Wei et al., 2024). The GFL behaves as a controlled current source, which uses the PLL to detect the grid state on the frequency and voltage and then accordingly provides a passive support (Kim et al., 2024). While the GFM behaves as a controlled voltage source, of which mechanism is similar with the power-angle transients of the synchronous generator and thus, which naturally can provide an active support (Zhang et al., 2023). In the event of a grid fault, a synchronous generator can inject 6 to 8 times its rated current (pu) to support the grid (Taul et al., 2020). However, the overcurrent tolerance of converters is relatively low. Without proper control, this could lead to disconnection of renewable energy generation equipment from the grid or damage to the converters. To address this, IEEE standard 2,800–2022 provides detailed technical requirements for renewable energy generation equipment regarding fault ride-through capabilities (IEEE, 2022). Currently, research mainly focuses on the transient processes of single GFL or single GFM converters during fault ride-through, with an emphasis on the control of fault current and power angle. For GFL, Zhang and Schuerhuber (2023) enhances system stability during grid faults and improves post-fault recovery performance by adjusting current injection via PLL frequency feedback. However, the steady-state operating points and stability become challenging to predict. Xu et al. (2021), by removing the frequency feedback loop and employing frequency-locking techniques, fixes the PLL frequency to maintain its output at the state of the previous moment. Nonetheless, this approach struggles to meet the requirements of grid codes. He et al. (2021) suggests locking only the integral part of the PLL during faults, but this method fails when there is no equilibrium point after the fault. Gao et al. (2023) adjusts the ratio of active to reactive current to match the grid impedance ratio, which helps ensure the existence of a post-fault equilibrium point. However, this approach still falls short of adhering to grid codes. For GFM, Li et al. (2022) highlights that under fault conditions, grid-forming control may need to switch to grid-following control. A backup PLL is essential for achieving seamless transitions, but stability issues may arise, particularly in weak grid environments. However, this process requires a backup PLL and may face stability issues in weak grid environments. Xi et al. (2022) adopt a current limiting method in the current loop of the converter's double closed-loop control to limit fault currents. Lu et al. (2023) introduces virtual impedance in the current control loop (CCL) to dynamically adjust the voltage compensation value, effectively limiting high-frequency transient overcurrent. Zheng et al. (2023) enhances the low voltage ride-through (LVRT) strategy by incorporating current reference limitation functionality within the current control loop, successfully constraining the peak value of short-circuit currents. However, the above methods turn the voltage source into a current source, making power control difficult, reducing stability, and potentially causing instability. Chen et al. (2020) proposes a strategy using voltage limiting to control fault current, locking the reactive voltage droop, and calculating the reference voltage based on the maximum allowable current. For hybrid grid-tied converters (HGCs), that is, GFL and GFM are coupled with each other through the grid impedance and integrated into the same power system. Cheng et al. (2022) analyzes the transient voltage angle stability of GFL and GFM converters. Tian et al. (2023) studies the impact of steady-state operating points and control parameters of GFL and GFM modes on islanded microgrid stability and proposes a virtual impedance design methodology to enhance system stability. However, there are relatively few studies on the fault ride-through problem under the hybrid grid conditions where converters based on GFM and GFL controls coexist. In fact, during faults, the cooperation between converters with different control strategies can provide better service to the grid.

To overcome the aforementioned limitations, this study introduces a hybrid fault ride-through control strategy aimed at improving the issue of fault ride-through during symmetrical voltage dips when low voltage faults occur in the grid. The main contributions of this strategy are as follows:

- A hybrid grid-tied system model consisting of GFL and GFM converters operating in parallel is developed in the context of their coexistence in power systems. Transient stability analysis is performed to investigate the coupling effects between the two converters through grid impedance.
- The phase plane trajectories of the GFL and GFM converters under fault conditions are plotted to visually illustrate the dynamic characteristics of both converters during faults. This approach reveals how the mutual coupling between GFM and GFL influences system stability.
- A fault ride-through strategy is proposed, which involves adjusting the GFM power angle based on the degree of voltage dip and incorporating this adjustment into the GFL to improve its PLL. Additionally, the strategy considers the impact of GFL current injection and imposes fault current limitations on the GFM, achieving coordinated fault ride-through control for the hybrid system.
- A hybrid grid-tied system model, integrating GFL and GFM converters, is constructed in Matlab/Simulink. The output characteristics of GFL and GFM converters during faults are analyzed, and the proposed fault ride-through control strategy is validated through simulation experiments.

The structure of this paper is organized as follows: Section 2 constructs the basic model of the grid-following/grid-forming converter HGS. Section 3 analyzes the interaction mechanism

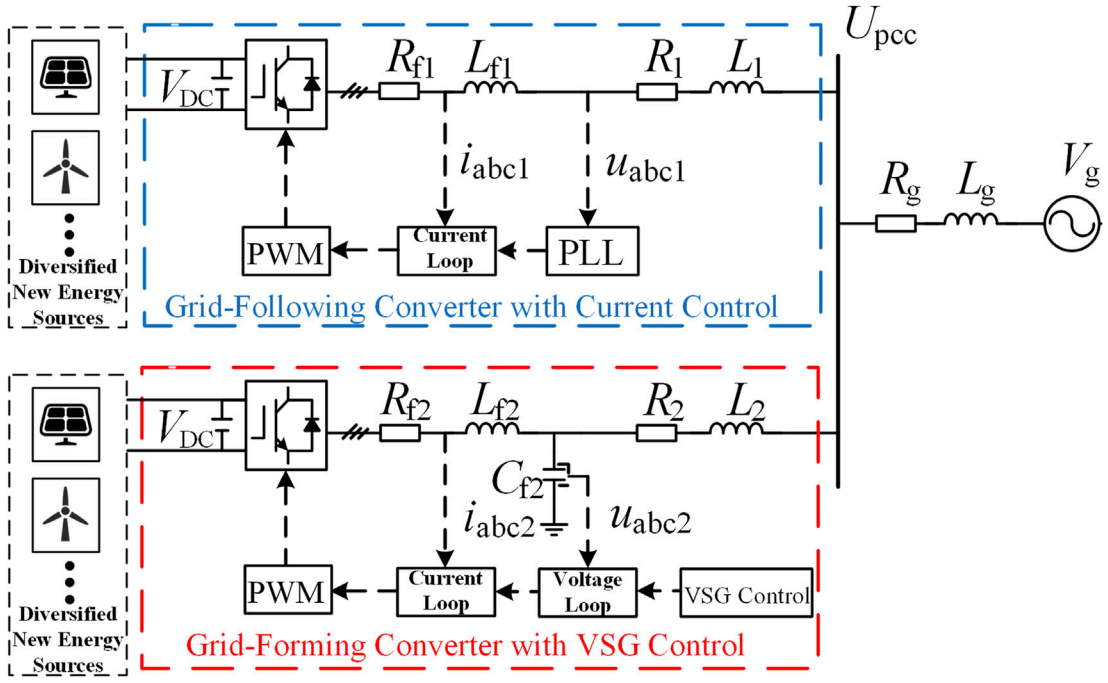

FIGURE 1
Parallel topology of grid-connected converters with GFL and GFM.

between GFL and GFM when a low-voltage fault occurs in the power grid. Section 4 proposes a GFM power angle control considering the influence of GFL current injection and a hybrid fault ride-through control strategy based on an improved grid-forming phase-locked loop. During the fault period, this strategy can not only ensure the power angle stability and limited fault current of the GFM but also enable the GFL to inject current in accordance with the grid guidelines. Section 5 verifies the correctness and effectiveness of the proposed control strategy through simulation.

2 The connection of grid-forming and GFL with the system

2.1 Main circuit system topology

The research object of this paper is the parallel system of grid-following and GFM, as illustrated in Figure 1. In this parallel system, the DC-side power of the two converters can be supplied by photovoltaic panels, wind turbines, energy storage devices, or other sources. However, since the focus of this study lies in the characteristics of the converters on the AC side, the structure of the DC-side power sources is disregarded.

The fundamental concept of the HGS system is to combine grid-following and grid-forming control strategies in parallel, thereby integrating the respective characteristics of these two control approaches. The grid-following converter employs a PLL for synchronization control, and its control structure includes sampling, the PLL, inner current control loops, and a PWM generator. In contrast, the grid-forming converter adopts a more mature Virtual Synchronous Generator (VSG) control strategy. Its control circuit primarily consists of active power and reactive power loops, coordinate transformation, dual-loop voltage and current control, and PWM signal modulation. The two converters are connected to the main power grid via PCC.

In Figure 1, V_{DC} is a constant DC voltage; R_{f1}, L_{f1}, R_{f2}, and L_{f2} are the filter resistances and filter inductances for the GFL and GFM converters, respectively; C_{f2} is the filter capacitor for the GFM converter; R_1, L_1, R_2, and L_2 are the line resistances and line inductances for the GFL and GFM converters, respectively; R_g and L_g represent the line resistance and inductance between the PCC and the grid; U_{pcc} is the voltage at the PCC; i_{abc1} and i_{abc2} are the converter-side currents for the GFL and GFM converters, respectively; u_{abc1} and u_{abc2} are the output voltages for the GFL and GFM converters, respectively; V_g is the grid voltage.

2.2 Grid-following converter based on current control

The control system of the GFL is shown in Figure 2. The core of the GFL control strategy is the PLL, and its control structure is shown in Figure 3. The PLL synchronizes the generating unit with the grid by estimating and tracking the phase of the grid voltage u_{abc1}. The outer-loop power control compares the reference values with the actual values to generate an error signal, which serves as the reference for the inner-loop current control. The inner-loop current control generates modulation signals, which are then processed by the PWM stage.

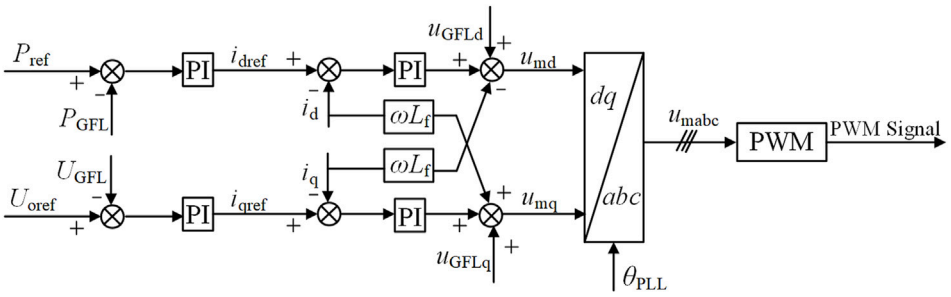

FIGURE 2
The control system of the GFL.

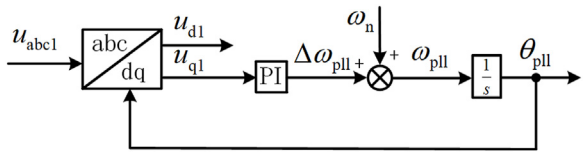

FIGURE 3
Schematic diagram of phase locked loop.

The mathematical model of the PLL can be expressed as follows:

$$\begin{cases} \dfrac{d\theta_{pll}}{dt} = \omega_{pll} \\ \dfrac{d\omega_{pll}}{dt} = k_i u_{q1} + k_p \dfrac{du_{q1}}{dt} \end{cases} \tag{1}$$

In Equation 1: θ_{pll} is the output phase angle of the PLL; ω_{pll} is the output angular frequency of the PLL; u_{d1} and u_{q1} are the d-axis and q-axis voltages of the grid-connected point, respectively; k_i and k_p are the proportional and integral gains of the PI controller. θ_{pll} is used as the angle for the Park transformation, achieving decoupled control of active and reactive power by aligning u_{abc1} with the d-axis, ensuring that $u_{q1} = 0$.

The PLL is used to provide the reference angle for the Park transformation. By aligning u_{abc1} to the d-axis, such that $u_{q1} = 0$, decoupled control of active and reactive power is achieved. This ensures precise power regulation and synchronization of the system with the grid.

$$\begin{cases} i_{dref} = k_{p\_p}(P_{ref} - P_{GFL}) + k_{i\_p}(P_{ref} - P_{GFL})/s \\ i_{dref} = k_{p\_udc}(U_{dcref} - U_{dc}) + k_{i\_udc}(U_{dcref} - U_{dc})/s \end{cases} \tag{2}$$

$$\begin{cases} i_{qref} = k_{p\_uo}(U_{oref} - U_{GFL}) + k_{i\_uo}(U_{oref} - U_{GFL})/s \\ i_{qref} = k_{p\_q}(Q_{ref} - Q_{GFL}) + k_{i\_q}(Q_{ref} - Q_{GFL})/s \end{cases} \tag{3}$$

In Equations 2, 3, i_{dref} and i_{qref} represent the d-axis and q-axis reference currents, respectively. k_{p_p} and k_{i_p}, k_{p_udc} and k_{i_udc}, k_{p_uo} and k_{i_uo}, and k_{p_q} and k_{i_q} are the proportional and integral gains of the respective PI controllers. P_{ref} denotes the active power reference value, and Q_{ref} represents the reactive power reference value. U_{dcref} is the reference value for the DC-side voltage, while U_{oref} is the reference value for the PCC voltage. Finally, U_{GFL} indicates the output voltage magnitude of the GFL converter.

The mathematical model of the inner current loop can be expressed as follows:

$$\begin{cases} u_{md} = u_{GFLd} + k_{p\_i}(i_{dref} - i_d) + k_{i\_i}(i_{dref} - i_d)/s - \omega L_f i_q \\ u_{mq} = u_{GFLq} + k_{p\_i}(i_{qref} - i_q) + k_{i\_i}(i_{qref} - i_q)/s + \omega L_f i_d \end{cases} \tag{4}$$

In Equation 4, u_{md} and u_{mq} represent the d-axis and q-axis components of the modulation signal, respectively. k_{p_i} and k_{i_i} are the proportional and integral gains of the PI controller, respectively. $L_f i_q$ and $L_f i_d$ denote the decoupling control terms.

2.3 Grid-forming converter based on VSG control

The control part of a VSG includes an active power loop, a reactive power loop, dual voltage-current control loops, and PWM signal modulation. The core of the control is the active and reactive power loops. VSG achieves synchronization with the grid by mimicking the rotor characteristic equations of a synchronous generator. Consequently, a grid-forming converter based on virtual synchronous generator control possesses the external characteristics of a synchronous generator. The schematic diagram is shown in Figure 4.

The control system of GFM converter is shown in Figure 5. The voltage control, current control, and PWM generator of the GFM converter are consistent with those of the grid-following converter.

The GFM converter achieves control over its output active and reactive power through the active power loop and reactive power loop. The mathematical model of the active power loop under VSG control can be expressed as follows:

$$\begin{cases} \dfrac{d\theta_{vsg}}{dt} = \omega_{vsg} \\ J\dfrac{d\omega_{vsg}}{dt} = P_{set} - P - D_p(\omega_{vsg} - \omega_n) \end{cases} \tag{5}$$

In Equation 5: θ_{vsg} is the output phase angle of the VSG; ω_{vsg} is the derivative of θ_{vsg}; P_{set} is the input mechanical power; P is the output active power of the VSG; ω_n is the nominal angular frequency; J is the moment of inertia; and D_p is the damping coefficient.

The active power loop adjusts θ_{vsg} to regulate the output active power P of the VSG, ultimately ensuring that $P = P_{set}$.

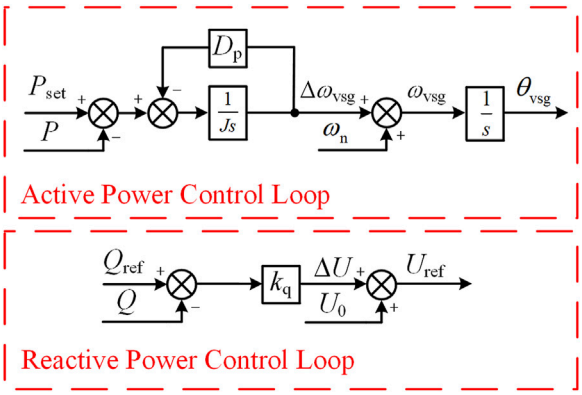

FIGURE 4
Virtual synchronous machine control schematic diagram.

The mathematical model of the reactive power loop can be expressed as:

$$\boldsymbol{U_{ref} = U_0 + k_q (Q_{ref} - Q)} \tag{6}$$

In Equation 6: U_{ref} is the output voltage of the VSG; U_0 is the set value of the output voltage; k_q is the droop coefficient of the reactive power loop; Q_{ref} is the reactive power reference value; and Q is the output reactive power of the VSG.

The reactive power loop adjusts the output voltage reference value based on the output reactive power.

3 Mathematical modeling of HGS

3.1 The mathematical model and transient characteristics of the grid-connected system

The bandwidth of the current loop in the GFL is significantly larger than the bandwidth of the PLL. By ignoring the dynamic process of the current loop, the GFL can be approximated as a current source. Similarly, in the GFM, the adjustment speed of the inner voltage and current loops is much faster than that of the active and reactive power loops. By neglecting the dynamic process of the inner voltage and current loops, the GFM can be approximated as a voltage source (Li et al., 2021). Circuit impedance is considered negligible, and the phase angle of the grid voltage is taken as the reference angle (Gursoy et al., 2023).The equivalent circuit diagram of Figure 1 is shown in Figure 6.

In this figure, I_1 is the RMS value of the output current of the current-controlled converter; U_1 is the RMS value of the output voltage of the GFL; θ_{pll} is the phase angle difference between the PLL and the grid, corresponding to the power angle of a synchronous generator, and for convenience, it will be referred to as the power angle hereafter; φ_1 is the phase angle difference between voltage U_1 and current I_1; U_2 is the RMS value of the output voltage of the GFM; δ_{vsg} is the power angle of the GFM; V_g is the RMS value of the grid voltage.

According to the superposition theorem, the PCC voltage $U_{pcc}\angle\delta_{pcc}$ in Figure 6 can be expressed in the stationary reference frame as:

$$\boldsymbol{U_{pcc}\angle\delta_{pcc} = jk_1 I_1 \angle(\delta_{pcc} + \varphi_1) + k_2 U_2 \angle\delta_{vsg} + k_3 V_g \angle 0°} \tag{7}$$

In Equation 7: $k_1 = \omega_{pll}\frac{L_2 L_g}{L_2+L_g}$; $k_2 = \frac{L_g}{L_2+L_g}$; $k_3 = \frac{L_2}{L_2+L_g}$.

The point where the PLL measures the voltage is $U_1\angle\delta_{pll}$, which can be expressed as:

$$\boldsymbol{U_1\angle\delta_{pll} = jk_4 I_1 \angle(\delta_{pll} + \varphi_1) + k_2 U_2 \angle\delta_{vsg} + k_3 V_g \angle 0°} \tag{8}$$

In Equation 8: $k_4 = \omega_{pll} L_1 + \omega_{pll}\frac{L_2 L_g}{L_2+L_g}$.

Transforming Equation 8 to the dq rotating reference frame based on the PLL, the q-axis voltage of U_1 can be obtained as:

$$\boldsymbol{u_{q1} = k_4 i_{d1} + k_2 U_2 \sin(\delta_{vsg} - \delta_{pll}) - k_3 V_g \sin\delta_{pll}} \tag{9}$$

In Equation 9: typically, δ_{vsg}, $\delta_{pll}\in[0,\pi/2]$.

Comparing Equation 9 with the case of a single GFL connected to the grid, it can be observed that the q-axis voltage u_{q1} of the GFL has an additional impedance drop coupling term (Paquette and Divan, 2015). The magnitude of this coupling term is related to k_2, U_2, δ_{vsg}, and δ_{pll}, indicating that the power angle of the PLL is also influenced by the GFM power angle δ_{vsg}.

From Figure 6, the single-phase output complex power of the GFM can be expressed as:

$$\dot{\boldsymbol{S}}_2 = \boldsymbol{U_2\angle\delta_{vsg}}\left(\frac{\boldsymbol{U_2\angle\delta_{vsg} - U_{pcc}\angle\delta_{pcc}}}{\boldsymbol{jX_2}}\right)^* \tag{10}$$

In Equation 10, $X_2 = \omega_n L_2$, where ω_n is the nominal angular frequency.

Substituting Equation 7 into Equation 10, we obtain:

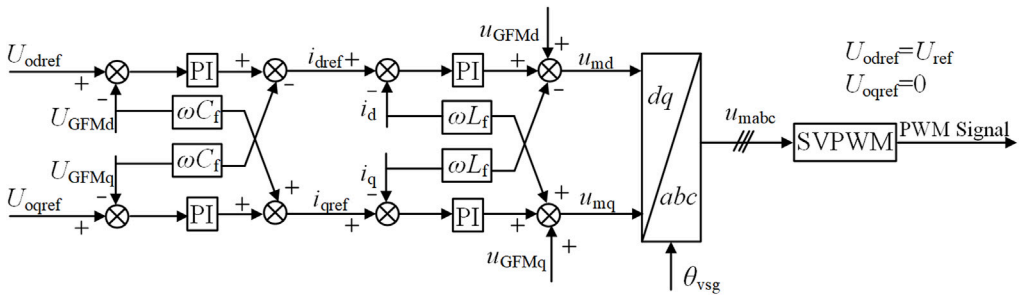

FIGURE 5
The control system of GFM converter.

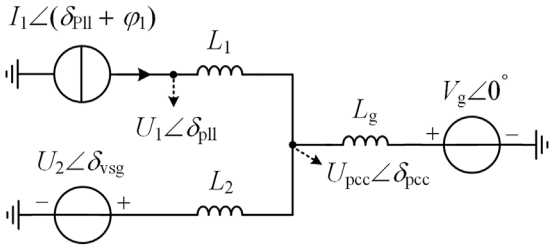

FIGURE 6
HGS equivalent circuit diagram.

$$P_2 = \frac{k_3 U_2 V_g}{X_2}\sin\delta_{vsg} - \frac{k_1 U_2 I_1}{X_2}\cos(\delta_{vsg}-\delta_{pll}-\varphi_1) \quad (11)$$

$$Q_2 = \frac{U_2^2 - k_2 U_2^2}{X_2} - \frac{k_3 U_2 V_g}{X_2}\cos\delta_{vsg} - \frac{k_1 U_2 I_1}{X_2}\sin(\delta_{vsg}-\delta_{pll}-\varphi_1) \quad (12)$$

From Equations 11, 12, it can be seen that the GFL affects both the active power loop and the reactive power loop of the GFM. Compared to the single machine case, an additional active power coupling term and a reactive power coupling term are introduced. The magnitude of this impact is related to k_1、U_2、I_1、X_2、δ_{vsg}, δ_{pll}, and φ_1. The power angle of the GFM is also influenced by the output current I_1 of the GFL. By calculating the three-phase active power using Equation 11 and substituting it into Equation 5, it can be obtained that the GFM in steady state satisfies Equation 13.

$$P_{set} - 3\frac{k_3 U_2 V_g}{X_2}\sin\delta_{vsg} + 3\frac{k_1 U_2 I_2}{X_2}\cos(\delta_{vsg}-\delta_{pll}-\varphi_1) = 0 \quad (13)$$

In summary, the transient analysis model of the HGS can be obtained, as shown in Figure 7. It can be seen that the integration of the GFL adds a power coupling term to the GFM; similarly, the GFM adds an impedance drop coupling term to the GFL (Zhang et al., 2024).

3.2 Transient stability analysis considering coupling effects

Setting Equation 9 to 0, the condition for the PLL to have an equilibrium point can be obtained as:

$$\sqrt{\left(\frac{k_2 U_2}{k_4}\right)^2 + \left(\frac{k_3 V_g}{k_4}\right)^2 + 2\frac{k_2 k_3 U_2 V_g}{k_4^2}\cos\delta_{vsg}} \geq i_{d1} \quad (14)$$

When the GFM operates stably, $\delta_{vsg} \in [0, \pi/2]$. If $i_{d1} > \frac{k_2 U_2 + k_3 V_g}{k_4}$, then Equation 14 cannot be satisfied, and there is no equilibrium

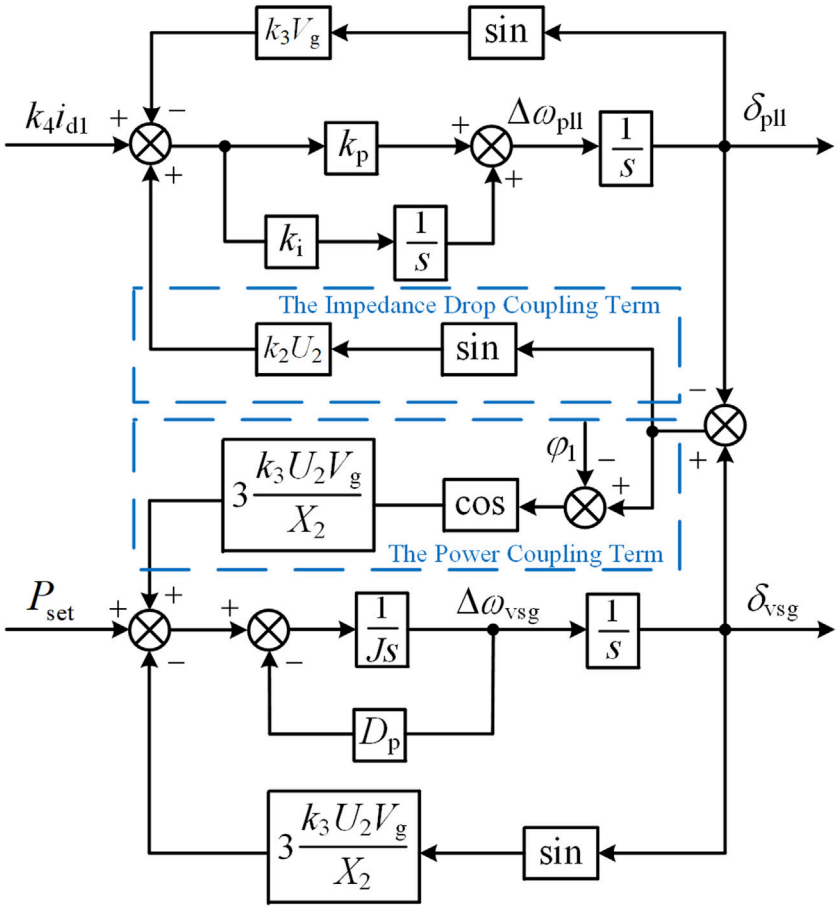

FIGURE 7
Transient analysis model of HGS.

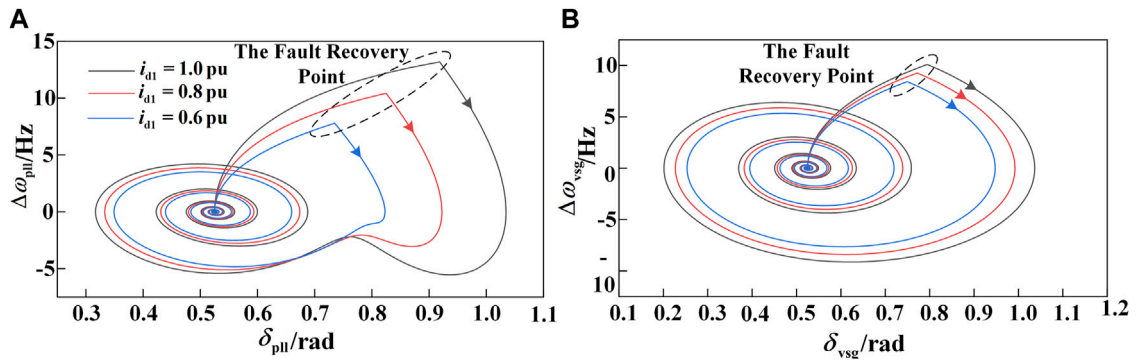

FIGURE 8
Phase portrait of different i_{d1} of GFL. **(A)** The phase plane of the GFL under fault conditions. **(B)** The phase plane of the GFM under fault conditions.

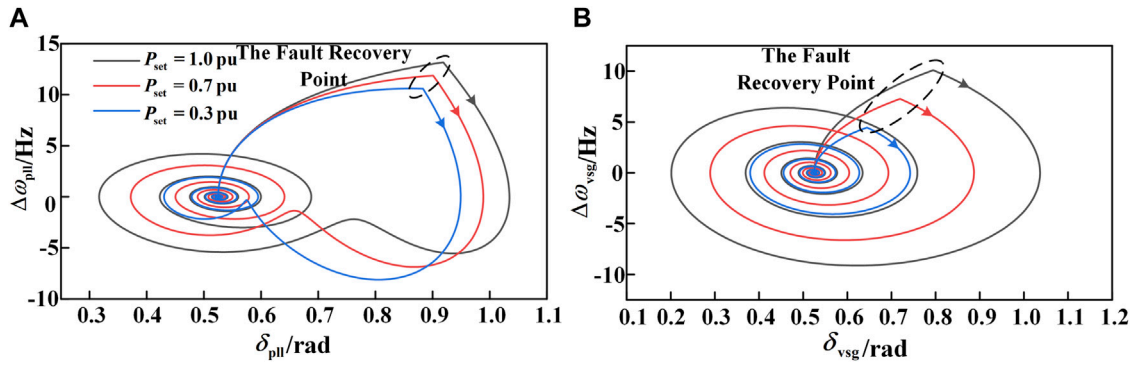

FIGURE 9
Phase portrait of different P_{set} of GFM. **(A)** The phase plane of the GFL under fault conditions. **(B)** The phase plane of the GFM under fault conditions.

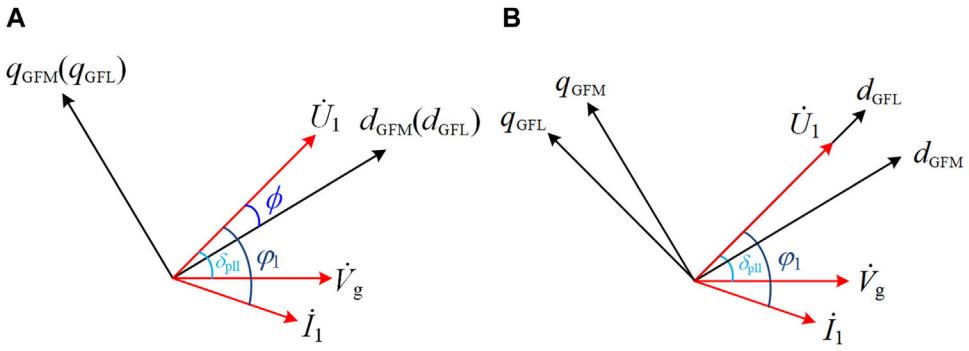

FIGURE 10
Voltage vector diagram. **(A)** Based on the GFM rotating coordinate system. **(B)** Based on the GFL rotating coordinate system.

point for the PLL. If $i_{d1} \leq \frac{k_2U_2+k_3V_g}{k_4}$, then Equation 14 can be satisfied, and an equilibrium point exists for the PLL.

From Equation 13, it can be seen that the presence of I_1 increases δ_{vsg}, reducing the stability margin of the GFM. The magnitude of δ_{vsg} is directly proportional to k_1, U_2, and I_1, and inversely proportional to X_2. If I_1 is too large, it may cause the initially stable GFM to lose power angle stability. If the GFM loses power angle stability due to a fault or other reasons, its output angle δ_{vsg} increases indefinitely. As

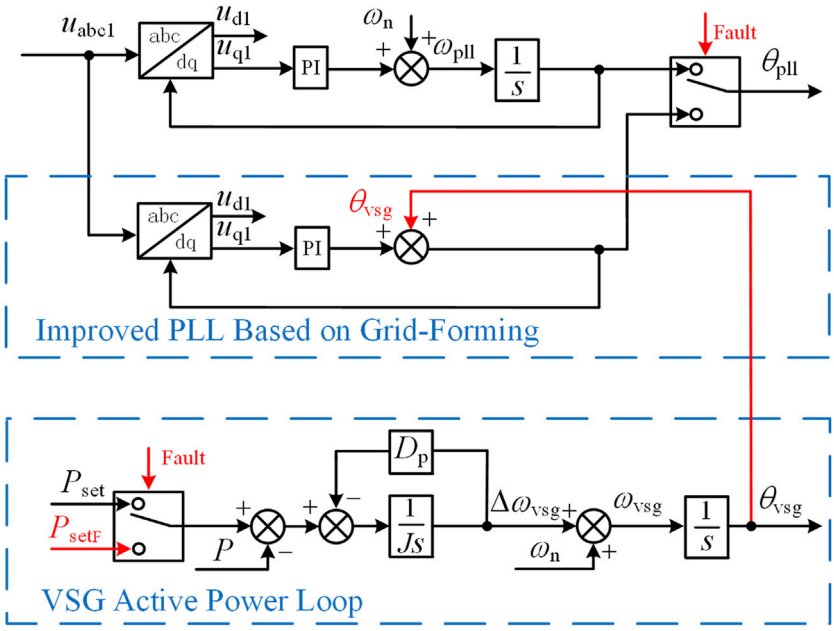

FIGURE 11
HGS transient power angle control.

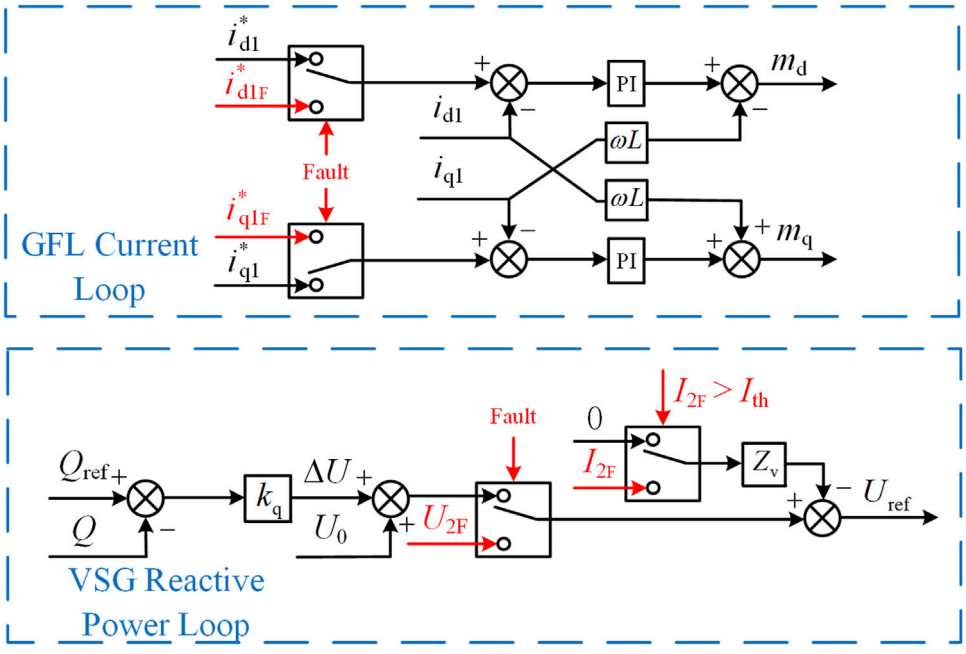

FIGURE 12
HGS fault current control.

indicated by Equation 14, when $\delta_{vsg} = 2k\pi + \pi$, $k \in Z$, the impact on the PLL is maximized, leading to two possible situations: ① If Equation 14 is not satisfied, the GFL becomes unstable. ② If Equation 14 is satisfied, since δ_{vsg} increases indefinitely, Equation 9 remains in a state of adjustment and cannot stabilize or converge to 0, indicating that the GFL becomes unstable.

Therefore, transient instability in the GFM will trigger a chain reaction, causing transient instability in the GFL.

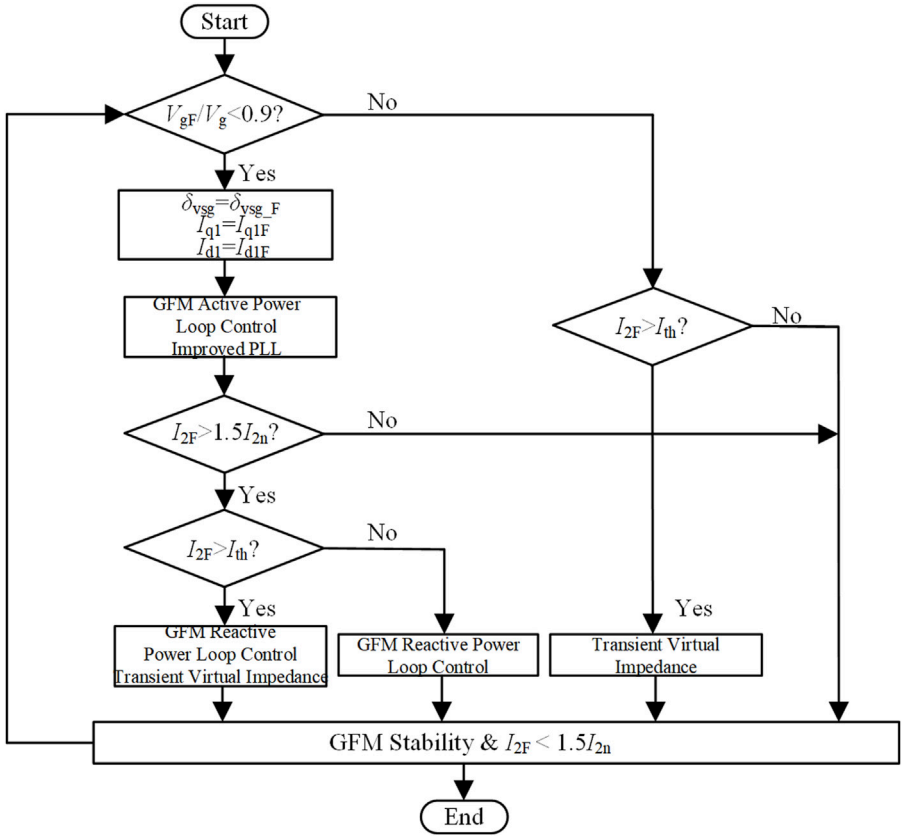

FIGURE 13
Fault ride-through control flowchart.

From Equation 13, the GFM has a steady-state point when the following condition is satisfied:

$$\sqrt{9\left(\frac{k_3U_2V_g}{X_2}\right)^2+9\left(\frac{k_1U_2I_1}{X_2}\right)^2-18\frac{k_1k_3U_2^2V_gI_1}{X_2^2}\sin\left(\delta_{pll}+\varphi_1\right)}\geq P_{set} \tag{15}$$

When the GFL operates stably, $\delta_{pll} \in [0, \pi/2]$ and $\varphi_1 \in [-\pi/2, 0]$. If $P_{set} > 3\frac{k_3U_2V_g+k_1U_2I_1}{X_2}$, Equation 15 cannot be satisfied, and there is no equilibrium point for the GFM. If $P_{set} \leq 3\frac{k_3U_2V_g+k_1U_2I_1}{X_2}$, then Equation 15 can be satisfied, and an equilibrium point exists for the GFM.

From Equation 9, it can be seen that when $\delta_{vsg} > \delta_{pll}$, δ_{pll} increases, and the stability margin of the GFL decreases. When $\delta_{vsg} < \delta_{pll}$, δ_{pll} decreases, and the stability margin of the GFL increases. When $\delta_{vsg} = \delta_{pll}$, the coupling term is zero, and δ_{pll} is not affected by the GFM. If the GFL loses synchronization stability due to a fault or other reasons, the PLL will have no equilibrium point, causing the power angle δ_{pll} to increase indefinitely, thereby affecting the GFM. There are two possible scenarios: ① If Equation 15 is not satisfied, the GFM becomes unstable. ② If Equation 15 is satisfied, due to δ_{pll} increasing indefinitely, Equation 13 remains in a state of adjustment and cannot converge to zero, indicating that the GFM becomes unstable.

Therefore, when the GFL experiences transient instability, the increase in its output phase also causes the GFM to experience transient instability.

In summary, it is essential to ensure the simultaneous stability of both converters; instability in either one will affect the stability of the other.

Additionally, during grid voltage sag, the GFM, being a voltage source type, can experience transient overcurrent and steady-state overcurrent. Under fault conditions, the circuit satisfies:

$$(L_2+L_g)\frac{di_{2F}}{dt}=u_{2F}-v_{gF}-L_g\frac{di_1}{dt} \tag{16}$$

In Equation 16: i_{2F} is the instantaneous value of the GFM output current during a fault; u_{2F} is the instantaneous value of the GFM output voltage during a fault; v_{gF} is the instantaneous value of the grid voltage during a fault; i_1 is the instantaneous value of the output current of the current-controlled converter.

From Equation 16, it can be seen that the presence of the GFL can reduce the fault current of the GFM.

During a fault, reducing the GFL output current i_{d1} not only ensures the existence of the PLL equilibrium point, but also, as seen from Equation 9, the reduction of i_{d1} can slow down the acceleration process of the GFL output ω_{pll} during the fault, thereby reducing the deviation of ω_{pll}. Since the inertia of the GFM is much larger than the equivalent inertia of the GFL, the increase rate of δ_{vsg} is slower than that of δ_{pll} during a fault. Additionally, because the fault duration is short, during the fault, $(\delta_{vsg} - \delta_{pll}) \in [-\pi/2, 0]$ (Cheng et al., 2022). For purely active power output, $\varphi_1 = 0$, and the reduction in i_{d1} is much greater than the change in the cosine function, so the effect of

TABLE 1 Parameters of HGS.

Parameter	Value
DC bus voltage (VDC/V)	800
Grid voltage amplitude (V_g/V)	311
Grid angular frequency [ω_g/(rad/s)]	314
GFL line inductance (L_1/mH)	3.2
GFM line inductance (L_2/mH)	3.2
Grid inductance (L_g/mH)	4
GFM moment of inertia [J/(kg/m^2)]	5
GFM active power damping coefficient (D_p)	130
GFM reactive power droop coefficient (k_q)	0.01

the cosine function can be ignored. Therefore, when i_{d1} is reduced, the power coupling term in Equation 11 is also reduced. From Equation 5, it can be seen that this also helps to slow down the acceleration of the GFM output ω_{vsg} during the fault, reducing the deviation of ω_{vsg}. The phase plane diagram of the HGS under different i_{d1} conditions during a fault is shown in Figure 8.

From Figure 8, it can be observed that reducing the active current of the GFL can slow down the acceleration process of both the GFL and GFM during a fault, thereby improving the synchronization stability of the two converters. Moreover, the smaller the i_{d1}, the better the synchronization stability of the two converters; conversely, the larger the i_{d1}, the worse the synchronization stability of the two converters.

During a fault, reducing the input mechanical power P_{set} of the GFM not only ensures the existence of the GFM's equilibrium point but, as shown in Equation 5, also slows down the acceleration process of the GFM's output ω_{vsg} during the fault, reducing the deviation of ω_{vsg}. A decrease in P_{set} during a fault causes the δ_{vsg} of the GFM, which has inertia, to increase more slowly than δ_{pll}. The smaller the P_{set}, the slower the increase of δ_{vsg}, the larger the $|\ \delta_{vsg} - \delta_{pll}\ |$, and the smaller the impedance drop coupling term in Equation 9, resulting in a smaller deviation of the GFL's output ω_{pll}. The phase plane diagram of the HGS under different P_{set} conditions during a fault is shown in Figure 9.

From Figure 9, it can also be seen that reducing the input mechanical power P_{set} of the GFM can similarly slow down the acceleration process of both the GFM and GFL during a fault, thereby enhancing the synchronization stability of the two converters. Moreover, the smaller the P_{set}, the better the synchronization stability of the two converters; conversely, the larger the P_{set}, the worse the synchronization stability of the two converters.

4 Fault ride-through control of the HGS

During a low voltage sag fault in the grid, the HGS faces three issues: power angle instability caused by the power imbalance between the GFM and GFL; outputting reactive current in compliance with grid codes to support the grid; and the risk of overcurrent due to the large short-circuit current of the GFM, which threatens power electronic equipment.

From the previous analysis, it is known that reducing i_{d1} and P_{set} during a grid fault helps ensure the existence of the equilibrium points of the GFL and GFM, and simultaneously enhances the transient stability of both converters. However, the conditions for the existence of the equilibrium points of both converters are coupled through the GFL power angle δ_{pll}, the GFL output current I_1, the GFM power angle δ_{vsg}, and the GFM output voltage U_2. Directly controlling the power angles by adjusting i_{d1} and P_{set} is quite challenging. Therefore, this paper first determines the values of the GFM power angle δ_{vsgF}, the fault currents I_{1F} and I_{2F} during the fault, and then calculates the required VSG output voltage U_{2F} and mechanical power P_{setF} based on the power angles.

4.1 Equations transient power angle control

During a grid fault, while maintaining power angle stability, the GFM power angle δ_{vsgF} is adjusted based on the extent of the grid voltage sag to modify the reactive component of the output current during the fault, thereby supporting the grid. The adjustment rules are as follows:

$$\boldsymbol{\delta_{vsgF}} = \begin{cases} \dfrac{\boldsymbol{V_{gF}}}{\boldsymbol{V_g}}\boldsymbol{\delta_2^0} & ,\ \boldsymbol{0.2 < \dfrac{V_{gF}}{V_g} < 0.9} \\ \boldsymbol{0} & ,\ \boldsymbol{\dfrac{V_{gF}}{V_g} \le 0.2} \end{cases} \tag{17}$$

In Equation 17, δ 0 2 is the power angle of the GFM before the fault;V_{gF} is the RMS value of the grid phase voltage after the fault. During the fault, by adjusting P_{set}, we can control the power angle of the GFM, making it reach δ_{vsgF} under the corresponding V_{gF}.

According to Equation 14, the equilibrium point of the PLL is not only related to the output current i_{d1} but also affected by the inductances L_1, L_2, and L_g. Therefore, by adjusting only the current, especially in a weak grid environment, it is impossible to ensure the existence of the equilibrium point. Hence, the output phase angle θ_{vsg} of the GFM is transmitted to the PLL. However, under this circumstance, the PLL becomes an open-loop system with a steady-state error, making it impossible to precisely align $\mathring{U}_1$ with the d-axis.

From Figure 10A, it can be seen that there is a fixed angular difference φ between $\mathring{U}_1$ and the d-axis d_{GFL} of the GFL. Therefore, the angle of the GFL needs to be adjusted by adding a fixed angle φ on the basis of θ_{vsg}. This can be obtained by measuring the deviation of u_{q1} and applying PI control.

$$\begin{cases} \boldsymbol{\theta_{pll} = \theta_{vsg} + \phi} \\ \boldsymbol{\phi = k_p u_{q1} + k_i \int u_{q1}} \end{cases} \tag{18}$$

Using Equation 18, an improved PLL based on the grid-forming model can be obtained, which can also precisely align U_1 with the d-axis of the two-phase rotating coordinate system of the GFL, as shown in Figure 10B. At this point, the active power and reactive power of the GFL are decoupled.

The P_{setF} during the fault can be obtained as:

$$\boldsymbol{P_{setF} = 3\dfrac{k_3 U_2 V_{gF}}{X_2}\sin\delta_{vsgF} - 3\dfrac{k_1 U_2 I_1}{X_2}\cos(\phi + \varphi_1)} \tag{19}$$

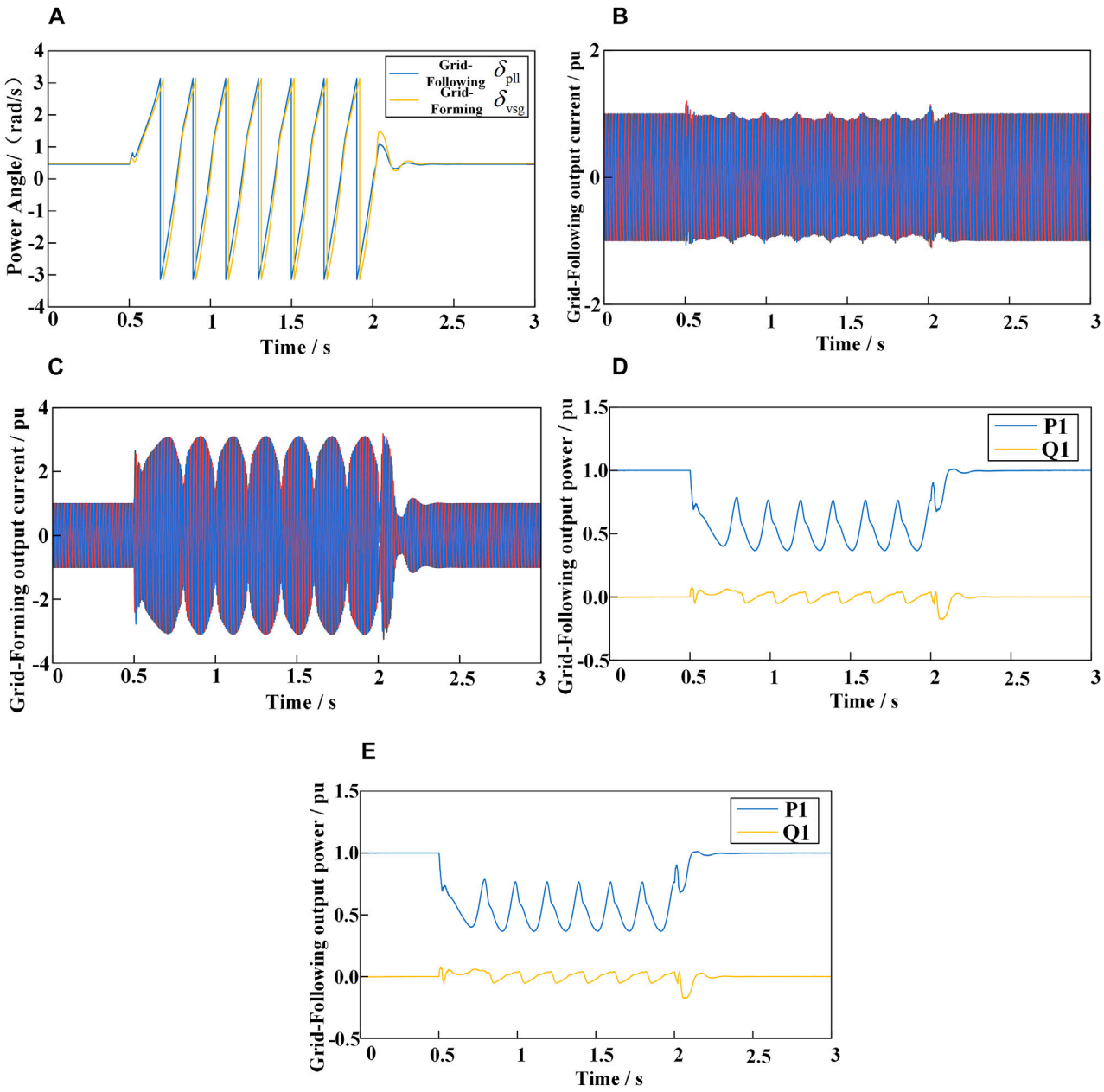

FIGURE 14
Output waveform under symmetrical fault of grid. **(A)** Power angle curve. **(B)** Grid-Following output current. **(C)** Grid-Forming output current. **(D)** Grid-Following output power. **(E)** Grid-Forming output power.

After introducing the input mechanical power adjustment loop in the GFM and adopting the improved PLL based on the grid-forming model in the GFL, the control block diagrams of the GFM and GFL are shown in Figure 11. In this case, as long as the GFM remains stable, the stability of the GFL can be ensured.

4.2 Fault current control

4.2.1 Steady-state current control

Although the GFM is stabilized by adjusting the input mechanical power, this does not effectively suppress the overcurrent phenomenon. Even though the presence of the GFL can reduce the fault current of the GFM, the GFM may still generate a significant fault current when there is a substantial drop in grid voltage. Therefore, when the fault current I_{2F} exceeds 1.5 times the rated current, the control of the GFM fault current I_{2F} is as follows:

$$\boldsymbol{I_{2F} = 1.5 I_{2n}} \tag{20}$$

In Equation 20: I_{2n} is the rated value of the GFM output current.

Since the GFL is a current source type, it will not generate steady-state overcurrent during a fault. However, to support the grid, it needs to output reactive current. The adjustment rules for the output current of the grid-following type are as follows:

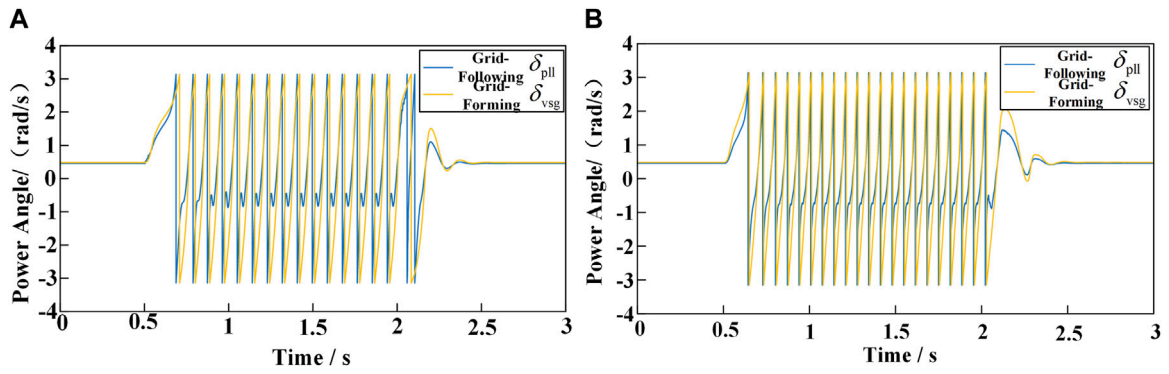

FIGURE 15
Change the reference value of the inverter. **(A)** Changing Grid-Following reference current. **(B)** Changing Grid-Forming input mechanical power.

$$I_{q1F} = \begin{cases} 0 & , \frac{V_{gF}}{V_g} \geq 0.9 \\ -1.5\left(0.9 - \frac{V_{gF}}{V_g}\right) I_{1n} & , 0.2 \leq \frac{V_{gF}}{V_g} < 0.9 \\ -1.05 I_{1n} & , \frac{V_{gF}}{V_g} < 0.2 \end{cases} \quad (21)$$

$$I_{d1F} = \begin{cases} \sqrt{I_{1n}^2 - I_{q1F}^2}, \frac{V_{gF}}{V_g} \geq 0.2 \\ 0, \frac{V_{gF}}{V_g} < 0.2 \end{cases} \quad (22)$$

In Equations 21, 22: I_{1n} is the rated value of the GFL output current;I_{d1F} is the d-axis output current of the GFL during a fault; I_{q1F} is the q-axis output current of the GFL during a fault.

Based on Equations 17, 21, 22, the values of δ_{vsgF}, I_{q1F}, and I_{d1F} are obtained, respectively. From Equations 7, 9, 11, 20, the following system of equations can be derived:

$$\begin{cases} (A - k_3 V_g)^2 + B^2 - 2(1.5 X_2 I_{2n})^2 = 0 \\ k_4 i_{d1F} - k_2 U_{2F} \sin\phi - k_3 V_g \sin(\delta_{vsgF} + \phi) = 0 \\ P_{setF} = C \sin\delta_{vsgF} - D\cos(\phi + \varphi_{1F}) \end{cases} \quad (23)$$

In Equation 23: $\varphi_{1F} = \arctan\left(\frac{I_{q1F}}{I_{d1F}}\right)$; $I_{1F} = \sqrt{I_{d1F}^2 + I_{q1F}^2}$; $A = U_{2F}\cos\delta_{vsgF} + k_1 I_{1F}\sin(\delta_{vsgF} + \phi + \varphi_{1F}) - k_2 U_{2F}\cos\delta_{vsgF}$; $B = U_{2F}\sin\delta_{vsgF} - k_1 I_{1F}\cos(\delta_{vsgF} + \phi + \varphi_{1F}) - k_2 U_{2F}\sin\delta_{vsgF}$; $C = 3\frac{k_3 U_{2F} V_g}{X_2}$.

Equation 21 can be solved using numerical methods to obtain the output voltage U_{2F} of the GFM and the input mechanical power P_{setF} during a fault. Since the reactive power loop adjusts the output voltage command, this may lead to inaccurate fault current control. Therefore, during a fault, the reactive power loop is locked, and the calculated U_{2F} is used to replace the output of the reactive power loop.

4.2.2 Steady-state current control

The transient current of the GFL is small and has a minimal impact on the system, so it can be neglected. However, the transient current of the GFM is relatively large, and adjusting the reference voltage of the reactive power loop alone is not effective. If left unchecked, it can damage transistors.

Therefore, transient virtual impedance is used to suppress transient overcurrent. The threshold current *I*th for the virtual impedance is set slightly above 1.5 times I_{2n}. When the detected fault current exceeds *I*th, the virtual impedance is activated; otherwise, the virtual impedance remains inactive. By combining the virtual impedance with the adjustment of the reactive power loop, the output voltage of the GFM can be expressed as:

$$U_{ref} = U_{2F} - I_{2F} Z_v \quad (24)$$

In Equation 24: Z_v is the virtual impedance.

The overall current control block diagram is shown in Figure 12:

4.3 Fault ride-through control process for HGS

The fault ride-through control process is illustrated in Figure 13. The system operates under normal conditions, monitoring V_g to determine whether a fault has occurred. In the event of a ground fault, the value of V_g decreases.

When the grid voltage drops above a specified threshold, the transient current is evaluated to determine whether it exceeds the current-limiting threshold, thereby deciding whether to activate transient virtual impedance control. If the grid voltage falls below the threshold, transient power angle control is first applied to the hybrid system. Using Equations 17, 21, 22, the fault power angle of the GFM converter and the reference current for the GFL converter are determined. Subsequently, the value of P_{setF} is calculated according to Equation 19.

Next, the fault current of the GFM converter is monitored. If the current exceeds the transient current-limiting threshold, both the reactive power loop and transient virtual impedance control for the GFM converter are activated. If the current only exceeds the steady-state current-limiting threshold of the GFM converter, only the reactive power loop control is applied.

Once the reactive power loop control is engaged in the GFM converter, the previously determined GFM fault power angle and GFL reference current are used to calculate P_{setF} and U_{2F} according to Equation 23. When V_g recovers above the threshold value, the hybrid system transitions back to the normal control strategy.

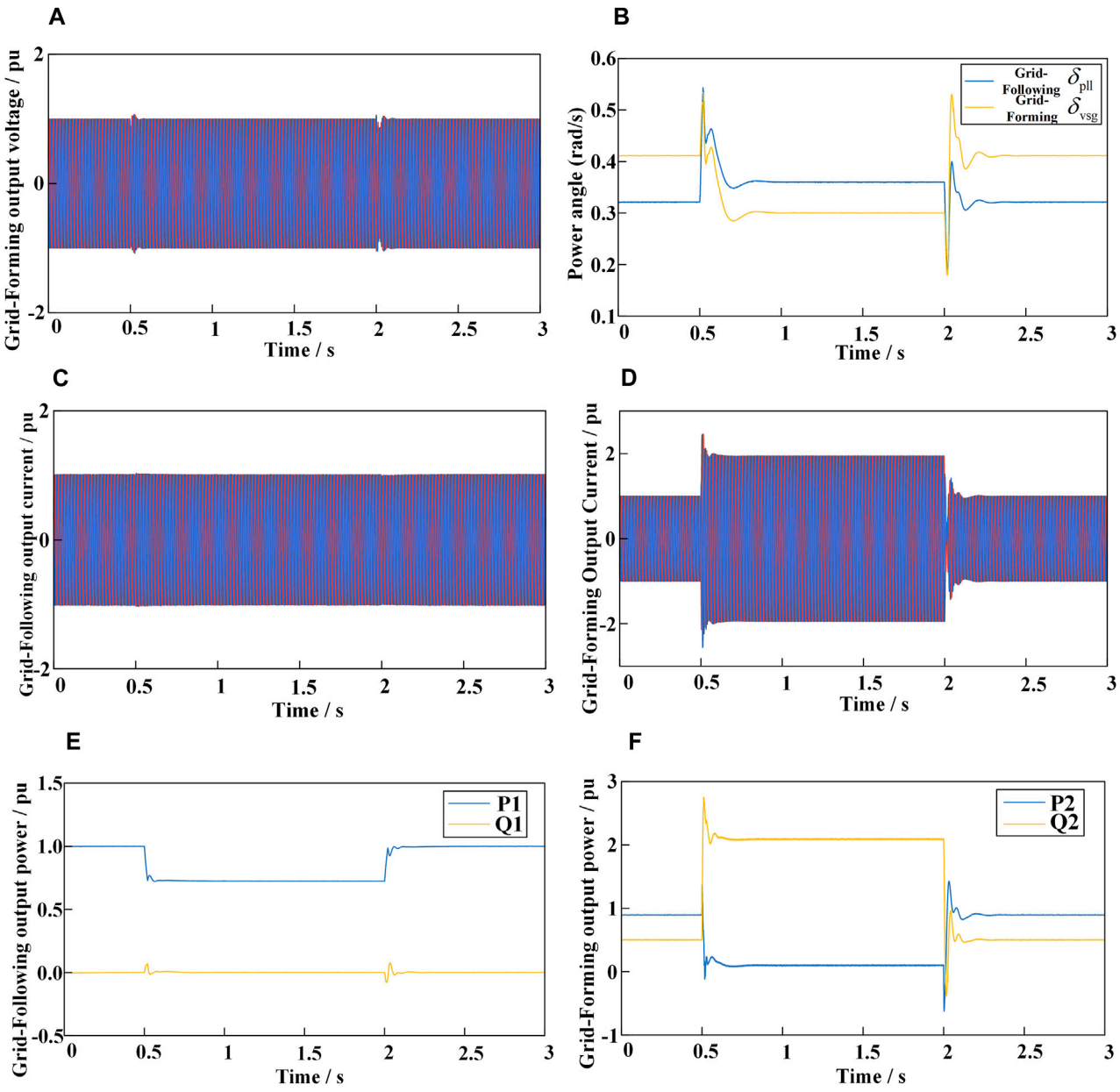

FIGURE 16
Output waveform under transient power Angle fault ride-through control only. **(A)** Grid-Forming output voltage. **(B)** Power angle curve. **(C)** Grid-Following output current. **(D)** Grid-Forming output current. **(E)** Grid-Following output power. **(F)** Grid-Forming output power.

5 Case study

To verify the theoretical analysis and the proposed fault ride-through control strategy, a hybrid grid-connected model of grid-following and GFM, as shown in Figure 1, was built in Matlab/Simulink. The system parameters are listed in Table 1.

5.1 Output characteristics of GFM and GFL during fault conditions

When the three-phase grid voltage drops to 0.5, the output currents and power angles of the GFM and GFL are shown in Figure 14. The simulation duration is set to 3 s, with a fault occurring at 0.5 s and clearing at 2 s. As seen in Figure 14, during the fault, the power angles of both the GFM and GFL increase indefinitely. The output currents of the two converters are affected by the power angles, resulting in oscillations. Since the GFM is a voltage source type, its maximum current amplitude reaches three times its rated operating value. The output active and reactive power of both converters also experience oscillations.

Figure 15A shows the power angle curves of both converters when the d-axis current reference value I *d1 of the grid-following converter is changed from 1 pu to 2.5 pu at 0.5 s and restored to 1 pu at 2 s. Figure 15B shows the power angle curves of both converters when the input mechanical power P_{set} of the grid-forming converter

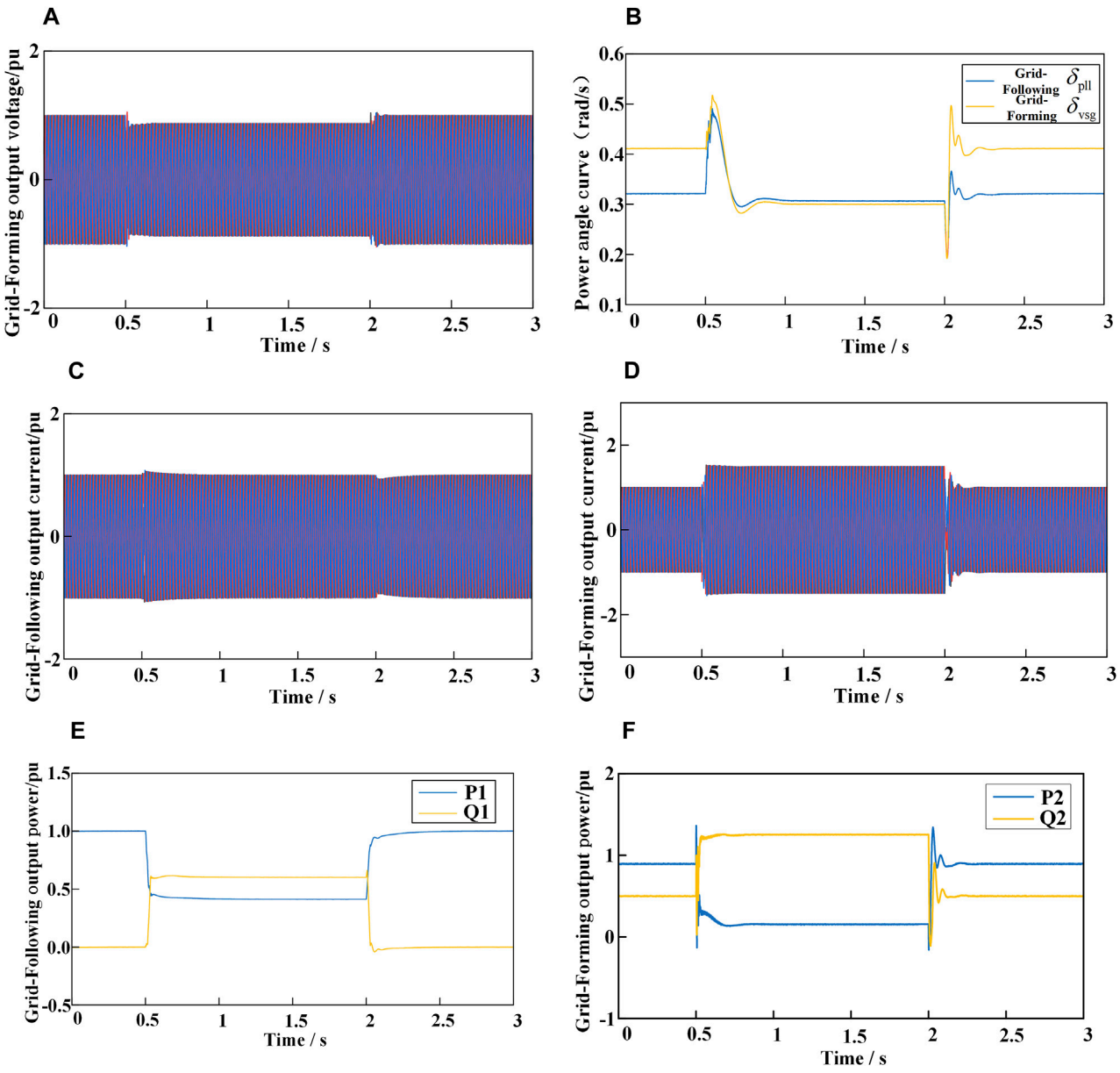

FIGURE 17
Output waveform under transient power Angle and current fault ride-through control. **(A)** Grid-Forming output voltage. **(B)** Power angle curve. **(C)** Grid-Following output current **(D)** Grid-Forming output current.**(E)** Grid-Following output power. **(F)** Grid-Forming output power.

is changed from 1 pu to 3 pu at 0.5 s and restored to 1 pu at 2 s. Based on the output power angles, it can be seen that the occurrence of power angle instability in the GFL immediately causes power angle instability in the GFM. Similarly, the occurrence of power angle instability in the GFM immediately causes power angle instability in the GFL. This verifies the analysis of the mutual influence between the two converters mentioned earlier.

5.2 Verification of the proposed fault ride-through control strategy

Figure 16 shows the output waveforms when the grid voltage symmetrically drops to 0.4 pu at 0.5 s and rises back to 1 pu at 2 s. During the fault, transient power angle control is applied to the HGS, and both the GFL and GFM remain stable after a brief transient process. As seen in Figure 16B, during the fault, by adjusting the input mechanical power P_{set} of the GFM and using the improved PLL based on the grid-forming model for the GFL, the power angles of both converters can be kept stable. However, as shown in Figure 16D, the transient current output by the GFM is too large, and the steady-state current also exceeds 1.5 pu, approaching 2 pu. From Figure 16F, it can be seen that this is due to the excessive reactive current output by the GFM. Although reactive current can support the grid, there is still a risk of damaging transistors. Therefore, it is necessary to suppress transient and steady-state overcurrents through fault current control.

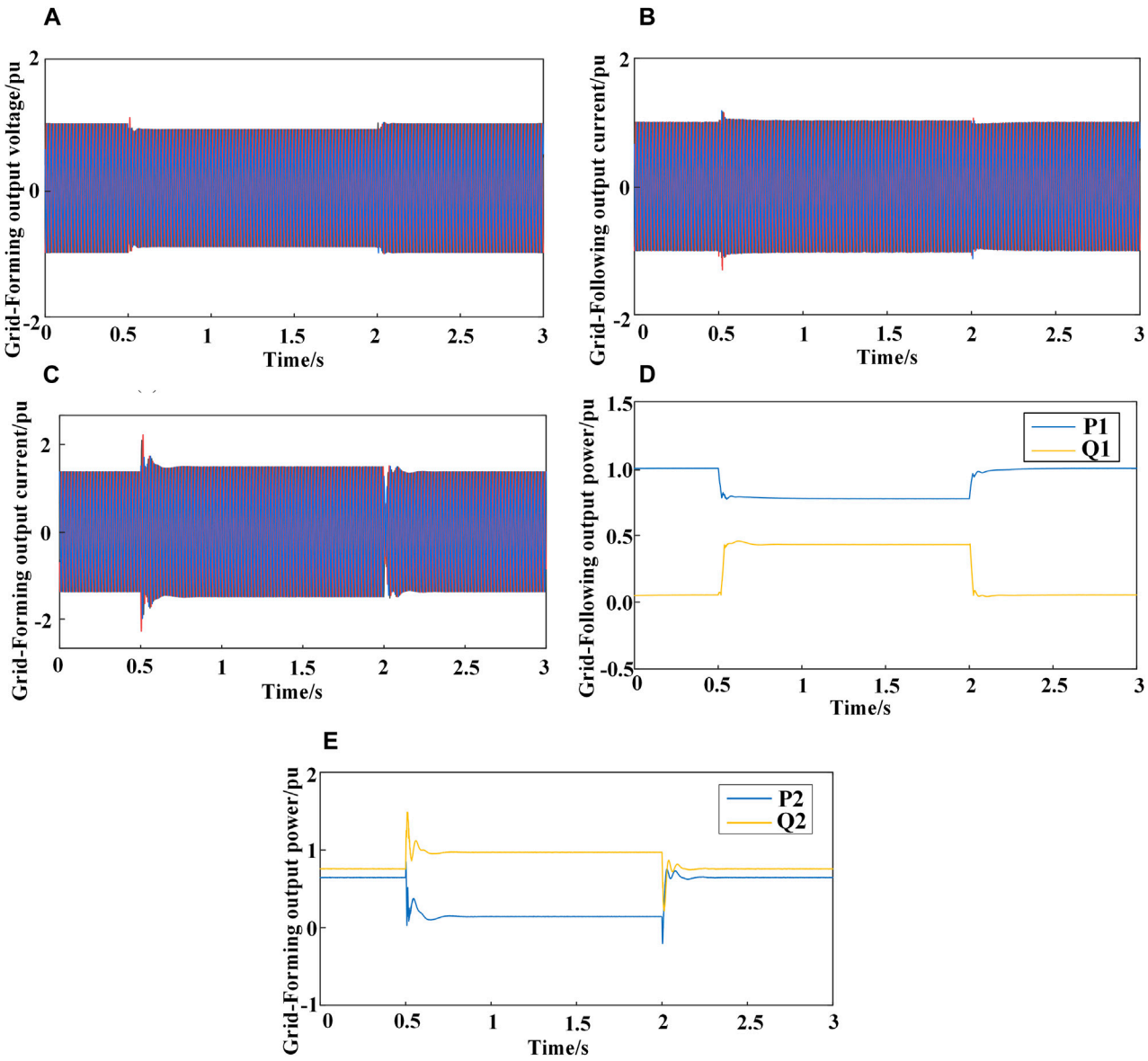

FIGURE 18
Transient power angle and fault current waveforms under fault ride-through control. **(A)** Grid-Forming output voltage. **(B)** Grid-Following output current. **(C)** Grid-Forming output current. **(D)** Grid-Following output power. **(E)** Grid-Forming output power.

Figure 17 shows the waveforms of the HGS when transient power angle and fault current control are implemented as the grid voltage symmetrically drops to 0.4 pu. Similarly, the GFL and GFM remain stable after a brief transient process. As shown in Figure 17D, during the fault, by reducing the output voltage of the GFM, the GFM's output current is precisely controlled to 1.5 pu. Thanks to the virtual impedance, the transient current is also effectively suppressed. As depicted in Figure 17E, the GFL, while remaining stable, is able to provide reactive current in accordance with grid codes, supporting the grid. After the fault is cleared, both converters can return to their pre-fault operating state after a brief transient process.

Figure 18 presents the waveforms of transient power angle and fault current control for the HGS system during a symmetrical grid voltage dip to 0.6 pu. Similarly, both the GFL and GFM converters remain stable after a brief transient process. As shown in Figure 17C, during the fault, the output current of the GFM converter is below 1.5 pu, in contrast to the scenario where the grid voltage symmetrically drops to 0.4 pu. This reduction is attributed to the implementation of virtual impedance, which effectively suppresses transient currents. As depicted in Figure 17D, the GFL converter, while maintaining stability, provides reactive current in compliance with grid codes, thereby supporting the grid. After the fault is

cleared, both converters recover to their normal operating conditions following a brief transient period.

6 Conclusion

This paper analyzes the transient stability of HGS with parallel GFL and GFM, and proposes a fault ride-through control strategy considering the interactive effects between GFL and GFM. By establishing a mathematical model of the HGS, the dynamic coupling mechanism between GFM and GFL is revealed, and the fault ride-through problem under symmetrical voltage drops is studied. The main conclusions are as follows:

1) Through the transient stability analysis of the HGS with parallel GFL and GFM, demonstrating that the two are mutually coupled through the grid impedance. The instability of one converter will lead to the instability of the other converter. During a fault, reducing the i_{d1} of GFL or the P_{set} of GFM can simultaneously improve the transient stability of both converters.
2) During a fault, the GFM adjusts the power angle according to the extent of the grid voltage drop and modifies the output voltage while considering the impact of the current injected by the GFL when limiting current. This approach can effectively suppress short-circuit overcurrent and maintain power angle stability. The GFL uses an improved PLL based on grid-forming control, which can effectively prevent GFL instability and inject current into the grid in accordance with grid codes.
3) Considering the interactive effects of GFL and GFM, a fault ride-through control strategy applicable to the HGS is proposed. By setting a threshold current *I*th slightly greater than 1.5 I_{2n} in the GFM, virtual impedance is introduced when the detected fault current exceeds *I*th, effectively suppressing transient overcurrent.
4) The transient current of the GFM is relatively large. By setting a threshold current *I*th slightly greater than 1.5I_{2n} in the GFM, virtual impedance is introduced when the detected fault current exceeds *I*th, effectively suppressing transient overcurrent. This approach addresses the shortcomings of reactive voltage reference adjustment alone, which is less effective and risks damaging transistors.

This study preliminarily explores the interaction mechanisms and fault ride-through control for GFL and GFM converters under symmetrical faults. However, the transient processes and fault control strategies under asymmetrical faults are more complex. Future work will focus on control strategies for asymmetrical fault conditions.

Data availability statement

The original contributions presented in the study are included in the article/supplementary material, further inquiries can be directed to the corresponding author.

Author contributions

BZ: Conceptualization, Methodology, Writing–original draft. SL: Conceptualization, Validation, Writing–review and editing. ZX: Software, Validation, Writing–review and editing. FD: Data curation, Writing–review and editing. JC: Funding acquisition, Project administration, Resources, Supervision, Writing–review and editing. HW: Formal Analysis, Investigation, Validation, Visualization, Writing–review and editing.

Funding

The author(s) declare that financial support was received for the research, authorship, and/or publication of this article. This research was funded by the Science and Technology Department of Xinjiang under grant No. 2022A01004.

Conflict of interest

Authors BZ, SL, ZX and HW were employed by the company Electric Power Research Institute of State Grid Xinjiang Electric Power Co., Ltd.

The remaining authors declare that the research was conducted in the absence of any commercial or financial relationships that could be construed as a potential conflict of interest.

Generative AI statement

The author(s) declare that no Generative AI was used in the creation of this manuscript.

Publisher's note

References

Chen, J., Prystupczuk, F., and O' Donnell, T. (2020). Use of voltage limits for current limitations in grid-forming converters. *CSEE J. Power Energy Syst.* 6 (2), 259–269. doi:10.17775/CSEEJPES.2019.02660

Cheng, H., Shuai, Z., Peng, Y., Huang, W., and Shen, Z. J. (2022). "Coupled problem of transient voltage/angle stability in paralleled synchronous and virtual synchronous generators with dynamic loads," in 2022 IEEE 5th International Electrical and Energy Conference (CIEEC), Nangjing, China, 2303–2308. doi:10.1109/CIEEC54735.2022.9846152

Gao, X., Zhou, D., Anvari-Moghaddam, A., and Blaabjerg, F. (2023). "Analysis of X/R ratio effect on stability of grid-following and grid-forming converters," in 2023 IEEE 17th International Conference on Compatibility, Power Electronics and Power Engineering (CPE-POWERENG), Tallinn, Estonia, 14-16 June 2023 (IEEE), 1–6.

Gu, Y., and Green, T. C. (2023). Power system stability with a high penetration of inverter-based resources. *Proc. IEEE* 111 (7), 832–853. doi:10.1109/jproc.2022.3179826

Gursoy, M., Sadeque, F., Fateh, F., and Mirafzal, B. (2023). "Direct control methods for grid-forming and grid-following inverters," in 2023 IEEE Energy Conversion Congress and Exposition (ECCE), Nashville, TN, USA, 1081–1088. doi:10.1109/ECCE53617.2023.10361995

He, X., Geng, H., Xi, J., and Guerrero, J. M. (2021). Resynchronization analysis and improvement of grid-connected VSCs during grid faults. *IEEE J. Emerg. Sel. Top. Power Electron.* 9 (1), 438–450. doi:10.1109/jestpe.2019.2954555

Huang, Z., Chen, D., Qiu, Y., and Ying, K. (2024). "Optimization of resource allocation for distributed energy consumption based on a meta-heuristic algorithm," in 2024 3rd International Conference on Energy and Electrical Power Systems (ICEEPS), Guangzhou, China, 198–201. doi:10.1109/ICEEPS62542.2024.10693062

IEEE (2022). "Ieee standard for interconnection and interoperability of inverter-based resources (ibrs) interconnecting with associated transmission electric power systems," in *Ieee std 2800-2022* (IEEE), 1–180. doi:10.1109/IEEESTD.2022.9762253

Kim, K.-H., Cui, S., and Jung, J.-J. (2024). Current-oriented phase-locked loop method for robust control of grid-connected converter in extremely weak grid. *IEEE Trans. Power Electron.* 39 (10), 11963–11968. doi:10.1109/tpel.2024.3419445

Li, M., Quan, X., Wu, Z., Li, W., Zhu, L., and Hu, Q. (2021). "Modeling and transient stability analysis of mixed-GFM-GFL-based power system," in 2021 IEEE Sustainable Power and Energy Conference (iSPEC), Nanjing, China, 2755–2759. doi:10.1109/iSPEC53008.2021.9735564

Li, Y., Gu, Y., and Green, T. C. (2022). Revisiting grid-forming and grid-following inverters: a duality theory. *IEEE Trans. Power Syst.* 37 (6), 4541–4554. doi:10.1109/tpwrs.2022.3151851

Lu, Y., Cao, W., Zhang, Z., and Hu, B. (2023). "Fault-current limiting strategy for grid-forming converters with virtual impedance from both inner CCL and outer VCL," in 2023 IEEE 7th Conference on Energy Internet and Energy System Integration (EI2), Hangzhou, China, 1907–1911. doi:10.1109/EI259745.2023.10512712

Paquette, A. D., and Divan, D. M. (2015). Virtual impedance current limiting for inverters in microgrids with synchronous generators. *IEEE Trans. Industry Appl.* 51 (2), 1630–1638. doi:10.1109/tia.2014.2345877

Taul, M. G., Wang, X., Davari, P., and Blaabjerg, F. (2020). Current limiting control with enhanced dynamics of grid-forming converters during fault conditions. *IEEE J. Emerg. Sel. Top. Power Electron.* 8 (2), 1062–1073. doi:10.1109/jestpe.2019.2931477

Tian, Z., Li, X., Zha, X., Tang, Y., Sun, P., Huang, M., et al. (2023). Transient synchronization stability of an islanded AC microgrid considering interactions between grid-forming and grid-following converters. *IEEE J. Emerg. Sel. Top. Power Electron.* 11 (4), 4463–4476. doi:10.1109/jestpe.2023.3271418

Wei, Y., Liu, J., Xiong, L., Chen, Z., Liu, J., You, L., et al. (2024). "Comparisons of dynamic characteristics between grid-forming and grid-following converters," in 2024 IEEE 10th International Power Electronics and Motion Control Conference (IPEMC2024-ECCE Asia), Chengdu, China, 4604–4610. doi:10.1109/IPEMC-ECCEAsia60879.2024.10567983

Xi, J., Wang, J., Zhang, J., Zhang, Y., Su, C., and Liu, C. (2022). "Current limiting strategy of grid-forming converter based on additional current loop," in 2022 4th International Conference on Smart Power and Internet Energy Systems (SPIES), Beijing, China, 328–332. doi:10.1109/spies55999.2022.10082058

Xu, J., Qian, H., Hu, Y., Bian, S., and Xie, S. (2021). Overview of SOGI-based single-phase phase-locked loops for grid synchronization under complex grid conditions. *IEEE Access* 9, 39275–39291. doi:10.1109/access.2021.3063774

Zhang, X., Huang, Z., Wang, Z., Li, G., Zheng, L., and Xia, S. (2024). "Transient stability analysis for hybrid GFM-GFL systems with current limit," in 2024 IEEE Power and Energy Society General Meeting (PESGM), Seattle, WA, USA, 1–5. doi:10.1109/PESGM51994.2024.10688760

Zhang, Y., Zhang, C., Yang, R., Molinas, M., and Cai, X. (2023). Current-constrained power-angle characterization method for transient stability analysis of grid-forming voltage source converters. *IEEE Trans. Energy Convers.* 38 (2), 1338–1349. doi:10.1109/tec.2023.3236620

Zhang, Z., and Schuerhuber, R. (2023). Impact of reactive current and phase-locked loop on converters in grid faults. *Energies* 16 (7), 3122. doi:10.3390/en16073122

Zhao, X., and Flynn, D. (2022). Stability enhancement strategies for a 100% grid-forming and grid-following converter-based Irish power system. *IET Renew. Power Gener.* 16, 125–138. doi:10.1049/rpg2.12346

Zheng, Y., Wang, T., He, S., Wu, Y., Kang, Y., and Liu, D. (2023). "Analytical expression of short circuit current for virtual synchronous generator with improved low voltage ride through control strategy," in 2023 IEEE Power and Energy Society General Meeting (PESGM), Orlando, FL, USA, 1–5. doi:10.1109/PESGM52003.2023.10253183

frontiers | Frontiers in Energy Research

TYPE Original Research
PUBLISHED 14 February 2025
DOI 10.3389/fenrg.2025.1537562

OPEN ACCESS

EDITED BY
Minghao Wang,
University of Macau, China

REVIEWED BY
Jipeng Gu,
Peking University, China
Aijuan Wang,
Chongqing University of Technology, China

*CORRESPONDENCE
Xu Zhuo,
zhuoxu1018@gmail.com

RECEIVED 01 December 2024
ACCEPTED 03 January 2025
PUBLISHED 14 February 2025

CITATION
Lou W, Zhu S, Zhuo X, Qin S, Li B, Zhou Y, Chen J and Gao Q (2025) Energy interaction strategy for multi-prosumer distribution systems based on game theory.
Front. Energy Res. 13:1537562.
doi: 10.3389/fenrg.2025.1537562

Energy interaction strategy for multi-prosumer distribution systems based on game theory

Wei Lou[1], Shenglong Zhu[1], Xu Zhuo[2]*, Shaorui Qin[1], Baodong Li[3], Ya Zhou[3], Jian Chen[3] and Qiang Gao[3]

[1]Electric Power Research Institute of State Grid Anhui Electric Power Co., Ltd., Hefei, China, [2]School of Electric Engineering and Automation, Hefei University of Technology, Hefei, China, [3]State Grid Anhui Electric Power Co., Ltd., Chuzhou Power Supply Company, Chuzhou, China

In flexible distribution systems, the strong uncertainty of generation and load demand poses challenges for energy interaction and resource coordination. However, existing energy interaction strategies generally focus only on economic benefits, neglecting safety performance, and are insufficient to ensure the reliable operation of the system. To address these issues, this paper proposes an energy interaction strategy for multi-prosumer flexible distribution systems, considering the economic benefits of all parties and the voltage safety of the system. First, a multi-agent energy interaction framework based on the Stackelberg game is established, and a bi-level optimization model for the distribution network operator and prosumers is constructed. Second, the paper innovatively introduces soft open point-based power flow control technology into the energy trading market. Then, the KKT conditions, dual theory, linearization, and relaxation techniques are applied to transform the original bi-level game problem into a single-level mixed-integer second-order cone programming problem, improving computational efficiency. Finally, the improved IEEE 33-bus distribution system is simulated and compared with two other scenarios. The results show that the proposed strategy can significantly improve the economic and safety performance of the energy interaction system, optimize the power flow distribution, and effectively enhance power quality. The approach offers a promising solution to the growing challenges of managing distributed energy resources in the context of flexible and reliable grid operation.

KEYWORDS

energy interaction, multiple-prosumer, soft open point, Stackelberg game, KKT condition

1 Introduction

With the proposal of the "dual carbon" goal, the widespread access of distributed energy and flexible resources has significantly increased the participation of prosumers in the power market (Yang et al., 2024). Under this background, the operation mode of power distribution system is changing to multi-direction and multi-agent. Flexible distribution systems refer to advanced distribution networks that integrate multiple energy resources and flexible control technologies and are capable of dynamic reconfiguration and real-time power flow adjustment to adapt to changing demand and supply conditions (Li et al., 2023). By incorporating advanced control strategies, flexible distribution systems have the potential to significantly enhance energy interaction capabilities, increase renewable energy utilization, and provide strong support for system stability.

Prosumers play a crucial role in reducing energy costs and promoting renewable energy. Under coordinated feed-in tariffs, prosumers can engage in energy trading with the distribution network (DN) to maintain energy supply-demand balance, thereby providing new support for enhancing the flexibility and reliability of power systems (Seppälä and Järventausta, 2024). However, as the share of prosumers in distribution systems continues to grow, energy interactions among multiple entities are becoming increasingly complex. The presence of intermittent demand response (DR) introduces additional challenges to maintaining power system balance. Consequently, there is an urgent need for more advanced strategies to effectively regulate and manage multi-agent energy interactions, ensuring the stability, economic efficiency, and flexibility of distribution networks.

Existing energy interaction methods for multiple prosumers can be broadly categorized into two types: direct control and regional market-based control (Manchalwar et al., 2024). Direct control, also referred to as prosumer-to-grid control, involves the upper-level grid directly accessing information from individual prosumers and directly managing all controllable resources for energy interaction as needed. While this method is straightforward in operation, it suffers from drawbacks such as transaction congestion, poor privacy protection, and limitations on prosumers' autonomy. In contrast, regional market-based control is a distributed control approach based on local energy trading markets and can be viewed as prosumer-to-distribution network operator (DNO) control. Under this framework, the DNO has pricing authority, and prosumers can adjust their flexible resources proactively based on the DNO's pricing signals, thereby autonomously determining energy exchange while indirectly influencing the DNO's pricing. This method balances the interests of all participants by coordinating dispersed prosumers to form a regional platform for energy generation and consumption, achieving resource sharing and preserving prosumer autonomy. Moreover, it offers excellent scalability. For instance, various approaches such as distributed trading mechanisms for demand-side energy interaction (Lou et al., 2023), optimization methods targeting models, solution techniques, and information transmission (Hou et al., 2022), dual-chain implementation methods for electricity rights trading (Gao et al., 2024), and multi-agent deep learning-based energy management techniques (Miyamoto et al., 2020) have been explored. Although these studies have achieved significant progress in energy interaction among multiple prosumers, they also exhibit notable limitations. Lou et al. (2023); Hu et al. (2022); Gao et al. (2024) neglect power quality issues and fail to account for voltage regulation, which may impact system stability. Similarly Miyamoto et al. (2020), focuses solely on power optimization without integrating economic considerations in market energy trading and distribution network regulation, potentially limiting the economic benefits for participants.

Economic efficiency and system security are two critical concerns for users, operators, and power grids. In practical applications, economic and security objectives often conflict with each other. For instance, prioritizing the economic benefits of transactions between prosumers and the distribution network operator (DNO) may compromise the reliability and safety of system operations, potentially leading to severe voltage violations or excessive utilization of grid assets (Tao et al., 2024). Moreover, the autonomous nature of prosumers, coupled with intermittent and concentrated power usage patterns, can result in imbalances between generation and consumption. This imbalance often causes power flow discrepancies across feeders, leading to frequent feeder power fluctuations and increased system losses (Liu et al., 2024). As a result, transaction control strategies that balance economic efficiency and system security have become a prominent research focus. Examples include transaction control algorithms based on attention mechanisms (Zheng et al., 2021), scheduling methods leveraging double-agent Q-learning (Liu et al., 2023), and game-theoretic scheduling strategies (Xiao et al., 2024; Guan and Hou, 2024; Zheng et al., 2024). These studies, through either deep learning algorithms or game-theory-based approaches, have demonstrated the ability to enhance DNO revenues, reduce prosumers' electricity costs, stabilize system operations, and maximize social welfare. However, they have not adequately addressed the challenge of handling surplus energy, leaving room for further improvement in energy management strategies.

The concept of "clearing price" has been widely discussed in recent studies (Izadi and Rastegar, 2024; Meng et al., 2024; Mohammadreza et al., 2024; Wu et al., 2024), where game-theoretic methods have been applied to achieve economic dispatch and system regulation within energy communities (Izadi and Rastegar, 2024). For instance, one study explored economic coordination and regulation using game theory (Meng et al., 2024), while another incorporated energy clearing and voltage regulation through a leader-follower (Stackelberg) game-based pricing mechanism to realize mutual benefits for the DNO and prosumers. By leveraging "clearing price" as an interaction signal within the Stackelberg game framework, these approaches facilitate communication between the upper-level leader (DNO) and lower-level followers (prosumers). This methodology prioritizes internal transactions in local energy markets, effectively managing surplus energy, promoting local energy utilization, and ensuring the system's economic efficiency. Additionally, the focus on price and power exchange as communication variables ensures robust user privacy protection (Mohammadreza et al., 2024). Despite their ability to enhance system revenues and operational security, these strategies lack consideration of active regulation in the distribution network (DN). Addressing this gap is essential to further improve system reliability and operational flexibility.

Network reconfiguration has been proposed as a method to adjust the topology of distribution networks (DN) for power flow optimization (Liang et al., 2024; Ashrafi et al., 2024), aiming to reduce power losses, lower operational costs, and prevent voltage violations. However, this approach is constrained by the operating frequency of tie switches, the need for more advanced control devices. Multi-Terminal Soft Open Points (MOP), are power electronic devices designed for efficient power transmission in electric power systems (Deakin et al., 2022; Taher et al., 2024; Li et al., 2024). MOP actively regulates active and reactive power on connected feeders, optimizes power flow distribution, and improves resource allocation, thereby increasing the flexibility and reliability of the network. Studies have demonstrated that MOP outperforms traditional network reconfiguration in power flow regulation and offers greater adaptability compared to conventional Soft Open Points (SOP) (Deakin et al., 2022), as it enables simultaneous control and optimization of multiple branch lines, providing

more versatile power distribution capabilities. Nevertheless, research and applications of MOP in the context of energy interaction remain limited, suggesting significant potential for further exploration in this area.

Therefore, based on the analysis of the aforementioned background, this paper comprehensively considers the energy interaction strategy between the DNO and multiple prosumers in a flexible distribution system. This strategy involves factors such as energy storage system (ESS) charging and discharging, MOP active regulation, DR, internal pricing, and voltage stability. A game-theoretic energy interaction model and strategy for multi-prosumer distribution systems are proposed, and mathematical methods such as Karush-Kuhn-Tucker (KKT) conditions are utilized to simplify the model solution process. The KKT conditions are a set of mathematical optimization conditions widely used in optimization problems to characterize the solutions of constrained nonlinear programming (Dempe and Franke, 2019). Unlike traditional iterative methods, which typically require extensive computation and data exchange between decision-making layers, the KKT-based transformation simplifies the optimization process by reducing the bi-level optimization problem to a single-layer form. This approach not only enhances computational efficiency but also ensures privacy by limiting the exchange of sensitive data.

This paper proposes a multi-agent energy interaction strategy based on MOP to solve the balance between economic benefits and operational security, so as to promote the construction of new power systems. Through the comparison with the existing research, the innovation of this paper is as follows:

1) A multi-agent energy interaction framework based on the Stackelberg game is developed in this study. Unlike most research that focuses solely on economic aspects without considering system security, or existing studies that prioritize voltage regulation without addressing flexible resource allocation, this work establishes an interaction framework that considers economic benefits, power quality, and demand response. This framework simultaneously addresses the economic and security issues of the DNO-multi-prosumer distribution network. Furthermore, in terms of power flow optimization for the distribution network (DN), this study introduces MOP for the active regulation of active and reactive power on the connected feeders, which not only reduces network losses but also prevent voltage over-limit rate, further enhancing the system's economic efficiency and security.
2) Different from most traditional approaches that use iterative methods to solve the Stackelberg bi-level optimization model for price determination, this study employs KKT conditions, dual theory, linearization techniques, relaxation methods, and the Big-M method to transform the bi-level model into a single-level mixed-integer second-order cone programming (MISOCP) problem. This transformation allows for solving the model using commercial solvers, thereby improving solution efficiency.

The remainder of this paper is organized as follows: Section 2 introduces the energy interaction framework for the DNO-multi-prosumer distribution system; Section 3 develops the DNO-prosumer optimization model based on the Stackelberg leader-follower game; Section 4 applies KKT conditions, linearization, and relaxation techniques to transform the bi-level model into a single-level model; Section 5 provides case studies and analysis; Section 6 presents the conclusion.

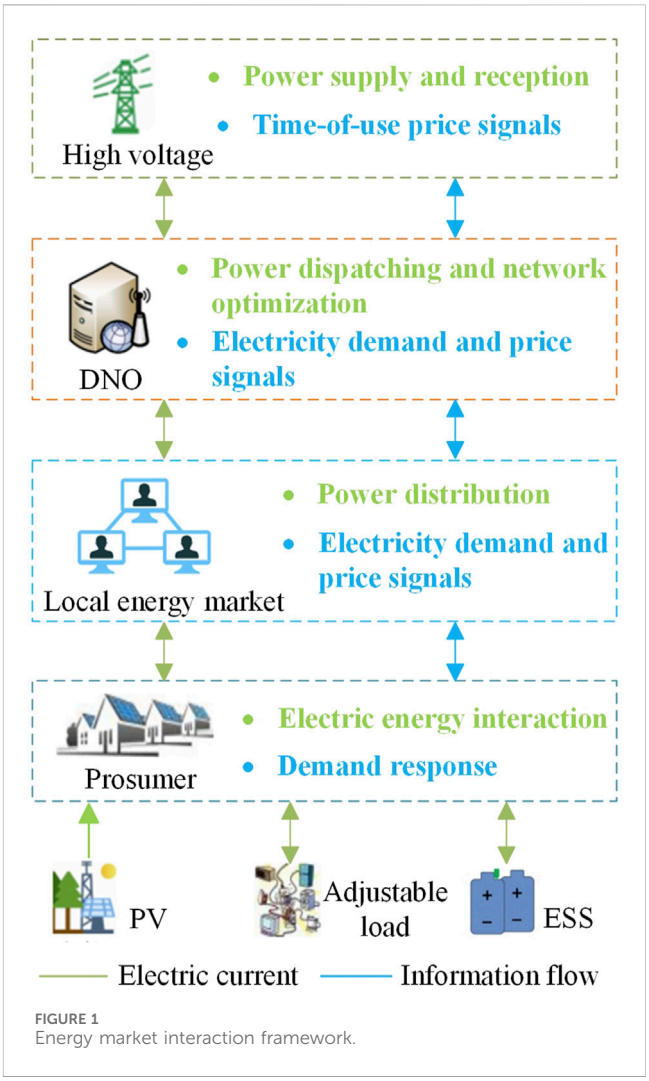

FIGURE 1
Energy market interaction framework.

2 Energy interaction framework for multiple consumer distribution systems

2.1 Energy market interaction framework

An energy market interaction framework that considers energy management issues between DNO and multiple prosumer is shown in Figure 1. The figure includes the high-voltage (HV) grid, which provides the required electrical energy and receives excess energy, the local energy interaction market that distributes electrical energy and transmits energy demand and price signals, and two key participants: the DNO, which serves as an intermediary for transactions between the HV grid and prosumers, and the photovoltaic prosumers who generate and consume their own electricity.

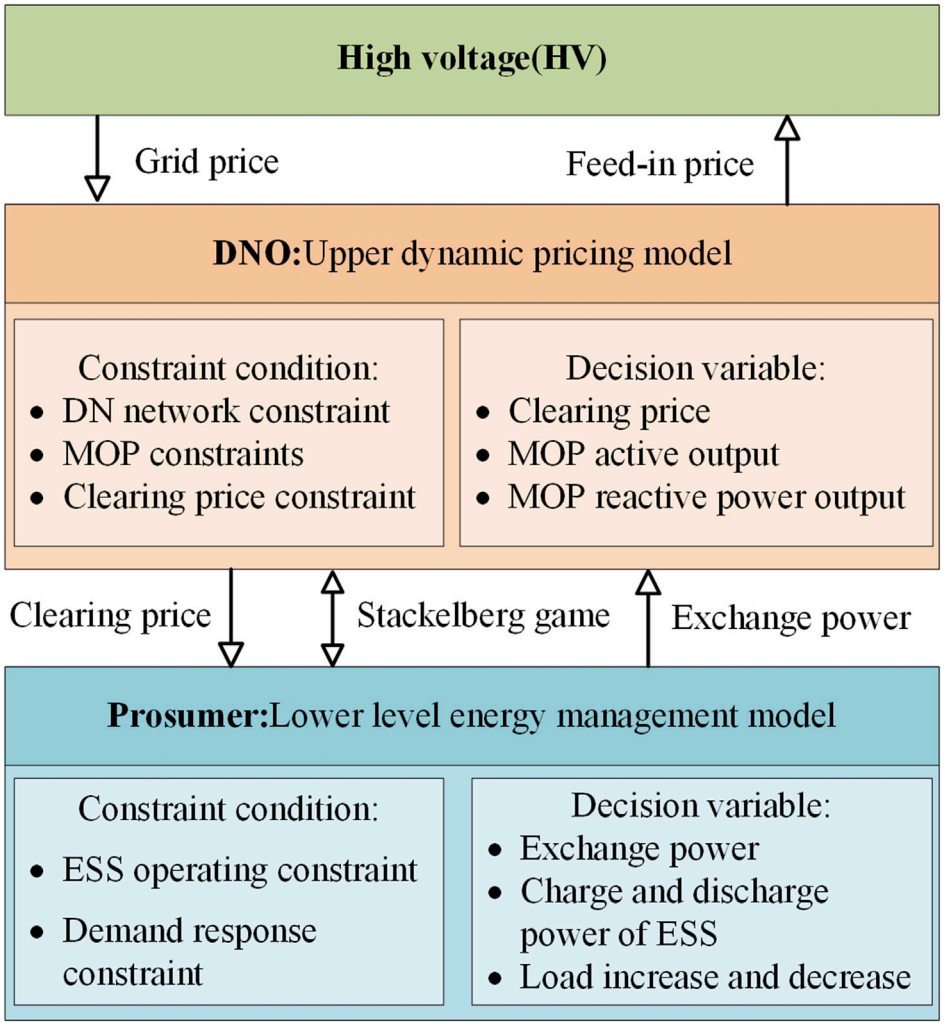

FIGURE 2
Energy interactive game framework.

As the energy interaction intermediary, the DNO acts as the operator of the distribution network (DN) and the internal price setter. Its responsibilities include: 1) overseeing the operation of the distribution network to ensure system safety and stability while meeting high-quality power requirements from users; 2) participating in the energy market and engaging in energy transactions with the HV grid to balance supply and demand when internal imbalances occur; 3) coordinating internal energy transactions by dynamically setting internal transaction prices based on economic and safety considerations, referencing users' electricity demand and feed-in tariffs, and allocating internal energy to improve consumption capacity.

As the main participants in the energy market, prosumers consist of photovoltaic (PV) systems, loads (both fixed and flexible), and energy storage systems (ESS). Among these, flexible loads, also referred to as transferable loads, are controllable loads that do not affect basic living needs, enabling demand response. This allows prosumers to adjust their loads based on the transaction prices set by the DNO and develop their own electricity consumption strategies. Additionally, to enhance the network optimization level of the DNO, Multi-Terminal Soft Open Points (MOP) are installed within the distribution network (DN).

2.2 Energy interactive game framework

As shown in Figure 2, this paper explores a bi-level energy trading framework based on the Stackelberg game, which shows the leader-follower relationship between DNO and prosumers, and both play interest games with exchanged power through clearing prices.

The upper-level leader, the DNO, can determine the operational strategy of the MOP and the internal clearing prices based on time-varying grid prices, feed-in tariffs, the exchange power between prosumers and the DNO, and the operational status of the distribution network (DN), aiming to maximize social welfare. Meanwhile, the lower-level follower, the prosumer, can adjust its electricity consumption and ESS charging/discharging strategy according to the clearing prices set by the DNO, and determine the exchange power with the DNO, in order to minimize its own costs.

It can be observed that this is a bi-directional decision-making problem, where the clearing price and exchange power serve as the communication bridge between the upper and lower levels. The DNO sets the clearing price based on the exchange power with the prosumers, while prosumers respond to the DNO's clearing price by determining their own energy scheduling plans. Therefore, although the DNO holds priority in the decision-making process, it must take into account the demand response (DR) of each prosumer, thus forming a leader-follower game of interests.

In summary, the proposed energy market interaction and game framework effectively solves the complexity of energy trading in flexible distribution networks involving multiple production-consumers. By integrating dynamic clearing prices, DR, and MOP-based network optimization, bidirectional coordination between DNO and prosumers is achieved, ensuring joint achievement of economic and operational objectives.

3 Energy interaction model of distribution system for prolific consumer

This chapter develops an energy interaction model based on the aforementioned framework. First, the objective of minimizing the DNO's operational costs is defined, along with the constraints for the distribution network (DN) operation. Next, the cost minimization objective for prosumers is outlined based on their characteristics, and the corresponding operational constraints are established. Finally, for the bi-level game problem, instead of using the traditional iterative methods, which are cumbersome, the study employs KKT conditions, the Big-M method, second-order cone relaxation techniques, and dual theory to transform the bi-level optimization model into a single-level model.

3.1 Optimization model of distribution network operator

3.1.1 Optimization objective

The DNO, as the coordinator between the grid and users, has the core objective of maximizing social welfare. This is specifically manifested in minimizing the transaction costs between the DNO, the HV, and prosumers, reducing network losses and voltage fluctuations in the DN, and enhancing the economic efficiency and stability of the system. Therefore, the objective function of the DNO can be expressed as:

$$\min F_{DNO} = a_o\left(f_{Grid} + f_{loss} - f_{inc}\right) + b_v f_{vd} \tag{1}$$

$$\begin{cases} f_{Grid} = \sum_{t=1}^{N_T}\left(\frac{X_t - W_t}{2}\left|g_t\right| + \frac{X_t + W_t}{2}g_t\right)\Delta t \\ f_{loss} = C_{loss}\left(\sum_{t=1}^{N_T}\sum_{ij\in\Omega_l} r_{ij}I_{t.ij}^2 + \sum_{t=1}^{N_T}\sum_{i=1}^{N_N} P_{t,i}^{mop,loss}\right)\Delta t \\ f_{inc} = \sum_{t=1}^{N_T}\sum_{n=1}^{N_p}\lambda_t P_{t,n}^{p}\Delta t \\ f_{vd} = \sum_{t=1}^{N_T}\sum_{i=1}^{N_N}\left|U_{t,i}^2 - \tilde{U}_{ref}^2\right| \end{cases} \tag{2}$$

Equation 1 represents the general form of the DNO optimization objective function, which is a linear weighted combination of operational costs and voltage deviation minimization. Where, a_o and b_v are the weight coefficients (Yang et al., 2023), which represent the relative importance of each element in the objective, with their sum being equal to 1; f_{Grid} and f_{inc} represent the transaction costs incurred between the DNO and HV, as well as the total revenue from transactions between the DNO and the prosumers, respectively. f_{loss} refers to the network loss cost of the DN, while f_{vd} represents the total voltage deviation. Equation 2 provides detailed expressions for each component, where X_t and W_t denote the purchase and sale prices of electrical energy between the DN and the HV grid, respectively; g_t represents the net load of the DN, with g_t indicating a positive value when the DN purchases energy from the HV grid and g_t indicating a negative value when the DN sells energy to the HV grid; C_{loss} refers to the cost coefficient associated with network losses; r_{ij} and x_{ij} represent the resistance and reactance of branch; $I_{t.ij}$ denotes the current flowing through branch ij at period t; $P_{t,i}^{mop,loss}$ accounts for the active power loss generated by the MOP during period t; N_T, N_N, and N_P represent the total time periods, total nodes, and total number of prosumers in the DN, respectively; Δt denotes the time interval; Ω_l refers to the set of all branches; λ_t represents the clearing price in the internal energy trading market at period t; $P_{t,n}^{p}$ denotes the net load of the nth prosumer at period t, which corresponds to its exchange power with the DN; $U_{t.i}$ is the voltage of bus i at period t; $\tilde{U}_{ref}$ is the reference voltage of the buses.

3.1.2 Constraint condition

3.1.2.1 Network constraints of the DN

The DN is modeled using the widely adopted Distflow branch model.

$$\sum_{ji\in\Omega_b}\left(P_{t,ji} - r_{ji}I_{t,ji}^2\right) + P_{t,i} = \sum_{ik\in\Omega_b} P_{t,ik} \tag{3}$$

$$\sum_{ji\in\Omega_b}\left(Q_{t,ji} - x_{ji}I_{t,ji}^2\right) + Q_{t,i} = \sum_{ik\in\Omega_b} Q_{t,ik} \tag{4}$$

$$U_{t,i}^2 - U_{t,j}^2 - 2\left(r_{ij}P_{t,ij} + x_{ij}Q_{t,ij}\right) + \left(r_{ij}^2 + x_{ij}^2\right)I_{ij}^2 = 0 \tag{5}$$

$$I_{t,ij}^2 U_{t,i}^2 = P_{t,ij}^2 + Q_{t,ij}^2 \tag{6}$$

$$P_{t,i} = P_{t,i}^{PV} + P_{t,i}^{MOP} - P_{t,i}^{L} + P_{t,i}^{L,move} + \left(P_{t,i}^{ess,c} - P_{t,i}^{ess,d}\right) \tag{7}$$

$$Q_{t,i} = Q_{t,i}^{MOP} - Q_{t,i}^{L} \tag{8}$$

Equations 3, 4 represent the active and reactive power balance for the branch, where $P_{t,ji}$ and $Q_{t,ji}$ are the active and reactive power flowing through branch ij at time t, $P_{t,i}$ and $Q_{t,i}$ are the active and reactive power injected at bus i at time t. Equations 5, 6 represent the voltage and branch current level constraints at bus i at period t. Equations 7, 8 represent the active and reactive power balance at the bus, where $P_{t,i}^{PV}$, $P_{t,i}^{VSC}$, $Q_{t,i}^{VSC}$ are the active and reactive power injected into bus i at period t by the PV and MOP, respectively. $P_{t,i}^{L}$ and $P_{t,i}^{L,move}$ are the fixed and transferable loads of the prosumer at period t, with a positive value indicating an increase in load demand and a negative value indicating a decrease. $P_{t,i}^{ess,c}$ and $P_{t,i}^{ess,d}$ represent the charging and discharging power of the ESS at period t at bus i.

3.1.2.2 Security constraints of the DN

DN During normal operation, the bus voltage and branch current cannot exceed the safety limit.

$$\underline{U}^2 \le U_{t,i}^2 \le \bar{U}^2 \tag{9}$$

$$I_{t,ij}^2 \le \bar{I}^2 \tag{10}$$

where, $\underline{U}$ and $\bar{U}$ are the upper and lower limits of voltage of buses respectively; $\bar{I}$ is the maximum current limit of the branch.

3.1.2.3 Operation constraints of MOP

The ideal MOP of 4 feeder lines is shown in Figure 3, and $P_{t,i}^{\mathrm{VSC}}$ in the figure is the power of the feeder connected to MOP flowing to MOP. It can be seen that it is determined by the feeder selection switch state b_i and the active power $P_{t,i}^{\mathrm{VSC}}$ transmitted by VSC_i, that is, MOP controls $P_{t,i}^{\mathrm{VSC}}$ and $Q_{t,i}^{\mathrm{VSC}}$ by controlling these two variables, and then controls the active and reactive power of the connected feeder.

$$\bar{P}_{t,i}^{\mathrm{VSC}} + P_{t,i}^{\mathrm{mop,loss}} = P_{t,i}^{\mathrm{VSC}}, \forall t, i \in \Omega_{\mathrm{VSC}} \tag{11}$$

$$\sum_{i=1}^{N_m} \bar{P}_{t,i}^{\mathrm{VSC}} = 0, \forall t, i \in \Omega_{\mathrm{VSC}} \tag{12}$$

$$P_{t,i}^{\mathrm{mop,loss}} = A_i^{\mathrm{VSC}} S_i^{\mathrm{L}}, \forall t, i \in \Omega_{\mathrm{VSC}} \tag{13}$$

$$\sqrt{\left(P_{t,i}^{\mathrm{VSC}}\right)^2 + \left(Q_{t,i}^{\mathrm{VSC}}\right)^2} \le S_i^{\mathrm{VSC}}, \quad \forall t, i \in \Omega_{\mathrm{VSC}} \tag{14}$$

$$S_n^{\mathrm{L}} \le B_{i,n} S_i^{\mathrm{VSC}}, \forall t, i \in \Omega_{\mathrm{VSC}}, \quad n \in \{1, 2, 3, \ldots N_m\} \tag{15}$$

$$\sum_{n=1}^{N} B_{i,n} = 1, \forall i \in \Omega_{\mathrm{VSC}} \tag{16}$$

$$-\bar{Q}_i^{\mathrm{VSC}} \le Q_{t,i}^{\mathrm{VSC}} \le \bar{Q}_i^{\mathrm{VSC}}, \forall t, i \in \Omega_{\mathrm{VSC}} \tag{17}$$

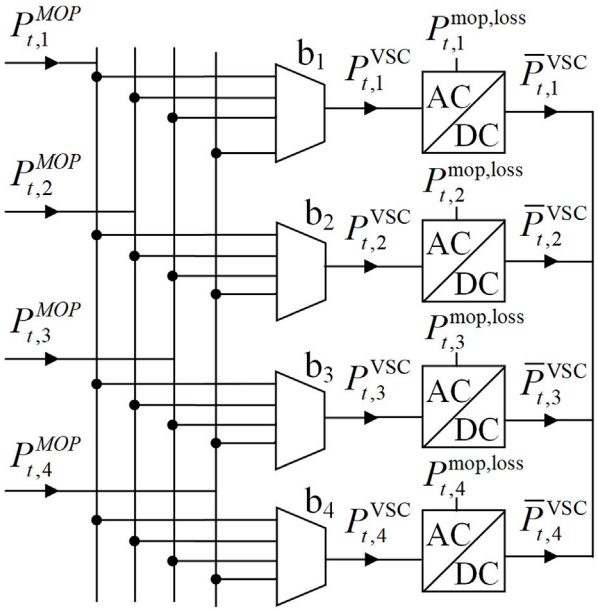

FIGURE 3
MOP Topology view.

Equations 11–13 represent the power balance constraints, where $\bar{P}_{t,i}^{\mathrm{VSC}}$ denotes the active power on the DC side of the VSC at bus i at period t, $P_{t,i}^{\mathrm{VSC}}$ represents the actual transmitted active power of VSC_i at period t, $P_{t,i}^{\mathrm{mop,loss}}$ is the active power loss of MOP_i at period t, A_i^{VSC} represents the loss coefficient of VSC_i, and Ω_{VSC} denotes the set of VSCs. Equations 14–17 describe the MOP capacity constraints, where S_n^{L} represents the power transmission capacity of the branch n connected to the MOP, S_i^{VSC} denotes the capacity of VSC_i, $Q_{t,i}^{\mathrm{VSC}}$ is the actual reactive power transmitted by VSC_i at period t, $\bar{Q}_i^{\mathrm{VSC}}$ denotes the reactive power output limit of VSC_i, and N_m represents the total number of branches connected to the MOP.

3.1.2.4 Price constraint

When determining the clearing price, the DNO must consider the responses of the prosumers. To encourage prosumers to actively participate in the internal energy market and ensure that they do not bypass the DNO to trade directly with the HV grid, the clearing price must satisfy certain constraints.

$$\lambda_t^{\min} \le \lambda_t \le \lambda_t^{\max} \tag{18}$$

$$\frac{1}{T}\sum_{t=1}^{T}\lambda_t \le \frac{1}{T}\sum_{t=1}^{T} X_t \tag{19}$$

Equation 18 specifies that λ_t must remain within the upper and lower bounds $\lambda_t^{\max}$ and $\lambda_t^{\min}$ to prevent excessive pricing, which could discourage prosumers from purchasing electricity and thereby affect their normal daily activities. Equation 19 ensures that the average clearing price does not exceed the average price of purchasing electricity from the HV grid, thereby protecting the interests of users.

3.2 Optimization model of prosumer

3.2.1 Optimization objective

Prosumers can respond to the clearing price set by the DNO by adjusting their electricity usage plans and energy storage utilization in the internal energy trading market, with the objective of minimizing their operational costs. Accordingly, the objective function for an individual prosumer is formulated as follows:

$$\min J_n = \sum_{t=1}^{T}\lambda_t P_{t,n}^{p}\Delta t + \sum_{t=1}^{T} v_n^{Disc}\left(P_{t,i}^{L,move}\right)\Delta t + \sum_{t=1}^{T} l_{\mathrm{deg}}\left(P_{t,i}^{ess,c}\eta^{ess,c} + \frac{P_{t,i}^{ess,d}}{\eta^{ess,d}}\right)\Delta t \tag{20}$$

$$P_{t,n}^{p} = P_{t,i}^{L} + P_{t,i}^{L,move} - P_{t,i}^{PV} + \sum_{e=1}^{N_e}\left(P_{t,i}^{ess,c} - P_{t,i}^{ess,d}\right) \tag{21}$$

Equation 20 represents the general formulation of the prosumer's optimization objective. The first term corresponds to the cost of participating in energy transactions, the second term represents the utility cost associated with load adjustments, and the third term accounts for the degradation cost of ESS operation. where v_n^{Disc} denotes the sensitivity coefficient of the prosumer n to load variation discomfort, $\eta^{ess,c}$ and $\eta^{ess,d}$ represent the charging and discharging efficiencies of the ESS, respectively, and l_{deg} indicates the degradation coefficient of the ESS. Equation 21 is the exchanged power between the prosumer and DNO, where a positive value represents the transmission power from DNO to the prosumer.

3.2.2 Constraint condition

3.2.2.1 Constraints of ESS

ESS must meet the relevant constraints of energy storage, charge and discharge power

$$\begin{cases} 0 \le P_{t,i}^{ess,c} \le u_{t,e}^{ess} P_e^{c,rat} \\ 0 \le P_{t,i}^{ess,d} \le \left(1 - u_{t,e}^{ess}\right) P_e^{d,rat} \end{cases} \tag{22}$$

$$S_{t,e} = S_{t-1,e} + \left(\frac{P_{t,i}^{ess,c} \eta^{ess,c}}{Cap_e^{ess}} - \frac{P_{t,i}^{ess,d}}{Cap_e^{ess} \eta^{ess,d}} \right) \Delta t \tag{23}$$

$$S_e^{\min} \le S_{t,e} \le S_e^{\max} \tag{24}$$

$$S_{1,e} = S_{N_T,e} \tag{25}$$

Equation 22 defines the charging and discharging power constraints of the ESS, where $u_{t,e}^{ess}$ represents the operational state of the ESS e at period t (1 for charging, 0 for discharging), $P_e^{c,rat}$ and $P_e^{d,rat}$ are the maximum charging and discharging powers of the ESS e, respectively. The constraints Equations 23, 24 are expressed as the energy storage constraints of the ESS. where $S_{t,e}$ represents the current energy stored in the ESS e at period t, while $S_{t-1,e}$ represents its energy level at the previous period step, with the two having a recursive relationship. $S_e^{\min}$ and $S_e^{\max}$ denote the lower and upper bounds of the ESS's energy storage, and Cap_e^{ess} represents its maximum capacity. Constraint Equation 25 is expressed as the equality between the initial energy storage $S_{1,e}$ and the final energy storage $S_{N_T,e}$ of the ESS.

3.2.2.2 Constraints on demand response

Prosumers can adjust their electricity demand based on the clearing price set by the DNO; however, to ensure their basic living needs, the following constraints must be satisfied:

$$L^{\min} \le P_{t,i}^{L,move} \le L^{\max} \tag{26}$$

$$\sum_{t=1}^{N_T} P_{t,i}^{L,move} = 0 \tag{27}$$

Equation 26 indicates that the adjustment of the prosumer's transferable load cannot exceed the specified range $[L^{\min}, L^{\max}]$. Constraint Equation 27 shows that the total load demand of the prosumer remains constant throughout the day.

4 Processing and transformation of the model

The optimization objective and constraints in the above model contain numerous nonlinear functions, which cannot be solved by existing commercial solvers. Therefore, in this section, linearization methods and second-order cone relaxation techniques are applied to process the model, converting it into a mixed-integer second-order cone programming (MISOCP) model. At the same period, to simplify the model's solution process, the bi-level optimization model is converted into a single-level optimization model.

4.1 Linearization

4.1.1 Processing of quadratic terms

Due to the nonlinear forms, such as current and voltage squared, in Equations 2–6, 9, 10, $v_{t,i}$ and $l_{t,ij}$ are used to replace $U_{t,i}^2$ and $I_{t,ij}^2$. The transformed function looks like Equations 28–34:

$$f_{loss} = C_{loss} \left(\sum_{t=1}^{N_T} \sum_{ij \in \Omega_l} r_{ij} l_{t,ij} \Delta t + \sum_{t=1}^{N_T} \sum_{t=1}^{N_N} P_{t,i}^{VSC,loss} \Delta t \right) \tag{28}$$

$$\sum_{ji \in \Omega_b} \left(P_{t,ji} - r_{ji} l_{t,ij} \right) + P_{t,i} = \sum_{ik \in \Omega_b} P_{t,ik} \tag{29}$$

$$\sum_{ji \in \Omega_b} \left(Q_{t,ji} - x_{ji} l_{t,ij} \right) + Q_{t,i} = \sum_{ik \in \Omega_b} Q_{t,ik} \tag{30}$$

$$\begin{aligned} &v_{t,i} - v_{t,j} - 2\left(r_{ij} P_{t,ij} + x_{ij} Q_{t,ij} \right) \\ &+ \left(r_{ij}^2 + x_{ij}^2 \right) l_{t,ij} = 0 \end{aligned} \tag{31}$$

$$l_{t,ij} v_{t,i} = P_{t,ij}^2 + Q_{t,ij}^2 \tag{32}$$

$$\underline{U}^2 \le v_{t,i} \le \bar{U}^2 \tag{33}$$

$$l_{t,ij} \le \bar{I}^2 \tag{34}$$

4.1.2 Handling of absolute value terms

Due to the absolute value term of the voltage deviation in Equation 2, an auxiliary variable $Aux_{t,i}$ is introduced to linearize it. The converted function is shown in Equations 35–38:

$$f_{vd} = \sum_{t=1}^{N_T} \sum_{i=1}^{N_N} Aux_{t,i} \tag{35}$$

$$Aux_{t,i} \ge 0 \tag{36}$$

$$Aux_{t,i} \ge \tilde{U}_{ref}^2 - v_{t,i} \tag{37}$$

$$Aux_{t,i} \ge v_{t,i} - \tilde{U}_{ref}^2 \tag{38}$$

4.2 Second-order cone transformation

Even after linearization in Equation 32, quadratic nonlinear terms in the form of $l_{t,ij} v_{t,i}$ still exist. Therefore, further processing is required, and the convex relaxation of the function is expressed as follows:

$$\left\| \begin{matrix} 2P_{t,ij} \\ 2Q_{t,ij} \\ l_{t,ij} - v_{t,i} \end{matrix} \right\|_2 \le l_{t,ij} + v_{t,ij}, \forall t \tag{39}$$

Similarly, Equation 14 also contains quadratic nonlinear terms, and the transformed second-order cone constraint is as follows:

$$\left(P_{t,i}^{VSC} \right)^2 + \left(Q_{t,i}^{VSC} \right)^2 \le 2 \frac{S_{t,i}^{VSC}}{\sqrt{2}} \frac{S_{t,i}^{VSC}}{\sqrt{2}} \tag{40}$$

Equation 41 is defined to verify the constraint effect. If the gap value is sufficiently small, it is considered that the accuracy after relaxation is reasonable, which also means that the initial model can be transformed into a model that can be solved by commercial solvers using the two processing methods described above.

$$\text{gap} = \left\| l_{t,ij} - \frac{P_{t,ij}^2 + Q_{t,ij}^2}{v_{t,i}} \right\|_\infty \tag{41}$$

4.3 Transformation of two-layer model

Based on the Stackelberg leader-follower game, and combining the above framework and model, the following bi-level optimization problem is formulated:

Upper level: min F_{DNO};
Subject to: Equations 7, 8, 11–13, 15–19, 29–31, 33, 34, 36–40;
Variables: $\lambda_t, P_{t,i}^{VSC}, Q_{t,i}^{VSC}, l_{t,ij}, v_{t,i}, Aux_{t,i}$
$\lambda_t \downarrow\downarrow P_{t,n}^{P} \uparrow\uparrow$
Lower level: min J_n;
Subject to: Equations 22–27;
Variables: $P_{t,n}^{P}, P_{t,i}^{L,move}, P_{t,i}^{ess,c}, P_{t,i}^{ess,d}, S_{t,e}$;

For the two-layer optimization model, the traditional iterative method is adopted, and the solving process is relatively complicated.

Furthermore, considering user privacy and security, and to avoid unnecessary information exchange between prosumers and the DNO, this paper applies the KKT conditions to transform the above bi-level model, thereby improving computational efficiency and protecting user privacy.

Let μ be the dual variable for the inequality constraints of the lower-level optimization problem, and λ be the dual variable for the equality constraints of the lower-level optimization problem. As shown in Equations 42, 43, the general form of the KKT condition obtained by the transformation is:

$$\nabla L = \left(P_{t,i}^{L,move}, P_{t,i}^{ess,c}, P_{t,i}^{ess,d}, S_{t,e}, \mu_i, \lambda_i\right) = 0 \tag{42}$$

$$0 \le \mu \perp g(x) \ge 0 \tag{43}$$

where, ∇L is the Lagrange function written using the KKT conditions (Zhu et al., 2022), $g(x) \ge 0$ representing the inequality constraints in the optimization problem. The specific expression is as follows:

1) Introduce the optimization objectives and constraints of the lower prosumers to write the Lagrange function:

$$\begin{aligned}
\nabla L = & \sum_{t=1}^{T}\sum_{n=1}^{N}\lambda_t\left[P_{t,i}^{L} + P_{t,i}^{L,move} - P_{t,i}^{PV} + \sum_{e=1}^{N_e}\left(P_{t,i}^{ess,c} - P_{t,i}^{ess,d}\right)\right]\Delta t + \sum_{t=1}^{T}\sum_{n=1}^{N}v_n^{Disc}P_{t,i}^{L,move}\Delta t \\
& + \sum_{t=1}^{T}\sum_{n=1}^{N}\sum_{e=1}^{Ne} l_{\deg}\left(P_{t,i}^{ess,c}\eta^{ess,c} + \frac{P_{t,i}^{ess,d}}{\eta^{ess,d}}\right)\Delta t \\
& - \sum_{t=1}^{T}\sum_{n=1}^{N}\sum_{e=1}^{Ne}\left[\mu_{1,t,n}^{ess,c}P_{t,i}^{ess,c} - \mu_{2,t,n}^{ess,c}\left(P_{t,i}^{ess,c} - u_{t,e}^{ess}P_e^{c,rat}\right)\right] \\
& - \sum_{t=1}^{T}\sum_{n=1}^{N}\sum_{e=1}^{Ne}\left\{\mu_{1,t,n}^{ess,d}P_{t,i}^{ess,d} - \mu_{2,t,n}^{ess,d}\left[P_{t,i}^{ess,d} - \left(1 - u_{t,e}^{ess}\right)P_e^{d,rat}\right]\right\} \\
& + \sum_{t=1}^{T}\sum_{n=1}^{N}\sum_{e=1}^{Ne}\left[\mu_{1,t,n}^{S}\left(S_e^{\min} - S_{t,e}\right) + \mu_{2,t,n}^{S}\left(S_{t,e} - S_e^{\max}\right)\right] \\
& + \sum_{t=1}^{T}\sum_{n=1}^{N}\left[\mu_{1,t,n}^{L,move}\left(L^{\min} - P_{t,i}^{L,move}\right) + \mu_{2,t,n}^{L,move}\left(P_{t,i}^{L,move} - L^{\max}\right)\right] \\
& + \sum_{n=1}^{N}\lambda_{1,n}\left(\sum_{t=1}^{T}P_{t,i}^{L,move}\right) + \sum_{n=1}^{N}\sum_{e=1}^{Ne}\lambda_{2,n}\left(S_{1,e} - S_{T,e}\right) \\
& + \sum_{t=1}^{T-1}\sum_{n=1}^{N}\sum_{e=1}^{Ne}\left[\lambda_{3,t,n}\left(S_{t,e} - S_{t-1,e} - \frac{P_{t,i}^{ess,c}\eta^{ess,c}\Delta t}{Cap_e^{ess}} - \frac{P_{t,i}^{ess,d}}{\eta^{ess,d}Cap_e^{ess}}\Delta t\right)\right]
\end{aligned} \tag{44}$$

2) Taking the partial derivative with respect to ∇L yields the equality constraint:

$$\frac{\partial L}{\partial P_{t,i}^{L,move}} = \lambda_t\Delta t + v_n^{Disc}\Delta t - \mu_{1,t,n}^{L,move} + \mu_{2,t,n}^{L,move} + \lambda_{1,n} = 0 \quad T \in [1,t] \tag{45}$$

$$\frac{\partial L}{\partial P_{t,i}^{ess,c}} = \begin{cases} \lambda_t\Delta t + l_{\deg}\eta^{ess,c}\Delta t - \mu_{1,t,n}^{ess,c} + \mu_{2,t,n}^{ess,c} - \lambda_{3,t,n}\eta^{ess,c}\Delta t \big/ Cap_e^{ess} = 0 & t \in [1, T-1] \\ \lambda_t\Delta t + l_{\deg}\eta^{ess,c}\Delta t - \mu_{1,t,n}^{ess,c} + \mu_{2,t,n}^{ess,c} = 0 & t = T \end{cases} \tag{46}$$

$$\frac{\partial L}{\partial P_{t,i}^{ess,d}} = \begin{cases} -\lambda_t\Delta t + \dfrac{l_{\deg}\Delta t}{\eta^{ess,d}} - \mu_{1,t,n}^{ess,d} + \mu_{2,t,n}^{ess,d} - \dfrac{\lambda_{3,t,n}\Delta t}{\eta^{ess,d}Cap_e^{ess}} = 0 & t \in [1, T-1] \\ -\lambda_t\Delta t - \dfrac{l_{\deg}\Delta t}{\eta^{ess,d}} - \mu_{1,t,n}^{ess,d} + \mu_{2,t,n}^{ess,d} = 0 & t = T \end{cases} \tag{47}$$

$$\frac{\partial L}{\partial S_{t,e}} = \begin{cases} -\mu_{1,t,n}^{S} + \mu_{2,t,n}^{S} + \lambda_{2,n} - \lambda_{3,t,n} = 0 & t = 1 \\ -\mu_{1,t,n}^{S} + \mu_{2,t,n}^{S} + \lambda_{3,t-1,n} - \lambda_{3,t,n} = 0 & t \in [2, T-1] \\ -\mu_{1,t,n}^{S} + \mu_{2,t,n}^{S} - \lambda_{2,n} + \lambda_{3,t-1,n} = 0 & t = T \end{cases} \tag{48}$$

$$\frac{\partial L}{\partial \lambda_{1,n}} = \sum_{t=1}^{T}P_{t,i}^{L,move} = 0 \tag{49}$$

$$\frac{\partial L}{\partial \lambda_{2,n}} = S_{1,e} - S_{T,e} = 0 \tag{50}$$

$$\frac{\partial L}{\partial \lambda_{3,t,n}} = S_{t,e} - S_{t-1,e} - \frac{P_{t,i}^{ess,c}\eta^{ess,c}}{Cap_e^{ess}} + \frac{P_{t,i}^{ess,d}\big/\eta^{ess,d}}{Cap_e^{ess}}\Delta t = 0 \quad t \in [1, T-1] \tag{51}$$

3) The inequality constraint is constructed by large M method

Since the complementary slack variables in the KKT condition have nonlinear terms of the form $\mu_i g_i(x) = 0$, a Boolean variable ε and a maximum positive number M are introduced to construct the following linear inequalities:

$$\begin{cases} 0 \le P_{t,i}^{ess,c} \le \varepsilon_1^{ess,c}M \\ 0 \le \mu_{1,t,n}^{ess,c} \le \left(1 - \varepsilon_1^{ess,c}\right)M \end{cases} \quad t \in [1,T] \tag{52}$$

$$\begin{cases} 0 \le u_{t,e}^{ess}P_e^{c,rat} - P_{t,i}^{ess,c} \le \varepsilon_2^{ess,c}M \\ 0 \le \mu_{2,t,n}^{ess,c} \le \left(1 - \varepsilon_2^{ess,c}\right)M \end{cases} \quad t \in [1,T] \tag{53}$$

$$\begin{cases} 0 \le P_{t,i}^{ess,d} \le \varepsilon_1^{ess,d}M \\ 0 \le \mu_{1,t,n}^{ess,d} \le \left(1 - \varepsilon_1^{ess,d}\right)M \end{cases} \quad t \in [1,T] \tag{54}$$

$$\begin{cases} 0 \le \left(1 - u_{t,e}^{ess}\right)P_e^{d,rat} - P_{t,i}^{ess,d} \le \varepsilon_2^{ess,d}M \\ 0 \le \mu_{2,t,n}^{ess,d} \le \left(1 - \varepsilon_2^{ess,d}\right)M \end{cases} \quad t \in [1,T] \tag{55}$$

$$\begin{cases} 0 \le S_{t,e} - S_e^{\min} \le \varepsilon_1^{S}M \\ 0 \le \mu_{1,t,n}^{S} \le \left(1 - \varepsilon_1^{S}\right)M \end{cases} \quad t \in [1,T] \tag{56}$$

$$\begin{cases} 0 \le S_e^{\max} - S_{t,e} \le \varepsilon_2^{S}M \\ 0 \le \mu_{2,t,n}^{S} \le \left(1 - \varepsilon_2^{S}\right)M \end{cases} \quad t \in [1,T] \tag{57}$$

$$\begin{cases} 0 \le P_{t,i}^{L,move} - L^{\min} \le \varepsilon_1^{L,move}M \\ 0 \le \mu_{1,t,n}^{L,move} \le \left(1 - \varepsilon_1^{L,move}\right)M \end{cases} \quad t \in [1,T] \tag{58}$$

$$\begin{cases} 0 \le L^{\max} - P_{t,i}^{L,move} \le \varepsilon_2^{L,move}M \\ 0 \le \mu_{2,t,n}^{L,move} \le \left(1 - \varepsilon_2^{L,move}\right)M \end{cases} \quad t \in [1,T] \tag{59}$$

4) Single layer optimization model

Substituting Equations 45–51 into Equation 44 can be obtained as follows:

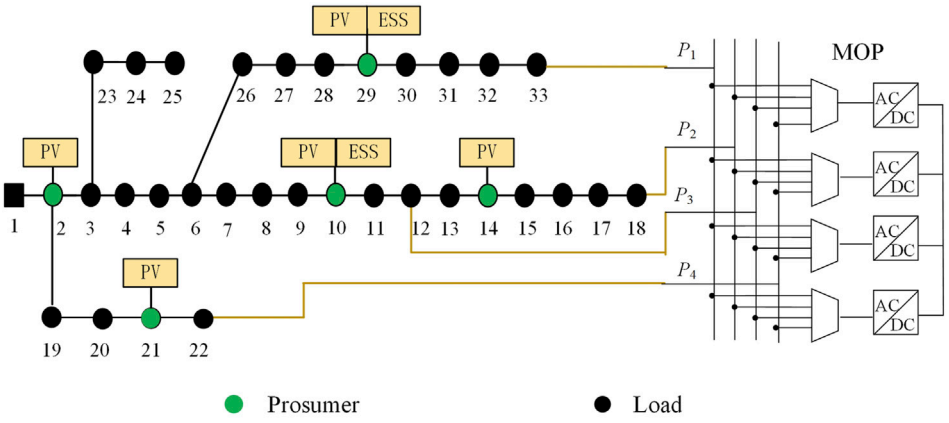

FIGURE 4
Diagram of the improved IEEE 33-bus system.

TABLE 1 IEEE 33-bus test system related parameters.

Entity	Device	Location	Parameter
Prosumer 1	PV	Bus 2	Power: 500 kW
Prosumer 2	PV	Bus 10	Power: 500 kW
	ESS	Bus 10	Power: 0.5 MWh, Capacity: 0.2 MW, efficiency: 0.95
Prosumer 3	PV	Bus 14	Power: 400 kW
Prosumer 4	PV	Bus 21	Power: 400 kW
Prosumer 5	PV	Bus 29	Power: 300 kW
	ESS	Bus 29	Power: 0.5 MWh, Capacity: 0.2 MW, efficiency: 0.95
DN	MOP	Bus 12, 22, 18, 33	Capacity: 0.75WVA

$$\nabla L = \sum_{t=1}^{T}\sum_{n=1}^{N}\lambda_t\left(P_{t,i}^{L} - P_{t,i}^{PV}\right)\Delta t - \sum_{t=1}^{T}\sum_{n=1}^{N}\mu_{2,t,n}^{ess,c}u_{t,e}^{ess}P_e^{c,rat} - \sum_{t=1}^{T}\sum_{n=1}^{N}\mu_{2,t,n}^{ess,d}\left(1-u_{t,e}^{ess}\right)P_e^{d,rat} + \sum_{t=1}^{T}\sum_{n=1}^{N}\mu_{1,t,n}^{S}S_e^{\min} - \sum_{t=1}^{T}\sum_{n=1}^{N}\mu_{2,t,n}^{S}S_e^{\max} + \sum_{t=1}^{T}\sum_{n=1}^{N}\mu_{1,t,n}^{L,move}L^{\min} - \sum_{t=1}^{T}\sum_{n=1}^{N}\mu_{2,t,n}^{L,move}L^{\max} \tag{60}$$

Equation 60 is combined with the upper DNO optimization objective Equation 1 to obtain the optimization objective of the single-layer optimization model as shown in Equation 61:

$$\begin{aligned}\min F = {} & a_o\left[f_{Grid} + f_{loss} + f_{switch} - \sum_{t=1}^{T}\sum_{n=1}^{N}\lambda_t\left(P_{t,i}^{L} - P_{t,i}^{PV}\right)\Delta t\right] + b_v f_{vd} + \\ & \sum_{t=1}^{T}\sum_{n=1}^{N}\left(\mu_{1,t,n}^{L,move}L^{\min} - \mu_{2,t,n}^{L,move}L^{\max}\right) \\ & + \sum_{t=1}^{T}\sum_{n=1}^{N}\left[-\mu_{2,t,n}^{ess,c}u_{t,e}^{ess}P_e^{c,rat} - \mu_{2,t,n}^{ess,d}\left(1-u_{t,e}^{ess}\right)P_e^{d,rat}\right] \\ & + \sum_{t=1}^{T}\sum_{n=1}^{N}\left[\mu_{1,t,n}^{S}S_e^{\min} - \mu_{2,t,n}^{S}S_e^{\max}\right]\end{aligned} \tag{61}$$

Subject to: Equations 7, 8, 11–13, 15–19, 29–31, 33–34, 36–40, 45–59;

Variables: $\lambda_t, P_{t,i}^{VSC}, Q_{t,i}^{VSC}, P_{t,n}^{P}, P_{t,i}^{L,move}, P_{t,i}^{ess,c}, P_{t,i}^{ess,d}, S_{t,e}$;

By the above methods, the two-layer game optimization problem has been transformed into a single-layer optimization problem.

5 Simulation and analysis

To verify the accuracy and feasibility of the proposed model, programming was implemented using MATLAB R2021b software. The optimization was solved in a 64-bit Windows environment, utilizing the YALMIP toolbox and the Gurobi solver. The hardware environment for optimization calculations was an Intel(R) Core(TM) i9-13900 K @ 3.00 GHz processor with 128 GB of memory.

5.1 Parameter setting

In the simulation tests, the modified IEEE-33 bus distribution system is used for analysis, which includes five prosumers with PV systems. Among them, the prosumers at buses 10 and 29 are equipped with ESS, as shown in Figure 4. The whole DN contains five PVS, two ESS and one four-feeder MOP. The relevant parameters are shown in Table 1, and the other bus branch parameters are the standard IEEE-33 bus system.

The DNO is set from the HV power purchase price reference (Qiao et al., 2025), and the DNO selling price is set to 400 ¥/MWh, without considering the reactive power influence of renewable

TABLE 2 Parameter settings.

Parameter	Value	Parameter	Value
Δt	1 h	$\bar{U}$	1.05p.u
a_o	0.833	$\underline{U}$	0.95p.u
b_v	0.167	$\tilde{U}_{ref}$	0.97 p.u.,1.03p.u
C_{loss}	0.08	$\lambda_t^{\min}$	W_t
l_{deg}	2.7$/MWh	$\lambda_t^{\max}$	X_t

energy. Other parameter Settings are shown in Table 2 (Yang et al., 2023).

The PV output and load demand forecast of each prosumer are shown in Figures 5A, B.

5.2 Results and analysis

In the energy trading market, DNO, as the leader, has the pricing power, and the settlement price determined is shown in Figure 6.

As followers, prosumer adjust their electricity consumption strategies according to the internal settlement price. The transferable load of each prosumer is shown in Figure 7A, and the total exchange power with DNO is shown in Figure 7B. The charging and discharging power of ESS1 connected to prosumer 2 is shown in Figure 8A, and the energy storage of each ESS is shown in Figure 8B.

As observed from Figures 5–8, the formulation of the electricity consumption strategy of the prosumer is affected by the clearing price set by the DNO, which is specifically shown as follows:

Between 0:00 and 5:00, with zero PV output and low prosumer loads, prosumers purchase electricity to maintain normal operations. Clearing prices remain high due to economic principles but are capped by time-of-use pricing. During this period, the ESS charges and the prosumer increases the transferable load. From 3:00 to 5:00, as the electricity price decreases, the ESS charging increases, resulting in a sharp rise in the exchanged power. Between 6:00 and 8:00, the PV generation and consumer load gradually rise, but the supply is still insufficient, leading to an increase in the clearing price. At the same time as the ESS discharges, the prosumer reduces the transferable load, which reduces the exchanged power. Between 9:00 and 10:00, higher PV generation and less load can achieve energy balance through energy interaction and resource adjustment without purchasing DNO, thus achieving price reduction and zero exchanged power. From 11:00 to 13:00, peak PV output exceeds demand, enabling prosumers to charge ESS, consume transferable loads, and sell surplus energy to the DNO. Exchange power becomes negative, and clearing prices drop to the minimum limit. Between 14:00 and 17:00, as PV generation and load are reduced, the supply temporarily meets the demand and maintains the minimum price. After that, the energy internal supply exceeds the demand leading to the clearing price increase, prompting the prosumer to reduce the load and the ESS discharge, so that the exchange power is positive. From 18:00 to 20:00, insufficient PV generation and gradually rising electricity demand lead to the maximum clearing price. The prosumer reduces the transferable load and the ESS discharges, at which point, the exchanged power reaches its peak. Between 21:00 and 24:00, demand remains high, but prices stabilize due to time-of-use pricing. Prosumers remaining transferable loads and discharge surplus ESS energy, reducing costs and exchange power as load demand declines.

The voltage situation of each bus within 24 h of the test system is shown in Figure 9. It can be seen that the per unit voltage value of

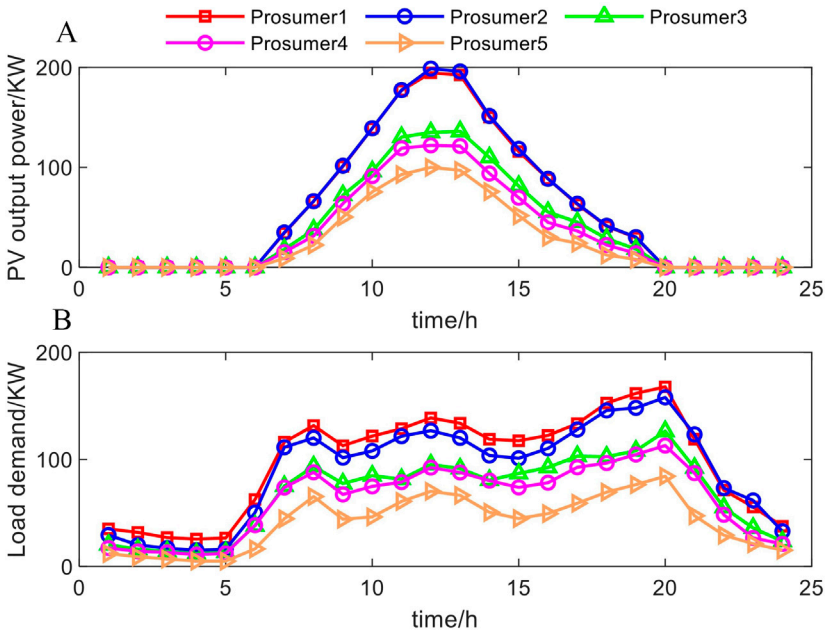

FIGURE 5
Initial data of each prosumer: **(A)** PV output; **(B)** Load demand.

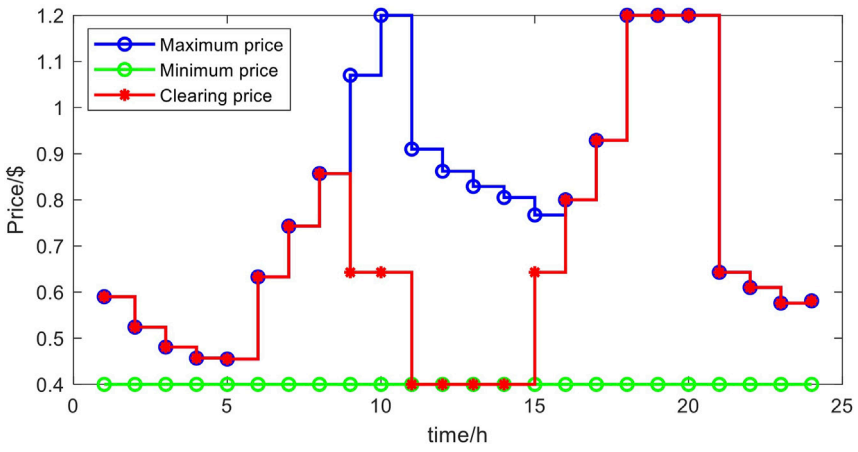

FIGURE 6
Clearing price.

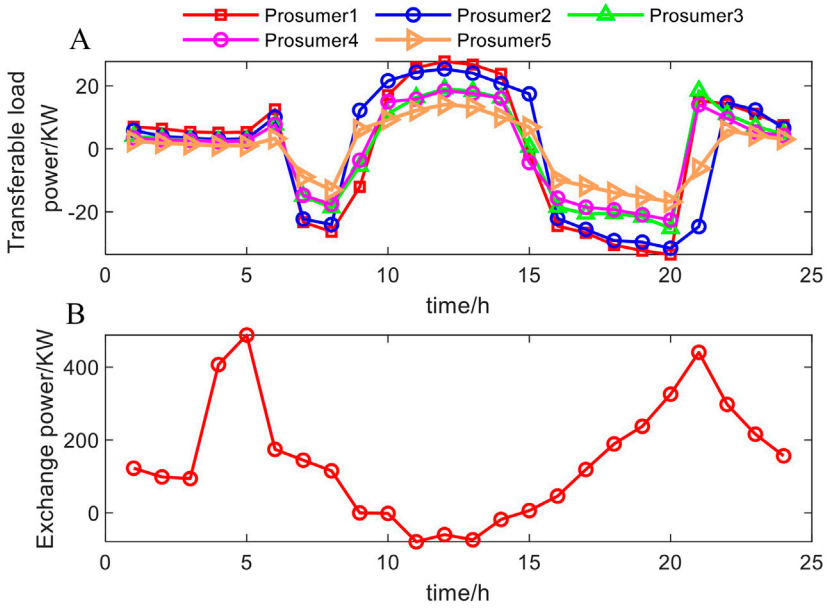

FIGURE 7
Load regulation strategies of prosumer: **(A)** Changes in transferable loads; **(B)** Exchange power.

each bus is within the expected range (0.96 p.u.–1.04p.u.), which meets the safety of the system operation.

The gap value of 24 h is shown in Figure 10. Combined with the definition of Equation 41, it can be found that the gap value of each time period is at the level of 10-6, so it can be proved that convex relaxation is accurate.

5.3 Scenario comparison and analysis

In order to verify the effectiveness and superiority of the proposed strategy, the following three scenarios are set in this section:

Scenario 1: Only the economy of the system is considered, and safety issues such as MOP power flow optimization, power loss, and voltage deviation are not considered.

Scenario 2: The adjustment of MOP is not considered in the proposed strategy.

Scenario 3: The strategy presented in this article.

As can be seen in Figures 11A, B and Figures 12 A, B, the voltage quality of scenario 3 is better than that of the comparison scenario, indicating that the proposed strategy can improve the stability of the system. Moreover, the action of MOP is consistent with that of energy storage, which indicates that MOP can optimize the power

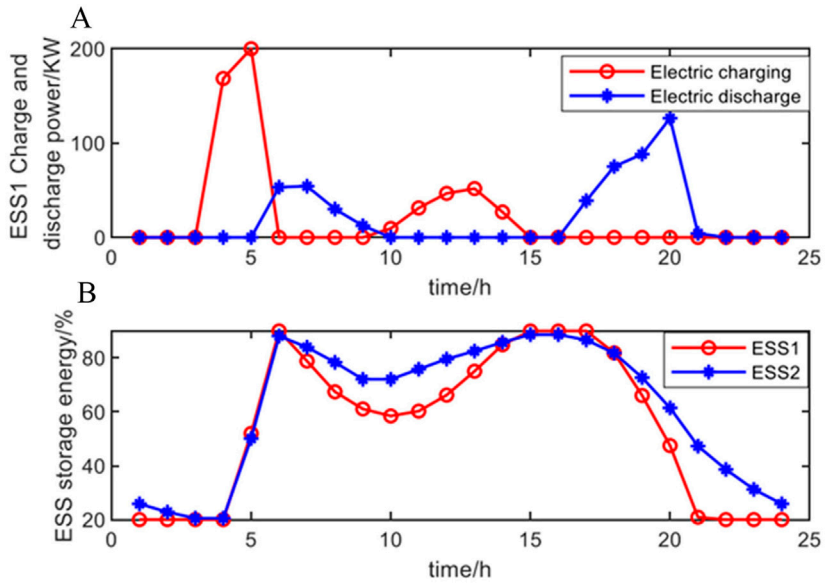

FIGURE 8
ESS control strategy: **(A)** Charge and discharge power of ESS1; **(B)** Energy storage of each ESS.

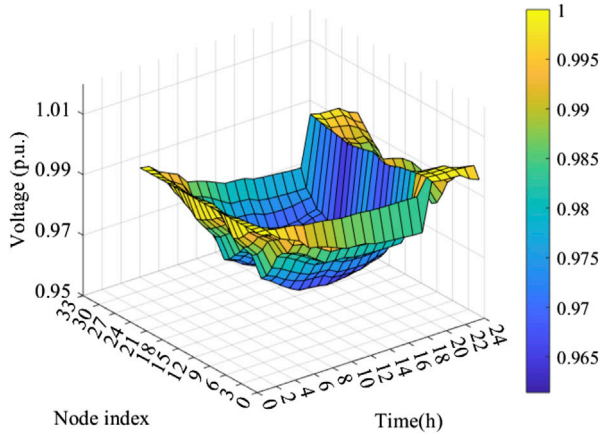

FIGURE 9
Voltage profiles of all 33 nodes.

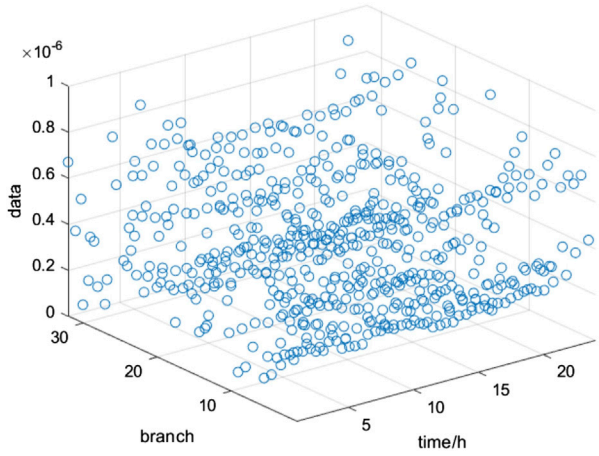

FIGURE 10
Gap value.

flow distribution and improve power quality by adjusting the active and reactive power of the connected feeders.

The test results are compared as shown in Table 3, including the system power loss cost (f_{loss}, including line power loss and MOP power loss), the converted voltage deviation cost (f_{vd}), the total operating cost of DNO (F_{DNO}), the total operating cost of the prosumer (J_n) and voltage over-limit rate. The voltage compliance range specified in this paper is 0.95p.u.–1.05p.u.

As shown in Table 3, the daily total operating cost of the DNO in Scenario 1, which considers only economic benefits, is \$13.95, representing a reduction of approximately 83.9% compared to \$86.72 in Scenario 3. However, the voltage deviation cost increases from \$0.13 to \$104.21, an increase of nearly 800 times, and the voltage over-limit rate increases from 0% to 26.39%. This indicates that in scenarios where safety performance is not considered, all controllable resources are allocated to maximize profits. While this approach effectively reduces system operating costs, it leads to significant grid fluctuations, poor power quality, and substantial safety risks, which are detrimental to the reliable operation of the system.

Compared to Scenario 2, Scenario 3 introduces the MOP, which increases the power loss cost of the MOP by \$30.94. However, both network loss and voltage deviation costs are reduced, resulting in a decrease in the total operating cost of the DNO from \$193.04 to \$86.72, a reduction of approximately 55.1%. Moreover, the voltage over-limit rate is reduced from

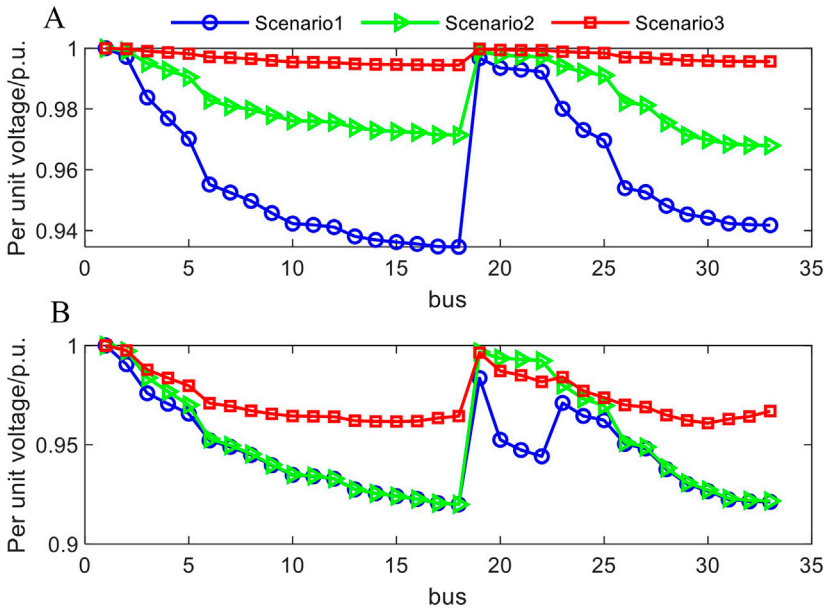

FIGURE 11
Comparison of voltage per unit value: **(A)** Maximum voltage; **(B)** Minimum voltage.

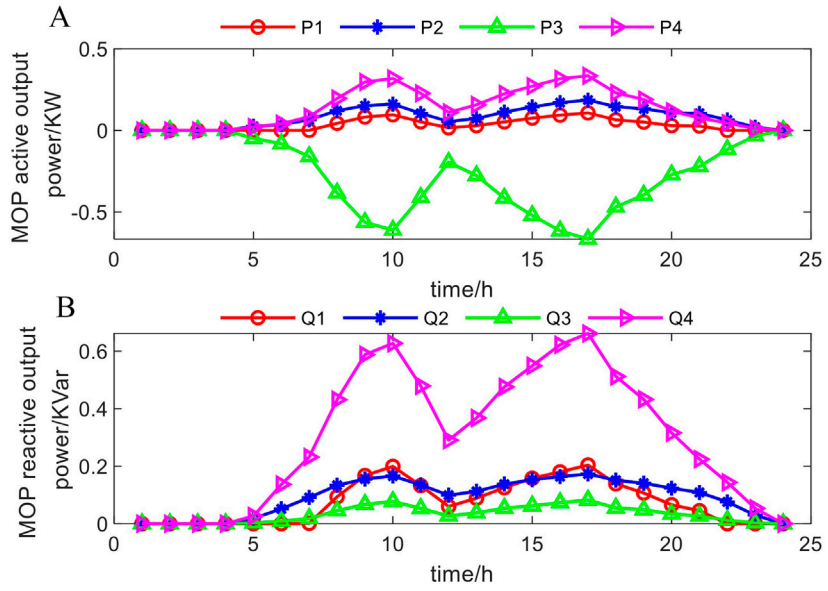

FIGURE 12
Power output of MOP: **(A)** The output of active power; **(B)** The output of reactive power.

65.03% to 0. This demonstrates a significant improvement in both economic efficiency and operational safety.

In summary, the proposed strategy not only addresses the energy transaction challenges in multi-prosumer distribution systems and ensures the economic benefits of all participants but also enhances the safety performance of the system. Additionally, it provides a novel solution for promoting local renewable energy utilization and optimizing energy interactions.

6 Conclusion

This study investigates the energy interaction challenges in flexible distribution systems with multiple prosumers. By analyzing the factors influencing the economic benefits of the DNO and prosumers, as well as the network security of the DN, a Stackelberg game-based energy interaction strategy for multi-prosumer distribution systems is proposed, considering both

TABLE 3 Test data comparison.

Test result		Scenario 1	Scenario 2	Scenario 3
f_{loss} ($)	Line	9,560.51	209.19	72.00
	MOP	0	0	30.94
f_{vd} ($)		104.21	2.96	0.13
F_{DNO} ($)		13.95	193.04	86.72
J_n ($)		2,704.10	2,700.75	2,712.97
Voltage over-limit rate		65.03%	26.39%	0%

economic and safety aspects. Unlike previous studies, this strategy not only addresses the economic issues between the DNO and prosumers but also optimizes DN operation by regulating the MOP, ensuring system operational safety and improving power quality. Additionally, the original bi-level energy interaction model is transformed using KKT conditions, enhancing computational efficiency. The main conclusions are as follows:

1) Different from traditional energy interaction models for multi-prosumer distribution systems, this paper proposes a novel energy interaction strategy based on game theory, considering the interests of all participants and the operational safety of the system. This strategy not only maximizes the benefits for all parties but also promotes the local utilization of PV energy while protecting user privacy.
2) The influencing factors in the energy interaction process were analyzed, and the MOP was introduced into the energy trading market. Different from traditional interaction models that focus solely on the coordination between the DNO and prosumers, this strategy also considers power flow regulation in the DN. Although the introduction of MOP increases device costs, it significantly reduces power losses across the system, improves power quality, and ensures the long-term operation of the system.
3) Different from traditional iterative methods for solving bi-level energy interaction game models to determine transaction prices, this paper employs KKT conditions, dual theory, linearization methods, and relaxation techniques to transform the bi-level optimization model, simplifying the solution process.

This study focuses on exploiting the potential of game theory in enhancing energy interaction in flexible distribution systems and innovating the introduction of interconnected devices to improve the regulation performance of distribution networks, but voltage overruns still exist. Therefore, future research should be oriented to dynamic uncertainty and real-time operation, and explore data-driven based intelligent control to further optimize energy trading, improve scalability, and ensure reliable grid operation.

Data availability statement

The original contributions presented in the study are included in the article/supplementary material, further inquiries can be directed to the corresponding author.

Author contributions

WL: Funding acquisition, Project administration, Writing–review and editing, Methodology. SZ: Investigation, Supervision, Writing–original draft. XZ: Methodology, Software, Writing–original draft. SQ: Data curation, Supervision, Writing–review and editing. BL: Formal Analysis, Writing–review and editing. YZ: Formal Analysis, Supervision, Writing–review and editing. JC: Writing–review and editing. QG: Writing–review and editing.

Funding

The author(s) declare that financial support was received for the research, authorship, and/or publication of this article. This work was financially supported by Technology Project of State Grid Anhui Electric Power Co., Ltd. China “Research on multi-agent interactive energy control technology of high proportion distributed photovoltaic flexible distribution system” (B31205230006).

Conflict of interest

Authors WL, SZ, and SQ were employed by Electric Power Research Institute of State Grid Anhui Electric Power Co., Ltd. Authors BL, YZ, JC, and QG were employed by State Grid Anhui Electric Power Co., Ltd., Chuzhou Power Supply Company.

The remaining author declares that the research was conducted in the absence of any commercial or financial relationships that could be construed as a potential conflict of interest.

The authors declare that this study received funding from Technology Project of State Grid Anhui Electric Power Co., Ltd. The funder had the following involvement in the study: study design, decision to publish, and preparation of the manuscript.

Generative AI statement

The author(s) declare that no Generative AI was used in the creation of this manuscript.

Publisher’s note

References

Ashrafi, M., Abbaspour, A., Firuzabad, M., Dehkordi, S., Bacha, S., and Caire, R. (2024). Fault-resilient energy management of grid-connected energy communities in presence of distance-driven P2P and P2G energy transactions. *Electr. Power Syst. Res.* 233, 110468. doi:10.1016/J.EPSR.2024.110468

Deakin, M., Taylor, P., Bialek, J., and Ming, W. (2022). Design and operation of hybrid multi-terminal soft open points using feeder selector switches for flexible distribution system interconnection. *Electr. Power Syst. Res.* 212, 108516. doi:10.1016/J.EPSR.2022.108516

Dempe, S., and Franke, S. (2019). Solution of bilevel optimization problems using the KKT approach. *Optimization* 68 (8), 1471–1489. doi:10.1080/02331934.2019.1581192

Gao, J., Shao, Z., Chen, F., and Lak, M. (2024). Robust optimization for integrated energy systems based on multi-energy trading. *Energy* 308, 132302. doi:10.1016/J.ENERGY.2024.132302

Guan, Y., and Hou, Q. (2024). Design of distributed trading mechanism for prosumers considering the psychological gap effect in community electricity markets. *Electr. Power Syst. Res.* 232, 110410. doi:10.1016/J.EPSR.2024.110410

Hou, P., Yang, G., Hu, J., Douglass, P., and Xue, Y. (2022). A distributed transactive energy mechanism for integrating PV and storage prosumers in market operation. *Engineering* 12, 171–182. doi:10.1016/J.ENG.2022.03.001

Izadi, A., and Rastegar, M. (2024). A stochastic iterative peer-to-peer energy market clearing in smart energy communities considering participation priorities of prosumers. *Sustain. Cities Soc.* 114, 105728. doi:10.1016/J.SCS.2024.105728

Li, J., Zhang, L., Zhang, B., and Tang, W. (2023). Coordinated planning for flexible interconnection and energy storage system in low-voltage distribution networks to improve the accommodation capacity of photovoltaic. *Glob. Energy Interconnect.* 6 (6), 700–713. doi:10.1016/J.GLOEI.2023.11.004

Li, J., Zhang, Y., Lv, C., Liu, G., Ruan, Z., and Zhang, F. (2024). Coordinated planning of soft open points and energy storage systems to enhance flexibility of distribution networks. *Appl. Sci.* 14 (18), 8309. doi:10.3390/APP14188309

Liang, J., Zhou, J., Yuan, X., Huang, W., Gong, X., and Zhang, G. (2024). An active distribution network voltage optimization method based on source-network-load-storage coordination and interaction. *Energies* 17 (18), 4645. doi:10.3390/EN17184645

Liu, D., Cheng, P., Cheng, J., Liu, J., Lu, M., and Jiang, F. (2023). Improved reinforcement learning-based real-time energy scheduling for prosumer with elastic loads in smart grid. *Knowledge-Based Syst.* 280, 111004. doi:10.1016/J.KNOSYS.2023.111004

Liu, J., Meng, X., and Wu, J. (2024). Multi-stage cooperative planning among shared energy storage operator and multiple prosumers in regional integrated energy system considering long-term uncertainty. *J. Energy Storage* 103 (PA), 114244. doi:10.1016/J.EST.2024.114244

Lou, W., Zhu, S., Ding, J., Zhu, T., Wang, M., Sun, L., et al. (2023). Transactive demand–response framework for high renewable penetrated multi-energy prosumer aggregators in the context of a smart grid. *Appl. Sci.* 13 (18), 10083. doi:10.3390/APP131810083

Manchalwar, A. D., Patne, N. R., Morey, C. D., and Pemmada, S. (2024). Prosumers and retailers based decentralized energy trading model in the smart grid considering network constraints. *Int. J. Electr. Power Energy Syst.* 160, 110108. doi:10.1016/J.IJEPES.2024.110108

Meng, H., Jia, H., Xu, T., Sun, J., Wang, R., and Wang, J. (2024). Trading mechanism of distributed shared energy storage system considering voltage regulation. *Appl. Energy* 374, 123904. doi:10.1016/J.APENERGY.2024.123904

Miyamoto, T., Kitamura, S., Naito, K., Mori, K., and Izui, Y. (2020). Distributed day-ahead scheduling of community energy management system group considering uncertain market prices using stochastic optimization. *IEEJ Trans. Electr. Electron. Eng.* 15 (3), 401–408. doi:10.1002/tee.23068

Mohammadreza, A., Taher, N., and Hossein, J. (2024). Economic operation of networked flexi-renewable energy hubs with thermal and hydrogen storage systems based on the market clearing price model. *Int. J. Hydrogen Energy* 50 (PD), 1–18. doi:10.1016/J.IJHYDENE.2023.06.144

Qiao, J., Mi, Y., Shen, J., Lu, C., Cai, P., Ma, S., et al. (2025). Optimization schedule strategy of active distribution network based on microgrid group and shared energy storage. *Appl. Energy* 377 (PD), 124681. doi:10.1016/J.APENERGY.2024.124681

Seppälä, J., and Järventausta, P. (2024). Analyzing supply reliability incentive in pricing regulation of electricity distribution operators. *Energies* 17 (6), 1451. doi:10.3390/EN17061451

Taher, A., Hasanien, H., Alsaleh, I., Aleem, A., Alassaf, A., and Almalaq, A. (2024). Optimizing active distribution microgrids with multi-terminal soft open point and hybrid hydrogen storage systems for enhanced frequency stability. *J. Energy Storage* 99 (PA), 113369. doi:10.1016/J.EST.2024.113369

Tao, C., Duan, Y., Gao, F., and Zhang, J. (2024). A game model based optimisation approach for generalised shared energy storage and integrated energy system trading. *J. Eng. Appl. Sci.* 71 (1), 172. doi:10.1186/S44147-024-00506-7

Wu, Y., Tian, X., Gai, L., Lim, B., Wu, T., Xu, D., et al. (2024). Energy management for PV prosumers inside microgrids based on Stackelberg–Nash game considering demand response. *Sustain. Energy Technol. Assessments* 68, 103856. doi:10.1016/J.SETA.2024.103856

Xiao, Y., Lin, X., Lei, Y., Gu, Y., Tang, J., Zhang, F., et al. (2024). Blockchain-assisted secure energy trading in electricity markets: a tiny deep reinforcement learning-based Stackelberg game approach. *Electronics* 13 (18), 3647. doi:10.3390/ELECTRONICS13183647

Yang, X., Song, Z., Wen, J., Ding, L., Zhang, M., Wu, Q., et al. (2023). Network-constrained transactive control for multi-microgrids-based distribution networks with soft open points. *IEEE Trans. Sustain. Energy* 14, 1769–1783. doi:10.1109/TSTE.2023.3246360

Yang, Y., Xu, X., Pan, L., Liu, J., Liu, J., and Hu, W. (2024). Distributed prosumer trading in the electricity and carbon markets considering user utility. *Renew. Energy* 228, 120669. doi:10.1016/J.RENENE.2024.120669

Zheng, S., Huang, G., and Lai, A. C. K. (2021). Techno-economic performance analysis of synergistic energy sharing strategies for grid-connected prosumers with distributed battery storages. *Renew. Energy* 178, 1261–1278. doi:10.1016/J.RENENE.2021.06.100

Zheng, W., Xu, S., Lu, H., Wu, W., and Zhu, J. (2024). Trading mechanism for social welfare maximization in integrated electricity and heat systems with multiple self-interested stakeholders. *Energy* 306, 132267. doi:10.1016/J.ENERGY.2024.132267

Zhu, X., Sun, Y., Yang, J., Dou, Z., Li, G., Xu, C., et al. (2022). Day-ahead energy pricing and management method for regional integrated energy systems considering multi-energy demand responses. *Energy* 251, 123914. doi:10.1016/J.ENERGY.2022.123914

frontiers | Frontiers in Energy Research

TYPE Brief Research Report
PUBLISHED 17 March 2025
DOI 10.3389/fenrg.2025.1561763

OPEN ACCESS

EDITED BY
Zhenjia Lin,
Hong Kong Polytechnic University, Hong Kong SAR, China

REVIEWED BY
Xi Lu,
Southeast University, China
Xiurong Zhang,
China Agricultural University, China

*CORRESPONDENCE
Jiong Yan,
yanjiong7172@vip.sina.com

RECEIVED 16 January 2025
ACCEPTED 17 February 2025
PUBLISHED 17 March 2025

CITATION
Wu Q, Zhou M, Yan J, Sang Z and Wang S (2025) A survey on investment efficiency-oriented power grid infrastructure planning.
Front. Energy Res. 13:1561763.
doi: 10.3389/fenrg.2025.1561763

A survey on investment efficiency-oriented power grid infrastructure planning

Qiang Wu[1], Ming Zhou[1], Jiong Yan[2]*, Zixia Sang[2] and Sicong Wang[2]

[1]State Grid Hubei Electric Power Company Limited, Wuhan, China, [2]State Grid Hubei Electric Power Company Limited Economic and Technical Research Institute, Wuhan, China

This paper proposes an investment efficiency-oriented strategy for power grid infrastructure planning with high penetration of renewable energy sources. First, a multi-objective investment portfolio optimization model based on data envelopment analysis is proposed to improve the cost efficiency of power grid infrastructure planning. Then, an evolutionary algorithm based on super-efficiency hyperplane projection transformation is developed to obtain the optimal Pareto frontier of the multi-objective investment portfolio. Furthermore, a super-efficiency envelope model with non-radial relaxation variables is formulated to identify an optimal investment efficiency-oriented solution from the Pareto frontier set. Comparative case studies have been implemented to demonstrate the superior performance of the proposed strategy for investment efficiency enhancement of power grid infrastructure planning.

KEYWORDS

cost efficiency, investment portfolio, power grid planning, renewable energy, multi-objective optimization

1 Introduction

Modern power grids are gradually being dominated by various renewable energy sources due to global low-carbon and environmental concerns (Yi et al., 2023). The integration of renewable energy into the grid will bring about an increase in the cost of various infrastructure investment categories because of its intermittent, volatile, and regional characteristics (Guo et al., 2023; Saxena and Shankar, 2024; Fu et al., 2022; Sha et al., 2023). Faced with mounting operational expenses and constrained investment capacities, power grids must devise portfolio optimization strategies to minimize costs while maximizing investment returns (Lu et al., 2022). The investment portfolio in power grid infrastructure is a dynamic, sequentially coupled, multi-objective discrete combinatorial optimization problem (Liu et al., 2023). Traditional infrastructure investment portfolio decisions that focus on maximizing a single benefit objective are inadequate for meeting the demands of high-quality development in power grids (Yan et al., 2022; Garifi et al., 2022; Ma et al., 2020; Guelpa et al., 2019). Therefore, this study provides practical models and algorithms for grid infrastructure investment planning oriented to maximize investment efficiency.

The main contributions of this work can be twofold, as follows: (1) a multi-objective cost efficiency-oriented investment portfolio optimization model based on

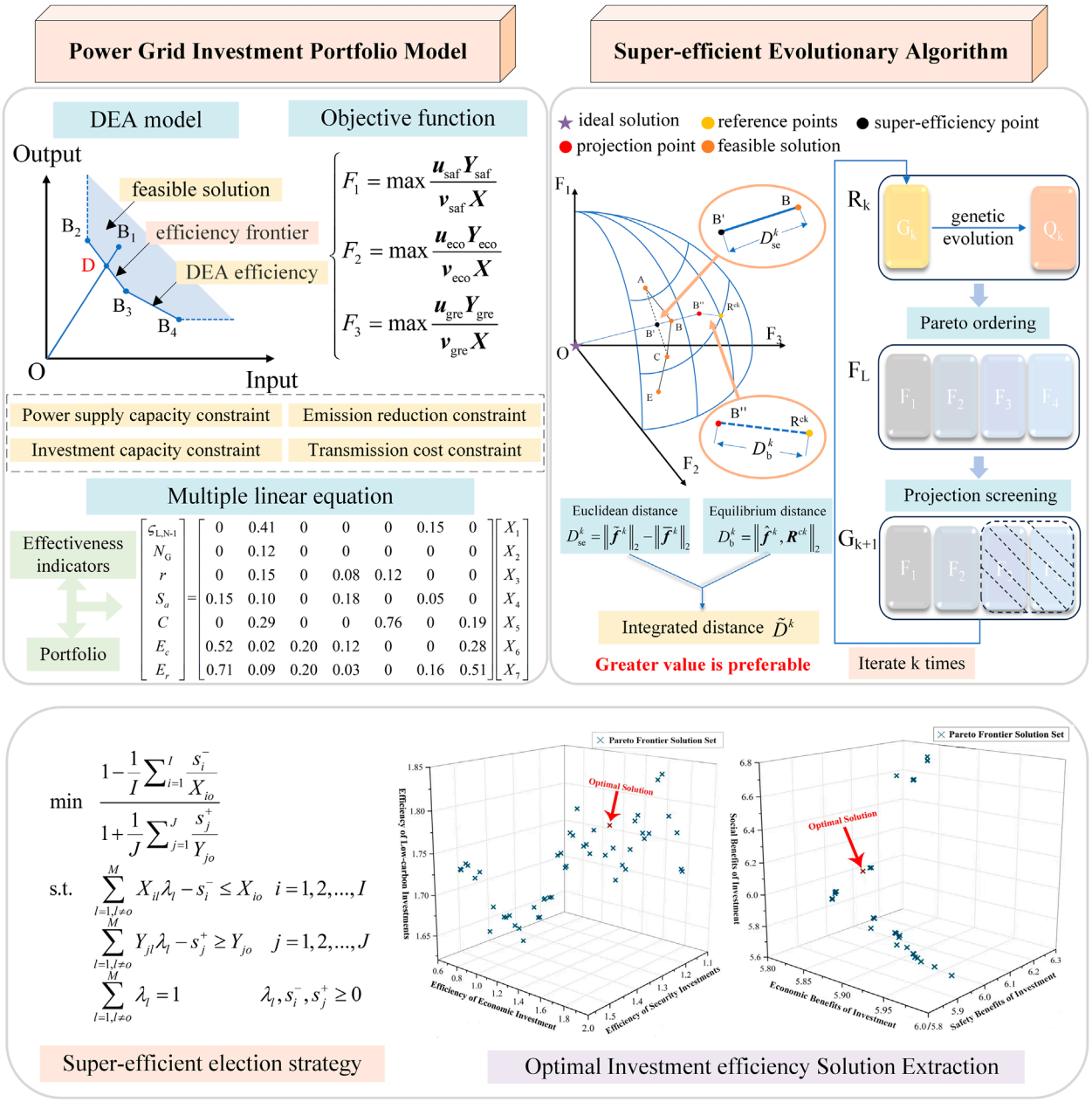

FIGURE 1
Multi-objective cost efficiency-oriented investment portfolio optimization model.

data envelopment analysis is proposed for power grid infrastructure planning, and a transformation matrix based on the LASSO regression model is established with the goal of reducing the complexity of the portfolio optimization, representing the relationship between the amount of investment and benefits. (2) An evolutionary algorithm based on super-efficiency hyperplane projection transformation is developed to obtain the optimal Pareto frontier of the multi-objective investment portfolio, and a super-efficiency envelope model with non-radial relaxation variables is formulated to identify the optimal investment efficiency-oriented solution from the Pareto frontier set.

2 Multi-objective cost efficiency-oriented investment portfolio optimization model

With the increase in investment demand and the concurrent decrease in investment capacity, it has become crucial for grid operators to prioritize investment efficiency when developing annual investment plans (Wu et al., 2022). Thus, it is necessary to establish a multi-objective cost efficiency-oriented investment portfolio optimization model that considers constraints such as investment capacity, power supply reliability (Cao et al., 2024a), energy conservation, and emission reduction. An investment

TABLE 1 Parameter settings of the investment portfolio optimization model.

Parameter	Value	Parameter description
X_{max}	27.6 billion yuan	Maximum investment capacity
M	100	Population size
τ_c	0.9	Population crossover probability
τ_v	0.1	Population mutation probability
N	200	Iteration times
$\varsigma_{L,N-1}^{min}$	98.80%	Lower limit value of N-1 line passing rate
N_{GZ}^{min}	1.2%	Lower limit value of the heavy overload equipment reduction rate
r^{min}	2.10 MVA/MW	Lower limit value of the capacity–load ratio
r^{max}	2.45 MVA/MW	Upper limit value of the capacity–load ratio
S_a^{min}	2.9 MVA per household	Lower limit value of the average household power distribution capacity
S_a^{max}	3.1 MVA per household	Upper limit value of the average household power distribution capacity
C^{min}	184.2 yuan/kWh	Lower limit value of transmission and distribution cost per unit of electricity
E_c^{min}	65,000 tons	Lower limit value of standard coal saved
E_r^{min}	165,000 tons	Lower limit value of pollutant emission reduction

efficiency-oriented model is formulated based on data envelopment analysis (DEA) by mapping power grid investment portfolios to efficiency indicators (Lee and Chen, 2024; Xu et al., 2024). Then, three investment efficiency objective functions are formulated through this approach: safety investment efficiency, economic investment efficiency, and green investment efficiency of power grid infrastructure investment, as outlined in Equation 1:

$$\begin{cases} F_1 = \max \dfrac{\boldsymbol{u}_{saf}\boldsymbol{Y}_{saf}}{\boldsymbol{v}_{saf}\boldsymbol{X}} \\ F_2 = \max \dfrac{\boldsymbol{u}_{eco}\boldsymbol{Y}_{eco}}{\boldsymbol{v}_{eco}\boldsymbol{X}} \\ F_3 = \max \dfrac{\boldsymbol{u}_{gre}\boldsymbol{Y}_{gre}}{\boldsymbol{v}_{gre}\boldsymbol{X}} \end{cases}, \quad \text{s.t.} \quad \frac{\sum_{j=1}^{J} u_j Y_j}{\sum_{i=1}^{I} v_i X_i} \le 1, \quad u_j \ge 0, v_i \ge 0, X_i \ge 0 \tag{1}$$

where $\boldsymbol{u}_{saf}$, $\boldsymbol{u}_{eco}$, and $\boldsymbol{u}_{gre}$, respectively, represent the output weight vector of infrastructure investment safety, economic, and green effectiveness indicators, which can be calculated by the combination of the analytic hierarchy process (Deng and Wang, 2020; Wang et al., 2017) and the entropy weighting method (Li et al., 2024; Qin et al., 2024); $\boldsymbol{v}_{saf}$, $\boldsymbol{v}_{eco}$, and $\boldsymbol{v}_{gre}$ represent the input weight vector of the investment scale of infrastructure portfolio categories; $\boldsymbol{X}$ represents the vector of the investment scale of infrastructure portfolio categories, and $\mathbf{X} = [X_1, X_2, \cdots, X_i, \cdots, X_7]^T$; $\boldsymbol{Y}_{saf}$, $\boldsymbol{Y}_{eco}$, and $\boldsymbol{Y}_{gre}$, respectively, represent the vector of the values of infrastructure investment safety, economic, and green effectiveness indicators, which can be calculated by the LASSO regression model (Tibshirani, 2011). The multi-objective cost efficiency-oriented investment portfolio optimization model is shown in Figure 1.

Several constraints have been introduced into the model to ensure that investments in grid infrastructure are rationalized (Yang et al., 2024). Constraint (2) stipulates that the total investment across all infrastructure drivers should not exceed the maximum investment capacity of the grid. The N-1 line passing rate $\varsigma_{L,N-1}$ and heavy overload equipment reduction rate N_G are used to reflect the degree of improvement in power reliability. In addition, the capacity–load ratio r and average household power distribution capacity S_a are used to reflect the limitation to power supply capacity. Transmission and distribution cost per unit of electricity C is selected to limit the profitability of the company. The amount of saved standard coal E_c and pollutant emission reduction E_r are chosen to reflect the effect of energy saving and emission reduction. Constraints are shown in Equations 2–4:

$$\sum_{i=1}^{I} X_i \le X_{max}, \tag{2}$$

$$\begin{bmatrix} \varsigma_{L,N-1}^{min} \\ N_{GZ}^{min} \\ r^{min} \\ S_a^{min} \\ C^{min} \\ E_c^{min} \\ E_r^{min} \end{bmatrix} \le \begin{bmatrix} \varsigma_{L,N-1} \\ N_G \\ r \\ S_a \\ C \\ E_c \\ E_r \end{bmatrix} = \begin{bmatrix} 0 & 0.41 & 0 & 0 & 0 & 0.15 & 0 \\ 0 & 0.12 & 0 & 0 & 0 & 0 & 0 \\ 0 & 0.15 & 0 & 0.08 & 0.12 & 0 & 0 \\ 0.15 & 0.10 & 0 & 0.18 & 0 & 0.05 & 0 \\ 0 & 0.29 & 0 & 0 & 0.76 & 0 & 0.19 \\ 0.52 & 0.02 & 0.20 & 0.12 & 0 & 0 & 0.28 \\ 0.71 & 0.09 & 0.20 & 0.03 & 0 & 0.16 & 0.51 \end{bmatrix} \begin{bmatrix} X_1 \\ X_2 \\ X_3 \\ X_4 \\ X_5 \\ X_6 \\ X_7 \end{bmatrix}, \tag{3}$$

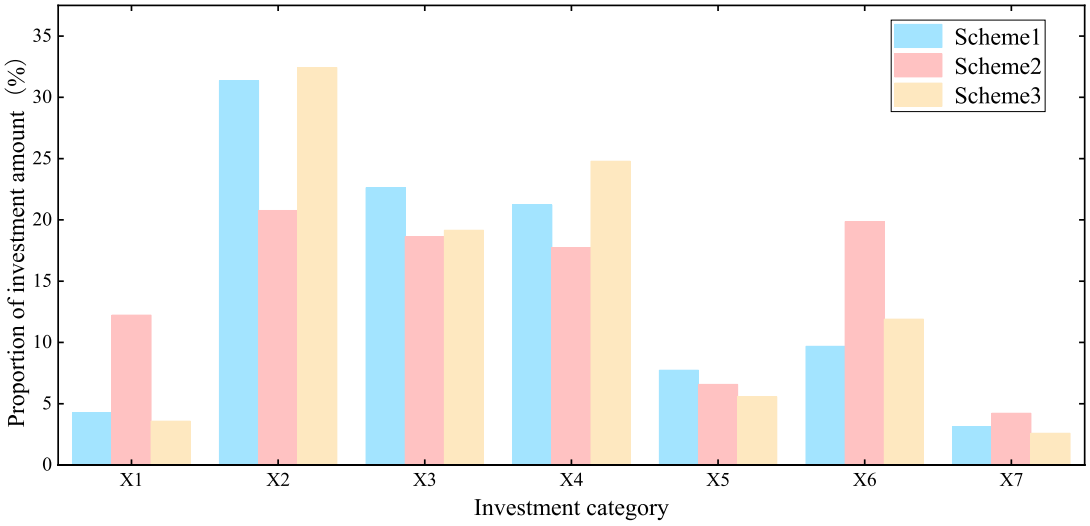

FIGURE 2
Power grid investment portfolios under different schemes.

$$\begin{bmatrix} r^{\max} \\ S_a^{\max} \end{bmatrix} \geq \begin{bmatrix} r \\ S_a \end{bmatrix} = \begin{bmatrix} 0 & 0.15 & 0.08 & 0.12 & 0 \\ 0.15 & 0.10 & 0.18 & 0 & 0.05 \end{bmatrix} \begin{bmatrix} X_1 \\ X_2 \\ X_4 \\ X_5 \\ X_6 \end{bmatrix}, \tag{4}$$

where $X_{\max}$ represents the maximum scale of annual infrastructure investment of the company; $\varsigma_{\mathrm{L,N-1}}^{\min}$ represents the lower limit value of the line N-1 passing rate; $N_{\mathrm{GZ}}^{\min}$ represents the lower limit value of the decline rate of heavy overload equipment solved; $r^{\max}$ and $r^{\min}$, respectively, represent the upper and lower values of the capacity–load ratio; $S_a^{\max}$ and $S_a^{\min}$, respectively, represent the upper and lower values of the average household power distribution capacity; $C^{\min}$ represents the lower limit value of the cost of transmission and distribution of electricity per unit of electricity; $E_c^{\min}$ represents the lower limit value of the saved standard coal; $E_r^{\min}$ represents the lower limit value of pollutant emission reduction. X_1 represents the investment in improving power access capacity; X_2 represents the investment in enhancing the transmission capacity; X_3 represents the investment in enhancing the flexibility capability; X_4 represents the investment to meet the growing load; X_5 represents the investment in improving the level of digitization; X_6 represents the investment in optimizing the grid structure; X_7 represents the investment in new models and new formats.

3 Evolutionary algorithm for power grid investment efficiency maximization

An evolutionary algorithm based on super-efficient hyperplane projection transformation (EASEHPT) is proposed to optimize multiple objectives within the model. The proposed algorithm is based on the principle of the NSGA-III algorithm (Deb and Jain, 2014), which selects sub-generation grid portfolio populations by calculating the integrated distance of non-dominated portfolio populations. Then, the grid portfolio populations are sorted according to the integrated distance, and populations that perform better in the same class will be retained. The optimal solution is selected from the Pareto efficiency frontier set of the multi-objective infrastructure portfolio through the super-efficiency selection strategy. The multi-objective evolutionary algorithm is shown in Figure 1.

This study compares all portfolio individuals in a new population with a size of 2M after the genetic evolution operation, according to three optimization objectives, F_1, F_2, and F_3, to achieve a Pareto non-dominated hierarchical sorting. Moreover, the single-objective optimal solution set is chosen to construct the spatial hyper-efficiency plane. Then, the Pareto non-dominated solution of the grid infrastructure investment portfolio is projected to the hyper-efficiency plane (Chen et al., 2021). The general expression for the super-efficiency plane of the three objectives is shown in Equation 5:

$$\boldsymbol{a}_1 \cdot \boldsymbol{f}_1 + \boldsymbol{a}_2 \cdot \boldsymbol{f}_2 + \boldsymbol{a}_3 \cdot \boldsymbol{f}_3 = 1, \tag{5}$$

where $(\boldsymbol{a}_1, \boldsymbol{a}_2, \boldsymbol{a}_3)$ denote the unit normal vector of the super-efficiency plane; $(\boldsymbol{f}_1, \boldsymbol{f}_2, \boldsymbol{f}_3)$ denote the extreme point vector. The ideal individuals $(f_{1,\min}, f_{2,\min}, f_{3,\min})$ are extracted and converted to zero vectors (Chen et al., 2020), and the target individuals are normalized and projected onto the super-efficient plane is shown in Equations 6, 7:

$$\bar{f}_i^k = \frac{f_i^k - f_{i,\min}^k}{f_{i,\max}^k - f_{i,\min}^k}, \tag{6}$$

$$\hat{f}_i^k = \frac{\bar{f}_i^k}{\sum_{i=1}^{3} \bar{f}_i^k}, \tag{7}$$

TABLE 2 Investment efficiency and convergence effect of the solution set under different schemes.

Scheme	Safety investment efficiency	Economic investment efficiency	Green investment efficiency	Comprehensive investment efficiency	Inverse generational distance	Spacing
Scheme 1	1.18	1.21	1.77	1.43	0.5374	0.1493
Scheme 2	1.50	0.76	1.62	1.33	—	—
Scheme 3	1.09	1.13	1.48	1.26	0.7226	0.2041

where $\overline{f}_i^k$ denotes the ith normalized target value under the kth grid infrastructure investment portfolio solution; $\hat{f}_i^k$ denotes the intercept of the ith target in the super-efficiency plane under the kth grid infrastructure investment portfolio solution; $f_{i,max}^k$ and $f_{i,min}^k$, respectively, denote the maximum and minimum values of the ith target under the kth grid infrastructure investment portfolio solution.

In this paper, the integrated distance is introduced to evaluate the super-efficiency and equilibrium performance of solutions. Assuming that the coordinates $\overline{\boldsymbol{f}}^k$ of the kth portfolio solution and its projection point $\hat{\boldsymbol{f}}^k$ in the super-efficiency plane are $\left(\overline{f}_1^k, \overline{f}_2^k, \overline{f}_3^k\right)$ and $\left(\hat{f}_1^k, \hat{f}_2^k, \hat{f}_3^k\right)$, and the coordinates of the intersection point with the new production frontier plane $\tilde{\boldsymbol{f}}^k$ in the super-efficiency plane are $\left(\tilde{f}_1^k, \tilde{f}_2^k, \tilde{f}_3^k\right)$, and the coordinates of the reference point $\boldsymbol{R}^{\mathrm{ck}}$ in the super-efficiency plane are $\left(r_1^{\mathrm{ck}}, r_2^{\mathrm{ck}}, r_3^{\mathrm{ck}}\right)$; then, the calculation method of the equilibrium distance D_{b}^k, the super-efficiency distance D_{se}^k, and the integrated distance $\tilde{D}^k$ is shown in Equations 8–10:

$$D_{\mathrm{b}}^k = \left\| \hat{\boldsymbol{f}}^k, \boldsymbol{R}^{ck} \right\|_2, \tag{8}$$

$$D_{\mathrm{se}}^k = \left\| \tilde{\boldsymbol{f}}^k \right\|_2 - \left\| \overline{\boldsymbol{f}}^k \right\|_2, \tag{9}$$

$$\tilde{D}^k = w_{\mathrm{b}}^k \cdot \frac{D_{\mathrm{b}}^{\max} - D_{\mathrm{b}}^k}{D_{\mathrm{b}}^{\max} - D_{\mathrm{b}}^{\min}} + w_{\mathrm{se}}^k \cdot \frac{D_{\mathrm{se}}^k - D_{\mathrm{se}}^{\min}}{D_{\mathrm{se}}^{\max} - D_{\mathrm{se}}^{\min}}, \tag{10}$$

where D_{b}^k denotes the Euclidean distance (Cao et al., 2024b) between the projection point of the kth grid infrastructure portfolio solution on the super-efficiency plane and the nearest super-efficiency plane reference point. The smaller the value of D_{b}^k, the higher is the balance of the investment portfolio solution regarding the three target efficiency values. D_{se}^k is the Euclidean distance between the kth investment portfolio solution and the new production frontier. The bigger the value of D_{se}^k, the higher the efficiency; w_{b}^k and w_{se}^k, respectively, indicate the weighting coefficients of balanced performance and super-efficiency performance of the kth infrastructure investment portfolio solution; $D_{\mathrm{b}}^{\max}$, $D_{\mathrm{b}}^{\min}$, $D_{\mathrm{se}}^{\max}$, and $D_{\mathrm{se}}^{\min}$, respectively, represent the maximum and minimum of all equilibrium and super-efficiency distance values calculated in the solution set of the grid infrastructure investment portfolio frontiers. The integrated distance $\tilde{D}^k$ serves as an indicator of the quality of the investment solution, with larger values reflecting superior performance.

In this paper, a super-efficient envelope model with non-radial relaxation variables is introduced to select the optimal solution from the Pareto efficient frontier set of the multi-objective infrastructure investment portfolio. In this model, the relaxation variable is used to measure the deviation between the solution and the hyper-efficiency plane. Specifically, s_i^- denotes the relaxation variable of the scale of the ith type of infrastructure investment portfolio, and s_j^+ denotes the relaxation variable of the value of the jth type of investment benefits. When $s_i^- > 0$, it means that there is a lot of waste in the investment portfolio. When $s_i^+ > 0$, it means that the output of the investment portfolio can be further improved. When the relaxation variable is zero, it means that the investment portfolio is optimal. Therefore, the optimal investment efficiency-oriented solution can be identified from the resulting Pareto frontier set. It can be found that a smaller value of $s_i^- + s_j^+$ in the solution indicates higher overall efficiency.

$$\begin{aligned} \min \quad & \frac{1 - \frac{1}{I}\sum_{i=1}^{I} \frac{s_i^-}{X_{io}}}{1 + \frac{1}{J}\sum_{j=1}^{J} \frac{s_j^+}{Y_{jo}}} \\ \text{s.t.} \quad & \sum_{l=1,l\neq o}^{M} X_{il}\lambda_l - s_i^- \le X_{io} \quad i = 1,2,...,I \\ & \sum_{l=1,l\neq o}^{M} Y_{jl}\lambda_l - s_j^+ \ge Y_{jo} \quad j = 1,2,...,J \\ & \sum_{l=1,l\neq o}^{M} \lambda_l = 1 \quad \lambda_l, s_i^-, s_j^+ \ge 0 \end{aligned}, \tag{11}$$

where I denotes the total number of infrastructure portfolio categories in the population individuals; J denotes the total number of investment effectiveness indicators in the population individuals; X_{io} denotes the investment scale of the ith infrastructure portfolio category of the oth population individual; Y_{jo} denotes the jth construction effectiveness value of the oth population individual; X_{il} denotes the investment scale of the ith infrastructure portfolio category of the lth population individual; Y_{jl} denotes the jth construction effectiveness value of the lth population individual; λ_l denotes the impact factor of the lth population individual. Because of the existence of bilinear variable division terms in Equation 11, it cannot be solved directly, so this paper adopts the simplex method and pairwise planning to linearize the model by introducing the transformed variables d, S_i^-, S_j^+,

and Λ_l. Let $d = 1/\left(1 + \Sigma_{j=1}^{J}\left(s_j^+/Y_{jo}\right)/J\right)$; then, Equation 11 can be expressed as follows:

$$\min \quad d - \frac{1}{I}\sum_{i=1}^{I}\frac{s_i^- d}{X_{io}}$$
$$\text{s.t.}\begin{cases} 1 = d + \frac{1}{J}\sum_{j=1}^{J}\frac{s_j^+ d}{Y_{jo}} \\ \sum_{l=1,l\neq o}^{M} X_{il}\lambda_l - s_i^- \le X_{io} \quad i = 1,2,...,I \\ \sum_{l=1,l\neq o}^{M} Y_{jl}\lambda_l - s_j^+ \ge Y_{jo} \quad j = 1,2,...,J \\ \sum_{l=1,l\neq o}^{M} \lambda_l = 1 \quad \lambda_l, s_i^-, s_j^+ \ge 0 \end{cases} . \tag{12}$$

Let $S_i^- = s_i^- d$, $S_j^+ = s_j^+ d$, and $\Lambda_l = \lambda_l d$; then, Equation 12 can be transformed into Equation 13:

$$\min \quad d - \frac{1}{I}\sum_{i=1}^{I}\frac{S_i^-}{X_{io}}$$
$$\text{s.t.}\begin{cases} 1 = d + \frac{1}{J}\sum_{j=1}^{J}\frac{S_j^+}{Y_{jo}} \\ S_i^- = s_i^- d, S_j^+ = s_j^+ d, \Lambda_l = \lambda_l d \\ \sum_{l=1,l\neq o}^{M} X_{il}\Lambda_l - S_i^- \le X_{io} d \quad i = 1,2,...,I \\ \sum_{l=1,l\neq o}^{M} Y_{jl}\Lambda_l - S_j^+ \ge Y_{jo} d \quad j = 1,2,...,J \end{cases} . \tag{13}$$

Through the above processing, the fractional planning problem is transformed into a general linear planning problem so as to obtain the optimal solution of the Pareto frontier solution.

4 Case studies

To validate the proposed model, taking a provincial power grid in central China as an example, three comparison schemes are established: scheme 1 uses the method proposed in this paper to select the optimal investment portfolio. Based on scheme 1, scheme 2 changes the super-efficiency selection strategy into a fuzzy multi-attribute decision-making method to obtain the optimal investment portfolio. Scheme 3 uses the NSGA-III algorithm for multi-objective optimization and combines the fuzzy multi-attribute decision-making method to select the optimal investment portfolio (Yu et al., 2019; Wang et al., 2024; Hussain et al., 2024). The parameter settings of the multi-objective cost efficiency-oriented investment portfolio optimization model are shown in Table 1. Power grid investment portfolios under different schemes are shown in Figure 2. The comparative results under different schemes are shown in Table 2.

The proposed scheme prioritizes power infrastructure investments on the transmission capacity and flexibility capability enhancements. It can be seen from Figure 2 that the investment portfolio obtained from scheme 2 prioritizes optimizing the grid structure, and the investment portfolio obtained from scheme 3 prioritizes enhancing the transmission capacity and meeting the growing load. It can be found from the analytical results that scheme 1 demonstrates superior performance on the comprehensive investment efficiency while maintaining the balanced performance in all efficiency indicators. Compared to scheme 3, the lower inverse generational distance and spacing in scheme 1 indicate that the solution set is close to the ideal Pareto front and has a better distribution of solutions. This is because the proposed algorithm employs a super-efficiency DEA model to rank these population individuals through equilibrium distances so that the better individuals can be selected from the non-dominated population individuals. Additionally, the algorithm utilizes a super-efficiency envelopment model to extract optimal solutions from the Pareto frontier set. As a result, the power grid investment portfolio achieves higher comprehensive efficiency while maintaining the balanced performance in all efficiency indicators.

The power grid investment portfolio obtained from scheme 2 demonstrates a stronger emphasis on safety investment efficiency while exhibiting notably lower economic investment efficiency and inferior comprehensive investment efficiency compared to those of scheme 1. These results stem from the decision making of scheme 2 to improve safety benefits for the goal of protecting people's livelihood and policies, and it easily leads to the lack of investment in enhancing economic benefits, resulting in the reduction in the comprehensive investment efficiency of power grids. Although scheme 3 shows relatively balanced performance in all indicators, all its investment efficiency indicators are lower than those of scheme 1. Moreover, the inverse generational distance and spacing of scheme 3 are significantly higher than those of scheme 1, indicating that its solution set is far away from the ideal Pareto frontier set.

5 Conclusion

In this paper, an investment efficiency-oriented strategy is proposed to improve the overall investment efficiency for power grid infrastructure planning with high penetration of renewable energy sources. The following are the key findings of this study: 1) the proposed investment portfolio model prioritizes enhancing the transmission capacity and flexibility capability of power grids with proportions of 31.35% and 22.62%, respectively, and thus, the system investment efficiency can be enhanced with renewable energy accommodation enhancement. 2) The proposed EASEHPT algorithm can improve the overall investment efficiency by 11.9% compared to traditional methods, and the obtained Pareto front solution set of the multi-objective investment portfolio exhibits both diversity and optimality.

Data availability statement

The original contributions presented in the study are included in the article/supplementary material; further inquiries can be directed to the corresponding author.

Author contributions

QW: writing–original draft and writing–review and editing. MZ: conceptualization, data curation, and writing–review and editing.

JY: writing–original draft and writing–review and editing. ZS: visualization and writing–review and editing. SW: formal analysis and writing–review and editing.

Funding

The author(s) declare that financial support was received for the research, authorship, and/or publication of this article. This work was supported by the State Grid Science and Technology Project (No. 5100-202456030A-1-1-ZN).

Conflict of interest

Authors QW and MZ were employed by State Grid Hubei Electric Power Company Limited. Authors JY, ZS, and SW were employed by State Grid Hubei Electric Power Company Limited Economic and Technical Research Institute.

Generative AI statement

The author(s) declare that no generative AI was used in the creation of this manuscript.

Publisher's note

All claims expressed in this article are solely those of the authors and do not necessarily represent those of their affiliated organizations, or those of the publisher, the editors and the reviewers. Any product that may be evaluated in this article, or claim that may be made by its manufacturer, is not guaranteed or endorsed by the publisher.

References

Cao, Y., Zhou, B., Chung, C. Y., Wu, T., Zheng, L., and Shuai, Z. (2024b). A coordinated emergency response scheme for electricity and watershed networks considering spatio-temporal heterogeneity and volatility of rainstorm disasters. *IEEE Trans. Smart Grid* 15, 3528–3541. doi:10.1109/TSG.2024.3362344

Cao, Y., Zhou, B., Chung, C. Y., Zhou, K., Zhu, L., and Shuai, Z. (2024a). Resilience-oriented coordinated topology reconfiguration of electricity and drainage networks with distributed mobile emergency resources. *IEEE Trans. Smart Grid* 16, 786–800. doi:10.1109/TSG.2024.3419086

Chen, C., Liu, H., Tang, L., and Ren, J. (2021). A range adjusted measure of super-efficiency in integer-valued data envelopment analysis with undesirable outputs. *J. Syst. Sci. Inf.* 9, 378–398. doi:10.21078/JSSI-2021-378-21

Chen, Y., Li, J., Sheng, K., Yang, T., Xu, X., Han, Z., et al. (2020). Many-criteria evaluation of infrastructure investment priorities for distribution network planning. *IEEE Access* 8, 221111–221118. doi:10.1109/ACCESS.2020.3043248

Deb, K., and Jain, H. (2014). An evolutionary many-objective optimization algorithm using reference-point-based nondominated sorting approach, Part I: solving problems with box constraints. *IEEE Trans. Evol. Comput.* 18, 577–601. doi:10.1109/TEVC.2013.2281535

Deng, Z., and Wang, J. (2020). Multi-sensor data fusion based on improved analytic Hierarchy process. *IEEE Access* 8, 9875–9895. doi:10.1109/ACCESS.2020.2964729

Fu, X., Wu, X., Zhang, C., Fan, S., and Liu, N. (2022). Planning of distributed renewable energy systems under uncertainty based on statistical machine learning. *Prot. Control Mod. Power Syst.* 7, 41. doi:10.1186/s41601-022-00262-x

Garifi, K., Johnson, E. S., Arguello, B., and Pierre, B. J. (2022). Transmission grid resiliency investment optimization model with SOCP recovery planning. *IEEE Trans. Power Syst.*, 1. doi:10.1109/PESGM48719.2022.9916881

Guelpa, E., Bischi, A., Verda, V., Chertkov, M., and Lund, H. (2019). Towards future infrastructures for sustainable multi-energy systems: a review. *Energy* 184, 2–21. doi:10.1016/j.energy.2019.05.057

Guo, M., Ren, M., Chen, J., Cheng, L., and Yang, Z. (2023). Tracking photovoltaic power output schedule of the energy storage system based on reinforcement learning. *Energies* 16, 5840. doi:10.3390/en16155840

Hussain, A., Ullah, K., Garg, H., and Mahmood, T. (2024). A novel multi-attribute decision-making approach based on T-spherical fuzzy Aczel Alsina Heronian mean operators. *Granul. Comput.* 9, 21. doi:10.1007/s41066-023-00442-6

Lee, C. Y., and Chen, Y. W. (2024). Reinforcement learning with data envelopment analysis and conditional value-at-risk for the capacity expansion problem. *IEEE Trans. Eng. Manag.* 71, 6469–6480. doi:10.1109/TEM.2023.3264566

Li, Q., Li, B., Jiang, Q., Liu, T., Yue, Y., and Zhang, Y. (2024). A novel location method for interline power flow controllers based on entropy theory. *Prot. Control Mod. Power Syst.* 9, 70–81. doi:10.23919/PCMP.2023.000504

Liu, C., Li, X., Liang, J., Sheng, K., Kong, L., Peng, X., et al. (2023). A multistep iterative ranking learning method for optimal project portfolio planning of smart grid. *Int. Trans. Electr. Energy Syst.* 2023, 1–10. doi:10.1155/2023/1358099

Lu, S., Yan, J., Zhang, Y., Qi, L., Wang, S., Wu, Q., et al. (2022). A R-GCN-based correlation characteristics extraction method for power grid infrastructure planning and analysis. *Front. Energy Res.* 10. doi:10.3389/fenrg.2022.888161

Ma, Y., Han, R., and Wang, W. (2020). Prediction-based portfolio optimization models using deep neural networks. *IEEE Access* 8, 115393–115405. doi:10.1109/ACCESS.2020.3003819

Qin, T., Liu, M., Ji, S., and Cai, D. (2024). Parameter weight analysis of synchronous induction electromagnetic coil launch system based on the entropy weight method. *IEEE Trans. Plasma Sci.* 52, 1865–1873. doi:10.1109/TPS.2024.3395284

Saxena, A., and Shankar, R. (2024). An interactive operating demand response approach for hybrid power systems integrating renewable energy sources. *Prot. Control Mod. Power Syst.* 9, 174–194. doi:10.23919/PCMP.2023.000282

Sha, J., Liu, Y., Sheng, K., Zhang, L., Jiang, T., Tan, M., et al. (2023). Opinions on power grid infrastructure investments for renewable energy accommodation in China. *Front. Energy Res.* 11. doi:10.3389/fenrg.2023.1221841

Tibshirani, R. (2011). Regression shrinkage and selection via the lasso: a retrospective. *J. R. Stat. Soc.* 73, 273–282. doi:10.1111/j.1467-9868.2011.00771.x

Wang, D., Li, Z., Dey, N., Ashour, A. S., Sherratt, R. S., and Shi, F. (2017). Case-based reasoning for product style construction and fuzzy analytic Hierarchy process evaluation modeling using consumers linguistic variables. *IEEE Access* 5, 4900–4912. doi:10.1109/ACCESS.2017.2677950

Wang, D., Zhang, C., Li, J., Zhu, L., Zhou, B., Zhou, Q., et al. (2024). A novel interval power flow method based on hybrid box-ellipsoid uncertain sets. *IEEE Trans. Power Syst.* 39, 6111–6114. doi:10.1109/TPWRS.2024.3391921

Wu, Y., Li, X., Zhang, L., Liu, C., Zhao, W., and Zhang, T. (2022). Machine learning–driven deduction prediction methodology for power grid infrastructure investment and planning. *Front. Energy Res.* 10. doi:10.3389/fenrg.2022.893492

Xu, L., Shen, C., Chen, J., Pan, X., and Xiao, G. (2024). Efficiency evaluation and improvement pathway of sulfur-oxide emissions in European ports based on Context-dependent SBM-DEA model. *Mar. Pollut. Bull.* 208, 117002. doi:10.1016/J.MARPOLBUL.2024.117002

Yan, J., Lu, S., Wang, S., Wu, A., Sang, Z., Huang, J., et al. (2022). A multi-level investment allocation indicator system for distribution network planning. *Front. Energy Res.* 10. doi:10.3389/fenrg.2022.889325

Yang, T., Cao, B., and Wang, C. (2024). Joint generation and voyage scheduling of all-electric ships considering power supply capacity constraints. *IEEE Trans. Appl. Supercond.* 34, 1–4. doi:10.1109/TASC.2024.3456556

Yi, Y., Zhao, H., Zeng, Y., Chen, F., Yang, D., Wang, B., et al. (2023). Accommodation capacity evaluation of renewable energy in power systems considering peak and frequency regulation. *Front. Energy Res.* 10. doi:10.3389/fenrg.2022.1067884

Yu, G. F., Fei, W., and Li, D. F. (2019). A compromise-typed variable weight decision method for hybrid multiattribute decision making. *IEEE Trans. Fuzzy Syst.* 27, 861–872. doi:10.1109/TFUZZ.2018.2880705

frontiers | Frontiers in Energy Research

TYPE Original Research
PUBLISHED 14 April 2025
DOI 10.3389/fenrg.2025.1566923

OPEN ACCESS

EDITED BY
Cong Zhang,
Hunan University, China

REVIEWED BY
Nan Chen,
University of Birmingham, United Kingdom
Tong Qian,
Hong Kong Polytechnic University, Hong Kong SAR, China

*CORRESPONDENCE
Liu Yang,
liuyangscu910@163.com

RECEIVED 06 February 2025
ACCEPTED 03 March 2025
PUBLISHED 14 April 2025

CITATION
Yuyan S, Yang L, Yongjie Z, Shuai Z, Xiaodi W, Fang L and Yunche S (2025) A coordinated control strategy for active transient voltage support in DFIG-based wind farms.
Front. Energy Res. 13:1566923.
doi: 10.3389/fenrg.2025.1566923

A coordinated control strategy for active transient voltage support in DFIG-based wind farms

Song Yuyan, Liu Yang*, Zhang Yongjie, Zhang Shuai, Wang Xiaodi, Liu Fang and Su Yunche

State Grid Sichuan Economic Research Institute, Chengdu, China

During the implementation of active voltage support in wind farms, coordinating the operation of multiple wind turbines presents significant challenges. The dynamic response of the entire wind farm becomes complex during grid faults, making it difficult to achieve coordinated voltage support across different wind turbines. To address this, a coordination control strategy for doubly fed wind farms is here proposed which is based on Q-learning informed by the sensitivity of voltage. First, a method for calculating the voltage sensitivity of DFIG-based wind farms is introduced, utilizing the arbitrary polynomial chaos approach. Additionally, the operational constraints of wind farms are defined based on the average short-circuit ratio of reactive power. The voltage support characteristics of multi-machine wind farms under grid fault conditions are then thoroughly explored. Subsequently, an improved Q-learning algorithm is developed, based on the sensitivity of voltage. This algorithm aids in optimizing the control commands, thus enhancing the effectiveness of the voltage support system. Finally, adopting this voltage sensitivity as the basis for the coordinated control commands and applying the improved Q-learning algorithm as the implementation mechanism, a coordinated control strategy for active voltage support in DFIG-based wind farms is proposed. Simulation results demonstrate that the proposed control strategy can provide effective active voltage support during grid faults.

KEYWORDS

active voltage support, Q-learning, reactive power voltage sensitivity, DFIG-based Wind farm, coordinated control

1 Introduction

The ongoing transition of renewable energy from a supplementary to a primary power source is crucial for energy transformation (Global Wind Energy Council, 2022; Global Wind Energy Council, 2020). Currently, wind power has been extensively deployed on a large scale and substantial capacity. The large-scale integration of wind energy significantly alters the voltage dynamics of power systems, leading to frequent and extensive voltage fluctuations. During grid faults, abrupt voltage changes can precipitate large-scale disconnection incidents in wind farms, posing a significant threat to the safe and stable operation of the power grid (Chengmao et al., 2023; Mathis, 2023; Liu et al., 2020; Liu and Cheng, 2021).

To enhance the voltage of the point of common coupling (PCC) during faults, reactive power compensation devices (Kafshgari et al., 2019; Abulanwar et al., 2016; Bian et al., 2015), including capacitor reactors, on-load tap-changing transformers, and SVCs are employed. However, challenges persist, such as high construction and maintenance costs, insufficient dynamic reactive capacity during faults, and inadequate control strategies (Abulanwar et al., 2016). Consequently, active voltage support technology for wind farms has attracted considerable research (Hu et al., 2016; Ouyang et al., 2019).

Doubly fed induction generators (DFIGs), a pivotal model in the contemporary wind power generation industry, possess the capability to decouple active and reactive power outputs (Llrab et al., 2020; Liu and Cheng, 2021; Zhang et al., 2020). This characteristic makes DFIG-based wind turbines an important measure for improving the reactive power operational environment of wind farms (Ouyang et al., 2019; Yujun et al., 2018). A variable droop control scheme for reducing PCC voltage fluctuations is proposed in Li et al. (2018). While previous studies have optimized the reactive power injected into the grid by DFIG-based wind farms, the transient operational characteristics necessitate further exploration.

A two-stage voltage control method for wind farms with energy storage systems (ESSs) is proposed in Peng et al. (2024) to enhance the reactive power support capability of wind farms. However, due to the addition of ESSs, the construction cost of wind farms has increased, and the complexity of their transient characteristics will further increase. A wind farm power control strategy based on model predictive control was proposed by Zhao et al. (2017) and Zhang et al. (2023), which optimized the reactive power capacity of wind farms by adjusting the active power output. However, the coordinated control characteristics among multiple WTs have not been considered. Self-allocation strategies were introduced in Botong et al. (2023) for distributing reactive power output among multiple wind turbines (WTs) within a wind farm. Distributed voltage control architectures for wind farms were introduced by Ahmidi et al. (2012) to coordinate the reactive power output among multiple WTs. An optimization operation framework for WTs was proposed in Bhyri et al. (2024) to enhance the reactive power output capability of wind farms during fault crossing. However, the reactive power operating limitations of each WT were not considered in the these studies.

Additionally, a method was proposed in Dong et al. (2020) to enhance the resilience of turbines to voltage fluctuations by minimizing the imbalance in power generation among multiple WTs, while in Huang et al. (2020), voltage support was achieved by optimizing control parameters and compensating for delays in wind farm control systems. Coordinated sequence control based on multi-machine coordination and fault isolation has also been proposed to enhance the overall reactive support capability of wind farms (Zhang et al., 2019; Xiao and Heng, 2021). However, the above studies have not considered the various operational scenarios and constraints of wind farms, indicating that the applicability of their control systems requires further research (Tong et al., 2020; Cai et al., 2024; Zheng et al., 2020).

This paper proposes a novel coordinated control strategy for active transient voltage support in DFIG-based wind farms that aims to optimize the dynamic reactive power response characteristics of wind turbines and improve the voltage support capability of wind farms. The main contributions of this paper are as follows.

(1) A method for calculating the voltage sensitivity of DFIG-based wind farms utilizing arbitrary polynomial chaos (aPC) is presented which quantifies the impact of each WT on the voltage at the PCC.
(2) An operational constraint based on the short-circuit ratio is established, with the average value of reactive power taken into consideration, which could effectively prevent excess reactive power after fault clearance.
(3) An improved Q-learning based on voltage sensitivity (VS-Q) is innovated; based on this, a coordinated control strategy for active transient voltage support in DFIG-based wind farms is proposed to effectively improve the voltage level of wind-connected power systems during grid faults.

2 Voltage support characteristics and operational constraints of DFIG-based wind farms under grid faults

2.1 Reactive power support capacity of DFIG-based wind farms

When a wind farm implements voltage support, its available reactive power capacity is obtained by adding the reactive power output from the wind turbines. The total available reactive power capacity under current operating conditions, Q_{ARC}, and the sum of reactive power capacity increase due to reduced active power output, Q_{IRC}, can be expressed by Equation 1.

$$Q_{RPC} = \underbrace{\sum_{g=1}^{G} Q_{gref\_AR} + \sum_{h=1}^{H} Q_{href\_RL}}_{Q_{ARC}} + \underbrace{\sum_{k=1}^{K} Q_{kref\_SA} - Q_{loss}}_{Q_{IRC}}, \quad G + H \le N, K \le N \tag{1}$$

where Q_{RPC} is the reactive power support capability of a wind farm, Q_{gref_AR} is the reference value for the reactive power output of the g^{th} WT under current operating conditions, Q_{href_RL} is the reactive power limit of the WT, Q_{kref_SA} is the reactive power added when the WT reduces its active power, and Q_{loss} is the reactive power loss of the wind farm. G represents the number of WTs that have implemented the active voltage support but have not yet reached the reactive power output limit. Under the same operating condition, the number of WTs that have reached the reactive power limit is H. K denotes the number of WTs that reduce the active power to increase the reactive power output, and N is the total number of WTs in the wind farm.

The reactive power support capability of DFIG-based wind farms is determined by the reactive capacity of WTs. During the implementation of voltage support, the use of available reactive power capacity should be prioritized by a wind farm to prevent WTs from operating under extreme conditions.

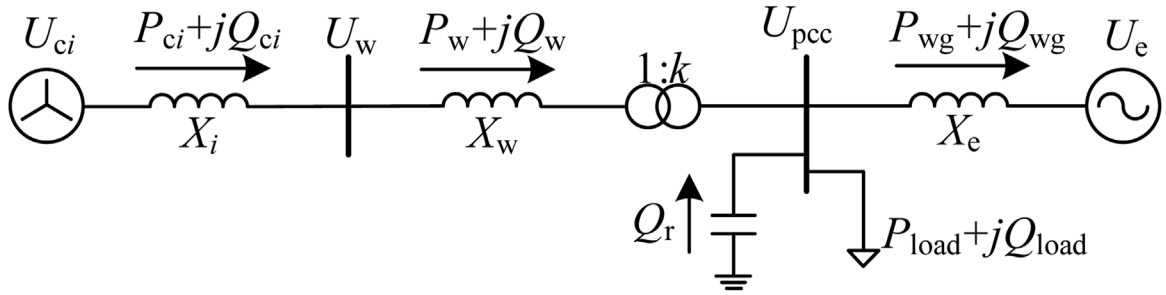

FIGURE 1
Grid-connected equivalent circuit of the DFIG-farm.

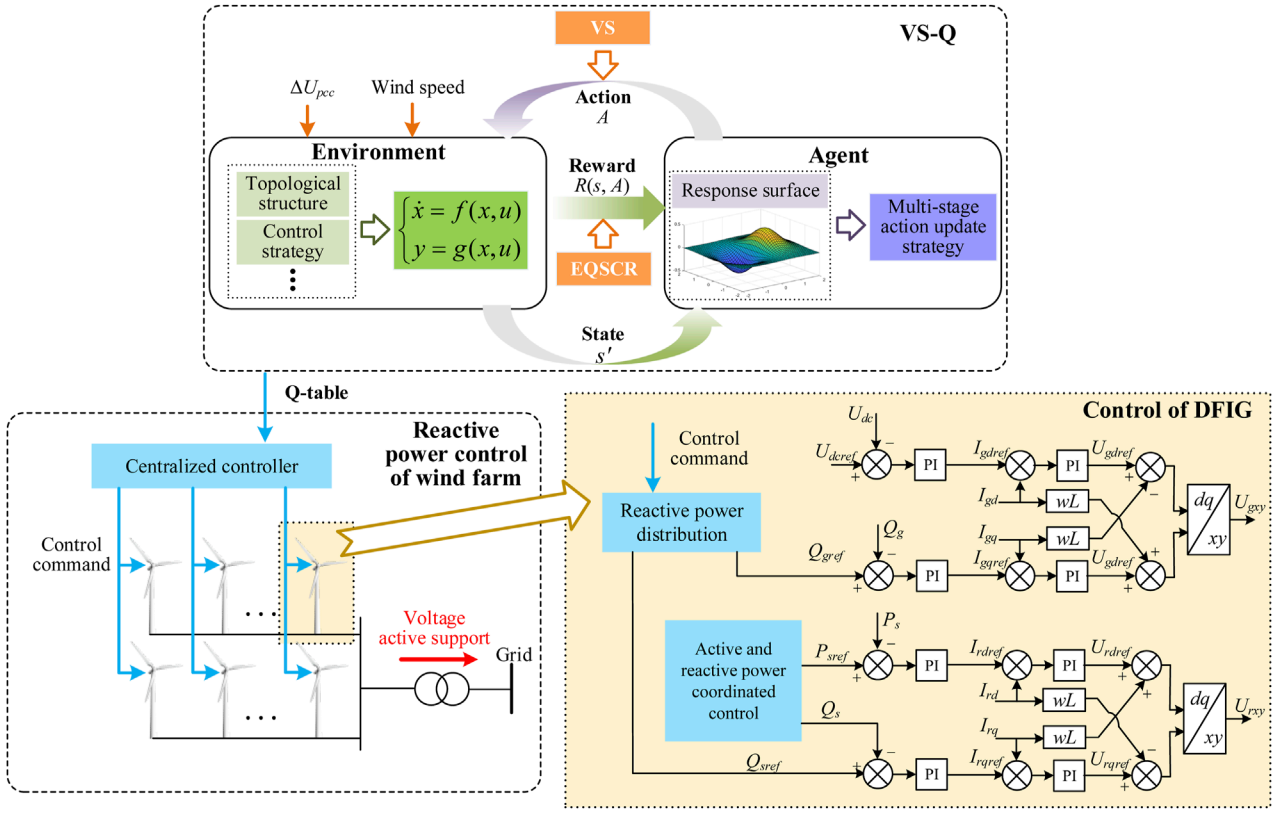

FIGURE 2
An overall coordinated control framework for transient voltage active support in DFIG-based wind farms based on VS-Q.

2.2 Voltage sensitivity of a wind farm based on aPC

The key to achieving active voltage support for a wind farm is to adjust the reactive power output of each WT reasonably and accurately based on the impact of the WTs on the PCC voltage, which can achieve optimal control effects. The physical significance of voltage sensitivity can be defined as the influence exerted on the PCC voltage by the reactive power output of a WT within a wind farm. Therefore, the voltage sensitivity of wind farms can be utilized as a predetermined basis for determining the coordinated control parameters of the active voltage support. The aPC utilizes orthogonal polynomial expansion to assess the dependence of model outputs on parameters, enabling the calculation of voltage sensitivity. Thus, the weighted sum of multivariate orthogonal polynomial bases can be used to represent the degree to which the PCC voltage of a wind farm is affected by the reactive power output of the WTs. The voltage response variation at the PCC can be approximated by the following polynomial representation:

$$\Upsilon(\mathbf{x},t;\boldsymbol{\omega}) \approx \sum_{j=0}^{M} c_j(\mathbf{x},t)\,\Psi_j(\boldsymbol{\omega}), \tag{2}$$

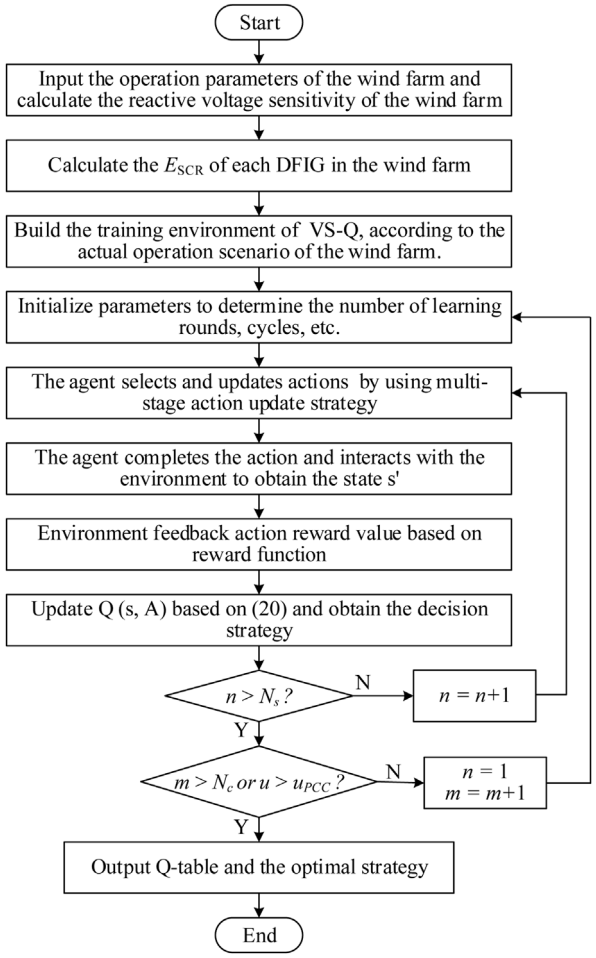

FIGURE 3
Flowchart of the coordinated control strategy.

where: $\boldsymbol{\omega}$ is the input of the model, representing the reactive power generated by the wind farm comprising multiple WTs; Υ is the output of the model, representing the transient voltage response of the PCC; M is the number of polynomials, and its value depends on the number of wind turbines N and the polynomial order d; c_j is a polynomial coefficient used to quantify the dependence of the model output Υ on the input parameter $\boldsymbol{\omega}$ for each expected point in space $\mathbf{x}$ at time t. The simplified representation of the multivariate orthogonal polynomial basis of $\boldsymbol{\omega}$ is $\boldsymbol{\Psi}$, which can be further expressed by Equations 3, 4.

$$\boldsymbol{\Psi}_k(\boldsymbol{\omega}) = \prod_{j=1}^{N} H_j^{(\alpha_j^r)}(\omega_j), \sum_{j=1}^{N} \alpha_j^r \le \mathrm{M}, r = 1, \ldots, N, \tag{3}$$

$$\begin{bmatrix} \mu_{0,j} & \mu_{1,j} & \cdots & \mu_{k,j} \\ \mu_{1,j} & \mu_{2,j} & \cdots & \mu_{k+1,j} \\ \vdots & \vdots & \ddots & \vdots \\ \mu_{k-1,j} & \mu_{k,j} & \cdots & \mu_{2k-1,j} \\ 0 & 0 & \cdots & 1 \end{bmatrix} \begin{bmatrix} H_{0,j}^{(k)} \\ H_{1,j}^{(k)} \\ \cdots \\ H_{k-1,j}^{(k)} \\ H_{k,j}^{(k)} \end{bmatrix} = \begin{bmatrix} 0 \\ 0 \\ \cdots \\ 0 \\ 1 \end{bmatrix}, \tag{4}$$

where H_j is an orthogonal basis parameter, α_j^r is a multivariate index that contains the combination information of all possible products of a univariate polynomial, and the index α is an M × N matrix. $\mu_{i,j}$ is the i^{th} original statistical moment of the variable ω_i.

The coefficient c_j is further evaluated in Equation 2. The formula configuration focuses on the voltage change at PCC when the reactive power output of the WT changes, and satisfies the linear equation system shown by Equation 5.

$$\mathbf{M}_\Psi(\boldsymbol{\omega})\mathbf{V}_c(\mathbf{x}, t) = \mathbf{V}_\Upsilon(\mathbf{x}, t; \boldsymbol{\omega}), \tag{5}$$

where $\mathbf{V}_c$ is an $M \times 1$ vector of coefficient c_j.The vector $\mathbf{V}_\Upsilon$ contains the model output for each configuration point. The $M \times N$ matrix $\mathbf{M}_\Psi$ contains polynomials evaluated at the configuration points.

Based on aPC, the analysis of voltage sensitivity in multiple WTs allows the response variation of the PCC voltage to be expressed on a normalized polynomial basis. Its mean μ_Ω and variance σ_Ω^2 can be represented by Equation 6. The Sobol index for sensitivity analysis can be derived from Equations 7–9. The multi-parameter reactive voltage weighted global sensitivity index within the wind farm is expressed as Equation 10, reflecting the impact of reactive power output from multiple WTs on the PCC voltage.

$$\mu_\Omega = c_0, \sigma_\Omega^2 = \sum_{j=1}^{M} c_j^2, \tag{6}$$

$$S_{i_1,\ldots,i_s} = \frac{\sum_{j=1}^{M} \chi_j c_j^2}{\sum_{j=1}^{M} c_j^2}, \tag{7}$$

$$S_j^T = \sum_{(i_1,,,i_s);j\in(i_1,,,i_s)} S_{i_1,,,i_s}, \tag{8}$$

$$\chi_j = \begin{cases} 1, \text{if } \alpha_j^k > 0, \forall j \in (i_1,,,i_s) \\ 0, \text{if } \alpha_j^k = 0, \forall j \in (i_1,,,i_s) \end{cases}, \tag{9}$$

$$S_{\omega_j}^2 = \sum_{k=0}^{M} c_k^2 \sum_{i=0}^{\alpha_j^k - 1} \left[b_i^{(\alpha_j^k - 1)} \right]^2 P_j^{(i)}(\omega_j), \tag{10}$$

where $S_{i_1,\ldots,i_s}$ is the Sobol index, which represents the contribution of variable ω_i to the total variance of the output space Υ, and S_j^T summarizes all Sobol indices of variable ω_i. Formula 10 reflects the impact of reactive power output of multiple WTs within the wind farm on PCC voltage and can be used as a measure of voltage sensitivity in wind farms.

2.3 Active support operation constraint of wind farms based on the average short-circuit ratio of reactive power

The reactive power output from wind farms may cause grid overvoltage after a fault is cleared. Therefore, it is essential to determine the maximum acceptable reactive power output of a wind farm under any grid disturbance. Constraints for voltage support and coordinated control can be defined based on the short-circuit ratio to prevent overvoltage issues in the power system with wind farms. The equivalent circuit of the power system with wind farms is shown in Figure 1.

Assuming that the DFIG operates at a constant power factor, the output power at the PCC can be expressed as Equation 11. The

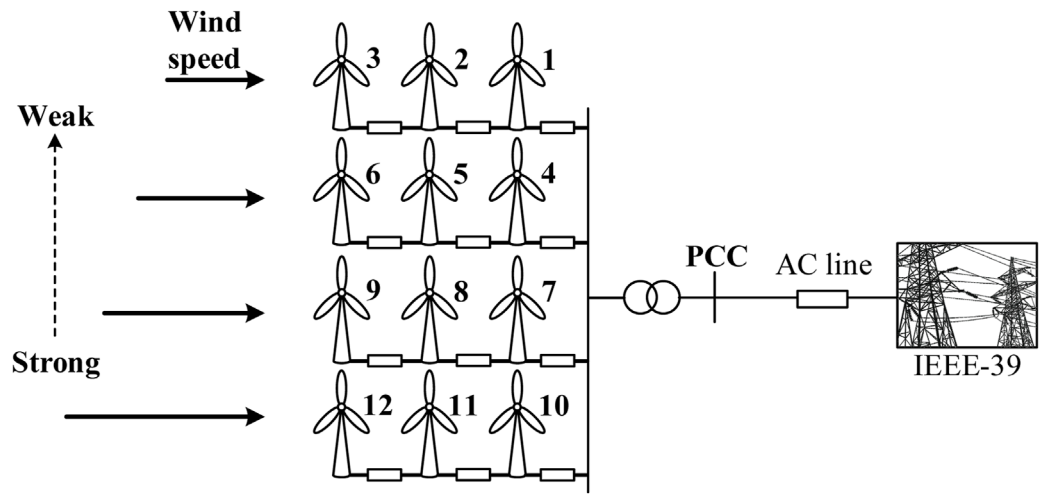

FIGURE 4
Simulation model.

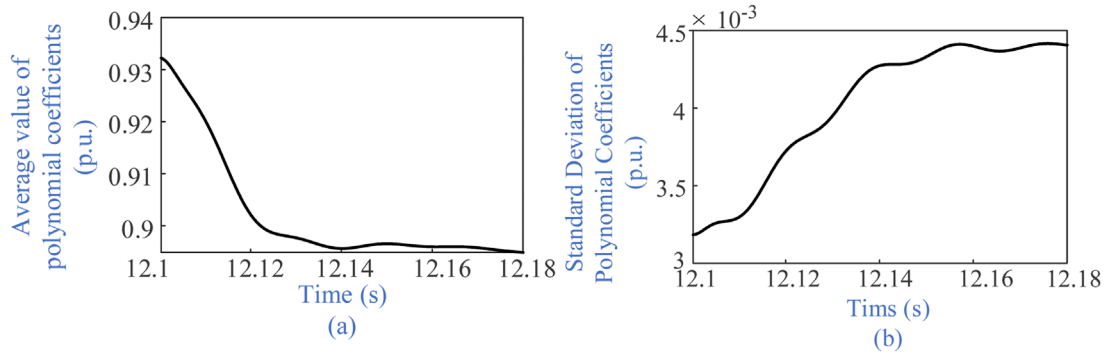

FIGURE 5
Statistical parameters of reactive power output from wind farms. **(a)** The average value of polynomial coefficients and **(b)** The standard deviation of polynomial coefficients.

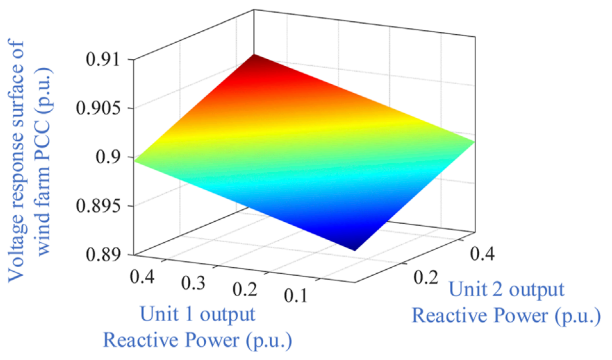

FIGURE 6
Voltage response surface of the PCC under grid fault based on dual parameters.

equivalent voltage at the PCC can be represented as Equation 12. After the grid fault cleared, the WTs gradually restore active output, at which point the output power at the PCC can be expressed as Equation 13, and the equivalent voltage of the PCC is represented as Equation 14.

$$\begin{cases} P_{wg} = \sum_{i=1}^{N} P_{ci} - P_{load} \\ Q_{wg} = Q_{rl} = Q_r - Q_{load}, \end{cases} \tag{11}$$

$$U_{pcc} = \sqrt{\left(U_e + \frac{Q_{wg}X_e}{U_e}\right)^2 + \left(\frac{P_{wg}X_e}{U_e}\right)^2}, \tag{12}$$

$$\begin{cases} P''_{wg} = \sum_{i=1}^{N} P_{ci} - P_{load} - \sum_{i=1}^{N} \Delta P_{ci} + \sum_{i=1}^{N} \Delta P'_{ci} = P_{wg} - \Delta P_w + \Delta P'_w \\ Q''_{wg} = Q''_r - Q_{load} + \sum_{i=1}^{N} \Delta Q_{ci} - \sum_{i=1}^{N} \Delta Q'_{ci} = Q''_{rl} + \Delta Q_w - \Delta Q'_w \end{cases}, \tag{13}$$

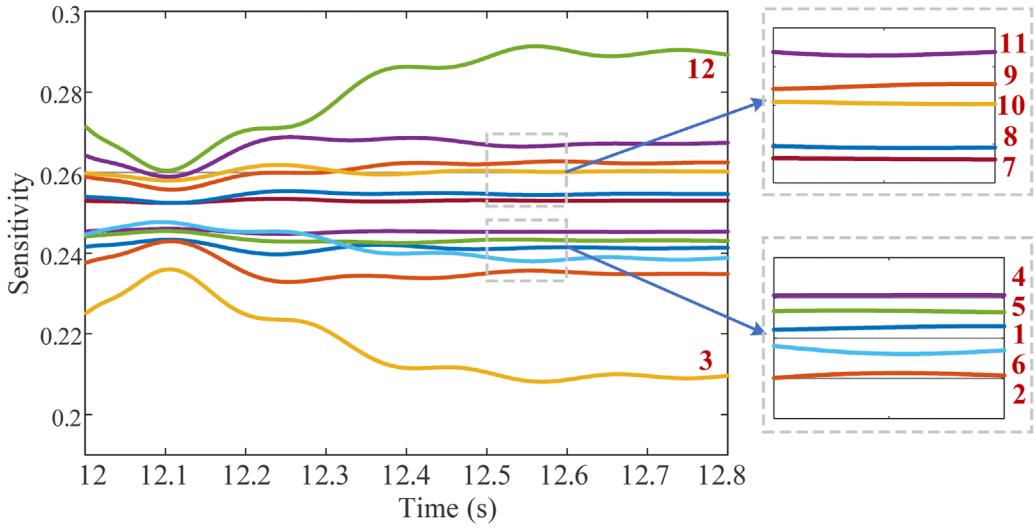

FIGURE 7
Voltage sensitivity of DFIG-based wind farms based on aPC.

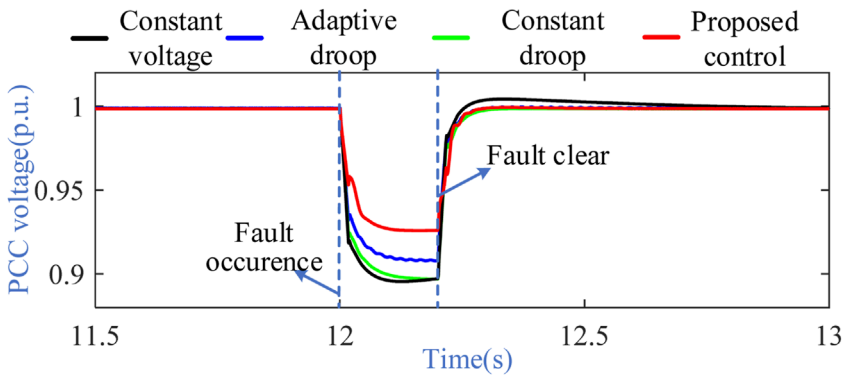

FIGURE 8
Voltage response waveform of a DFIG-based wind farm (PCC voltage drops by 0.1 p. u.).

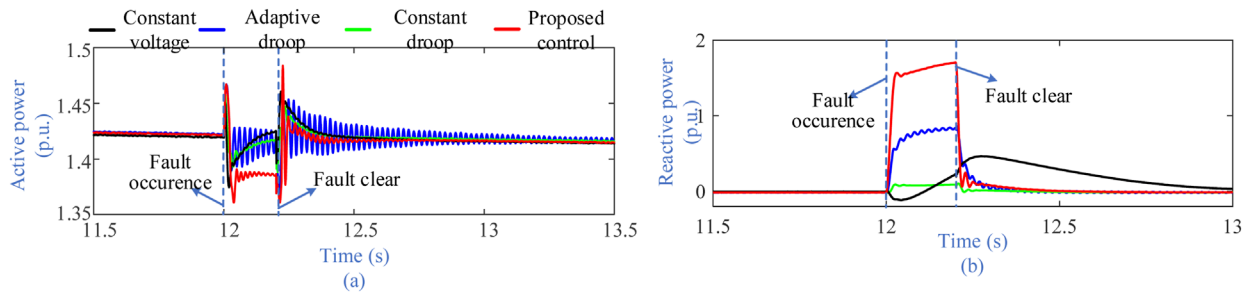

FIGURE 9
Output power waveform of a DFIG-based wind farm (PCC voltage drops by 0.1 p. u.). **(a)** active power of the WT and **(b)** is reactive power of the WT.

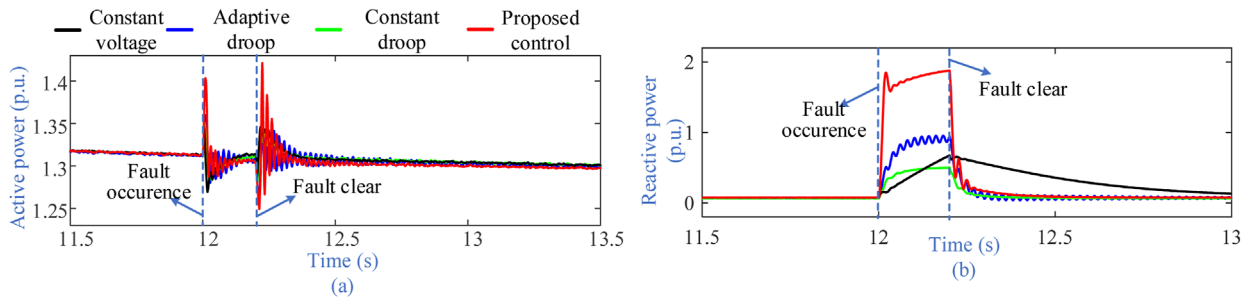

FIGURE 10
Waveform of WT 3. **(a)** active power of the WT and **(b)** is reactive power of the WT.

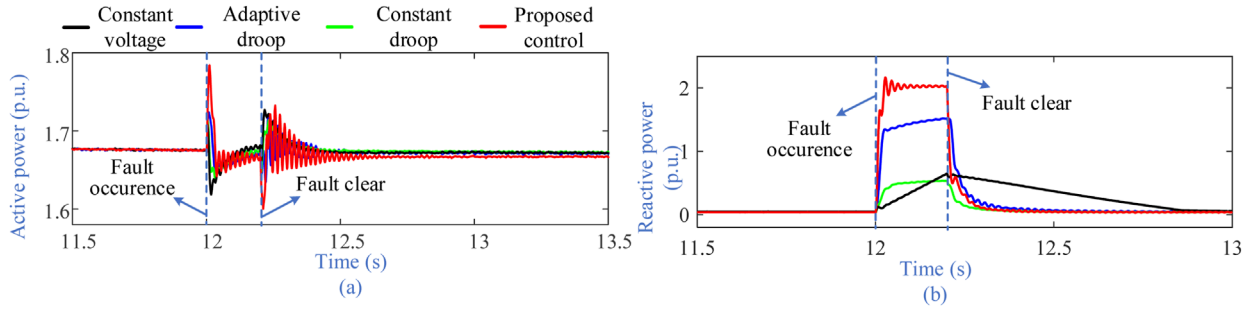

FIGURE 11
Waveform of WT 5. **(a)** active power of the WT and **(b)** is reactive power of the WT.

$$U''_{\mathrm{pcc}} = \sqrt{\left(U''_{\mathrm{e}} + \frac{Q''_{\mathrm{rl}}X_{\mathrm{e}}}{U''_{\mathrm{e}}} + \frac{\Delta Q_{\mathrm{w}}X_{\mathrm{e}}}{U''_{\mathrm{e}}} - \frac{\Delta Q'_{\mathrm{w}}X_{\mathrm{e}}}{U''_{\mathrm{e}}}\right)^2 + \left(\frac{P_{\mathrm{wg}}X_{\mathrm{e}}}{U''_{\mathrm{e}}} - \frac{\Delta P_{\mathrm{w}}X_{\mathrm{e}}}{U''_{\mathrm{e}}} + \frac{\Delta P'_{\mathrm{w}}X_{\mathrm{e}}}{U''_{\mathrm{e}}}\right)^2}, \tag{14}$$

where P_{wg} and Q_{wg} are the active and reactive power outputs of the wind farm, respectively. Q_{r} is the reactive power output by the reactive power compensation device, and Q_{load} is the reactive load at the PCC. X_{e} is the equivalent reactance of the connected system. Q''_{r} is the output reactive power of the reactive power compensation device after the fault cleared. $\Delta P'_{ci}$ and $\Delta Q'_{ci}$ represent the changes in active and reactive power output of the i^{th} WT after the fault cleared, respectively. At this time, the active and reactive power recovery values of the wind farm are $\Delta P'_{\mathrm{w}}$ and $\Delta Q'_{\mathrm{w}}$, respectively. U''_{pcc} is the equivalent potential of the PCC after the fault cleared.

The steady-state operating voltage of the system is defined as 1p.u. If the constant component influence of the equivalent potential at the PCC is ignored and $X_{\mathrm{e}} = U_{\mathrm{e}}^2/S_{\mathrm{cg}}$, the equivalent potential can be expressed as Equation 15.

$$U''_{\mathrm{pcc}} = 1 + \frac{Q''_{\mathrm{rl}}}{S_{\mathrm{cg}}} + \frac{\sum_{i=1}^{N}\Delta Q_{ci}}{S_{\mathrm{cg}}}, \tag{15}$$

where S_{cg} is the short-circuit capacity of the power system connected by the wind farm. To avoid overvoltage issues in the power system after fault clearance, the average reactive power output of all WTs in the wind farm at the moment of fault clearance is defined as Equation 16. Consequently, the operational constraint for voltage support coordination in the wind farm should satisfy Equation 17, which considers the reactive power characteristics of the wind farm. The proposed operational constraint enables a more precise evaluation of voltage support capability during the operation of multiple WTs, which can guide the allocation of reactive power output under grid faults. E_{SCR}

$$Q_{\mathrm{eve}} = \frac{1}{N}\sum_{i=1}^{N}\Delta Q_{ci,} \tag{16}$$

$$E_{\mathrm{SCR}} > \frac{NS_{\mathrm{cg}}}{0.3S_{\mathrm{cg}} - Q''_{\mathrm{rl}}.} \tag{17}$$

3 Coordinating the control of the overall structure

The issue of active voltage support in multiple WT DFIG-based wind farms can be described as coordinating the reactive power output of each WT based on their operational differences, aiming to maximize the wind farm's reactive support capability. The voltage support problem under coordinated control in such wind farms exhibits Markov properties, which can be represented in the tuple Equation 18.

$$\boldsymbol{\chi} = [\boldsymbol{S}, \boldsymbol{A}, \boldsymbol{T}], \tag{18}$$

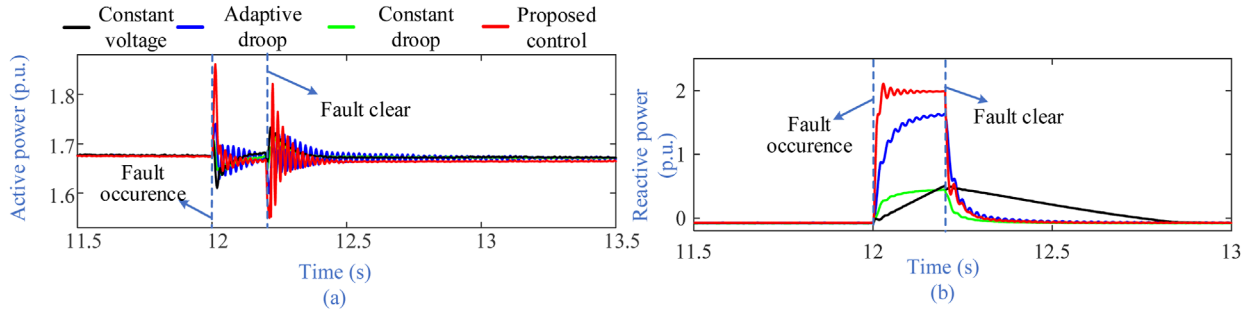

FIGURE 12
Waveform of WT 8. **(a)** active power of the WT and **(b)** is reactive power of the WT.

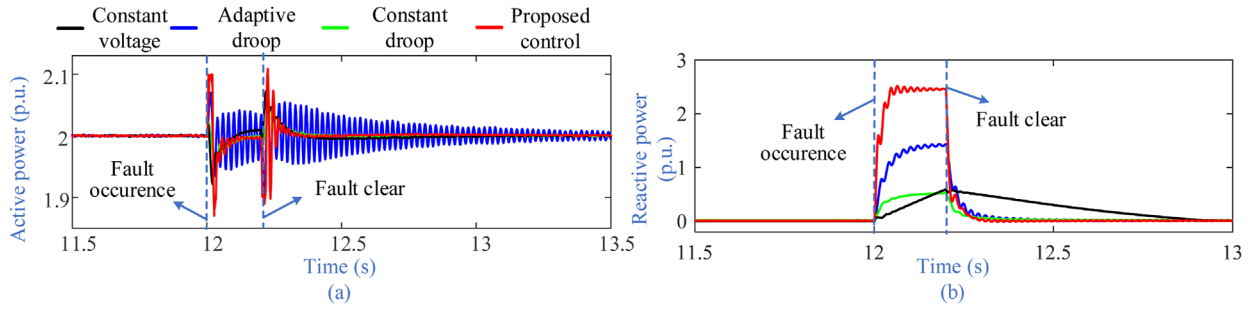

FIGURE 13
Waveform of WT 12. **(a)** active power of the WT and **(b)** is reactive power of the WT.

where: $\boldsymbol{S}$ is the state space of the power system connected by wind farms, represented as $\boldsymbol{S} = [\boldsymbol{s}_0, \boldsymbol{s}_1, \boldsymbol{s}_2, ..., \boldsymbol{s}_x]$; $\boldsymbol{A}$ is the operation space of multiple WTs in the wind farm, which can be represented as $\boldsymbol{A} = [\boldsymbol{A}_0, \boldsymbol{A}_1, \boldsymbol{A}_2, ..., \boldsymbol{A}_x]$; $\boldsymbol{T}$ is the probability of state transition.

Because of the Markov property, the voltage support issue in multiple WT DFIG-based wind farms can be solved through Q-learning for coordinated reactive power control under grid faults. The coordination control framework based on VS-Q is shown in Figure 2. Based on VS-Q, a coordinated control strategy for the transient voltage active support of DFIG-based wind farms is proposed, wherein the voltage sensitivity is utilized to characterize the impact of each WT on the PCC voltage and the reactive power output scheme of the wind farm is determined based on Q-learning to enhance the ability of wind farms to participate in power system voltage regulation.

4 Coordination control strategy for voltage support in DFIG-based wind farms based on VS-Q

The coordination control of active voltage support in multiple WT DFIG-based wind farms exhibits Markov properties. Reinforcement learning can effectively derive decision-making strategies among multiple WTs. Therefore, an improved Q-learning method based on voltage sensitivity is proposed to achieve active voltage support for wind farms. The state set of VS-Q is represented as Equation 19, and the action set is represented as Equation 20. The reward function is crucial for an agent's assessment of actions, fundamentally shaping its decision-making logic (Equation 21).

$$\begin{aligned} &\boldsymbol{s}_x = [\boldsymbol{P}_{cx}, \boldsymbol{Q}_{cx}, \boldsymbol{U}_{cx}, \boldsymbol{U}_{\mathrm{PCC}x} | \boldsymbol{P}_{cx} = [P_{1x}, P_{2x}, ..., P_{Nx}], \\ &\boldsymbol{Q}_{cx} = [Q_{1x}, Q_{2x}, ..., Q_{Nx}], \boldsymbol{U}_{cx} = [U_{1x}, U_{2x}, ..., U_{Nx}]], \\ &x = 1, 2, 3.... \end{aligned} \tag{19}$$

$$\begin{aligned} &\boldsymbol{A}_x = [a_1, a_2, ..., a_N] \\ &a_{1,2,...,N} \in \left[Q_{c_0}^{\mathrm{ref}}, Q_{c_{AR}}^{\mathrm{ref}}, Q_{c_{RL}}^{\mathrm{ref}}, Q_{c_{SA}}^{\mathrm{ref}} \right], \end{aligned} \tag{20}$$

$$R = \begin{cases} \lambda_{\mathrm{pun}} \sum_{i=1}^{N} \dfrac{E_{\mathrm{SCR}} - \frac{S_{cg}}{\Delta Q_{ci}}}{E_{\mathrm{SCR}}} & \boldsymbol{s}_x \notin \boldsymbol{S}_{\mathrm{con}}, \\ \Delta U_{\mathrm{PCC}} \cdot \lambda_{\mathrm{rew}} & \boldsymbol{s}_x \in \boldsymbol{S}_{\mathrm{con}} \end{cases} \tag{21}$$

where x is the environmental state number of the wind farm connected system and each state set constitutes the state space S of the environment. $Q_{c\_0}^{\mathrm{ref}}$ is the current action taken by the WT to maintain the existing reactive power output. $Q_{c\_AR}^{\mathrm{ref}}$ represents the reactive power output action taken by the WT. $Q_{c\_RL}^{\mathrm{ref}}$ is the action taken by the WT to output the reactive power limit. $Q_{c\_SA}^{\mathrm{ref}}$ is the action to reduce the active power and increase the reactive power for the WT. λ_{pun} is the penalty coefficient, and λ_{rew} is the reward coefficient. $\boldsymbol{S}_{\mathrm{con}}$ is the feasible state space, which is the set of system states that satisfy constraints.

To maximize voltage support at the PCC using a limited number of WTs, a multiple WT active voltage support coordination control based on VS-Q is proposed. This control utilizes a multi-stage action

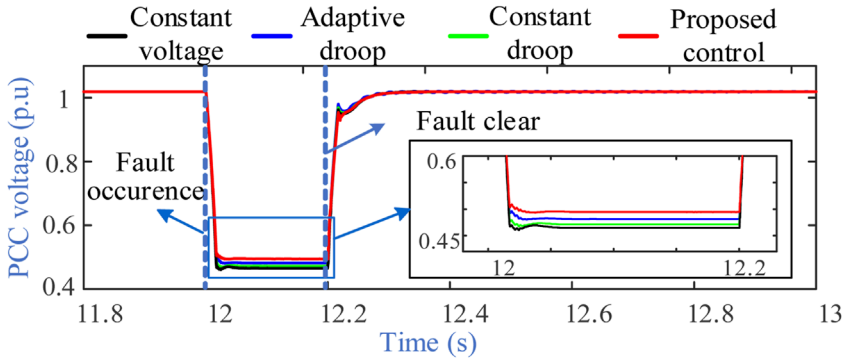

FIGURE 14
Voltage response waveform of a DFIG-based wind farm (PCC voltage drops by 0.45 p. u.).

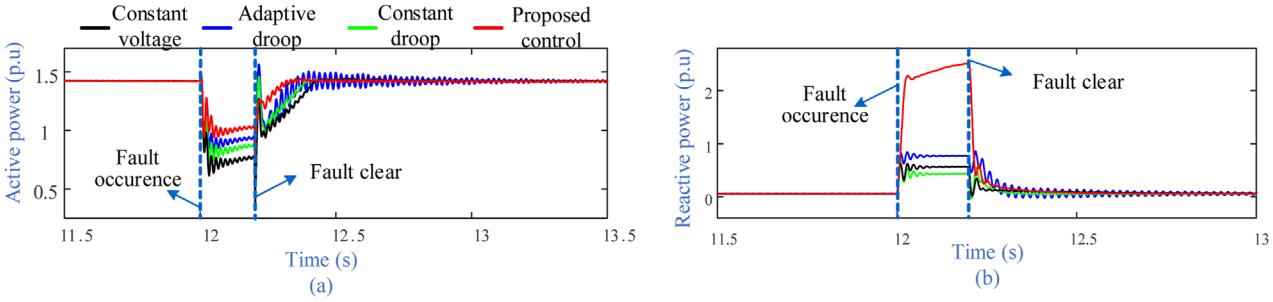

FIGURE 15
Output power waveform of a DFIG-based wind farm (PCC voltage drops by 0.45 p. u.). **(a)** active power of the WT and **(b)** is reactive power of the WT.

updating strategy for intelligent agents, allowing for the adjustment of individual output power and the coordination of reactive power among multiple machines. In the element selection phase of the strategy, the action transfer probabilities based on voltage sensitivity are represented as Equation 22. The element selection strategy is expressed as Equation 23, and the action updating strategy is represented as Equation 24. After the agent takes an action, the expected return of the system state can be expressed as Equation 25.

$$P_{ai} = \begin{cases} \dfrac{S_{\omega 1}}{\sum_{k=1}^{N} S_{\omega k}} & i = 1 \\ P_{ai-1} + \dfrac{S_{\omega i}}{\sum_{k=1}^{N} S_{\omega k}} & i = 2,\ldots,N, \end{cases} \tag{22}$$

$$\Pi_A = \begin{cases} f_c(a_1 | \alpha \in (0,1]) \\ f_c(a_i | \alpha \in [P_{ai-1}, P_{ai}]) \end{cases} \quad i = 2,\ldots,N \;\; \alpha = rand(0,1], \tag{23}$$

$$a_i = \begin{cases} Q_{c\_l+1}^{ref} & \beta \in (0, 1-\gamma], l = 0,1,2 \\ Q_{c\_l}^{ref} & \beta \in (\gamma, 1], l = 3 \end{cases} \quad \beta = rand(0,1], \tag{24}$$

where f_c is the action element selection function used to select elements that meet the requirements. $Q_{c\_l}^{ref}$ is the current action value of the selected element by the intelligent agent. γ is the action update factor used to achieve a balance between agent development and deep learning. $Q_{c\_1}^{ref}$, $Q_{c\_2}^{ref}$, and $Q_{c\_3}^{ref}$ correspond to $Q_{c\_AR}^{ref}$, $Q_{c\_RL}^{ref}$, and $Q_{c\_SA}^{ref}$ in the action set, respectively. The probability of the system transitioning from current state s to next state $\boldsymbol{s}'$ at the moment when the intelligent agent takes action A can be expressed as $T(\boldsymbol{s}, \boldsymbol{A}, \boldsymbol{s}')$. At this point, the expected return of system state s can be expressed as:

$$V(\boldsymbol{s}) = R(\boldsymbol{s}) + \max_{\boldsymbol{A}} \zeta \sum \boldsymbol{s}' T(\boldsymbol{s}, \boldsymbol{A}, \boldsymbol{s}') V(\boldsymbol{s}'), \tag{25}$$

where ζ is the discount factor that satisfies $\zeta \in [0,1]$, representing the impact of future rewards on current rewards. The goal of VS-Q is to find the optimal strategy (Equation 26). The update of the expected return for state transitions is represented as Equation 27. Finally, the optimal strategy is obtained in Equation 28.

$$\Pi^*(\boldsymbol{s}) = \arg\max_{\boldsymbol{A}} \sum \boldsymbol{s}' T(\boldsymbol{s}, \boldsymbol{A}, \boldsymbol{s}') V^*(\boldsymbol{s}'), \tag{26}$$

$$V^{\Pi}(\boldsymbol{s}) = V^{\Pi}(\boldsymbol{s}) + \mu\left(R(\boldsymbol{s}) + \zeta V^{\Pi}(\boldsymbol{s}') - V^{\Pi}(\boldsymbol{s})\right), \tag{27}$$

$$Q(\boldsymbol{s}, \boldsymbol{A}) \leftarrow Q(\boldsymbol{s}, \boldsymbol{A}) + \mu\left[R(\boldsymbol{s}) + \zeta \max_{\boldsymbol{A}} Q(\boldsymbol{s}', \boldsymbol{A}) - Q(\boldsymbol{s}, \boldsymbol{A})\right]. \tag{28}$$

Figure 3 shows the implementation process of voltage active support coordination control for a multiple WT DFIG-based wind farm based on voltage sensitivity and improved Q-learning.

5 Simulation

This section calculates the voltage sensitivity of a multiple WT DFIG-based wind farm using MATLAB and develops a detailed

electromagnetic transient model of the wind farm using PSCAD. The topology of the wind farm is shown in Figure 4. Each WT has a rated capacity of 2 MW, and the wind farm accounts for 42.7% of the total installed capacity of the system.

First, set node 14 of the wind power grid connection system to experience a three-phase grounding fault at 12 s, lasting for 0.2 s. The statistical parameters of the aPC coefficient, namely the mean and standard deviation, are shown in Figure 5. Considering only the WT with the maximum operational difference, the results are shown in Figure 6. It can be seen that the output reactive power of the random group increases, and the voltage at the connection point shows an upward trend, indicating that the wind turbines significantly enhance the reactive power support of the grid connection system.

The voltage sensitivity of the wind farm is illustrated in Figure 7. As shown, there are significant differences in voltage sensitivity among the WTs due to factors such as geographical environment, operating wind speed, and the topology structure of the wind farm.

At node 14 of the wind power grid connection system, a three-phase ground fault occurred at 12 s, lasting 0.2 s. The voltage responses at the PCC under various controls (Fortmann et al., 2008; Kim et al., 2016) are shown in Figure 8, while the active and reactive power outputs of the wind farm are depicted in Figure 9. Figures 9–13 compares the active and reactive power output of different WTs in the wind farm under the proposed control and existing control (Fortmann et al., 2008; Kim et al., 2016). The proposed VS-Q enhances the reactive power output level of the wind farm, raising the average voltage at the grid connection point during the fault from 0.906 p. u. to 0.9357 p. u., and increasing the reactive power injected into the grid from 0.0106 p.u. to 1.5176 p. u.

We introduce the increase rate of PCC voltage to characterize the control effect of different controls on the PCC voltage, specifically expressed as

$$\rho = \frac{U^{\mathrm{eve}}_{\mathrm{PCC\_}C} - U^{\mathrm{eve}}_{\mathrm{PCC\_}u}}{U^{\mathrm{eve}}_{\mathrm{PCC\_}u}} \times 100\%, \tag{29}$$

where $U^{\mathrm{eve}}_{\mathrm{PCC\_}u}$ and $U^{\mathrm{eve}}_{\mathrm{PCC\_}C}$ are the PCC voltages under the constant voltage control and the other control effects, respectively. During the fault period, the increase rates of PCC voltage by the constant droop control, the adaptive droop control, and the proposed control were 0.33%, 1.51%, and 3.38%, respectively. The proposed control can adjust the reactive power output of WTs according to the actual operational state while avoiding the power oscillation caused by the adaptive droop control.

To further validate the proposed control, the output active and reactive power of WTs 3, 5, 8, and 12 during the fault period were extracted, with their power waveforms shown in Figures 10–13. The figures indicate that, compared to the other three controls, the proposed control can output more reactive power during grid faults and provide voltage support to the grid.

To further verify the control effect of the proposed control under different fault levels, a three-phase ground fault occurred at node 16, with a fault duration of 0.2 s. The voltage responses at the PCC under various control are shown in The voltage responses at the PCC under various control are shown in Figure 14, while the active and reactive power outputs under various controls (Proposed control; Fortmann et al., 2008; Kim et al., 2016) of the wind farm are depicted in Figure 15.

The calculation results show that the proposed control increases the average voltage of PCC during the fault from 0.454 to 0.4836 p. u. and increases the reactive power injected into the grid from 0.5442 to 2.2428 p. u. The increase rates of PCC voltage by the constant droop control, the adaptive droop control, and the proposed control were 1.41%, 3.47%, and 6.13%, respectively. The proposed control achieves active voltage support of the wind farm for the connected system.

6 Conclusion

This study has discussed the voltage support characteristics of multiple WT DFIG-based wind farms under grid faults. It proposes a method for calculating voltage sensitivity based on aPC and an active support operational constraint based on the average short-circuit ratio. Additionally, a coordination control for active voltage support based on VS-Q is proposed. Key conclusions include the following.

1. The aPC-based voltage sensitivity reflects the impact of each WT on the PCC voltage.
2. The active support constraint accounts for reactive power output and grid strength, preventing transient overvoltage after fault clearance.
3. VS-Q coordination control optimizes voltage support using sensitivity as a directive, enabling intelligent coordination of reactive power among turbines during grid faults, thereby enhancing transient voltage stability.

Data availability statement

The original contributions presented in the study are included in the article/Supplementary Material; further inquiries can be directed to the corresponding author.

Author contributions

SoY: conceptualization, data curation, formal analysis, funding acquisition, investigation, methodology, project administration, resources, software, supervision, validation, visualization, writing–original draft, writing–review and editing. LY: conceptualization, data curation, formal analysis, funding acquisition, investigation, methodology, project administration, resources, software, supervision, validation, visualization, writing–original draft, and writing–review and editing. ZY: data curation, formal analysis, investigation, methodology, project administration, software, validation, and writing–review and editing. ZS: conceptualization, investigation, methodology, project administration, resources, software, and writing–review and editing. WX: conceptualization, data curation, investigation, methodology, software, validation, and writing–review and

editing. LF: conceptualization, data curation, formal analysis, investigation, methodology, project administration, resources, and writing–review and editing. SuY: data curation, formal analysis, funding acquisition, investigation, methodology, project administration, resources, software, and writing–review and editing.

Funding

The author(s) declare that financial support was received for the research and/or publication of this article. This work was supported by Science and Technology Project of State Grid Sichuan Electric Power Company (521996230009).

Conflict of interest

The authors declare that the research was conducted in the absence of any commercial or financial relationships that could be construed as a potential conflict of interest.

The authors declare that this study received funding from State Grid Sichuan Electric Power Company. The funder had the following involvement in the study design, collection, analysis, interpretation of data, the decision to submit it for publication.

Generative AI statement

The authors declare that no generative AI was used in the creation of this manuscript.

Publisher's note

Supplementary material

The Supplementary Material for this article can be found online at: https://www.frontiersin.org/articles/10.3389/fenrg.2025.1566923/full#supplementary-material

References

Abulanwar, S., Hu, W., Chen, Z., and Iov, F. (2016). Adaptive voltage control strategy for variable-speed wind turbine connected to a weak network. *IET Renew. Power Gener.* 10, 238–249. doi:10.1049/iet-rpg.2015.0239

Ahmidi, A., Guillaud, X., Besanger, Y., and Blanc, R. (2012). A multilevel approach for optimal participating of wind farms at reactive power balancing in transmission power system. *IEEE Syst. J.* 6 (02), 260–269. doi:10.1109/jsyst.2011.2163003

Bhyri, A. K., Senroy, N., and Saha, T. K. (2024). Enhancing the grid support from dfig-based wind farms during voltage events. *IEEE Trans. Power Syst.* 39 (1), 733–744. doi:10.1109/tpwrs.2023.3239503

Bian, X. Y., Geng, Y., Lo, K. L., Fu, Y., and Zhou, Q. B. (2015). Coordination of PSSs and SVC damping controller to improve probabilistic small-signal stability of power system with wind farm integration. *IEEE Trans. Power Syst.* 31, 2371–2382. doi:10.1109/tpwrs.2015.2458980

Botong, L. I., Dingchuan, ZHENG, Bin, L. I., Jiao, X., Hong, Q., and Ji, L. (2023). Analysis of low voltage ride-through capability and optimal control strategy of doubly-fed wind farms under symmetrical fault. *Prot. Control Mod. Power Syst.* 8 (1), 36. doi:10.1186/s41601-023-00310-0

Cai, Z., Huang, S., Wu, Q., Tai, N., Huang, W., Huang, S., et al. (2024). Nonlinear hybrid flatness control for suppressing overcurrent of DFIG during high voltage ride through. *Electr. Power Syst. Res.* 229 (Apr), 1.1–1.11. doi:10.1016/j.epsr.2024.110190

Chengmao, D. U., Xiong, D. U., Tong, C., Li, Y., and Zhou, P. (2023). Stability analysis for DFIG-based wind farm grid-connected system under all wind speed conditions. *IEEE Trans. Industry Appl.* 59 (2 Pt.2), 2430–2445. doi:10.1109/TIA.2022.3218022

Dong, Z., Li, Z., Du, L., Liu, Y., and Ding, Z. (2020). Coordination strategy of large-scale DFIG-based wind farm for voltage support with high converter capacity utilization. *IEEE Trans. Sustain. Energy* 12 (02), 1416–1425. doi:10.1109/tste.2020.3047273

Fortmann, J., Wilch, Koch, F. and M., and Erlich, I. (2008). A novel centralised wind farm controller utilising voltage control capability of wind turbines. *Fifth Power Syst. Comput. Conf.*

Global Wind Energy Council (2020). *Global wind report 2019*. Brussels, Belgium: Global Wind Energy Council. Available online at: https://gwec.net/global-wind-report-2019/ (Accessed on December 07, 2021).

Global Wind Energy Council (2022). Brussels, Belgium, Global wind report. Available online at: https://gwec.net/global-wind-report-2022/ (Accessed on October 26, 2024).

Hu, W., Abulanwar, S., Iov, F., and Chen, Z. (2016). Adaptive voltage control strategy for variable-speed wind turbine connected to a weak network. *IET Renew. Power Gener.* 10 (02), 238–249. doi:10.1049/iet-rpg.2015.0239

Huang, S., Wu, Q., Guo, Y., and Rong, F. (2020). Hierarchical active power control of DFIG-based wind farm with distributed energy storage systems based on ADMM. *IEEE Trans. Sustain. Energy* 11 (02), 1528–1538. doi:10.1109/tste.2019.2929820

Kafshgari, N. A., Ramezani, N., and Nouri, H. (2019). Effects of high frequency modeling and grounding system parameters on transient recovery voltage across vacuum circuit breakers for capacitor switching in wind power plants. *Int. J. Electr. Power Energy Syst.* 104, 159–168. doi:10.1016/j.ijepes.2018.06.046

Kim, J., Seok, J., Muljadi, E., and Kang, Y. C. (2016). Adaptive Q-V scheme for the voltage control of a DFIG-based wind power plant. *IEEE Trans. Power Electron.* 31 (05), 3586–3599. doi:10.1109/tpel.2015.2464715

Li, Y., Xu, Z., Zhang, J., and Meng, K. (2018). Variable droop voltage control for wind farm. *IEEE Trans. Sustain. Energy* 9 (1), 491–493. doi:10.1109/tste.2017.2726355

Liu, J.-H., and Cheng, J.-S. (2021). Online voltage security enhancement using voltage sensitivity-based coherent reactive power control in multi-area wind power generation systems. *IEEE Trans. Power Syst.* 36, 2729–2732. doi:10.1109/tpwrs.2021.3053139

Liu, Y., Lin, Z., Li, M., and Wu, Q. H. (2020). On the state-dependent switched energy functions of DFIG-based wind power generation systems. *CSEE J. Power Energy Syst.* 6, 318–328.

Llrab, C., Oacv, B., Ercd, C., Jmg, D., and Ajsf, C. (2020). Generalized Predictive Control applied to the DFIG power control using state-space model and voltage constraints. *Electr. Power Syst. Res.* 182, 106227. doi:10.1016/j.epsr.2020.106227

Mathis, WILLIAM (2023(). UK will speed up grid connections to boost clean power capacity. *Environ. and Energy Rep.*, 121–122.

Ouyang, J., Tang, T., Yao, J., and Li, M. (2019). Active voltage control for DFIG-based wind farm integrated power system by coordinating active and reactive powers under wind speed variations. *IEEE Trans. Energy Convers.* 34 (03), 1504–1511. doi:10.1109/tec.2019.2905673

Peng, H., Huang, S., Wei, J., Wei, C., Wu, Q., Shen, F., et al. (2024). Two-stage decentralized optimal voltage control in wind farms with hybrid ESSs. *IEEE Trans. Power Syst.* 39 (5), 6552–6565. doi:10.1109/tpwrs.2024.3360451

Tong, N., Lin, X., Li, Z., Fang, J., Zhuo, Y., Sui, Q., et al. (2020). Coordinated sequential control of individual generators for large-scale DFIG-based wind farms. *IEEE Trans. Sustain. Energy* 11 (03), 1679–1692. doi:10.1109/tste.2019.2936757

Xiao, J. I. N., and Heng, NIAN (2021). Overvoltage suppression strategy for sending AC grid with high penetration of wind power in the LCC-HVDC system under commutation failure. *IEEE Trans. Power Electron.* 36 (9), 10265–10277. doi:10.1109/tpel.2021.3066641

Yujun, L. I., Zhao, X. U., Zhang, J., and Meng, K. (2018). Variable droop voltage control for wind farm. *IEEE Trans. Sustain. Energy* 9 (1), 491–493. doi:10.1109/tste.2017.2726355

Zhang, K., Geng, G., and Jiang, Q. (2020). Online tracking of reactive power reserve for wind farms. *IEEE Trans. Sustain. Energy* 11 (02), 1100–1102. doi:10.1109/tste.2019.2929673

Zhang, Y., Kou, P., Zhang, Z., Li, H., Li, X., and Liang, D. (2023). Coordinated frequency and voltage optimal control of wind farm with nonlinear power constraints. *IEEE Syst. J.* 17 (3), 4934–4945. doi:10.1109/jsyst.2023.3273569

Zhang, H., Gruson, F., Rodriguez, D. M. F., and Saudemont, C. (2019). Overvoltage limitation method of an offshore wind farm with DC series-parallel collection grid. *IEEE Trans. Sustain. Energy* 10 (1), 204–213. doi:10.1109/tste.2018.2829929

Zhao, H., Wu, Q., Wang, J., Liu, Z., Shahidehpour, M., and Xue, Y. (2017). Combined active and reactive power control of wind farms based on model predictive control. *IEEE Trans. Energy Convers.* 32 (3), 1177–1187. doi:10.1109/tec.2017.2654271

Zheng, Z., Wang, Y., Xiao, X., Huang, C., Xie, Q., et al. (2020). Response mechanism of DFIG to transient voltage disturbance under commutation failure of LCC-HVDC system. 35(6):2972–2979. doi:10.1109/TPWRD.2020.3005720

frontiers | Frontiers in Energy Research

TYPE Original Research
PUBLISHED 28 August 2025
DOI 10.3389/fenrg.2025.1535211

OPEN ACCESS

EDITED BY
ZhaoYang Dong,
City University of Hong Kong, Hong Kong SAR, China

REVIEWED BY
Qianzhi Zhang,
Cornell University, United States
Jun Yang,
Northeastern University, China

*CORRESPONDENCE
Chuanhong Ru,
15271023788@163.com

RECEIVED 27 November 2024
ACCEPTED 06 August 2025
PUBLISHED 28 August 2025

CITATION
Ru C, Li L, Lu J and Jiang B (2025) Data-driven industrial park microgrids robust optimization method.
Front. Energy Res. 13:1535211.
doi: 10.3389/fenrg.2025.1535211

Data-driven industrial park microgrids robust optimization method

Chuanhong Ru[1]*, Lei Li[2], Ji Lu[1] and Beini Jiang[1]

[1]State Grid TaiZhou Power Supply Company, Taizhou, China, [2]State Grid ZheJiang Electric Power Corporation, Hangzhou, China

In order to accurately describe the impact of the volatility and randomness of renewable energy output power on the operation of industrial park microgrids, a data-driven robust optimization method for industrial park microgrids is proposed. Firstly, based on the traditional interval set, the uncertain parameters of renewable energy output are modeled using a polyhedral set. Then, an ellipsoidal uncertainty set is established using historical data of renewable energy output. By connecting high-dimensional ellipsoidal vertices, a data-driven convex hull polyhedron set is established. Then, the uncertain parameters are better enveloped by scaling the convex hull set. A data-driven robust optimization model for industrial park microgrid was further established, and the column and constraint (C&CG) generation algorithm was used to solve the model. Finally, simulation comparisons were conducted through examples, and the results showed that the data-driven industrial park microgrids robust optimization method can reduce conservatism and improve the robustness of optimization results, demonstrating the effectiveness of the proposed method.

KEYWORDS

industrial park microgrids, data-driven, robust optimization, convex hull set, column and constraint generation algorithm

1 Introduction

With the increasingly prominent environmental and climate issues caused by excessive reliance on traditional fossil fuels, accelerating energy transition and sustainable development on a global scale has become a widely accepted consensus (Farh et al., 2024). To address the challenges of energy supply diversity and the intermittency of renewable energy sources, the industrial park microgrids featuring complementary and coupled forms of multiple energy supplies has emerged (Ishaq and Dincer, 2024). However, due to the instability of renewable energy outputs, power generation is affected by various factors such as climate, weather, and seasons, leading to significant fluctuations in power supply. These fluctuations can potentially trigger instability or even collapse of the industrial park microgrids, posing significant challenges to its safety and stability (Poodeh et al., 2025).

Existing research on the industrial park microgrids operation planning focuses on energy utilization efficiency and enhancing system stability. For instance, in Arooj (2024), system stability is improved by adopting demand-side response under the premise of considering flexible resources. In Rezazadeh and Avami (2024), a comprehensive energy system with detailed power-to-gas conversion and carbon cycling is established

through the utilization of the carbon trading market. In Rahman et al. (2025), the grid partitioning of the integrated energy system is optimized by taking into account the characteristics of the load, thereby achieving cost reduction. Synthesizing these studies, there is a noticeable lack of consideration given to the uncertainty of renewable energy output.

To address the issue of uncertainty in renewable energy output, existing uncertainty optimization methods are mainly categorized into two types: stochastic optimization methods (Davidsdottir et al., 2024; Son and Kim, 2024; Aliasghar et al., 2022) and robust optimization methods (Vulusala and Madichetty, 2018; Stewart and Bingham, 2016). Robust optimization methods typically use a set-based approach to describe the distribution range of uncertain parameters. Unlike stochastic methods, robust optimization does not require the probability distribution of uncertain parameters and avoids the high-dimensional problems introduced by numerous scenarios. Consequently, it has gained increasing attention in the optimal operation of industrial park microgrids.

To enhance the reliability of robust optimization results and describe the correlations among uncertain parameters, recent studies have employed historical data of uncertain variables to explore the relationships between the variations of random variables, leading to the proposal of data-driven uncertainty sets (Sulaiman et al., 2024; Freitas et al., 2007; Ibraheemi and Janabi, 2024). For instance (Zhang et al., 2024a), constructed the uncertainty of photovoltaic power generation using historical data from smart meters and phasor measurement units to solve the problem of voltage regulation (Zhang et al., 2024b). constructed an uncertainty set using historical vehicle travel data to analyze the impact of large-scale transportation electrification on power systems (Lorca and Sun, 2015). established a polyhedral uncertainty set based on historical wind power data for economic dispatch modeling, analysis, and optimization (Jalilvand-Nejad et al., 2016). Proposed a correlated polyhedral uncertainty set model by bending the boundaries of a polyhedral set through mathematical analysis, building on the polyhedral set approach (Hamed and Rasoul, 2021). further refined the approach of Jalilvand-Nejad et al. (2016) by constructing a generalized correlated polyhedral uncertainty set model, allowing the polyhedral set to better envelop the range of uncertain parameters (Degefa et al., 2015). Constructed an ellipsoidal set to describe photovoltaic (PV) output and proposed an affine adjustable robust optimization strategy for active distribution networks. Although the ellipsoidal set effectively considers the correlations among uncertain parameters, its nonlinear structure increases the difficulty of solving the model. While Lorca and Sun (2015), Jalilvand-Nejad et al. (2016), Hamed and Rasoul (2021), and Degefa et al. (2015) consider the correlations within the uncertainty sets, the broader coverage of the uncertainty sets they establish can lead to increased conservatism in decision-making.

In addition to polyhedral and ellipsoidal sets, another common method is constructing uncertainty sets based on extreme scenarios. In Moradian et al. (2024) and Akter et al. (2025), historical data is first selected to form the uncertainty set. Then, extreme scenarios are identified based on the historical data, and convex hull sets are constructed from these scenarios. An appropriate scaling factor is introduced to cover all historical data, and finally, a robust optimization model based on extreme scenarios is established. The method in Ayene and Yibre (2024) and Bifei et al. (2022) does not predefine the shape of the uncertainty set but represents it as the convex hull of historical scenarios. These studies have made improvements regarding the conservativeness of polyhedral sets. However, although the uncertainty sets based on extreme scenarios can address the conservatism issue, they have a large number of vertices, making them difficult to solve. Therefore, this paper proposes a data-driven convex hull uncertainty set model. This model can not only reduce the conservatism of the solution but also decrease the difficulty of solving.

Against this research backdrop, considering the lack of attention to uncertain energy inputs in industrial park microgrids, this paper proposes a data-driven robust optimization method for industrial park microgrids. First, traditional polyhedral set modeling is conducted based on interval sets. Then, ellipsoidal sets are constructed based on historical scenarios, and the vertices of the ellipsoids are connected to form convex hull polyhedral sets. Finally, the constructed convex hull set is scaled to cover all historical scenarios. Furthermore, the data-driven convex hull model is embedded into the robust optimization model of the industrial park microgrids. The effectiveness of iu-the proposed method is verified through a case study of an integrated energy system in a specific region.

This paper will mainly make contributions in the following aspects:

1. In view of the current situation that the integrated energy system insufficiently considers the injection of uncertain energy sources, a data-driven robust optimization method for industrial park microgrids is proposed.
2. Aiming at the deficiencies of traditional uncertain set modeling, traditional polyhedron set modeling is first carried out on the interval set. Then, an elliptical set is constructed based on historical scenarios. Subsequently, the vertices of the ellipse are connected to construct a convex hull polyhedron set, and all historical scenarios are covered by scaling, thus establishing a unique data-driven modeling method.
3. The well-constructed data-driven convex hull set model is successfully embedded into the robust optimization model of the industrial park microgrids. Moreover, with the help of an example of an industrial park microgrid in a certain region, the effectiveness of the proposed method is verified.

The rest of this article is organized as follows: Section 2 introduces the different uncertain set modeling. The industrial park microgrid optimization model is introduced in Section 3. In Section 4, the specific objective function and constraints is presented. Section 5 studies the robust optimization method for microgrid in industrial park. Finally, Section 6 concludes.

2 Uncertain set modeling

2.1 Traditional uncertain set modeling

In this paper, the budget uncertainty set U is used to express the range of fluctuations in the magnitude of PV as

well as wind power output. The specific expression is shown in Equation 1:

$$\boldsymbol{U} = \begin{cases} \boldsymbol{u} = \left[\tilde{P}_t^{\mathrm{PV}}, \tilde{P}_t^{\mathrm{WT}}\right] \\ \boldsymbol{z} = \left[z_t^{\mathrm{PV}}, z_t^{\mathrm{WT}}\right] \\ \tilde{P}_t^{\mathrm{PV}} = P_t^{\mathrm{PV,f}} + \Delta P^{\mathrm{PV,max}} z_t^{\mathrm{PV}} \\ \tilde{P}_t^{\mathrm{WT}} = P_t^{\mathrm{WT,f}} + \Delta P^{\mathrm{WT,max}} z_t^{\mathrm{WT}} \end{cases} \tag{1}$$

where $\tilde{P}_t^{\mathrm{PV}}$ and $\tilde{P}_t^{\mathrm{WT}}$ denote the actual magnitude of output at the moment t for PV and wind power, respectively; z_t^{PV} and z_t^{WT} represent the actual output levels of PV and wind power generation at the moment t respectively. $P_t^{\mathrm{PV,f}}$ and $P_t^{\mathrm{WT,f}}$ represent the predicted power output levels of PV and wind energy at the moment t respectively; $\Delta P^{\mathrm{PV,max}}$ and $\Delta P^{\mathrm{WT,max}}$ denote the maximum fluctuation values of PV and wind power generation, respectively; $\boldsymbol{u}$ represents the vector set of PV and wind power output; $\boldsymbol{z}$ stands for the vector set of uncertain variables in PV and wind power generation.

When there is no spatiotemporal correlation between uncertain variables, to better represent the range of variation of uncertain variables, this paper first characterizes them using traditional box sets and polyhedral sets, as shown below.

2.1.1 Box set

The specific expression for a box set can be given as:

$$\boldsymbol{U} = \left\{\boldsymbol{z} \in \boldsymbol{R}^{N\times 1} | \beta \boldsymbol{z}_{\mathrm{down}} \le \boldsymbol{z} \le \beta \boldsymbol{z}_{\mathrm{up}}\right\} \tag{2}$$

where $\boldsymbol{R}^{N\times 1}$ represents the dimension of the uncertain variable; $\boldsymbol{z}_{\mathrm{down}}$ and $\boldsymbol{z}_{\mathrm{up}}$ represent the maximum and minimum values of the uncertain variables, with values set to 1 and −1, respectively; β, which is the adjustment coefficient used to regulate the conservativeness of the uncertain set, is set to $(0, 1]$.

From Equation 2, it can be seen that the box set is merely an interval representation of the uncertain variable, and under normal circumstances, the values are often taken at the boundaries. However, since the extreme conditions corresponding to the boundary values have a lower probability of occurrence, the box set fails to accurately represent most other cases. Therefore, a polyhedral set is often required.

2.1.2 Polyhedral set

The specific expression is shown in Equation 3:

$$\boldsymbol{U} = \left\{ \boldsymbol{z} \in \boldsymbol{R}^{N\times 1} \middle| \begin{matrix} \beta \boldsymbol{z}_{\mathrm{down}} \le \boldsymbol{z} \le \beta \boldsymbol{z}_{\mathrm{up}} \\ \sum_i^N z_i \le \Gamma \end{matrix} \right\} \tag{3}$$

where Γ represents the uncertainty of the polyhedral set of uncertain variables, used to constrain the range of uncertainty of the polyhedral set. When the uncertain variables are two-dimensional, the envelope ranges of the polyhedral sets corresponding to different matrices Γ are illustrated as shown in Figure 1.

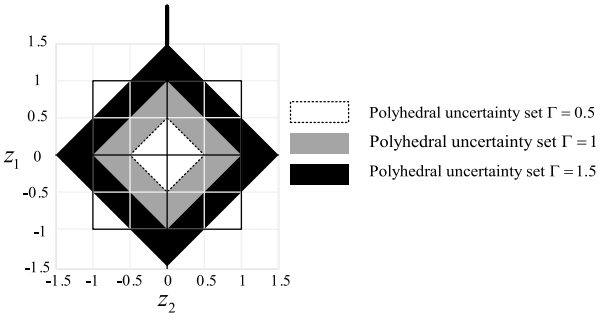

FIGURE 1
The impact of uncertainty on polyhedral sets.

2.2 Data-driven modeling of uncertain set

When there is spatiotemporal correlation among uncertain parameters, envelope lines can be adopted to represent different sets based on the scatter plots formed by the historical data of uncertain renewable energy output. Figure 2 illustrates the difference in envelope ranges when using box sets and ellipsoid sets.

As can be seen in Figure 2a, the box set envelopes all possible outcomes of distributed PV and wind power generation. However, due to the inherent spatiotemporal correlation of distributed PV at different times and locations, the PV output data predominantly clusters around the $y = x$ and $y = -x$ function lines. In this scenario, using a box set to describe the uncertainty of PV output may lead to overly conservative optimization solutions, since the box set not only encompasses all possible fluctuations but also covers areas with low probability of occurrence, which are essentially blank spaces. Therefore, it is necessary to adopt a more suitable modeling approach for uncertain sets.

2.2.1 Ellipsoid set

The specific expression is shown in Equation 4:

$$\boldsymbol{U} = \left\{\boldsymbol{z} \in \boldsymbol{R}^{N\times 1} | (\boldsymbol{z} - \boldsymbol{c})^{\mathrm{T}} \boldsymbol{\Sigma}^{-1} (\boldsymbol{z} - \boldsymbol{c}) \le 1\right\} \tag{4}$$

where $\boldsymbol{c}$ represents the center point of a high-dimensional ellipsoid, while $\Sigma \in \boldsymbol{R}^{N\times N}$ is a positive definite matrix indicating the offset direction of the high-dimensional ellipsoid relative to the coordinate axes.

As illustrated in Figure 2b, the ellipsoid set, similar to the box set, envelopes all possible outcomes of distributed power generation. Unlike the box set, however, the ellipsoid set reduces the envelopment of blank areas with low probability of fluctuation occurrence, thereby decreasing the conservativeness of the decision results. However, due to the quadratic form of the ellipsoid set's expression, it introduces complexity in the robust optimization process, increasing the difficulty of the solution.

2.2.2 Generalized convex hull set

Building upon this (Moradian et al., 2024), proposed a generalized convex hull set, which not only effectively reduces the conservativeness of optimization outcomes but also avoids the introduction of quadratic forms during the modeling process. Thus, based on Moradian et al. (2024), this paper constructs a data-driven uncertain set, with the modeling process illustrated in Figure 3.

Step (1): Firstly, construct a high-dimensional ellipsoidal uncertainty set that covers all historical data fluctuations

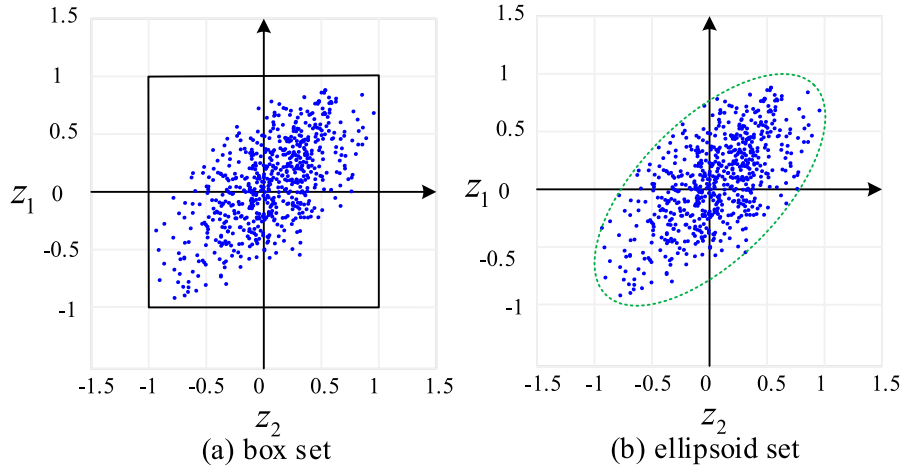

FIGURE 2
The envelope range of an uncertain set. **(a)** Box set. **(b)** Ellipsoid set.

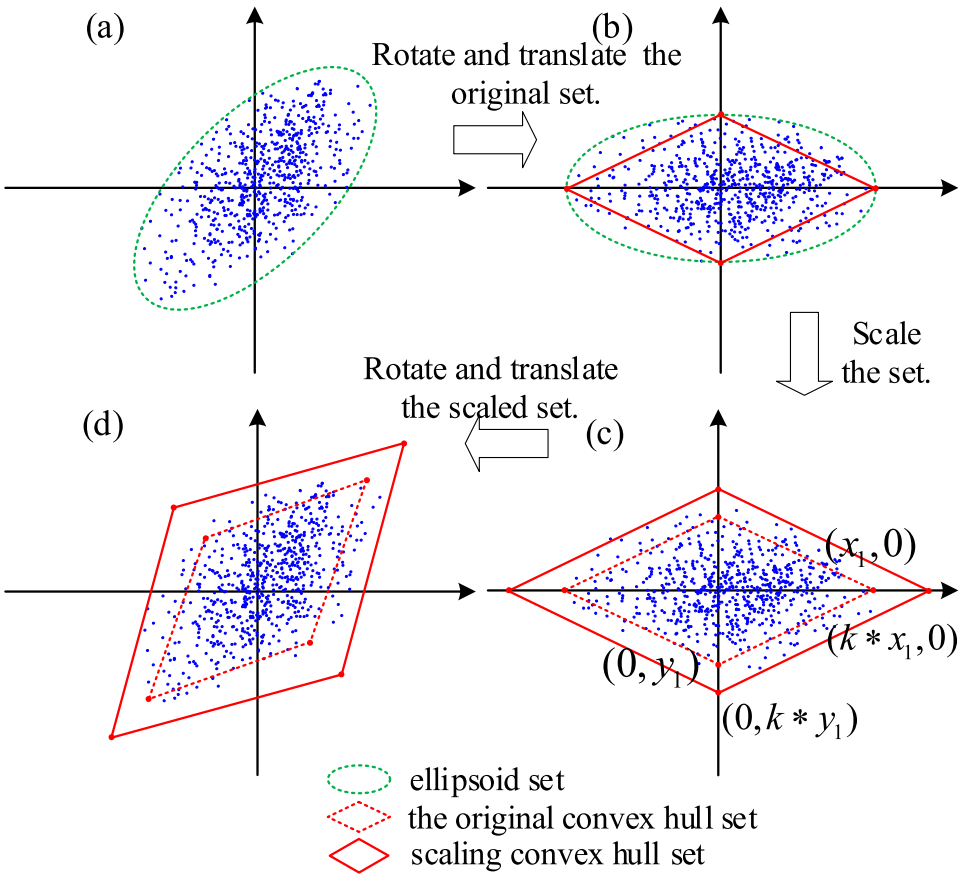

FIGURE 3
The modeling process for the convex hull uncertainty set (parts **(a–d)** illustrate key transformation steps).

with minimal volume, as illustrated in Figure 3a. The specific representation is given by Equation 5, which is:

$$\boldsymbol{U}_{e1} = \left\{ \boldsymbol{z} \in \boldsymbol{R}^{N\times 1} | (\boldsymbol{z}-\boldsymbol{c})^{\mathrm{T}} \boldsymbol{\Sigma}^{-1} (\boldsymbol{z}-\boldsymbol{c}) \le 1 \right\} \tag{5}$$

Step (2): On the basis of the original high-dimensional ellipsoid, perform an orthogonal decomposition of the positive definite matrix $\boldsymbol{\Sigma}$ into matrix $\boldsymbol{\Sigma} = \boldsymbol{P}^{T}\boldsymbol{J}\boldsymbol{P} = \boldsymbol{P}^{-1}\boldsymbol{J}\boldsymbol{P}$. Rotate and translate the existing ellipsoid so that its center coincides with the origin of the coordinate

axes, as shown by the green dashed line in Figure 3b. At this point, the high-dimensional ellipsoidal uncertainty set becomes $\boldsymbol{U}_{e2}$, which is shown in Equation 6:

$$\boldsymbol{U}_{e2} = \left\{ \boldsymbol{z}' \in \boldsymbol{R}^{N\times 1} | (\boldsymbol{z}')^{\mathrm{T}} \boldsymbol{J}^{-1} (\boldsymbol{z}') \le 1 \right\} \tag{6}$$

$$\boldsymbol{z}' = \boldsymbol{P} \times (\boldsymbol{z} - \boldsymbol{c}) \tag{7}$$

where $\boldsymbol{J}$ is a diagonal matrix, denoted as $\boldsymbol{J} = \mathrm{diag}(\lambda_1 \dots \lambda_N)$; P is a transformation matrix, representing the offset angle of the matrix.

Given the diagonal matrix $\boldsymbol{J}$, the coordinates of the vertices $z_{c,i}{}'$ of the transformed high-dimensional ellipsoid are shown in Equation 8:

$$\begin{cases} z_{c,1}{}' = \left[1/\sqrt{\lambda}_1, 0 \dots 0\right], z_{c,N+1}{}' = -\left[1/\sqrt{\lambda}_1, 0 \dots 0\right] \\ z_{c,2}{}' = \left[0, 1/\sqrt{\lambda}_2 \dots 0\right], z_{c,N+2}{}' = -\left[0, 1/\sqrt{\lambda}_2 \dots 0\right] \\ \vdots \\ z_{c,N}{}' = \left[0, 0 \dots 1/\sqrt{\lambda}_{N_{\mathrm{PV}}}\right], z_{c,2N}{}' = -\left[0, 0 \dots 1/\sqrt{\lambda}_N\right] \end{cases} \tag{8}$$

where m_i represents the weight coefficient of the i-th vertex.

Step (3): Due to the high-dimensional linear polyhedral set obtained from step 2, a small number of data points fall outside the envelope. Therefore, a scaling process is necessary for the original set, as shown by the solid lines in Figure 3c. After scaling, the vertices of the high-dimensional linear polyhedron are shown in Equation 9:

$$\begin{cases} kz_{c,1}{}' = \left[k/\sqrt{\lambda}_1, 0 \dots 0\right], kz_{c,N+1}{}' = -\left[k/\sqrt{\lambda}_1, 0 \dots 0\right] \\ kz_{c,2}{}' = \left[0, k/\sqrt{\lambda}_2 \dots 0\right], kz_{c,N+2}{}' = -\left[0, k/\sqrt{\lambda}_2 \dots 0\right] \\ \vdots \\ kz_{c,N}{}' = \left[0, 0 \dots k/\sqrt{\lambda}_N\right], kz_{c,2N}{}' = -\left[0, 0 \dots k/\sqrt{\lambda}_N\right] \end{cases} \tag{9}$$

At this point, the scaled high-dimensional linear polyhedral uncertainty set $\boldsymbol{U}_{p2}$ is shown in Equation 10:

$$\boldsymbol{U}_{p2} = \left\{ \boldsymbol{z}' \in \boldsymbol{R}^{N\times 1} \left| \begin{array}{l} \boldsymbol{z}' = \sum_{i=1}^{2N} m_i k \boldsymbol{z}_{c,i}{}' \\ \sum_{i=1}^{2N} m_i = 1; \quad 0 \le m_i \le 1 \end{array} \right. \right\} \tag{10}$$

where k is the scaling factor, used to adjust the conservativeness of the high-dimensional linear polyhedral envelope range. The calculation method for k is detailed in Moradian et al. (2024), thus there exists a minimum $k_{\min}$ that ensures the scaled polyhedral set precisely envelops all possible data points. The derivation process of $k_{\min}$ is shown in Supplementary Appendix SA1. Consequently, the valid range for k is $[0, k_{\min}]$, and the polyhedral sets formed by different values of k are illustrated in Figure 4.

The scaling factor influences the degree to which the convex hull set envelops data points. When $k = 1$, the convex hull set, formed by connecting the ellipsoid's endpoints, does indeed envelop all historical PV output points. However, it fails to fully account for certain extreme scenarios, which, while reducing the conservativeness of the optimization outcomes, compromises the system's robustness. By gradually increasing the scaling factor of the convex hull set until it equals $k_{\min}$, the set now fully encompasses all historical output points. Unlike the box set, it minimally envelops blank areas, thus, while decreasing the conservativeness of the optimization results, it enhances the robustness of the outcomes simultaneously.

Step (4): Rotate and translate the scaled high-dimensional linear polyhedron so that it conforms to the original data points' range. From Equation 7, it is known that after rotation and translation, the high-dimensional linear polyhedral uncertainty set $\boldsymbol{U}_{p1}$ is shown in Equation 11:

$$\boldsymbol{U}_{p1} = \left\{ \boldsymbol{z} \in \boldsymbol{R}^{N\times 1} \left| \begin{array}{l} \boldsymbol{z} = \sum_{i=1}^{2N} m_i (\boldsymbol{c} + k\boldsymbol{P}^{-1} \boldsymbol{z}_{c,i}{}') \\ \sum_{i=1}^{2N} m_i = 1; \quad 0 \le m_i \le 1 \end{array} \right. \right\} \tag{11}$$

In summary, when the box set is used to describe the fluctuation of photovoltaic output, because it is an interval set, as shown in the black box square box line in Figure 4. Although it completely envelopes all the possibilities of photovoltaic output, due to the existence of a large number of blank areas, the results obtained by using this set are conservative to a certain extent. When the convex hull set is used, it is shown in the color diamond box in Figure 4. Since it is connected by the endpoints of the elliptical set and the polyhedron set obtained by scaling, it has a good ability to describe the historical output points of the photovoltaic, and reduces the envelope of the blank area while completely enveloping. This solves the disadvantage of high conservatism brought by the box set.

3 Industrial park microgrid optimization modeling

3.1 Industrial park microgrid system

The power-to-gas industrial park microgrid system is an integrated system that combines electricity, thermal energy, and gas energy, typically involving various energy conversion and utilization technologies, aiming to achieve efficient energy utilization and complementarity.

The typical power-to-gas industrial park microgrid system established in this paper consists of the following components, and the industrial park microgrid system diagram is shown in Figure 5.

Renewable energy facilities, including solar photovoltaic (PV) systems and wind turbine generation (WT) systems, which primarily convert renewable energy such as solar and wind power into electricity to supply electric loads; energy storage facilities, including battery energy storage systems (ES), heat storage systems (HS), and cold storage systems (CS), which not only provide energy to the system but also store excess energy for future use; heating equipment, such as gas boilers (GB) and excess heat boilers (EH); cooling equipment, such as absorption refrigerators (AC); and various energy conversion equipment, including gas turbines (GT), electroliers (EG), methane reactors (MR), hydrogen storage tanks (CH), hydrogen fuel cells (HFC), and electric chillers (EC).

3.2 Demand-side response model

In order to better accommodate clean energy and enhance the stability and economic efficiency of the system, a demand-side

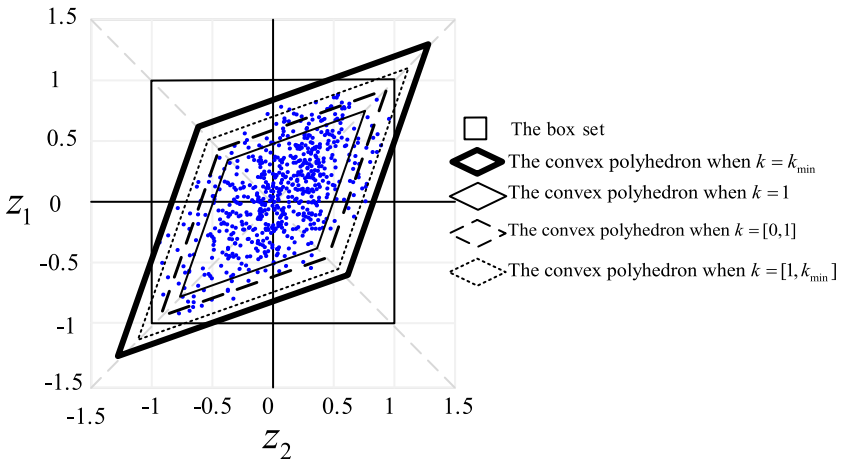

FIGURE 4
The range of convex hull sets under different values of k.

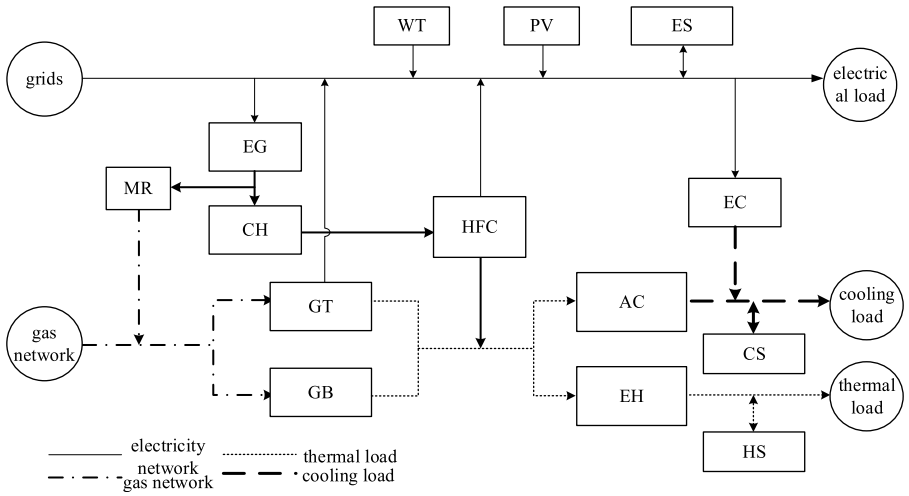

FIGURE 5
Industrial park microgrid system diagram.

response model needs to be established on the load side. The model is constructed as follows:

$$-\xi_t = \frac{\Delta P_t^{\mathrm{D}}}{\Delta \rho_t^{\mathrm{D}}} = \frac{P_t^{\mathrm{D,cur}} - P_t^{\mathrm{D}}}{\rho_t^{\mathrm{D,cur}} - \rho_t^{\mathrm{D}}} \tag{12}$$

$$\sum_{t=1}^{T} P_t^{\mathrm{cur}} = \sum_{t=1}^{T} P_t^{\mathrm{D}} \tag{13}$$

$$\rho_t^{\mathrm{cur,max}} \le \rho_t^{\mathrm{cur}} \le \rho_t^{\mathrm{cur,min}} \tag{14}$$

$$\rho_t^{\mathrm{cur}} = \begin{cases} \rho^{\mathrm{peak}} & t \in T^{\mathrm{peak}} \\ \rho^{\mathrm{valley}} & t \in T^{\mathrm{valley}} \end{cases} \tag{15}$$

where ξ_t represents the price elasticity coefficient at the moment t; ΔP_t^{D} represents the change in the demand-side load before and after the response is implemented at the moment t; $\Delta \rho_t$ represents the change in the demand-side electricity price before and after the response is implemented at the moment t; ρ_t^{D} and $\rho_t^{\mathrm{D,cur}}$ respectively represent the electricity price before and after the demand side response is applied at the moment t; $\rho_t^{\mathrm{cur,max}}$ and $\rho_t^{\mathrm{cur,min}}$ respectively represent the upper and lower limits of the electricity price before and after the demand side response are applied at the moment t; ρ^{peak} and ρ^{valley} represent the peak and valley power before the demand-side response is implemented; T^{peak} and T^{valley} respectively represent the time periods of peak and valley power after the demand-side response is implemented. Equation 12 defines the elastic relationship between electricity price and load. Equation 13 ensures the balance of total electricity consumption before and after the response. Equation 14 defines the value range of electricity price. Equation 15 defines the peak and valley values of electricity price. The modeling of thermal load response follows the same logic.

3.3 IDR model

However, the demand-side response model only focuses on making response strategies for a single type of demand-side resource, in the power-to-gas industrial park microgrid system, due to the coordinated operation of multiple energy forms and equipment, the demand-side response model is difficult to coordinate the operation of multiple types of energy and equipment, an efficient adjustment model is needed to manage and optimize the operation of the system. Therefore, this paper adopts the Integrated Demand Response (IDR) model.

$$0 \le \Delta P_t^{0,\mathrm{IDR}} \le P_t^{\mathrm{IDR}} \tag{16}$$

$$P_t^{\mathrm{IDR}} \le P_{\max}^{\mathrm{IDR}} \tag{17}$$

where $\Delta P_t^{0,\mathrm{IDR}}$ represents the change of load when the system adopts the IDR model, P_t^{IDR} represents the IDR reserve capacity of the load at the moment t, and $P_{\max}^{\mathrm{IDR}}$ represents the maximum value of the IDR load. Equation 16 defines the range of load change, and Equation 17 specifies the conditions that the load reserve capacity must satisfy.

4 Objective function and constraints

4.1 Objective function

In this paper, we consider the electricity-gas multi-energy complementary microgrid model that minimizes the integrated cost of energy purchase cost, operation and maintenance cost, IDR cost, and standby cost, and is shown in Equation 18:

$$\min\ \mathrm{C} = \mathrm{C}_{\mathrm{buy}} + \mathrm{C}_{\mathrm{main}} + \mathrm{C}_{\mathrm{SP}} + \mathrm{C}_{\mathrm{IDR}} \tag{18}$$

Equations 19–22 respectively demonstrate the calculation methods for energy purchase cost, operation and maintenance cost, Integrated Demand Response (IDR) cost, and standby cost.

$$\mathrm{C}_{\mathrm{buy}} = \sum_t^T \left[\left(\frac{b_t^{\mathrm{e}} + s^e}{2} P_t^{\mathrm{E}} + \frac{b_t^{\mathrm{e}} - s^e}{2} \left| P_t^{\mathrm{E}} \right| \right) + b_t^{\mathrm{g}} Q_t^{\mathrm{G}} \right] \tag{19}$$

where $\mathrm{C}_{\mathrm{buy}}$ represents the cost of energy purchased by the system from the higher grid as well as from the gas grid; P_t^{E} represents the power of interaction between the system and the grid at time t. A positive value indicates that power is purchased from the grid, while a negative value indicates that power is sold to the grid; Q_t^{G} represents the natural gas purchased by the system at time t; b_t^{e} and b_t^{g} represent the price of the electricity and natural gas, respectively, at the time of purchase at time t; and s^e represents the price of the electricity at the time of sale.

$$\mathrm{C}_{\mathrm{main}} = \sum_n^N \sum_t^T c^n P_t^n \tag{20}$$

where c^n denotes the number of O&M coefficients of the nth device; P_t^n denotes the output of the nth device at time t.

$$\mathrm{C}_{\mathrm{SP}} = \sum_t^T \left(c_{\mathrm{sp}}^+ P_t^{\mathrm{sp},+} + c_{\mathrm{sp}}^- P_t^{\mathrm{sp},-} \right) \tag{21}$$

where c_{sp}^+ and c_{sp}^- denote the upward and downward standby cost coefficients of the grid; $P_t^{\mathrm{sp},+}$ and $P_t^{\mathrm{sp},-}$ denote the upward and downward standby capacity of the grid at time t, respectively.

$$\mathrm{C}_{\mathrm{IDR}} = \sum_t^T \left(c_{\mathrm{IDR}} P_t^{\mathrm{IDR}} \right) \tag{22}$$

where $\mathrm{C}_{\mathrm{IDR}}$ denotes the cost factor when the user participates in IDR.

4.2 Constraint condition

4.2.1 Energy balance constraints

The expression for the electrical power balance of the system is shown in Equation 23:

$$\begin{aligned} &P_t^{\mathrm{E}} - P_t^{\mathrm{EG}} + \eta^{\mathrm{HFCE}} P_t^{\mathrm{CH,out}} + \eta^{\mathrm{GTE}} Q_t^{\mathrm{GT}} + P_t^{\mathrm{WT}} \\ &+ P_t^{\mathrm{PV}} + P_t^{\mathrm{ES,dis}} - P_t^{\mathrm{ES,ch}} - P_t^{\mathrm{EC}} = P_t^{\mathrm{D,cur}} - \Delta P_t^{0,\mathrm{IDR}} \end{aligned} \tag{23}$$

where P_t^{EG}, $P_t^{\mathrm{CH,out}}$, P_t^{WT}, P_t^{PV}, $P_t^{\mathrm{ES,dis}}$, $P_t^{\mathrm{ES,ch}}$, P_t^{EC} indicate the size of the electrolyzer, hydrogen storage tank, distributed wind power, distributed photovoltaic, battery storage, electric refrigeration machine at the moment t to consume or send out the size of the electric energy; Q_t^{GT} indicates that the gas turbine at the moment t of the size of the gas-to-electricity power; η^{HFCE} indicates that the electric efficiency of the hydrogen fuel cell; η^{GTE} indicates that the gas turbine gas-to-electricity efficiency.

The gas balance expression for the system is shown in Equation 24:

$$Q_t^{\mathrm{G}} + \eta^{\mathrm{MR}} Q_t^{\mathrm{MR}} - Q_t^{\mathrm{GT}} - Q_t^{\mathrm{GB}} = 0 \tag{24}$$

where Q_t^{MR} represents the amount of natural gas injected into the system by the methane reactor at the moment t; Q_t^{GB} represents the amount of natural gas consumed by the gas boiler at the moment t; and η^{MR} represents the natural gas generation efficiency of the methane generator.

The heat balance expression of the system is shown in Equation 25:

$$\eta^{\mathrm{EH}} P_t^{\mathrm{EH}} + P_t^{\mathrm{HS,dis}} - P_t^{\mathrm{HS,ch}} = P_t^{\mathrm{H}} \tag{25}$$

where P_t^{EH} represents the thermal power produced by the waste heat boiler at the moment t; $P_t^{\mathrm{HS,dis}}$ and $P_t^{\mathrm{HS,ch}}$ represent the thermal power issued or stored in the heat storage tank at the moment t respectively; P_t^{H} represents the thermal load of the system at the moment t; η^{EH} represents the heat production efficiency of the waste heat boiler.

The cold balance expression of the system is shown in Equation 26:

$$\eta^{\mathrm{AC}} P_t^{\mathrm{AC}} + \eta^{\mathrm{EC}} P_t^{\mathrm{EC}} + P_t^{\mathrm{CS,dis}} - P_t^{\mathrm{CS,ch}} = P_t^{\mathrm{C}} \tag{26}$$

where P_t^{AC} represents the cold energy power issued by the absorption chiller at the moment t; $P_t^{\mathrm{CS,dis}}$ and $P_t^{\mathrm{CS,ch}}$ represent the cold energy power issued or stored in the cold storage tank at the moment t, respectively; P_t^{C} represents the cold load of the system at the moment t; η^{AC} and η^{EC} represent the refrigeration efficiency of the absorption chiller, respectively.

4.2.2 Energy coupling constraints

Electricity - gas conversion mainly includes two aspects of electricity hydrogen and hydrogen methanization, the system of electricity - gas conversion coupling constraints expression is shown in Equation 27:

$$\eta^{\mathrm{EG}} P_t^{\mathrm{EG}} - Q_t^{\mathrm{MR}} - P_t^{\mathrm{CH,in}} = 0 \tag{27}$$

where η^{EG} represents the efficiency of the electrolyzer to convert gas; $P_t^{\mathrm{CH,in}}$ represents the amount of hydrogen input to the hydrogen storage tank at the moment t. The system heat-cooling conversion is mainly to convert part of the system heat power into cold power.

The heat-cooling conversion is mainly to convert part of the input thermal power of the system into cold power, and the expression of the coupling constraints of heat-cooling conversion of the system is as follows

$$\eta^{\mathrm{HFCH}} P_t^{\mathrm{CH,out}} + \eta^{\mathrm{GB}} Q_t^{\mathrm{GB}} + \eta^{\mathrm{GT}} Q_t^{\mathrm{GT}} = P_t^{\mathrm{AC}} + P_t^{\mathrm{EH}} \tag{28}$$

where η^{HFCH} represents the thermal efficiency of the hydrogen fuel cell, η^{GB} and η^{GT} represent the thermal efficiency of the gas boiler and gas turbine respectively.

4.2.3 Operation constraints of energy supply equipment

The operation constraints of each device in the system are expressed as Equations 29, 30

$$P^n_{\min} \le P^n_t \le P^n_{\max} \tag{29}$$

$$\Delta P^n_{\min} \le P^n_{t+1} - P^n_t \le \Delta P^n_{\max} \tag{30}$$

where $P^n_{\min}$ and $P^n_{\max}$ represent the upper and lower limits of the n-th equipment output, $\Delta P^n_{\min}$ and $\Delta P^n_{\max}$ represent the upper and lower limits of the nth equipment output change in the neighboring time period.

4.2.4 Energy storage operation constraints

$$S_t^m = S_{t-1}^m + \eta^{m,\mathrm{ch}} P_t^{m,\mathrm{ch}} - \frac{P_t^{m,\mathrm{dis}}}{\eta^{m,\mathrm{dis}}} \tag{31}$$

$$\begin{cases} 0 \le P_t^{m,\mathrm{ch}} \le P_{\max}^{m,\mathrm{ch}} D_t^{m,\mathrm{ch}} \\ 0 \le P_t^{m,\mathrm{dis}} \le P_{\max}^{m,\mathrm{dis}} D_t^{m,\mathrm{dis}} \\ D_t^{m,\mathrm{ch}} + D_t^{m,\mathrm{dis}} \le 1 \end{cases} \tag{32}$$

$$S^m_{\min} \le S^m_t \le S^m_{\max} \tag{33}$$

$$S^m_T = S^m_1 \tag{34}$$

where S_t^m denotes the size of energy stored in the m-th storage device at the moment t, $P_t^{m,\mathrm{ch}}$ and $P_{\max}^{m,\mathrm{ch}}$ denote the maximum charging and discharging power of the m-th storage device at the moment t, $\eta^{m,\mathrm{ch}}$ and $\eta^{m,\mathrm{dis}}$ denote the charging and discharging efficiency of the m-th storage device, $D_t^{m,\mathrm{ch}}$ and $D_t^{m,\mathrm{dis}}$ denote the charging and discharging state of the m-th storage device at the moment t, respectively. Equations 31–34 sequentially define the dynamic change relationship of the stored energy of energy storage devices, the constraints on charging/discharging power and status, the limitation on the range of stored energy, and the closed - loop condition for the stored energy at the start and end of the period, regulating the operation process of the energy storage system.

4.2.5 Hydrogen storage tank operation constraints

Similar to the battery energy storage, the hydrogen storage tank can also be regarded as an energy storage device.

$$S_t^{\mathrm{CH}} = S_{t-1}^{\mathrm{CH}} + \eta^{\mathrm{CH,in}} P_t^{\mathrm{CH,in}} - \frac{P_t^{\mathrm{CH,out}}}{\eta^{\mathrm{CH,out}}} \tag{35}$$

$$\begin{cases} 0 \le P_t^{\mathrm{CH,in}} \le P_{\max}^{\mathrm{CH,in}} D_t^{\mathrm{CH,in}} \\ 0 \le P_t^{\mathrm{CH,out}} \le P_{\max}^{\mathrm{CH,out}} D_t^{\mathrm{CH,out}} \\ D_t^{\mathrm{CH,in}} + D_t^{\mathrm{CH,out}} \le 1 \end{cases} \tag{36}$$

$$S^{\mathrm{CH}}_{\min} \le S_t^{\mathrm{CH}} \le S^{\mathrm{CH}}_{\max} \tag{37}$$

$$S_T^{\mathrm{CH}} = S_1^{\mathrm{CH}} \tag{38}$$

where S_t^{CH} represents the amount of hydrogen stored in the hydrogen storage tank at the moment t, $P_t^{\mathrm{CH,in}}$ and $P_t^{\mathrm{CH,out}}$ represent the maximum hydrogen filling and discharging capacities of the hydrogen storage tank at the moment t, $\eta^{\mathrm{CH,in}}$ and $\eta^{\mathrm{CH,out}}$ represent the hydrogen filling and discharging efficiency of the hydrogen storage tank, $D_t^{\mathrm{CH,in}}$ and $D_t^{\mathrm{CH,out}}$ represent the hydrogen filling and discharging energy state of the hydrogen storage tank at the moment t. Equations 35–38 sequentially define the dynamic change of hydrogen storage amount in hydrogen storage tanks, the constraints on hydrogen charging/discharging power and status, the range of hydrogen storage amount, and the periodic closed-loop condition.

4.2.6 Power exchange constraints in large power grids

$$P_t^{\mathrm{E}} + P_t^{\mathrm{sp},+} \le P_{\max}^{\mathrm{E}} \tag{39}$$

$$P_t^{\mathrm{E}} - P_t^{\mathrm{sp},+} \ge P_{\min}^{\mathrm{E}} \tag{40}$$

where $P_{\max}^{\mathrm{E}}$ and $P_{\min}^{\mathrm{E}}$ respectively represent the upper and lower limits of power exchange with the large power grid. Equation 39 defines the upper limit of the power exchange combined with the upward reserve, and Equation 40 specifies the lower limit of the power exchange after deducting the upward reserve.

4.2.7 Constraint on reserve capacity

In order to ensure the reasonable reserve capacity of the system, the constraints are set as Equations 41–43.

$$0 \le P_t^{\mathrm{sp},+} \le P_{\max}^{\mathrm{sp},+} \tag{41}$$

$$P_{\min}^{\mathrm{sp},-} \le P_t^{\mathrm{sp},-} \le P_{\max}^{\mathrm{sp},-} \tag{42}$$

$$P_t^{\mathrm{sp},+} + P_t^{\mathrm{IDR}} \ge P_{\min}^{\mathrm{sp},+} \tag{43}$$

where $P_{\max}^{\mathrm{sp},+}$ and $P_{\max}^{\mathrm{sp},-}$ respectively represent the maximum values of upward and downward reserves, and $P_{\min}^{\mathrm{sp},-}$ represents the minimum value of downward reserves.

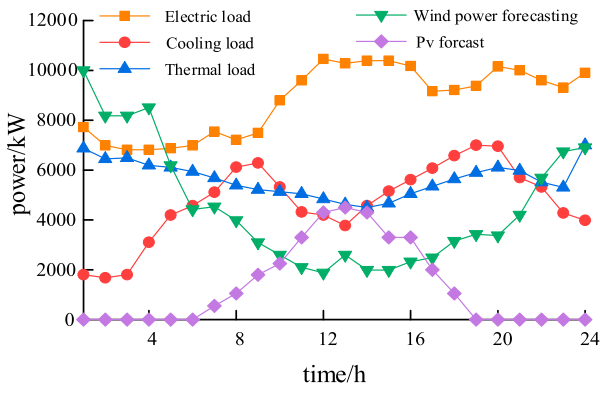

FIGURE 6
Renewable energy forecast output and load size.

4.2.8 Constraint on output of renewable energy

The constraints of renewable energy are as Equations 44, 45.

$$0 \le P_t^{\mathrm{WT}} \le \tilde{P}_t^{\mathrm{WT}} \tag{44}$$

$$0 \le P_t^{\mathrm{PV}} \le \tilde{P}_t^{\mathrm{PV}} \tag{45}$$

5 Robust optimization method for microgrid in industrial park

5.1 Robust optimization model establishment

Let the renewable energy constraint variable of the system be vector $\boldsymbol{P}^{\mathrm{RE}} = \left\{P_t^{\mathrm{PV}}, P_t^{\mathrm{WT}}\right\}$; the constraint variable of energy storage equipment be vector $\boldsymbol{P}^{\mathrm{ES}} = \left\{S_t^m, P_t^{m,\mathrm{ch}}, P_t^{m,\mathrm{dis}}\right\}$; the constraint variable of energy supply equipment be vector $\boldsymbol{P}^{\mathrm{E}} = \left\{P_t^n\right\}$; the operation constraint variable of hydrogen storage tank be vector $\boldsymbol{P}^{\mathrm{CH}} = \left\{S_t^{\mathrm{CH}}, P_t^{\mathrm{CH,in}}, P_t^{\mathrm{CH,out}}\right\}$; the energy purchase constraint variable be vector $\boldsymbol{P}^{\mathrm{SP}} = \left\{P_t^{\mathrm{E}}, Q_t^{\mathrm{G}}, P_t^{\mathrm{sp},+}, P_t^{\mathrm{sp},-}\right\}$; and the IDR constraint variable be vector $\boldsymbol{P}^{\mathrm{IDR}} = \left\{\Delta P_t^{0,\mathrm{IDR}}, P_t^{\mathrm{IDR}}\right\}$. Then, the matrix form of the robust optimization model for the microgrid in the industrial park established in this paper is as Equation 46.

$$\begin{aligned} &\min_{x}\left(\max_{u\in U}\ \min_{y\in\Omega(x,u)}\ \boldsymbol{c}^{\mathrm{T}}\boldsymbol{y}\right) \\ &s.t.\ \boldsymbol{A}\boldsymbol{x} \le \boldsymbol{d}\ \text{(a)} \\ &\boldsymbol{G}\boldsymbol{y} \le \boldsymbol{h} - \boldsymbol{E}\boldsymbol{x} - \boldsymbol{M}\boldsymbol{u}\ \text{(b)} \end{aligned} \tag{46}$$

where $\boldsymbol{x}$ and $\boldsymbol{y}$ are the decision variables of the model, and $\boldsymbol{u}$ is the uncertain variable. Among them, the first-stage decision variables $\boldsymbol{x} = \left\{D_t^{m,\mathrm{ch}}, D_t^{m,\mathrm{dis}}\right\}$, $D_t^{m,\mathrm{ch}}$, and $D_t^{m,\mathrm{dis}}$ represent the charging and discharging states of the m-th energy storage system; the second-stage decision variable is $\boldsymbol{y} = \left\{\boldsymbol{P}^{\mathrm{RE}}, \boldsymbol{P}^{\mathrm{ES}}, \boldsymbol{P}^{\mathrm{E}}, \boldsymbol{P}^{\mathrm{CH}}, \boldsymbol{P}^{\mathrm{SP}}, \boldsymbol{P}^{\mathrm{IDR}}\right\}$; the second-stage uncertain variable is $\boldsymbol{u} = \left\{\tilde{P}_t^{\mathrm{PV}}, \tilde{P}_t^{\mathrm{WT}}\right\}$. The constant matrix $\boldsymbol{A}$ represents the coefficient matrix related to the decision variable $\boldsymbol{x}$. The column vector $\boldsymbol{d}$ is a constant and represents the coefficient vector related to the decision variable $\boldsymbol{x}$. The constant matrices $\boldsymbol{G}$ and $\boldsymbol{E}$ represent the coefficient matrices related to the decision variable $\boldsymbol{y}$. The column vector $\boldsymbol{h}$ is a constant vector and represents the coefficient vector related to the decision variable $\boldsymbol{y}$. The constant matrix $\boldsymbol{M}$ represents the coefficient matrix related to the uncertain variable $\boldsymbol{u}$. $\Omega(\boldsymbol{x},\boldsymbol{u})$ is the feasible region of the continuous variable $(\boldsymbol{x},\boldsymbol{u})$ when $\boldsymbol{y}$ is given. $\boldsymbol{c}^{\mathrm{T}}\boldsymbol{y}$ represents the objective function of the second stage, corresponding to Equations 19 and 47 corresponds to the constraint condition related to the first-stage variable $\boldsymbol{x}$; (47-b) corresponds to the constraint condition related to the second-stage variable $\boldsymbol{y}$.

For a two-stage robust optimization model like Equation 47, since it contains both continuous variables and integer variables, and the second stage of the model contains uncertain parameter $\boldsymbol{u}$, it cannot be directly solved. Therefore, this paper uses method C&CG (Nayak et al., 2025; Michos et al., 2024) to transform it into a master-slave problem for solution. Among them, the master problem is to solve the integrated energy optimization model with the minimum comprehensive cost under the worst case; the sub-problem is to first solve the integer solution of the master problem (such as the charging and discharging state of the energy storage battery), and then optimize the remaining continuous variables to minimize the comprehensive cost obtained by the system under the worst case.

5.2 C&CG iterative solution method

The master-slave problem corresponding to Equation 47 is modeled as

$$\mathrm{MP1}:\begin{cases} \min\limits_{x,y,u}(\eta) \\ s.t.\ \boldsymbol{A}\boldsymbol{x} \le \boldsymbol{d} \\ \quad \boldsymbol{G}\boldsymbol{y}^l \le \boldsymbol{h} - \boldsymbol{E}\boldsymbol{x} - \boldsymbol{M}\boldsymbol{u}^l\ \forall l \le k \\ \quad \eta \ge \boldsymbol{c}^{\mathrm{T}}\boldsymbol{y}^l\ \forall l \le k \end{cases} \tag{47}$$

$$\mathrm{SP1}:\begin{cases} \max\limits_{u\in U}\ \min\limits_{y\in\Omega(x,u)}\ \boldsymbol{c}^{\mathrm{T}}\boldsymbol{y} \\ s.t.\ \ \boldsymbol{G}\boldsymbol{y} \le \boldsymbol{h} - \boldsymbol{E}\boldsymbol{x}^* - \boldsymbol{M}\boldsymbol{u}:\boldsymbol{\pi} \end{cases} \tag{48}$$

The main problem MP1 corresponding to Equation 48 is solved first, at this point, MP1 belongs to the mixed-integer second-order cone programming problem. After solving the first-stage variable solution $\boldsymbol{x}^*$ corresponding to MP1 and the auxiliary variable η introduced in $k+1$ iterations, which is C&CG-cut. Then, the variable solution $\boldsymbol{x}^*$ derived in the first stage is brought into the second stage subproblem SP1 to find the worst-case scenario $\boldsymbol{u}^l$, where l is the number of historical iterations and k is the number of current iterations. Finally, the worst-case scenario $\boldsymbol{u}^l$ solved in the second stage is brought into the main problem MP1 of the first stage and iterated. Where the last three constraints of Equation 48 are the set of optimal and feasible cut planes resulting from the previous k iterations, respectively. $\boldsymbol{\pi}$ is the dyadic variable of the subproblem constraints.

5.2.1 Sub-problem solution method

Equation 49 is a max-min optimization problem, therefore, in this paper, the pairwise theorem is used to convert the inner

TABLE 1 Operation parameters of each device.

Device type	Device parameters	Value
EG	Transformation efficiency	0.8
	Operation and maintenance cost (Yuan/kWh)	0.01
CH	Capacity (kWh)	20,000
	Charging and discharging efficiency	0.95
	Upper and lower limits of gas charging and discharging power (kW)	4,000
	Initial gas volume	10,000
	Operation and maintenance cost (Yuan/kWh)	0.01
GT	Electrical transformation efficiency	0.26
	Thermal transformation efficiency	0.68
	Operation and maintenance cost (Yuan/kWh)	0.03
GB	Operational efficiency	0.1
	Operation and maintenance cost (Yuan/kWh)	0.8
AC	Operational efficiency	0.8
	Operation and maintenance cost (Yuan/kWh)	0.03
EH	Operational efficiency	0.8
	Operation and maintenance cost (Yuan/kWh)	0.025
EC	Operational efficiency	3
	Operation and maintenance cost (Yuan/kWh)	0.03
ES	Capacity (kWh)	5,000
	Charging and discharging efficiency	0.9
	Upper and lower limits of charging and discharging power (kW)	2,000
	State of charge at start”	0
	Operation and maintenance cost (Yuan/kWh)	0.02
CS	Capacity (kWh)	5,000
	Charging and discharging efficiency	0.9
	Upper and lower limits of charging and discharging power (kW)	1,000
	Initial capacity (kWh)	0
	Operation and maintenance cost (Yuan/kWh)	0.02
HS	Capacity (kWh)	5,000
	Charging and discharging efficiency	0.9
	Upper and lower limits of charging and discharging power (kW)	1,000
	Initial capacity	1,000
	Operation and maintenance cost (Yuan/kWh)	0.02

TABLE 2 The effect of scaling factor k on various costs.

Various costs/dollar	k = 0.4	k = 0.6	k = 0.8	k = 1.0	k = 1.2
Operation and maintenance cost	238	236	234	232	231
	44.1	62.2	79.4	96.7	21.6
Energy purchase cost	152	153	155	156	157
	071.9	636.1	202.1	768	816.3
Standby cost	864	864	864	864	864
	0	0	0	0	0
IDC cost	298	298	298	298	304
	92.5	92.5	92.5	92.5	24.5
Total cost	214	215	217	218	220
	448.5	830.8	214	597.2	002.4

TABLE 3 The influence of the three aggregations on individual costs.

Various costs/$	Cassette set	Polyhedral set (%change)	Convex packet ensemble (%change)
Operation and maintenance cost	22927.4	22984.8 (+0.25%)	23121.6 (+1.24%)
Energy purchase cost	159509.5	159044.5 (−0.29%)	157816.3 (−1.06%)
standby costs	8,640	8,640 (0.00%)	8,640 (0.00%)
IDR costs	30497.7	30497.7 (0.00%)	30424.5 (−0.24%)
system cost	221574.6	221,167 (−0.18%)	220002.4 (−0.71%)

min problem of Equation 49 into its pairwise form to merge it into a maximization problem, which is shown in the form of Equation 50.

$$\begin{aligned} &\max_{u,\pi} -(\boldsymbol{h}-\boldsymbol{M}\boldsymbol{u}-\boldsymbol{E}\boldsymbol{x})^{\mathrm{T}}\boldsymbol{\pi} \\ s.t.\ \ &\boldsymbol{c}+\boldsymbol{N}^{\mathrm{T}}\boldsymbol{\pi}=0 \\ &\boldsymbol{\pi},\boldsymbol{\tau}^{a},\boldsymbol{\tau}^{b}\geq 0 \end{aligned} \tag{49}$$

in Equation 50, there exists a bilinear term $(\boldsymbol{M}\boldsymbol{u})^{\mathrm{T}}\boldsymbol{\pi}$, which is solved here by using the outer approximation of the bilinear term. The master problem MP2 and subproblem SP2 are obtained as shown in Equations 51 and 52.

$$\mathrm{SP2}:\begin{cases} \max\limits_{u,\pi} -(\boldsymbol{h}-\boldsymbol{M}\boldsymbol{u}-\boldsymbol{E}\boldsymbol{x})^{\mathrm{T}}\boldsymbol{\pi} \\ s.t.\ \ \boldsymbol{c}+\boldsymbol{N}^{\mathrm{T}}\boldsymbol{\pi}=0 \\ \quad \boldsymbol{\pi},\boldsymbol{\tau}^{a},\boldsymbol{\tau}^{b}\geq 0 \end{cases} \tag{50}$$

$$\mathrm{MP2}:\begin{cases} \max\limits_{u,\pi} -(\boldsymbol{h}-\boldsymbol{E}\boldsymbol{x})^{\mathrm{T}}\boldsymbol{\pi}+\boldsymbol{\beta} \\ s.t.\ \ \boldsymbol{c}+\boldsymbol{N}^{\mathrm{T}}\boldsymbol{\pi}=0 \\ \quad \boldsymbol{\pi},\boldsymbol{\tau}^{a},\boldsymbol{\tau}^{b}\geq 0 \\ \quad \boldsymbol{\beta}\leq G^{m}(\boldsymbol{u},\boldsymbol{\pi}),\forall m\leq n \end{cases} \tag{51}$$

where MP2 and SP2 are used to solve the upper and lower bounds of Equation 38, respectively, m is the number of historical iterations, and n is the number of current iterations. An auxiliary variable $\boldsymbol{\beta}$ is introduced to replace the bilinear term in the original equation, and a bilinear term exists in Equation 52 $G^{m}(\boldsymbol{u},\boldsymbol{\pi})=(\boldsymbol{M}\boldsymbol{u})^{\mathrm{T}}\boldsymbol{\pi}$. Therefore, it is necessary to use the outer approximation method for linearization, and the linearization formula is shown in (53).

$$G^{n}(\boldsymbol{u},\boldsymbol{\pi})=(\boldsymbol{u}^{n})^{\mathrm{T}}\boldsymbol{\pi}_{sp}^{n}+(\boldsymbol{u}-\boldsymbol{u}^{n})^{\mathrm{T}}\boldsymbol{\pi}_{sp}^{n}+\left(\boldsymbol{\pi}-\boldsymbol{\pi}_{sp}^{n}\right)^{\mathrm{T}}\boldsymbol{u}^{n} \tag{52}$$

6 Example analysis

This section is validated using the IEEE-RTS 24 node example system. To reflect the planning requirements of the power generation and transmission system, the load will be increased by 1.4 times. At the same time, 400 MW wind farms were connected at nodes 3, 6, 15, 18, and 23, respectively. According to Equation 28, the predicted wind power output value is about 115 MW, and the fluctuation of wind power output is ±30% of the predicted value. The typical value of sub transient reactance for all units is 0.1 (standard value). This example has two voltage levels, namely, 138 kV and 230 kV, and the maximum allowable current of the circuit breaker is 31.5 kA and 35 kA, respectively. The abandonment cost and load

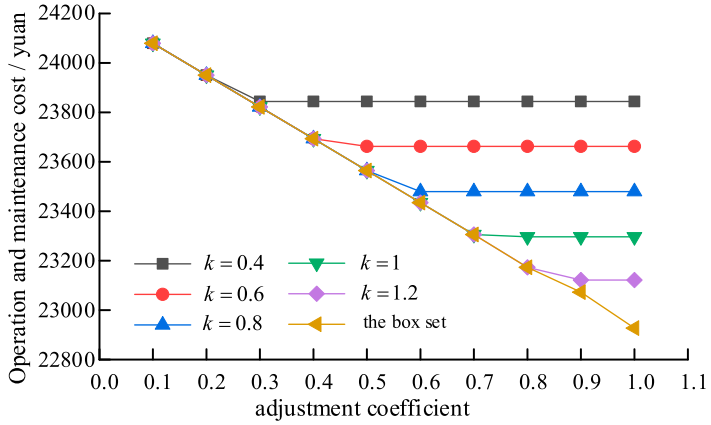

(a) Influence of robust adjustment coefficient β on O&M Costs

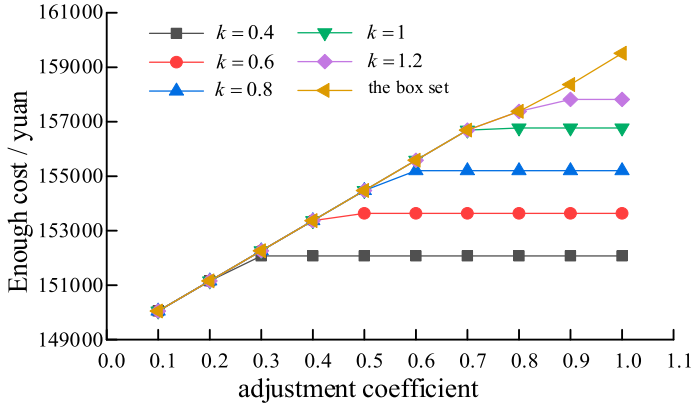

(b) Influence of the robust adjustment coefficient β on the cost of purchased energy

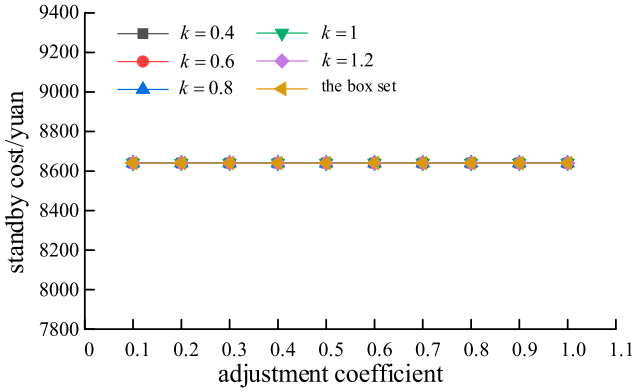

(c) Influence of the robust adjustment coefficient β on standby costs

FIGURE 7
(Continued).

shedding cost are \$150/(MWh) and \$5,000/(MWh) respectively. This article considers N-1 random faults in power generation and transmission, and the convergence threshold of the C&CG algorithm ζ Set to 0.001.

6.1 Example setting

In order to verify the effectiveness of the data-driven industrial park microgrids robust optimization method established in this

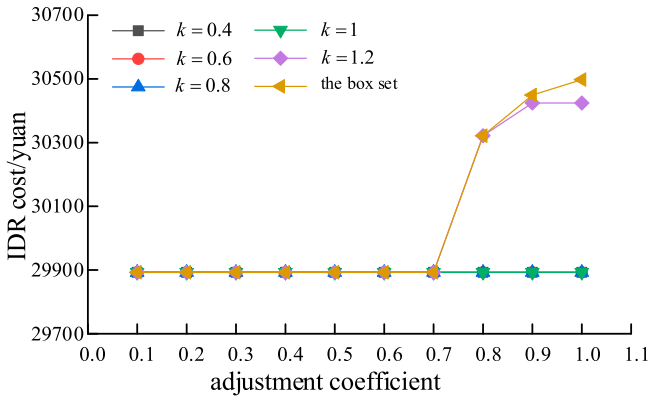

(d) Influence of the robust adjustment coefficient β on IDR costs

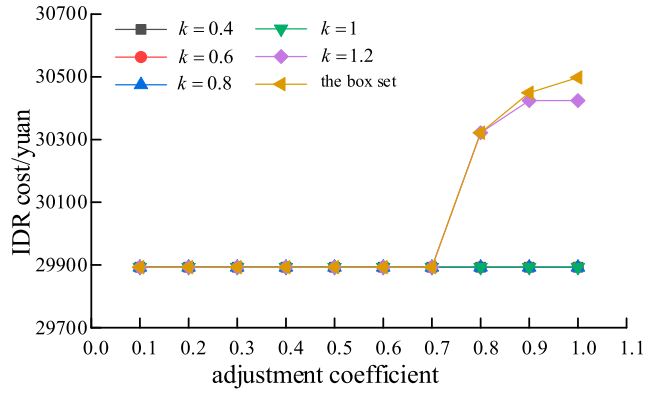

(e) Influence of the robust adjustment coefficient β on total costs

FIGURE 7
(Continued). Influence of robust adjustment coefficient β on each cost. **(a)** Influence of robust adjustment coefficient β on O&M costs. **(b)** Influence of the robust adjustment coefficient β on the cost of purchased energy. **(c)** Influence of the robust adjustment coefficient β on standby costs. **(d)** Influence of the robust adjustment coefficient β on IDR costs. **(e)** Influence of the robust adjustment coefficient β on total costs.

paper, this section cites a 24-h operation example of an industrial park in Hubei Province for verification. The equipment installed in the industrial park includes wind power, photovoltaic, gas boiler and waste heat boiler. Absorption chillers, gas turbines, electroliers, methane reactors, hydrogen storage tanks, hydrogen fuel cells, electric chillers, energy storage systems, etc. Among them, the wind power, photovoltaic prediction and load size of the system are shown in Figure 6. The operating parameters of each device are shown in. The operating parameters of each device are shown in Schedule A1. According to the calculation method given in (Hamed and Rasoul, 2021), the value k_{min} here is 1.22.

6.2 Result analysis and verification

6.2.1 The influence of scaling factor k on the optimization results

The impact of the scaling factor on the robust optimization of the industrial park microgrid is shown in Table 2. The size of the scaling factor determines the extent to which the constructed convex hull set covers historical data. As seen from Table 2, with the increase of the scaling factor, the system's operational cost gradually decreases, while the energy purchase cost continues to increase. This is because the increase in the scaling factor expands the envelope range of the convex hull uncertainty set over the historical output data, meaning that the fluctuation range of renewable energy output becomes larger, making the worst-case scenario more likely to occur. When volatile renewable energies such as distributed photovoltaics and wind power continuously inject into the distribution network, in order to maintain supply-demand balance and reduce disturbances caused by the injection of uncertain energy, the system needs to filter out a large portion of the power injected by distributed photovoltaics and wind power. This leads to a reduction in the maintenance cost of photovoltaic and wind power equipment, and as a result, the overall operational cost decreases. Meanwhile, since the injection of distributed energy is reduced, more injection power from the grid is needed to meet the system's electricity supply, thereby gradually increasing the energy purchase cost. Reserve cost refers to the margin cost incurred to account for the system's response to possible

random events and depends on the system's contingency plan for the worst-case scenario. Therefore, regardless of changes in the scaling factor, the reserve cost shows little variation. Similar to the reserve cost, the IDR (Interruptible Demand Response) cost is an added cost to enhance the system's stability margin. When the scaling factor is less than or equal to 1, the convex hull set does not envelop the extreme worst-case conditions, and thus the IDR cost remains unchanged. However, when the scaling factor exceeds 1, the convex hull set covers all possible scenarios, including the worst-case scenario. To improve the overall efficiency of the system, users need to appropriately shed load, which results in an increase in IDR cost.

6.2.2 The influence of robust adjustment coefficient β on the optimization results

Figure 7 demonstrates the influence of the robust adjustment coefficient β on the results of the robust optimization of the industrial park microgrid. From the figure, it can be seen that as the robust adjustment coefficient increases, each of the costs changes more or less, except for the standby cost, which is unaffected by system changes, which stays constant at $8640. When the robust adjustment coefficient of the system is small, the uncertain energy injected into the system at this time will be approximated as deterministic energy, the various equipment of the system will operate stably, and the photovoltaic and wind power equipment of the system will operate at full efficiency, so the operation and maintenance cost is the largest, and at the same time, due to the injection of the deterministic energy, the system purchased energy from the port decreases, so the system's purchased energy cost is the smallest, and with the increase in the robust adjustment coefficient, this uncertainty energy injection will rise and the amount of energy purchased by the system from the port will keep on rising, which in turn leads to the rise of the system's energy purchase cost and the decrease of the O&M cost. For the IDR cost, when $\beta \leq 0.7$, the envelope always fails to cover the extreme conditions for both the boxed set and the convex packet set with different deflation multiples, so the IDR cost always stays the same; while when β is large, at this time, when the deflation multiples $k = k_{min}$, the convex packet set will completely envelope the worst case when the deflation multiples are large, which will increase the IDR cost at this time, but due to the fact that the boxed set can not accurately envelope the distribution of the uncertain parameters, resulting in the blank area of the envelope. Region, resulting in more blank regions in the envelope, so the boxed set corresponds to the largest IDR cost compared to the convex packet set.

As the robust adjustment coefficient increases, the magnitude of the change in the cost of purchased energy and O&M cost will remain stable when the convex packet ensemble is used, specifically, when the deflation multiplier increases from 0.4 to 1.2, the magnitude of the change in the cost of purchased energy and O&M cost will be stabilized at the time when the robust adjustment coefficient is equal to 0.3, 0.4, 0.6, 0.7, and 0.8, which is related to the renewable energy equipment's power output situation. When β is small, the system is poorly adapted to the renewable energy perturbation and the cost does not change much no matter what

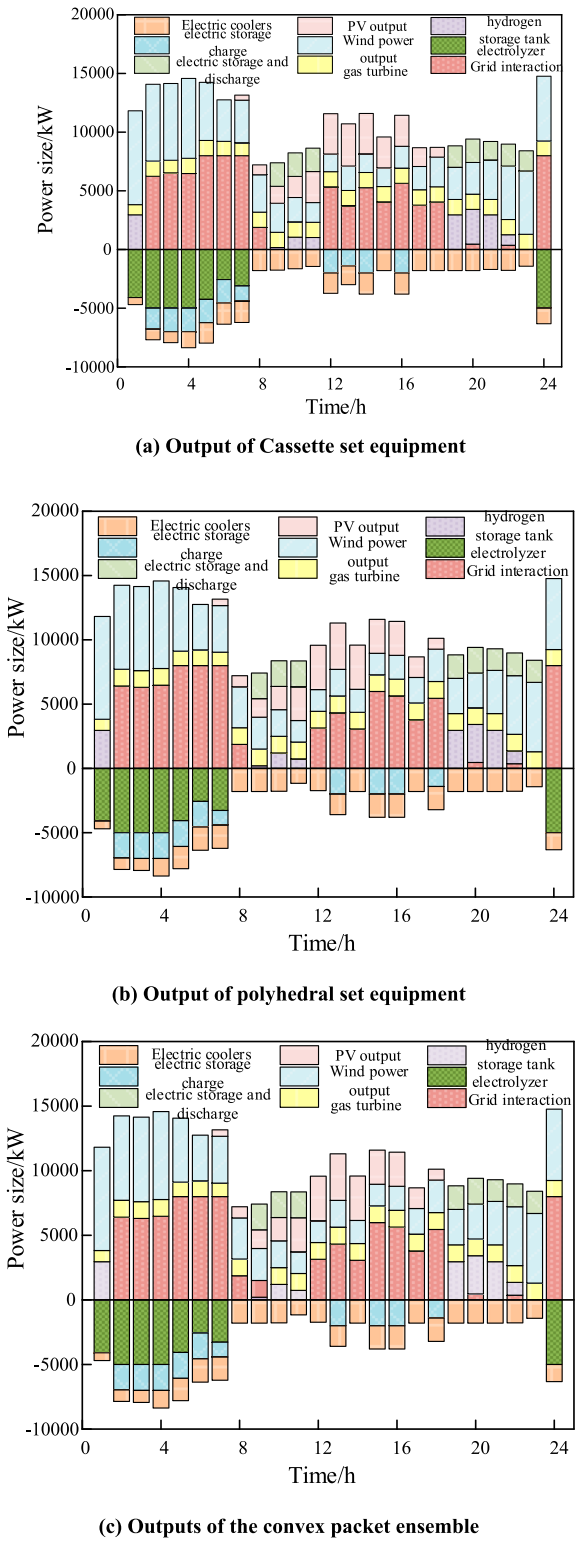

(a) Output of Cassette set equipment

(b) Output of polyhedral set equipment

(c) Outputs of the convex packet ensemble

FIGURE 8
Output of each device under three aggregations. **(a)** Output of Cassette set equipment. **(b)** Output of polyhedral set equipment. **(c)** Outputs of the convex packet ensemble.

TABLE 4 Comparative analysis of optimization methods.

Comparison item	Scheduling cycle: 24 h		Scheduling cycle: 72 h	
	Convex hull set	Scenario-based stochastic optimization	Convex hull set	Scenario-based stochastic optimization
Scheduling time/s	25	65	42	97

kind of ensemble is used, on the contrary, when β is large, the system is better adapted to the distributed PV perturbation. However, when the convex packet ensemble is used, the envelope range of the convex packet ensemble is different due to different deflation multiples. When the deflation multiplier $k = 0.4$, the envelope range of the convex packet ensemble is also smaller. In this case, changing the size of the robust regulation coefficient β will not significantly affect the renewable energy output size, so the effect of changing β to a certain extent on the renewable energy output will be minimal. However, when the deflation facto $k = k_{\min}$, the convex packet uncertainty set will encompass all the historical data, so it will be adjusted accordingly to the increase of the robust regulation coefficient β, which will affect the size of the renewable energy output. Since the purchased energy cost of the system accounts for a large proportion of the total cost, the trend of the total cost of the system is similar to that of the purchased energy cost.

6.2.3 The influence of the three aggregations on individual costs

The effects of the three uncertainty sets on each cost are further compared when the deflation multiplier $k = k_{\min}$, the robust adjustment coefficient $\beta = 1$, and the uncertainty $\Gamma = 0.9$ are used, as shown in Table 3. From Table 3, it can be seen that when different sets are used, the total cost of using the convex packet set is lower than that of the box set and the polyhedral set, except that the standby cost remains basically the same. This is due to the fact that when there is spatio-temporal correlation of the uncertain parameters, the convex packet ensemble can change the envelope range of the convex packet ensemble by deflation to make it fit the distribution region of the uncertain parameters better, which enhances the robustness of the system and reduces the conservatism. On the other hand, the polyhedral set changes the envelope of the polyhedral set by changing the uncertainty, and in order to encompass the historical data of all renewable energy outputs, the polyhedral set needs to increase the uncertainty, which enables the expansion of the envelope of the polyhedral set in an untargeted manner, although this enhances the robustness of the solution results, but over-expansion for the sake of a few scenarios of the data increases the conservatism of the solution instead. The boxed ensemble, on the other hand, is a preliminary characterization of the uncertain parameter distribution range, and therefore the conservativeness and robustness of the solution results are the worst.

6.2.4 Output of each device in three pools

Figure 8 gives the output of each device at the electric power balance under the three uncertainty sets. From the figure, it can be seen that in the multi-energy complementary microgrid system, the individual devices coordinate with each other and work together to maintain the electric power balance. In the PV big hairy time period (12–16 h), the system purchases the lowest electric power from the ports, the polyhedral ensemble is the second, and the box ensemble is the most when the convex packet ensemble is used, which is the same as the conclusion obtained in the previous paper, and further verifies that the use of the convex packet ensemble enhances the robustness of the solution results and reduces the conservatism.

6.2.5 Computational efficiency analysis

To verify the computational efficiency of the convex hull uncertainty set, we supplemented simulation analyses comparing the convex hull set method with scenario-based stochastic optimization in the revised manuscript. The comparative results are shown in the table below.

As shown in Table 4, when handling problems of the same scale, the convex hull set method proposed in this paper exhibits significant computational efficiency advantages over scenario-based stochastic optimization. Even as the problem scale increases, the convex hull set method still outperforms scenario-based stochastic optimization in computational efficiency.

7 Conclusion

In this paper, a research model of the industrial park microgrids robust optimization method based on data-driven is constructed and solved by C&CG algorithm. Finally, by comparing the industrial park microgrids robust optimization methods under different sets, the simulation results show that:

1. Compared with the interval set which can only take extreme conditions at the boundary, the polyhedron set has a better envelope for the range of uncertain parameters, which makes the operation result more robust.
2. When the robust adjustment coefficient is the same, the total system cost of using the convex hull set is 0.71% lower than that of the box set and 0.53% lower than that of the polyhedron set. For the convex hull set with different scaling multiples, this not only increases the envelope of the region with higher distribution of uncertain parameters, but also reduces the envelope of the blank region with low probability. Therefore, compared with the polyhedral set, the industrial park microgrids robust optimization method using the convex hull set is less conservative and more robust.

In the future, we will explore the comparative analysis between convex hull sets and advanced data-driven methods such as distributionally robust optimization and machine learning-based uncertainty sets, with a view to providing more comprehensive

and forward-looking research results for the field of multi-energy microgrid optimization.

Data availability statement

The original contributions presented in the study are included in the article/Supplementary Material, further inquiries can be directed to the corresponding author.

Author contributions

CR: Investigation, Methodology, Writing – original draft. LL: Investigation, Methodology, Writing – original draft. JL: Validation, Writing – review and editing. BJ: Validation, Writing – review and editing.

Funding

The author(s) declare that financial support was received for the research and/or publication of this article. This work is supported by Science and Technology Project of State Grid Zhejiang Electric Power Co., Ltd. (No. 5211TZ230002).

Conflict of interest

Authors CR, JL, and BJ were employed by State Grid TaiZhou Power Supply Company.

Author LL was employed by State Grid ZheJiang Electric Power Corporation.

The authors declare that this study received funding from State Grid Zhejiang Electric Power Co. The funder participated in the research design phase. During this phase, combining the actual operation requirements of industrial park microgrids, it put forward relevant suggestions on the research direction (e.g., the industrial load characteristics that need to be focused on in microgrid robust optimization) and the practicality of the technical framework.

Generative AI statement

The author(s) declare that no Generative AI was used in the creation of this manuscript.

Any alternative text (alt text) provided alongside figures in this article has been generated by Frontiers with the support of artificial intelligence and reasonable efforts have been made to ensure accuracy, including review by the authors wherever possible. If you identify any issues, please contact us.

Publisher's note

Supplementary Material

The Supplementary Material for this article can be found online at: https://www.frontiersin.org/articles/10.3389/fenrg.2025.1535211/full#supplementary-material

References

Akter, K., Rahman, M., Islam, R. M., Sheikh, M. R. I., and Hossain, M. (2025). Attack-resilient framework for wind power forecasting against civil and adversarial attacks. *Electr. Power Syst. Res.* 238, 238111065–111065. doi:10.1016/j.epsr.2024.111065

Aliasghar, B., Baseem, K., and Navid, P. (2022). Guest editorial: introduction to the special section on application of advanced machine/deep learning in electrical power and energy systems (VSI-mlep). *Comput. Electr. Eng.*, 102. doi:10.1016/j.compeleceng.2022.108245

Arooj, Q. (2024). FedWindT: Federated learning assisted transformer architecture for collaborative and secure wind power forecasting in diverse conditions. *Energy* 309, 133072–133072. doi:10.1016/j.energy.2024.133072

Ayene, M. S., and Yibre, M. A. (2024). Wind power prediction based on deep learning models: the case of adama wind farm. *Heliyon* 10 (21), e39579. doi:10.1016/j.heliyon.2024.e39579

Bifei, T., Haoyong, C., and Xiaodong, Z. (2022). Two-stage robust optimization dispatch for multiple microgrids with electric vehicle loads based on a novel data-driven uncertainty set. *Int. J. Electr. Power Energy Syst.*, 134. doi:10.1016/j.ijepes.2021.107359

Davidsdottir, B., Ásgeirsson, I. E., Fazeli, R., Gunnarsdottir, I., Leaver, J., Shafiei, E., et al. (2024). Integrated energy systems modeling with multi-criteria decision analysis and stakeholder engagement for identifying a sustainable energy transition. *Energies* 17 (17), 4266. doi:10.3390/en17174266

Degefa, M., Lehtonen, M., Millar, R., Alahäivälä, A., and Saarijärvi, E. (2015). Optimal voltage control strategies for day-ahead active distribution network operation. *Electr. Power Syst. Res.* 127, 12741–12752. doi:10.1016/j.epsr.2015.05.018

Farh, H. M. H., Shamma'a, A. A. A., Alaql, F., Omotoso, H. O., Alfraidi, W., and Mohamed, M. A. (2024). Optimization and uncertainty analysis of hybrid energy systems using monte carlo simulation integrated with genetic algorithm. *Comput. Electr. Eng.* 120 (PC), 109833. doi:10.1016/j.compeleceng.2024.109833

Freitas, W., Asada, N. E., Zobaa, F. A., and McConnach, J. S. (2007). Policy and economic issues of electrical power and energy systems. *Int. J. Glob. Energy Issues* 27 (3), 253–261. doi:10.1504/ijgei.2007.014347

Hamed, D., and Rasoul, S. (2021). A new correlated polyhedral uncertainty set for robust optimization. *Comput. Industrial Eng.*, 157. doi:10.1016/j.cie.2021.107346

Ibraheemi, A. Z., and Janabi, A. S. (2024). Sustainable energy: advancing wind power forecasting with grey wolf optimization and GRU models. *Results Eng.* 24, 102930–102930. doi:10.1016/j.rineng.2024.102930

Ishaq, M., and Dincer, I. (2024). Development of a novel renewable energy-based integrated system coupling biomass and H2S sources for clean hydrogen production. *Renew. Energy* 237 (PC), 121642. doi:10.1016/j.renene.2024.121642

Jalilvand-Nejad, A., Shafaei, R., and Shahriari, H. (2016). Robust optimization under correlated polyhedral uncertainty set. *Comput. Industrial Eng.*, 92. doi:10.1016/j.cie.2015.12.006

Lorca, A., and Sun, X. A. (2015). Adaptive robust optimization with dynamic uncertainty sets for multi-period economic dispatch under significant wind. *IEEE Trans. Power Systems: A Publ. Power Eng. Soc.* 30 (4), 1702–1713. doi:10.1109/tpwrs.2014.2357714

Michos, D., Catthoor, F., Foussekis, D., and Kazantzidis, A. (2024). Ultra-short-term wind power forecasting in complex terrain: a physics-based approach. *Energies* 17 (21), 5493. doi:10.3390/en17215493

Moradian, S., Gharbia, S., and Nezhad, M. M. (2024). Enhancing the accuracy of wind power projections under climate change using geospatial machine learning models. *Energy Rep.*, 123353–123363. doi:10.1016/j.egyr.2024.09.007

Nayak, K. A., Sharma, C. K., Bhakar, R., and Tiwari, H. (2025). Probabilistic online learning framework for short-term wind power forecasting using ensemble bagging regression model. *Energy Convers. Manag.* 323 (PA), 119142. doi:10.1016/j.enconman.2024.119142

Poodeh, S. M., Hooshmand, A. R., and Khah, S. M. (2025). Reliability-constrained configuration optimization for integrated power and natural gas energy systems: a stochastic approach. *Reliab. Eng. Syst. Saf.* 254, 110600. doi:10.1016/j.ress.2024.110600

Rahman, J., Jacob, A. R., and Zhang, J. (2025). Multi-timescale power system operations for electrolytic hydrogen generation in integrated nuclear-renewable energy systems. *Appl. Energy* 377 (PA), 124346. doi:10.1016/j.apenergy.2024.124346

Rezazadeh, A. A., and Avami, A. (2024). An integrated policy approach for sustainable decarbonization pathways of energy system in a city under climate change scenarios. *Energy Policy* 195, 114394. doi:10.1016/j.enpol.2024.114394

Son, G. Y., and Kim, Y. S. (2024). Optimal planning and operation of integrated energy systems in South Korea: introducing a novel ambiguity set based distributionally robust optimization. *Energy* 307, 132503. doi:10.1016/j.energy.2024.132503

Stewart, P., and Bingham, C. (2016). Electrical power and energy systems for transportation applications. *Energies* 9 (7), 545. doi:10.3390/en9070545

Sulaiman, H. M., Mustaffa, Z., Saari, M. M., and Abas, M. F. (2024). Wind power forecasting with metaheuristic-based feature selection and neural networks. *Clean. Energy Syst.* 9, 100149. doi:10.1016/j.cles.2024.100149

Vulusala, V. S., and Madichetty, S. (2018). Application of superconducting magnetic energy storage in electrical power and energy systems: a review. *Int. J. Energy Res.* 42 (2), 358–368. doi:10.1002/er.3773

Zhang, Q., Bu, F., Guo, Y., and Wang, Z. (2024a). Tractable data enriched distributionally robust chance-constrained conservation voltage reduction. *IEEE Trans. Power Syst.* 39 (1), 821–835. doi:10.1109/tpwrs.2023.3244895

Zhang, Q., Liu, Y. S., Gao, H., and You, F. (2024b). A data-aided robust approach for bottleneck identification in power transmission grids for achieving transportation electrification ambition: a case study in New York state. *Adv. Appl. Energy* 14, 100173. doi:10.1016/j.adapen.2024.100173

Frontiers in
Energy Research

Advances and innovation in sustainable, reliable and affordable energy

Explores sustainable and environmental developments in energy. It focuses on technological advances supporting Sustainable Development Goal 7: access to affordable, reliable, sustainable and modern energy for all.

Discover the latest Research Topics

See more →

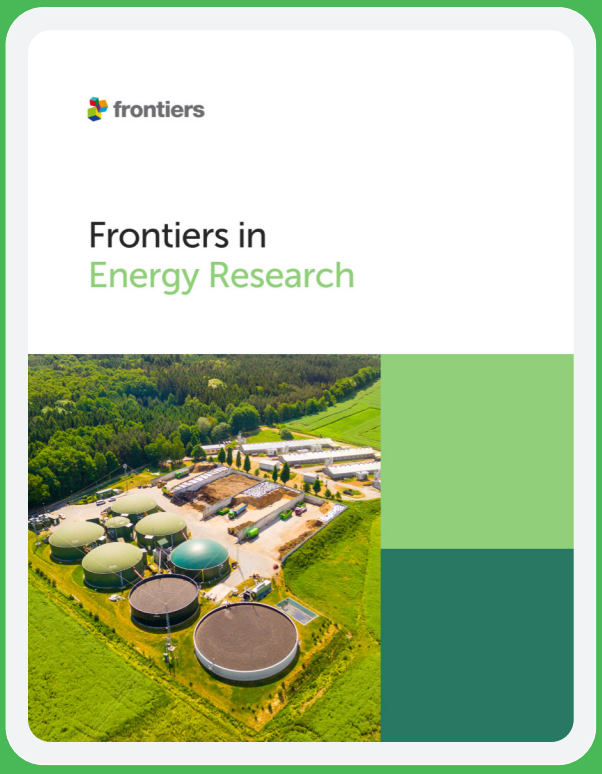

Frontiers

Avenue du Tribunal-Fédéral 34
1005 Lausanne, Switzerland
frontiersin.org

Contact us

+41 (0)21 510 17 00
frontiersin.org/about/contact